Preparation and Characterization of Novel Palladacycles and their Evaluation as Anticancer Agents

by
Angelique Blanckenberg

Dissertation presented for the degree of Doctor of Chemistry in the Faculty of Science at Stellenbosch University

Promoter: Prof. Selwyn Frank Mapolie

December 2016

Declaration

By submitting this thesis/dissertation electronically, I declare that the entirety of the work contained therein is my own, original work, that I am the sole author thereof (save to the extent explicitly otherwise stated), that reproduction and publication thereof by Stellenbosch University will not infringe any third party rights and that I have not previously in its entirety or in part submitted it for obtaining any qualification.

December 2016

Dedication

This thesis is dedicated in memory of my grandfather, Edwin Enoch Owen Virét, who lost his battle against cancer on 24 August 2013.

Abstract

Mononuclear and binuclear (unsubstituted and substituted) palladacycles based on benzylidene-2,6-diisopropylphenylamine, were designed and synthesised for evaluation as anti-cancer agents. The design of these complexes was based on the structure and properties of **AJ5**, a binuclear palladacycle with significant anti-cancer activity, but poor solubility. In an attempt to improve water solubility the Schiff base ligands, employed to prepare the palladacycles, were modified by introducing hydrophilic functional groups on the aldehyde starting material. Furthermore, the μ-chloro bridged palladacycles were cleaved with either the hydrophilic tertiary phosphine, 1,3,5-triaza-7-phosphaadamantane (PTA), or bis(tertiary phosphine) ligands as a further attempt at improving the water-solubility, whilst maintaining the anti-cancer activity. The synthesised complexes were fully characterised by a range of analytical techniques. The solubilities of the palladacycles were determined in water, dimethyl sulfoxide and water/dimethyl sulfoxide mixtures. None of the complexes were entirely water-soluble, however, the substituted binuclear palladacycles were found to show the highest solubility in dimethyl sulfoxide, with some analogues exhibiting improved solubility, compared to **AJ5**.

NMR spectra of the mononuclear palladacycles showed that these PTA-cleaved, mononuclear palladacycles exhibit fluxional behaviour, especially with regard to the isopropyl substituents on the imine ligand. This fluxionality manifests itself as varying degrees of resolution of the isopropyl signals in the proton NMR spectroscopy, leading to this signal having different shapes depending on the nature of the imine ligand. The variety of peak shapes observed for the methyl signals of the isopropyl groups were thought to be due to a reversible symmetric site-exchange and fortunately this could be simulated by way of a computational model developed in-house. The free energy of activation ($\Delta G^{\#}$) and other thermodynamic parameters for the site-exchange process were calculated and found to correspond with aryl ring rotation. Slight deviations in the expected chemical shifts were attributed to concentration-dependent chemical exchange processes. Both molecular aggregation via PTA self-association and dimerisation by imine dissociation were proposed and shown to be plausible. Furthermore, we were able to show that the “ortho effect” accounts for the influence of the ortho-substituents on the free energy of activation. We were also able to attribute the ability for these species to undergo the proposed chemical exchange processes to the phosphorous ligand, PTA, specifically its small cone angle and nitrogen donor atoms.

In vitro evaluation of the mono- and binuclear palladacycles was performed to determine their biological activity as anti-cancer agents against human breast adenocarcinoma MCF7 (estrogen receptor positive) and MDA-MB231 (estrogen receptor negative) cell lines. These studies show that most of the complexes are cytotoxic, with the binuclear palladacycles showing better activity than the mononuclear palladacycles. IC_{50} values of some of the palladacycles were better than those of cisplatin (below 20 μM) and the IC_{50} values for the substituted-binuclear palladacycle, **BTC2**, were found to be comparable to those of **AJ5**. The complexes were found to induce DNA damage and apoptosis. DNA binding studies were carried out on the most active palladacycle in each series to determine the mode of action. DNA binding studies by electrophoresis, ultraviolet-visible-, circular dichroism- and nuclear magnetic resonance spectroscopy suggest that the palladacycles bind to DNA non-covalently, by a mode different to that of cisplatin. The most likely mode of DNA binding was identified as an electrostatic binding mode. Thus, the formation of an aquated cationic species was proposed to form via hydrolysis of the Pd-Cl bond.

Opsomming

Monokernige en bikernige (ongesubstitueerde en gesubstitueerde) palladasikliese verbindings gebaseer op die bensilideen-2,6-diisopropielfenielamien ligand, is ontwerp en gesintetiseer vir evaluering as kankermiddels. Die ontwerp van hierdie komplekse is gebaseer op die struktuur en eienskappe van **AJ5**, 'n bikernige palladasikliese verbinding wat beduidende aktiewiteit as 'n kankermiddel toon, maar deur swak oplosbaarheid belemmer word. In 'n poging om die wateroplosbaarheid te verbeter is die Schiff-basis ligande, wat gebruik is in die voorbereiding van die palladasikliese verbindings, gemodifiseer deur die byvoeging van hidrofiliese funksionele groepe op die aldehied uitgangstof. Die μ-chloor oorbrugde palladasikliese verbindings is daarna gesplits deur die hidrofiliese tersiêre fosfien, 1,3,5-triasa-7-fosfaadamantaan (PTA), of bis(tersiêre fosfien) ligande, as 'n verdere poging om die wateroplosbaarheid te verbeter sonder om die biologiese aktiewiteit te belemmer. Die gesintetiseerde komplekse is volledig gekarakteriseer met 'n reeks analitiese tegnieke. Die oplosbaarheid van die gesplete palladasikliese verbindings is in water, dimetielsulfoksied en 'n mengsel van water/dimetielsulfoksied bepaal. Geeneen van die komplekse is in water oplosbaar nie, maar die gesubstitueerde, bikernige palladasikliese verbindings toon die hoogste oplosbaarheid in dimetielsulfoksied. 'n Paar van die bikernige palladasikliese verbindings toon ook beter oplosbaarheid as **AJ5**.

KMR spektra van die monokernige palladasikliese verbindings wys dat hierdie PTA-gesplete, monokernige palladasikliese verbindings fluksionele gedrag toon, veral ten opsigte van die isopropiel substituente op die imien ligand. Die fluksionele gedrag manifesteer as die mate waarin die resolusie van die isopropiel sein in die proton KMR voorkom. As gevolg hiervan word daar 'n reeks verskillende vorms vir hierdie seine, afhangend van die aard van die imien ligand, gevind. Die verskillende piekvorms wat waargeneem is vir die isopropiel metiel seine word geag om deur simmetriese plek uitruiling veroorsaak te word. Dit kan gelukkig deur middel van 'n interne teoretiese model gesimuleer word. Die aktiveringsenergie ($\Delta G^{\#}$) en ander termodinamiese parameters vir die plek verruiling is bereken en gevind om ooreen te stem met ariel ring rotasie. Effense afwykings vanaf die verwagte chemiese sein verskuiwing word aan konsentrasie-afhanklike chemise uitruiling prosesse toegeskryf. Beider molekulêre aggregasie deur self-assosiasie van PTA en dimerisasie deur imien dissociasie is voorgestel en gewys om haalbaar te wees. Daar is gevind dat die "orto effek" die invloed van die orto substituente op die aktiveringsenergie kon verklaar. Ons kon ook die vermoë van hierdie komplekse om die voorgestelde chemise uitruiling prosesse te ondergaan aan die fosfien ligand, PTA, toeskryf, spesifiek die klein keel hoek en die stikstof skenkeratome.

In vitro evaluering van die monokernige en bikernige palladasikliese verbindings is uitgevoer om hul biologiese aktiwiteit as kankermiddels teen menslike bors adenokarsinoom MCF7 (estrogeen reseptor positief) en MDA-MB231 (estrogeen reseptor negatief) sellyne te bepaal. Hierdie studies toon dat die meeste van die komplekse sitotoksies is en dat die bikernige palladasikliese verbindings better aktiewiteit toon as die monokernige palladasikliese verbindings. Die IC_{50} waardes van ‘n paar van die komplekse is beter as dié van cisplatin (onder 20 μM) en die IC_{50} waardes van die gesubstitueerde, bikernige palladasikliese verbinding, **BTC2**, was vergelykbaar met dié van **AJ5**. Daar is gevind dat die komplekse DNS dubbelstring breke en apoptose veroorsaak. DNS bindingstudies is uitgevoer op die mees aktiewe palladasikliese verbindings in elkeen van hierdie reekse, om die manier van interaksie te bepaal. DNS bindingstudies met behulp van elektroforese, ultraviolet-sig-, sirkulêredichroïsme-, kern magnetise resonansie spektroskopie dui daarop dat die palladasikliese verbindings DNS op ‘n nie-kovalente wyse bind, deur ‘n manier anders as dié van cisplatin. Die mees waarskynlikste manier van DNS verbind is geidentifiseer as ‘n elektrostatiese binding wyse. Dus was die formasie van ‘n kationiese spesies voorgestel wat vorm deur die hidroliese van die Pd-Cl binding.

Acknowledgements

Firstly, to my supervisor, Prof. Mapolie, thank you for your patient guidance and the invaluable knowledge that you have imparted to me throughout my studies.

Secondly, to Prof. Prince, Dr. Aliwaini and the rest of the Tbox laboratory at the UCT Medical School, thank you for your assistance and contributions in the *in vitro* testing of the complexes.

To Dr. Gerber and his students, a big thank you for your assistance with the kinetic calculations and modelling for the NMR spectroscopy study.

To the students of the organometallic group, Stellenbosch University, from 2011 to 2015, thank you for your inputs and guidance, especially for the great atmosphere in and around the laboratory.

I would also like to thank Dr. Brand and Elsa Malherbe for their assistance with NMR- and CD spectroscopy, Dr. Smith, Prof. Haynes and Prof. Guzei for the solving of crystal structures and assistance with the interpretation of single crystal X-ray diffraction data, Trudy Jansen and Peta Steyn for their assistance and guidance with the gel electrophoresis, the Central Analytical Facility for their services, the staff and technical assistants of the Department of Chemistry and Polymer Science for their assistance in the completion of this project.

The financial assistance of the National Research Foundation (NRF) towards this research is hereby acknowledged. Opinions expressed and conclusions arrived at, are those of the author and are not necessarily to be attributed to the NRF.

Thank you to the Medical Research Council (MRC) and Stellenbosch University, for providing further financial support for this project.

Finally, to my husband and my family, a special word of thanks for always supporting and encouraging me.

Conference Contributions and Publications

Angelique Blanckenberg

Oral presentation: ***Development of novel palladacycles for testing as anti-cancer agents***. Western Cape Organometallic Mini-Symposium, Cape Town, South Africa, 2013.

Angelique Blanckenberg and Selwyn Mapolie

Poster presentation: ***Development of novel palladacycles for in-vitro testing as anti-cancer agents***. South African Chemical Institute (SACI) Inorganic Chemistry Conference (INORG2013), Durban, South Africa, 2013.

Saeb Aliwaini, Andrew J. Swarts, Angelique Blanckenberg, Selwyn Mapolie and Sharon Prince

Journal article: ***A novel binuclear palladacycle complex inhibits melanoma growth in vitro and in vivo through apoptosis and autophagy***. Biochemical Pharmacology, 2013, 86, 1650-1663.

Angelique Blanckenberg

Oral presentation: ***Development of novel palladacycles for testing as anti-cancer agents***. American Chemical Society (ACS) Fall Meeting, San Francisco, California, 2014.

Saeb Aliwaini, Jade Peres, Wendy L. Kröger, Angelique Blanckenberg, Jo de la Mare, Adrienne L. Edkins, Selwyn Mapolie and Sharon Prince.

Journal article: ***The palladacycle, AJ-5, exhibits anti-tumour and anti-cancer stem cell activity in breast cancer cells***. Cancer letters, 2014, 357, 206-218.

Angelique Blanckenberg and Selwyn Mapolie

Oral and Poster presentation: ***Development of novel palladacycles for testing as anti-cancer agents***. South African Chemical Institute (SACI) Inorganic Chemistry Conference (INORG2015), Grahamstown, South Africa, 2015.

Table of Contents

List of Figures

List of Schemes

List of Equations

List of Tables

List of Abbreviations

ADF	Amsterdam density functional
AIDS	Acquired Immune Deficiency Syndrome
AIL	Atomic interaction line
APL	Acute Promyelocytic Leukemia
asn	asparagine
ATR	Attenuated Total Reflectance
BCP	bond critical point
bipy	bipyridine
C_{Ar}	aromatic carbon
CD	circular dichroism
CNpy	4-cyanopyridine
CSD	Crystal Structure Database
cyclohex	cyclohexylamine
cyclopent	cyclopentadiene
DACH	1,2-diaminocyclohexane
DCM	dichloromethane
DFT	density functional theory
DMEM	Dulbecco's Modified Eagle's Medium
DMSO	dimethyl sulfoxide
DNA	deoxyribonucleic acid
dppe	1,2-bis(diphenylphosphino)ethane
DTP	Developmental Therapeutics Program
ECL	enhanced chemiluminescence
EDA	energy decomposition analysis
en	ethylenediamine
ESI-MS	Electrospray Ionisation Mass Spectroscopy
FBS	fetal bovine serum
FDA	Food and Drug Administration
FT-IR	Fourier Transform-Infra Red
GSH	glutathione
IARC	International Agency on Cancer

IC_{50}	half maximal inhibitory concentration
ICD	induced circular dichroism
IdMOC	independent discrete multiple organ coculture
Ind	indazole
Im	imidazole
^{i}Pr	isopropyl
ITC	isothermal calorimetry
KD	kilodalton
mal	malonate
Me	methyl
MeCN	acetonitrile
m.p.	melting point
MTT	3-(4,5-dimethylthiazol-2-yl)-2,5-diphenyltetrazolium bromide
N7	number 7 nitrogen atom in guanine nucleoside base
NCI	National Cancer Institute
NCI-analysis	non-covalent interaction analysis
NMR	Nuclear Magnetic Resonance
NSCLC	non-small cell lung cancer
OMe	methoxy
Ox	oxalate
PDT	photodynamic therapy
Ph	phenyl
pKa	acid dissociation constant
ppm	parts per million
PTA	1,3,5-triaza-7-phosphaadamantane
QTAIM	quantum theory of atoms in molecules
RAPTA	ruthenium/arene/PTA
ROS	reactive oxygen species
RPMI	Roswell Park memorial Institute
sac	saccharinate
TB	tuberculosis
terpy	2,2':6',2"-terpyridine
TMS	tetramethyl silane

Chapter 1
Palladium and its complexes as potential anti-cancer agents

1.1 Introduction

The first record of cancer can be found in a copy of an ancient Egyptian textbook on trauma surgery, viz. the Edwin Smith Papyrus, dating back to approximately 3000 BC. Eight cases of tumours or ulcers of the breast were recorded in this textbook. According to the text, the tumours were removed by cauterisation and it states that there is no treatment for the disease [1]. In 2012, the GLOBOCAN project estimated that there were 14.1 million new cases of cancer worldwide, 32.6 million people living with cancer and 8.2 million cancer related deaths, which amounts to approximately 22 thousand deaths a day [2]. This is a significant increase from the 12.7 million new cancer cases, reported in 2008. Five centuries since its discovery, cancer is responsible for one in eight deaths. Worldwide, it causes more deaths than AIDS, TB and malaria combined [3].

Cancer is defined as a “group of diseases characterised by uncontrolled growth and spread of abnormal cells” [3]. The causes of cancer are numerous and can be classified into two groups, external- and internal factors. External factors, known as carcinogens, include: chemicals (tobacco smoke is the most well-known respiratory carcinogen [4]), radiation and viruses, whilst internal factors include: inherited genetic mutations, hormones and immune conditions. Most types of cancer develop over a long period of time and are the result of multiple factors. All types of cancer involve the mutation of the genes which control cell growth, -division and -death [1;3]. Generally, however, the risk of developing cancer increases with age and exposure to carcinogens. Treatments range from surgery, radiation and chemotherapy to hormone and immunotherapy [1;3].

Oncology is the study of cancer which includes the fields of anatomy, physiology, epidemiology and chemistry. It is one of the most rapidly evolving areas of modern medicine, as is evident from the 15% decrease in mortality due to cancer since the 1990’s [1].

This review will focus on the latter field, viz. chemistry, more specifically the use of palladium-based chemical compounds as chemotherapeutic agents.

1.1.1 Transition metals as anti-cancer agents

The term chemotherapy was defined by Paul Ehrlich, when he used it to describe the use of chemicals to treat a disease; however, it was not until the late 1960's that curing cancer with drugs was even considered to be possible [5]. Traditionally, chemotherapeutic agents were organic molecules, as inorganic metal-based compounds were known to be carcinogenic [6]. Nevertheless, Paracelsus, the founder of the field of toxicology, quoted the following: "Dosis facit venenum". Translated, it means that the dose makes the poison. He theorised that harmful or poisonous materials in small doses could be beneficial [7;8]. Despite his theory, research in the field of inorganic and organometallic compounds as anti-cancer agents only gained interest after the discovery of cisplatin, the first platinum-containing anti-cancer agent.

1.1.1.1 Cisplatin and platinum anti-cancer drugs

In 1969, Rosenberg and co-workers discovered the potential anti-cancer properties of cisplatin (*cis*-$[Pt(NH_3)_2Cl_2]$) during a study to determine the effects of electrical current on the cell division of *E.coli*. It was noted that cell division was inhibited, but that cell growth was not, resulting in long filamentous cells instead of rods (Figure 1.1). This type of cell division inhibition is a sought after property in anti-cancer agents. Further investigation showed that the observed inhibition was not due to the electrical current, but rather due to platinum from the electrodes which was forming $[PtCl_6]^-$ by platinum hydrolysis. This led to testing of other platinum complexes for similar properties. The complexes were tested in mice with sarcoma 180. It was found that cisplatin (Figure 1.2) was the most effective of the complexes, resulting in complete inhibition of the development of a solid tumour [9].

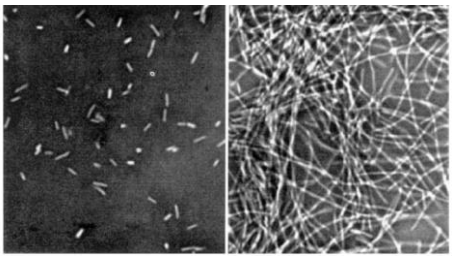

Figure 1.1: Normal rod-shaped *E.coli* (left) and filamentous *E.coli* (right) [9].

Following Rosenberg's work, testing was continued at the United States National Cancer Institute where cisplatin entered clinical trials. In 1971, the first patient was treated. Cisplatin has since been used to treat various cancers, including head and neck, ovarian and testis cancer, with a large number of patients being completely cured after treatment. Currently, it is one of the most successful anti-cancer drugs on the market. The discovery and success of cisplatin led to increased interest in the use of metal compounds to treat cancer [10-13].

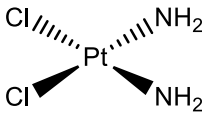

Figure 1.2: Chemical structure of cisplatin.

Despite the increase in research in the field of platinum-based anti-cancer agents and the thousands of compounds being synthesised and evaluated as anti-cancer agents every year, only a limited number of platinum complexes have entered clinical trials and been approved for clinical use. The main problems with these new platinum compounds were severe toxicity, limited application and drug-resistance. This lack of advancement, coupled with limited application of the approved drugs due to toxicity, led to the ongoing search for new anti-cancer agents with increased specificity, reduced toxicity and the ability to overcome resistance [14].

1.1.1.2 Alternative transition metal anti-cancer drugs

Over the years, many different transition metals have been tested as anti-cancer agents, including vanadium, iron, copper, ruthenium, palladium, silver and gold [14;15].

Among the more promising transition metal-based drugs are those of ruthenium, specifically, the ruthenium/arene/PTA or RAPTA (where PTA is 1,3,5-triaza-7-phosphaadamantane) complexes (Figure 1.3). Essentially, these complexes consist of an arene-capped ruthenium (II) centre and contain the water-soluble phosphine ligand, PTA.

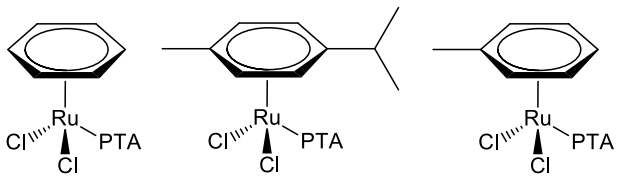

Figure 1.3: RAPTA complexes.

First discovered by Dyson *et al.*, these structures present an ideal scaffold for rational drug design [16]. Not only do they exhibit favourable pharmacokinetic properties, but their pharmacological properties are promising, as well [17]. As with many ruthenium complexes, the RAPTA complexes have a pH dependant mechanism which makes them highly selective for cancer cells *in vitro* and well tolerated *in vivo*. Despite having lower cytotoxicity than platinum-based drugs, the overall lower toxicity and controllable chemistry of these ruthenium complexes makes them very good candidates for clinical evaluation [18].

Another metal, notorious for its toxicity, yet surprising with respect to its therapeutic capability, is arsenic. The arsenic complex, arsenic trioxide (A_2O_3), was first reported to have anti-leukemic properties in the 1800's (Figure 1.4), whilst orally administered potassium arsenite (K_3AsO_3) was used in the 1950's to treat chronic myelogenous leukaemia. Both drugs were later discarded in favour of more modern treatments.

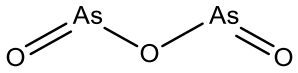

Figure 1.4: Chemical structure of arsenic trioxide.

However, recently arsenic compounds have resurfaced in medicinal applications, driven by the discovery of the efficacy of arsenic trioxide against acute promyelocytic leukaemia (APL). In 2000, the Food and Drug Administration (FDA) approved arsenic trioxide for the treatment of relapsed and refractory APL [19;20] by intravenous administration. By 2003, a group at the University of Hong Kong reported the redevelopment of an oral preparation of arsenic trioxide, as an alternative to the current intravenous administration. Preliminary studies with the orally active drug showed results comparable to those of the intravenously administered form [20].

In contrast to the examples given above, research into palladium-based complexes has been rather disappointing in terms of progress beyond the laboratory. Based on the similarities in the physical and chemical properties of platinum and palladium and the proven near identical coordination chemistry of the Pd^{2+} and Pt^{2+} oxidation states, there is some degree of expectation for analogous complexes to have comparable properties. Aside from the early studies of palladium complexes, which proved rather insignificant with regards to anti-cancer activity, there are several examples of palladium(II) complexes with significantly lower toxicity than their platinum(II) counterparts and comparable activity throughout the literature. Recently, an example of a palladium complex with 10-fold higher activity than cisplatin was reported by ourselves [21;22]. Despite some promising results, there has been little to no progress beyond laboratory evaluation of these palladium complexes. To date, there are only a few photodynamic therapy palladium-based drugs in clinical trials [23].

1.1.2 (A closer look at) Palladium

Although palladium is best known for its use as catalysts for a range of organic transformations, it has been shown to have promising biological activity. Radioactive palladium and palladium complexes with chlorophyll-type ligands have been successfully employed as brachytherapy- and photodynamic therapy agents against cancer, respectively [24].

Brachytherapy was discovered soon after the discovery of X-rays in 1895. It was Pierre Curie, who proposed that a small tube of radioactive radium be inserted directly into a tumour, thus inventing the term “brachytherapy” [25]. By the early 1970s, brachytherapy had been proven to be successful in increasing the life expectancy of cancer patients. Currently, brachytherapy is used as a less invasive form of radiation therapy, where small radioactive seeds (theraseeds) are implanted into the tumour (Figure 1.5) [26].

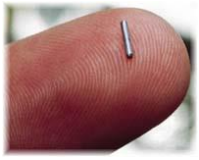

Figure 1.5: Image of a theraseed [26].

Radioactive palladium-103 (^{103}Pd) seeds (Figure 1.6), were introduced in 1986 and are currently in clinical use as an alternative to radioactive iodine-125 (^{125}I). The palladium-103 isotope is a source of low energy photons, with a half-life of 17 days. This results in a significantly decreased dose with increasing distance from the source relative to that of higher energy photons, such as those generated by the decay of iodine-125. This ensures that the radiation is localised and that radiation exposure to people in contact with patients undergoing brachytherapy is limited. Furthermore, the short half-life of palladium-103 provides higher initial dose rates than iodine-125, which has a half-life of 60 days [27]. These differences make palladium-103 a safer alternative to iodine-125, with fewer complications; however, both are frequently used in treatments [28;29].

Photodynamic therapy (PDT) is a cancer treatment where an inactive form of the drug is administered and is then locally activated and controlled by light. The principle is to administer a non-toxic photosensitiser and then activate it at which point, it generates cytotoxic reactive oxygen species (ROS) which are responsible for cell death and necrosis. Damage is limited or localised as the drug is only activated in a specific target area. Selectivity of PDT drugs is usually based on differential drug accumulation within tumour- and normal tissues. PDT has been used to treat a range of different cancers. Palladium-bacteriopheophorbide (TOOKAD), shown in Figure 1.7, is a fast acting PDT drug which leads to vascular thrombosis and secondary tumour destruction, clearing the system within a few hours. This drug is currently involved in clinical trials, evaluating its efficacy against prostate cancer. Thus far, it has proven to be as safe and effective as current photosensitisers, with the added benefit of having a rapid clearance rate [30;31].

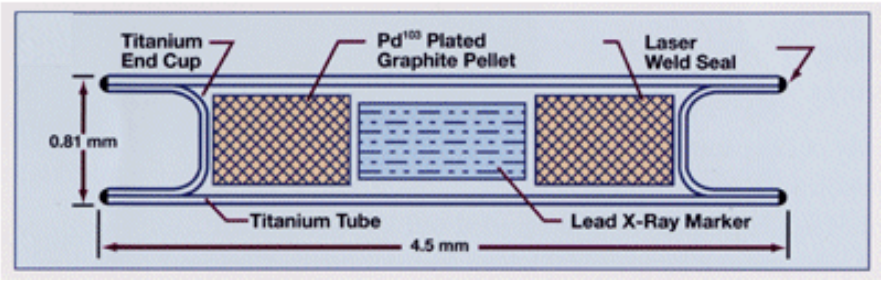

Figure 1.6: Diagram of palladium-103 theraseed design [32].

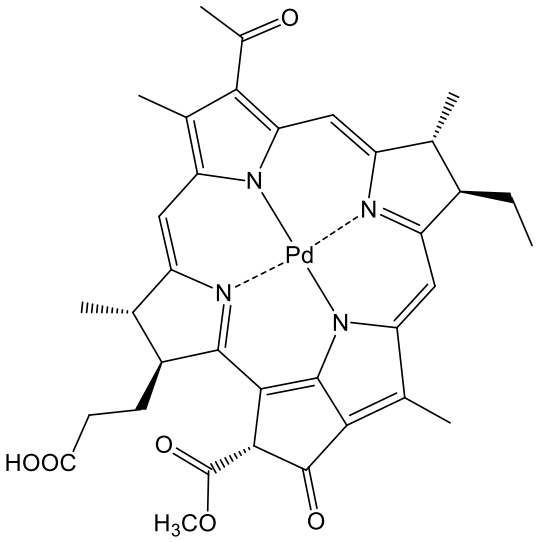

Figure 1.7: Chemical structure of TOOKAD.

1.1.3. Platinum vs. palladium with respect to designing chemotherapeutics

As mentioned previously, platinum and palladium have very similar physical and chemical properties, with the exception of their ligand exchange kinetics. The ligand exchange rate for palladium is 10^5 times faster than that of platinum. The most significant implication of this difference, in terms of designing chemotherapeutic agents, is that palladium species will be far more reactive in biological environments than their platinum analogues.

Considering the similarities between platinum and palladium, especially their very similar coordination abilities, and the overall lower toxicity of palladium, it is plausible that palladium complexes could be used for synthesising analogues of existing platinum anti-cancer drugs which are more active and less toxic [33].

The next section will discuss some of the significant developments in the design of palladium anti-cancer drugs, as well as the more the promising complexes reported in the literature. The work discussed below is aimed at providing a timeline for the developments and discoveries in this field and to establish a guide for future investigators. This review is by no means a full account of all the palladium complexes designed as potential anti-cancer drugs.

1.2 Palladium complexes as anti-cancer agents

1.2.1 Palladium analogues of platinum drugs (1970s-1980s)

Following the success of cisplatin, Cleare published a review in 1974, with the aim of encouraging research in the direction of inorganic coordination complexes [34]. The ideal anti-cancer drug was defined as having selective toxicity for cancer cells. It was also pointed out that a drug such as this was yet to be discovered. In the review, it was speculated that palladium(II) complexes were too reactive to be effective *in vivo*, due to the significantly higher ligand exchange kinetics of palladium, as compared to platinum. This was based on the lack of activity of some reported palladium(II) analogues of active platinum(II) complexes when tested against Sarcoma 180 in Swiss white mice [35]. Even the more stable palladium complexes, with bidentate ligands, showed unimpressive results. The activity for these complexes was measured as the weight of a treated tumour compared with that of an untreated (control) tumour, also referred to as a T/C value (Table 1.1). T/C values below 50 were considered to be significant, however, none of the tested complexes met this requirement [34].

Table 1.1: *In vivo* results for palladium(II) analogues of active platinum(II) complexes.

Complex	Dose range (mg/kg)	Toxicity level (mg/kg)	T/C[a]
cis-$[Pd(NH_3)_2Cl_2]$	1.25-10	>10	83
$[Pd(en)Cl_2]$	5-40	>40	79
$[Pd(NH_3)_2mal]$	25-200	150-200	55
[Pd(en)mal]	25-100	>100	75
[Pd(en)ox]	1.25-75	>40	104
$[Pd(NH_3)_2ox]$	1.25-200	~100	80

Abbreviations: en: ethylenediamine; mal: malonate; ox: oxalate. [a]Weight of treated tumour compared to control tumour (expressed as a percentage).

During the same period (1979), Graham and Williams [36] followed the research trends set by Furst [37] and Rosenberg [9] to consider the incorporation of group VIIIB metals into potential anti-cancer drugs. They studied the anti-bacterial, -cancer, -viral and fungicidal properties of several palladium and nickel complexes. Table 1.2 is an abbreviated table, showing the anti-cancer screening data for the palladium complexes tested. From their results, they concluded that active palladium complexes do not follow the structural criteria, as determined for active platinum complexes. This is clear from entries 4-6, for compounds which do not have nitrogen donor atoms (with at least one active hydrogen) in their carrier ligands, as stipulated for designing active platinum drugs, yet these complexes are active. Entry 3 is another example of a complex which is biologically active, yet its octahedral geometry does not allow for metal-metal stacking, a property thought to be essential for anti-cancer activity, based on cisplatin and other active platinum anti-cancer drugs. Furthermore, they were able to confirm that selectivity varies with the central metal ion, in the same way that it varies with nitrogen ligand substitution in the platinum species. Their most significant observation was that the neutral species was the active drug in the case of platinum complexes, whereas palladium complexes exchange ligands too quickly for the initial neutral complex to be the active species. Thus, the anions, $PdCl_6^{2-}$ and $PdCl_4^{2-}$, were the more likely active species. This observation cleared up the misconception that palladium complexes are inferior to their platinum counterparts, as initially found by Cleare and Hoeschele [35]. This publication brought to light one of the issues still of concern today, the need to determine the nature of the active species under physiological conditions [36].

Further studies looking at the palladium analogues of cisplatin and its derivatives were reported in 1990 by Castan *et al*. [38]. By this time, a handful of palladium complexes with nitrogen-donor ligands, $[Pd(L)(NO_3)_2]$ [where L = ethylenediamine (en), bipyridine (bipy) or 1,2-diaminocyclohexane (DACH)], had been reported to have “noticeable” activity against sarcoma 180 [39], yet the overall results remained unsatisfactory in comparison to the platinum analogues. The authors ascribed these “disappointing results” to an inappropriate selection of ligands, suggesting that the ligands were not lowering the reactivity of the metal sufficiently for the complex to be active. Their hypothesis was that the high reactivity of palladium could be counteracted by relatively inert leaving groups and that cis-trans isomerisation could be prevented by suitable ligands, such as chelating ligands. In an attempt to prove their hypothesis, they tested platinum and palladium complexes with the general formula, N_2ML, where N_2, the inert ligand, was one mole of DACH or 2 moles of ammonia, M, the metal and L, the leaving group, was the dianion of 3-methyl orotic acid. The complexes were tested against leukemia cell lines, L1210 and P388, in CDF_1 hybrid female (BALB/C x DBA/2) mice and sarcoma 180 cells in Swiss mice. The highest non-lethal dose (LD_0) values

and T/C values were reported, where T/C was defined as the median survival time of the treated mice (excluding the survivors) compared to the median life span of untreated mice, expressed as a percentage. In this case, a T/C percentage of 125 or greater indicated significant activity. The results are shown in an abbreviated table, Table 1.3.

Table 1.2: Anti-cancer screening data from work published by Graham and Williams [36].

Compound	Anti-cancer screening			Cytotoxicity (μg/mL)
	Landschutz ascites *in vitro/ in vivo*[a]	Landschutz ascites *in vivo*[b]	Sarcoma 180 *in vivo*[c]	
cis-$Pd(NH_3)_2Cl_2$	100% at 1.95	75% at 12.5	1.6% at 25	0 at 50
trans-$Pd(NH_3)_2Cl_2$		48% at 50	43% at 50	Toxic at 100 mg/kg
cis-$Pd(NH_3)_2Cl_4$	100% at 15.6 55% at 1.9	92% at 50	86% at 100	0 at 50
Na_2PdCl_6	100% at 7.8 25% at 1.9	36% at 50	2.5% at 50	0 at 50
$(NH_4)_2PdCl_4$	100% at 15.6 60% at 3.9	49% at 50	11% at 50	0 at 50
enH_2PdCl_4	100% at 7.8 76% at 1.9	34% at 25	27% at 50	0 at 50
$(\pi C_3H_5PdCl)_2$	100% at 1.9 34% at 0.04	0 at 12.5	40% at 12.5	Toxic at 12.5
$Pd(cyclopent)_2Cl_2$	100% at 3.9	14.7% at 50 70.3% at 25	4.0% at 50 41.2% at 25	
$Pd(cyclohex)_2Cl_2$ (red isomer)	100% at 31.25	31.2% at 50 6.4% at 25	13.3% at 50 68.4% at 25	
$Pd(cyclohex)_2Cl_2$ (pink isomer)	100% at 3.9	11.1% at 50 63.0% at 25	0 at 50 27.4 at 25	
$Pt(cyclohex)_2Cl_2$	100% at 1000	63.3% at 50 49.6% at 25	0 at 50 0 at 25	
$Pd(asn)Cl_2$	100% at 250 27% at 1.9			
$Pd(asn)_2$ (pale yellow isomer)	100% at 31 64% at 1.9			
$Pd(asn)_2$ (lilac grey isomer)	100% at 62.5 54% at 1.0			

Abbreviations: en: ethylenediamine; cyclopent: cyclopentylamine; cyclohex: cyclohexylamine; asn: asparagine. [a]Percentage inhibition at μg/mL concentration. [b]Percentage inhibition at mg/kg/dose concentration. [c]Percentage inhibition at mg/kg/dose concentration.

Table 1.3: *In vivo* anti-tumour activity of N_2ML-type complexes against Sarcoma 180 [38].

Compounds	LD_0 (mg/kg)	T/C[a]
$[Pt(NH_3)_2(3\text{-Me-orot})]$	400	130
	200	129
$[Pd(NH_3)_2(3\text{-Me-orot})]$	150	TOXIC
	75	122
[Pt(DACH)(3-Me-orot)]	500	130
	250	109
[Pd(DACH)(3-Me-orot)]	300	152
	150	267
$K_2[Pd(3\text{-Me-orot})_2]$	400	117
	200	139
$[Pd(DACH)(NO_3)_2]$	150	142
	75	120
cis-$[Pt(NH_3)_2Cl_2]$	8	TOXIC
	4	277

Abbreviations: 3-Me-orot: 3-methyl orotic acid. [a]Median survival time of treated mice (excluding the survivors) compared to the median life span of untreated mice (expressed as a percentage).

From Table 1.3, the complex reported by Gill in 1984 [39], $[Pd(DACH)(NO_3)_2]$, had reasonable anti-tumour activity, despite the potential for isomerisation in aqueous media. Furthermore, [Pd(DACH)(3-Me-orot)], where 3-Me-orot = 3-methyl orotic acid, had significant activity with T/C values of 150 and 267, which is higher than that observed for Gill's complex. Another observation was the significant drop in activity for the platinum analogues containing the orotate anion. This could be ascribed to the reduction in reactivity due to the strong chelating effects of the orotate anion.

The low activity observed for $[Pd(NH_3)_2(3\text{-Me-orot})]$ was thought to be due to isomerisation from the cis isomer to the thermodynamically stable trans isomer, thus rendering the species inactive, in the same way that $[Pd(NH_3)_2Cl_2]$ is inactive compared to its platinum counterpart which is not plagued by the trans-effect.

Despite this lack of activity and the very limited number of active palladium complexes, researchers were not discouraged, as Kirschner *et al.* had already proven that a palladium complex could have significant anti-cancer activity. In 1966, they published their paper, "Anti-cancer and Potential Anti-viral Activity of Complex Inorganic Compounds" where they studied twenty-six inorganic compounds for their ability to alter cancer-producing viruses. They

proposed that these compounds would target the protein and nucleic acid units in the virus, by coordination or chelation of the metal ion to atoms in these large macromolecules, thus altering the structure of the macromolecules and consequently the virus. They looked at platinum metals, as these are good sulphur coordinators, aluminium metals were considered for their oxygen-binding potential and iron and cobalt were selected as nitrogen coordinators. The ligands employed were chosen for their inherent biological activity.

Five of the compounds showed significant anti-cancer activity and in each case, the activity of the complex was higher than that of the ligand. $Na_2[Pt(mp)_2Cl_4]\cdot 2H_2O$, $Na_2[Pd(mp)_2Cl_2]\cdot H_2O$ and $[Pd(butp)_3Cl]Cl$ (where mp = 6-mercaptopurine and butp = butylthiopurine) were among the active compounds. The results in Table 1.4 show that palladium can not only exhibit similar activity to its platinum analogues, but that palladium-based compounds as anti-cancer agents is a valid and worthwhile field of research [40].

Table 1.4: Anti-tumour activity results for active complexes with biologically active ligands, 6-mercaptopurine and butylthiopurine [40].

Compound	Test system	Daily dose (mg/kg)	Survivors	% tumour weight decrease
$Na_2[Pt(mp)_2Cl_4]\cdot 2H_2O$	S180[a]	100	6/6	10
	Ca755[b]	16	10/10	0
		8	10/10	4
$Na_2[Pd(mp)_2Cl_2]\cdot H_2O$	S180[a]	100	5/6	18
	Ca755[b]	18	9/10	0
		9	10/10	10
$Pd(butp)_3Cl]Cl$	Ca755[b]	15	9/9	28
		7.5	10/10	85

[a]Swiss mice used as host. [b]BDF_1 mice used as host.

1.2.2 Palladium and its lability solved (1990s)

The work by Khan and co-workers, in 1991, generated the first genuine interest in palladium complexes as anti-tumour drugs [41]. As mentioned previously, the lability of palladium complexes posed a problem for application as anti-cancer agents. Khan and co-workers reasoned that if the palladium complexes could be stabilised enough to reach their biological targets, they could be tested as anti-tumour agents. Much the same as the approach by Castan *et al.* [38], they made use of chelating ligands, such as methionine (meth) and mercaptopyrimidine (mercaptopy), to reduce the lability of mixed ligand complexes of *cis*-dichloromethioninepalladium(II). At this early stage of the investigation into palladium-based anti-tumour agents, the requirement for these complexes to be considered as potential anti-

tumour agents, was that they would have to exhibit half maximal inhibitory concentration (IC_{50}) values of 10 μg/mL or lower.

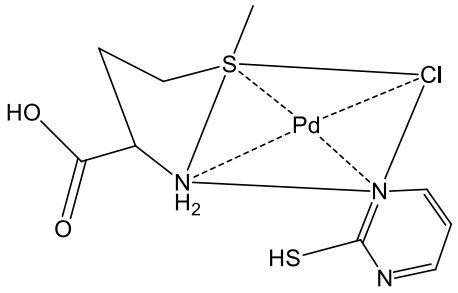

Figure 1.8: Chemical structure of [Pd(meth)(2mercaptopy)Cl]Cl.

The anti-tumour activity of the six reported square planar complexes was evaluated by *in vitro* cytotoxicity against CHO (Chinese hamster ovary) and Hela (Epidermoid Carcinoma Cervix) cell lines. Based on the results, chloro2-mercaptopyrimidinemethioninepalladium(II)chloride {[Pd(meth)(2mercaptopy)Cl]Cl}, shown in Figure 1.8, proved to be the most cytotoxic with IC_{50} values in the range of 6.25 μg/mL and 6.17 μg/mL for the CHO and Hela cell lines, respectively. This complex not only met the requirement, but showed that palladium complexes could indeed be powerful anti-tumour agents [6;41].

In the early 1990's, Navarro-Ranninger and co-workers published a paper on the use of spermidine [(*N*-(3-aminopropyl)-1,4-diaminobutane), (sper)] as the ligand in palladium(II) complexes to be evaluated as potential anti-tumour agents [42]. Based on previous work, such as the examples discussed above, this chelating ligand was selected for its biological activity and the ability to reduce the reactivity of the palladium metal centre, as well as the potential to manipulate the cis-trans isomerisation to favour the formation of the active cis isomer. They were able to prove that $[PdCl_2(sperH)]_2[PdCl_4]$ and $[(PdCl_2)_3(sper)_2]$ (Complexes **1** and **2** in Figure 1.9) had similar or enhanced activity compared to cisplatin, against MDA-MB 468 breast cancer cells, as shown in Table 1.5.

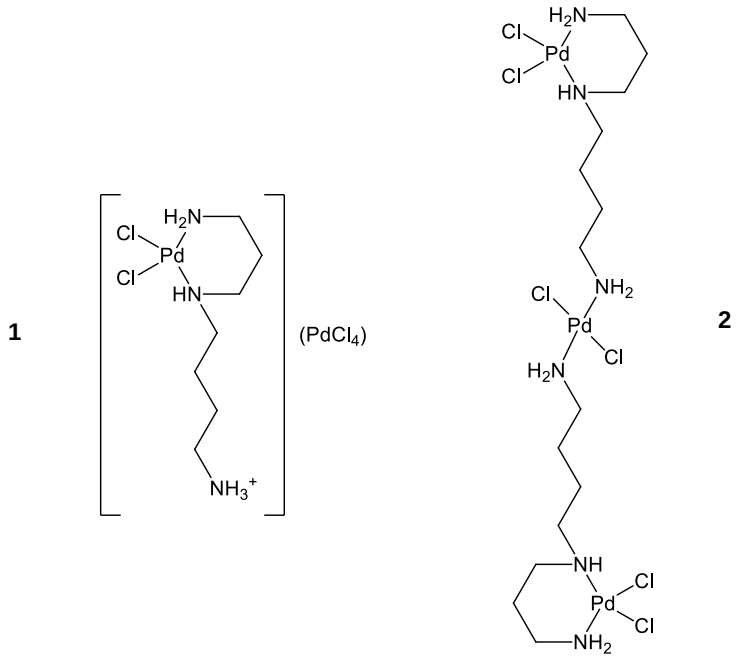

Figure 1.9: Palladium complexes with spermidine ligands [42].

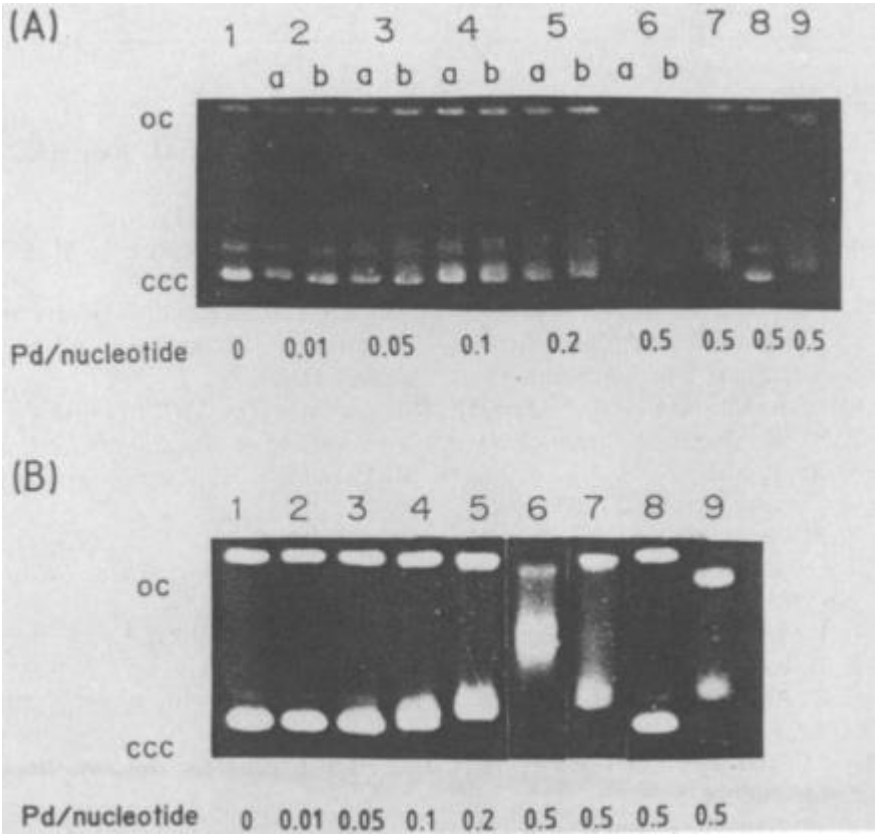

Figure 1.10: Electrophoresis gels showing changes in electrophoretic mobility of the oc and ccc forms of the pUC8 plasmid DNA. Lanes 7-9 are the controls, K_2PdCl_4, spermidine and cisplatin. (A) shows the results for $[(PdCl_2)_3(sper)_2]$ in lanes labelled a. (B) shows the results for $[PdCl_2(sperH)]_2[PdCl_4]$, with increasing Pd/nucleotide concentrations [42].

Table 1.5: *In vitro* testing results of palladium complexes with spermidine-type ligand [42].

Complex	ID_{50} values (μg/mL)[a]
$[sperH_3]_2[PdCl_4]_3$	9.30
$[PdCl_2(sperH)]_2[PdCl_4]$	0.56
$[(PdCl_2)_3(sper)_2]$	0.74
Cisplatin	0.80

[a]50% inhibition of cell growth.

Furthermore, they investigated the drug-induced changes in DNA conformations, by studying changes in the electrophoretic mobility of covalently closed circular (ccc)- and open circular (oc) plasmid DNA (Figure 1.10). Both complexes induced changes in both the ccc and oc plasmids, but the change observed for $[PdCl_2(sperH)]_2[PdCl_4]$ is far more significant. The change in electrophoretic mobility is even more extensive than the change observed for cisplatin (lane 9) [42].

With these promising results in hand, they extended their study of these types of complexes, using both putrescine [(1,4-butanediamine), (put)] and spermine {[*N*,*N*'-bis(3-aminopropyl)-1,4-butanediamine], (sperm)} as ligands. As shown in Figure 1.11, the ligands were used as bridging ligands to form binuclear complexes. These complexes were again evaluated against the MDA-MB 468 cell line. The ID_{50} values obtained for compounds **3**-**5** are considerably more favourable, compared to the value obtained for cisplatin (Table 1.6) [43].

Table 1.6: Anti-proliferative activity of Pd(II) putrescine and Pd(II) spermine complexes [43].

Complex	ID_{50} values (μg/mL)[a]	Dose (μM)
$[PutH_2][PdCl_4]$ (**3**)	0.39	1.60
$[Pd_2Cl_4(Put)_2]$ (**4**)	0.37	0.70
$[PdCl_2(Put)]+ [Pd_2Cl_4(Put)_2]$ (**5**)	0.42	0.53
$[PdCl_2(SpermH_2)][PdCl_4]$ (**7**)	7.25	11.51
$[Pd_2Cl_4(Sperm)]$ (**6**)	4.70	8.44
K_2PdCl_4	1.79	5.50
Cisplatin	0.80	2.50

Abbreviations: Put: putrescine; Sperm: spermine. Compound structures are reported in Figure 1.11.

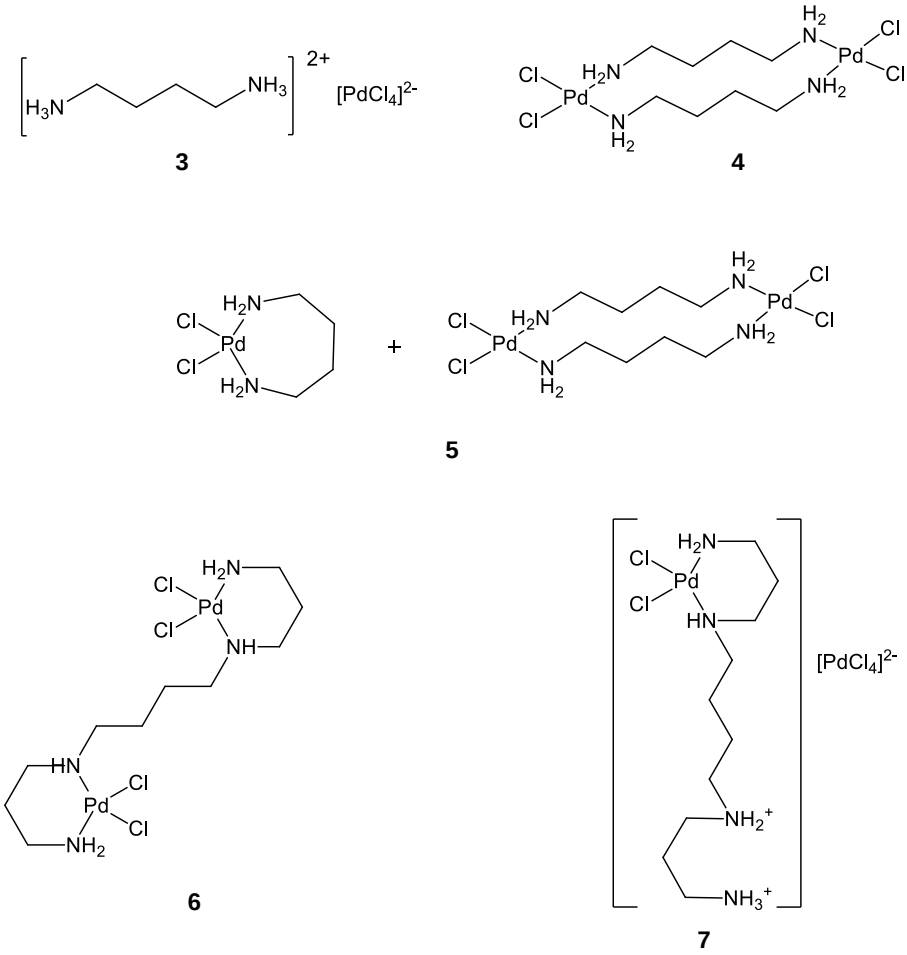

Figure 1.11: Palladium complexes with putrescine and spermine ligands.

As with the previous complexes, the drug-DNA interactions were investigated. UV-Vis- and CD spectroscopy, as well as electrophoresis, were used. Plasmid DNA was used for all of these assays, instead of linear DNA, which is more common in current literature on spectroscopic techniques for investigation DNA-binding studies. UV-Vis spectra showed that the complexes induced a hyperchromic effect, which is the opposite of the effect induced by the ligands. Similarly to cisplatin and K_2PdCl_4, $[PdCl_2(SpermH_2)][PdCl_4]$ and $[Pd_2Cl_4(Sperm)]$ induced a bathochromic shift, as well. These observations pointed to drug-induced conformational changes in the secondary structure of the DNA, more specifically, a distortion of the base stacking. CD spectra showed shifted and decreased intensities for both the positive and negative ellipticity values. In this instance, the most significant changes were observed for $[Pd_2Cl_4(Put)_2]$ and $[Pd_2Cl_4(Sperm)]$, along with the controls, K_2PdCl_4 and cisplatin. The changes point to the opening and rotation of the stacked bases in the DNA double helix. The electrophoresis data, however, showed no change in the electrophoretic mobility of the oc form, as was observed for the control compounds. This suggests that these compounds do not induce tighter coiling which would consequently shorten the DNA, as was observed

previously with the control compounds. The complexes with putrescine as ligand, retarded the mobility of the ccc form of the pUC8 plasmid DNA. $[Pd_2Cl_4(Put)_2]$ had a higher retention of the ccc form than cisplatin. Based on these results, it was concluded that Pd(II) putrescine complexes altered both the secondary and tertiary structure of DNA. These changes are likely the formation of local microloops which result in partial uncoiling of the DNA helix. This suggested that the spermine and putrescine ligands result in the formation of different adducts.

Navarro-Ranninger and co-workers made a significant contribution to research in this area by showing just how significant the correct choice of ligand is and how extensive the effects can be in terms of drug-DNA interaction and anti-proliferative activity. Another important observation was made in that the spectroscopic data suggest that both the Pd(II) putrescine and the Pd(II) spermine complexes produced similar degrees of modification in the DNA, whilst the *in vitro* assays showed that the Pd(II) putrescine complexes possessed higher anti-proliferative activity. The *in vitro* and *in vivo* data cannot necessarily be correlated, as there are numerous factors which could cause these differences, but it should again become clear that testing potential anti-cancer activity by only one assay or method is insufficient to obtain a true indication of the anti-cancer potential of a compound [43].

Realising the importance of ligand choice, Higgins III *et al.* [44] followed the work by Newkome [45] and others, from as early as 1985, where bidentate bipyridines were observed to form palladacyclic complexes capable of binding to DNA [45]. Based on this literature, phenanthroline ligands were investigated for their planarity, as a planar ligand may result in a planar complex capable of intercalating into the DNA double helix. This ability to intercalate into the DNA helix was a sought after property for potential anti-cancer agents at the time [44;46]. Figure 1.12 depicts the intercalation of ethidium bromide, a well-known DNA-intercalating agent, into the DNA helix.

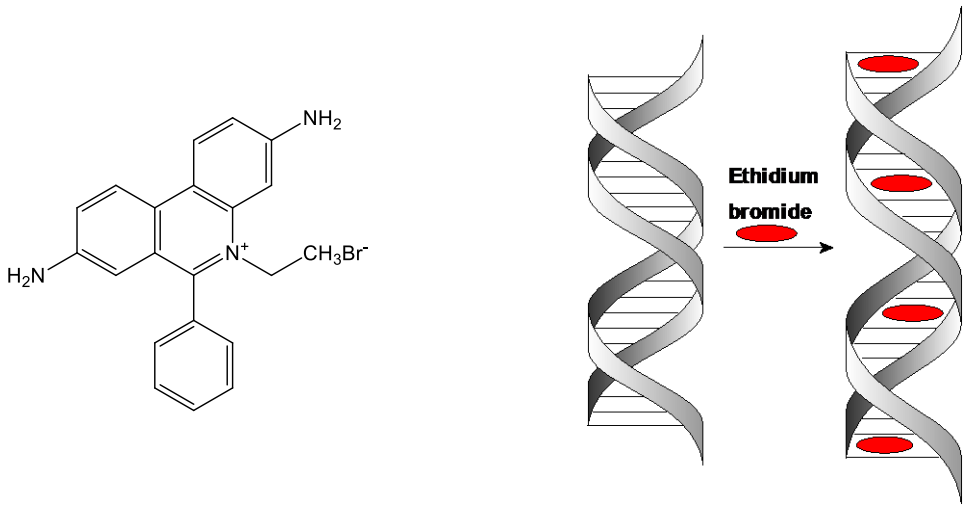

Figure 1.12: Planar structure of ethidium bromide (left) and diagram showing the intercalation of ethidium bromide into the DNA double helix (right) [47].

When investigating their own complexes with phenanthroline-type ligands in 1989, Higgins III *et al.* discovered a unique palladacycle compound, complex **8** (Figure 1.13) [48]. Complex **8** is a mononuclear palladacycle with 2-arylphenanthroline as ligand. Evaluation of this complex against a tumour panel showed "potent" anti-cancer activity (Table 1.7) [44;46].

After their initial success, they continued their investigation into the use of amine ligands in 1993, where they studied various amines for their bridge opening abilities, thus forming mononuclear complexes from binuclear bridged palladacycles [44].

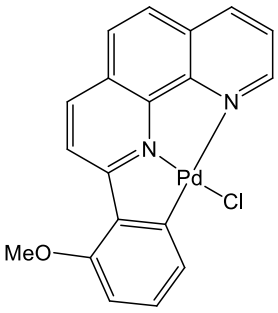

8

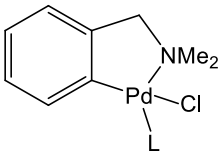

9a/b

Figure 1.13: Unique palladacycle complex, complex 8, and the follow up complex 9 (where L = pyridine for 9a and ^{i}Pr-NH$_2$ for 9b), both reported by Higgins III *et al*. [44].

Table 1.7: Anti-cancer activity of complex 8 and complex 9 [44].

Human Cancer Cell Line	IC_{50} value (μM)		
	Complex 8	Complex 9a	Complex 9b
SW6020	5	44	30
SW1116	7	44	26
SW403[a]	6	-	-
ZR75-1	7	50	9
HT1376	8	8	9
SK-OV-3	7	20	10

[a]No data obtained.

Their choice of mononuclear target compounds over the dimeric species was based on solubility considerations. The limited solubility of the dimeric complexes in most organic solvents forced them to consider lower molecular weight species. Therefore, they considered the mononuclear analogues, as these lower molecular weight complexes were more likely to be soluble. The use of amines was based on earlier work where these ligands produced complexes with DNA binding ability, which could lead to anti-tumour activity, as well as their potential to increase solubility. Both aromatic and aliphatic amines were used. Most of the

complexes were found to have improved solubility and two of these complexes were found to be water-soluble. When evaluated for their cytotoxicity against a number of cancer cell lines, most of the complexes displayed IC_{50} values in the range of 10 μg/mL across the panel, making them effective, but not necessarily selective for different cells, be it various cancerous cell lines or healthy cells. However, the complexes derived from *N*,*N*-dimethylbenzyl amine, complex **9a** and **9b** (where L = pyridine for **9a** and L = ^{i}Pr-NH_2 for **9b**), displayed differential cytotoxicity. A 3-5 fold difference in activity was observed between the HT1376 and the SW6020 cell lines, making these the most promising leads for the design of an effective yet less toxic drug [44].

1.2.3 Cis and trans isomers (early 2000s)

In 2001, Al-Allaf and Rashan synthesised a large number of novel palladium complexes in both their cis and trans forms. A variety of ligands were employed, including pyrazoles, DMSO and ferrocenylphenylphosphanes. The complexes were tested against a series of tumour cell lines and solid tumours. The results showed that trans-palladium complexes are generally more cytotoxic than their cis-palladium and -platinum analogues. Some of these complexes were also more active *in vitro*, than cisplatin, carboplatin and oxaliplatin [49]. This followed on the earlier work by Tusek-Bozic and co-workers, who reported trans-palladium complexes with mono- and diethylphosphonate ligands for improved solubility, as potential anti-cancer agents. Their results showed that the trans-palladium complexes have improved activity with respect to their cis analogues. A representative structure is shown in Figure 1.14 [46;50;51].

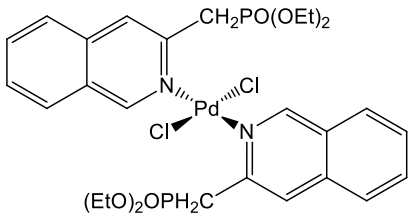

Figure 1.14: Representative structure in early work on active trans-palladium complexes as anti-tumour agents.

Abu-Surrah and co-workers reported on a chiral trans-palladium complex with a bulky amine ligand, *endo*-(1*R*)-1,7,7-trimethylbicyclo[2-2-1]-heptan-2-amine [52], the year after the extensive work by Al-Allaf and Rashan [49]. This complex was evaluated against three cell lines, L929 (murine fibrosarcoma), K562 (human myelogenous leukemia) and HeLa (human cervical carcinoma) cells. The results again showed similar activity to the standard platinum drugs, cisplatin, carboplatin and oxaliplatin [46;52].

It is well known that trans-platinum complexes are generally inactive as anti-cancer agents; hence the early studies of palladium complexes considered cis isomers, assuming the same structure rules applied to palladium, yet here clear violations of these rules were observed. The trans-palladium species not only outperformed their cis isomers, but also the cis-platinum analogues. From these results, it was clear that the known structure-activity rules for designing active platinum drugs did not apply to palladium drugs. This also suggested that palladium drugs may have a different mode of action to platinum drugs.

1.2.4 Significant complexes and their influence on palladium drug design (2000-2015)

Research leading up to the early 2000s proved that the structure-activity relationship for active platinum complexes cannot be applied in the design of active palladium anti-cancer drugs. However, based on the early research, it is clear that chelating or strongly binding ligands are necessary for reducing the reactivity of the metal centre in order to obtain an active compound. Aside from this requirement, researchers could try almost anything. In the following sections, we report some of the more successful designs.

In 2003, Rodrigues *et al.* reported palladacycles with the bisphosphinic ligand, dppe [11]. The dppe ligand was used to decrease the lability of palladium and to stabilise the complex. This should allow for the use of lower dosages and consequently lower toxicity. These complexes showed promise as anti-tumour agents against a syngeneic B16F10 murine melanoma model, both *in vitro* and *in vivo*. The novel palladacycles were classified as ionic mononuclear [Pd(*C*,*N*-cycle)(dppe)Cl], molecular mononuclear [Pd(C^2,*N*-cycle)(dppe)Cl] and binuclear [Pd_2(*C*,*N*-cycle)$_2$(μ-dppe)Cl_2] complexes.

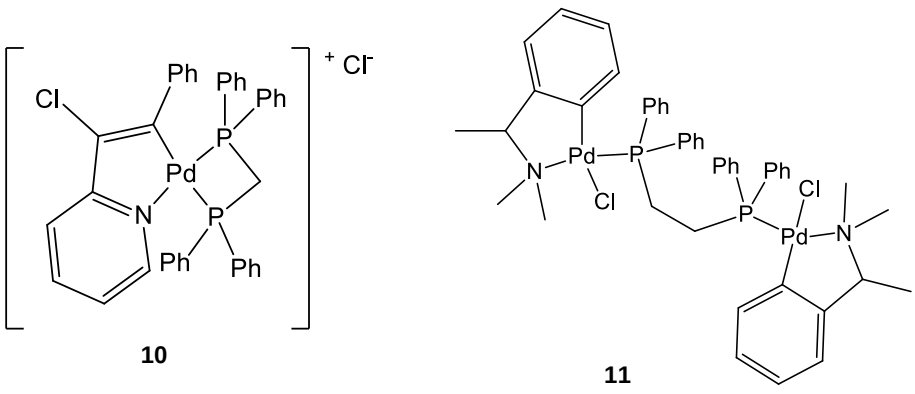

Figure 1.15: Dppe-type palladacycles reported by Rodrigues *et al*.

In vitro evaluation of the compounds against B16-Nex2 cells (subline of B16F10 murine melanoma model) showed that complexes **10**, **11a** and **11b** (where **11a** and **11b** were the S(-) and R(+) enantiomers, respectively) were highly active, resulting in 100% tumour cell death at concentrations below 1.25 μM (Figure 1.15), whilst the other complexes required concentrations above 10 μM to produce the same effect. When these three complexes were evaluated *in vivo*, only complex **11a** showed anti-tumour activity; however, it is important to note that none of the complexes were toxic to the host mice, even at a dosage of 60 μM/animal/week (where a 1 mM stock solution of **11a** was prepared in 1% DMSO in 50 mM phosphate buffer and further dilution was achieved with phosphate-buffered saline).

Evaluation of the other complexes *in vivo*, showed that two of the less active complexes (based on the *in vitro* work), [Pd(*o*-NC_5H_4)(Cl)C=C(Ph)(dppe)Cl] and [Pd(CH_2-$N(CH_3)_2$(Cl)C=C(Ph)(dppe)], were active and showed similar activity to complex **11a**. Further investigation of these three active complexes showed that all three induced an apoptosis-like effect in the tumour cells via a caspase-1 and caspase-3 independent pathway.

The binuclear complex **11a** showed good activity in both *in vitro* and *in vivo* testing with 100% cell death occurring at a concentration lower that 1.25 μM [11]. Interestingly, however, the two mononuclear palladacycles showed very little activity *in vitro*, yet *in vivo* they showed significantly improved activity.

Circular dichroism spectroscopy, a spectroscopic technique used to elucidate changes in secondary structure of macromolecules upon interaction with potential drug complexes, was used to determine if the complexes interacted with DNA. Complex **11a** was found to interact with plasmid DNA, inducing changes in the CD spectrum, as shown in Figure 1.16. These changes suggested that the complex intercalated between base pairs in the DNA double helix.

This work emphasises the potential of palladacycles with dppe ligands as highly active anti-tumour agents, both *in vitro* and *in vivo* [11].

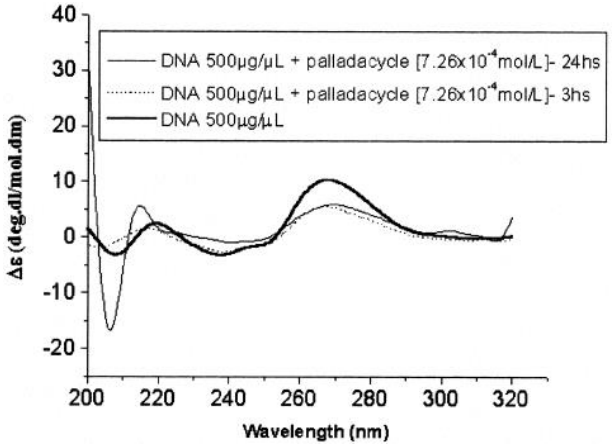

Figure 1.16: CD spectra of DNA and complex 11a [11].

Ray *et al*. reported on palladium *N*-heterocyclic carbene (NHC) complexes with 1-benzyl-3-tert-butylimidazol-2-ylidene as the ligand. Their motivation was two-fold. Firstly, NHC complexes have proven to be very successful in the field of catalysis. Secondly, the usefulness of NHC ligands in potential anti-cancer drugs was assumed based on previous success of palladium complexes with amine- and pyridine ligands which showed considerable anti-proliferative properties against tumour cells. Their NHC compounds were modelled on the potent anti-cancer pro-drug, *trans*-(pyridine)$_2$PtCl$_2$, [53] where the pyridine ligands were replaced by a more electron-donating NHC ligand, to further stabilise the highly reactive palladium centre.

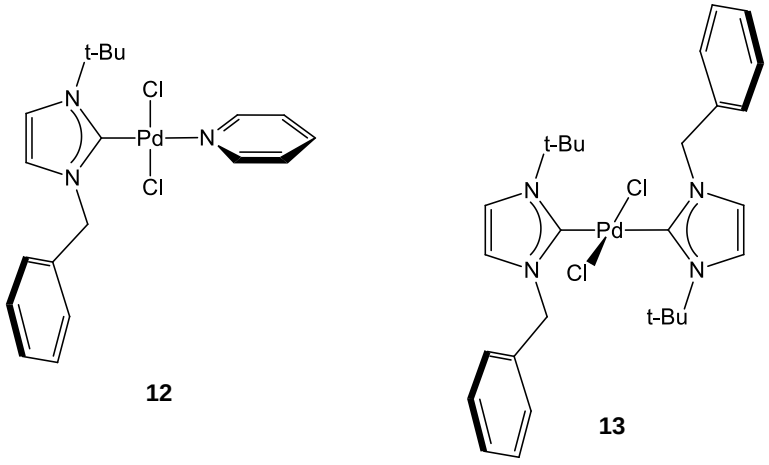

Figure 1.17: Palladium-NHC complexes synthesised by Ray *et al*. [53].

These Pd-NHC complexes (Figure 1.17) showed promising anti-cancer activity against HeLa cells. At a concentration of 10 µM, complex **12** inhibited proliferation by 35%, whilst complex **13** resulted in 85% inhibition of tumour proliferation. Complex **13** also exhibited anti-proliferative activity that was far more effective than that of cisplatin (Table 1.8) in the following human tumour cells: cervical cancer (HeLa), breast cancer (MCF7) and colon adenocarcinoma (HCT116).

Table 1.8: *In vitro* assay results for complex 1b compared to cisplatin [53].

Compound	IC_{50} (μM)		
	HeLa	MCF7	HCT116
13	4 ± 0.2	1 ± 3	0.8 ± 0.05
Cisplatin	8 ± 1	15 ± 2	16 ± 3

The observation that complex **13** was more active than complex **12** could be ascribed to the more electron-rich metal centre of complex **13**, as compared to that of complex **12**. This was due to the coordination of two NHC ligands in the case of complex **13**, whilst complex **12** only had one of these electron donating ligands [53]. This work has continued since and in 2013, a very promising example of substituted Pd-NHC complex was reported by Haque *et al.* (Figure 1.18). Evaluation of this complex against colorectal cancer cell lines (HCT116) showed high levels of activity at very low concentrations (6.6 μM) [46;54].

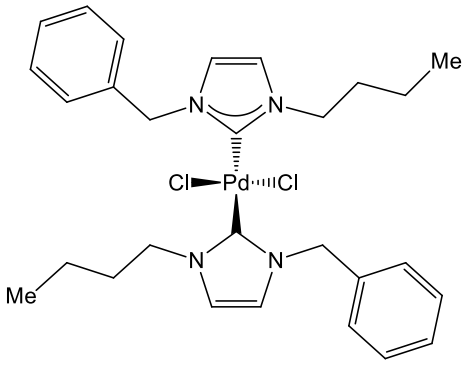

Figure 1.18: Substituted NHC-Pd complex reported by Haque *et al*. [54].

With current trends in anti-cancer research moving in the direction of orally active drugs, there is a greater need to improve the overall solubility of many of these palladium complexes, and more specifically, the water solubility. In 2013, Guerrero *et al.* reported novel palladium complexes with the water-soluble phosphine, PTA, and its derivative, 3,7-diacetyl-1,3,7-triaza-5-phosphabicyclo[3.3.1]nonane (DAPTA) [55]. These ligands were chosen based on the success of the RAPTA complexes, with these ligands. Thus, trans-platinum and –palladium complexes were synthesised using these water-soluble ligands. Thionate moieties were also incorporated, based on the authors' previous success with such ligands in water-soluble gold and platinum complexes [56]. The complexes shown in Figure 1.19 were found to be poorly water-soluble (0.1-0.8 mg/mL), with the exception of two of the palladium complexes which were moderately water-soluble. These were *trans*-[Pd(*S*-methylpyrimidine-2-thionate)$_2$(DAPTA)$_2$ (complex **16**) and *trans*-[Pd(*S*-methylpyrimidine-2-thionate)$_2$(PTA)$_2$ (complex **14**) with 12.6 mg/mL and 23.4 mg/mL solubility in water, respectively. All of the

complexes were evaluated as anti-cancer agents against human ovarian cancer cell lines, A2780 and A2780cisR (cisplatin-resistant). The palladium complexes had activity comparable to that of cisplatin against A2780; however, remarkably high cytotoxicity was observed when tested against A2780cisR, thus, exhibiting the ability of these palladium complexes to overcome cisplatin resistance [55].

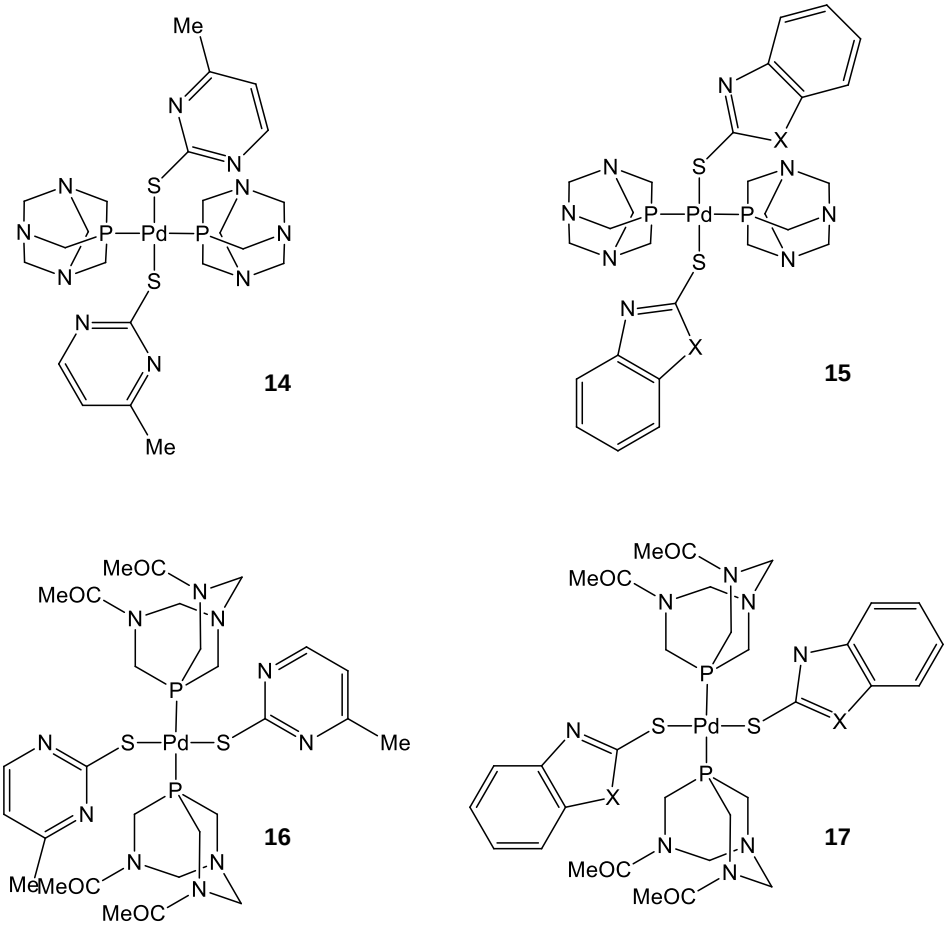

Figure 1.19: PTA-based palladium complexes as potential water-soluble anti-cancer agents [55].

Still focusing on the solubility of potential drugs, Albert *et al.* investigated the efficacy of doubly cyclopalladated diimines with linker molecules, $N(CH_2)_2N$ and $N(CH_2)_2O(CH_2)_2O(CH_2)_2N$ (complexes **18** and **19** in Figure 1.20, respectively) [57]. These linkers varied in length and flexibility, but more importantly, they differed in their hydrophilicity and lipophilicity. The diimine palladacycles were evaluated against a panel of adenocarcinoma cell lines: HCT116 (colon), MCF7 (breast) and MDA-MB231 (breast). Interestingly, complexes with the shorter linker, $N(CH_2)_2N$, were inactive (IC_{50} values >100 μM), whilst those with the longer oxygen-containing linker showed activity comparable to cisplatin against all cell lines.

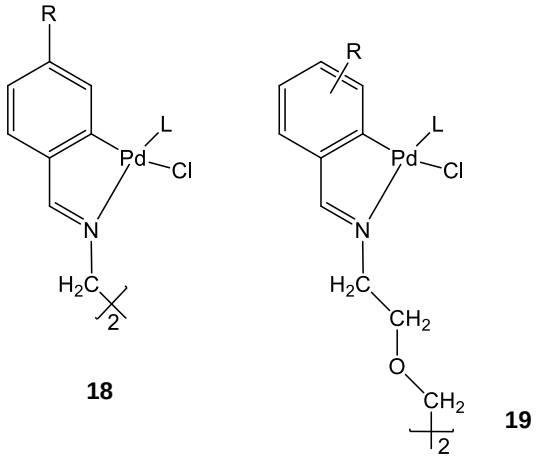

Figure 1.20: Doubly cyclopalladated diimines with linker molecules, where R = *p*-Cl, *p*-OMe, *p*-NO_2 and *o*-Cl [57].

The authors correlated the biological results to the chemical structures. The significantly higher activity observed for the longer linker was firstly ascribed to the flexibility of the linker, which would allow the formation of flexible adducts with DNA. This is the same rationalisation applied to the high activity observed for polymetallic species, such as the trinuclear platinum drug, BBR3464 [({*trans*-$PtCl(NH_3)_2$-(μ-*trans*-$[Pt(NH_3)_2(CH_2)_6NH_2)_2]$})$^{4+}$], which is currently undergoing clinical evaluation [57]. The second reasoning for the significant activity is the presence of the oxygen atoms, which allow hydrogen-bond formation and consequently enhanced hydrophilicity. Furthermore, the activity of chemotherapeutic agents has been linked to the cellular accumulation within cancer cells, where higher accumulation leads to enhanced cytotoxicity and lower toxicity. This accumulation is related to the lipophilicity, which is an indication of the amount of drug which can enter the cell. It is also well known that the balance between hydrophilicity and lipophilicity is important, which, in this instance, is obtained by the presence of the oxygen atoms in the linker molecule.

Further evaluation of these complexes showed that they were less effective at uncoiling DNA than cisplatin. This suggested that there may be an alternative mode of action to that of cisplatin, or a different target than DNA [57].

Recently, a very promising binuclear palladacycle, **AJ5**, was identified and evaluated by our group (Figure 1.21). Originally designed as a catalyst, this complex was evaluated against human breast cancer cell lines, MCF7 and MDA-MB231, and melanoma cell lines, ME1402, WM1158 and 501 mel. In each instance, **AJ5** outperformed cisplatin [21;22].

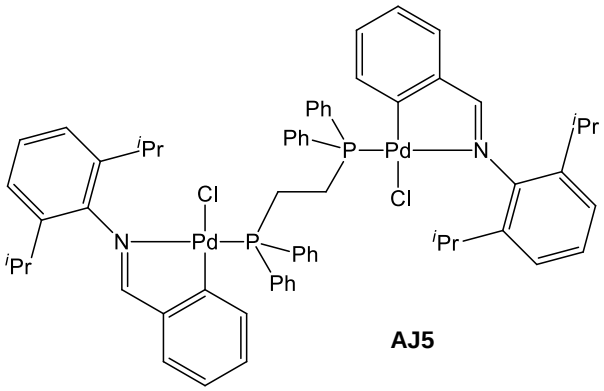

AJ5

Figure 1.21: Promising palladacycle, AJ5.

Initially, **AJ5** was evaluated against malignant melanoma cell lines, as this is an aggressive and notoriously difficult cancer to treat. It is also one of the more prevalent cancers in South Africa. *In vitro* testing showed that **AJ5** was more effective at inhibiting the cancerous cell lines compared to the normal non-malignant fibroblast cell lines, FGO, DNB and CT1 (Table 1.9). It was noted that at a concentration of 0.4 μM, **AJ5** killed 90% of the melanoma cells whilst 70% of the fibroblast cells survived. This is important since many of the severe side effects caused by chemotherapeutic agents are due to the high concentrations required to kill cancer cells. Furthermore, comparison of the IC_{50} values of **AJ5** and cisplatin, 0.2 μM and 10 μM respectively, showed that **AJ5** was approximately 50 fold more active than cisplatin. Taken together, this means that **AJ5** is likely to be far less toxic than cisplatin due to its high potency and degree of selectivity for cancerous cells over non-malignant tissue.

Table 1.9: IC_{50} results for AJ5 [21].

Cell line	IC_{50} (μM)
ME1402	0.1945
WM1158	0.2008
501 mel	0.2500
FGO	0.4049
DNB	0.4631
CT1	0.4296

Investigations into the mode of action of **AJ5** showed that it induced both apoptosis and the formation of autophagosomes. While apoptosis is a recognised mechanism of cell death, autophagy, a catabolic process which involves the degradation and recycling of macromolecules and organelles, was thought to be a mode of survival, delaying the onset of apoptosis. However, there have been a number of reports showing that autophagy can be a mode of cell death as well. To test this, autophagy was inhibited in the **AJ5**-treated cells. There

was a significant decrease in the levels of PARP cleavage (an indicator of apoptosis) and the level of cell death, thus, confirming that **AJ5**-induced autophagy is a mode of cell death.

Following the *in vitro* assays, *in vivo* assays were performed on nude mice. Cisplatin (CDDP) was used as a control. **AJ5** was found to reduce the tumour growth in these melanoma-bearing mice. Increased levels of apoptosis and autophagy were also observed. Figure 1.22 shows the autophagosomes observed in tumour sections taken from the melanoma-bearing mice. Furthermore, the treated mice showed no obvious side effects, suggesting that **AJ5** was less toxic than cisplatin, as predicted from the *in vitro* results [21].

To probe the scope of this drug, **AJ5** was also evaluated against breast cancer. As stated earlier, **AJ5** exhibited far better results than cisplatin. Not only was **AJ5** more active against the cancerous cell lines (MCF7 and MDA-MB231) than the normal fibroblast cells (FGO and DNB), but it was also more effective against the more resistant and difficult to treat cell line, MDA-MB231. The mode of cell death was once again found to be both apoptosis and autophagy [22].

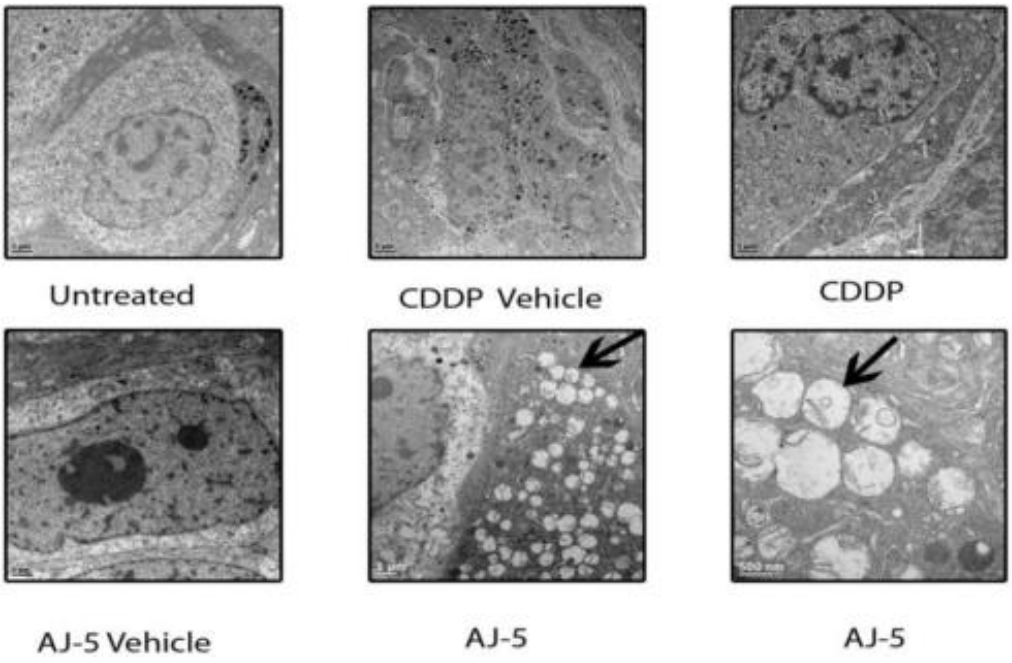

Figure 1.22: Representative transmission electron photomicrographs of tumour sections from melanoma-bearing mice showing autophagosomes, indicated by black arrows. Note the CDDP vehicle is a sodium chloride solution, whilst the AJ5 vehicle is dimethyl sulfoxide (DMSO) [58].

1.3 Conclusion

From this brief overview, it is clear that cancer is a serious disease which is still affecting a large percentage of the world population, as it has been for the past five centuries. It should also be noted that significant progress has been made in the field of chemotherapy with the most notable of these being the discovery of cisplatin in 1965. A 15% decrease in mortality since the 1990's emphasises this progress. However, problems such as toxicity and tumour cell resistance continue to hamper successful treatments. As shown here, palladium complexes have potential as viable alternatives to the current drugs, both in terms of reduced toxicity and the ability to overcome cisplatin/platinum drug resistance. The literature provides a vast library of these palladium complexes, including some very promising examples where the palladium complexes are significantly more active than cisplatin, yet not as toxic. Despite the overwhelming number of promising palladium complexes in the literature, there has been limited success with these complexes beyond the laboratory. This lack of advancement has been ascribed to the absence of data regarding the mode of action of these drugs. This need for more in-depth information justifies the ongoing research in this field.

1.4 Aims and objectives

Palladacycles have been found to be active *in vitro* as anti-cancer agents, especially those with methyl amino functionalities [44]. There are also reports of dppe-bridged palladacycles which are effective against certain cancers [11;59]. Our group has recently started testing palladacycles with imine functionalities as possible anti-cancer drugs [21;22]. Some of the binuclear complexes developed have shown promise. Palladium and platinum are both group 10 transition metals. Although they form similar structures, the reactivities vary greatly, particularly in that palladium complexes are less toxic than platinum complexes [11;59]. However, a major problem with these types of complexes is solubility, even more so, solubility in aqueous media [44].

The aim of this project was to synthesise novel water-soluble palladacycles for testing as anti-cancer agents. In an attempt to improve water solubility, the Schiff base ligands were modified by introducing hydrophilic functional groups on the aldehyde starting materials. The bridged palladacycles were then cleaved with the hydrophilic tertiary phosphine, 1,3,5-triaza-7-phosphaadamantane (PTA) or bis(tertiary phosphine) ligands [60].

The new palladacycle complexes were tested for their efficacy as anti-cancer agents *in vitro*. The tests were against mammalian breast cancer cell lines, MCF7 and MDA-MB231. Cell

viability tests were also done in the presence of the most promising complexes. In addition, DNA binding studies using the some of the prepared palladacycles were conducted.

1.5 Thesis outline

Chapter 1 – Palladium and its complexes as potential anti-cancer agents

This review provides a brief timeline of the significant developments in the design of palladium anti-cancer drugs, as well as the most promising palladacycle complexes reported in the literature.

Chapter 2 – Mononuclear palladacycles: Synthesis and characterisation

This chapter introduces palladacycle chemistry and its biological application. It also discusses the significance of mononuclear palladacycles as anti-cancer agents, as well as the synthesis and characterisation of the novel mononuclear PTA-based palladacycles.

Chapter 3 – NMR spectroscopic study of PTA-based palladacycles

The symmetric site-exchange and concentration effects of the PTA-based palladacycles were investigated by NMR spectroscopy. The study is discussed in this chapter.

Chapter 4 – Binuclear palladacycles: Synthesis and characterisation

This chapter discusses the significance of binuclear palladacycles as anti-cancer agents, as well as the synthesis and characterisation of the binuclear palladacycles.

Chapter 5 – Biological evaluation and DNA binding studies of synthesised palladacycles

All biological results and DNA binding study results are reported and discussed in this section.

Chapter 6 – Conclusions and future work

Some general conclusions and suggestions for future work are provided in this final chapter.

1.6 References

1. American Cancer Society: The History of Cancer. Accessed at www.cancer.org/cancer/cancerbasics/thehistoryofcancer/index on April 10, 2012.
2. GLOBOCAN 2012: Estimated Cancer Incidence, Mortality and Prevalence Worldwide in 2012. Accessed at www.globocan.iarc.fr/Pages/fact_sheets_cancer.aspx on February 27, 2015.
3. American Cancer Society: Global Cancer Facts & Figures. Accessed at www.cancer.org/research/cancerfactsfigures/globalcancerfactsfigures/global-facts-figures-2nd-ed on November 5, 2012.
4. J. H. Duffus and H. G. J. Worth, *Fundamental toxicology for chemists*, Cambridge: Royal Society of Chemistry, 1996.
5. V. T. DeVita, Jr. and E. Chu, *Cancer Res.*, 2008, **68**, 8643-8653.
6. A. C. F. Caires, *Anti-Cancer Agents Med. Chem.*, 2007, **7**, 484-491.
7. C. Webster, *Paracelsus: Medicine, Magic and Mission at the End of Time*. New Haven: Yale University Press, 2008.
8. Paracelsus, dritte defensio, 1538.
9. B. Rosenberg, *Pt. Metals Rev.*, 1971, **15**, 42-51.
10. M. J. McKeage, J. D. Higgins III and L. R. Kelland, *Br. J. Cancer*, 1991, **64**, 788-792.
11. E. G. Rodrigues, L. S. Silva, D. M. Fausto, M. S. Hayashi, S. Dreher, E. L. Santos, J. B. Pesquero, L. R. Travassos and A. C. F. Caires, *Int. J. Cancer*, 2003, **107**, 498-504.
12. J. Reedijk, *Chem. Rev*., 1999, **99**, 2499-2510.
13. R. A. Alderden, M. D. Hall and T. W. Hambley, *J. Chem. Ed.*, 2006, **83**, 728-734.
14. I. Ott and R. Gust, *Arch. Pharm.*, 2007, **340**, 117-126.
15. T. Boulikas, A. Pantos, E. Bellis and P. Christofis, *Cancer Therapy*, 2007, **5**, 537-583.
16. A. D. Phillips, L. Gonsalvi, A. Romerosa, F. Vizza and M. Peruzzini, *Coord. Chem. Rev.*, 2004, **248**, 955-993.
17. W. H. Ang, A. Casins, G. Sava and P. J. Dyson, *J. Organomet. Chem.*, 2011, **696**, 989-998.
18. W. H. Ang, E. Daldini, C. Scolaro, R. Scopelliti, L. Juillerat-Jeannerat and P. J. Dyson, *Inorg. Chem.*, 2006, **45**, 9006-9013.
19. K. H. Antman, *Oncologist*, 2001, **6**, 1-2.
20. B. Desoize, *Anticancer Res.*, 2004, **24**, 1529-1544.
21. S. Aliwaini, A. J. Swarts, A. Blanckenberg, S. F. Mapolie and S. Prince, *Biochem. Pharmacol.*, 2013, **86**, 1650-1663.
22. S. Aliwaini, J. Peres, W. L. Kröger, A. Blanckenberg, J. de la Mare, A. L. Edkins, S. Mapolie and S. Prince, *Cancer Lett.*, 2015, **357**, 206-218.

23. J.L. Butour, S. Wimmer, F. Wimmer and P. Castan, *Chemico. Biol. Interact.*, 1997, **104**, 165-178.
24. National Cancer Institute, NCI Drug Dictionary: *Palladium*. Accessed at http://www.cancer.gov/publications/dictionaries/cancer-drug?search=palladium&contains=true on January 7, 2016.
25. P. M. Devlin, *Brachytherapy: Applications and Techniques*, Philadelphia: Lippincott Williams and Wilkins, 2007, 50-51.
26. National Cancer Institute and United States Food and Drug Administration, *40 Years of progress against cancer: Advances since the National Cancer Act of 1971*, 2005. Accessed at http://www.cancer.net/about-us/about-asco/progress-against-cancer on January 8, 2016.
27. Radioactive seeds. Accessed at http://www.aboutcancer.com/seed6.htm on December 17, 2014.
28. S. Hosseini, M. Sadeghi and V. Ataeinia, *Medical Physics*, 2009, **36**, 3080-3085.
29. D. Baltas, G. Lymperopoulou, E. Löffler and P. Mavroidis, *Medical Physics*, 2010, **37**, 2572-2586.
30. N. V. Koudinova, J. H. Pinthus, A Brandis, O. Brenner, P. Bredel, J. Ramon, Z. Eshhar, A. Scherz and Y. Salomon, *Int. J. Cancer*, 2003, **104**, 782-789.
31. J. H. Woodhams, A. J. MacRobert, M. Novelli and S. G. Bown, *Int. J. Cancer*, 2006, **118**, 477-482.
32. RADA Radiation Application Development Association. Accessed at http://www.rada.or.jp/database/home4/normal/ht-docs/member/synopsis/030145.html on January 5, 2016.
33. A. S. Abu-Surrah, H. H. Al-Sa'doni and M. Y. Abdalla, *Cancer Ther.*, 2008, **6**, 1-10.
34. M. J. Cleare, *Coord. Chem. Rev.*, 1974, **12**, 349-405.
35. M. J. Cleare and J. D. Hoeschele, *Bioinorg. Chem.*, 1973, **2**, 187-210.
36. R. D. Graham and D. R. Williams, *J. Inorg. Nucl. Chem.*, 1979, **41**, 1245-1249.
37. A. Furst, *Chemistry of Chelation in Cancer*, C.C. Thomas, Springfield, Illinois: *American Lectures in Living Chemistry Series*, 1963.
38. P. Castan, S. Wimmer, E. Colacio-Rodriguez, A. L. Beauchamp and S. Cros, *J. Inorg. Biochem.*, 1990, **38**, 225-239.
39. D. S. Gill, *Platinum Coordination Complexes in Cancer Chemotherapy*, 1984, M. P.Hacker, E. B. Douple, and I. K. Krakoff, Eds., Boston: Martinus Nijhoff Publishing, 267-278.
40. S. Kirschner, Y.- K. Wei, D. Francis and J. G. Bergman, *J. Med. Chem.*, 1966, **9**, 369-372.

41. B. T. Khan, J. Bhatt, K. Najmuddin, S. Shamsuddin and K. J. Annapoorna, *J. Inorg. Biochem.*, 1991, **44**, 55-63.
42. C. Navarro-Ranninger, F. Zamora, J. M. Pérez, I. López-Solera, S. Martínez-Carrera, J. R. Masaguer and C. Alonso, *J. Inorg. Biochem.*, 1992, **46**, 267-279.
43. C. Navarro-Ranninger, J. M. Pérez, F. Zamora, V. M. González, J. R. Masaguer and C. Alonso, *J. Inorg. Biochem.*, 1993, **52**, 37-49.
44. J. D. Higgins III, L. Neely and S. Fricker, *J. Inorg. Biochem.*, 1993, **49**, 149-156.
45. G. R. Newkome, W. E. Puckett, G E. Kiefer, V. K. Gupta, F. R. Fronczek, D. C. Pantaleo, G. L. McClure, J. B. Simpson and W. A. Deutsch, *Inorg. Chem.*, 1985, **24**, 811-826.
46. A. R. Kapdi and I. J. S. Fairlamb, *Chem. Soc. Rev.*, 2014, **43**, 4751-4777.
47. T. A. Brown, Genomes. 2nd edition. Oxford: Wiley-Liss; 2002. Chapter 14, Mutation, Repair and Recombination. Accessed at http://www.ncbi.nlm.nih.gov/books/NBK21114/ on April 27, 2015.
48. J. W. Suggs, J. D. Higgins III, R. W. Wagner and J. T. Millard, *Metal-DNA Chemistry*, 7, Tullius, Ed., Washington, D.C.: American Chemical Society Symposium Series No. 402, 1989, p146-158.
49. T. A Al-Allaf and L. J Rashan, *Boll. Chem. Farmac.*, 2001, **140**, 205-210.
50. L. j. Tušek-Božić, I. Matijašić, G. Bocelli, G. Calestani, A. Furlani, V. Scarcia and A. Papaioannou, *J. Chem. Soc. Dalton Trans.*, 1991, 195-201.
51. M. Ćurić, L. j. Tušek-Božić, D. Vikić-Topić, V. Scarcia, A. Furlani, J. Balyarini and E. de Clercq, *J. Inorg. Biochem.*, 1996, **63**, 125-142.
52. A. S. Abu-Surrah, T. A. K. Al-Allaf, L. J. Rashan, M. Klinga abd M. Leskelä, *Eur. J. Med. Chem.*, 2002, **37**, 919-922.
53. S. Ray, R. Mohan, J. K. Singh, M. K. Samantaray, M. M. Shaikh, D. Panda and P. Ghosh, *J. Am. Chem. Soc.*, 2007, **129**, 15042-15053.
54. R. A. Haque, A. W. Salman, S. Badagumpi, A. A. Abdullah and A. M. S. A. Majid, *Metallomics*, 2013, **5**, 760-769.
55. E. Guerrero, S. Miranda, S. Lüttenberg, N. Fröhlich, J.-M. Koenen, F. Mohr, E. Cerrada, M. Laguna and A. Mendía, *Inorg. Chem.,* 2013, **52**, 6635-6647.
56. S. Miranda, E. Vergara, F. Mohr, D. de Vos, E. Cerrada, A. Mendía and M. Laguna, *Inorg. Chem.*, 2008, **47**, 5641-5648.
57. J. Albert, R. Bosque, M. Cadena, L. D'Andrea, J. Granell, A. González, J. Quirante, C. Calvis, R. Messeguer, J. Badía, L. Baldomà, T. Calvet, and M. Font-Bardia, *Organomet.*, 2014, **33**, 2862-2873.
58. S. Aliwaini, PhD Thesis, University of Cape Town, 2014.

59. J. Spencer, A. Casini, O. Zava, R. P. Rathnam, S. K. Velhanda, M. Pfeffer, S. K. Callear, M. B. Hursthouse and P. J. Dyson, *Dalton Trans.*, 2009, **48**, 10731-10735.
60. J. Bravo, S. Bolaño, L. Gonsalvi and M. Peruzzini, *Coord. Chem. Rev.*, 2010, **254**, 555-607.

Chapter 2
Mononuclear Palladacycles: Synthesis and Characterisation

2.1 Introduction

Palladacycles are defined as any palladium compound containing at least one palladium-carbon sigma bond which is intramolecularly stabilised by one or two neutral two-electron donors (including nitrogen, phosphorous, oxygen and sulfur), whilst the organic moiety acts as a carbon-anionic four- or six-electron donor ligand. These complexes were first reported by Cope *et al*. [1], who synthesised such species by cyclopalladation of azobenzene derivatives [2-4]. Palladacycles can be classified as one of two types with those being either anionic four-electron donors or anionic six-electron donors, as shown in Figure 2.1.

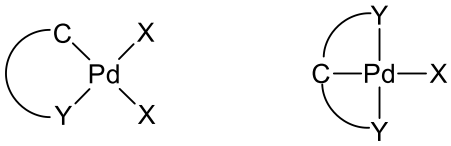

Figure 2.1: General structure of C-anionic four-electron donor (left) and C-anionic six-electron donor (right) type palladacycles, where X is an anionic ligand and Y is a two-electron donor [2].

After the initial discovery by Cope *et al*. [1], a number of years passed before palladacycles became a popular area of research. This occurred when Herrmann *et al*. produced a palladacycle of the tri-*o*-tolyl-phosphane ligand as a precatalyst for Heck and other cross-coupling reactions catalysed by palladium [5]. This discovery increased interest from the chemical industry as palladacycles could be used to elaborate lower value substrates which were currently in use. Since then, palladacycles have become synonymous with Heck and other C-C coupling reactions [2;4]. However, in the last four decades, a wide range of palladacycles have been synthesised and studied for diverse applications. Thus, the chemistry of these complexes is fairly well understood and documented [2].

2.1.1 Palladacycle chemistry

The rich chemistry associated with palladacycles is due to the facile redox interchange between the palladium(II) and palladium(0) oxidation states. Another contributing property is the compatibility of palladacycles with most functional groups, which sets them apart from

several other transition metal complexes [4]. Complimenting this rich chemistry are properties such as stability and robustness, availability, ease of handling and versatility, making these complexes attractive to industry and the research community. Besides these assets, palladacycles are also easily and rapidly synthesised [2;4].

There are a number of methods used to synthesise palladacycles, including C-H bond activation, transmetallation and oxidative addition. Of these, C-H bond activation, which often involves orthopalladation, is the simplest and most direct method. It is also the method which was employed to synthesise the series of mononuclear palladacycles reported here. It usually involves the use of a tetrachloropalladated salt and a base, or palladium acetate and acetic acid or benzene. The resultant palladacycles are usually five- or six-membered chelate rings [4].

2.1.2 Biological application of palladacycles

The appeal of palladacycles for medicinal and biological applications arises from their rich chemistry, ease of synthesis and handling (due to the stability), as well as the potential for rapid library development. These properties are especially significant when one considers the application of these complexes in cancer treatment, where there is still no clear structure-activity guideline for palladacycles.

By using existing information on palladacycle synthesis and chemistry, a large number of complexes can be generated in a short period of time, allowing more time for biological evaluation of the complexes. The stability allows for simple long term storage and ease of testing [4]. Furthermore, there are a number of articles which compare palladacycles to their platinum analogues and often the use of palladacycles has been shown to be more advantageous. The choice of cyclometallated- over non-cyclometallated palladium complexes is due to the former's increased stability, slower reaction kinetics and consequently lower toxicity, as non-cyclometallated complexes of palladium were found to be highly labile in biological fluids [4].

As described in the previous chapter, palladacycles can be either mononuclear, binuclear or multinuclear complexes. In this chapter, we focus on mononuclear palladacycles.

The consideration of mononuclear over binuclear palladacycles is mainly driven by the need to improve solubility. In 1993, Higgins *et al*. prepared dimeric palladacycles for testing as anti-cancer agents; however, the limited solubility led them to consider mononuclear analogues [2]. Since the mononuclear analogues have lower molecular weights, it was reasoned that

these palladacycles would be more soluble. The authors made use of various amines to cleave the chloro-bridged dimeric species, obtaining much more soluble mononuclear analogues (Scheme 2.1). However, it was found that the mononuclear species were not water-soluble, but were quite stable in organic solvents. The mononuclear palladacycles were tested against a tumour panel of human carcinomas and most complexes exhibited uniform cytotoxicity for all cell lines in the range of 10 μg/mL [2].

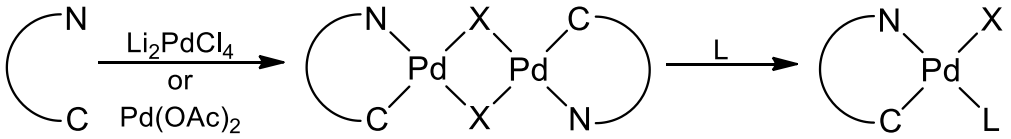

Scheme 2.1: General synthetic scheme for dimeric and monomeric palladacycles prepared by Higgins III *et al*. Where X = Cl or OAc and L = amine [2].

Despite the improved solubility, most mononuclear palladacycles have been reported to be less cytotoxic than their dimeric analogues. One of the many examples of this trend was presented by Karami *et al*. in 2012 [6]. The IC_{50} values of the two mononuclear complexes, Pd(*C*,*N*)-$C_6H_4CH_2NH$(Et)Cl(Py) and Pd(*C*,*N*)-$C_6H_4CH_2NH$(*t*-Bu)Cl(PPh_3) were approximately two-fold higher than those for the binuclear analogue, Pd_2(*C*,*N*-dmba)$_2$(μ-dppe)$(Cl)_2$ [6], as shown in the Table 2.1.

Table 2.1: IC_{50} values (μM ± SD) of palladacycles against tumour panel, as reported by Karami *et al.* [6].

Complex	Hela	HT-29	K562	MDA-MB-468
Pd(*C*,*N*)-$C_6H_4CH_2NH$(Et)Cl(Py)	7.5 ± 0.60	4.3 ± 0.04	3.7 ± 0.04	2.4 ± 0.05
Pd(*C*,*N*)-$C_6H_4CH_2NH$(*t*-Bu)Cl(PPh_3)	7.7 ± 0.40	5.3 ± 0.28	3.3 ± 0.04	3.3 ± 0.05
Pd_2(*C*,*N*-dmba)$_2$(μ-dppe)$(Cl)_2$	2.1 ± 0.05	2.2 ± 0.04	1.4 ± 0.06	2.3 ± 0.01

As stated in the aims, the series of mononuclear palladacycles reported here was based on a dimeric palladacycle (**AJ5**) which had been previously synthesised in our laboratory [7] and has been shown to exhibit significant anti-cancer activity. However, its activity is hindered by poor solubility. Since **AJ5** is not water-soluble and dimeric palladacycles are known for their poor solubility, it was decided to synthesise mononuclear analogues, using the rationale proposed by Higgins *et al*. that lower molecular weight products are more soluble. Hence, the aim was to replace the dppe ligand with a water-soluble tertiary phosphine, 1,3,5-triaza-7-phosphaadamantane (PTA) (Figure 2.2) [8]. The decision to use PTA, rather than the more directly comparable triphenylphosphane, PPh_3, was based on the trend of reduced cytotoxicity for mononuclear palladacycles relative to their dimeric analogues, as discussed above. PTA is not only a water soluble phosphine, but it is non-toxic and biocompatible, which may lead to a less significant reduction in cytotoxicity or even improved cytotoxicity [9]. Additionally, it was

set out to investigate the effects of various ortho substituents (R) on solubility and efficacy of these complexes.

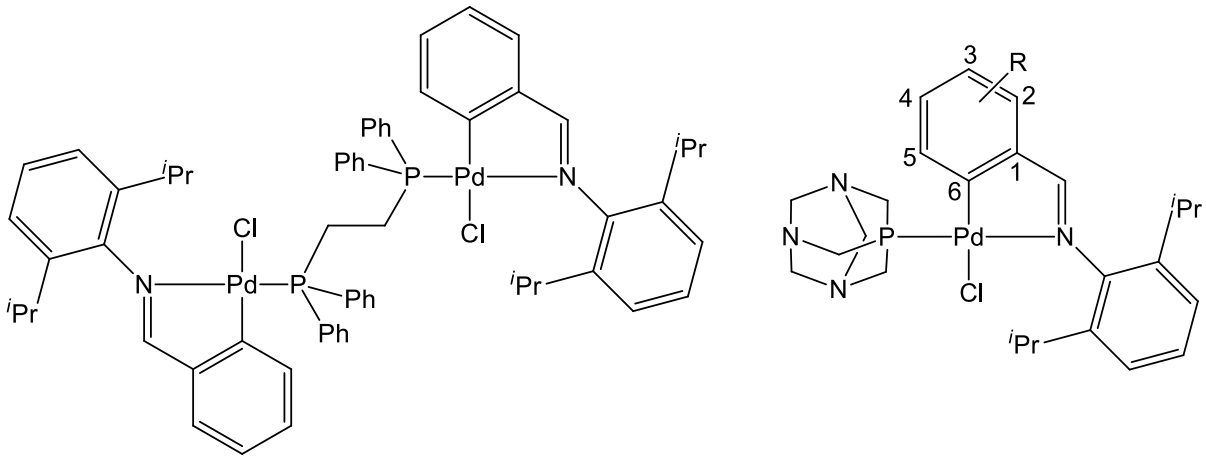

Figure 2.2: Structure of AJ5 (left) and mononuclear analogues (right) where R = 2-H, 2-Cl, 2-Br, 2-Me, 4-Me, 2-F, 2-NO_2 or 2-OMe.

2.2 Synthetic route

The series of mononuclear palladacycles was synthesised in a three-step process. The monosubstituted ligands were synthesised by Schiff base condensation of 2,6-diisopropylaniline with various monosubstituted benzaldehydes. These Schiff base ligands were cyclopalladated by the reaction of the ligands with the palladium precursor, bis(acetonitrile)palladium dichloride, $[(MeCN)_2PdCl_2]$. An excess of sodium acetate was used as the base. The resulting μ-chloro bridged palladacycles were then cleaved by the addition of a basic tertiary phosphine, PTA, producing the desired mononuclear palladacycle target molecules for anti-cancer testing.

The synthesised complexes were characterised by FT-IR- and NMR (^{1}H, ^{13}C and ^{31}P) spectroscopy, mass spectrometry and microanalysis, as well as melting point- and single crystal analysis, where applicable. In addition, the solubilities were determined in water, dimethyl sulfoxide and a water/dimethyl sulfoxide mixtures.

2.3 Results and Discussion

2.3.1 Preparation of Schiff base ligands

The Schiff base ligands were synthesised as described by Mungwe *et al*. [7]. The ligands were prepared by reacting various monosubstituted benzaldehydes with 2,6-diisopropylaniline in dry ethanol, as shown in Scheme 2.2.

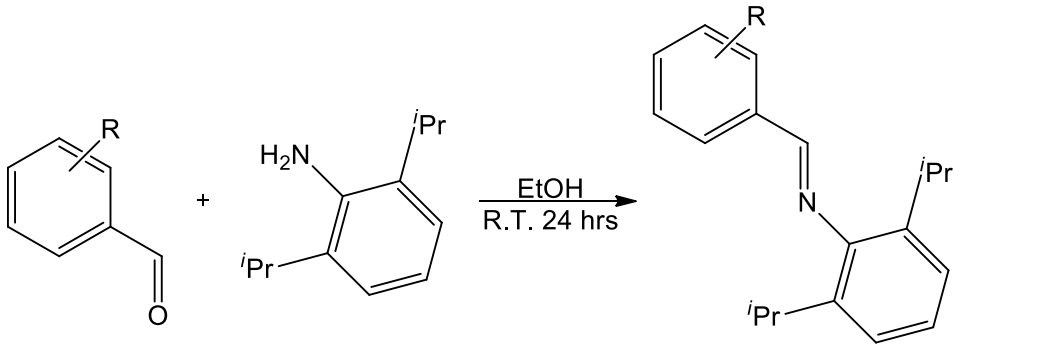

L1: R = 2-H **L2**: R = 2-Cl

L3: R = 2-Br **L4**: R = 2-Me

L5: R = 4-Me **L6**: R = 2-F

L7: R = 2-NO_2 **L8**: R = 2-OMe

Scheme 2.2: Synthetic scheme for Schiff base ligands.

The ligands, **L1**-**L5**, have been prepared previously by our group [10;11] and **L6** and **L7** have been reported previously [12;13]. The synthetic method employed in this project produced higher yields for **L6** and an alternative synthetic method for the previously reported **L7**. **L8**, however, is a novel ligand. The ligands were isolated as yellow crystalline solids in low to high yields (29-81%). The ligands were found to be stable both in the solid state, as well as in solution. As reported [7], the ligands were soluble in polar organic solvents.

The ligands were characterised by various analytical techniques and these are discussed below. Table 2.2 contains some general characterisation data for comparison of the various analogues.

FT-IR spectroscopy was used to determine whether the imine had been formed successfully. The strong aldehyde carbonyl (C=O) stretch band for an aldehyde conjugated with a phenyl ring occurs in the region 1700-1660 cm^{-1} [14]. The imine C=N stretch occurs in the region 1690-1640 cm^{-1} and has variable-intensity absorption. The disappearance of the C=O band and the appearance of the C=N band was monitored using FT-IR spectroscopy. In all cases, there were no bands in the $\nu_{C=O}$ region and a medium to strong band in the $\nu_{C=N}$ region, as shown in the spectrum below (Figure 2.3) [14]. The $\nu_{C=N}$ bands of the various ligands prepared, occurred between 1640-1625 cm^{-1}.

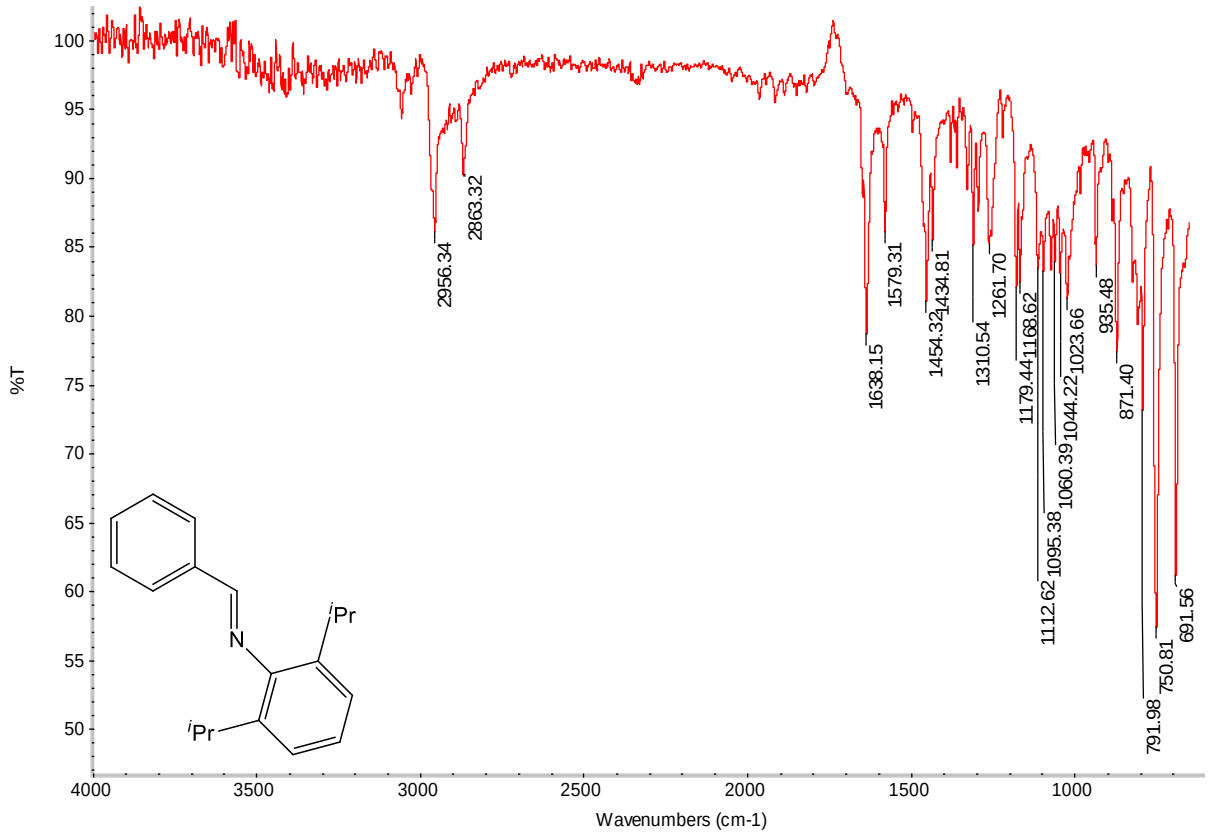

Figure 2.3: FT-IR spectrum of L1 (4000-600 cm^{-1}).

Table 2.2: Analytical data for ligands, L1-L8.

Ligand	FT-IR ($\nu_{C=N}$, cm^{-1})[a]	ESI-MS (*m/z*) $[M+H]^+$	Melting point (˚C)[b]
L1*	1638	266	63-64
L2*	1626	301	52-53
L3*	1627	345	78-79
L4	1629	280	62-66
L5*	1636	280	93-94
L6	1631	284	75-79
L7	1643	311	63-66
L8	1638	296	124-128

[a]IR spectra were recorded neat using an ATR accessory. [b]Melting points were recorded in glass capillaries and are reported as uncorrected. *Data from previously published results [10].

^{1}H NMR spectra of the ligands showed the imine signal in the region 8.22-8.76 ppm as a singlet. It is easily identified as the signal which occurs furthest downfield. No aldehyde or amine signals were present in the 9.00-10.0 ppm and 0.50-4.00 ppm regions, respectively.

The complexity of the aromatic region (overlapping multiplets), also confirms the formation of the ligand. The septet observed at approximately 3.00 ppm represents the methine protons of the isopropyl substituents and the doublet at approximately 1.20 ppm represents the methyl groups of the isopropyl moieties. The presence of only one methine and one methyl signal suggest that the two isopropyl groups are in the same chemical environment. Hence, there is free rotation of the 2,6-diisopropylaniline group and the two isopropyl groups, around the N-C bond and the C-C bonds, as shown in Figure 2.4.

Table 2.3 contains the ^{1}H NMR spectroscopy data for the Schiff base ligands. From the data, it is clear that the imine signal shifts relative to the substituent on the benzene ring. The difference in the chemical shift of the 2-methyl and 4-methyl protons indicates that the para position (4) is more shielded from the effects of the imine than the ortho position (2). The more electronegative halogen analogues (**L2**, **L3** and **L6**) show imine signals which are shifted more downfield compared to the chemical shift of the unsubstituted analogue (**L1**). The electron-withdrawing nitro group caused a downfield shift, as was expected; however, the methoxy group (**L8**) was expected to cause a shift similar to that of the methyl group or an even further upfield shift, as it is a donating group, yet the observed chemical shift is close to that of the nitro analogue (**L7**). Although unexpected, literature reports showed that methoxy substituents can be electron withdrawing or electron donating, depending on the electronic interactions in the system [15].

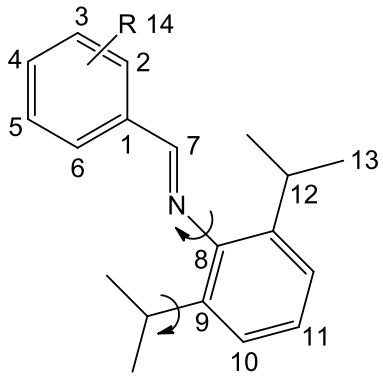

Figure 2.4: Free rotation of 2,6-diisopropylaniline moiety in ligands.

Table 2.3: ^{1}H NMR data for ligands, L1-L8.

Ligand	C*H*=N (H^{7})	Aromatic Region	Aliphatic region			
			Ar-OC*H*$_3$ (H^{14})	$(CH_3)_2CH$ (H^{12})	Ar-C*H*$_3$ (H^{14})	$CH(CH_3)_2$ (H^{13})
L1*	8.22 (s, 1H)	7.92-7.95 (m, 2H, $H^{2,6}$); 7.52-7.54 (m, 3H, $H^{3,4,5}$); 7.09-7.20 (m, 3H, $H^{10,11}$)		2.99 (sept, 2H, $^{3}J_{H-H}$ 6.9 Hz)		1.19 (d, 12H, $^{3}J_{H-H}$ 6.9 Hz)
L2*	8.76 (s, 1H)	8.27-8.29 (m, 1H, H^{3}); 7.44-7.48 (m, 3H, $H^{4,5,6}$); 7.12-7.20 (m, 3H, $H^{10,11}$)		2.98 (sept, 2H, $^{3}J_{H-H}$ 6.9 Hz)		1.20 (d, 12H, $^{3}J_{H-H}$ 6.8 Hz)
L3*	8.60 (s, 1H)	8.27 (dd, 1H, $^{3}J_{H-H}$ 7.8 Hz, $^{4}J_{H-H}$ 1.9 Hz, H^{3}); 7.66 (dd, 1H, $^{3}J_{H-H}$ 8.1 Hz, $^{4}J_{H-H}$ 1.3 Hz, H^{6}); 7.44-7.49 (m, 1H, H^{4}); 7.35-7.40 (m, 1H, H^{5}); 7.12-7.22 (m, 3H, $H^{10,11}$)		2.99 (sept, 2H, $^{3}J_{H-H}$ 6.9 Hz)		1.21 (d, 12H, $^{3}J_{H-H}$ 6.9 Hz)
L4*	8.52 (s, 1H)	8.11 (dd, 1H, $^{3}J_{H-H}$ 7.6 Hz, $^{4}J_{H-H}$ 1.4 Hz, H^{6}); 7.34-7.44 (m, 2H, $H^{4,5}$); 7.27-7.29 (m, 1H, H^{3}); 7.11-7.20 (m, 3H, $H^{10,11}$)		3.02 (sept, 2H, $^{3}J_{H-H}$ 7.0 Hz)	2.56 (2, 3H)	1.20 (d, 12H, $^{3}J_{H-H}$ 7.0 Hz)
L5*	8.18 (s, 1H)	7.87 (d, 2H, $^{3}J_{H-H}$ 8.0 Hz, $H^{2,6}$); 7.37 (d, 2H, $^{3}J_{H-H}$ 7.8 Hz, $H^{3,5}$); 7.13-7.22 (m, 3H, $H^{10,11}$)		3.04 (sept, 2H, $^{3}J_{H-H}$ 6.8 Hz)	2.49 (s, 3H)	1.22 (d, 12H, $^{3}J_{H-H}$ 6.8 Hz)
L6	8.53 (s, 1H)	8.21-8.27 (m, 1H, H^{3}); 7.47-7.52 (m, 1H); 7.27-7.33 (m, 1H); 7.10-7.20 (m, 4H, $H^{10,11}$)		2.98 (sept, 2H, $^{3}J_{H-H}$ 6.9 Hz)		1.20 (d, 12H, $^{3}J_{H-H}$ 6.9 Hz)
L7	8.65 (s, 1H)	8.35 (dd, 1H, $^{3}J_{H-H}$ 7.8 Hz, $^{4}J_{H-H}$ 1.6 Hz); 8.13 (dd, 1H, $^{3}J_{H-H}$ 8.2 Hz, $^{4}J_{H-H}$ 1.3 Hz); 7.78-7.83 (m, 1H); 7.65-7.71 (m, 1H); 7.12-7.22 (m, 2H); 7.06 (d, 1H, $^{3}J_{H-H}$ 7.6 Hz)		3.03 (sept, 2H, $^{3}J_{H-H}$ 6.9 Hz)		1.22 (d, 12H, $^{3}J_{H-H}$ 6.8 Hz)
L8	8.76 (s, 1H)	8.32 (dd, 1H, $^{3}J_{H-H}$ 7.6 Hz, $^{4}J_{H-H}$ 1.8 Hz); 7.58-7.61 (m, 1H); 7.28 (d, 1H, $^{3}J_{H-H}$ 7.6 Hz); 7.20-7.23 (m, 2H); 7.10 (d, 1H, $^{3}J_{H-H}$ 8.2 Hz)	3.88 (s, 3H)	3.02 (sept, 2H $^{3}J_{H-H}$ 7.0 Hz)		1.20 (d, 12H, $^{3}J_{H-H}$ 6.5 Hz)

*Data from previously published results [10;11]. Spectra run in $CDCl_3$ at 25 °C. Chemical shifts reported in ppm, referenced relative to residual solvent peak. Superscript numbering denotes proton assignments as per Figure 2.4.

Electrospray ionisation mass spectrometry (ESI-MS) was used as further confirmation that the correct product was formed. The spectra show a large base peak and in some cases, a few smaller peaks. The base peak corresponds to the molecular ion, $[M+H]^+$, of the ligand, as shown in Figure 2.5. The isotopic clusters result from nitrogen and its isotopes, as well as the various halogen isotopes in the case of the ortho-halogenated analogues. Comparison of the fragmentation pattern for the $[M+H]^+$ fragment with the simulated pattern showed that the assignment of the fragment was correct.

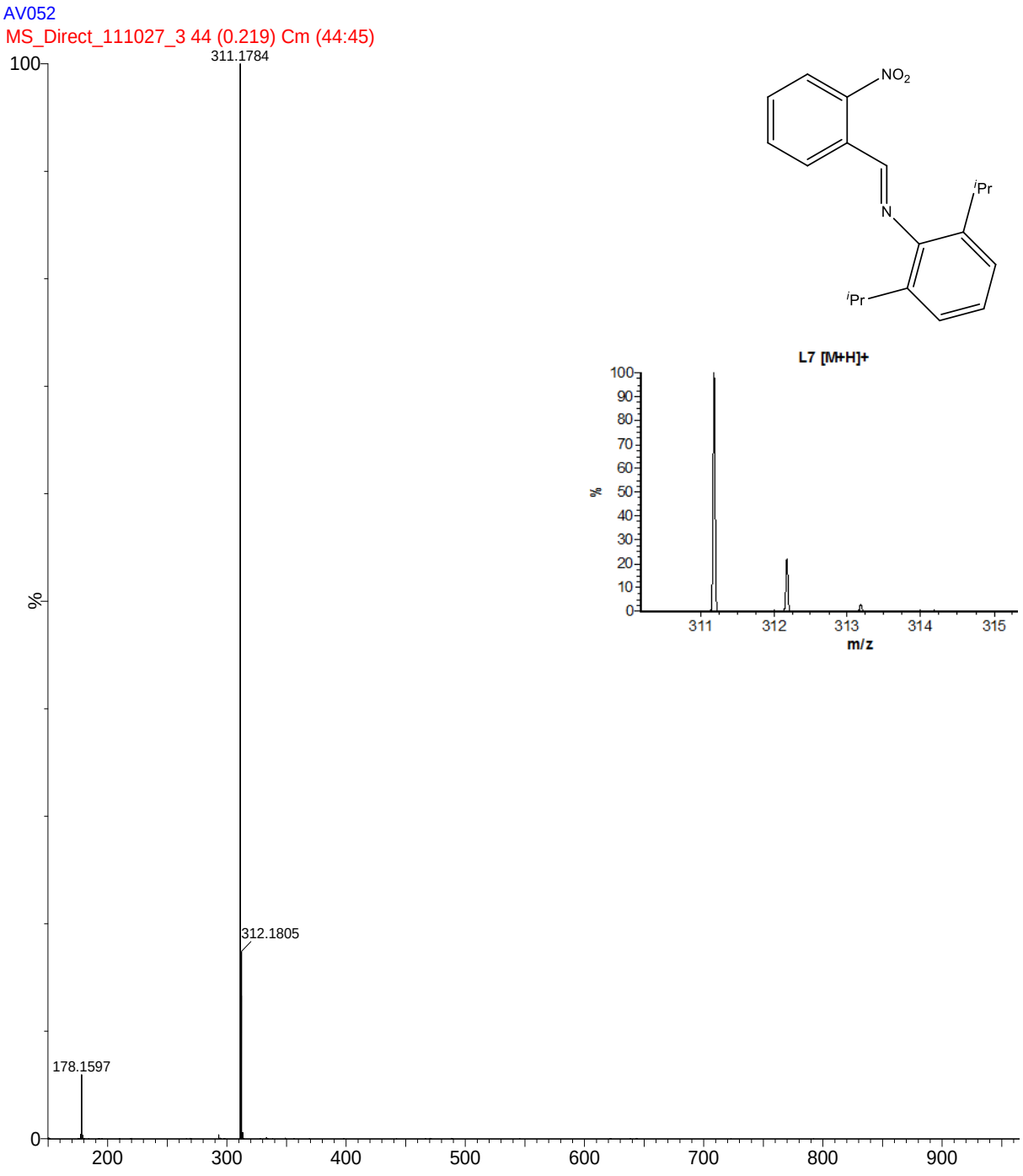

Figure 2.5: Mass spectrum of L7 and simulated fragment pattern for $[M+H]^+$ fragment.

A crystal structure was obtained for **L7**, the nitro analogue. The crystals were obtained by recrystallisation from DCM layered with cold methanol at low temperature (-16 °C). The crystal structure was determined by single crystal X-ray diffraction.

The asymmetric unit (ASU) contains two molecules, A and B, as shown in Figure 2.6, which have slight structural differences. The planes of the aromatic rings in A are almost perpendicular, whilst the angle between those in B is much smaller. This is evident from the torsion angle C1-C7-N2-C8 (τ), which is different for A (τ_A = 177.6(1)˚) and B (τ_B = -173.3(1)˚). These structural differences result in different orientations and different packing. Alternating columns of A and B are observed in the crystal packing (Figure 2.7) as an ···ABAB··· array of offset columns which repeat along the *c*-axis. The crystal structure also shows a complex network of C-H···O and C-H···N inter- and intramolecular hydrogen bonds. Molecules A and B are linked by two intermolecular C-H···O bonds, C3A-H3A···O1B and C4B-H4B···O2A. Further numerical data on the hydrogen bonds can be found in Table 2.4. Additionally, there is an O1A···O1B intermolecular interaction between the nitro groups of A and B molecules, with a bond distance of 2.900(1) (Figure 2.7). Other crystallographic data can be found in Table 2.5 and geometric parameters can be found in Appendix 1, Tables A1.1 and A1.2.

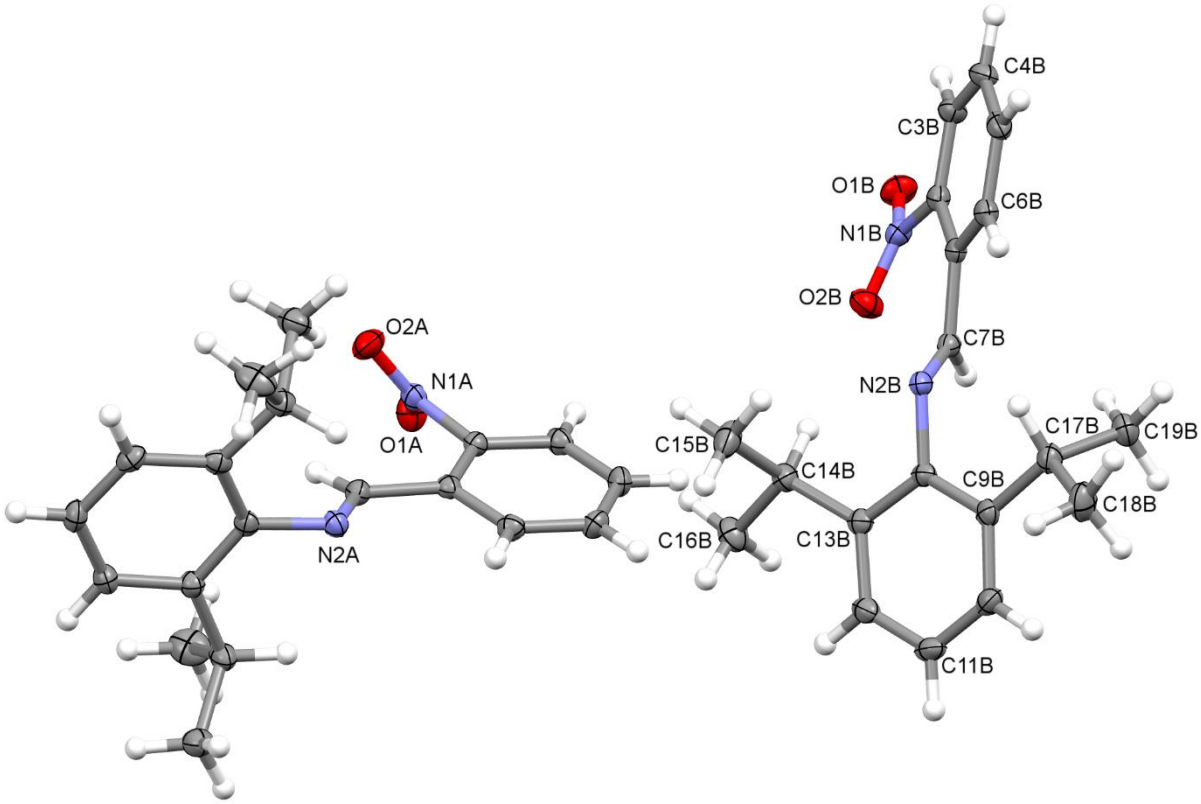

Figure 2.6: Asymmetric unit (ASU) for Schiff base ligand, L7, with thermal ellipsoids rendered at the 50% probability level. H atoms are rendered as spheres with arbitrary fixed radii. Selected non-H atoms are labelled.

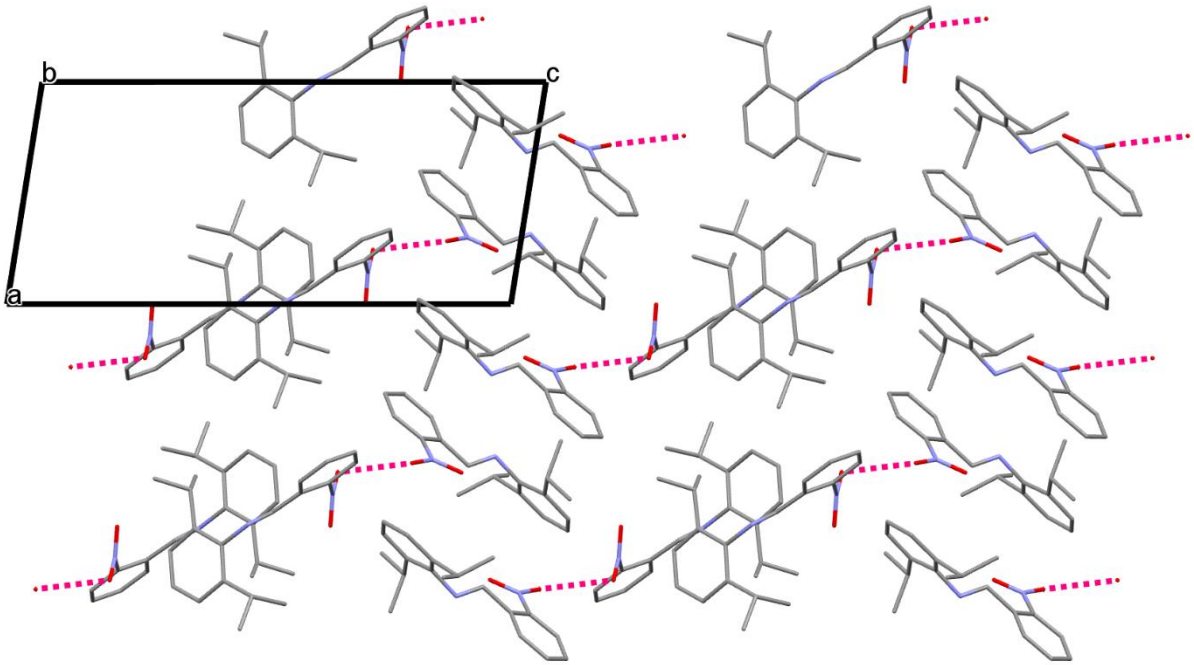

Figure 2.7: Crystal packing showing alternating columns of A and B along the *c*-axis and the O1A···O1B intermolecular interaction. Hydrogen atoms have been omitted for clarity.

Table 2.4: Numerical details of the hydrogen bonds in L7.

D-H···A	D-H (Å)	H···A (Å)	D···A (Å)	D-H···A (º)
C3A—H3A···O1B^{i}	0.95	2.40	3.269(2)	152
C7A—H7A···O2A	0.95	2.47	2.928(2)	110
C14A—H14A···N2A	1.00	2.48	2.969(2)	109
C14B—H14B···O2B	1.00	2.57	3.572(2)	178
C15B—H15D···N2B	0.98	2.56	3.180(2)	121
C17A—H17A···N2A	1.00	2.38	2.805(2)	104
C17B—H17B···N2B	1.00	2.42	2.814(2)	103
C18B—H18I···O2B^{ii}	0.98	2.57	3.295(2)	131
C19B—H19G···O2B^{iii}	0.98	2.60	3.514(2)	155

Note: D-H = proton donor group, A = proton acceptor atom;
Symmetry codes: (i) -*x*+1, -*y*+1, -*z*; (ii) *x*, *y*+1, *z*; (iii) -*x*+2, -*y*+2, -*z*.

Table 2.5: Crystallographic data for L7.

Parameter	L7
Chemical formula	$C_{19}H_{22}N_2O_2$
Formula weight	310.39
Temperature (K)	100(2)
Wavelength (Å)	0.71073
Crystal system	Triclinic
Space group	*P*-1
a (Å)	9.0009(13)
b (Å)	10.1457(14)
c (Å)	19.758(3)
α (°)	100.105(2)
β (°)	95.811(2)
γ (°)	105.637(2)
V (Å^3)	1689.4(4)
Z	4
D_{calc} [Mg/m^3]	1.220
Absorption coefficient (mm^{-1})	0.080
F(000)	664
Final *R* indices [$I>2\sigma(I)$]	R_1 = 0.0451, wR_2 = 0.1010
Reflections collected	20633
Completeness to θ_{max} (%)	91.6
Goodness-of-fit on F^2	1.040
Largest difference peak and hole (e Å^{-3})	0.287, -0.216

2.3.2 μ-Chloro palladacycles

Cyclopalladation of the Schiff base ligands, via electrophilic C-H bond activation was carried out to obtain μ-chloro palladacycles. The synthesis was performed as described by Mungwe *et al.* [7], using two equivalents of Schiff base ligand, two equivalents of bis(acetonitrile)palladium dichloride and four equivalents of sodium acetate to form one equivalent of bridged palladacycle (Scheme 2.3). The duration of the reaction depended on the nature of the Schiff base ligand [7].

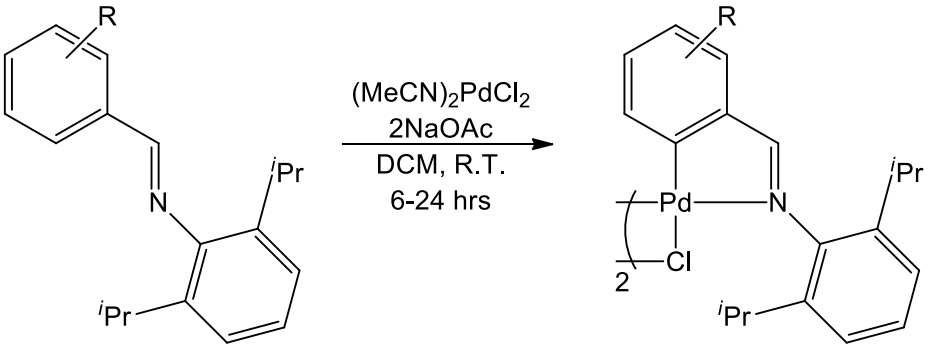

B1: R = 2-H **B2**: R = 2-Cl

B3: R = 2-Br **B4**: R = 2-Me

B5: R = 4-Me **B6**: R = 2-F

B7: R = 2-NO_2 **B8**: R = 2-OMe

Scheme 2.3: Synthetic scheme for μ-chloro palladacycles.

The chloro-bridged palladacycles, **B1**-**B5**, have been reported previously [10;11], whilst **B6**-**B8** are novel. The complexes were isolated as yellow solids (amorphous or crystalline), except for the nitro analogue which is an orange solid. The yields were in the range of 33-89%. The palladacycles are stable in both the solid state and in solution. All analogues were found to be soluble in chlorinated organic solvents, but **B2** and **B3** were found to be only sparingly soluble. Characterisation of the palladacycles involved the use of various analytical techniques, as will be discussed below.

FT-IR spectroscopy was used to determine if the cyclopalladation had occurred. The imine $\nu_{C=N}$ stretch of the bridged palladacycle is expected to shift to a lower wavenumber if coordination occurs. If the coordination of the nitrogen atom to the palladium is through its lone pair, the shift is expected to be small, approximately 30 cm^{-1}. However, if coordination through the C=N double bond, via a η^2 interaction, would result in a larger shift [16]. For all the bridged complexes, there was only one medium to strong band in the $\nu_{C=N}$ region, as shown in the spectrum below [14]. The $\nu_{C=N}$ bands of the various complexes occur at lower wavenumbers, approximately 30-40 cm^{-1} lower than those of the ligands, confirming that the coordination to the palladium metal centre is through the nitrogen lone pair (Table 2.6).

As shown in the Table 2.6, melting points determined for the bridged palladacycles are significantly higher than those of the ligands, indicating the increased stability of the palladacycle.

Table 2.6: Analytical data for bridged palladacycles, B1-B8.

Complex	FT-IR ($\nu_{C=N}$, cm^{-1})[a]	Melting point (˚C)[b]
B1*	1599	317-320
B2*	1594	330-332
B3*	1584	300-302
B4*	1594	303-305
B5*	1597	305-307
B6	1605	>250
B7	1600	>250
B8	1593	>250

[a]IR spectra were recorded neat using an ATR accessory. [b]Melting points were recorded in glass capillaries and are reported as uncorrected. *Data from previously published results [11].

^{1}H NMR spectroscopic results (Table 2.7) showed the imine signal as a singlet in the region 7.69-8.72 ppm. The imine signal was shifted slightly upfield (0.4-0.7 ppm), relative to the free ligand, again indicating that the coordination occurs through the nitrogen atom lone pair and not through the imine double bond. It is known that if the coordination was through the double bond, the shift would have been larger, by approximately 2 ppm [17]. This confirms what was observed from the FT-IR spectroscopic data, which also suggested coordination through the lone pair. Additionally, the isopropyl methine signal was shifted downfield compared to the ligand and the signal was no longer a septet, but a multiplet, integrating for four protons. The methyl signal had changed significantly; the doublet which integrated for twelve protons was now observed as two doublets, which integrated for twelve protons each. This, as well as the change in the methine signal, indicated that these groups were no longer equivalent. Hence, the free rotation observed in the free ligand was now restricted in the complex.

In the free ligand, it is expected that there is free rotation about the N-C bond and the two C-C bonds of the isopropyl moieties. If all bonds were restricted, there would be two methine signals and four methyl signals. However, this is not the case. Should the N-C bond have free rotation whilst the C-C bonds are restricted (Figure 2.8, left), we expect one methine signal and two methyl signals. If the opposite were the case, we expect two methine signals and two methyl signals. The latter is most likely (Figure 2.8, right). This is supported by the significant difference in chemical shifts for the methyl groups (indicating significantly different chemical environments). Hence, it is proposed that the N-C bond does not rotate, but the C-C bonds do, therefore making the methines inequivalent - evident from the differences in coupling constants within what appears to be a septet, but is in fact two overlapping signals.

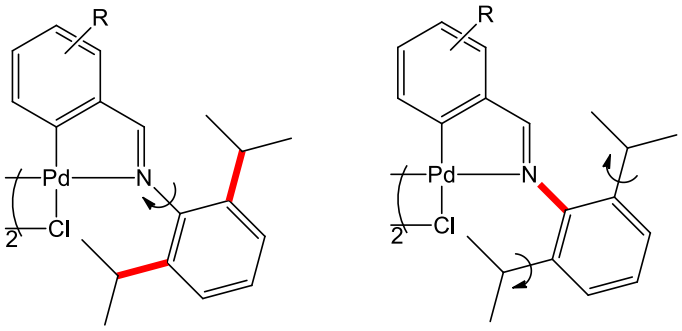

Figure 2.8: Possible restrictions to rotation in the bridged palladacycles indicated as bold red bonds.

As for the ligands, the difference in chemical shift of the 2-methyl and 4-methyl protons (2.28-2.40 ppm) indicates that the para position is once again more shielded from the effects of the imine compared to the ortho position. The imine proton signals of the more electronegative halogen analogues (**B2**, **B3** and **B6**) and the nitro analogue (**B7**) are shifted more downfield than the unsubstituted analogue (**B1**), as was expected. The methoxy analogue (**B8**) behaves the same as in the ligand, behaving more like an electron withdrawing group than an electron donating group.

ESI-MS was used as further confirmation that the correct product was formed. The spectra showed a large base peak and in some cases, a few smaller peaks (Figure 2.9). The base peak corresponded to the $[(M/2)\text{-}Cl+MeCN]^{2+}$ ion fragment, as shown in Figure 2.10. The coordination of acetonitrile in place of the chlorine ion (or the acetate ion for acetate-bridged palladacycles) is a phenomenon which has been reported previously by Tjosaas *et al*., who reported dimerisation and acetonitrile/acetate exchange occurring in acetonitrile solutions [18]. In some cases, the $[M\text{-}Cl]^{+}$ ion fragment (Figure 2.9) can also be observed. The isotopic clusters observed in Figure 2.9 result from palladium, nitrogen and chlorine isotopes. Palladium has six naturally occurring stable isotopes, whilst nitrogen and chlorine each have two stable isotopes. The simulated fragment patterns correspond to the observed fragments, however, the $[M\text{-}Cl]^{+}$ fragment is overlapped with another fragment, making the comparison more complex.

Table 2.7: ^{1}H NMR data for bridged palladacycles, B1-B8.

Complex	C*H*=N (H^{7})	Aromatic Region	Aliphatic region			
			Ar-OC*H*$_3$ (H^{18})	$(CH_3)_2CH$ ($H^{14,16}$)	Ar-C*H*$_3$ (H^{18})	$CH(CH_3)_2$ ($H^{15/17}$)
B1*	7.75 (s, 2H)	7.28-7.35 (m, 4H, $H^{2,3}$); 7.19-7.21 (m, 6H, $H^{10,11,12}$); 7.05-7.09 (m, 4H, $H^{4,5}$)		3.53 (m, 4H)		1.39 (d, 12H, $^{3}J_{H-H}$ 6.6 Hz); 1.15 (d, 12H, $^{3}J_{H-H}$ 6.6 Hz)
B2*	8.13 (s, 2H)	7.31-7.36 (m, 2H, H^{3}); 7.19-7.22 (m, 4H); 6.97-7.08 (m, 6H)		3.49 (m, 4H)		1.39 (d, 12H, $^{3}J_{H-H}$ 6.6 Hz); 1.18 (d, 12H, $^{3}J_{H-H}$ 6.6 Hz)
B3*	8.13 (s, 2H)	7.31-7.34 (m, 2H, H^{3}); 7.17-7.22 (m, 6H, $H^{10,11,12}$); 7.10-7.13 (m, 2H, H^{4}); 6.85-6.90 (m, 2H, H^{5});		3.49 (m, 4H)		1.39 (d, 12H, $^{3}J_{H-H}$ 6.6 Hz); 1.18 (d, 12H, $^{3}J_{H-H}$ 6.6 Hz)
B4*	8.01 (s, 2H)	7.31-7.33 (m, 2H, H^{3}); 7.20-7.22 (m, 4H); 6.80-7.03 (m, 6H)		3.54 (m, 4H)	2.40 (s, 6H)	1.39 (d, 12H, $^{3}J_{H-H}$ 5.9 Hz); 1.16 (d, 12H, $^{3}J_{H-H}$ 6.4 Hz)
B5*	7.69 (s, 2H)	7.30-7.35 (m, 2H,H^{2}); 7.16-7.21 (m, 6H, $H^{10,11,12}$); 7.01 (s, 2H, H^{5}); 6.88 (d, 2H, $^{3}J_{H-H}$ 7.5 Hz, H^{3})		3.53 (m, 4H)	2.28 (s, 6H)	1.39 (d, 12H, $^{3}J_{H-H}$ 6.6 Hz); 1.15 (d, 12H, $^{3}J_{H-H}$ 7.0 Hz)
B6	8.02 (s, 2H)	7.31-7.36 (m, 2H); 7.19-7.22 (m, 4H); 7.03-7.11 (m, 2H); 6.94-6.97 (m, 2H); 6.71-6.77 (m, 2H)		3.42-3.55 (m, 4H)		1.40 (d, 12H, $^{3}J_{H-H}$ 6.6 Hz); 1.18 (d, 12H, $^{3}J_{H-H}$ 6.8 Hz)
B7	8.72 (s, 2H)	7.87 (d, 2H, $^{3}J_{H-H}$ 8.1 Hz); 7.55-7.58 (m, 2H); 7.36-7.41 (m, 2H); 7.23-7.28 (m, 6H)		3.40-3.49 (m, 4H)		1.39 (d, 12H, $^{3}J_{H-H}$ 6.5 Hz); 1.19 (d, 12H, $^{3}J_{H-H}$ 6.8 Hz)
B8	8.06 (s, 2H)	7.27-7.32 (m, 2H); 7.17-7.19 (m, 4H); 6.97-7.03 (m, 2H); 6.78 (d, 2H, $^{3}J_{H-H}$ 7.8 Hz); 6.53 (d, 2H, $^{3}J_{H-H}$ 8.4 Hz)	3.77 (s, 6H)	3.47-3.60 (m, 4H)		1.39 (d, 12H, $^{3}J_{H-H}$ 6.8 Hz); 1.16 (d, 12H, $^{3}J_{H-H}$ 6.8 Hz)

*Data from previously published results [10;11]. Spectra run in $CDCl_3$ at 25 °C. Chemical shifts reported in ppm, referenced relative to residual solvent peak. Superscript numbering denotes proton assignments as per Figure 2.4.

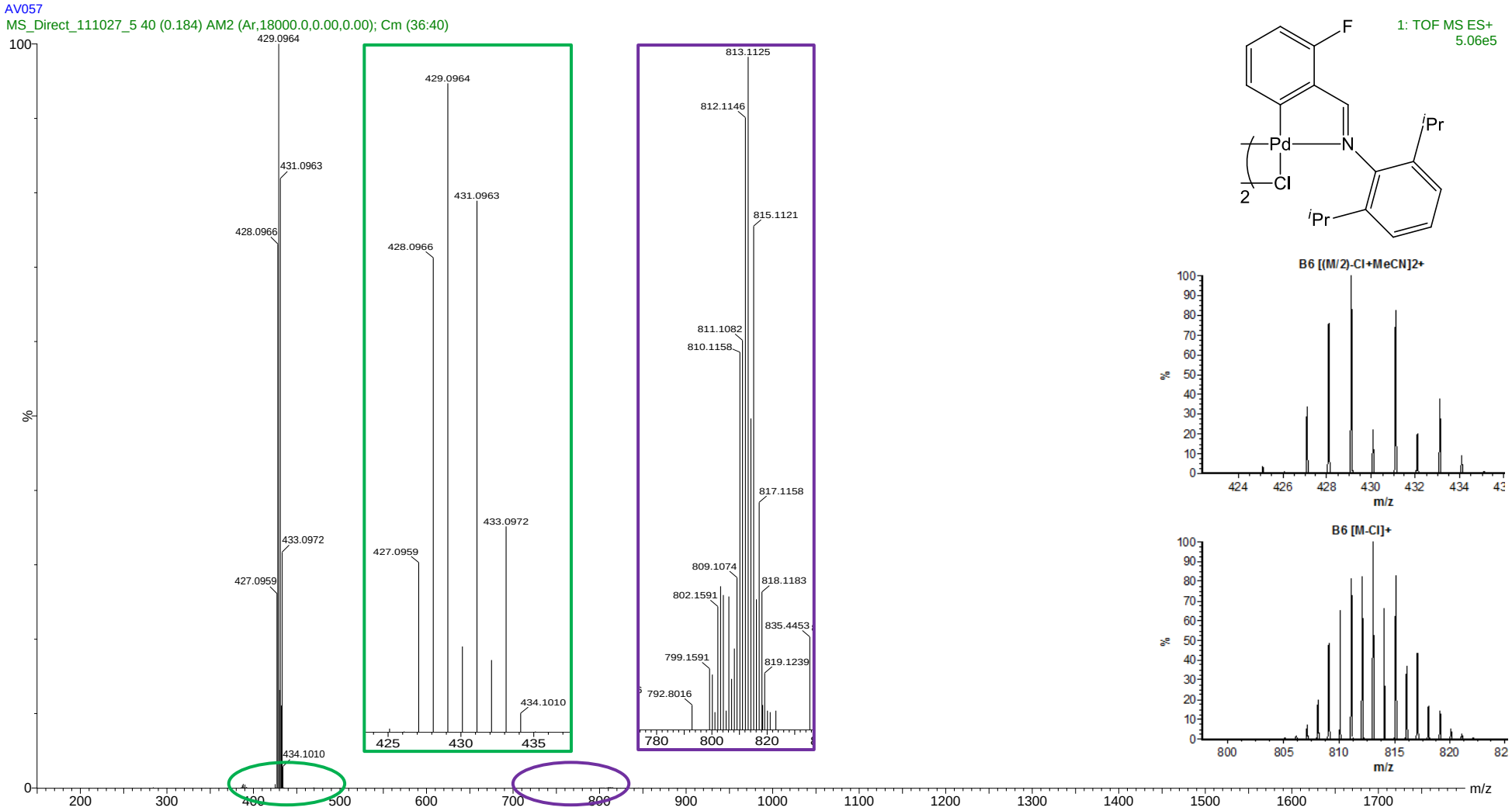

Figure 2.9: Mass spectrum of B6 with insets of zoomed in spectra showing the $[(M/2)\text{-Cl+MeCN}]^{2+}$ cluster (green) and the $[M\text{-Cl}]^{+}$ cluster (purple), as well as simulated fragment patterns.

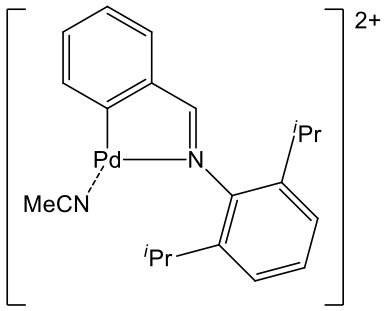

Figure 2.10: [(M/2)-Cl+MeCN]$^{2+}$ ion fragment.

Single crystals of **B6**, the fluoro analogue, were obtained by slow evaporation of a DCM/hexane solution at room temperature. The resultant yellow crystals were analysed by single crystal X-ray diffraction.

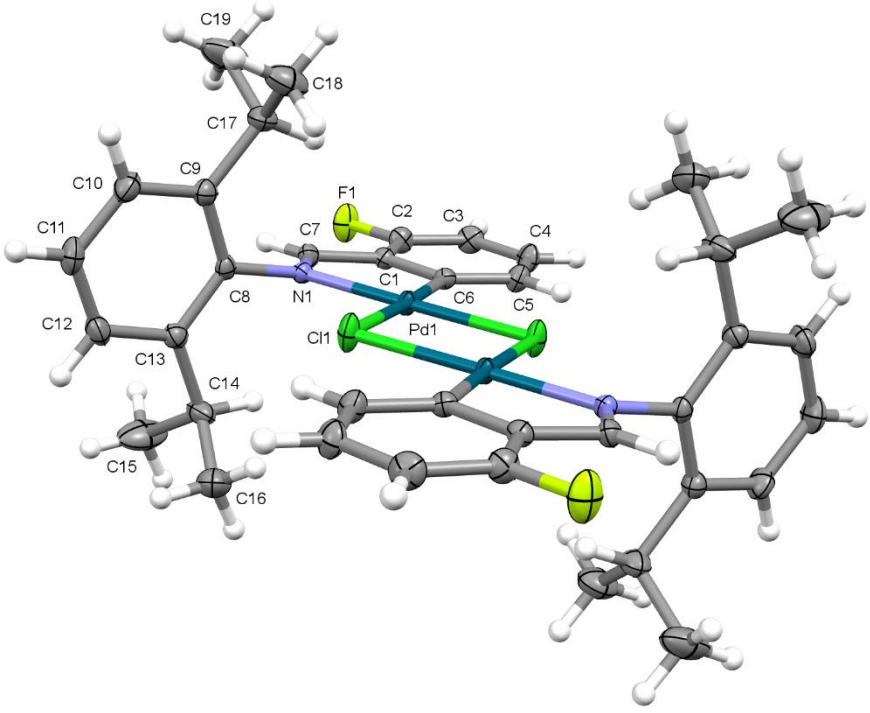

Figure 2.11: Complete molecular structure for dinuclear palladacycle, B6, with thermal ellipsoids rendered at 50% probability level. The atoms in the ASU have been labelled. H atoms are rendered as spheres with arbitrary fixed radii.

The chloro-bridged palladacycle, $C_{38}H_{42}Cl_2F_2N_2Pd_2$, has half a molecule in the asymmetric unit and the dinuclear molecule resides on a crystallographic inversion centre (Figure 2.11). The symmetry around the palladium centres is a distorted square planar geometry. Several atoms of the isopropyl moieties are disordered over two positions. The disorder is most likely via fluxional motion about a carbon (sp^2)-carbon (sp^3) bond axis. The carbon atoms in the major component of the disorder are labelled C15 and C16, as shown in Figure 2.11, whilst the minor component is labelled C21 and C22 (not shown in the figure for the sake of clarity). The major and minor components have site occupancy factors of 0.76(3) and 0.24(3), respectively. The molecules in the crystal structure associate via centrosymmetric hydrogen bonded rings with

Etter notation $R^2_2(10)$ [19]. These hydrogen bonds link the molecules to form infinite chains along the diagonal of the *ab* plane (Figure 2.12). Table 2.8 contains the numerical details of the C-H···F hydrogen bonds involved in the association of the molecules.

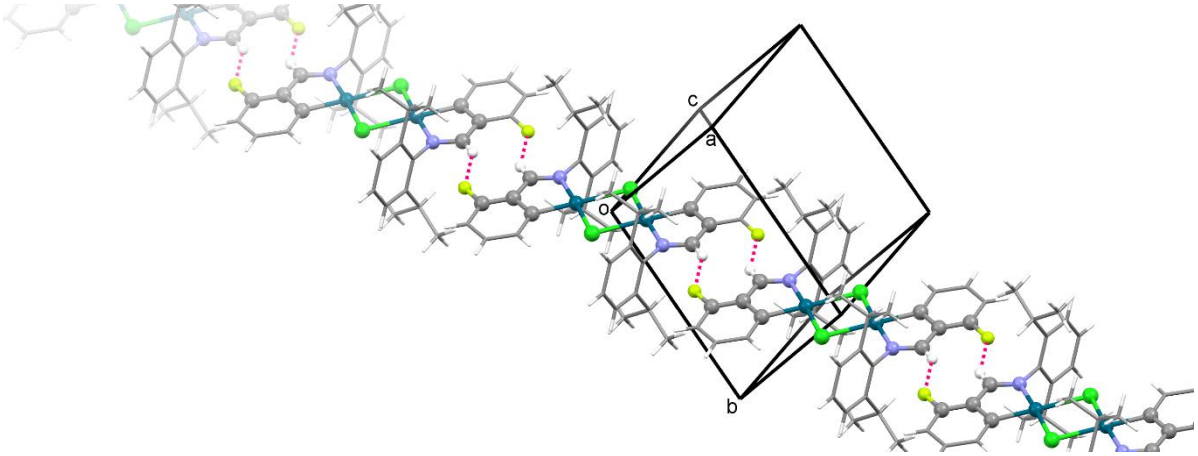

Figure 2.12: Structure of B6 showing infinite chain, where the atoms in the chain are depicted as balls.

The nature of C-H···F interactions in molecular crystals has been studied extensively. It has previously been found that these interactions act as weak hydrogen bonds when the fragments involved are neutral [20], as in the case of **B6**. C-H···F interactions are important in organising molecules in the crystal lattice often forming dimers and chains [21]. Although these interactions are weak, they can be as important as C-H···O and C-H···N hydrogen bonds in stabilising specific crystal structures [22].

CSD database screening found that C-H···F interactions have a mean distance of 2.6 Å and the mean F···H-C angle was found to be approximately 135 °C [23]. Similar C-H···F hydrogen bonding has been reported for the crystal structure of bis(μ_2-chloro)-bis(2-(((2,6-diisopropylphenyl)imino)methyl)-5-fluorophenyl)-di-palladium(II) (**Literature compound A**), where the C-H···F hydrogen bonding interactions form an infinite chain [24]. This data is included in Table 2.8. From the table, it is clear that the hydrogen bonding observed for **B6** is very similar to that of the **Literature compound A**, with the literature example being a slightly weaker bond, as indicated by the slightly longer C···F bond length. Furthermore, the hydrogen bond distance and angle fit the mean values reported.

Table 2.8: Numerical details of the C-H···F hydrogen bonds in B6 and the Literature compound A [24]

Compound	D-H···A	D-H (Å)	H···A (Å)	D···A (Å)	D-H···A (º)
B6	C7-H7···F1^{i}	0.95	2.46	3.282(2)	145
Literature compound A	C9-H9B···F1^{ii}	0.96	2.52	3.359(4)	145

Note: D-H = proton donor group, A = proton acceptor atom;
Symmetry codes: (i) −*x*+1, −*y*+1, −*z*; (ii) 1-*x*, 0.5+*y*, 0.5-*z*.

Two of the previously reported bridged palladacycles, **B1** and **B2**, were found in the CSD [7;25]. Table 2.9 contains all the coordination bond distances and bond angles for these two palladacycles, as well as **B6**.

From the table, it is appears as though the Pd(1)-N(1) bond distance increases with more electron withdrawing ortho-substituents (2-Cl in **B2** and 2-F in **B6**, if the large error is taken into account), thus, electron withdrawing substituents tend to weaken (lengthen) the bond as they draw electron density out of the metallocyclic ring system, whilst the unsubstituted complex (2-H in **B1**) has a slightly longer bond length, as the proton does not draw electron density out of the metallocyclic ring system. The same trend is observed for the Pd(1)-C(6) and C(7)-N(1) bonds. Thus, electron withdrawing ortho-substituents appear to weaken the coordination bonds. The bond angles clearly illustrate the distorted square planar geometry of the palladium centres, with all the angles being close to 90° or 180°.

Table 2.9: Selected bond distances (Å) and bond angles (°) [7;25].

Complex	B1*	B2*	B6
Pd(1)-N(1)	2.022(1)	2.028(5)	2.03(1)
Pd(1)-C(6)	1.965(1)	1.979(6)	1.98(2)
C(7)-N(1)	1.279(2)	1.288(8)	1.292(2)
Pd(1)-Cl(1)	2.326(5)	2.447(2)	2.319(4)
Pd(1)-Cl(A)	2.451(5)	2.329(2)	2.445(5)
Pd(1)···Pd(A)	3.457	3.477	3.450
N(1)-Pd(1)-C(6)	81.13(7)	81.5(2)[1]	81.37(7)
N(1)-Pd(1)-Cl(1)	176.1(4)	176.3(2)	176.7(4)
N(1)-Pd(1)-Cl(A)	96.59(4)	96.9(2)	96.06(4)
C(6)-Pd(1)-Cl(1)	94.98(5)	94.9(2)	95.33(5)
C(6)-Pd(1)-Cl(A)		178.2(2)	177.3(5)
Cl(1)-Pd(1)-Cl(A)	87.31(2)	86.59(6)	87.3(2)

*Previously reported data [7;25]. [1]Note that the bond angle was incorrectly reported as 178.2(2), but it was measured and found to be 81.5(2) [7].

Table 2.10: Crystallographic data for B6.

Parameter	**B6**
Chemical formula	$C_{38}H_{42}Cl_2F_2N_2Pd_2$
Formula weight	848.44
Temperature (K)	100(2)
Wavelength (Å)	0.71073
Crystal system	Triclinic
Space group	*P*-1
a (Å)	9.6171(4)
b (Å)	9.8094(5)
c (Å)	10.6917(5)
α (°)	96.677(1)
β (°)	111.131(1)
γ (°)	94.141(1)
V (Å^3)	927.31(7)
Z	1
D_{calc} [Mg/m^3]	1.519
Absorption coefficient (mm^{-1})	1.152
F(000)	428
Final *R* indices [$I>2\sigma(I)$]	R_1 = 0.0215, wR_2 = 0.0497
Reflections collected	11297
Completeness to θ_{max} (%)	91.2
Goodness-of-fit on F^2	1.020
Largest difference peak and hole (e Å^{-3})	0.395, -0.421

Additional structural data can be found in Table 2.10 and geometric parameters can be found in Appendix 1, Tables A1.3 and A1.4.

2.3.3 Mononuclear palladacycles

The binuclear μ-chloro palladacycles were reacted with the water-soluble tertiary phosphine, PTA, to obtain mononuclear palladacycles. The reaction conditions are shown in Scheme 2.4. The mononuclear palladacycles are all novel and were characterised completely, using a wide range of analytical techniques. They were isolated as yellow solids (crystalline or amorphous) in good yields (55-89%), except for the bromo analogue which was obtained in a yield of only 35%.

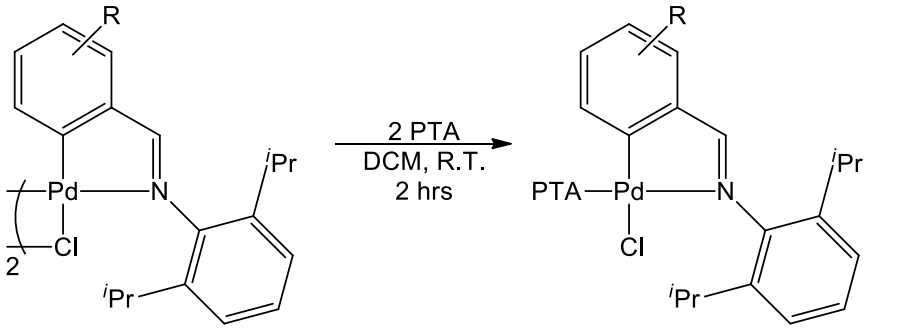

C1: R = 2-H **C2**: R = 2-Cl

C3: R = 2-Br **C4**: R = 2-Me

C5: R = 4-Me **C6**: R = 2-F

C7: R = 2-NO_2 **C8**: R = 2-OMe

Scheme 2.4: Reaction scheme for cleavage of dimeric palladacycles to obtain mononuclear species.

FT-IR spectroscopy was used to determine whether the chloro-bridged palladacycle was cleaved successfully. The $\nu_{C=N}$ stretch of the cleaved, mononuclear palladacycle is expected to shift to a higher wavenumber due to coordination of the two electron donor phosphine ligand. This is due to the better sigma-donor ability of the phosphine compared to that of the chloride. This consequently increases the electron density on the metal centre, which then leads to increased back-donation from the metal to the ligands. Since the phosphine is a better pi-acceptor ligand than the imine, there is less back-donation to the imine. Therefore, the imine bond is stronger and the corresponding shift to higher wavenumbers is observed [26,27]. For all the bridged complexes, there was only one medium to strong band in the $\nu_{C=N}$ region [14]. The $\nu_{C=N}$ bands of the various mononuclear palladacycles occur at slightly higher wavenumbers than those of the bridged complexes (Table 2.11).

Table 2.11: Analytical data for mononuclear palladacycles, C1-C8.

Complex	FT-IR ($\nu_{C=N}$, cm^{-1})[a]	ESI-MS (*m/z*) $[M-Cl]^+$	Melting point (˚C)[b]
C1	1606	527	222-226
C2	1600	563	215-219
C3	1599	607	173-178
C4	1601	541	197-202
C5	1608	541	198-202
C6	1605	545	219-222
C7	1599	572	216-221
C8	1597	557	203-207

[a]IR spectra were recorded neat using an ATR accessory. [b]Melting points were recorded in glass capillaries and are reported as uncorrected.

Studying these complexes with ^{1}H NMR spectroscopy produced some interesting results of which the salient points are summarised in Table 2.12. In all the PTA complexes, the imine signal occurs in the region of 7.90-8.80 ppm. This is slightly downfield when compared to that of the chloro-bridged complexes. This can, once again, be explained by the fact that the phosphine is a better sigma donor than the chloride ligand, thus leading to increased electron density on the metal centre and subsequent back-donation. Since the imine has more double bond character (due to its reduced pi-acceptor ability relevant to the presence of the phosphine), it experiences greater anisotropic effects [14;26;27]. The most likely explanation for this is that the better sigma-donor ability of the phosphine ligand compared to the chloride ligand, leads to an increase in the delocalisation of electron density in the metallocyclic ring, resulting in a greater degree of deshielding of the imine protons. Furthermore, the imine signal occurs as a doublet. This is due to $^4J_{H\text{-}P}$ coupling between the imine proton and the phosphorous atom of the PTA ligand.

Cleavage of the μ-chloro bridge leads to changes in the aromatic region of the NMR spectrum, producing many multiplets with fine splitting. An additional multiplet occurs in the region of 4.5-4.6 ppm. This signal integrates for the twelve protons associated with PTA. Free PTA has a singlet and a doublet at 4.61 ppm and 4.05 ppm; however, upon coordination it appears as though these signals shift and have some degree of overlap. As with the bridged complex, the methine signal is a multiplet, integrating for two protons. Again the multiplet is due to overlapping septets with very similar shifts. The methyl signals vary in multiplicity. Some analogues produced the expected two doublets, as was observed for the chloro-bridged palladacycles, whilst others showed signals with varying extents of broadening. **C4**, the

2-methyl analogue, showed a signal which resembles a broad singlet instead of the two doublets. These varyingly broad signals were unexpected and once again indicated a variation in the degree of bond rotation. This phenomenon is not observed in the analogous triphenylphosphane and trimethylphosphane series [10;11]. On closer investigation it was observed that these complexes exhibit dynamic motion in solution, in other words, the varying degrees of signal broadening observed are likely due to a dynamic phenomenon such as a chemical exchange process. This was explored further using variable temperature NMR, the details of which are discussed in Chapter 3.

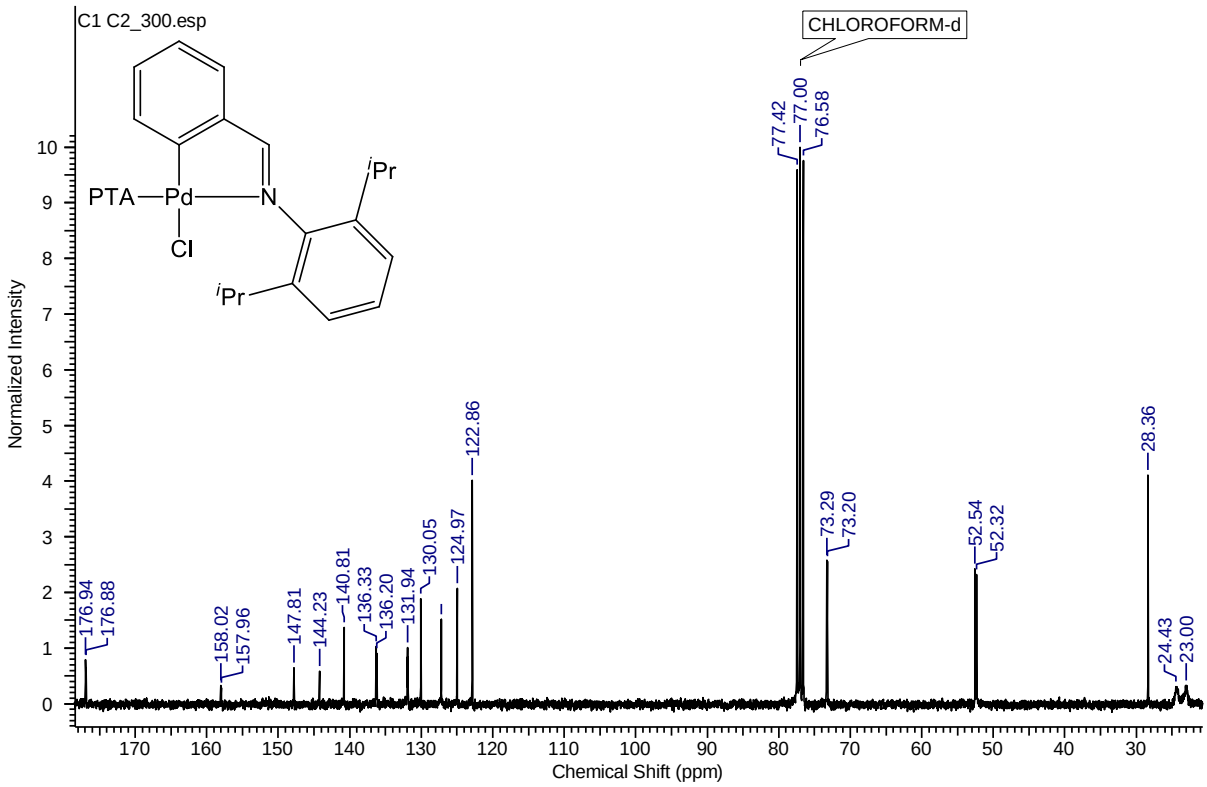

Figure 2.14: ^{13}C NMR spectrum of C1.

^{13}C NMR spectroscopy (Figure 2.14) also showed the imine carbon as the most downfield signal. As with the ^{1}H NMR spectra, these spectra showed heteronuclear splitting. The imine carbon signal (177 ppm) is a doublet due to three-bond coupling between ^{13}C and ^{31}P ($^{3}J_{C\text{-}P}$) which is of the order 3.1-4.5 Hz. The signals for the PTA carbons occur as two doublets, due to heteronuclear coupling of these carbons to phosphorous. The signal at approximately 70 ppm represents the N-CH_2-N carbon atom with $^{3}J_{C\text{-}P}$, whilst the doublet at 52 ppm represents the N-CH_2-P carbon atom with $^{1}J_{C\text{-}P}$.

Table 2.12: ^{1}H NMR data for mononuclear palladacycles, C1-C8.

Complex	C*H*=N (H^{7})	Aromatic Region	Aliphatic region				
			PTA H's	Ar-OC*H*$_3$ (H^{18})	$(CH_3)_2CH$ ($H^{14,16}$)	Ar-C*H*$_3$ (H^{18})	$CH(CH_3)_2$ ($H^{15/17}$)
C1	7.99 (d, 1H, $^{4}J_{H-P}$ 7.6 Hz)	7.46-7.48 (m, 1H, H^{3}); 7.16-7.35 (m, 6H)	4.53-4.64 (m, 12H)		3.16-3.29 (m, 2H)		1.07-1.39 (br s, 12H)
C2	8.48 (d, 1H, $^{4}J_{H-P}$ 7.6 Hz)	7.13-7.30 (m, 6H)	4.52-4.63 (m, 12H)		3.14-3.27 (m, 2H)		1.33 (d, 6H, $^{3}J_{H-H}$ 6.9 Hz) 1.16 (d, 6H, $^{3}J_{H-H}$ 6.8 Hz)
C3	8.48 (d, 1H, $^{4}J_{H-P}$ 7.6 Hz)	7.31-7.34 (m, 1H, H^{3}); 7.25-7.28 (m, 1H); 7.18-7.22 (m, 3H); 7.07-7.13 (m, 1H, H^{4})	4.52-4.63 (m, 12H)		3.14-3.28 (m, 2H)		1.33 (d, 6H, $^{3}J_{H-H}$ 6.8 Hz) 1.17 (d, 6H, $^{3}J_{H-H}$ 6.9 Hz)
C4	8.31 (s, 1H)	7.26-7.27 (m, 2H); 7.16-7.19 (m, 4H); 6.96 (d, 1H, $^{3}J_{H-H}$ 7.3 Hz, H^{3})	4.53-4.61 (m, 12H)		3.21-3.28 (m, 2H)	2.47 (2, 3H)	1.05-1.40 (br s, 12H)
C5	7.93 (d, 1H, $^{4}J_{H-P}$ 7.8 Hz)	7.36 (d, 1H, $^{3}J_{H-H}$ 7.6 Hz, H^{3}); 7.21-7.24 (m, 1H, H^{11}); 7.17 (s, 1H); 7.12-7.14 (m, 2H); 7.01-7.04 (m, 1H, H^{5})	4.53-4.63 (m, 12H)		3.15-3.28 (m, 2H)	2.44 (s, 3H)	1.13-1.29 (m, 12H)
C6	8.33 (dd, 1H, $^{4}J_{H-P}$ 7.6 Hz, $^{4}J_{H-F}$ 0.7 Hz)	7.24-7.35 (m, 2H, $H^{3,11}$); 7.16-7.19 (m, 2H); 7.04-7.08 (m, 1H, H^{5}); 6.83-6.89 (m, 1H, H^{4})	4.53-4.64 (m, 12H)		3.12-3.26 (m, 2H)		1.33 (d, 6H, $^{3}J_{H-H}$ 6.6 Hz) 1.15 (d, 6H, $^{3}J_{H-H}$ 6.8 Hz)
C7	8.80 (d, 1H, $^{4}J_{H-P}$ 7.8 Hz)	7.84 (dd, 1H, $^{3}J_{H-H}$ 8.1 Hz, $^{4}J_{H-H}$ 1.0 Hz, H^{3}); 7.52-7.56 (m, 1H, H^{5}); 7.41-7.46 (m, 1H, H^{4}); 7.27-7.32 (m, 1H, H^{11}); 7.18-7.21 (m, 2H, $H^{10,12}$)	4.53-4.63 (m, 12H)		3.09-3.23 (m, 2H)		1.17-1.32 (br m, 12H)
C8	8.41 (d, 1H, $^{4}J_{H-P}$ 7.5 Hz)	7.26-7.30 (m, 1H); 7.21-7.24 (m, 2H); 7.14-7.17 (m, 2H); 6.84-6.88 (m, 1H, H^{5}); 6.67-6.70 (m, 1H)	4.54-4.63 (m, 12H)	3.81 (s, 3H)	3.17-3.31 (m, 2H)		1.32 (br d, 6H, $^{3}J_{H-H}$ 6.8 Hz); 1.15 (br d, 6H, $^{3}J_{H-H}$ 6.8 Hz)

Spectra recorded in $CDCl_3$ at 25 °C. Chemical shifts reported in ppm, referenced relative to residual solvent peak. Superscript numbering denotes proton assignments as per Figure 2.4.

^{31}P NMR spectra show singlets at approximately -47 ppm (Table 2.13). This is a significant shift from the free PTA signal at -102 ppm. Similar shifts were observed for other palladium compounds upon coordination of PTA [28;29].

Table 2.13: ^{31}P NMR shifts of mononuclear palladacycles, C1-C8.

Complex	δ (ppm)
C1	-47.02
C2	-47.61
C3	-47.89
C4	-48.30
C5	-47.58
C6	-46.91
C7	-48.15
C8	-48.08

To further probe this large chemical shift, the ^{31}P NMR spectroscopic signals for analogous group 10 metal-PTA compounds from the literature were compared (Table 2.14). Additionally, the M-P bond length from the crystal structures of the analogous protonated compounds, $[M(PTAH)_4]Cl_4$, were compared. These values are reported in Table 2.15.

Table 2.14: Group 10 metal-PTA compounds from the literature and their ^{31}P NMR shifts [28;30;31].

PTA compound	^{31}P NMR shift (D_2O) (ppm)	Change in chemical shift relative to free PTA (ppm)
PTA	-96	0
$Ni(PTA)_4$	-46	50
$Pd(PTA)_4$	-59	37
$Pt(PTA)_4$	-75 with Pt satellites(J_{Pt-P} = 3590 Hz)	21
cis-$PdCl_2(PTA)_2$	-23	73
cis-$PtCl_2(PTA)_2$	-51 with Pt satellites(J_{Pt-P} = 3350 Hz)	45

Table 2.15: M-P bond lengths for reported $[M(PTAH)_4]Cl_4$ structures from the literature [30;32].

PTA compound	M-P bond distance (Å)	Electron density on M (gcm^{-1})
$[Ni(PTAH)_4]Cl_4$	2.133(2)	8.90
$[Pd(PTAH)_4]Cl_4$	2.203(3)	12.0
$[Pt(PTAH)_4]Cl_4$	2.254(3)	21.5

From the tables above, it is clear that the group 10 metal to which the PTA ligand coordinates has a significant influence on the ^{31}P NMR chemical shift of the compound and the M-P bond length.

Coordination of the two electron donor, PTA, increases the electron density on the metal, resulting in increased back donation. The larger the extent of back donation, the longer the bond length and consequently, the weaker the M-P bond. Therefore, the high electron density on platinum leads to a greater extent of back donation and results in a weaker M-P bond. Furthermore, from the ^{31}P NMR chemical shifts, it appears as though the degree of deshielding of the phosphorous correlates with the extent of back donation. Since nickel has a lower electron density than platinum, there is less back donation to the PTA ligands and thus, there is lower electron density on the phosphorous atoms. Consequently, there is a lower degree of shielding of the phosphorous nuclei from the magnetic field, hence, the large downfield shift observed in the ^{31}P NMR spectra.

Having determined that the large downfield shift in the ^{31}P NMR spectra is most likely due to the higher electron density on palladium, the next step was to compare the ^{31}P NMR spectra for the PTA complexes with the previously reported PPh_3 and PMe_3 analogues. The extent of the deshielding (55 ppm downfield shift) observed for the PTA complexes was close to that observed for PMe_3 (57-58 ppm) and larger than that observed for PPh_3 (47 ppm) [8;9]. Thus, similarly to PMe_3, PTA is a better sigma donor than PPh_3 due to its higher basicity, where the pKa's of PMe_3, PTA and PPh_3 are 8.65, 5.68 and 2.73, respectively [8;33]. Therefore, coordination of the PTA ligand increases the electron density on the palladium centre, leading to increased back donation and consequent deshielding of the phosphorous atoms in the PTA complexes, as explained above.

ESI-MS was again used as further confirmation that the correct products had been isolated. Mass spectra showed the $[M+H]^+$ and $[M-Cl]^+$ ion fragments for all the analogues (Figure 2.15). **C2**-**C8** also showed the $[M-Cl-PTA+MeCN]^+$ ion fragment, as shown in Table 2.16. Some of the analogues also show two dimeric ion fragments in the region of 800-1200 *m/z*. This dimerisation occurs during the ionisation process and has been reported previously [18]. Again, isotope clusters were observed and were indicative of the atoms present in the fragment. Furthermore, the simulated fragmentation patterns matched the observed experimental fragments for all cases, except the $[M+H]^+$ fragment, which is overlapped with a second fragment, thus the fragmentation pattern is obscured.

Table 2.16: Ion fragments detected by ESI-MS for mononuclear palladacycles, C1-C8.

Complex	$[M+H]^+$	$[M-Cl]^+$	$[M-Cl-PTA+MeCN]^+$
C1	564	527	-
C2	599	563	447
C3	643	607	491
C4	579	541	425
C5	579	541	425
C6	583	545	429
C7	610	572	456
C8	595	557	441

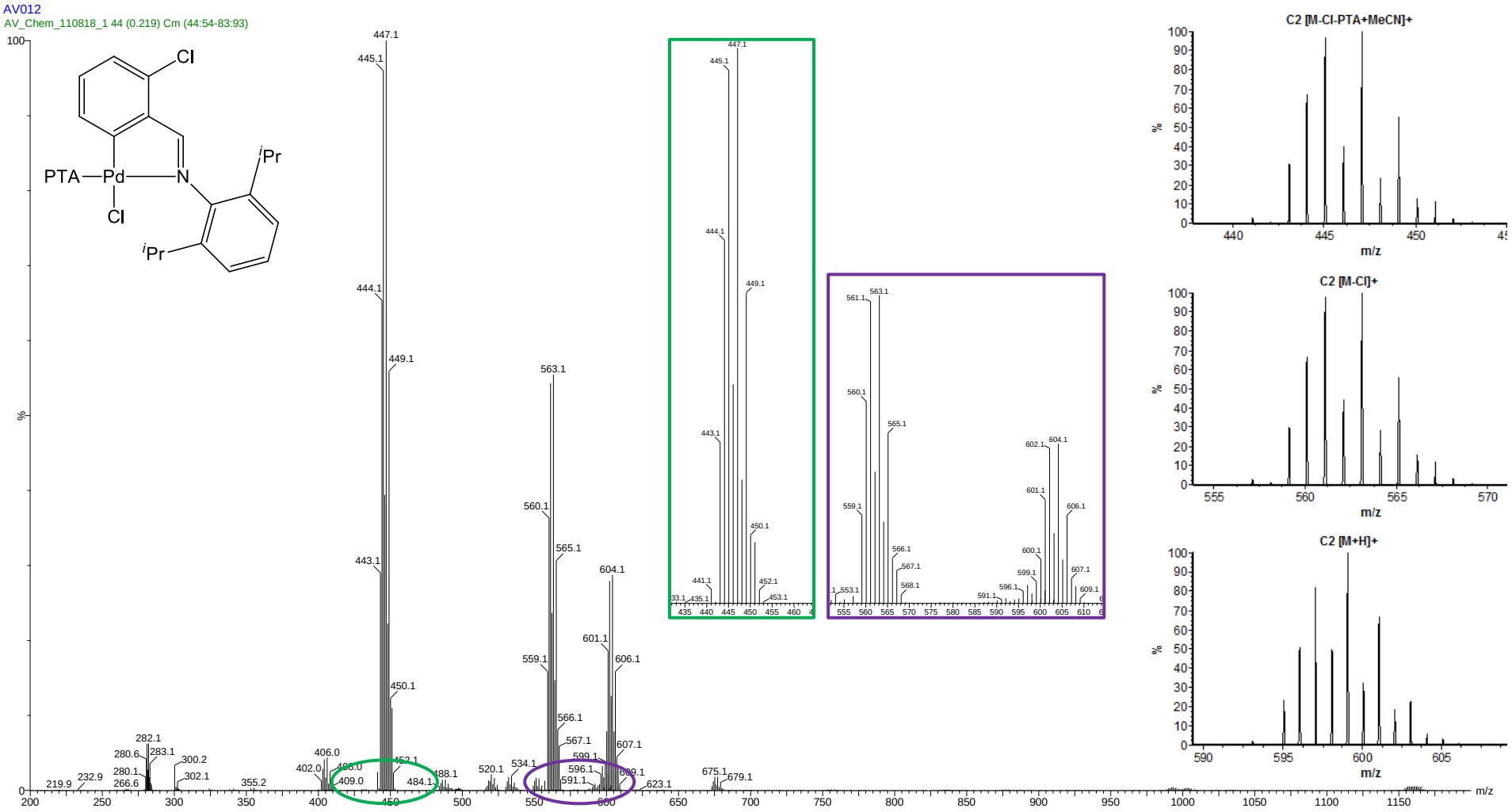

Figure 2.15: Mass spectrum of C2 with insets of zoomed in spectra showing the $[M\text{-}Cl\text{-}PTA+MeCN]^+$ cluster (green), the $[M\text{-}Cl]^+$ and $[M+H]^+$ clusters (purple), as well as simulated fragment patterns.

Solubility of the compounds was tested in water, DMSO and a DMSO/water mixture. Quantitative testing was done by adding the respective solvent, water or DMSO, to a known mass of the complex, drop-wise, until dissolution was achieved. This was continued until the solid dissolved (clear solution) or until a maximum of 10 mL was reached. None of the complexes were completely water-soluble by this method. To obtain a relative solubility in a DMSO/water mixture, water was added drop-wise to the complex, dissolved in DMSO, until the complex precipitated out (turbid solution). The results are reported as the minimum percentage of DMSO required for the complex to remain dissolved in a DMSO/water solution. Table 2.17 shows the results of this study.

Table 2.17: Solubilities for mononuclear palladacycles, C1-C8.

Complex	Water (mg/mL)	DMSO (mg/mL)	Minimum %DMSO in DMSO/water solution
AJ5	0	4.38	57
C1	0	8.32	66
C2	0	1.91	72
C3	0	2.34	72
C4	0	6.72	69
C5	0	12.3	49
C6	0	10.6	68
C7	0	0.459	57
C8	0	6.32	58

Based on the results in Table 2.17, these complexes are not water-soluble. Complexes **C4** and **C6** show the highest solubility in DMSO, whilst complex **C5** shows the highest tolerance for water, requiring only 11% DMSO in an aqueous medium to remain dissolved. When compared to **AJ5**, **C7** is more soluble in DMSO; however, the tolerance for water is significantly lower and **C5**, has higher water tolerance than **AJ5**, but it is far less soluble in DMSO.

Suitable crystals of **C1**, **C2** and **C4** were obtained by slow evaporation of DCM/diethyl ether solutions at room temperature. The resultant yellow crystals were analysed by single crystal X-ray diffraction and the experimental data are recorded in Table 2.18. Additional geometric parameters can be found in Appendix 1, Tables A1.5 – A1.10.

Table 2.18: Crystallographic data for C1, C2 and C4.

Parameter	**C1**	**C2**	**C4**
Chemical formula	$C_{25}H_{34}ClN_4PPd$	$C_{25}H_{33}Cl_2N_4O_{0.05}PPd$	$C_{26}H_{37}ClN_4O_{0.5}PPd$
Formula weight	563.38	598.56	586.41
Temperature (K)	100(2)	100(2)	173(2)
Wavelength (Å)	0.71073	0.71073	0.71073
Crystal system	Monoclinic	Monoclinic	Triclinic
Space group	*P*2$_1$/*n*	*P*2$_1$/*c*	*P*-1
a (Å)	19.101(3)	12.1991(4)	13.3048(9)
b (Å)	13.413(2)	23.1995(8)	13.7674(10)
c (Å)	19.575(3)	18.2034(6)	17.0288(12)
α (°)	90.00	90.00	104.843(1)
β (°)	94.160(2)	93.563(2)	105.172(1)
γ (°)	90.00	90.00	109.699(1)
V (Å^3)	5001.8(15)	5141.8(3)	2622.8(3)
Z	8	8	4
D_{calc} [Mg/m^3]	1.496	1.546	1.485
Absorption coefficient (mm^{-1})	0.933	1.013	0.894
F(000)	2320	2451	1212
Final *R* indices [*I*>2σ(*I*)]	R_1 = 0.0374, wR_2 = 0.0751	R_1 = 0.0199, wR_2 = 0.0507	R_1 = 0.0304, wR_2 = 0.0698
Reflections collected	31961	170673	32275
Completeness to θ_{max} (%)	91.5	94.5	91.2
Goodness-of-fit on F^2	1.028	1.060	1.031
Largest difference peak and hole (e Å^{-3})	0.613, -0.565	0.607, -0.493	0.600, -0.518

The asymmetric units of all three compounds contain two molecules each due to slight structural differences, including differences in bond lengths and angles, as well as disorder of the isopropyl groups for **C2** and **C4**. The geometry around the palladium centres is distorted square planar, with the phosphine ligand trans to the imine nitrogen and the angle between the planes of the two aromatic rings varying between 73.60° and 88.41°.

For **C1** (Figure 2.16), the structural differences are evident from the torsion angle C1-C7-N1-C8 (τ), which is different for the two molecules, A (τ_A = 178.8(2)˚) and B (τ_B = 177.0(2)˚). These differences result in different orientations and different packing. **C1** shows interesting packing

of the two molecules, as shown in Figure 2.17, where A (green) and B (purple), form alternating rows along the diagonal of the *ac* plane.

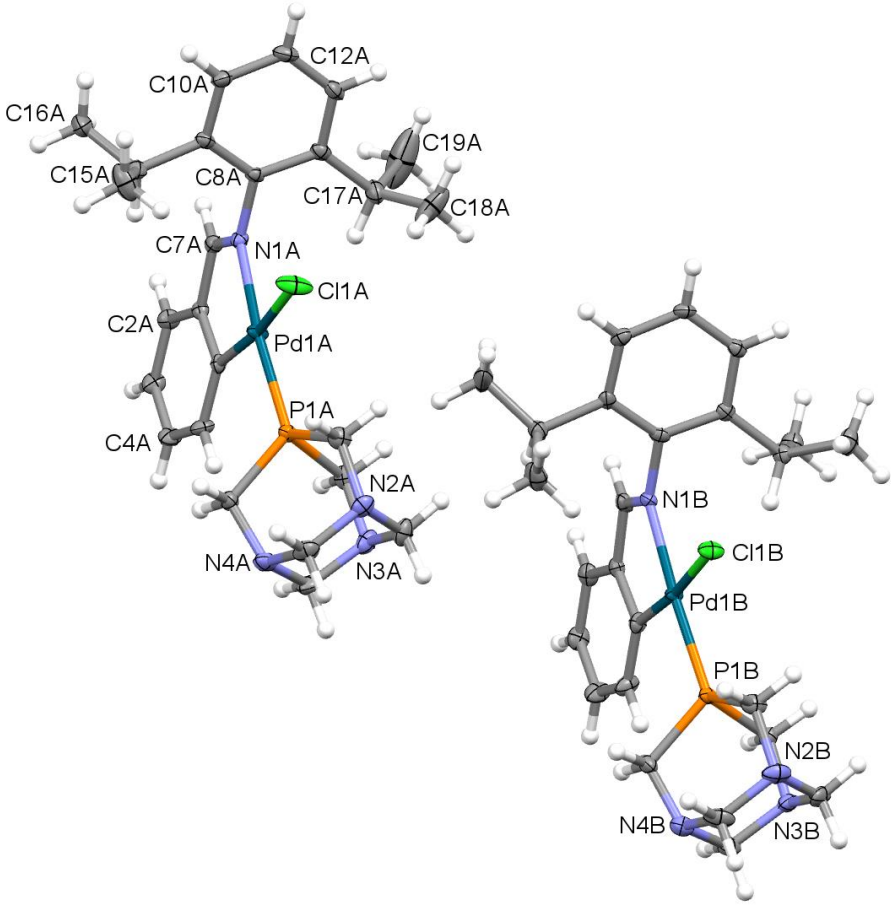

Figure 2.16: Asymmetric unit of C1, with thermal ellipsoids rendered at the 50% probability level. H atoms are rendered as spheres with arbitrary fixed radii. Selected non-H atoms are labelled.

Similarly, a 1.1° difference in the C1-C7-N1-C8 torsion angle of the two symmetry-independent molecules was also observed in **C2** (Figure 2.18). Additionally, there was disorder of several atoms in the isopropyl moiety of molecule A, whilst no disorder was observed in molecule B. The disorder is most likely a result of fluxional motion about a carbon (sp^2)-carbon (sp^3) bond axis. The carbon atoms in the major component of the disorder are labelled C15A and C16A, whilst the carbon atoms in the minor component are labelled C15C and C16C. The major and minor components have site-occupancy factors of 0.72(2) and 0.28(2), respectively.

The packing of **C2** shows an ···ABAB··· array along the *a*-axis, similar to that observed for **L7** and **C1**. Furthermore, an intermolecular hydrogen bond between a PTA nitrogen and a molecule of water was observed (Figure 2.19), the details of which are reported in Table 2.17. Note that the hydrogen atoms on the water molecule involved in this hydrogen bond could not be modelled satisfactorily, thus only an oxygen atom is displayed in the ASU (Figure 2.18). Consequently, some of the bond lengths and angles pertaining to the hydrogen bond could

not be measured. From the literature, it is known that these O-H···N hydrogen bonds are common in compounds containing PTA ligands [34].

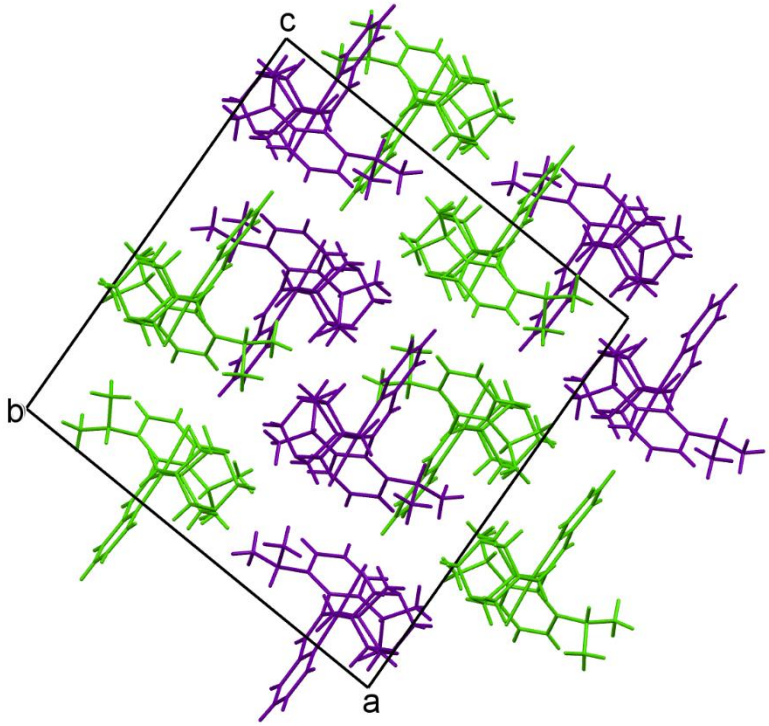

Figure 2.17: Crystal packing of C1 showing alternating molecules A (green) and B (purple). Viewed down the *b*-axis.

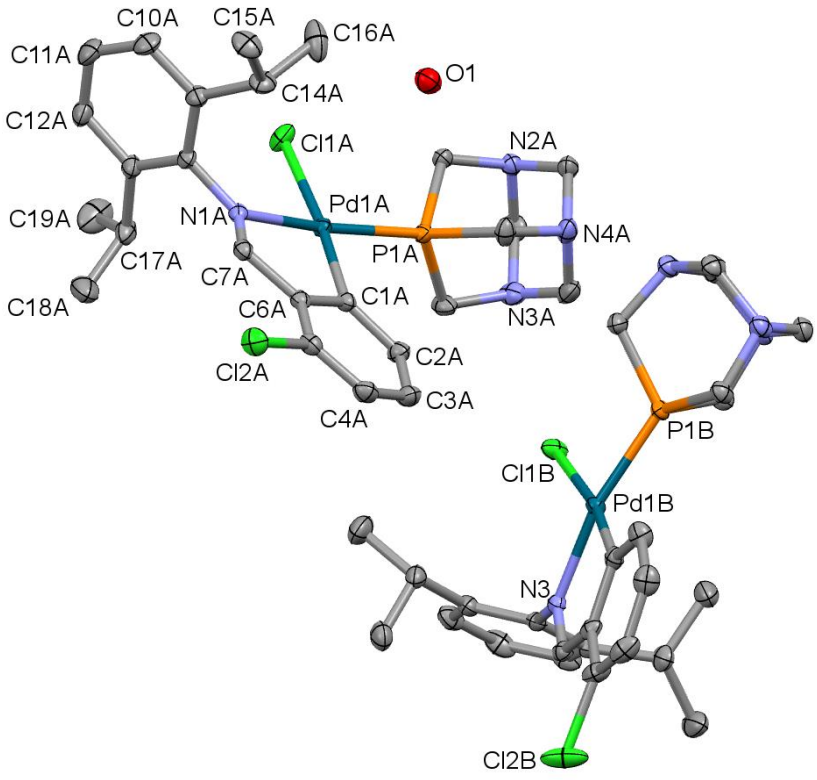

Figure 2.18: Asymmetric unit of C2, with thermal ellipsoids rendered at the 50% probability level. H atoms have been omitted for clarity. Selected non-H atoms are labelled.

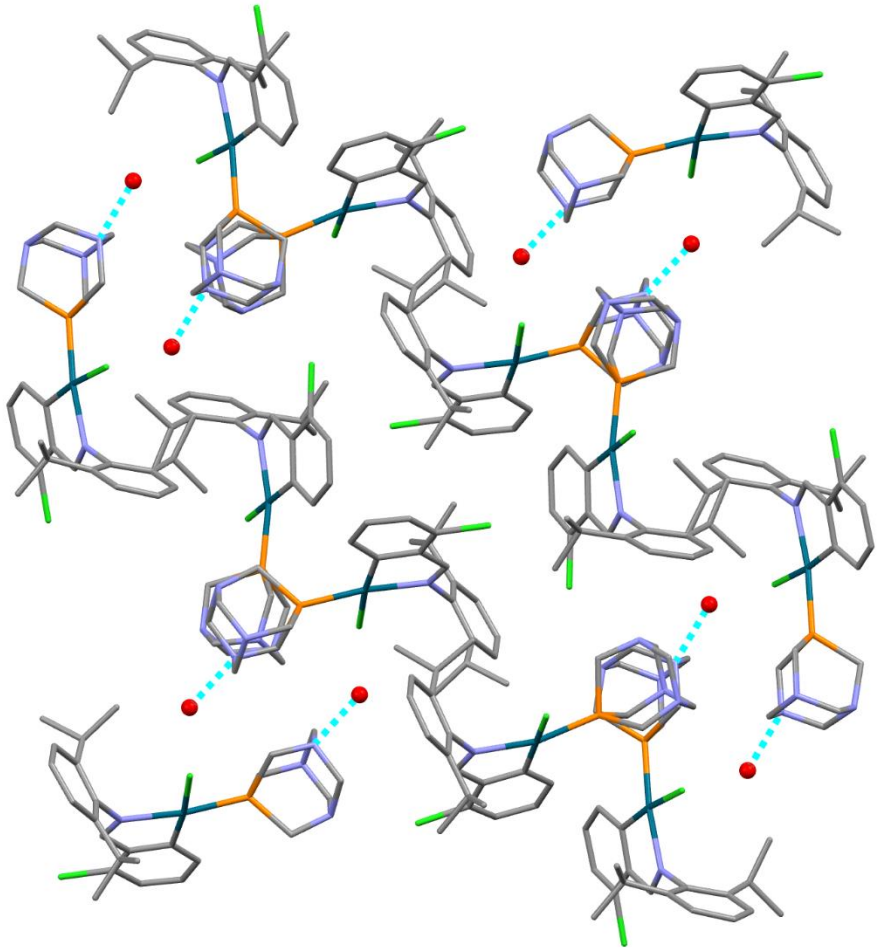

Figure 2.19: Hydrogen bond between PTA nitrogen of C2 and an entrapped water molecule. Hydrogens have been omitted for clarity.

Table 2.19: Numerical details of the O-H···N hydrogen bond in C2 and C4.

Compound	D-H···A	D-H (Å)	H···A (Å)	D···A (Å)	D-H···A (º)
C2	O1-H···N2A^{i}	-	-	2.89(1)	-
C4	O1-H2···N2B^{ii}	0.901	2.01	2.90(4)	167

Note: D-H = proton donor group, A = proton acceptor atom; Symmetry codes: (i) 1−*x*, 1−*y*, 2−*z*; (ii) -1+*x*, *y*, *z*.

C4, shown in Figure 2.20, is very similar to **C2**, with a difference of 5.1˚ in the torsion angle C1-C7-N1-C8 (τ) for molecule A and B. Disorder is observed in the isopropyl moiety of molecule B, with major and minor components assigned as C15B, C16B and C15C, C16C. Site occupancy factors are 0.853(6) for the major component and 0.147(6) for the minor component. As for **C2**, the disorder is most likely due to fluxional motion about a carbon (sp^2)-carbon (sp^3) bond axis. Packing is similar to **C1** and **C2**, but the ···ABAB··· array repeats along the *c*-axis.

As for **C2**, there is an intermolecular hydrogen bond between a nitrogen of a PTA ligand and an entrapped water molecule, as shown in the Figure 2.21. The details of this bond are recorded in Table 2.19.

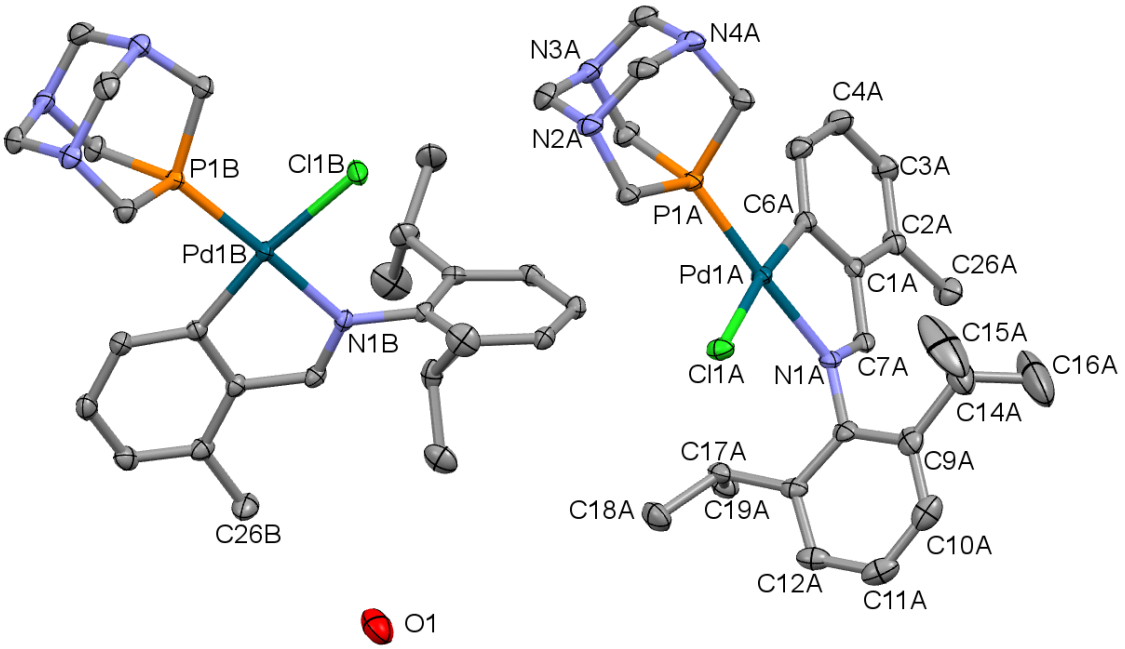

Figure 2.20: Asymmetric unit of C4, with thermal ellipsoids rendered at the 50% probability level. H atoms have been omitted for clarity. Selected non-H atoms are labelled.

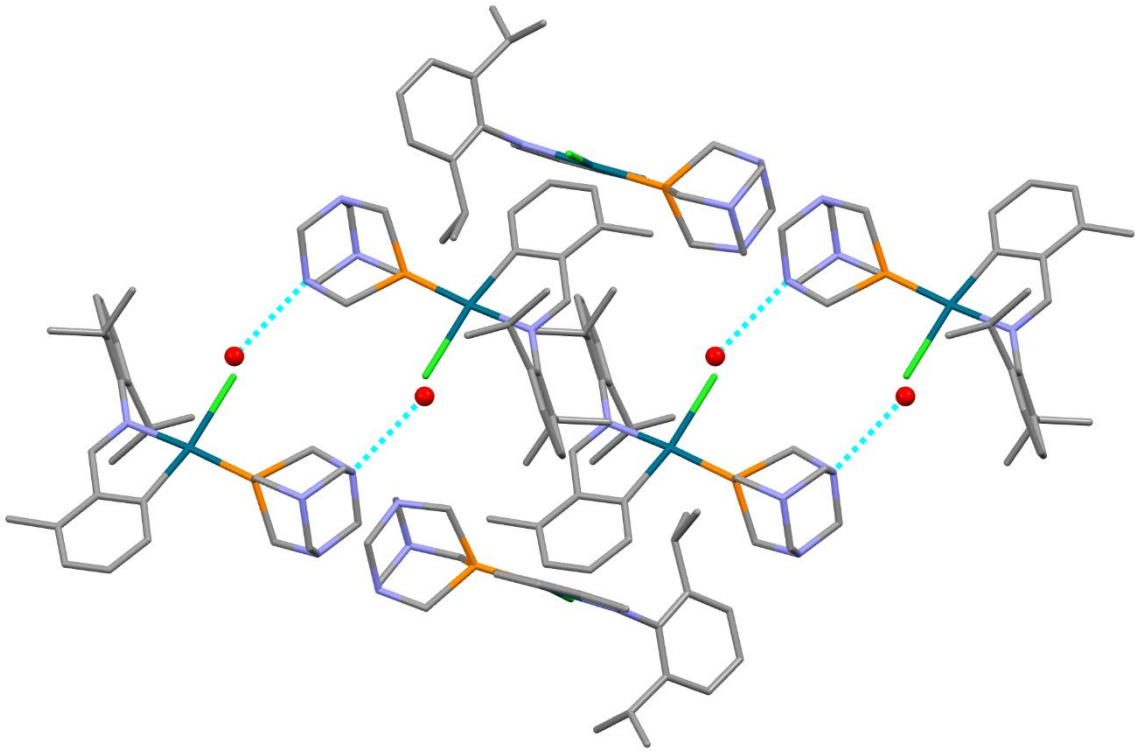

Figure 2.21: Hydrogen bond between PTA nitrogen of C4 and an entrapped water molecule. Hydrogens have been omitted for clarity and the oxygen atoms of the water molecules are represented as balls.

Next, the coordination bond lengths in the three palladacycles were considered and compared with analogous literature compounds.

The coordination bond lengths for **C1**, **C2** and **C4** are recorded in Table 2.20, followed by that of analogous PPh_3 palladacycles from the literature. All structures referred to in Table 2.20 are represented in Figure 2.22.

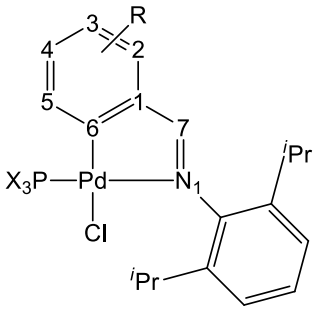

Figure 2.22: Novel and reported palladacycles with similar coordination spheres [10;11]. R = 2-H, 2-Cl, 2-Me and 4-Me and PX_3 = PTA and PPh_3.

Table 2.20: Bond lengths for C1, C2, C4 and analogous palladacycles from the literature, represented in Figure 2.22.

Complex	Pd-N1 (Å)	Pd-P (Å)	Pd-C6 (Å)	Pd-Cl (Å)	C7-N1 (Å)
C1	2.101(2)^A	2.2176(8)^A	2.011(3)^A	2.3750(8)^A	1.275(3)^A
PX_3 = PTA; R = 2-H	2.112(2)^B	2.2220(8)^B	2.015(3)^B	2.3701(8)^B	1.286(3)^B
C2	2.092(1)^A	2.2321(3)^A	2.0052(13)^A	2.3667(3)^A	1.287(2)^A
PX_3 = PTA; R = 2-Cl	2.092(1)^B	2.2404(3)^B	2.0047(12)^B	2.3721(3)^B	1.284(2)^B
C4	2.088(2)^A	2.2229(6)^A	2.022(2)^A	2.3832(6)^A	1.279(3)^A
PX_3 = PTA; R = 2-Me	2.087(2)^B	2.2347(6)^B	2.018(2)^B	2.3773(6)^B	1.283(3)^B
***Literature Compound B** **PX_3 = PPh_3; R = 2-Me**	2.104^A 2.109^B	2.267^A 2.265^B	2.026^A 2.025^B	2.358^A 2.365^B	1.289^A 1.284^B
Literature Compound C **PX_3 = PPh_3; R = 4-Me**	2.102(3)	2.2520(9)	2.011(3)	2.3647(7)	1.285(5)

*No errors reported in the references [10;11]; ^{A}Bond distance for molecule A in the ASU; ^{B}Bond distance for molecule B in the ASU.

From the Table 2.20, it is clear that the substituent on the aromatic ring influences the Pd-N1, Pd-P and Pd-C6 bond lengths. Unfortunately, the crystal data for **C4** was collected at a much higher temperature, so the bond lengths could not be compared. However, comparing the unsubstituted complex, **C1**, and the chloro-analogue, **C2**, revealed that the electron withdrawing substituent results in shorter Pd-N1 and Pd-C6 bonds and a longer Pd-P bond. However, a clear trend in terms of the electronic effects of the substituents cannot be established from the three complexes reported here. Furthermore, it was noted that the phosphine ligand has a significant influence on the Pd-P bond distance, with the bond lengths

for the PPh_3 complexes being longer and therefore, weaker as compared to the bond lengths in the PTA compounds, where the bond is approximately 0.03 Å shorter. The shorter Pd-P bond distance in the PTA analogues could be due to less steric strain, as the cone angle of PTA is considerably smaller than that of PPh_3. Overall, the coordination bonds appear very similar for the novel palladacycles, **C1**, **C2** and **C4**, and the reported PPh_3 analogues, **Literature compounds B** and **C**.

2.4 Conclusions

Novel PTA-based palladacycles were synthesised and fully characterised. The complexes were found to have dynamic motion in solution, as shown in the ^{1}H and ^{13}C NMR spectra. None of the complexes were water-soluble and no clear trend was observed for the influence of the ortho-substituents on the solubility. Crystal structures of some of the complexes showed two molecules in the asymmetric unit due to slight structural differences. Preliminary studies into improving the solubility of the complexes showed that simply reducing the molecular weight and including a water-soluble ligand is not sufficient, and more work needs to be done in this respect.

2.5 Materials and Methods

Reagents were obtained from Sigma Aldrich, Kimix and Merck. The palladium precursor, bis(acetonitrile)palladium dichloride, was prepared by refluxing $PdCl_2$ in excess acetonitrile for 3-4 hours, followed by filtration and drying [35]. Reactions were performed under nitrogen in sealed Schlenk tubes. All solvents for syntheses were distilled before use or dried over ZANTECH Alusorb ZT200 2-5 mm sieves in Innovative Technology PS-Micro solvent purifiers.

Novel compounds were characterised using the following analytical techniques: FT-IR-, NMR spectroscopy (^{1}H, ^{13}C, ^{31}P), mass spectrometry, microanalysis, melting point determinations, solubility and single crystal XRD structure determination where applicable.

FT-IR spectra were recorded on a Thermo Nicolet AVATAR 330 instrument equipped with a smart performer ATR. Samples were recorded neat. NMR (^{1}H: 300 and 400 and 600 MHz; ^{13}C: 300, 400 and 600 MHz, ^{31}P: 300 and 600 MHz) spectra were recorded on Varian NMR spectrometers at 273 K and chemical shifts are referenced to the residual protons of the deuterated solvents and external tetramethyl silane (TMS) of ^{1}H and ^{13}C NMR spectra, whilst ^{31}P NMR spectroscopy chemical shifts are referenced relative to external 85% phosphoric acid

(H_3PO_4). Chemical shifts (δ) and coupling constants (*J*) are reported in ppm and Hertz (Hz), respectively. The data in brackets are as follows: multiplicity, number of atoms (as per integration), coupling constants and assignment of atoms (where ',' denotes 'and' and '/'denotes 'or'). The following abbreviations were used to describe multiplicity of signals: s = singlet, d = doublet, t = triplet, q = quartet, sept = septet, m = multiplet and br = broad signals. ESI-MS (positive ion mode) analyses were performed on either a Waters API Quattro Micro or a Waters API Q-TOF Ultima instrument by direct injection of sample with acetonitrile as solvent. Fragmentation patterns were simulated using IsoPro 3.0 MS/MS Software [36]. Microanalysis was done at the University of Cape Town, Department of Chemistry on a Thermo Elemental Analyser CHNS-O instrument. Melting points were determined using a Stuart Scientific SMP3 melting point apparatus and are reported as uncorrected.

Quantitative solubilities of the mononuclear PTA-based palladacycles, in water and DMSO, were determined by adding the solvent drop-wise to a known mass of compound until the compound dissolved or remained insoluble at a maximum volume of 10 mL. Relative solubilities in DMSO/water mixtures were obtained by adding water drop-wise to a solution of the complex in DMSO, until the complex precipitated out, making the solution turbid.

For the X-ray structural determination, single crystals were mounted on nylon loops. Single crystal X-ray diffraction data were recorded using a Bruker Apex2 diffractometer with graphite monochromated Mo-K_α radiation (λ = 0.71073 Å). An Oxford Cryostream cooling system was used to record data sets at 100 and 173 K. Data reduction and absorption corrections were carried out with the Bruker software packages SAINT and SADABS [37;38]. Crystal structures were solved and refined using SHELXS97and SHELXL97, respectively [39]. Molecular graphics from Mercury 3.7 were used [40]. Additional geometric parameters can be found in Appendix 1. *Note that single crystal X-ray diffraction data was recorded and solved by Dr. Vincent Smith and Prof. Delia Haynes from Stellenbosch University and Prof. Ilia Guzei from the University of Wisconsin, Madison.

Synthesis of monofunctional imine ligands (L1-L8)

Benzylidene-2,6-diisopropylphenylamine (L1)

L1 was synthesised by stirring a solution of 2,6-diisopropylaniline (1.07 mL, 5.64 mmol) in dry ethanol (10 mL) in a Schlenk tube. Benzaldehyde (0.573 mL, 5.64 mmol) was added to the solution and the resulting yellow solution was stirred for 24 hours in an oil bath at ± 28 °C. The solvent was removed on a rotary evaporator to obtain a yellow oily residue. The residue was dissolved in dichloromethane (15 mL) and the solution was washed with water (10 x 15 mL

portions). The yellow organic layer was dried over anhydrous magnesium sulphate after which the magnesium sulphate was removed by filtration. The solvent was then removed from the yellow filtrate to obtain a yellow oily residue. The product was recrystallised from the residue by dissolving the residue in dichloromethane (2-3 mL) and then layering with cold methanol at low temperature. The solution was kept at low temperature (-16 °C) overnight. Yellow crystals which subsequently formed were isolated by vacuum filtration and rinsing with cold methanol. The yellow crystals were air dried. Yield: 0.648 g, 43%. FT-IR ($\nu_{C=N}$, cm^{-1}) 1638.

2-Chlorobenzylidene-2,6-diisopropylphenylamine (L2)

L2 was synthesised according to the method above using 2-chlorobenzaldehyde instead of benzaldehyde. Yield: 0.909 g, 54%. FT-IR ($\nu_{C=N}$, cm^{-1}) 1626.

2-Bromobenzylidene-2,6-diisopropylphenylamine (L3)

L3 was synthesised according to the method above using 2-bromobenzaldehyde instead of benzaldehyde. Yield: 1.556 g, 80%. FT-IR ($\nu_{C=N}$, cm^{-1}) 1627.

2-Methylbenzylidene-2,6-diisopropylphenylamine (L4)

L4 was synthesised according to the method above using 2-methylbenzaldehyde instead of benzaldehyde. Yield: 0.911 g, 57%. FT-IR ($\nu_{C=N}$, cm^{-1}) 1629.

4-Methylbenzylidene-2,6-diisopropylphenylamine (L5)

L5 was synthesised according to the method above using 4-methylbenzaldehyde instead of benzaldehyde. Yield: 1.237 g, 79%. FT-IR ($\nu_{C=N}$, cm^{-1}) 1636.

2-Fluorobenzylidene-2,6-diisopropylphenylamine (L6)

L6 was synthesised by stirring a solution of 2,6-diisopropylaniline (1.07 mL, 5.64 mmol) in dry ethanol (10 mL) in a Schlenk tube. 2-Fluorobenzaldehyde (0.605 mL, 5.64 mmol) was added to the solution. The resulting yellow solution was stirred for 24 hours in an oil bath at ± 28 °C. The solvent was removed to obtain yellow oily residue. The residue was dissolved in dichloromethane (15 mL). The solution was washed with water (10 x 15 mL portions). The yellow organic layer was dried over anhydrous magnesium sulphate. The magnesium sulphate was removed by filtration. The solvent was removed from the yellow filtrate to obtain

a yellow oily residue. The product was recrystallised by dissolving the residue in dichloromethane (2-3 mL) and then layering the solution with cold methanol at low temperature (-16 °C). The solution was kept at low temperature (-16 °C) overnight. Yellow needle-like crystals were isolated by vacuum filtration and rinsing with cold methanol. The crystals were air dried. Yield: 1.30 g, 81%. FT-IR ($\nu_{C=N}$, cm^{-1}) 1631. m.p.: 74.9-79.0 °C. ^{1}H NMR (299.74 MHz, $CDCl_3$): δ 8.53 (s, 1H, C*H*=N); δ 8.21-8.27 (m, 1H, Ph); δ 7.47-7.52 (m, 1H, Ph); δ 7.27-7.33 (m, 1H, Ph); δ 7.10-7.20 (m, 4H, Ph); δ 2.98 (sept, 2H, $^{3}J_{H-H}$ 6.9 Hz, ^{i}Pr-C*H*); δ 1.20 (d, 12H, $^{3}J_{H-H}$ 6.9 Hz, ^{i}Pr-C*H*$_3$). ^{13}C{1H} NMR ($CDCl_3$, 75.38 MHz): δ 161.12 (*C*H=N); δ 155.63 (d, J_{C-F} 4.5 Hz, C_{Ar}-F); δ 149.27 (C_{Ar}); δ 137.52 (C_{Ar}); δ 132.96 (d, J_{C-F} 8.9 Hz, C_{Ar}); δ 127.69 (d, J_{C-F} 2.5 Hz, C_{Ar}); δ 124.54 (d, J_{C-F} 3.8 Hz, C_{Ar}); δ 124.29 (C_{Ar}); δ 123.03 (C_{Ar}); δ 116.10 (C_{Ar}); δ 115.82 (C_{Ar}); δ 27.93 (^{i}Pr-*C*H); δ 23.46 (^{i}Pr-*C*H$_3$). ESI-MS: $[M+H]^+$ 284.18.

2-Nitrobenzylidene-2,6-diisopropylphenylamine (L7)

L7 was synthesised according to the method above using 2-nitrobenzaldehyde instead of 2-fluorobenzaldehyde. Yield: 0.507 g, 29%. FT-IR ($\nu_{C=N}$, cm^{-1}) 1643. m.p.: 63.2-65.7 °C. ^{1}H NMR (299.74 MHz, $CDCl_3$): δ 8.65 (s, 1H, C*H*=N); δ 8.35 (dd, 1H, $^{3}J_{H-H}$ 7.8 Hz and $^{4}J_{H-H}$ 1.6 Hz, Ph); δ 8.13 (dd, 1H, $^{3}J_{H-N}$ 8.2 Hz and $^{4}J_{H-H}$ 1.3 Hz, Ph); δ 7.78-7.83 (m, 1H, Ph); δ 7.65-7.71 (m, 1H, Ph); δ 7.12-7.22 (m, 2H, Ph); δ 7.06 (d, 1H, $^{3}J_{H-H}$ 7.6 Hz, Ph); δ 3.06 (sept, 2H, $^{3}J_{H-H}$ 6.9 Hz, ^{i}Pr-C*H*); δ 1.22 (d, 12H, $^{3}J_{H-H}$ 6.8 Hz, ^{i}Pr-C*H*$_3$). ^{13}C{1H} NMR ($CDCl_3$, 75.38 MHz): δ 158.24 (*C*H=N); δ 149.30 (C_{Ar}); δ 148.28 (C_{Ar}); δ 137.51 (C_{Ar}); δ 133.79 (C_{Ar}); δ 131.35 (C_{Ar}); δ 131.03 (C_{Ar}); δ 129.69 (C_{Ar}); δ 124.68 (d, $^{2}J_{C-N}$ 12.0 Hz, C_{Ar}); δ 123.13 (C_{Ar}); δ 122.77 (C_{Ar}); δ 27.94 (^{i}Pr-*C*H); δ 23.51 (^{i}Pr-*C*H$_3$). ESI-MS: $[M+H]^+$ 311.18.

2-Methoxybenzylidene-2,6-diisopropylphenylamine (L8)

L8 was synthesised according to the method above using 2-methoxybenzaldehyde instead of 2-fluorobenzaldehyde. Yield: 0.879 g, 53%. FT-IR ($\nu_{C=N}$, cm^{-1}) 1638. m.p.: 124-129 °C. ^{1}H NMR (599.98 MHz, $CDCl_3$): δ 8.76 (s, 1H, C*H*=N); δ 8.32 (dd, 1H, $^{3}J_{H-H}$ 7.6 Hz and $^{4}J_{H-H}$ 1.8 Hz, Ph); δ 7.58-7.61 (m, 1H, Ph); δ 7.28 (d, 2H, $^{3}J_{H-H}$ 7.6 Hz, Ph); δ 7.20-7.23 (m, 2H, Ph); δ 7.10 (d, 1H, $^{3}J_{H-H}$ 8.2 Hz, Ph); δ 3.88 (s, 3H, -OC*H*$_3$); δ 3.02 (sept, 2H, $^{3}J_{H-H}$ 7.0 Hz, ^{i}Pr-C*H*); δ 1.20 (d, 12H, $^{3}J_{H-H}$ 6.5 Hz, ^{i}Pr-C*H*$_3$). ^{13}C{1H} NMR ($CDCl_3$, 75.38 MHz): δ 159.48 (*C*H=N); δ 158.46 (C_{Ar}); δ 150.01 (C_{Ar}); δ 137.78 (C_{Ar}); δ 132.56 (C_{Ar}); δ 127.28 (C_{Ar}); δ 124.63 (C_{Ar}); δ 123.85 (C_{Ar}); δ 122.89 (C_{Ar}); δ 120.87 (C_{Ar}); δ 111.19 (C_{Ar}); δ 55.59 (-O*C*H$_3$); δ 27.85 (^{i}Pr-*C*H); δ 23.50 (^{i}Pr-*C*H$_3$). ESI-MS: $[M+H]^+$ 296.

Synthesis of μ-chloro palladacycles (B1-B8)

[PdCl(C_6H_4)CH=N{2,6-^{i}Pr$_2$-C_6H_3}]$_2$ (B1)

B1 was synthesised by stirring a solution of bis(acetonitrile)palladium dichloride (0.100 g, 0.386 mmol) in DCM (10 mL) in a Schlenk tube. **L1** (0.102 g, 0.386 mmol) and sodium acetate (0.063 g, 0.77 mmol) were added to the solution. The resulting dark red solution was stirred for 18 hours in an oil bath at ± 28 °C. The solvent was removed to obtain yellow solid residue. The residue was dissolved in DCM (20 mL) and the solution was filtered through celite. The solvent was removed from the filtrate on a rotary evaporator to obtain an oily residue. The product was recrystallised from the residue by dissolving it in DCM and then layering the solution with hexane at room temperature. The solution was kept at room temperature overnight after which a yellow solid was isolated by vacuum filtration and rinsing with hexane. The solid was air dried. Yield: 0.118 g, 76%. FT-IR ($\nu_{C=N}$, cm^{-1}) 1599.

[PdCl(2-Cl-C_6H_3)CH=N{2,6-^{i}Pr$_2$-C_6H_3}]$_2$ (B2)

B2 was synthesised according to the method above using **L2** instead of **L1**. Yield: 0.112 g, 66%. FT-IR ($\nu_{C=N}$, cm^{-1}) 1594.

[PdCl(2-Br-C_6H_3)CH=N{2,6-^{i}Pr$_2$-C_6H_3}]$_2$ (B3)

B3 was synthesised according to the method above using **L3** instead of **L1** and reacting for only 6 hours. Yield: 0.166 g, 89%. FT-IR ($\nu_{C=N}$, cm^{-1}) 1584.

[PdCl(2-Me-C_6H_3)CH=N{2,6-^{i}Pr$_2$-C_6H_3}]$_2$ (B4)

B4 was synthesised according to the method above using **L4** instead of **L1** and reacting for 24 hours. Yield: 0.090 g, 56%. FT-IR ($\nu_{C=N}$, cm^{-1}) 1594.

[PdCl(4-Me-C_6H_3)CH=N{2,6-^{i}Pr$_2$-C_6H_3}]$_2$ (B5)

B5 was synthesised according to the method above using **L5** instead of **L1** and using 0.308 mmol of ligand and precursor and 0.616 mmol of sodium acetate. Yield: 0.075 g, 58%. FT-IR ($\nu_{C=N}$, cm^{-1}) 1597.

[PdCl(2-F-C_6H_3)CH=N{2,6-^{i}Pr$_2$-C_6H_3}]$_2$ (B6)

B6 was synthesised by stirring a solution of bis(acetonitrile)palladium dichloride (0.100 g, 0.386 mmol) in dichloromethane (10 mL) in a Schlenk tube. **L6** (0.109 g, 0.386 mmol) and sodium acetate (0.063 g, 0.772 mmol) were added to the solution. The resulting orange solution was stirred for 24 hours in an oil bath at ± 28 °C. The solvent was removed to obtain yellow solid residue. The residue was dissolved in dichloromethane (20 mL). The solution was filtered through celite. The solvent was removed from the yellow filtrate to obtain a yellow oily residue. The product was recrystallised from the residue by layering with hexane at room temperature. The solution was kept at room temperature overnight. A yellow solid was isolated by vacuum filtration and rinsed with hexane. The solid was air dried. Yield: 0.053 g, 32%. FT-IR ($\nu_{C=N}$, cm^{-1}) 1604. m.p.: >250 °C. ^{1}H NMR (299.74 MHz, $CDCl_3$): δ 8.02 (s, 2H, C*H*=N); δ 7.31-7.36 (m, 2H, Ph); δ 7.19-7.22 (m, 4H, Ph); δ 7.03-7.11 (m, 2H, Ph); δ 6.94-6.97 (m, 2H, Ph); δ 6.71-6.77 (m, 2H, Ph); δ 3.42-3.55 (m, 4H, ^{i}Pr-C*H*); δ 1.39 (d, 12H, 6.8 Hz, ^{i}Pr-CH_3); δ 1.18 (d, 12H, 6.8 Hz, ^{i}Pr-CH_3). ^{13}C{^{1}H} NMR ($CDCl_3$, 75.38 MHz): δ 171.30 (*C*H=N); δ 161.35 (C_{Ar}); δ 157.87 (C_{Ar}); δ 156.21 (C_{Ar}); δ 144.25 (C_{Ar}); δ 141.45 (C_{Ar}); δ 132.91-133.12 (m, C_{Ar}); δ 129.56 (C_{Ar}); δ 128.00 (C_{Ar}); δ 123.31(C_{Ar}); δ 111.32 (d, $^2J_{C-F}$ 19.1 Hz, C_{Ar}); δ 28.25 (^{i}Pr-*C*H); δ 24.45 (^{i}Pr-*C*H_3); δ 22.97 (^{i}Pr-*C*H_3). ESI-MS: [M-Cl]$^+$ 813.11, [(M/2)-Cl+MeCN]$^{2+}$ 429.01. Anal. Found: C, 53.4; H, 4.97; N, 2.48. Calc. for $C_{38}H_{42}N_2F_2Cl_2Pd_2$: C, 53.8; H, 4.99; N, 3.30.

[PdCl(2-NO_2-C_6H_3)CH=N{2,6-^{i}Pr$_2$-C_6H_3}]$_2$ (B7)

B7 was synthesised according to the method above using **L7** instead of **L6**. Yield: 0.054 g, 50%. FT-IR ($\nu_{C=N}$, cm^{-1}) 1596. m.p.: >250 °C. ^{1}H NMR (299.74 MHz, $CDCl_3$): δ 8.72 (s, 2H, C*H*=N); δ 7.87 (d, 2H, $^3J_{H-H}$ 8.1 Hz, Ph); δ 7.55-7.58 (m, 2H, Ph); δ 7.36-7.41 (m, 2H, Ph); δ 7.23-7.28 (m, 6H, Ph); δ 3.40-3.49 (m, 4H, ^{i}Pr-C*H*); δ 1.39 (d, 12H, 6.5 Hz, ^{i}Pr-CH_3); δ 1.19 (d, 12H, 6.8 Hz, ^{i}Pr-CH_3). ^{13}C{^{1}H} NMR ($CDCl_3$, 75.38 MHz): δ 174.90 (*C*H=N); δ 157.87 (C_{Ar}); δ 146.17 (C_{Ar}); δ 144.23 (C_{Ar}); δ 141.17 (C_{Ar}); δ 139.49 (C_{Ar}); δ 137.81 (C_{Ar}); δ 131.16 (C_{Ar}); δ 128.50 (C_{Ar}); δ 123.51(C_{Ar}); δ 121.17 (C_{Ar}); δ 28.47 (^{i}Pr-*C*H); δ 24.44 (^{i}Pr-*C*H_3); δ 22.92 (^{i}Pr-*C*H_3). ESI-MS: [M-Cl]$^+$ 867.10, [(M/2)-Cl+MeCN]$^{2+}$ 456.09. Anal. Found: C, 47.5; H, 4.50; N, 5.03. Calc. for $C_{38}H_{42}N_4O_4Cl_2Pd_2 \cdot CH_2Cl_2$: C, 47.4; H, 4.49; N, 5.67.

[PdCl(2-OMe-C_6H_3)CH=N{2,6-^{i}Pr$_2$-C_6H_3}]$_2$ (B8)

B8 was synthesised according to the method above using **L8** instead of **L6**. Yield: 0.120 g, 71%. FT-IR ($\nu_{C=N}$, cm^{-1}) 1593. m.p.: >250 °C. ^{1}H NMR (299.74 MHz, $CDCl_3$): δ 8.06 (s, 2H, C*H*=N); δ 7.27-7.32 (m, 2H, Ph); δ 7.17-7.19 (m, 4H, Ph); δ 6.97-7.03 (m, 2H, Ph); δ 6.78 (d, 2H, $^3J_{H-H}$ 7.8 Hz, Ph); δ 6.53 (d, 2H, $^3J_{H-H}$ 8.4 Hz, Ph); δ 3.77 (s, 6H, -OCH_3); δ 3.47-3.60 (m,

4H, ^{i}Pr-C*H*); δ 1.39 (d, 12H, $^{3}J_{H-H}$ 6.8 Hz, ^{i}Pr-CH_3); δ 1.16 (d, 12H, 6.8 Hz, ^{i}Pr-CH_3). $^{13}C\{^{1}H\}$ NMR ($CDCl_3$, 75.38 MHz): δ 173.04 (*C*H=N); δ 158.27 (C_{Ar}); δ 157.36 (C_{Ar}); δ 144.77 (C_{Ar}); δ 141.75 (C_{Ar}); δ 133.78 (C_{Ar}); δ 132.70 (C_{Ar}); δ 127.48 (C_{Ar}); δ 126.26 (C_{Ar}); δ 123.10 (C_{Ar}); δ 106.72 (C_{Ar}); δ 55.33 (-OCH_3); δ 28.11 (^{i}Pr-*C*H); δ 24.50 (^{i}Pr-*C*H_3); δ 23.01 (^{i}Pr-*C*H_3). ESI-MS: $[(M/2)-Cl+MeCN]^{2+}$ 441.1. Anal. Found: C, 52.8; H, 5.95; N, 2.98. Calc. for $C_{40}H_{48}N_2O_2Cl_2Pd_2 \cdot 2H_2O$: C, 52.9; H, 5.77; N, 3.08.

Cleavage of μ-chloro palladacycles with monodentate phosphine, PTA, to produce the phosphine containing palladacycles, (C1-C8)

[Pd(PTA)(C_6H_4)CH=N{2,6-^{i}Pr-C_6H_3}Cl] (C1)

C1 was synthesised by stirring a solution of **B1** (0.060 g, 0.074 mmol) in dichloromethane (5 mL) in a Schlenk tube. PTA (0.023 g, 0.15 mmol) was added. The solution was stirred for 2 hours in an oil bath at ± 28 °C. The solvent was removed on a rotary evaporator to obtain a yellow oily residue. The product was recrystallised by layering a dichloromethane solution with ether at room temperature. The solution was kept at room temperature overnight. The yellow crystals were isolated by vacuum filtration and rinsed with ether. The crystals were air dried. Yield: 0.118 g, 89%. FT-IR ($\nu_{C=N}$, cm^{-1}) 1606. m.p.: 222-226 °C. ^{1}H NMR (299.74 MHz, $CDCl_3$): δ 7.99 (d, 1H, $^{4}J_{H-P}$ 7.6 Hz, C*H*=N); δ 7.46-7.48 (m, 1H, Ph); δ 7.16-7.35 (m, 6H, Ph); δ 4.53-4.64 (m, 12H, PTA); δ 3.16-3.29 (m, 2H, ^{i}Pr-C*H*); δ 1.07-1.39 (br s, 12H, ^{i}Pr-CH_3). $^{13}C\{^{1}H\}$ NMR ($CDCl_3$, 75.38 MHz): δ 176.91 (d, $^{3}J_{C-P}$ 4.5 Hz, *C*H=N); δ 157.99 (d, J_{C-P} 4.5 Hz, C_{Ar}); δ 147.81 (C_{Ar}); δ 144.23 (C_{Ar}); δ 140.81 (C_{Ar}); δ 136.27 (d, J_{C-P} 9.5 Hz, C_{Ar}); δ 131.91 (d, J_{C-P} 4.5 Hz, C_{Ar}); δ 130.05 (C_{Ar}); δ 127.19 (C_{Ar}); δ 124.97 (C_{Ar}); δ 122.86 (C_{Ar}); δ 73.25 (d, $^{3}J_{C-P}$ 6.4 Hz, N-*C*H_2-N); δ 52.43 (d, $^{1}J_{C-P}$ 16.5 Hz, P-*C*H_2-N); δ 28.36 (^{i}Pr-*C*H); δ 24.43 (^{i}Pr-*C*H_3); δ 23.00 (^{i}Pr-*C*H_3). $^{31}P\{^{1}H\}$ NMR (121.34 MHz, $CDCl_3$): δ -47.02 (s). ESI-MS: $[M+H]^+$ 564.1; $[M-Cl]^+$ 527.2. Anal. Found: C, 53.4; H, 6.08; N, 9.29. Calc. for $C_{25}H_{34}N_4PClPd$: C, 53.3; H, 6.08; N, 9.94. Solubility: DMSO 4.65 mg/mL; 51% DMSO in water.

[Pd(PTA)(2-Cl-C_6H_3)CH=N{2,6-^{i}Pr$_2$-C_6H_3}Cl] (C2)

C2 was synthesised as above, using **B2** as the reagent and the amounts as indicated here: **B2** (0.080 g, 0.0910 mmol) and PTA (0.029 g, 0.182 mmol). Yield: 0.119 g, 88%. FT-IR ($\nu_{C=N}$, cm^{-1}) 1600. m.p.: 215-219 °C. ^{1}H NMR (299.74 MHz, $CDCl_3$): δ 8.48 (d, 1H, $^{4}J_{H-P}$ 7.6 Hz, C*H*=N); δ 7.13-7.30 (m, 6H, Ph); δ 4.52-4.63 (m, 12H, PTA); δ 3.14-3.27 (m, 2H, ^{i}Pr-C*H*); δ 1.33 (d, 6H, $^{3}J_{H-H}$ 6.9 Hz, ^{i}Pr-CH_3); δ 1.16 (d, 6H, $^{3}J_{H-H}$ 6.8 Hz, ^{i}Pr-CH_3). $^{13}C\{^{1}H\}$ NMR ($CDCl_3$, 75.38 MHz): δ 175.21 (d, $^{3}J_{C-P}$ 4.5 Hz, *C*H=N); δ 160.19 (d, J_{C-P} 3.8 Hz, C_{Ar}); δ 144.44 (d, J_{C-P}

8.3 Hz, C_{Ar}); δ 140.76 (d, J_{C-P} 1.3 Hz, C_{Ar}); δ 134.85 (C_{Ar}); δ 134.73 (C_{Ar}); δ 134.43 (C_{Ar}); δ 133.21 (d, J_{C-P} 4.5 Hz, C_{Ar}); δ 127.41 (C_{Ar}); δ 125.82 (C_{Ar}); δ 122.94 (C_{Ar}); δ 73.24 (d, $^{3}J_{C-P}$ 7.0 Hz, N-*C*H_2-N); δ 52.41 (d, $^{1}J_{C-P}$ 15.9 Hz, P-*C*H_2-N); δ 28.42 (^{i}Pr-*C*H); δ 24.52 (^{i}Pr-*C*H_3); δ 22.87 (^{i}Pr-*C*H_3). $^{31}P\{^{1}H\}$ NMR (121.34 MHz, $CDCl_3$): δ -47.61 (s). ESI-MS: $[M+H]^+$ 599.1; $[M-Cl]^+$ 563.1; $[M-Cl-PTA+MeCN]^+$ 447.1. Anal. Found: C, 50.0; H, 5.54; N, 9.49. Calc. for $C_{25}H_{33}N_4Cl_2PPd$: C, 50.2; H, 5.56; N, 9.37. Solubility: DMSO 3.05 mg/mL; 64% DMSO in water.

[Pd(PTA)(2-Br-C_6H_3)CH=N{2,6-^{i}Pr-C_6H_3}Cl] (C3)

C3 was synthesised as above, using **B3** as the reagent and the amounts as indicated here: **B3** (0.130 g, 0.134 mmol) and PTA (0.042 g, 0.268 mmol). Yield: 0.061 g, 36%. FT-IR ($\nu_{C=N}$, cm^{-1}) 1599. m.p.: 173-178 °C. ^{1}H NMR (299.74 MHz, $CDCl_3$): δ 8.48 (d, 1H, $^{4}J_{H-P}$ 7.6 Hz, C*H*=N); δ 7.31-7.34 (m, 1H, Ph); δ 7.25-7.28 (m, 1H, Ph); δ 7.18-7.22 (m, 3H, Ph); δ 7.07-7.13 (m, 1H, Ph); δ 4.52-4.63 (m, 12H, PTA); δ 3.14-3.28 (m, 2H, ^{i}Pr-C*H*); δ 1.33 (d, 6H, $^{3}J_{H-H}$ 6.8 Hz, ^{i}Pr-CH_3); δ 1.17 (d, 6H, $^{3}J_{H-H}$ 6.9 Hz, ^{i}Pr-CH_3). $^{13}C\{^{1}H\}$ NMR ($CDCl_3$, 75.38 MHz): δ 177.08 (d, $^{3}J_{C-P}$ 3.8 Hz, *C*H=N); δ 159.88 (d, J_{C-P} 3.8 Hz C_{Ar}); δ 145.36 (C_{Ar}); δ 143.91 (C_{Ar}); δ 140.33 (C_{Ar}); δ 135.01 (d, J_{C-P} 9.5 Hz, C_{Ar}); δ 132.92 (d, J_{C-P} 5.1 Hz, C_{Ar}); δ 128.69 (C_{Ar}); δ 126.99 (C_{Ar}); δ 123.02 (C_{Ar}); δ 122.52 (C_{Ar}); δ 72.81 (d, $^{3}J_{C-P}$ 7.0 Hz, N-*C*H_2-N); δ 51.97 (d, $^{1}J_{C-P}$ 15.9 Hz, P-*C*H_2-N); δ 28.02 (^{i}Pr-*C*H); δ 24.12 (^{i}Pr-*C*H_3); δ 22.43 (^{i}Pr-*C*H_3). $^{31}P\{^{1}H\}$ NMR (161.90 MHz, $CDCl_3$): δ -47.89 (s). ESI-MS: $[M+H]^+$ 643.0; $[M-Cl]^+$ 607.1; $[M-Cl-PTA+MeCN]^+$ 491.0. Anal. Found: C, 46.5; H, 6.38; N, 9.14. Calc. for $C_{25}H_{33}N_4PClBrPd$: C, 46.8; H, 5.18; N, 8.72. Solubility: DMSO 3.03 mg/mL; 67% DMSO in water.

[Pd(PTA)(2-Me-C_6H_3)CH=N{2,6-^{i}Pr$_2$-C_6H_3}Cl] (C4)

C4 was synthesised as above, using **B4** as the reagent and the amounts as indicated here: **B4** (0.075 g, 0.0892 mmol) and PTA (0.028 g, 0.178 mmol). Yield: 0.076 g, 74%. FT-IR ($\nu_{C=N}$, cm^{-1}) 1601. m.p.: 197-202 °C. ^{1}H NMR (599.98 MHz, $CDCl_3$): δ 8.31 (s, 1H, C*H*=N); δ 7.26-7.27 (m, 2H, Ph); δ 7.16-7.19 (m, 4H, Ph); δ 6.96 (d, 1H, $^{3}J_{H-H}$ 7.3 Hz, Ph); δ 4.53-4.61 (m, 12H, PTA); δ 3.21-3.28 (m, 2H, $^{3}J_{H-H}$ 6.9 Hz, ^{i}Pr-C*H*); δ 2.47 (s, 3H, CH_3); δ 1.05-1.40 (br s, 12H, ^{i}Pr-CH_3). $^{13}C\{^{1}H\}$ NMR ($CDCl_3$, 75.38 MHz): δ 174.53 (*C*H=N); δ 159.05 (C_{Ar}); δ 145.52 (C_{Ar}); δ 144.79 (C_{Ar}); δ 140.89 (C_{Ar}); δ 140.11 (C_{Ar}); δ 134.33 (C_{Ar}); δ 132.43 (C_{Ar}); δ 127.15 (C_{Ar}); δ 127.11 (C_{Ar}); δ 122.94 (C_{Ar}); δ 73.25 (d, $^{3}J_{C-P}$ 6.4 Hz, N-*C*H_2-N); δ 52.27 (d, $^{1}J_{C-P}$ 15.3 Hz, P-*C*H_2-N); δ 28.32 (^{i}Pr-*C*H); δ 24.11 (^{i}Pr-*C*H_3); δ 20.45 (*C*H_3). $^{31}P\{^{1}H\}$ NMR (121.34 MHz, $CDCl_3$): δ -48.64 (s). ESI-MS: $[M+H]^+$ 579.1; $[M-Cl]^+$ 541.2; $[M-Cl-PTA+MeCN]^+$ 425.1. Anal.

Found: C, 52.6; H, 6.27; N, 9.23. Calc. for $C_{26}H_{36}N_4PClPd \cdot H_2O$: C, 52.4; H, 6.43; N, 9.41. S Solubility: DMSO 0.43 mg/mL; 51% DMSO in water.

[Pd(PTA)(4-Me-C_6H_3)CH=N{2,6-^{i}Pr$_2$-C_6H_3}Cl] (C5)

C5 was synthesised as above, using **B5** as the reagent and the amounts as indicated here: **B5** (0.100 g, 0.119 mmol) and PTA (0.037 g, 0.238 mmol). Yield: 0.076 g, 56%. FT-IR ($\nu_{C=N}$, cm^{-1}) 1608. m.p.: 198-202 °C. ^{1}H NMR (299.74 MHz, $CDCl_3$): δ 7.93 (d, 1H, $^4J_{H-P}$ 7.8 Hz, C*H*=N); δ 7.36 (d, 1H, $^3J_{H-H}$ 7.6 Hz, Ph); δ 7.21-7.24 (m, 1H, Ph); δ 7.17 (s, 1H, Ph); δ 7.12-7.14 (m, 2H, Ph); δ 7.01-7.04 (m, 1H, Ph); δ 4.53-4.63 (m, 12H, PTA); δ 3.15-3.28 (m, 2H, ^{i}Pr-C*H*); δ 2.44 (s, 3H, CH_3); δ 1.13-1.29 (m, 12H, ^{i}Pr-CH_3). ^{13}C{^{1}H} NMR ($CDCl_3$, 100.57 MHz): δ 176.40 (d, $^3J_{C-P}$ 4.0 Hz, *C*H=N); δ 157.89 (C_{Ar}); δ 145.06 (C_{Ar}); δ 144.31 (C_{Ar}); δ 142.54 (d, J_{C-P} 5.0 Hz, C_{Ar}); δ 140.91 (C_{Ar}); δ 137.56 (d, J_{C-P} 10.1 Hz, C_{Ar}); δ 129.86 (C_{Ar}); δ 127.10 (C_{Ar}); δ 125.57 (C_{Ar}); δ 122.83 (C_{Ar}); δ 73.29 (d, $^3J_{C-P}$ 7.0 Hz, N-*C*H_2-N); δ 52.43 (d, $^1J_{C-P}$ 16.1 Hz, P-*C*H_2-N); δ 28.36 (^{i}Pr-*C*H); δ 24.41 (*C*H_3); δ 22.98 (^{i}Pr-*C*H_3); δ 22.46 (^{i}Pr-*C*H_3). ^{31}P{^{1}H} NMR (121.34 MHz, $CDCl_3$): δ -47.58 (s). ESI-MS: $[M+H]^+$ 579.1; $[M-Cl]^+$ 541.2; [M-Cl- PTA+MeCN]$^+$ 425.1. Anal. Found: C, 53.0; H, 6.25; N, 9.20. Calc. for $C_{26}H_{36}N_4PClPd \cdot H_2O$: C, 52.4; H, 6.43; N, 9.41. Solubility: DMSO 0.43 mg/mL; 51% DMSO in water.

[Pd(PTA)(2-F-C_6H_3)CH=N{2,6-^{i}Pr$_2$-C_6H_3}Cl] (C6)

C6 was synthesised as above, using **B6** as the reagent and the amounts as indicated here: **B6** (0.073 g, 0.0860 mmol) and PTA (0.027 g, 0.172 mmol). Yield: 0.066 g, 66%. FT-IR ($\nu_{C=N}$, cm^{-1}) 1605. m.p.: 219-222 °C. ^{1}H NMR (299.74 MHz, $CDCl_3$): δ 8.33 (dd, 1H, $^4J_{H-P}$ 6.9 Hz and $^4J_{H-F}$ 0.7 Hz, C*H*=N); δ 7.24-7.35 (m, 2H, Ph); δ 7.16-7.19 (m, 2H, Ph); δ 7.04-7.08 (m, 1H, Ph); δ 6.83-6.89 (m, 1H, Ph); δ 4.53-4.64 (m, 12H, PTA); δ 3.12-3.26 (m, 2H, ^{i}Pr-C*H*); δ 1.33 (br d, 6H, $^3J_{H-H}$ 6.6 Hz, ^{i}Pr-CH_3); δ 1.15 (br d, 6H, $^3J_{H-H}$ 6.8 Hz, ^{i}Pr-CH_3). ^{13}C{^{1}H} NMR ($CDCl_3$, 75.38 MHz): δ 171.49 (d, $^3J_{C-P}$ 3.8 Hz, *C*H=N); δ 163.15 (C_{Ar}); δ 160.19-160.30 (m, C_{Ar}); δ 159.65 (C_{Ar}); δ 144.35 (C_{Ar}); δ 140.81 (C_{Ar}); δ 134.79 (d, J_{C-P} 4.5 Hz, C_{Ar}); δ 131.96 (dd, J_{C-P} 8.9 Hz and J_{C-P} 3.2 Hz, C_{Ar}); δ 127.36 (C_{Ar}); δ 122.91 (C_{Ar}); δ 111.91 (d, J_{C-P} 20.4 Hz, C_{Ar}); δ 73.25 (d, $^3J_{C-P}$ 7.0 Hz, N-*C*H_2-N); δ 52.49 (d, $^1J_{C-P}$ 16.5 Hz, P-*C*H_2-N); δ 28.40 (^{i}Pr-*C*H); δ 24.47 (^{i}Pr-*C*H_3); δ 22.93 (^{i}Pr-*C*H_3). ^{31}P{^{1}H} NMR (121.34 MHz, $CDCl_3$): δ -46.91 (s). ESI-MS: $[M+H]^+$ 583.1; [M-Cl]+ 545.1; [M-Cl-PTA+MeCN]$^+$ 429.1. Anal. Found: C, 51.6; H, 5.52; N, 8.65. Calc. for $C_{25}H_{33}N_4FPClPd$: C, 51.6; H, 5.72; N, 9.64. Solubility: DMSO 0.43 mg/mL; 51% DMSO in water.

[Pd(PTA)(2-NO_2-C_6H_3)CH=N{2,6-^{i}Pr_2-C_6H_3}Cl] (C7)

C7 was synthesised as above, using **B7** as the reagent and the amounts as indicated here: **B7** (0.065 g, 0.0720 mmol) and PTA (0.023 g, 0.144 mmol). Yield: 0.057 g, 65%. FT-IR ($\nu_{C=N}$, cm^{-1}) 1599. m.p.: 216-221 °C. ^{1}H NMR (299.74 MHz, $CDCl_3$): δ 8.80 (d, 1H, $^4J_{H-P}$ 7.8 Hz, C*H*=N); δ 7.84 (dd, 1H, $^3J_{H-H}$ 8.0 Hz and $^4J_{H-H}$ 1.0 Hz, Ph); δ 7.52-7.56 (m, 1H, Ph); δ 7.41-7.46 (m, 1H, Ph); δ 7.27-7.32 (m, 1H, Ph); δ 7.18-7.21 (m, 2H, Ph); δ 4.53-4.63 (m, 12H, PTA); δ 3.09-3.23 (m, 2H, ^{i}Pr-C*H*); δ 1.17-1.32 (br m, 12H, ^{i}Pr-CH_3). ^{13}C{^{1}H} NMR ($CDCl_3$, 75.38 MHz): δ 174.22 (d, $^3J_{C-P}$ 3.8 Hz, *C*H=N); δ 161.97 (C_{Ar}); δ 148.71 (C_{Ar}); δ 144.22 (C_{Ar}); δ 141.49 (d, J_{C-P} 9.5 Hz, C_{Ar}); δ 140.52 (C_{Ar}); δ 139.55 (C_{Ar}); δ 132.01 (d, J_{C-P} 4.5 Hz, C_{Ar}); δ 127.72 (C_{Ar}); δ 123.00 (C_{Ar}); δ 120.72 (C_{Ar}); δ 73.22 (d, $^3J_{C-P}$ 7.0 Hz, N-*C*H_2-N); δ 52.41 (d, $^1J_{C-P}$ 15.9 Hz, P-*C*H_2-N); δ 28.58 (^{i}Pr-*C*H); δ 24.38 (^{i}Pr-*C*H_3); δ 22.88 (^{i}Pr-*C*H_3). ^{31}P{^{1}H} NMR (121.34 MHz, $CDCl_3$): δ -48.15 (s). ESI-MS: $[M+H]^+$ 610.1; $[M-Cl]^+$ 572.1; $[M-Cl-PTA+MeCN]^+$ 456.1. Anal. Found: C, 49.1; H, 5.53; N, 11.6. Calc. for $C_{25}H_{33}N_5O_2PClPd$: C, 49.4; H, 5.47; N, 11.5. Solubility: DMSO 0.368 mg/mL; 76% DMSO in water.

[Pd(PTA)(2-OMe-C_6H_3)CH=N{2,6-^{i}Pr_2-C_6H_3}Cl] (C8)

C8 was synthesised as above, using **B8** as the reagent and the amounts as indicated here: **B8** (0.060 g, 0.0688 mmol) and PTA (0.022 g, 0.138 mmol). Yield: 0.054 g, 67%. FT-IR ($\nu_{C=N}$, cm^{-1}): 1597. m.p.: 203-207 °C. ^{1}H NMR (299.74 MHz, $CDCl_3$): δ 8.41 (d, 1H, $^4J_{H-P}$ 7.5 Hz, C*H*=N); δ 7.26-7.30 (m, 1H, Ph); δ 7.21-7.24 (m, 1H, Ph); δ 7.14-7.17 (m, 2H, Ph); δ 6.84-6.88 (m, 1H, Ph); δ 6.67-6.70 (m, 1H, Ph); δ 4.54-4.63 (m, 12H, PTA); δ 3.81 (s, 3H, CH_3); δ 3.17-3.31 (m, 2H, ^{i}Pr-C*H*); δ 1.32 (br d, 6H,$^3J_{H-H}$ 6.8 Hz, ^{i}Pr-CH_3); δ 1.15 (br d, 6H,$^3J_{H-H}$ 6.8 Hz, ^{i}Pr-CH_3). ^{13}C{^{1}H} NMR ($CDCl_3$, 75.38 MHz): δ 173.13 (*C*H=N); δ 159.73 (C_{Ar}); δ 159.32 (C_{Ar}); δ 144.43 (C_{Ar}); δ 140.62 (C_{Ar}); δ 135.06 (C_{Ar}); δ 133.50 (d, J_{C-P} 3.2 Hz, C_{Ar}); δ 128.17 (d, J_{C-P} 8.9 Hz, C_{Ar}); δ 126.53 (C_{Ar}); δ 122.32 (C_{Ar}); δ 107.09 (C_{Ar}); δ 72.81 (d, $^3J_{C-P}$ 7.0 Hz, N-*C*H_2-N); δ 55.06 (C_{Ar}); δ 51.98 (d, $^1J_{C-P}$ 15.9 Hz, P-*C*H_2-N); δ 27.84 (^{i}Pr-*C*H); δ 24.08 (^{i}Pr-*C*H_3); δ 22.52 (^{i}Pr-*C*H_3). ^{31}P{^{1}H} NMR (121.34 MHz, $CDCl_3$): δ -48.08 (s). ESI-MS: $[M+H]^+$ 595.1; $[M-Cl]^+$ 557.2; $[M-Cl-PTA+MeCN]^+$ 441.1. Anal. Found: C, 52.5; H, 6.09; N, 9.46. Calc. for $C_{26}H_{36}N_4OPClPd$: C, 52.6; H, 6.11; N, 9.44. Solubility: DMSO 4.07 mg/mL; 62% DMSO in water.

2.6. References

1. A. C. Cope and R. W. Siekman, *J. Am. Chem. Soc.*, 1965, **87**, 3272-3273.
2. J. D. Higgins III, L. Neely and S. Fricker, *J. Inorg. Biochem.*, 1993, **49**, 149-156.
3. J. Spencer, A. Casini, O. Zava, R. P. Rathnam, S. K. Velhanda, M. Pfeffer, S. K. Callear, M. B.Hursthouse and P. J. Dyson, *Dalton Trans.*, 2009, **48**, 10731-10735.
4. E. G. Rodrigues, L. S. Silva, D. M. Fausto, M. S. Hayashi, S. Dreher, E. L. Santos, J. B. Pesquero, L. R. Travassos and A. C. F. Caires, *Int. J. Cancer*, 2003, **107**, 498-504.
5. W.A. Herrmann, C. Brossmer, Karl Öfele, C.-P. Reisinger, T. Priermeier, M. Beller and H. Fischer, *Angew. Chem. Int. Ed. Engl.*, 1995, **34**, 1844-1848.
6. K. Karami, M. H. Kharat, H. Sadeghi-Aliabadi, J. Lipkowski and M. Mirian, *Polyhedron*, 2012, **50**, 187-192.
7. N. Mungwe, A. J. Swarts, S. F. Mapolie and G. Westman, *J. Organomet. Chem.*, 2011, **696**, 3527-3535.
8. J. Bravo, S. Bolaño, L. Gonsalvi and M. Peruzzini, *Coord. Chem. Rev.*, 2010, **254**, 555-607.
9. P. Bergamini, L. Marvelli, A. Marchi, F. Vassanelli, M. Fogagnolo, P. Formaglio, T. Bernardi, R. Gavioli and F. Sforza, *Inorg. Chim. Acta*, 2012, **391**, 162-170.
10. A. J. Swarts, *Mononuclear and multinuclear palladacycles as catalyst precursors*, M.Sc. Thesis Stellenbosch University, 2011.
11. D. M. E. van Niekerk, *Reactivity of metallacycles of palladium: experimental and computational studies*, M.Sc. Thesis Stellenbosch University, 2012.
12. J. Long, H. Gao. K. Song, F. Liu, H. Hu, L. Zhang, F. Zhu and Qing Wu, *Eur. J. Inorg. Chem.*, 2008, **27**, 4296-4305.
13. Y. Zhou, Q. Pang, R. Ben, Y. Qian and J. Zhao, *Organometallics*, 2013, **32**, 3753-3759.
14. D. L. Pavia, *Introduction to Spectroscopy*, Australia; Belmont, CA: Brooks/Cole Cengage Learning, 2009.
15. G. S. D. Sharma and S. V. Eswaran, *Resonance*, 1997, **2**, 73-75.
16. H. Onoue and I. Moritani, *J. Organomet. Chem.*, 1972, **43**, 431-436.
17. I. Omae, *Chem. Rev.*, 1979, **79**, 287-321.
18. F. Tjosaas and A. Fiksdahl, *J. Organomet. Chem.*, 2007, **692**, 5429-5439.
19. J. Bernstein, R. E. Davies, L. Shimoni and N.-L. Chang, *Angew. Chem., Int. Ed. Engl.*, 1995, **34**, 1555-1573.
20. E. D'Oria and J. J. Novoa, *Cryst. Eng. Comm.*, 2008, **10**, 423-436.
21. D. Chopra and T.N Guru Row, *Cryst. Eng. Comm*., 2011, **13**, 2175-2186.
22. V. R. Thalladi, H.-C. Weiss, D. Bläser, R. Boese, A. Nangia and G. R. Desiraju, *J. Am. Chem. Soc.*, 1998, **120**, 8702-8710.

23. L. Shimoni and J. P. Glusker, *Struct. Chem*., 1994, **5**, 383-397.
24. D.-Y. Ma, L.–E. Zhang, X.-Y. Rao, T.-L Wu, D.-H. Li, X.-Q. Xie, H.-F. Guo and L. Qin, *J. Coord Chem*., 2013, **66**, 3261-3271.
25. C.-L. Chen, Y.-H. Liu, S.-M. Peng and S.-T. Liu, *J. Organomet. Chem*., 2004, **689**, 1806-1815.
26. H. Masui, *Coord. Chem. Rev*., 2001, **219**-**221**, 957-992.
27. J. Albert, M. Gomez, J. Granell, X. Solans and J. Sales, *Organometallics*, 1990, **9**, 1405-1413.
28. A. D. Philips, L. Gonsalvi, A. Romerosa, F. Vizza and M. Peruzzini, *Coord. Chem. Rev*., 2004, **248**, 955-993.
29. J. Ruiz, N. Cutillas, F. López, G. López and D. Bautista, *Organometallics*, 2006, **25**, 5768-5773.
30. D. J. Darensbourg, T. J. Decuir, N. White Stafford, J. B. Robertson, J. D. Draper and J. H. Reinenspies, *Inorg. Chem.*, 1997, **36**, 4218-4226.
31. D. J. Darensbourg, J. B. Robertson, D. L. Larkins and J. H. Reinenspies, *Inorg. Chem.*, 1999, **38**, 2473-2481.
32. RSC interactive periodic table. Accessed at www.rsc.org/periodic-table/trends on 19 March 2016.
33. D. M. P. Mingos, *Essential trends in inorganic chemistry*, Oxford: Oxford University Press, 1998.
34. J. M. Forward, Z. Assefa, R. J. Staples and J. P. Fackler, Jr., *Inorg. Chem.*, 1996, **35**, 16-22.
35. F. R. Hartley, S. G. Murray and C. A. McAuliffe, *Inorg. Chem.*, 1979, **18**, 1394-1397.
36. M. Senko, IsoPro 3.0 MS/MS Software. Downloaded from https://sites.google.com/site/isoproms/.
37. SAINT, data reduction software; version 5.629. Bruker AXS Inc., Madison, WI, 2003.
38. R. H. Blessing, *Acta Crystallogr., Sect. A: Found. Adv.*, 1995, **51**, 33-38.
39. G. M. Sheldrick, *Acta Crystallogr., Sect. A: Found. Adv.*, 2008, **64**, 112-122.
40. C. F. Macrae, P. R. Edgington, P. McCabe, E. Pidcock, G. P. Shields, R. Taylor, M. Towler and J. van de Streek, *J. Appl. Cryst.*, 2006, **39**, 453-457.

Chapter 3
NMR spectroscopic study of PTA-based palladacycles

3.1 Introduction

Nuclear magnetic resonance (NMR) spectroscopy is a common, yet powerful analytical tool for determining the molecular structure of matter. NMR spectroscopy is a fairly versatile technique and can be used to investigate the structure of both small molecules and high molecular weight macromolecules. It is used to determine the way in which proteins fold and to examine phase changes [1]. NMR spectroscopy allows one to determine the number of magnetically distinct atoms of a specific type (^{1}H, ^{13}C and others) present in a sample and provides information about the environment of each type of atom, as well as changes occurring in the environment on the spectral timescale. Most other spectroscopic techniques (infrared- and ultraviolet-visible spectroscopy) cannot detect dynamic motion in molecules as the frequency at which the spectra are recorded is too high, relative to the frequency of the motion, resulting in a seemingly static spectrum [2;3]. The combination of IR- and NMR spectroscopy, as analytical techniques, is often sufficient to determine a structure completely [3]. This was clearly shown in the use of these techniques for the characterisation of the PTA-based palladacycles in Chapter 2. This chapter will focus on the use of NMR spectroscopy to investigate the kinetics of a dynamic NMR process observed for the PTA-based palladacycles, in which the methyl signals of the diisopropyl moieties showed spectral broadening as a result of the fluxional behaviour of these moieties. Hence, a short introduction to dynamic NMR spectroscopy and chemical exchange is provided.

3.1.1 Dynamic NMR spectroscopy

The chemical shift of a nucleus is sensitive to changes in the chemical environment around it. Dynamic NMR spectroscopy systems are systems in which changes in the spectra (changes in various chemical shifts) are observed due to dynamic phenomena, such as chemical exchange (either inter- or intra-molecular) [2;4-6]. The use of NMR spectroscopy to study dynamic phenomena in chemistry has seen rapid growth and development in the past few

years. The most common applications are the study of internal mobility of a molecule, including restricted rotation about a bond, ring inversions, and reversible rearrangements [7].

Molecular motion occurs over a wide range of timescales. NMR spectroscopy can be used to detect molecular motion occurring in the timescale range from picoseconds to seconds. The influence on the observed spectrum depends on the nature of the motion and the timescale in which it occurs. Below follows a short discussion on the types of motion and their influence on NMR spectra [1].

3.1.2 Molecular motion

Molecular motion can be divided into the following groups: molecular vibration, local rotation, chemical exchange, molecular rotation and molecular translations.

The most common types of motion are molecular vibration and local rotations. All atoms in a molecule vibrate around their mean position, the smaller the atom and molecule, the faster the vibration [1]. Molecular vibrations are typically on the picosecond timescale. This motion is faster than the spectral timescale and therefore has no effect on the NMR spectrum. Local rotations, such as the rotation of a methyl group (Figure 3.1) also occur on the picosecond timescale, unless the rotation is hindered in which case it may be slowed to the micro- or millisecond timescale. In some cases, the rotation may be prevented completely. As with molecular vibration, the chemical shift of the mean position for these atoms is usually observed as the motion is generally too fast to be observed by NMR spectroscopy [1].

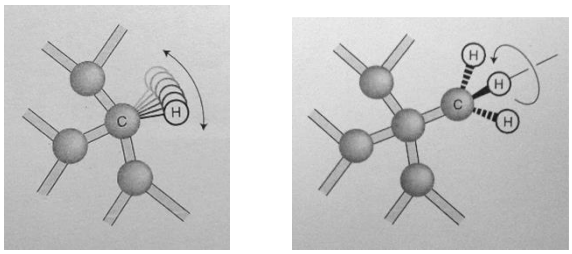

Figure 3.1: Diagrams of molecular vibration and local rotation [1].

Chemical exchange is a motional process including the formation and breaking of bonds (in chemical reactions) and conformational exchange. These processes occur over a wide range of timescales (nanoseconds to seconds). During chemical reactions, the intermolecular exchange of a nucleus between two molecules can be monitored, whilst for conformational exchange, the intramolecular exchange of a nucleus between two conformations can be monitored (Figure 3.2) [6;8]. Examples include internal cyclisation and cis-trans isomerisation.

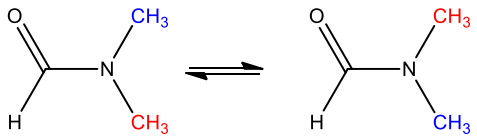

Figure 3.2: Diagram of intramolecular chemical exchange [6].

Molecular rotations and translations occur in solution. These are random rotations or movements through space which change the anisotropic spin interactions (e.g. direct dipole-dipole coupling), hence allowing the motion to be detected by NMR spectroscopy.

Of the types of molecular motion mentioned above, chemical exchange is most commonly observed to influence a NMR spectrum [1;8]. This will be discussed in detail in the next section.

3.1.3 Chemical exchange

As stated above, chemical exchange is a motional process which involves the breaking and forming of bonds, as well as changes in conformation. The advantage of using NMR spectroscopy to study these dynamic systems is that the chemical exchange process can be detected, even if the system is at equilibrium. This is not the case for other analytical techniques, which require non-equilibrium states of the chemical system in order to detect a form of chemical exchange [2;9].

During chemical exchange, the nucleus of an atom experiences two or more different chemical environments. As the nucleus is exposed to one environment and then another, the chemical shift is influenced and the changes can be observed in the NMR spectrum as a variety of line shapes, depending on the rate of exchange [2;4;5]. Examples of several exchange reactions are tabulated below (Table 3.1) [9].

Table 3.1: Examples of chemical exchange processes [9].

Intermolecular chemical exchange	Intramolecular chemical exchange
Binding of ligand to macromolecule	Unfolding of protein and motion of side chains
Protonation/deprotonation equilibria of ionisable groups	Helix-coil transitions of DNA and RNA
Exchange of labile protons with solvent	Conformational exchange
Enzyme catalysed reactions	Tautomerisation

3.1.3.1 Conformational exchange

One of the most commonly reported examples of chemical exchange is the intramolecular conformational change occurring in dimethylformamide. This type of chemical exchange is a two-site exchange. In this example, the C-N bond has partial double bond character due to the lone pair on the nitrogen which is delocalised into the carbonyl bond, as shown in Figure 3.3. The exchange or rotation of the methyl groups around this partial double bond can be detected by NMR spectroscopy, as the two sites are not chemically equivalent (since the molecule is not symmetrical); hence the magnetic field experienced by the nuclei differs and changes when the two groups exchange sites. These changes are observed as changes in the chemical shifts and line shapes of the NMR spectroscopic signals [1;9].

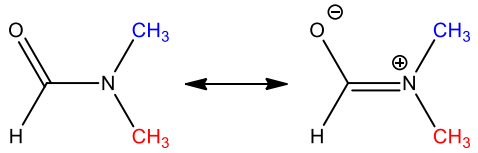

Figure 3.3: Resonance structures of dimethylformamide.

This process is usually represented as shown below, where A and B are the two conformations (CH_3* '*E*' or 'Z' with oxygen) and *k* is the rate constant.

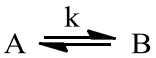

If *k* is dependent on temperature, increasing the temperature results in faster exchange and consequently, the coalescence of the NMR spectroscopic signals [9]. The difference in the chemical shift frequencies relative to the rate of exchange determines the effect of the exchange on the NMR spectrum [1;4;5;10]. The effects can be divided into two types, slow intermediate exchange and fast intermediate exchange.

Slow intermediate exchange

Slow-intermediate exchange is infrequent, rather than slow. The site-exchange causes changes in the precessing frequency of the nuclear spin. This leads to dephasing of the transverse magnetisation and consequent decay of the signal. Since the rate of exchange is smaller than the frequency difference, only slight motional broadening is observed. The faster or more frequent the exchange, the faster the decay. This leads to broader NMR spectroscopic signals which start to overlap. [1;4;5;11]. The point at which the signals coalesce is called the crossover point (Figure 3.4).

Fast intermediate exchange

Fast exchange is considered to be past the point of coalescence (crossover point) of the signals. As the exchange occurs more frequently, the decay slows down due to a decreased rate of dephasing, hence reducing the NMR spectroscopic signal width (Figure 3.4). The exchange between the sites occurs so quickly that an average precession frequency is experienced, rather than two different frequencies. The signal still experiences motional broadening due to the exchange, but the broadening is of the same magnitude as that of the natural line width and the inhomogeneity of the magnetic field [1;4;5;11].

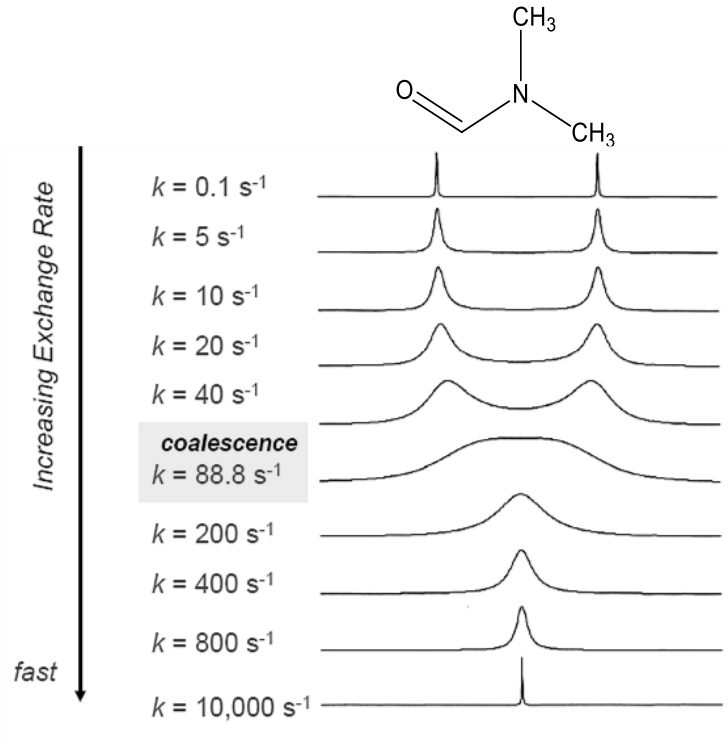

Figure 3.4: Example of intermediate two-site exchange process of dimethylformamide [12].

The example in Figure 3.4 is a very simple two-site exchange where the signals show no scalar (*J)* coupling, as the exchanging signals are the methyl groups of dimethylformamide. There are more complex systems where the exchanging signals show *J* coupling, an example of which is *N*,*N*-dimethyl-4-nitrosoaniline (Figure 3.5) [9;13]. The signals shown in Figure 3.5 are those of the aromatic protons. Each of the four aromatic protons is observed as a doublet at low temperature, however, as the temperature increases and the nitroso group flips from side to side more frequently, the signals broaden until there are only two signals, a broad flat singlet (2300 Hz) which accounts for one proton and a sharp doublet (2000 Hz) which accounts for the remaining three protons. The scalar coupling and involvement of more than two signals makes interpretation and modelling of such systems more complex.

These systems (both the simple and more complex systems) can be modelled by kinetic computational methods and further data may also be gained from the NMR spectra, such as rates of exchange and activation parameters for the exchange process. These methods are well documented in a number of books and reviews on dynamic NMR spectroscopy, therefore, they will not be discussed here [1;9;13;14]. The above theory and techniques were applied to analyse the changes observed in the NMR spectra previously reported in Chapter 2.

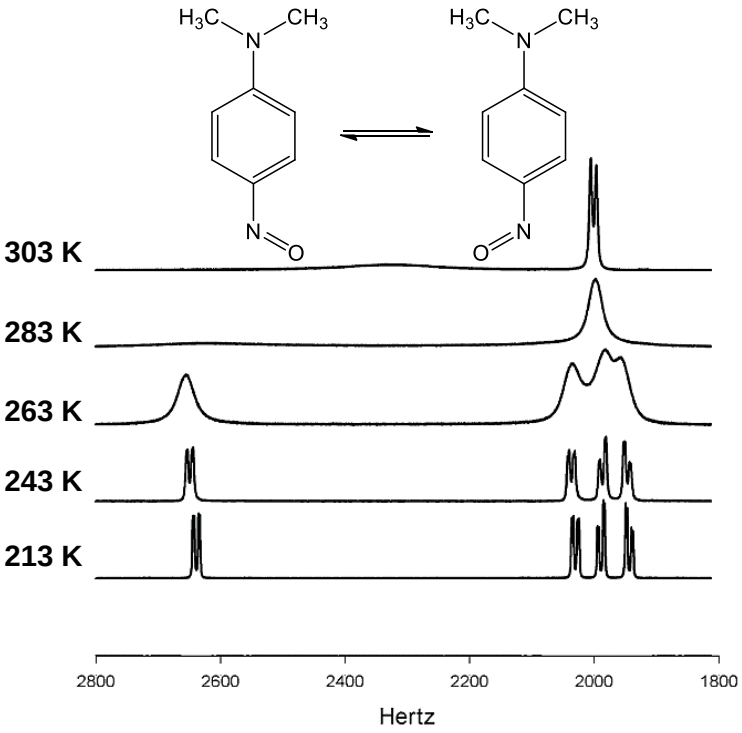

Figure 3.5: Site-exchange process in *N,N*-dimethyl-4-nitrosoaniline [11].

3.2 Results and Discussion

As mentioned in Chapter 2, the ^{1}H NMR spectra of the PTA-based palladacycles (Figure 3.6) produced interesting results, particularly regarding the isopropyl methyl signals. One would expect the methyl groups to appear as two doublets in the ^{1}H NMR spectra, as was the case for analogous triphenylphosphane (PPh_3) and trimethylphosphane (PMe_3) palladacycle structures (Figure 3.7) [15;16]. The representation of the methyl signals as two doublets implies that the protons are in two distinct chemical environments due to restricted rotation about the N-C bond between the imine nitrogen and the carbon on the 2,6-diisopropylaniline ring. However, the resonance signals of the corresponding PTA complexes ranged from fully resolved doublets to broad singlets (Figure 3.8), which were not observed for the analogous PPh_3 and PMe_3 complexes. The cause and possible mechanism for the observed broadening of these signals were investigated.

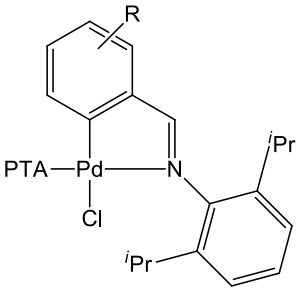

C1: R = 2-H **C2**: R = 2-Cl

C3: R = 2-Br **C4**: R = 2-Me

C5: R = 4-Me **C6**: R = 2-F

C7: R = 2-NO_2 **C8**: R = 2-OMe

Figure 3.6: Series of PTA-based mononuclear palladacycles with various R groups.

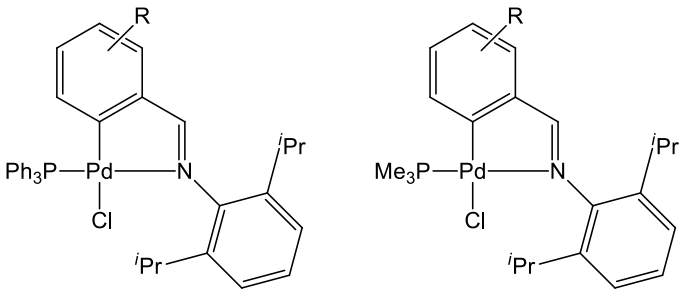

Figure 3.7: Trimethyl- and triphenylphosphane analogues of PTA-based palladacycles.

Since the differences in the observed signals are due to dynamic motion, it was decided to use variable temperature NMR spectroscopy in an attempt to understand the dynamic behaviour of these complexes. NMR spectra and relevant data not discussed in the following sections are included in Appendix 2. Variable temperature data are included in Section A2.1 and computational data are included in Section A2.2.

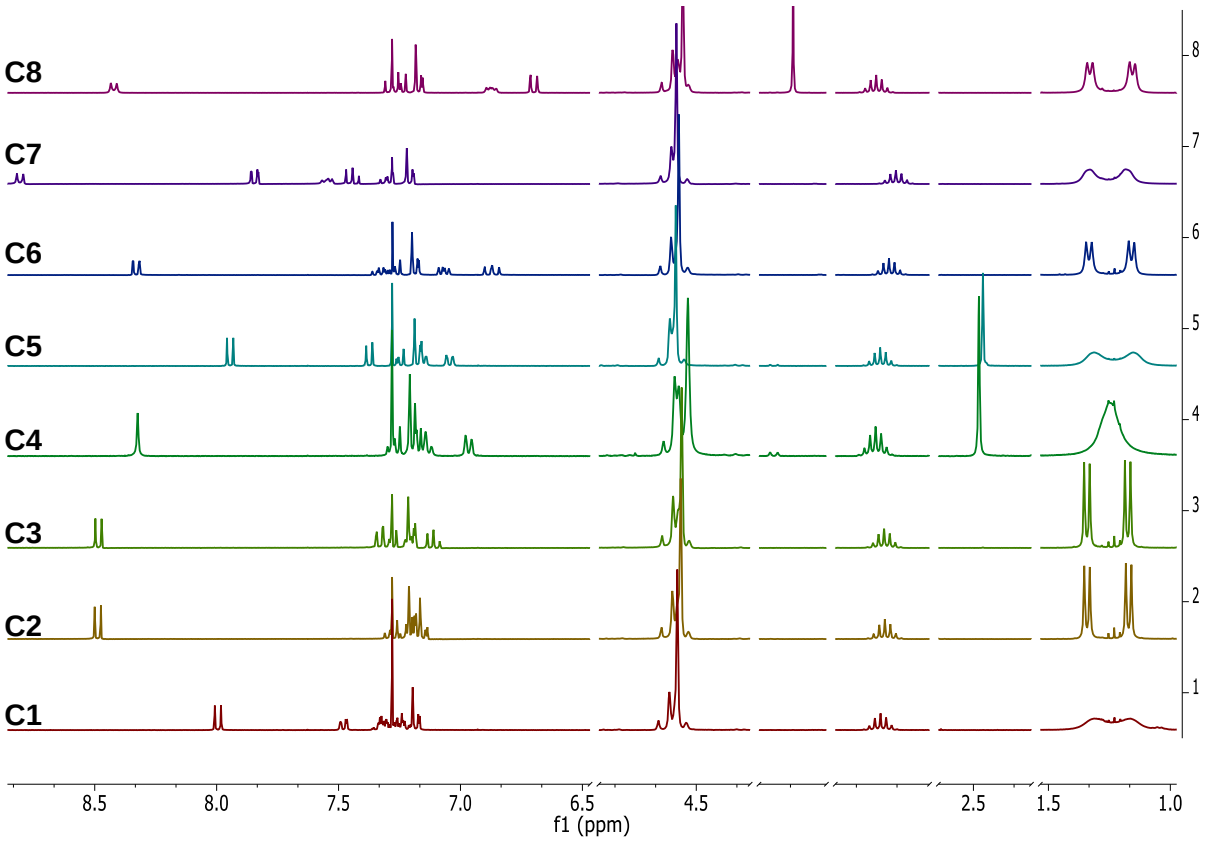

Figure 3.8: ^{1}H NMR spectra of C1-C8 in $CDCl_3$ at 25 °C, showing varying degrees of broadening in isopropyl group methyl signals between 1.00 and 1.50 ppm.

3.2.1 Variable temperature NMR spectroscopy

Variable temperature NMR spectroscopy can be used to monitor the rate of dynamic molecular motion of a molecule, by adjusting the temperature either up or down. Thus, the first step in the investigation was to record the NMR spectra over a wide range of temperatures, from -50 °C to 120 °C, using deuterated chloroform ($CDCl_3$) and deuterated tetrachloroethane (TCE-d2) as solvents.

Figures 3.9 and 3.10 show the array of NMR spectra recorded for **C2**, the 2-chloro analogue. At low temperature, the methyl signals of the isopropyl substituents were observed as two doublets (1.16 and 1.33 ppm). Increasing the temperature resulted in the coalescence of the two doublet signals into one broad doublet (20-25 °C). Further temperature increases led to the signals coalescing to a broad singlet at approximately 50 °C. Finally, the signal split into a single doublet at 75-100 °C, indicating that the methyl sites were magnetically equivalent at this temperature. Accompanying the change in the signal shape was a gradual downfield shift, suggesting that the methyl groups experience a degree of deshielding. Similarly, the ^{1}H NMR imine signal which starts off as a broad doublet at low temperature appears to become broader with increasing temperature until it is observed as a broad singlet and then sharpens distinctly

with further increases in temperature. The change in imine signal shape may also be due to weakening and eventual loss of the $^{4}J_{H\text{-}P}$ coupling. As observed for the isopropyl methyl signals, the imine signal also shifts slightly downfield with increasing temperature. Furthermore, some changes were observed in the fine structure and/or chemical shifts of the isopropyl methine signal at 3.00-3.20 ppm and the PTA signal at 4.40-4.55 ppm. Relatively small changes were observed in the aromatic signals. Similar changes were observed in the variable temperature ^{1}H NMR spectra of **C4**, the 2-methyl analogue, (Figure 3.11) and the other PTA-based palladacycles (A2.1-A2.8).

Once it was confirmed that these changes were observed for all of the PTA-based analogues, the reversibility of the dynamic event was tested. This was done by recording the ^{1}H NMR spectrum of **C2** at 25 °C (1), followed by heating the sample to 100 °C, and then recording the ^{1}H NMR spectrum at 25 °C again once the sample had cooled down (2). The final step was to cool the sample to -50 °C and then record the ^{1}H NMR spectrum at 25 °C for a third and final time once the sample had warmed up sufficiently (3). The three spectra recorded at 25 °C were compared and found to be qualitatively unchanged (Figure A2.9). Thus, it was concluded that the observed dynamic event is reversible.

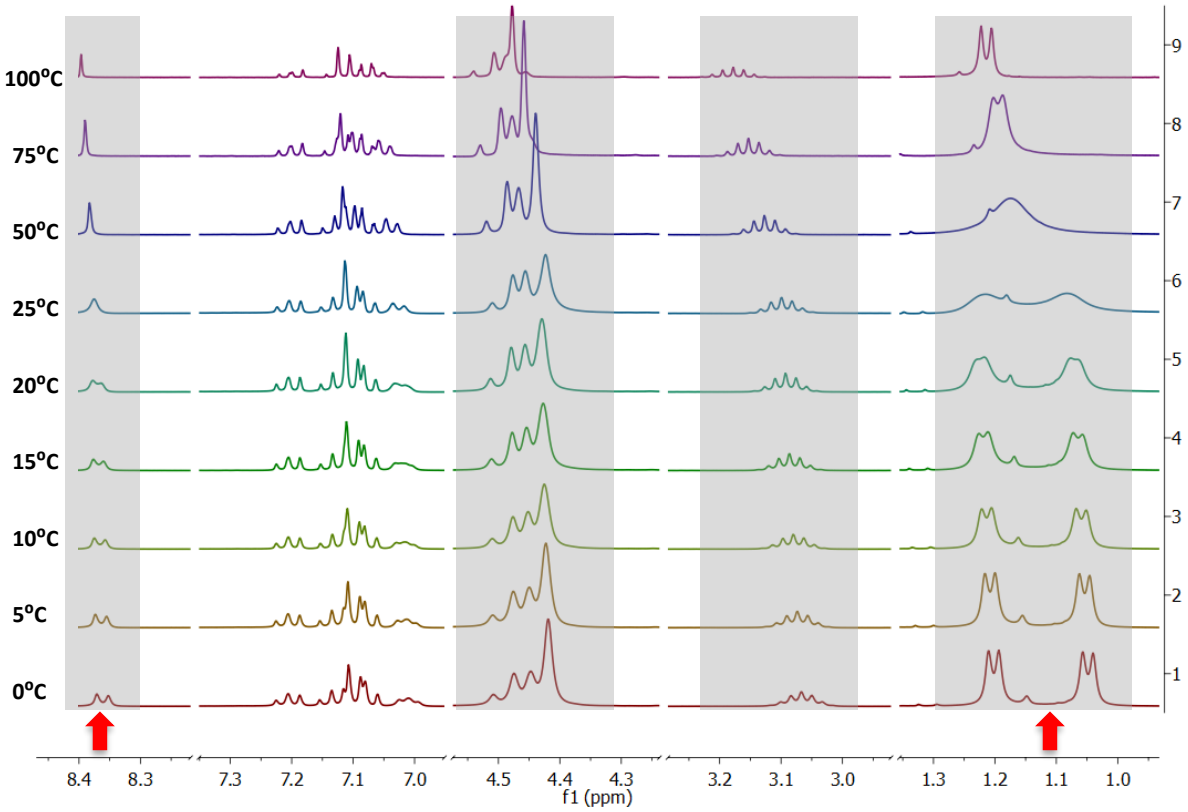

Figure 3.9: ^{1}H NMR spectroscopic array of C2 in TCE-d2 (0 to 100 °C). Red arrow shows broadening signals and grey areas indicate signals with significant fine structural changes and/or changes in chemical shifts.

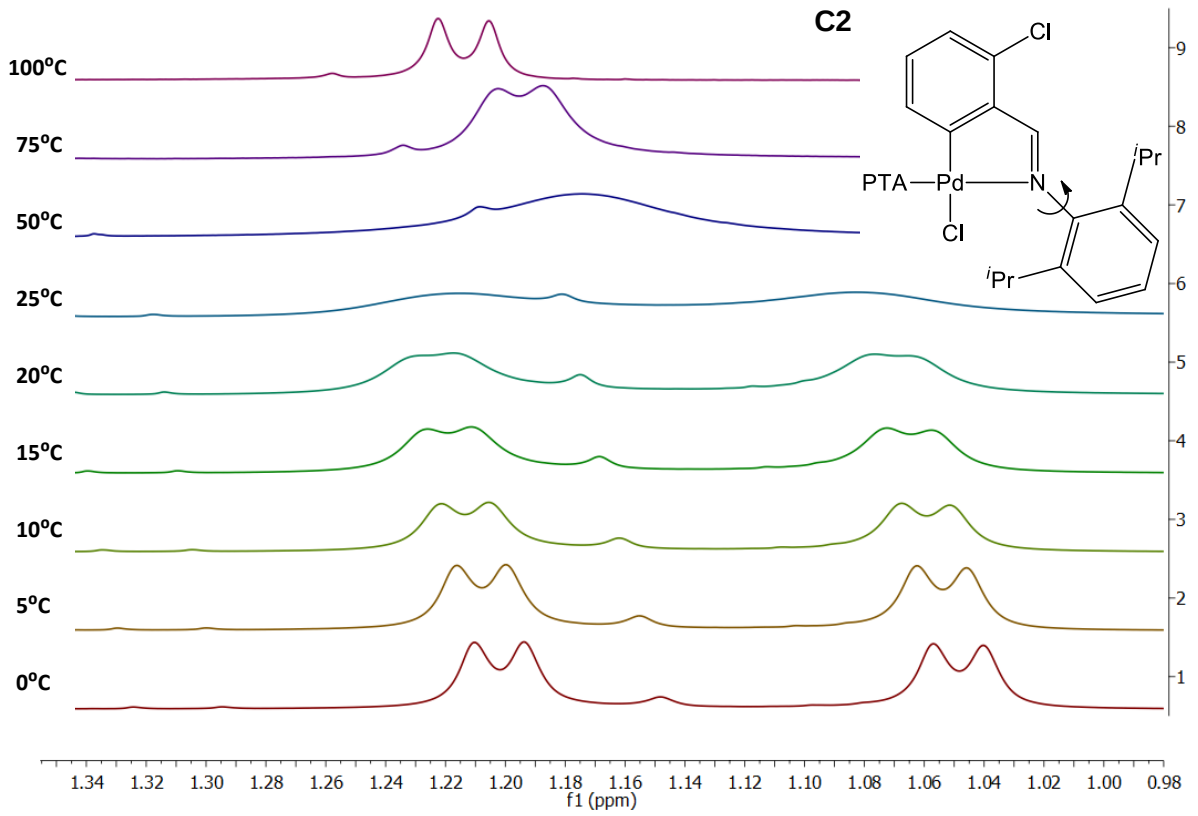

Figure 3.10: ^{1}H NMR spectroscopic array of C2 isopropyl methyl signals in TCE-d2 (0 to 100 °C), showing change in signal shape and chemical shift. Inset: Chemical structure of C2 showing possible rotation about the N-C bond.

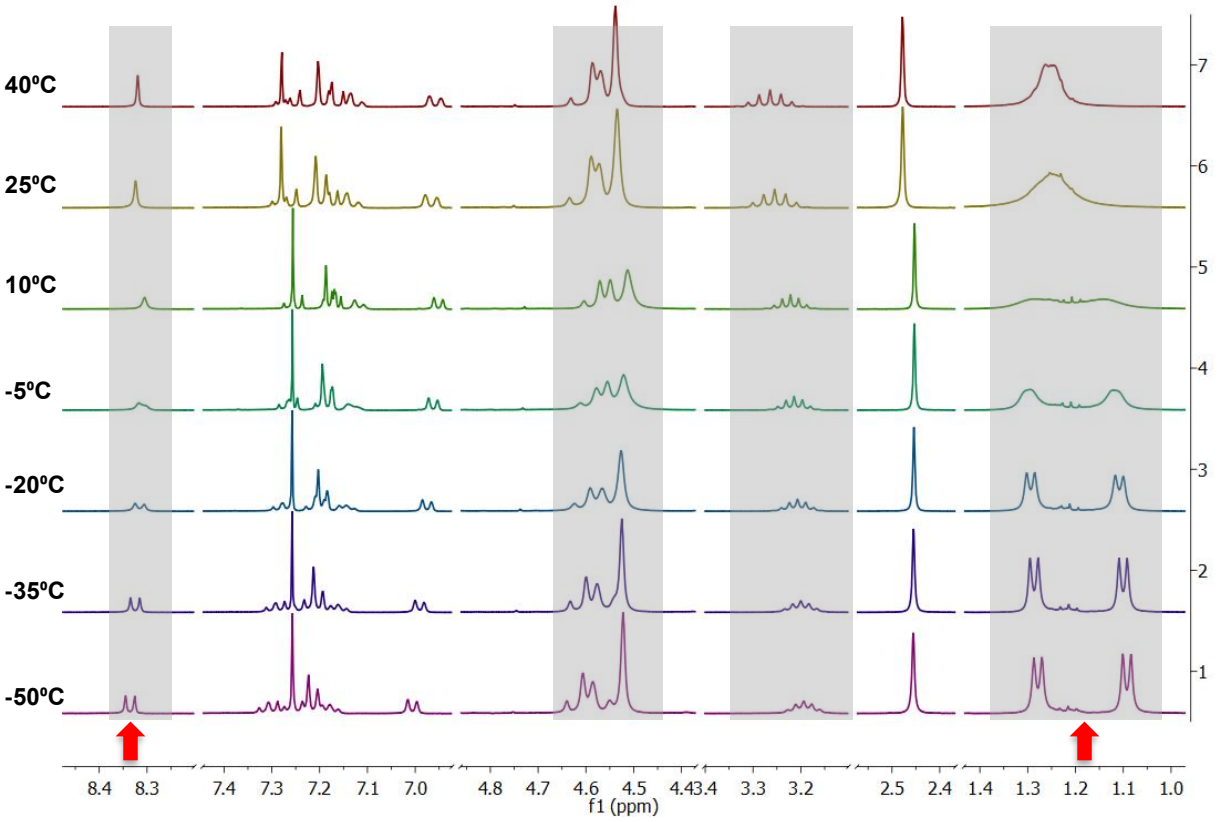

Figure 3.11: ^{1}H NMR spectroscopic array of C4 in $CDCl_3$ (-50 to 40 °C). Red arrow shows broadening signals and grey areas indicate signals with significant fine structural changes and/or changes in chemical shifts.

As stated previously, a chemical exchange process involves the nucleus of an atom experiencing two or more different chemical environments. As the nucleus is exposed to one environment and then another, the chemical shift is influenced and the changes can be observed in the NMR spectrum as a variety of line shapes, depending on the rate of exchange [2;4;5]. Based on the changes observed in the variable temperature spectra of the palladacycles in the current study, two possible chemical exchange processes were proposed (Scheme 3.1), a site-exchange event which results in the broadening of the methyl signals of the isopropyl groups and possibly the imine proton signal (indicated by red arrows on spectra i.e., possible rotation about the N-C bond, as indicated in Figure 3.10) and a bond breaking or bond forming event which results in fine structure and chemical shift changes of certain signals (indicated as grey areas on spectra i.e., possible PTA ligand dissociation). The proposed processes may or may not be linked. Each of these processes are discussed in Sections 3.2.2 and 3.2.3, respectively.

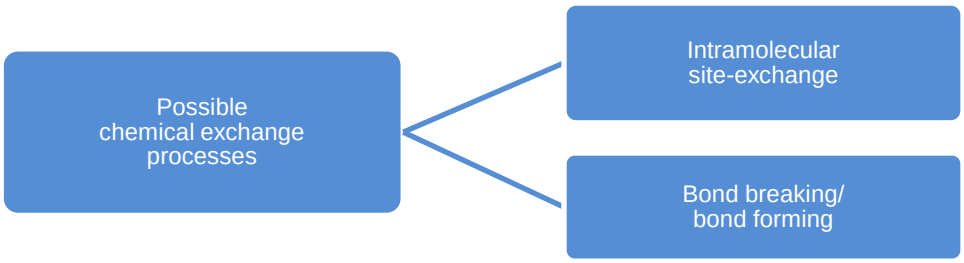

Scheme 3.1: Possible chemical exchange processes occurring in solution.

3.2.2 Proposed intramolecular two-site exchange process

Since the only signals displaying a variety of line shapes were the isopropyl methyl signals and the imine proton signal and the changes in the imine signal could be due to loss of $^{4}J_{H\text{-}P}$ rather than an exchange event, a symmetric two-site exchange process was proposed. This is a chemical exchange process where an isolated nuclear spin is exposed to two different chemical environments, with different chemical shifts, but the molecule is identical in both environments [1].

An example of how the ^{1}H NMR resonance signals change as a function of temperature for a symmetric two-site exchange is shown in Figure 3.12 [12]. The methyl signals of the isopropyl groups, shown in Figures 3.9 and 3.10, exhibit similar behaviour, where the two doublets (at low temperature) first condense and then become more resolved again at higher temperature. However, if only symmetric two-site exchange was taking place it is expected that the resonance signal in the regime of fast exchange would be exactly in the middle of the two

isopropyl methyl doublets in the regime of slow exchange. Yet, in the case of the PTA-based palladacycles, it was observed that the isopropyl methyl doublets shift downfield as temperature increases, indicating that another exchange process or some other reaction is taking place in addition to the site-exchange. Since the processes are not necessarily linked, the next section focuses only on the site-exchange process, whilst the second or additional process will be addressed in later sections.

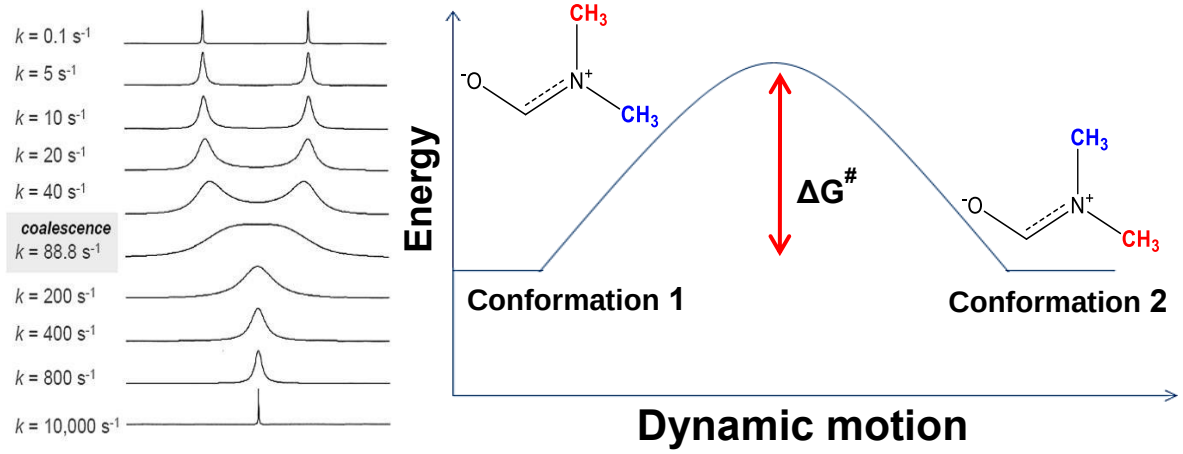

Figure 3.12: Variable temperature ^{1}H NMR spectra of dimethylformamide showing increasing exchange from the top to the bottom (left) [12] and general scheme showing symmetric site-exchange process as a function of Energy, where $\Delta G^{\#}$ is the energy barrier to rotation (right).

3.2.2.1 Symmetric two-site exchange model

The symmetric two-site exchange of the isopropyl methyl signals about the N-C bond was modelled using an in-house program, NMRfitv12, which was written by one of our collaborators, Dr. Gerber and his research group. The calculations employed in the program are based on the work by Vallurupalli [17]. Such calculations are reported extensively in the literature and are fairly well understood, therefore, the calculation details are not discussed here [1;4;5;9;18;19]. Although the program does not explicitly model symmetric site-exchange, the forward and reverse rate constants must be the same for such a process. Whilst significantly different rate constants mean that the site-exchange is not symmetric, viz. there is more than one stable conformer of the molecule. Further details of the program, NMRFitV12, can be found in the thesis of O'Kennedy [20]. The NMR line fit plots for the calculated data relative to the experimental data are shown in Figure 3.13.

At 0 °C, the methyl signals were observed as two doublets at 1.13 and 1.28 ppm. These signals represented a static system, where no site-exchange occurred. The spectrum at 10 °C showed broadening of the doublets and a very slight downfield shift to approximately 1.14 and 1.30 ppm. At 20 °C, it can be seen that the doublets had broadened quite significantly

and the signals were shifted to 1.15 and 1.31 ppm. The signal observed as two doublets at 0 °C appears as a broad doublet at 25 °C with a chemical shift of 1.23 ppm. This shift was slightly downfield from the average shift of the original doublets. Jumping to 50 °C, the signal was observed as a broad singlet at approximately 1.25 ppm. The broad singlet represented a system where the methyl sites are exchanging fast enough that an average signal of the two sites was observed. Increasing the temperature further was expected to increase the rotation/exchange beyond the detectable limit for NMR time-scale, thus the methyl signals are expected to collapse into a single doublet, representing two equivalent sites. The 75 °C and 100 °C spectra clearly showed this process, where the broad doublet became more resolved as the temperature was increased further.

The experimental data fit the model well with the exception of some minor peaks resulting from residual solvent impurities in the experimental spectra (1.2-1.4 ppm). The corresponding forward and reverse rate constants are reported in Table 3.2 and were found to be similar for each temperature, thus confirming the symmetric nature of the site-exchange.

Table 3.2: Forward and reverse rate constants, k_1 and k_2, for C2 at various temperatures.

Temperature (°C)	k_1 (s^{-1})	k_2 (s^{-1})
0	11.29	10.86
10	15.54	16.08
20	25.96	26.54
25	61.90	55.64
50	164.7	162.2
75	255.9	264.9
100	2511	2518

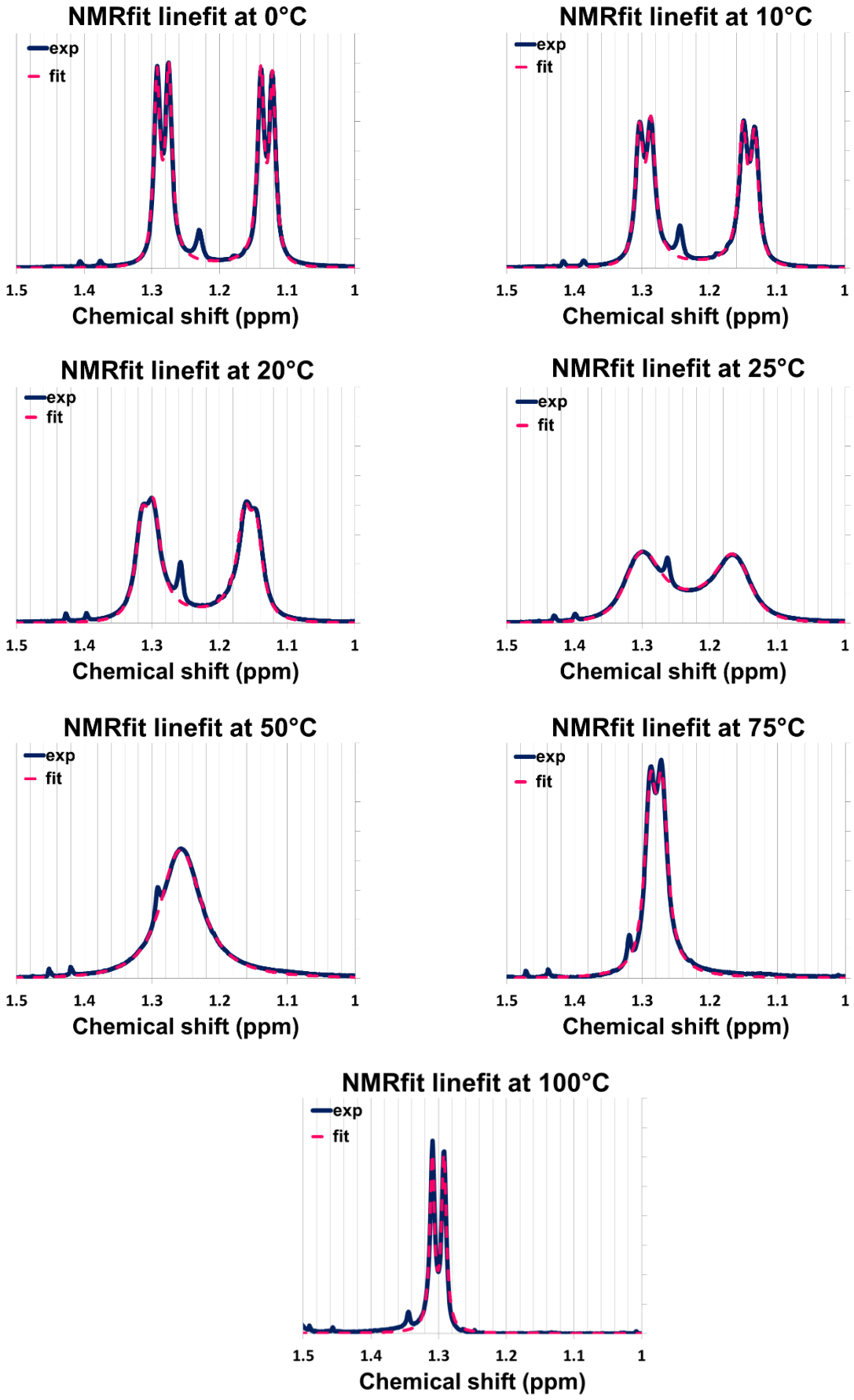

Figure 3.13: Excel plots showing correlation between experimental and calculated spectra of C2 in TCE-d2.

3.2.2.2 Determining the nature of the symmetric site-exchange

Having established that a symmetric site-exchange occurs in solution, the nature of the site-exchange was investigated. The aim of the investigation was to determine if the mechanism of interconversion leading to the observed broadening in the isopropyl methyl signals correlates with rotation about the N-C bond.

Therefore, the study was extended by calculating the rotational energy barrier. The enthalpy ($\Delta H^{\#}$), entropy ($\Delta S^{\#}$) and free energy of activation ($\Delta G^{\#}$) were calculated using the obtained rate constants to construct Eyring plots which depicts the reaction rate constant as a function of temperature (Equation 3.1) [2;14]. Eyring plots for all complexes yielded linear trends (Figures 3.14 and A2.10-2.16). The enthalpy ($\Delta H^{\#}$) and entropy ($\Delta S^{\#}$) of activation were calculated from the slopes and intercepts of these graphs (Equations 3.2 and 3.3) and were listed in Table 3.3. The activation energy ($\Delta G^{\#}$) was then calculated using Equation 3.4 and tabulated (Table 3.3).

Equation 3.1: Eyring equation.

$$ln\frac{k}{T} = -\frac{\Delta H^{\#}}{R}\frac{1}{T} + \frac{\Delta S^{\#}}{R} + ln\frac{k_B}{h}$$

Equation 3.2: Slope of the Eyring plot.

$$slope\colon\ -\frac{\Delta H^{\#}}{R}$$

Equation 3.3: Intercept of the Eyring plot.

$$intercept\colon \frac{\Delta S^{\#}}{R} + ln\frac{k_B}{h}$$

Equation 3.4: Energy of activation.

$$\Delta G^{\#} = \Delta H - T\Delta S$$

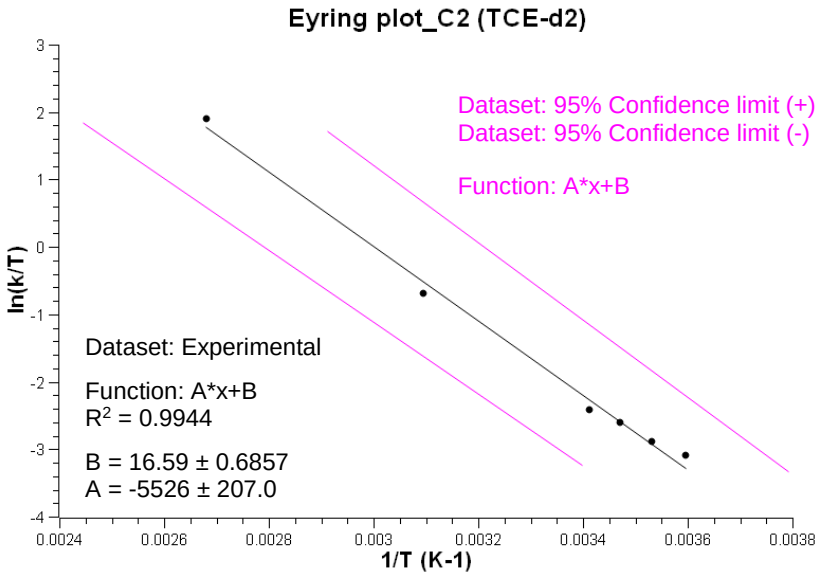

Figure 3.14: Eyring plot of C2 in TCE-d2.

Table 3.3: Calculated thermodynamic data from the Eyring plots of C1-C8 in $CDCl_3$.

Complex	$\Delta H^{\#}$ (kJ.mol^{-1})	$\Delta S^{\#}$ (kJ.mol^{-1}K^{-1})	$\Delta G^{\#}$ (kJ.mol^{-1})
C1 (2-H)	32.21 ± 0.9254	-0.1018 ± 0.003342	60.01 ± 1.838
C2 (2-Cl)	42.61 ± 0.6119	-0.09395 ± 0.001986	68.27 ± 1.155
C4 (2-Me)	39.74 ± 0.9803	-0.06635 ± 0.003577	57.87 ± 1.957
C5 (4-Me)	35.51 ± 0.8289	-0.09071 ± 0.002950	60.29± 1.635
C6 (2-F)	37.63 ± 0.8921	-0.09885 ± 0.003026	64.63 ± 1.719
C7 (2-NO_2)	35.88 ± 1.236	-0.09355 ± 0.004227	61.43 ± 2.390
C8 (2-OMe)	39.87 ± 1.198	-0.09089 ± 0.004057	64.69 ± 2.306

*No thermodynamic data were obtained for **C3**, as the thermodynamics of this compound are too slow and therefore cannot be detected by NMR.

The Eyring plots showed that the experimental data lie within the 95% confidence band for all complexes that were modelled [14]. The linear Eyring plots confirmed that the observed broadness of the isopropyl methyl signals resulted from a symmetric site-exchange.

Since one of the most likely mechanisms by which the isopropyl methyl groups can exchange is the rotation of the 2,6-diisopropylaniline aryl ring about the N-C bond, the literature was consulted in order to evaluate this proposal. A search for aryl ring rotation did not yield many results, however, the most relevant examples are included in Table 3.4. The literature rotational energy barriers were compared with the calculated rotational energy barriers in Table 3.3.

The rotational energy barriers for the PTA-palladacycles were found to be in the range of 58-68 kJ/mol. When comparing the rotational energy barrier of the C_6F_6 aryl ring with larger groups involving aryl rings, it is clear that the energy barrier tends to increase with the size of the moiety that is rotating. Based on the examples in Table 3.4, the range of energy barriers for aryl ring rotations or moieties containing aryl rings is 48-87 kJ/mol. If the large size of the rotating moiety in the last entry is regarded as being too large for comparison with the 2,6-diisopropylaniline moiety in the PTA-palladacycle system, the range can be refined to approximately 48-56 kJ/mol. This matches the observed rotational energy barriers quite well. Thus, based on the rotational energy barriers, it was quite possible that aryl ring rotation about the N-C bond occurs in solution [21-23].

Table 3.4: Comparison of rotational energy barriers from the literature.

Structure showing rotating moieties	$\Delta G^{\#}$ (kJ/mol)
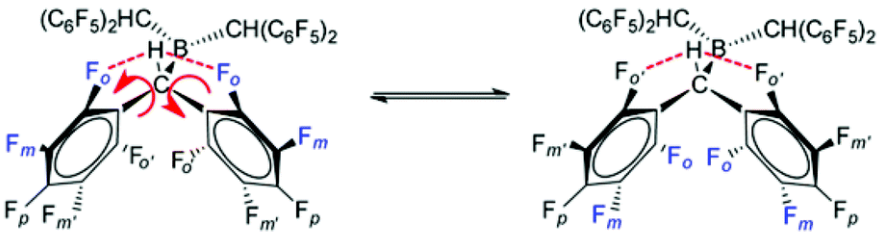	48 (C-C; red arrows) 56 (C-B; not indicated) [21]
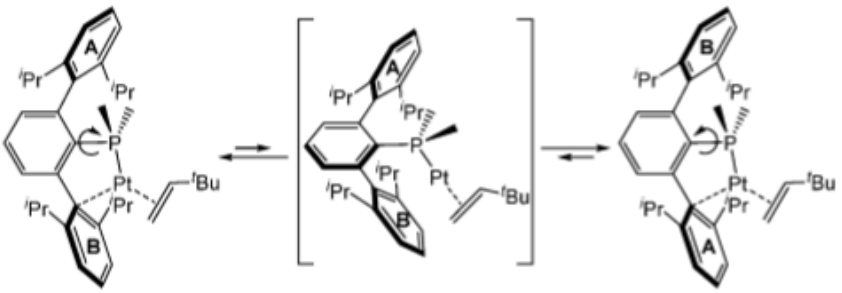	53 [22]
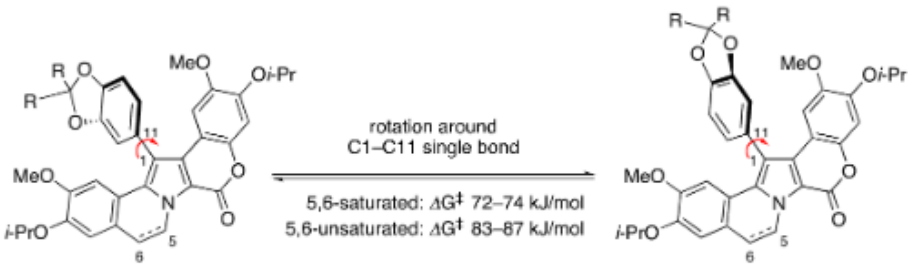	72 – 87 [23]

Variable temperature ^{1}H, ^{13}C and ^{31}P NMR spectra were collected for **C2** (Figures 3.15-3.18), to determine if all of the NMR signals, not just the isopropyl methyl signals, could corroborate the above finding.

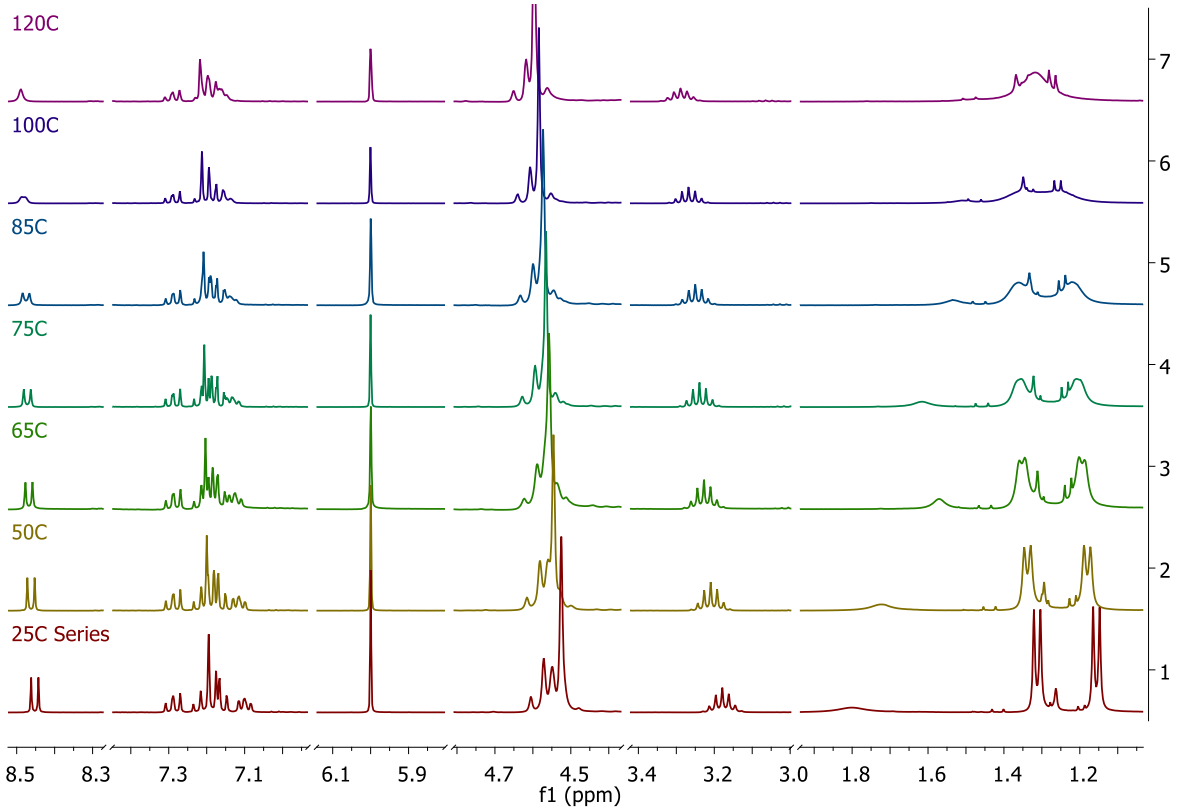

Figure 3.15: ^{1}H NMR spectroscopic array (25-120 °C) of C2 in TCE-d2.

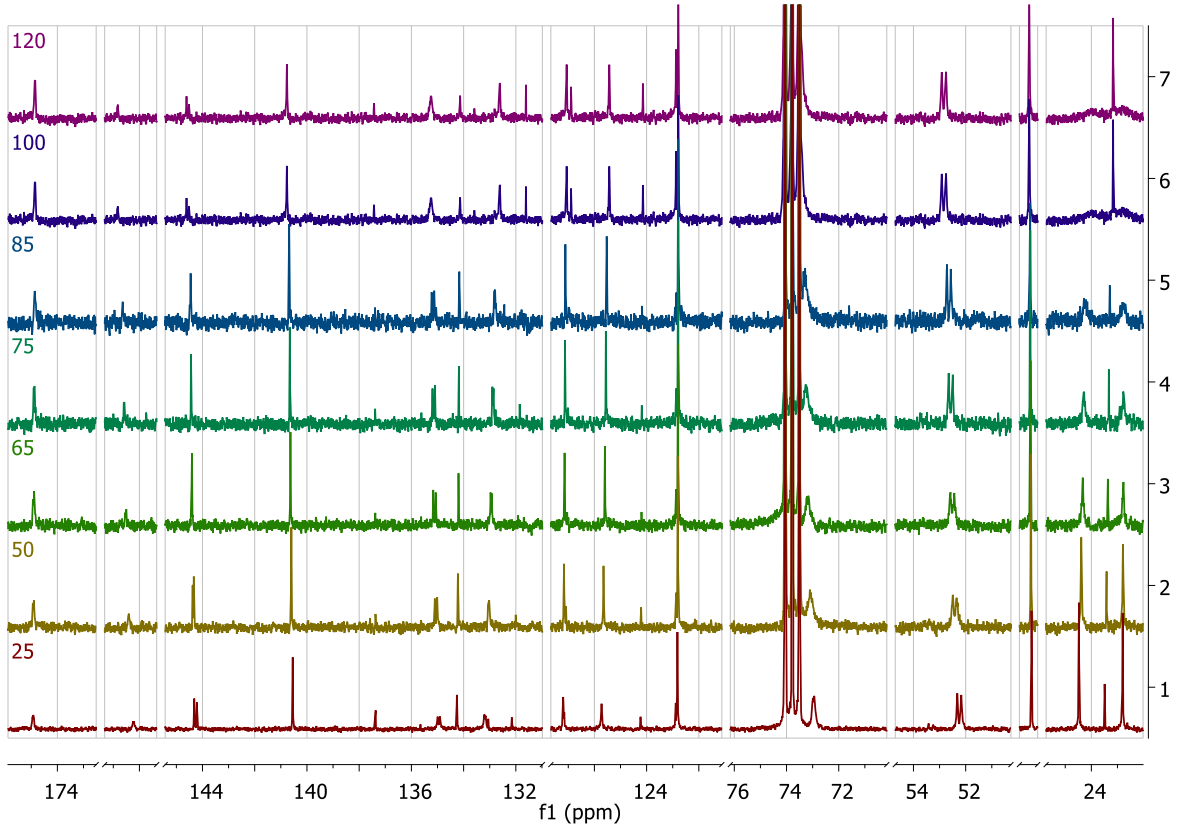

Figure 3.16: ^{13}C NMR spectroscopic array (25-85 °C) of C2 in TCE-d2.

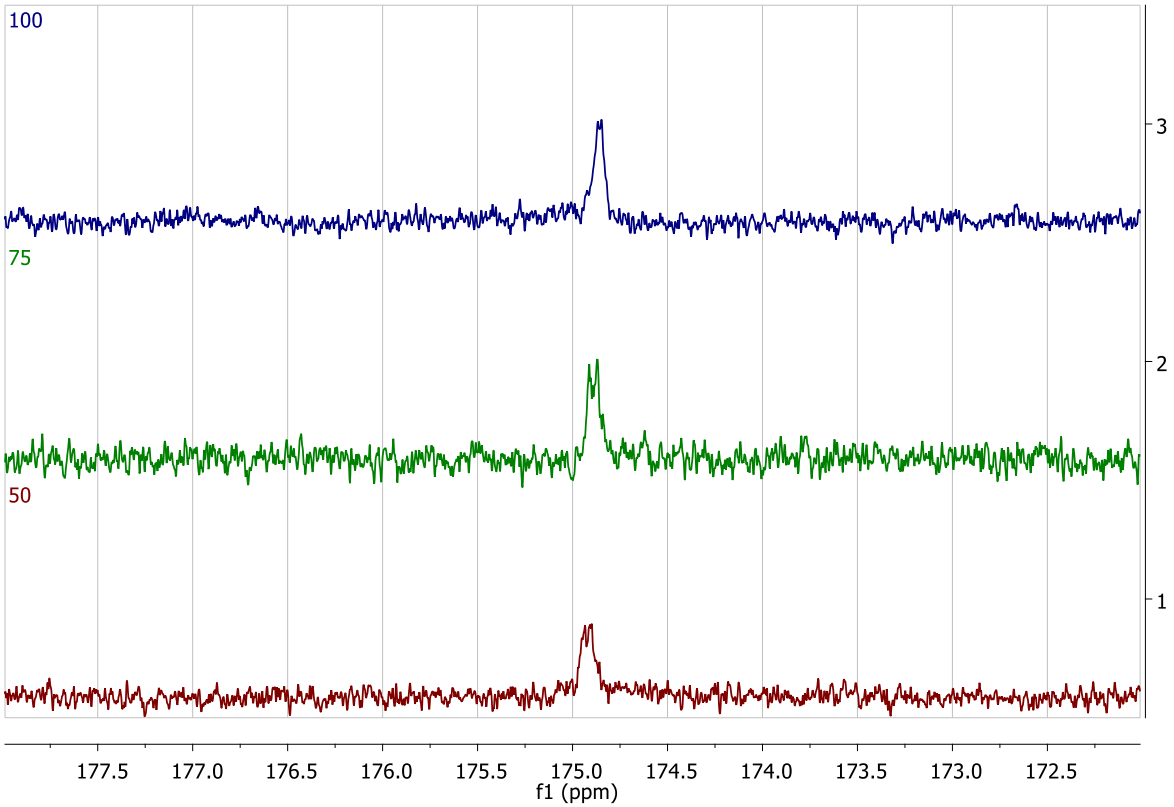

Figure 3.17: ^{13}C NMR spectroscopic array (50-100 °C) of C2 in TCE-d2 showing the expected broadening and an upfield shift in the imine carbon signal.

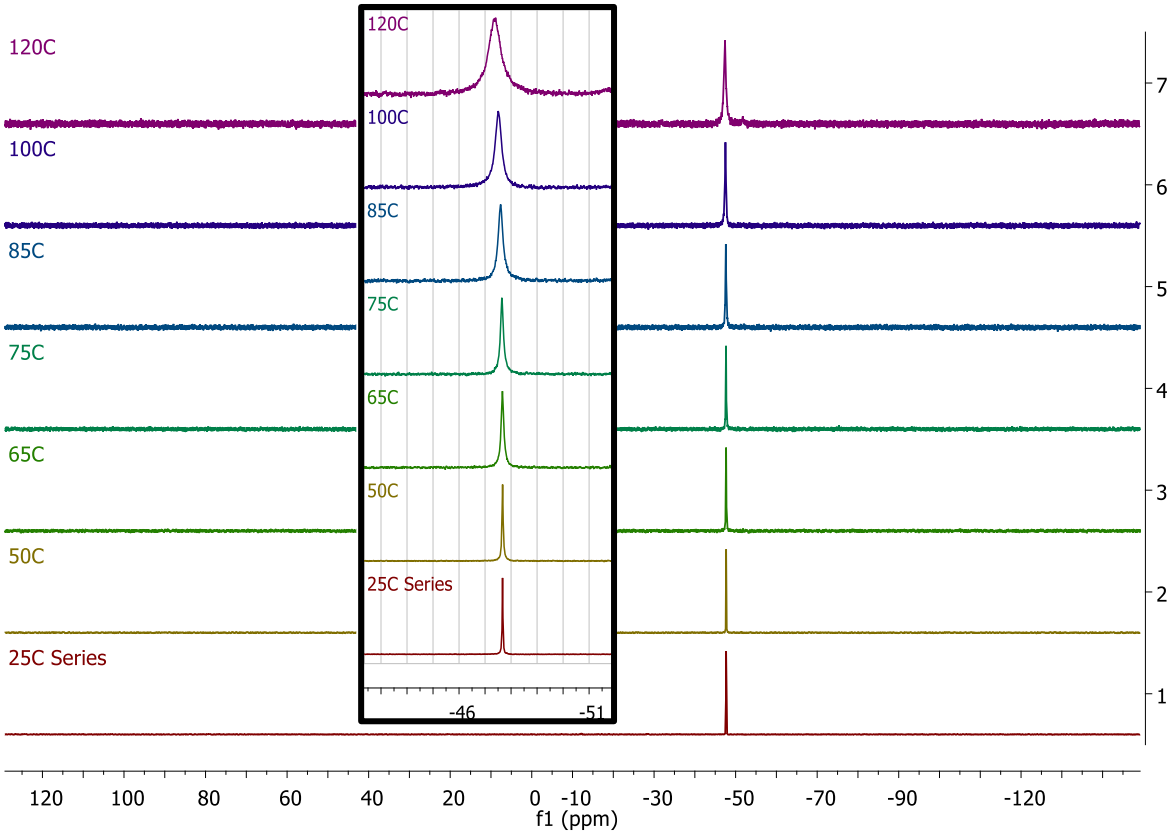

Figure 3.18: ^{31}P NMR spectroscopic array (25-120 °C) of C2 in TCE-d2 with inset of zoomed-in region.

The ^{1}H NMR spectra (Figure 3.16) showed that the isopropyl methyl signals coalesce from two doublets to a broad singlet and shift approximately 0.085 ppm downfield. The multiplet observed for the methine groups is in fact two overlapping septets (as determined by the presence of two different coupling constants) which have almost identical chemical shifts, as determined in Chapter 2. No clear change in the multiplicity of these signals was observed with increasing temperature, but the downfield shift was observed to be 0.11 ppm. The PTA signal showed fine structural changes and a 0.06 ppm downfield shift. There were also some changes to the fine structure of the aromatic signals. The imine signal showed coalescence from a doublet to a singlet and a 0.04 ppm downfield shift.

From the variable temperature ^{13}C NMR spectra (Figures 3.17 and 3.18), the methyl signals show slight broadening and a relatively small upfield shift. The CH signal shifts downfield by 0.9 ppm shift and no change in multiplicity was observed. Since the CH signals in the ^{1}H NMR spectra overlap quite closely, the CH signals in the ^{13}C NMR spectrum are presumed to be so close that they overlap perfectly and are observed as a singlet, as was the case for the μ-chloro palladacycles and the PPh_3- and PMe_3 analogues, where the N-C bond was restricted and the methyl signals were inequivalent and only one CH signal was observed [15;16]. The P-CH_2-N doublet showed a decrease in the coupling constant and a downfield shift of 0.59 ppm. The N-CH_2-N doublet overlapped with the solvent peak, but at lower temperatures, the signal could be observed just upfield of the solvent signal. A 0.22 ppm downfield shift was observed with increasing temperature, before the signal was completely masked by the solvent signal. Unfortunately, the multiplicity could not be determined due to the overlap with the solvent signal. The changes observed in the PTA signals suggest that there are slight changes in the chemical environment around the PTA ligand. The aromatic region did not show any large shifts, however, the three signals that initially showed $J_{C\text{-}P}$ coupling seem to lose the coupling with increasing temperature. Finally, the imine signal shows coalescence from a clear doublet to a broad unresolved doublet.

The variable temperature ^{31}P NMR spectra (Figure 3.18) show one signal at approximately -47.5 ppm which broadens slightly with increasing temperature and shifts slightly downfield.

Taken together, the NMR spectral arrays show the isopropyl methine and methyl signals were each represented by two signals at lower temperatures, thus confirming that the two sites are inequivalent when there is no site-exchange. Furthermore, the broadening of the isopropyl methyl signals with increasing temperature and the absence of broadening and significant changes in other signals (aside from the imine signal) suggested that the site-exchange occurs via rotation about the C-N bond, as determined from the rotational energy barriers. Loss of $^{4}J_{H\text{-}P}$ coupling in the imine signal with increasing temperature was also observed in both the

^{1}H and ^{13}C NMR spectra. However, these changes cannot be accounted for by simply having aryl ring rotation as proposed earlier. As stated previously, the changes in the imine signal may be caused by a bond breaking process, rather than a simple site-exchange process. The PTA signals in all three spectral arrays showed both fine structural changes and changes in the chemical shifts of certain signals. These changes could possibly be attributed to a second dynamic process occurring in solution. At this stage it is not certain whether the two processes are linked or not.

Based on these observations, the rotation of the 2,6-diisopropylaniline ring is likely restricted by steric and/or electronic interactions at low temperature, hence, the methyls and methines are in two distinct environments. Whilst at higher temperature, the species in solution either takes on a less sterically strained conformation or the electronic interactions are overcome by the increased energy in the system, thus allowing the 2,6-diisopropylaniline ring to rotate about the N-C bond, resulting in the methyl and methine signals being equivalent. It is thought that the process by which the site-exchange is facilitated must involve the PTA ligand, as this process was not observed for the analogous PPh_3 and PMe_3 complexes [15;16].

As indicated before, the computational model described earlier in this chapter seems to support the experimental observations to some degree and suggests that a symmetric site-exchange process occurs in solution (Scheme 3.2), most likely via rotation of the 2,6-diisopropyl aniline ring about the N-C bond. This is suggested by the fact that the rotational energy barriers which were calculated approximate those reported for aryl ring rotation. However, despite a reasonable fit of the model, there was one apparent discrepancy in the variable temperature results for the PTA-based palladacycles, viz. the slight downfield shift in the methyl signals of the isopropyl groups as the temperature was increased (Figure 3.15). This was attributed to the effects of a second possible dynamic process occurring in solution. Therefore, the next step was to investigate the second process occurring in solution which was thought to be either a bond-breaking or -forming process.

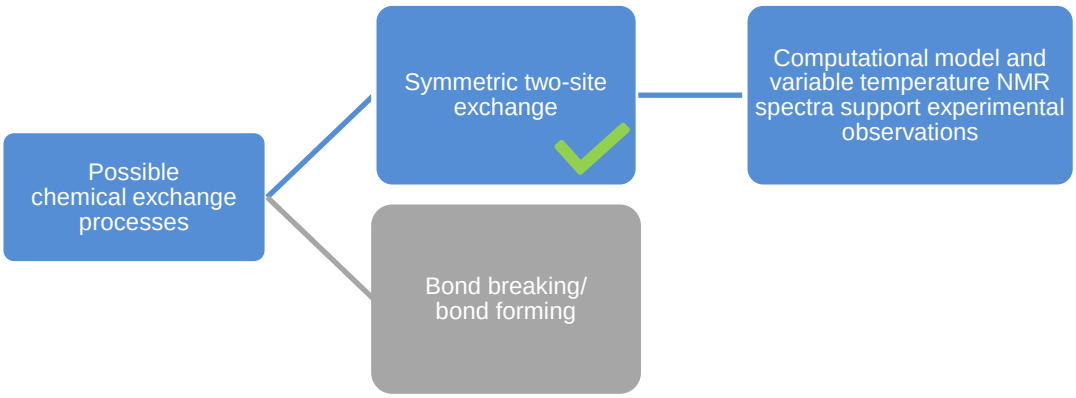

Scheme 3.2: Symmetric site-exchange was confirmed as a chemical exchange process occurring in solution.

3.2.3 Possible PTA ligand dissociation

The fine structural and chemical shift changes observed in the variable temperature NMR spectra are indicative of either bond breaking or bond forming events, where the species before and after the bond breaking/forming process are different. Since the extent of the changes in the signals increased with increasing temperature, a bond breaking process was potentially more favoured, as increasing the temperature facilitates breaking of bonds. One of the possible bonds that could be involved in the bond breaking process is the Pd-P bond.

The possible dissociation of the PTA ligand was thus considered, based largely on the changes observed in the imine signal. As stated earlier, the splitting of the imine signal is due to $^{4}J_{H\text{-}P}$ coupling between the imine proton and the PTA phosphorous atom. Thus, loss of the coupling at higher temperatures could be a consequence of possible PTA dissociation under these conditions. Should this be the case, one would expect that the PTA proton signals should change from those of the coordinated PTA ligand to those of the free PTA ligand. Thus, variable temperature ^{1}H and ^{31}P NMR spectra of **C2** and **C4** were recorded and compared to the NMR spectra of free PTA. The results of this study are discussed in the next section.

3.2.3.1 PTA ligand dissociation

In order to monitor the coordination of the PTA ligand, the ^{1}H and ^{31}P NMR spectra of the free ligand were recorded in deuterated TCE (Figure 3.19). The variable temperature ^{1}H and ^{31}P NMR spectra of **C2** and **C4** were also recorded in deuterated TCE in the range of 25 – 120 °C (Figures 3.20 - 3.23, respectively).

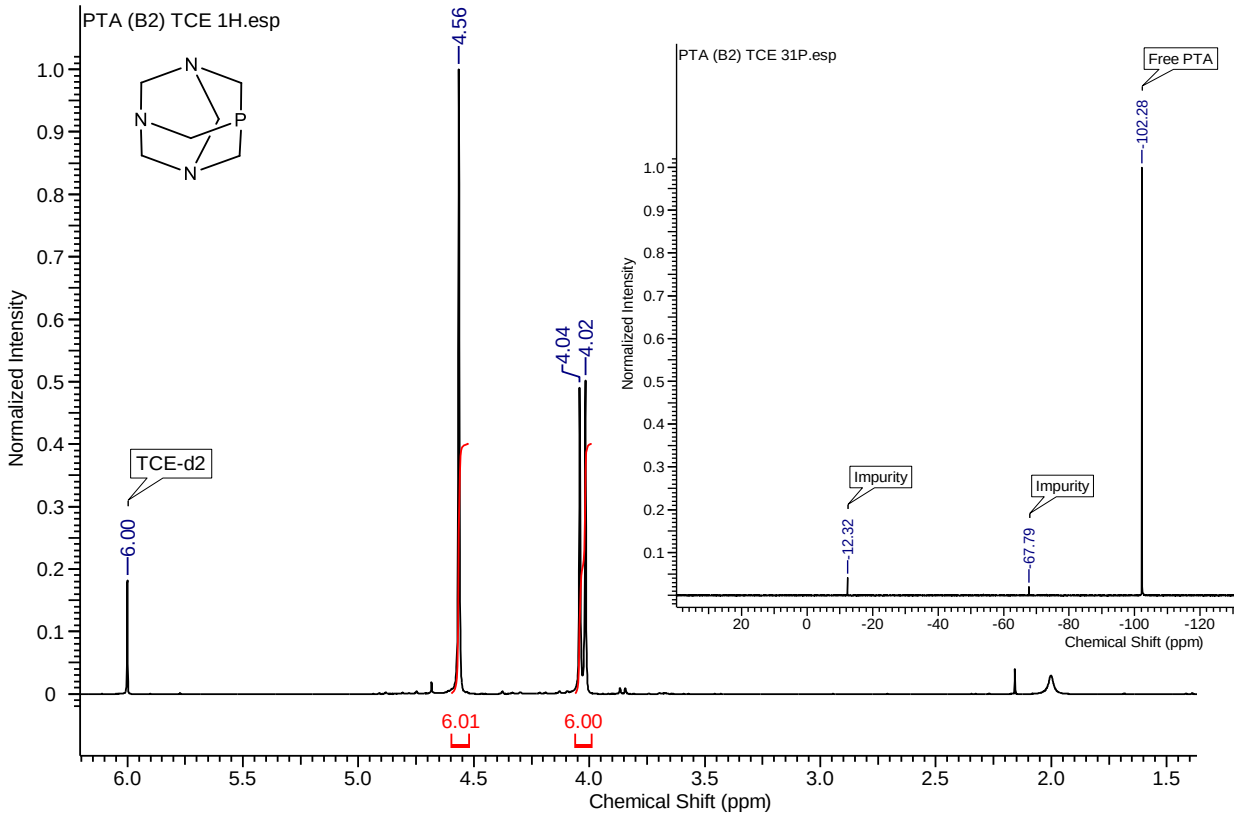

Figure 3.19: ^{1}H NMR spectrum (25 °C) of PTA in TCE-d2 with inset of ^{31}P NMR spectrum (25 °C) of PTA in TCE-d2.

The ^{1}H NMR spectrum for the free PTA ligand shows two well resolved signals (Figure 3.19), viz. a doublet at 4.03 ppm (NC*H*$_2$N) and a singlet at 4.56 ppm (PC*H*$_2$N). Although unusual, the singlet resonance for the PC*H*$_2$N signal has been reported previously [24]. The ^{31}P NMR signal for free PTA occurs at -102.28 ppm (Figure 3.19 inset).

The variable temperature ^{1}H NMR spectra of **C2** and **C4** (Figures 3.20 and 3.22) showed the coalescence of the imine signal from a doublet to a singlet, accompanied by a slight downfield shift. Changes in the fine structure of the PTA signal at approximately 4.5-4.6 ppm were observed; however, the well resolved singlet and doublet of the free ligand in the region of 4.0-4.6 ppm were not observed. More importantly, the ^{31}P NMR signals of **C2** and **C4** (Figures 3.21 and 3.23) both showed only a very slight downfield shift and broadening of the coordinated PTA signal at approximately -48 ppm, but no signals were observed at -102 ppm, the region for the free PTA ligand.

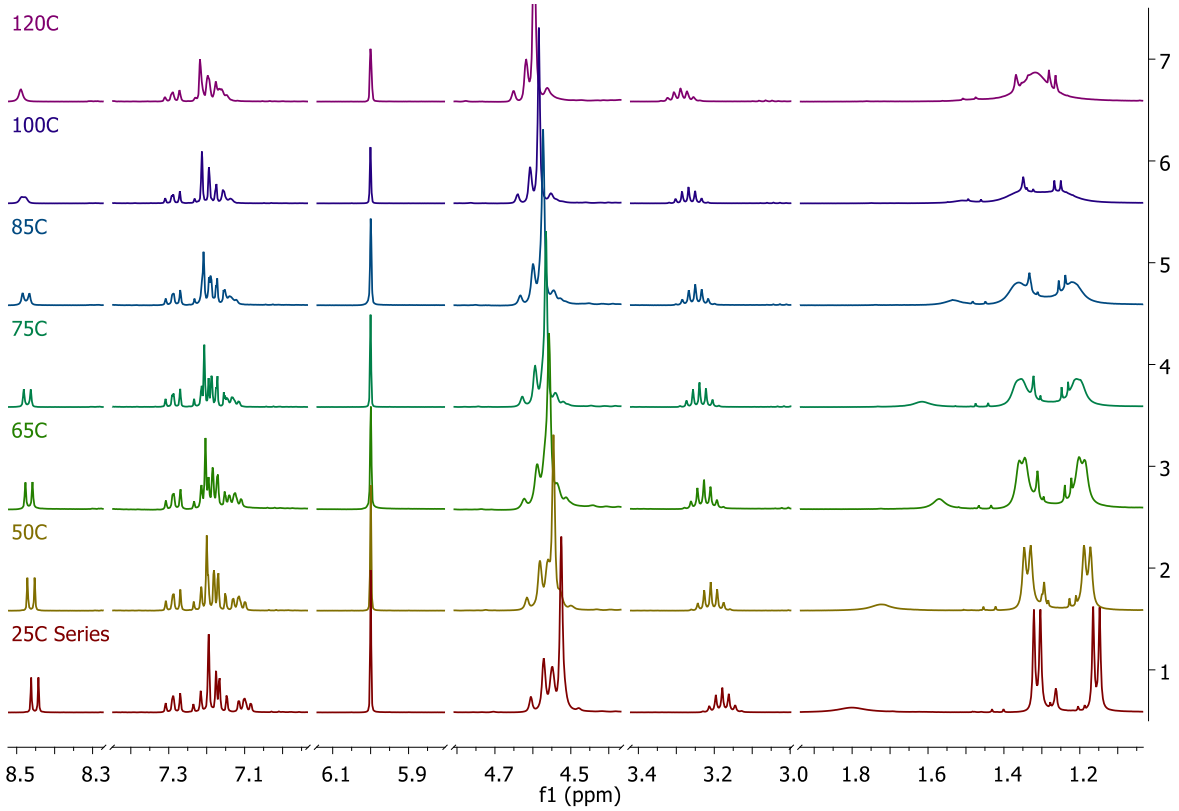

Figure 3.20: ^{1}H NMR spectroscopic array (25-120 °C) of C2 in TCE-d2.

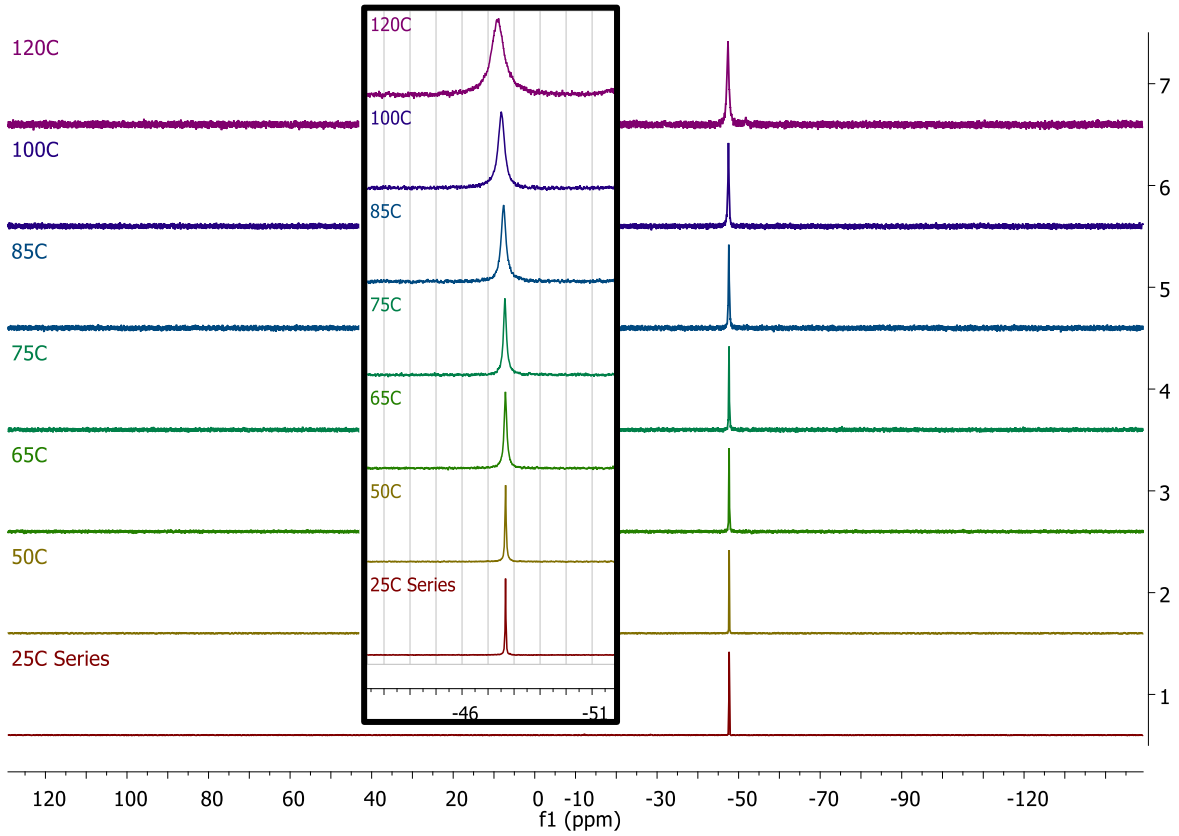

Figure 3.21: ^{31}P NMR spectroscopic array (25-120 °C) of C2 in TCE-d2 with inset of zoomed-in region.

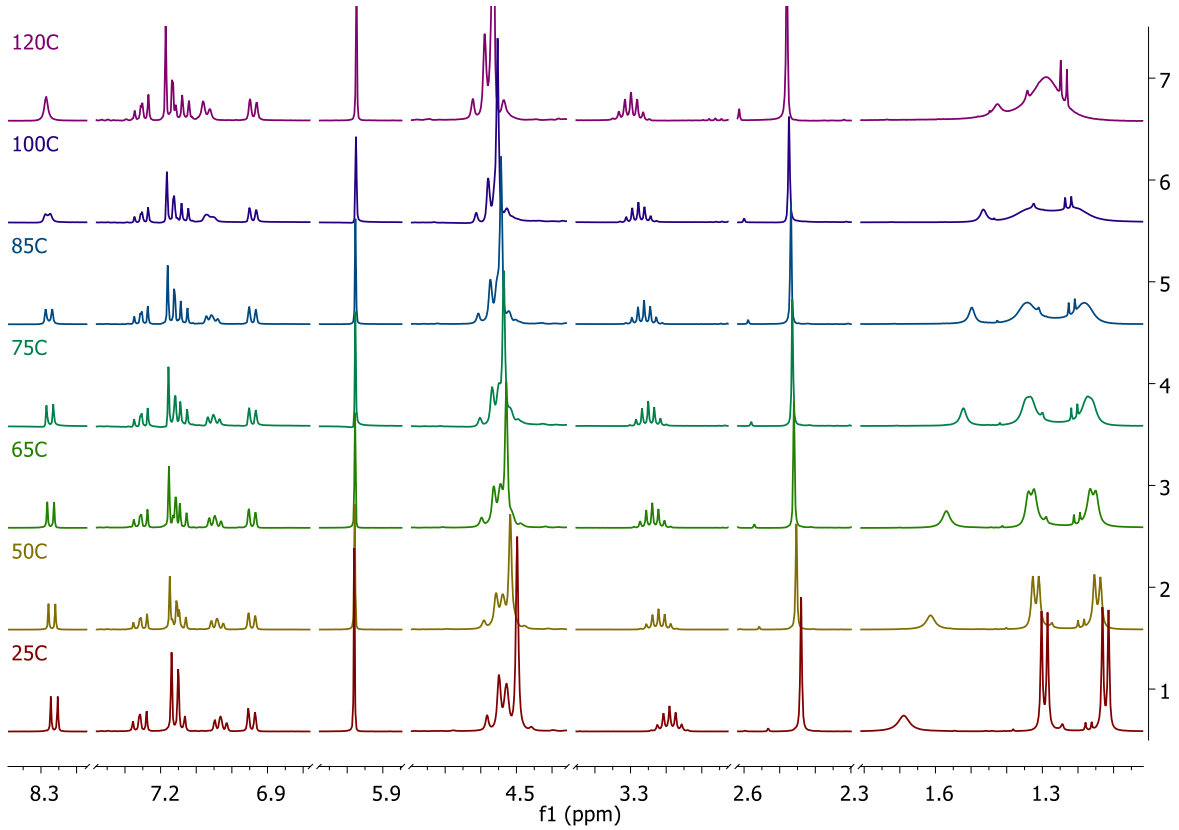

Figure 3.22: ^{1}H NMR spectroscopic array (25-120°C) of C4 in TCE-d2.

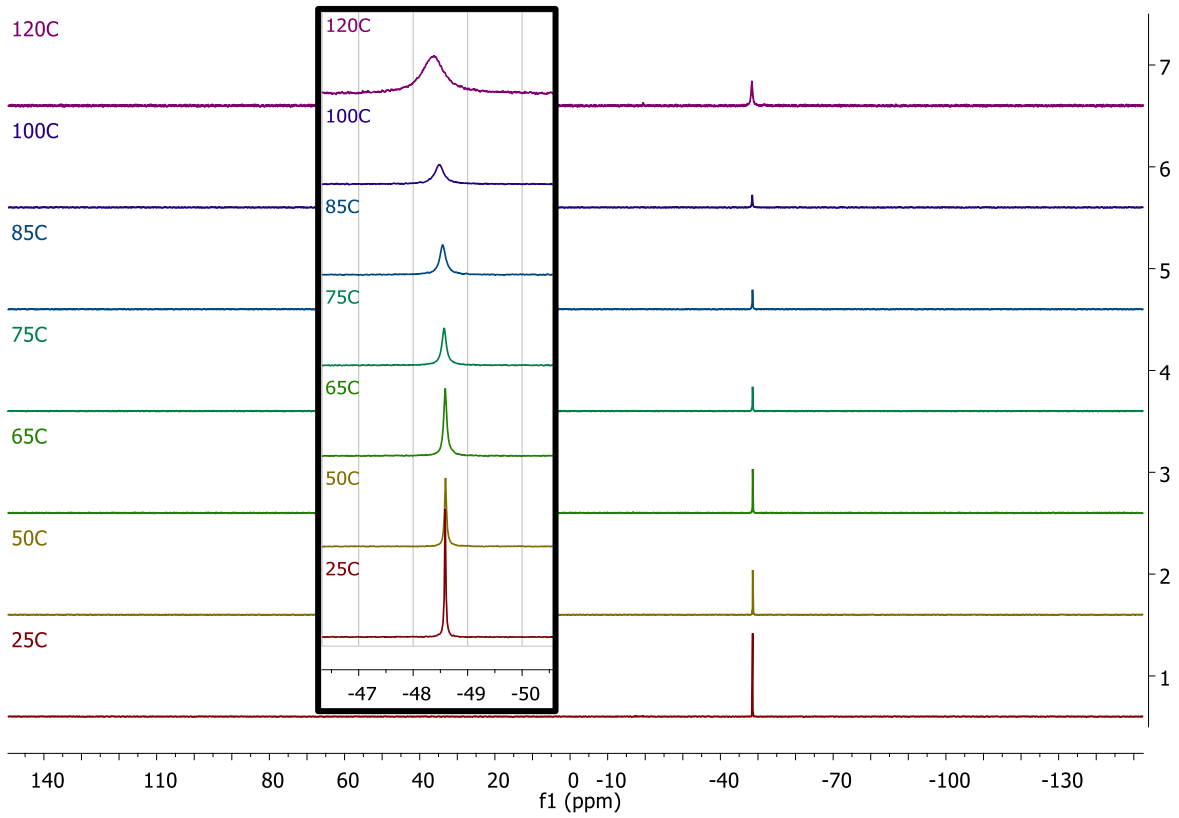

Figure 3.23: ^{31}P NMR spectroscopic array (25-120 °C) of C4 in TCE-d2.

Based on these observations, it was concluded that the change in the imine signal from a doublet (low temperature) to a singlet (high temperature) was not due to dissociation of the PTA ligand. Thus, there had to be an alternative bond breaking or bond forming process in solution to account for the observed changes in the signals for the imine and PTA protons in the variable temperature spectra.

Close examination of the variable temperature ^{1}H NMR spectra of **C2** and **C4** (Figures 3.20 and 3.22) revealed that besides the isopropyl signals, the PTA signals showed significant changes in signal shape or fine structure accompanied by a 0.07 ppm downfield shift with increasing temperature. Since the proton signals of PTA showed significant changes and the ^{31}P signal showed almost no change besides peak broadening, a bond forming process was considered to try and account for the observed spectra. In a search of the literature, a few examples were found that describe processes in which PTA undergoes self-association. Therefore, PTA self-association was considered as a possibility (Scheme 3.3). The results of this investigation are discussed in the following section.

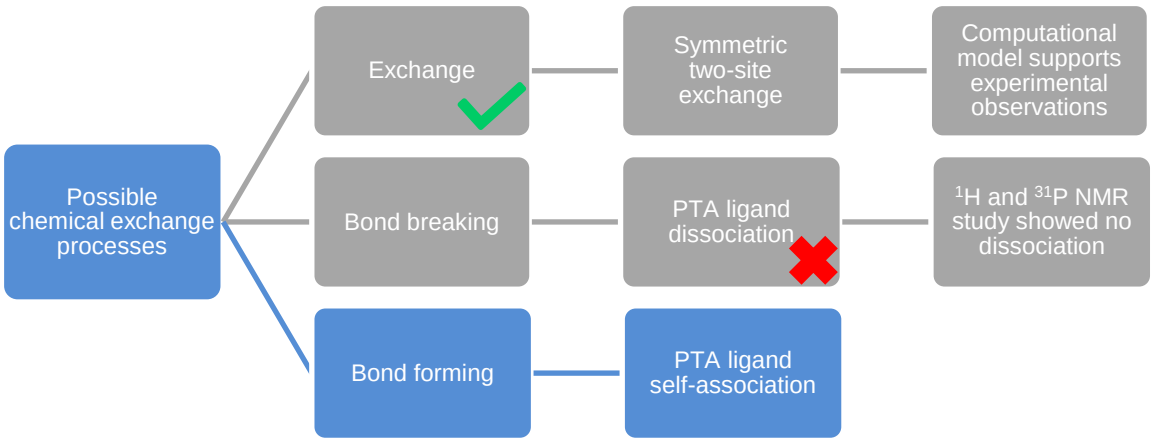

Scheme 3.3: Possible PTA ligand self-association proposed as an alternative bond forming process, since PTA ligand dissociation does not occur.

3.2.4 Possible PTA self-association

From a literature investigation, a number of reports seemed to indicate that the PTA ligand has the ability to form hydrogen-bonded networks between its nitrogen atoms and solvated water molecules in crystals [25;26]. Furthermore, $N^{+}H\cdots N$ bonding between PTA ligands has also been demonstrated (Figure 3.24) [25]. These interactions directed aggregation through hydrogen bond formation. Thus, an aggregation process via self-association of the PTA ligands is a plausible process to consider.

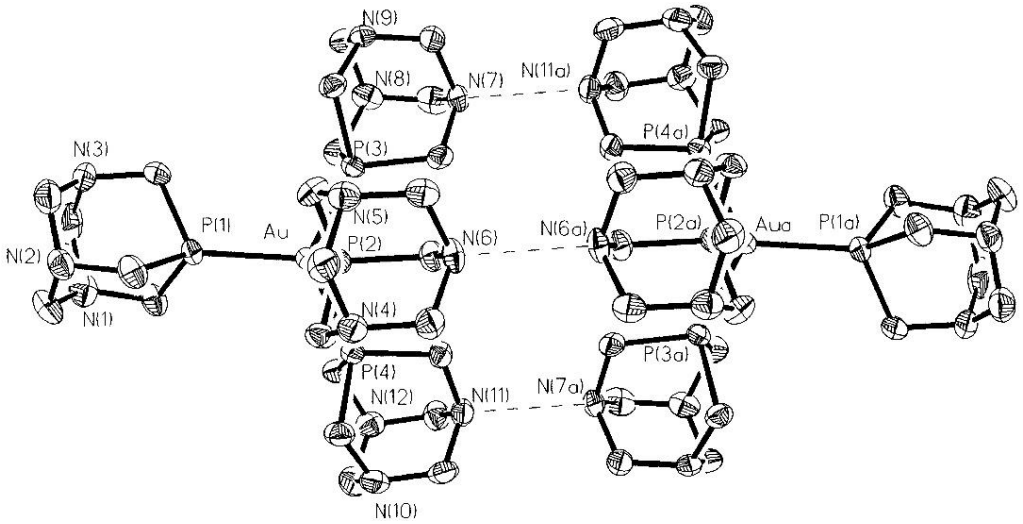

Figure 3.24: N-H^{+}···N interactions between six PTA ligands of [(TPA)$_4$Au](PF$_6$)·1.5HCl·H$_2$O [25].

Weak, non-conventional C-H···O contacts in 2,6-bis(acylamino)pyridines [27] with a C-O bond distance of 3.405(3), as shown in Figure 3.25, have been reported in the literature. These non-covalent interactions were also observed in non-covalent dimers of 2-acylaminopyrimidines, in addition to N-H···N hydrogen bonds, therefore, providing further stabilisation of the dimer. Since these weak C-H···O interactions exist, it is possible that there could be similar C-H···N interactions between two PTA ligands.

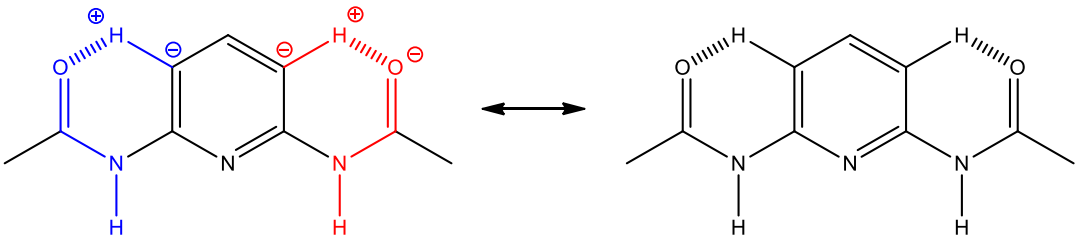

Figure 3.25: An example of weak, non-conventional C-H···O interactions detected in 2,6-bis(acylamino)pyridines [27].

To establish whether PTA can self-associate, a simple NMR spectroscopy experiment was performed, in which an additional amount of PTA was added to a NMR sample containing a known amount of PTA. The ^{1}H and ^{31}P NMR spectra were recorded for the various concentrations of PTA and the chemical shift changes were monitored. The results of this study are shown in Figures 3.26 and 3.27.

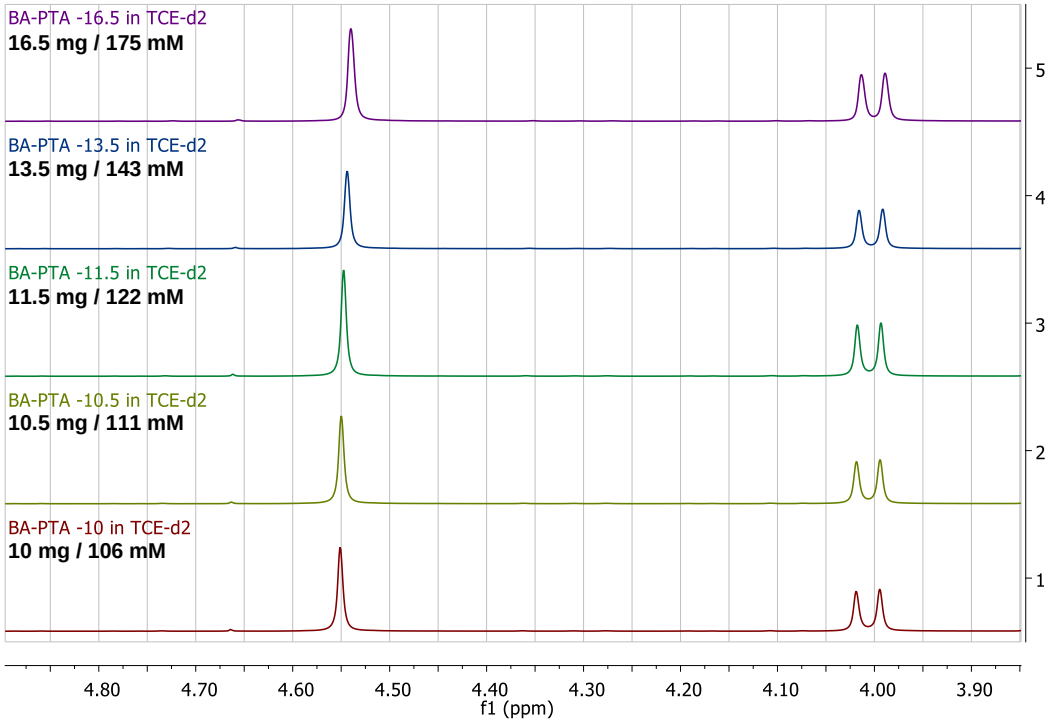

Figure 3.26: ^{1}H NMR spectra of PTA (10 mg to 16.5 mg/ 106-174 mM) showing slight upfield shift with increasing concentration.

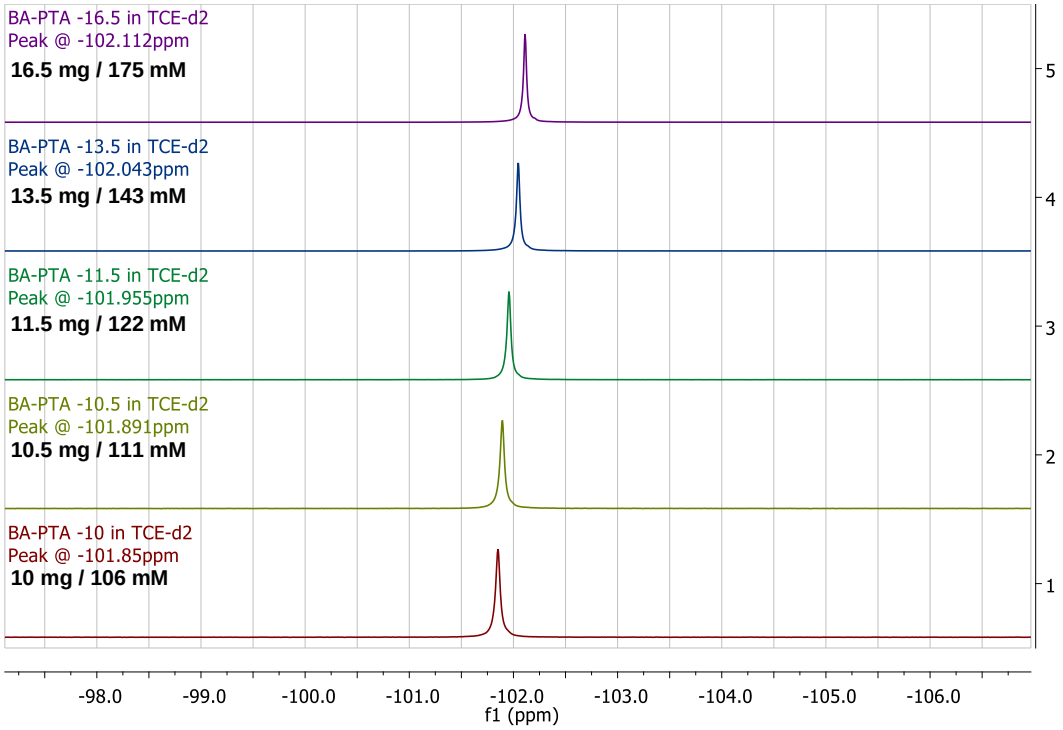

Figure 3.27: ^{31}P NMR spectra of PTA (10 mg to 16.5 mg/ 106-175 mM) showing upfield shift with increasing concentration.

From Figures 3.26 and 3.27, it appears as if there is some indication that PTA self-associates based on the fact that the chemical shifts of the PTA signals change with increasing concentration. It would however seem that the association (if indeed present) is very weak, since only small changes in the NMR spectra were observed.

Work done by LaPlante *et al*. [28], showed that many potential drug compounds were able to aggregate (where aggregate is defined by IUPAC as an assemblage of primary particles exhibiting an identifiable collective behaviour) in aqueous media, leading to false-positives in high-throughput screening for biological activity. They stated that aggregators exhibit unusual NMR trends. Thus, they developed an NMR spectroscopy assay which distinguishes between aggregators and non-aggregators. The assay is a simple dilution assay and the results of such an assay are shown in Figure 3.28. By employing similar NMR spectroscopy experiments, it was attempted to probe the possibility of PTA self-association.

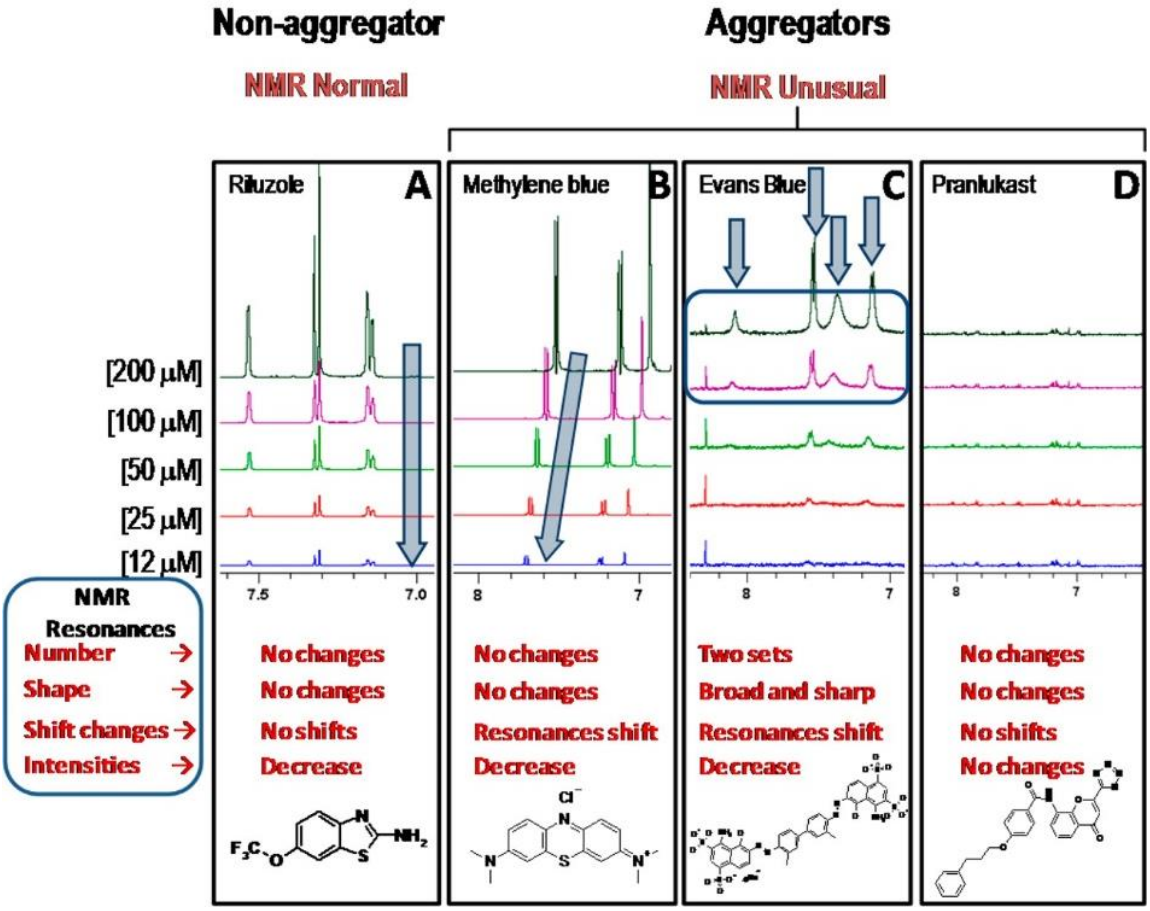

Figure 3.28: Examples of the NMR spectroscopic assay where the ^{1}H NMR spectra at various concentrations are shown [28].

3.2.4.1 PTA complex self-association

Similar experiments to those employed by LaPlante [28] were conducted using the palladacycle complexes, where the NMR spectra of the compounds were recorded at different concentrations, ranging from dilute to saturated samples. The NMR spectra recorded for this assay are shown in Figures 3.29-3.31.

Varying the concentration of the complex led to a variation in the degree of signal broadening of the isopropyl methyl signals (1.1-1.4 ppm) and a very slight downfield shift in the isopropyl methine (3.1-3.3 ppm) and imine (~8.4-8.5 ppm) signals (Figure 3.29 to 3.31). Unlike the other signals, the PTA signal (4.5-4.7 ppm) shifted slightly upfield with increasing concentration. It also showed fine structural changes. Furthermore, both the variable concentration- and variable temperature NMR spectroscopy experiments yielded spectra which, at face value, showed similar features with increasing temperature and concentration. It should, however, be pointed out that the broadening of the methyl signals of the isopropyl groups and the imine proton signal could possibly be a simple concentration effect (such as signal broadening due to increased viscosity) rather than being due to an aggregation process. Essentially, both these processes (increased viscosity and aggregation) could lead to the same spectral changes that were observed.

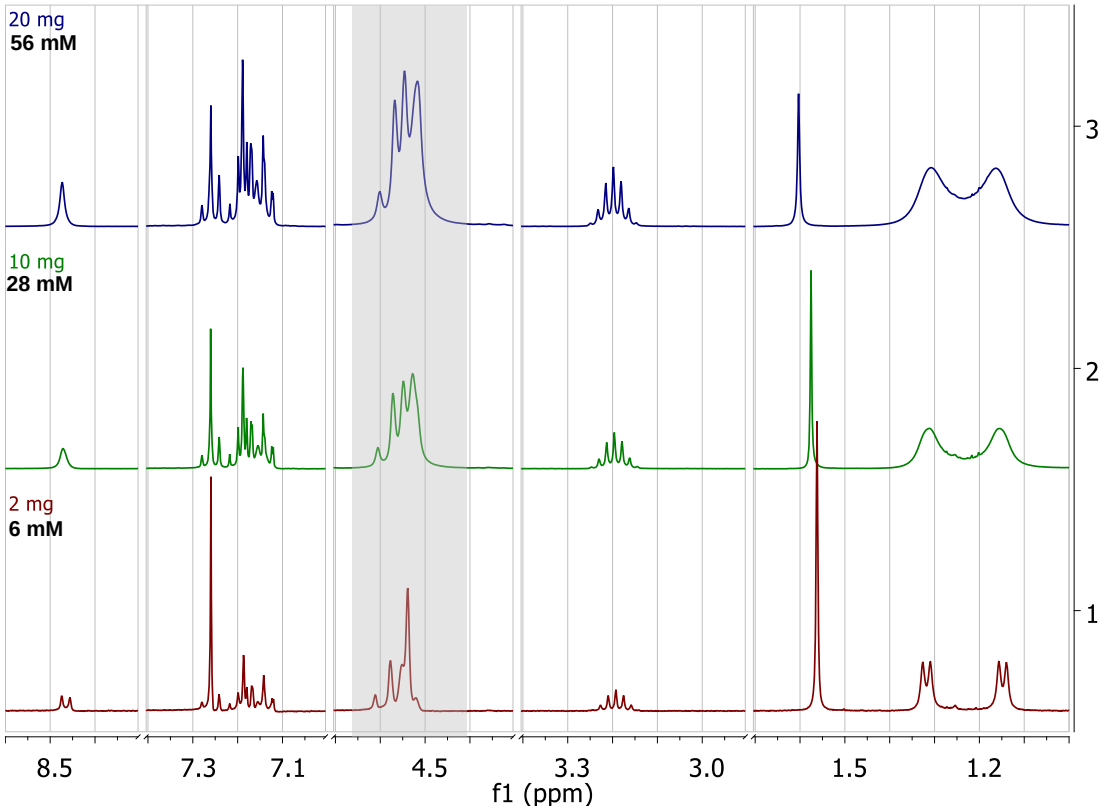

Figure 3.29: ^{1}H NMR spectroscopic array of C2 in $CDCl_3$ (2-20 mg/ 6-56 mM), showing changing spectra for the different concentrations. The PTA signal is highlighted in grey.

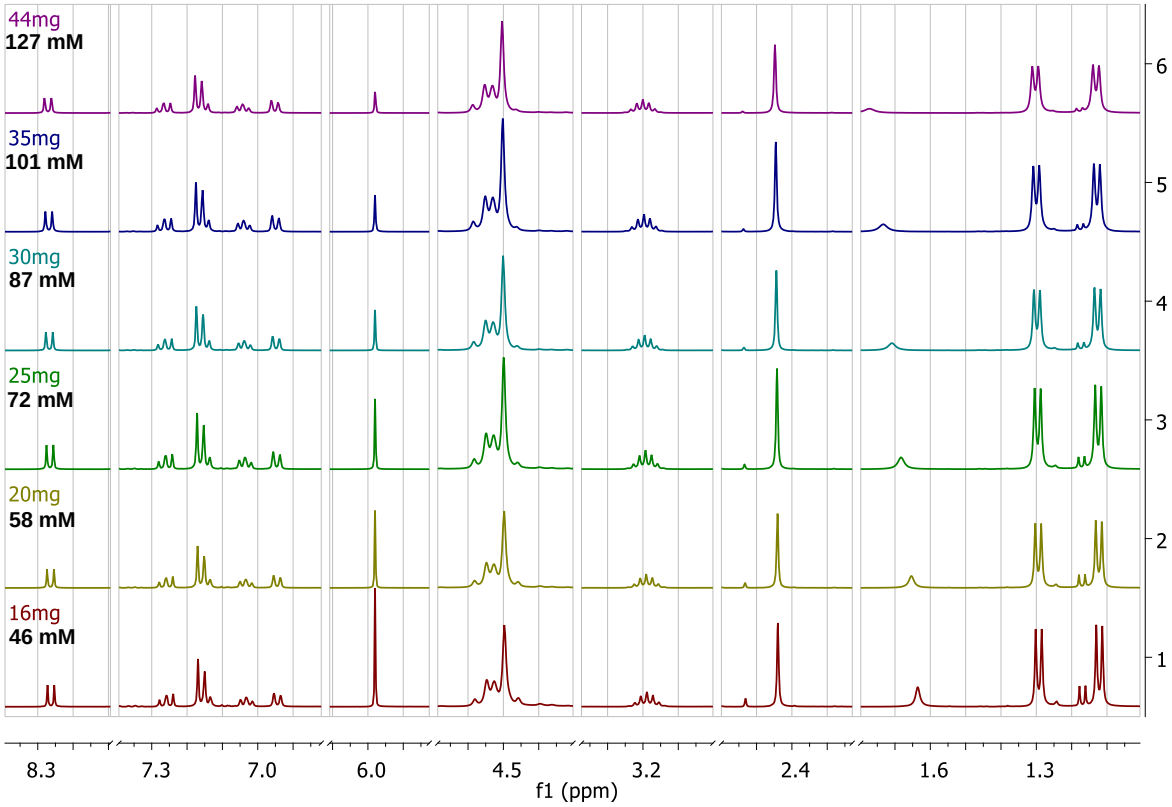

Figure 3.30: ^{1}H NMR spectroscopic array of C4 in TCE-d2 (16-44 mg/ 46-127 mM), showing slight change in spectra for the different concentrations.

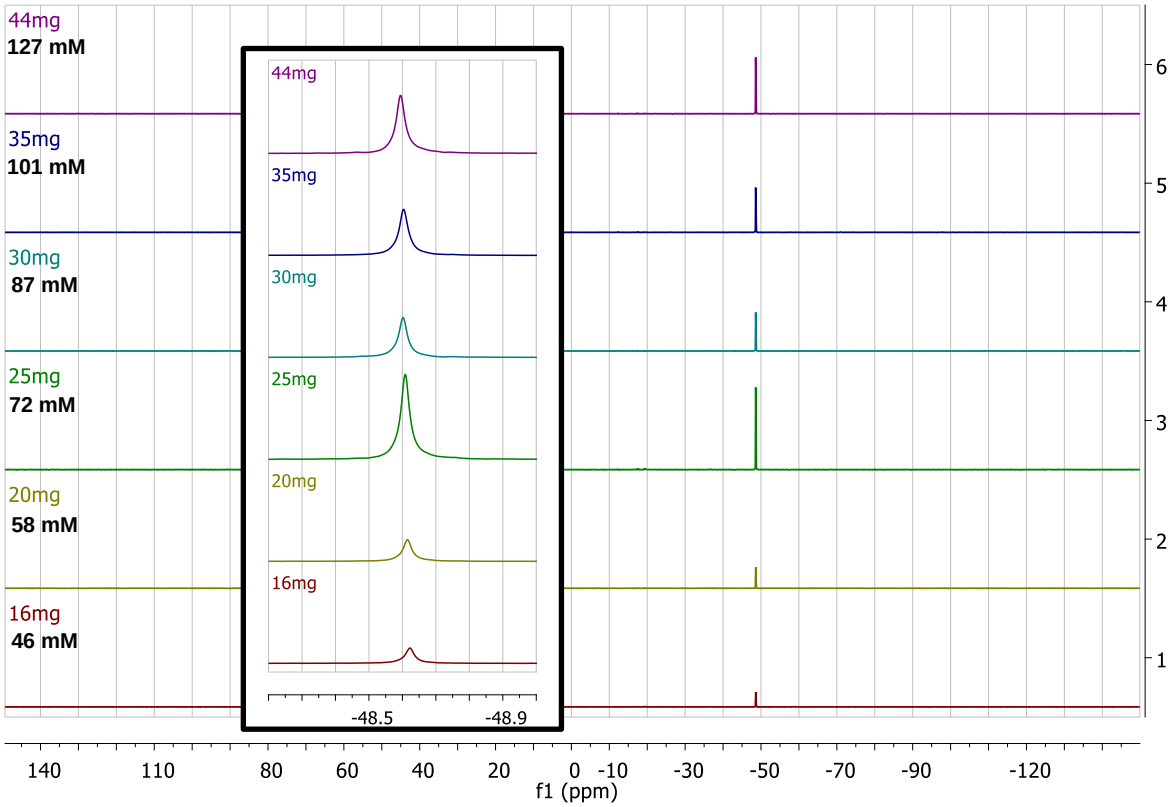

Figure 3.31: ^{31}P NMR spectroscopic array of C4 in TCE-d2 (16-44 mg/ 46-127 mM), showing slight shift and broadening in the phosphorous signal for different concentrations.

The question then also arises whether the spectral changes observed with increasing concentration are linked to those changes seen in the variable temperature NMR experiments. Again, at face value, similar signal broadening is observed with both an increase in temperature on the one hand and an increase in concentration on the other. However, the extent of the changes is more dramatic in the case of temperature. If, as proposed, the signal broadening as a result of concentration changes is associated with molecular aggregation then, intuitively, one would reasonably expect that recording the spectra at higher temperatures would lead to less aggregation and consequently less signal broadening. If, however, one for example compares the low temperature spectrum of **C2** with that of the high temperature (120 °C) spectrum in Figure 3.32, it is clear that at high temperature there is increased broadening which is contrary to what one would expect for the case of decreased association as a result of higher temperature. Thus, it is clear that the temperature and concentration effects are independent processes and that the temperature effects outweigh the concentration effects.

Further confirmation that the two processes are independent can be seen when comparing the trends in the PTA signals. In the two cases, changing concentration and temperature (Figures 3.29 and 3.32, respectively; signals highlighted in grey), opposite trends were observed. For the concentration data, the PTA signal becomes less resolved with increasing concentration, but with increasing temperature, the signal becomes more resolved. The signal shapes for the lowest concentration and the highest temperature spectra are very similar. Additionally, the variable concentration spectra showed a slight upfield shift in the PTA signals with increasing concentration, whilst the variable temperature data showed a slight downfield shift in the signal with increasing temperature. As stated above, these observations suggest that the site-exchange process and the aggregation process are not linked.

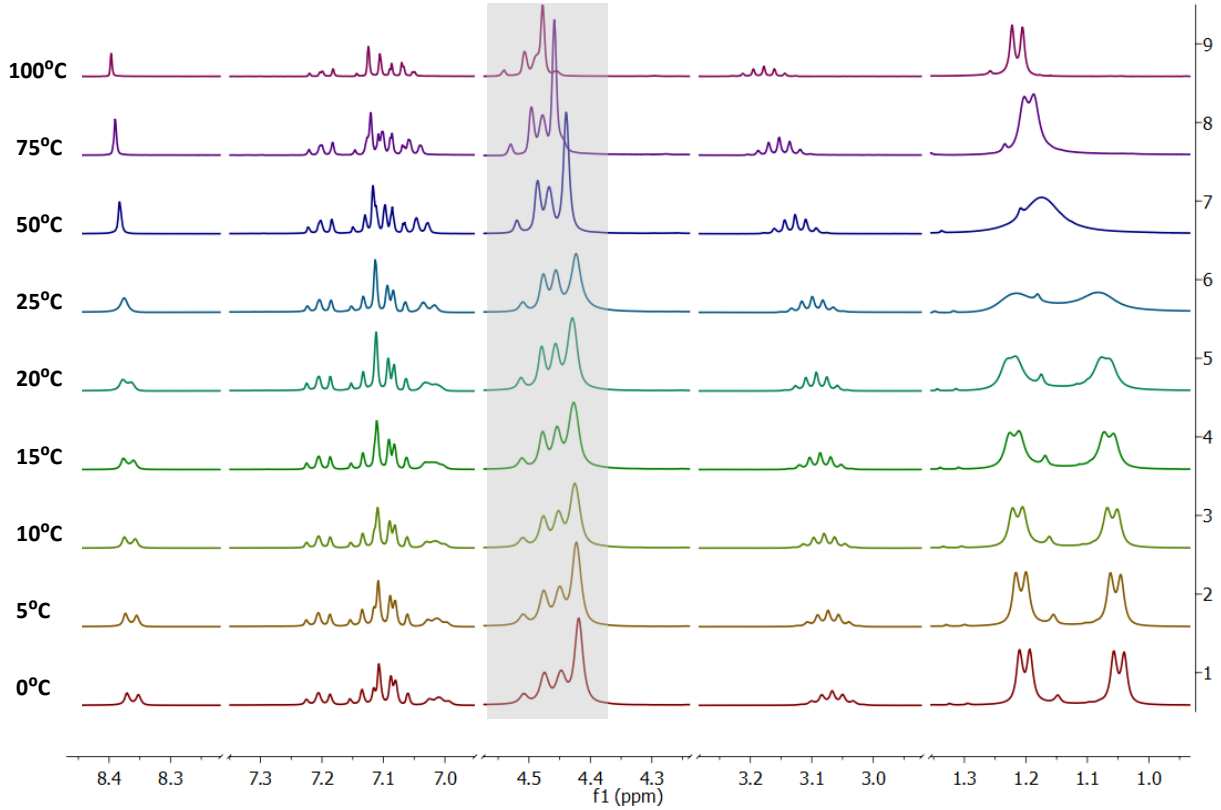

Figure 3.32: Variable temperature ^{1}H NMR spectra of C2. The PTA signal is highlighted in grey.

Having established that there was a concentration effect that could possibly involve PTA self-association, the next step was to propose a likely structure for the aggregate. Computational modelling was used to determine the nature of the species and the intermolecular interactions.

3.2.4.2 Self-associated aggregate via PTA ligands

Based on the changes in the NMR spectra and the structural studies taken from the literature, it is suspected that there could possibly be non-covalent interactions between the PTA moieties of two distinct complexes (Figures 3.33 and 3.34), leading to some sort of non-covalent dimer. The extent of dimerisation is expected to be greater at higher concentrations.

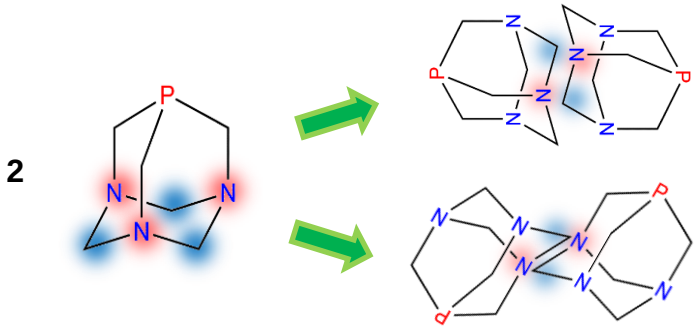

Figure 3.33: Possible associations between PTA ligands, where red = high electron density and blue = low electron density.

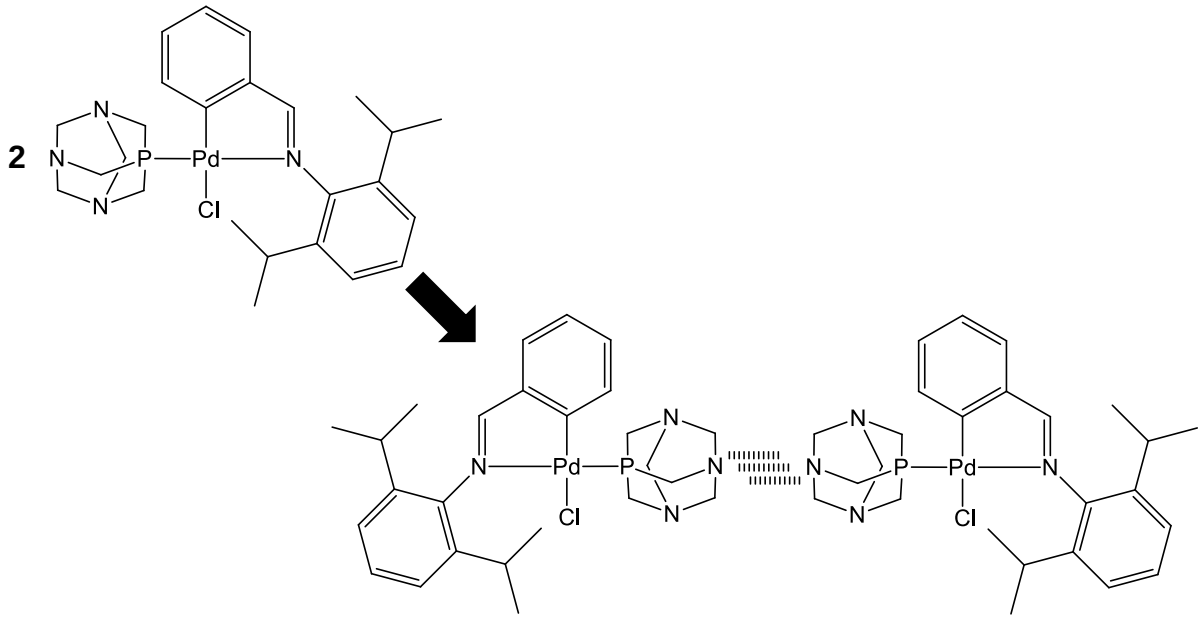

Figure 3.34: Possible dimerisation by association between two PTA ligands, forming a non-covalent dimer.

In order to test the validity of the proposed non-covalent dimer and obtain a more concrete description of the intermolecular interactions, a computational study using density functional theory (DFT) was carried out by our collaborators to model the proposed self-association process via the PTA ligands. Some of the preliminary computational work is reported here.

3.2.4.2.1 Monomer and dimer geometry optimisation and frequency scans of **C2**

Geometry optimisation and frequency scans were performed with the initial geometry being constructed from 2D molecular structures of the mononuclear PTA-based palladacycle, **C2**. The monomer and dimer were both optimised successfully using the computational methodologies described in Section 3.4. Minima on the potential energy surface were identified and confirmed by the non-negative vibrational frequencies. The optimised geometry of the monomer is shown in Figure 3.35, where the 2,6-diisopropylaniline moiety has a slanted T-shaped configuration relative to the square planar metallocyclic ring (Figure 3.35, right).

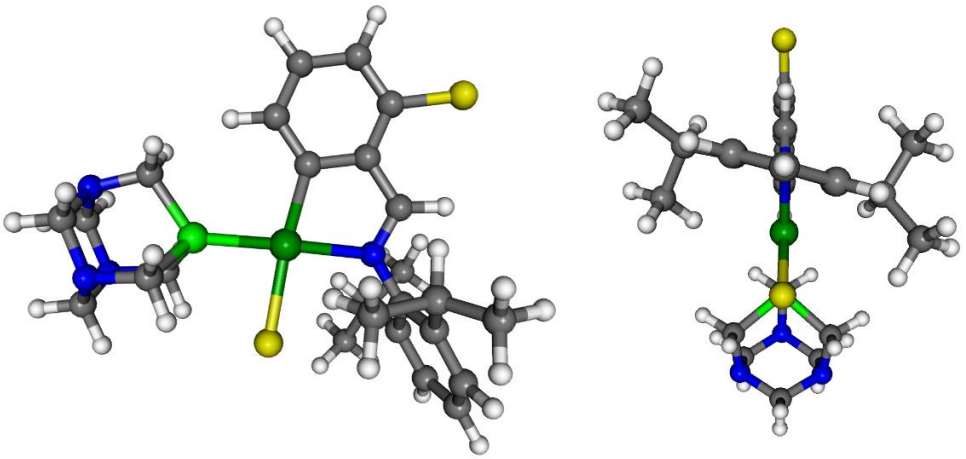

Figure 3.35: Optimised geometry of the monomer shown from two angles.

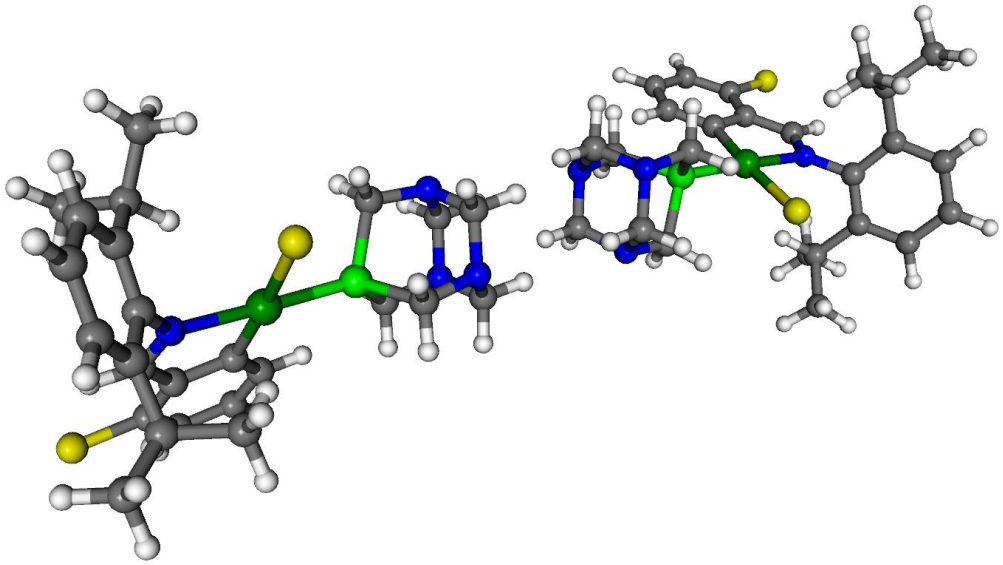

Figure 3.36: Optimised geometry of the PTA self-association aggregate.

Similarly, the optimised geometry of the non-covalent dimer (Figure 3.36) also showed the slanted T-shaped configuration of the 2,6-diisopropylaniline moiety. Overall, there was very little change in the configuration of the monomer upon PTA complex self-association. This is best illustrated by the relatively small changes in the atomic bond distances upon dimer formation. Selected bond distances are reported in Table 3.5. The change in electron density upon aggregation was also determined and found to be relatively small with changes in the 3rd and 4th decimals.

Table 3.5: Selected bond distances for the optimised monomer- and adduct geometries.

Bond Pair	Monomer (Bond distance in Å)	Aggregate (Monomer 1) (Bond distance in Å)	Aggregate (Monomer 2) (Bond distance in Å)
Pd-C	2.018	2.019	2.019
Pd-N	2.120	2.118	2.119
Pd-P	2.259	2.259	2.259
Pd-Cl	2.418	2.417	2.417
N-C1 (imine)	1.297	1.296	1.297
N-C2 (aniline ring)	1.422	1.423	1.423

3.2.4.2.2 Non-covalent interaction analysis (NCI)

Next, a non-covalent interaction (NCI-) analysis was performed [29] to calculate the inter- and intra-molecular topographical features of the electron density of the aggregate. It was hoped to gain further insight into specific regions of interest for non-covalent interactions and the relative strength of these interactions. In NCI analysis, the reduced density gradient (RDG) must be close to zero to indicate an attractive or repulsive interaction. Therefore, the RDG iso-surface was constructed (Figure 3.37), where regions of attraction are illustrated in orange and regions of repulsion are indicated in blue. Regions of attraction (orange) may also indicate bond critical points or 2D minima in the electron density.

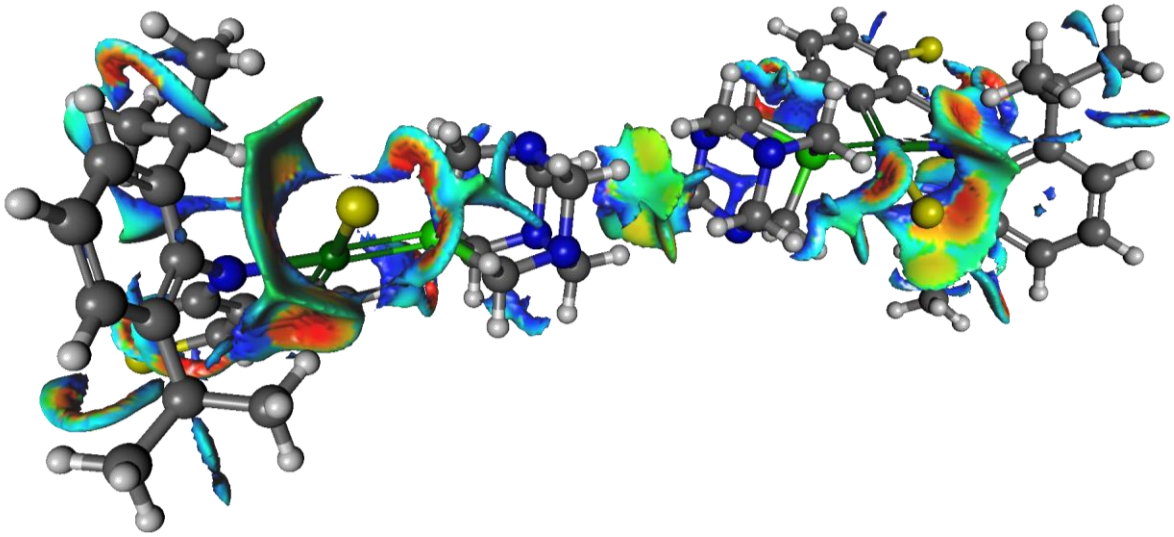

Figure 3.37: Non-covalent interaction RDG iso-surface of the PTA self-association adduct, where s = 1 with sign$\lambda_2\rho(r)$ colour mapping, $\rho(r) \in$ [-0.01 (orange); 0.01 (blue)].

From Figure 3.37, it is clear that there are some attractive non-covalent interactions between the monomers in the aggregate, however, compared to the electron density around the chloride in the Pd-Cl bond, these intermolecular interactions are relatively weak. Additionally,

it is noteworthy, that the large isosurface between the Cl atom and the 2,6-diisopropylaniline ring may explain the hindered/restricted rotation about the N-C bond. It is also possible that there is an intramolecular interaction between the chloride ion and a methyl group, as seen by the pocket of red in the isosurface in the lower left-hand corner of Figure 3.37 (and to a lesser extent in the top right-hand side). This interaction may be responsible for the slanted T-shape of the monomers and more importantly, it could possibly be the intramolecular interaction which must be overcome for there to be free rotation about the N-C bond.

In summary, the modelled non-covalent dimer is feasible based on the optimisation of the structure as a true energy minima on the potential energy surface. However, it is shown that there is very little configurational change in the monomer upon aggregation. Thus, it is unlikely that the broad methyl and imine signals could be accounted for by the formation of the aggregate. Instead, it is more likely that the broadening of the methyl signals of the isopropyl groups and the imine proton signal may be a concentration effect (such as signal broadening due to increased viscosity). Should this be the case, the temperature-induced site-exchange process and the aggregation process are not linked and it is purely coincidental that the variable temperature and variable concentration NMR spectra, at first glance, show similar trends.

Due to the interesting and unusual nature of the work, this process is being investigated further by our collaborators with the aim of obtaining data which provides a complete understanding of this system; however, the extent of this additional computational work required is beyond the ambit of this project and thus only the preliminary results are reported here. Hence, the final conclusion on this process, as shown in Scheme 3.4, is that aggregation via PTA self-association is feasible, as shown by the modelled data. However, there may be an alternative or additional concentration driven process occurring in solution which better or more fully explains the trends observed in the NMR spectra.

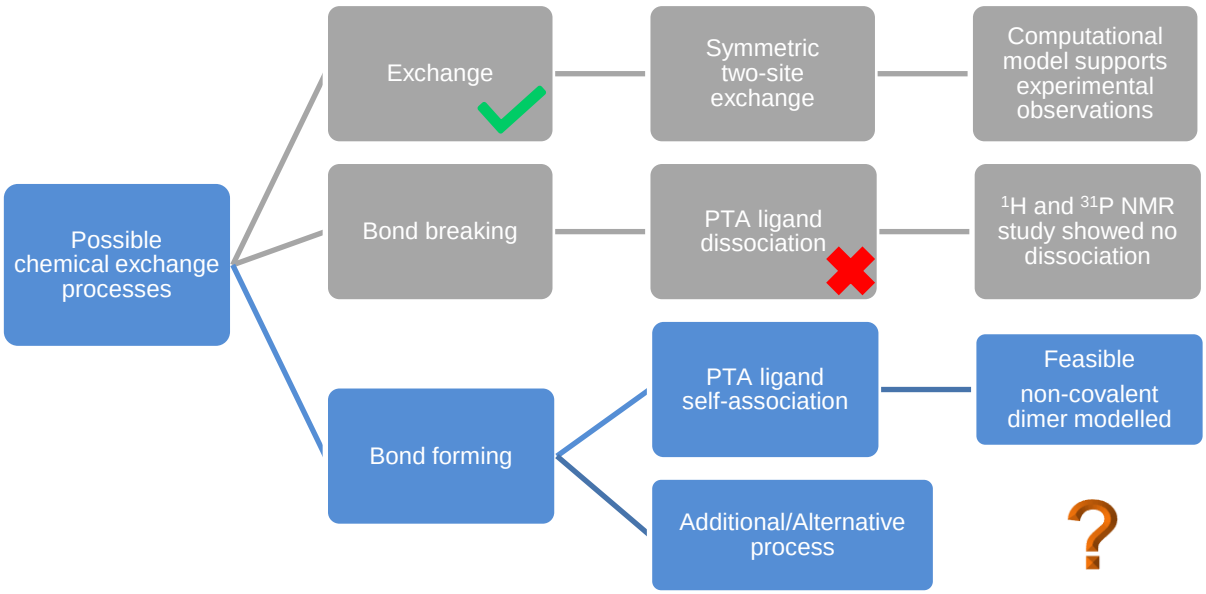

Scheme 3.4: PTA ligand self-association proven to be feasible, but alternative or additional concentration driven processes need to be considered.

3.2.5 Possible additional or alternative concentration driven process

In Chapter 2, it was noted that mononuclear palladacycles showed the tendency to dimerise during the ionisation process when analysing these compounds by electrospray ionisation mass spectrometry. Thus, some of the ionisation fragments detected in the mass spectra of some of the mononuclear PTA-based palladacycles were dimeric in nature, where two metal centres are linked via a chloride bridge. Since dimerisation in solution is also a concentration driven process, this was considered as an alternative to the molecular aggregation described earlier.

The simplest dimer that could form in solution is the μ-chloro palladacycle. To form this dimer, the phosphine ligand would have to dissociate and then two monomeric coordinatively unsaturated fragment species would combine to form the dimer (Figure 3.38).

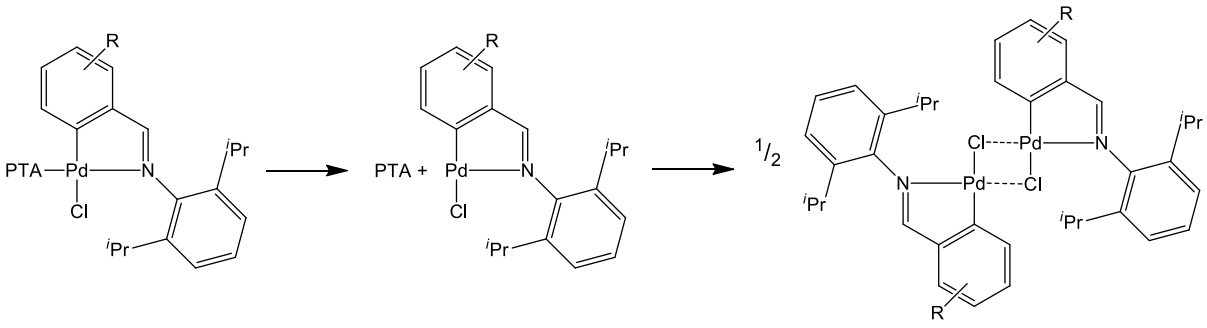

Figure 3.38: Possible dimerisation scheme.

This dimer, depicted in Figure 3.38, is identical to the chloro-bridged species which was used originally to form the PTA-based palladacycles. Thus, we compared the high concentration ^{1}H NMR spectrum of **C2** (Figure 3.39 – spectrum 2) with that of the corresponding bridged palladacycle, **B2** (Figure 3.39 – spectrum 1). From Figure 3.39, it was clear that the imine proton chemical shift of the dimer, **B2** (Figure 3.39 – spectrum 1) is approximately 0.3 ppm more upfield from the PTA-based palladacycle, **C2**, (Figure 3.39 – spectrum 2), whilst, the CH proton signal for the dimer (3.5 ppm) is further downfield from that of **C2** (3.2 ppm). These findings, accompanied by the fact that the PTA ligand did not dissociate upon increasing concentration (Figures 3.30 and 3.31), led to the conclusion that the μ-chloro palladacycle without PTA as a ligand was not the species being formed in solution at higher concentrations.

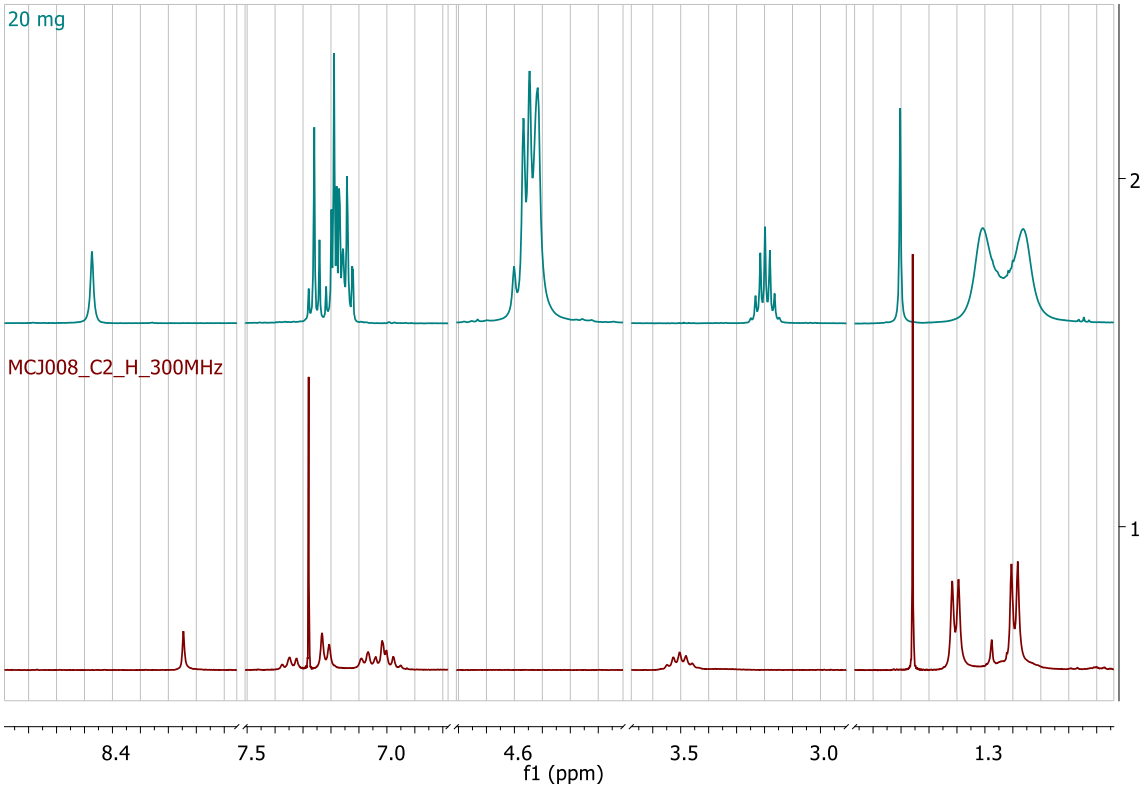

Figure 3.39: ^{1}H NMR spectrum of C2 in $CDCl_3$ (20 mg) - spectrum 2, showing the species detected at high concentration and ^{1}H NMR spectrum of B2 in $CDCl_3$ (10 mg) - spectrum 1.

Since dimerisation via PTA ligand dissociation does not occur, another possibility viz. the dissociation of the imine ligand, as shown in Figure 3.40, was considered. Literature shows that a number of analogous palladacycles with various phosphine ligands and substituents on the phenyl ring (coordinated to the palladium) have been synthesised and employed in catalysis (Figure 3.41). Therefore, the coordination sphere is a stable conformation and the proposed dimer is plausible. The reversibility of the dimer formation may be questioned since the analogous dimers were stable enough to be isolated, but none of the reported systems

have a substituent in the position of the imine, which could compete with the second chloride ligand for coordination to the palladium centre [30;31].

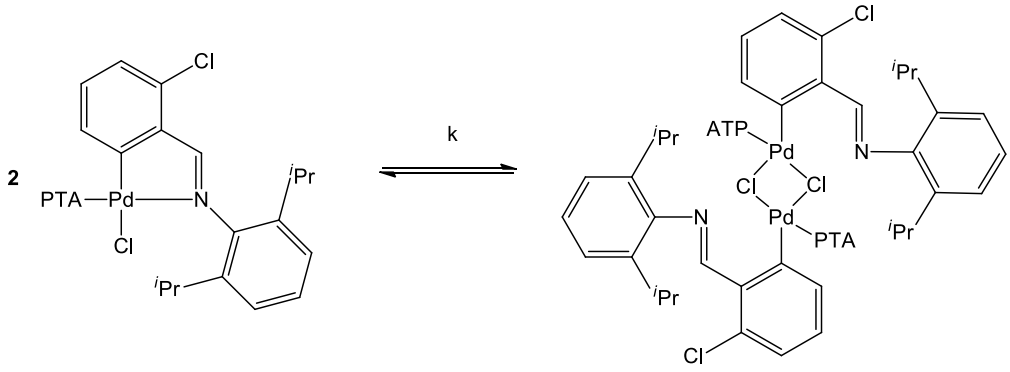

Figure 3.40: Proposed dimerisation via imine ligand dissociation. The dimerisation process represented here is not necessarily a single step process, there may be intermediates and/or transition states.

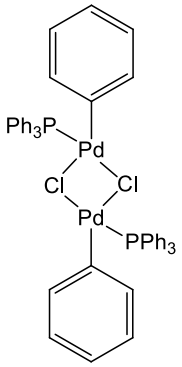

Figure 3.41: Structure of reported chloro-bridged dimer with coordinated phosphine ligands [31].

The expected changes in the NMR spectra are discussed here, should the dimer in Figure 3.40 represent the high concentration species. Upon increasing the monomer concentration, there would be more monomer in solution, thus more dimer can form. Accompanying the formation of the proposed dimer is the loss of $^{4}J_{H\text{-}P}$ coupling of the imine proton signal, so that a singlet is expected on dimer formation. This correlates with what is found in the NMR experiments conducted at high concentrations. Furthermore, the change in the coordination around the palladium metal centre would lead to changes in the PTA proton and phosphorous signals. Finally, the dissociation of the Pd-N bond, would allow the 2,6-diisopropylaniline moiety to move to a less sterically hindered position, thus allowing free rotation of the ring about the N-C bond, thus leading to increased broadening of the isopropyl methyl signals. These changes would also lead to shifts in the isopropyl methine and methyl signals. This situation is what is observed in the NMR of the free ligand, where the isopropyl methyls give rise to an individual doublet.

Similarly, increased temperature would provide the energy required to break the Pd-N bond, thus facilitating the formation of the dimer in Figure 3.40. Hence, similar trends would be expected in the variable temperature and variable concentration NMR spectra.

Comparison of these expected changes in the NMR spectra with the observed changes in the variable temperature and variable concentration NMR spectra show that this process correlates with most of the experimental observations. However, a much larger shift in the imine proton signal was expected upon dissociation. However, a closer comparison of the imine proton chemical shifts of various analogous ligands and compounds revealed an interesting trend. These ^{1}H NMR imine proton shifts are summarised in Table 3.6.

The compound, **NC1** (Figure 3.42), reported in Table 3.6 is a non-cyclometallated analogue of **C1**, synthesised by cleaving the chloro-bridged palladacycle with excess PTA, instead of two equivalents, as used for the synthesis of **C1**. The two PTA ligands coordinated at the palladium centre, trans to each other, thus forcing the imine ligand to dissociate. Similar structures with PMe_3 have been previously reported [16].

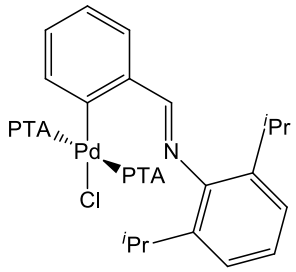

Figure 3.42: Chemical structure of NC1.

Table 3.6: ^{1}H NMR chemical shifts for the imine proton.

Compound	*H*C=N chemical shift (ppm)	Change in chemical shift relative to C1 (ppm)
L1	8.22	+0.23
B1	7.75	-0.24
C1	7.99	0.00
NC1	8.49	+0.50

The observed shift in the imine signal of palladacycle complexes with increasing temperature was a 0.05 ppm downfield shift. From Table 3.6, it was noted that the dissociation of the imine should lead to a downfield shift, whilst the formation of the chloro-bridged coordination should lead to an upfield shift. Since the changes in the coordination around the palladium centre in the two cases (free imine vs. chloro-bridged dimer) have opposite effects on the shielding of

the imine proton, the change in the chemical shift as a result of dimerisation will be smaller than expected.

Thus, the next step was to look for some evidence which could possibly support the formation of this dimer in solution.

3.2.5.1 Possible dimerisation via imine dissociation

In the previous section, it was argued that it was reasonably plausible that a dimer could form via dissociation of the imine ligand and that this species could possibly explain the experimentally observed variable temperature and concentration NMR data. However, some experimental evidence was required to prove that such dimers can indeed form. Since dimeric species have often been detected in the mass spectra of mononuclear palladium complexes [32;33], the higher *m/z* fragments in the ESI-MS spectra of the mononuclear palladacycles reported in this thesis were examined for evidence of the proposed dimer.

A $[M_2\text{-Cl}]^+$ fragment was detected for some of the mononuclear palladacycles. This fragment represents the proposed dimer, M_2, with the loss of a chloride ion (Figure 3.43).

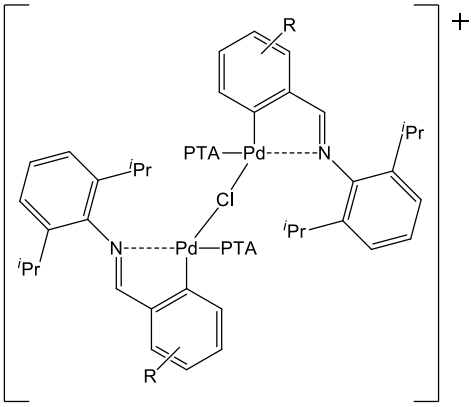

Figure 3.43: $[M_2\text{-Cl}]^+$ dimer fragment detected in high *m/z* regions of mass spectra of mononuclear palladacycles. Pd-N bond indicated as dashed line, as it is not possible to determine whether or not the bond is broken.

The mass spectrum of **C3** is shown in Figure 3.44 with the simulated fragmentation pattern. The observed fragmentation pattern matched the simulated pattern well. The $[M_2\text{-Cl}]^+$ fragments detected for the other mononuclear palladacycles are summarised in Table 3.7.

Table 3.7: Dimer fragment, $[M_2\text{-}Cl]^+$, detected at high *m/z* values, for the mononuclear PTA-based palladacycles.

Complex	$[M_2\text{-}Cl]^+$ (*m/z*)
C1	1091.28
C2	1159.20
C3	1249.10
C5	1119.31

Based on the detection of the $[M_2\text{-}Cl]^+$ fragment, the proposed dimerisation via dissociation of the imine ligand is feasible.

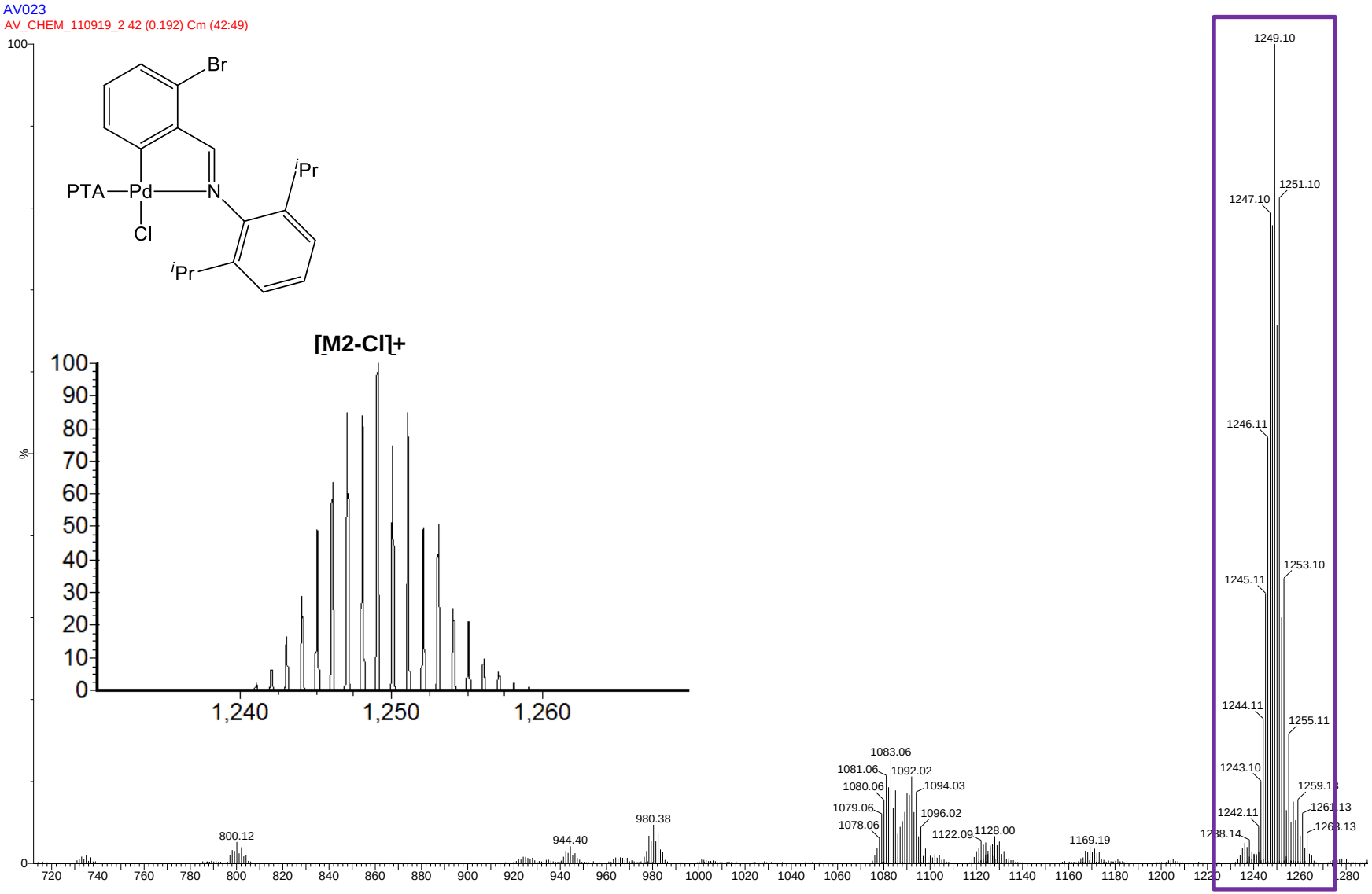

Figure 3.44: Mass spectrum of C3 with showing $[M_2\text{-Cl}]^+$ cluster (purple) with inset of the simulated fragmentation pattern.

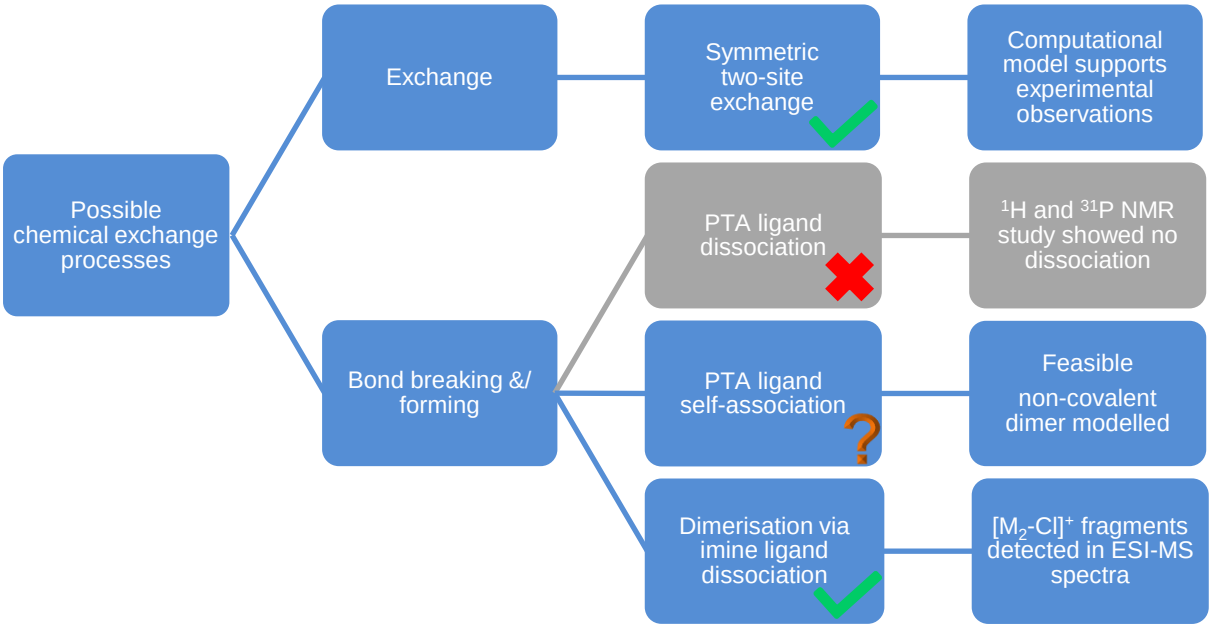

Scheme 3.5: Summary of the possible chemical exchange processes occurring in solution and detected by NMR spectroscopy.

To summarise (Scheme 3.5), variable temperature NMR spectra showed that there is an exchange process occurring in solution. The process was identified as a symmetric two-site exchange and it was confirmed with a computational model that showed that the experimental data lie within the 95 % confidence limits. Furthermore, the calculated activation energies ($\Delta G^{\#}$) were found to lie in the range for aryl ring rotations, thus the symmetric two-site exchange involved the rotation of the 2,6-diisopropylaniline moiety about the N-C bond with the isopropyl methyl signals in the NMR spectra clearly displaying line broadening due to the site-exchange process.

A second process was also present, as observed by changes in the chemical shifts of signals with increasing temperature. Loss of $^{4}J_{H\text{-}P}$ coupling in the imine proton signal suggested that the PTA ligand dissociates, however, further NMR spectroscopy studies did not support this proposal. Next, non-covalent aggregation via PTA self-association was proposed. Both variable concentration NMR spectroscopy studies and the computationally modelled adduct showed that this process was feasible, but whether or not it could fully account for all the experimental observations was questioned. Therefore, alternative concentration driven processes were considered, specifically, dimerisation via ligand dissociation. Since it had already been established that the PTA ligand does not dissociate, the dissociation of the imine ligand was considered. Not only did the proposed dimerisation process account for all observed changes in the NMR spectra with variable concentration and temperature, but literature precedence was also found for the proposed structure of the dimer. Finally, mass

spectrometry was used to confirm the formation of the dimer in solution, by detecting the dimer fragment with the loss of a chloride ion, $[M_2\text{-}Cl]^+$.

With the dynamic motion in the NMR spectra elucidated, the next steps were to determine the role or influence of the PTA ligand and the ortho-substituents on the chemical exchange processes.

3.2.6 PTA vs PPh_3 and PMe_3

Having established that there are two, possibly three, chemical exchange processes occurring in solution, the next step was to determine why these processes were only observed for the TPA-based palladacycles and not their PPh_3 and PMe_3 counterparts.

If at all likely to occur, the formation of the non-covalent dimer can be facilitated by PTA self-association. It is likely that the nitrogen donor atoms in PTA would facilitate this process. Although, the computationally modelled dimer showed only weak intermolecular interaction, it was thought that the difference in electronegativity of the carbon and nitrogen atoms on the PTA facilitated the aligning of the monomers through areas of high and low electron density (Figures 3.33 and 3.37), therefore allowing close enough contact between the monomer units for these weak intermolecular interactions to occur. The proposed involvement of the nitrogen donor atoms in this process immediately eliminates the possibility of this process occurring in the analogous PPh_3 and PMe_3 analogues, as these phosphines do not contain atoms other than carbon and hydrogen in addition to the phosphorous, thus, there can be no significant differences in the electron density of the atoms in the phosphine, effectively preventing the sort of “close fit” illustrated in Figure 3.37.

In order to determine why the site-exchange and the covalent dimer formation was only observed for the PTA series and not the analogous PPh_3 and PMe_3 series, the physical and chemical properties of the various phosphine ligands were compared (Table 3.8).

Table 3.8 shows the various phosphine analogues, the ^{1}H and ^{31}P NMR spectroscopy data for the corresponding palladacycle complexes, as well as the pKa’s and cone angles of the phosphines. From examining the NMR spectra, it was clear that only the PTA analogue had broad NMR spectroscopic signals and that the nature of tertiary phosphine influenced the imine proton shifts [34-46]. Comparison of the pKa values and the NMR spectroscopic signals and chemical shifts shows that the basicity of the phosphines could not be used to explain the observed trends; however, differences in the cone angles [37] correlated with the chemical shifts and degree of broadening. The other significant difference between the phosphines

studied was the presence of additional nitrogen donor atoms in PTA and absence of donor atoms, other than phosphorous, in PPh_3 and PMe_3. However, since similar covalent dimers, substituted with a range of phosphine ligands, none of which contain atoms other that carbon and hydrogen, was reported by Chaudhari *et al.* [31] (Figure 3.45), the nitrogen donor atoms in PTA could be ruled out as the factor responsible for facilitating or hindering dynamic chemical exchange processes. Thus, the property of PTA which is thought to facilitate the covalent dimer formation is the small cone angle and the related steric factor, which is smaller in this case.

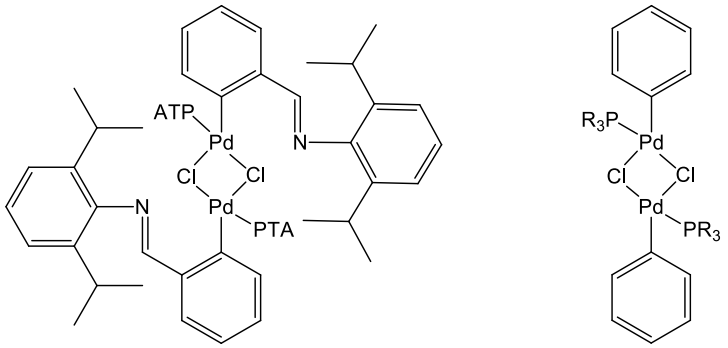

Figure 3.45: PTA-based palladacycle covalent dimer (left) compared to similar covalent dimers reported in the literature (right), where PR_3 = PEt_3, PMe_2Ph, $PMePh_2$ and PPh_3 [31].

Since the reported structure in Figure 3.45 (right) does not have the bulky 2,6-diisopropylaniline moiety on the phenyl ring, there is less steric hindrance about the square planar palladium system, thus allowing the dimer formation even with the bulky PPh_3 ligand. Contrastingly, in the PTA-based palladacycle system in Figure 3.46 (left), the large 2,6-diisopropylaniline moiety most likely occupies the same space required by larger phosphine ligands, thus preventing the dimer formation for bulkier phosphines, such as PPh_3 and even the slightly smaller PMe_3.

Table 3.8: NMR spectroscopic data and properties for phosphine analogues.

Phosphine	PPh_3	PMe_3	PTA
Structure	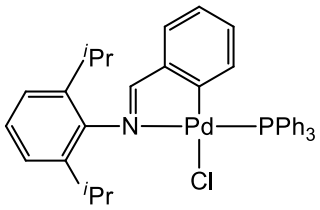	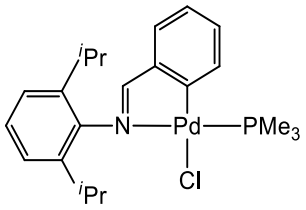	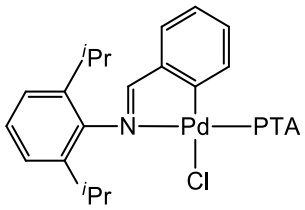
^{1}H ^{i}Pr methyl signal and chemical shift (ppm)	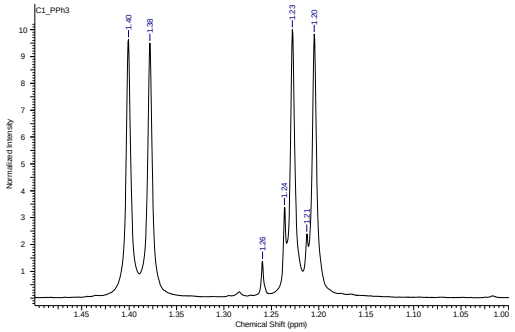	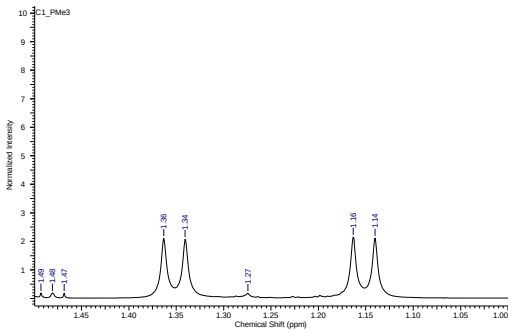	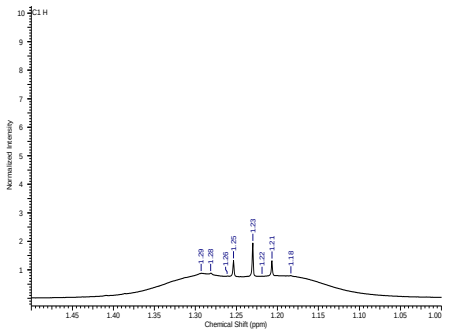
	1.37 (d, 6H, $^3J_{H-H}$ 6.90 Hz); 1.21 (d, 6H, $^3J_{H-H}$ 6.90 Hz)	1.33(d, 6H, $^3J_{H-H}$ 6.75 Hz); 1.13 (d, 6H, $^3J_{H-H}$ 6.90 Hz)	1.08-1.39 (d, 12H, broad)
^{1}H imine chemical shift (ppm)	8.11-8.13	8.00-8.03	7.96-7.99
^{31}P chemical shift (ppm)	42.21	-4.28	-47.02
pKa [35;36]	2.73	8.65	5.63
Cone angle (˚) [37]	145	118	102

3.2.7 Role of ortho-substituents

Since all of the palladacycles in the series showed different thermodynamic data for the symmetric site-exchange process (Table 3.3), the next section attempts to explain how the ortho-substituents could possibly affect the activation energy ($\Delta G^{\#}$) for the site-exchange, as shown below in Table 3.9. The change in the activation energy for the various analogues is quite small when compared to the overall activation energy, but it is an effect than can be explained. Note that **C3** data have been excluded as no thermodynamic data were obtained for this compound and **C5** has been excluded as it is a para-substituted species.

Table 3.9: Influence of ortho-substituents on activation energy for site-exchange compared with ortho-substituent properties from the literature.

Complex	$\Delta G^{\#}$ (kJ.mol^{-1})[a]	Radius (Å)[b]	Steric factor[b]
C4 (2-Me)	57.86	1.73	0.52
C1 (2-H)	60.01	-	-
C7 (2-NO_2)	61.43	-	-
C8 (2-OMe)	64.69	1.47	0.35
C6 (2-F)	64.63	1.39	0.31
C2 (2-Cl)	68.30	1.89	0.61

[a]Experimental data from Section 3.2.2; [b]Literature data [38]. Note that radius refers to the iodic group radii derived from the ortho-substituted biphenyls. This value was used as an estimate of the size for the various groups.

Simple steric and electronic effects were considered first. Steric effects were ruled out by using the size and steric factor data from literature. The literature data in Table 3.9 are from a report by Hussey and Diefenderfer [38]. This shows the radii of various ortho-substituents and their associated steric factors, where the steric factor is a relative term indicating the degree of hindrance caused by the group. The trend in Table 3.9 for the literature data does not correspond to the trend observed in the experimental $\Delta G^{\#}$ values calculated from the variable temperature NMR spectroscopy experiments. If electronic effects were the cause, then higher activation energy would have been expected for the electron-withdrawing groups due to reduced electron delocalisation, while lower activation energy (broad peaks) was expected for the electron-donating groups due to increased electron delocalisation. However the nitro- and fluoro-substituents, which are both strongly electronegative, have lower activation energies than the chloro-analogue.

The so-called ortho effect was then considered, as it takes into account both steric and electronic effects of ortho-substituents, as well as resonance influences, using Hammet σ_o values [38]. Hammett σ values give an indication of the relative electron withdrawing or

–donating ability of a substituent as compared to hydrogen, and is expressed as a ratio of log K_a's. These values were initially created to explain why some aromatic substituted analogous were more readily reduced than others. Both σ_m and σ_p values were calculated for various substituents, σ_o values were not determined so readily due to the "ortho effect" where ortho-substituted aromatic compounds were more readily reduced than was predicted (ortho enhancement).This behaviour is ascribed to a change in electron density at the reaction site due to decreased resonance contributions and increased inductive contributions. In 1967, Hussey and Diefenderfer created a reaction series and calculated σ_o values for phenyl halides. In 1969, Tribble and Traynham [39] did similar work, calculating the values for a series of ortho-substituted phenols, using an improved method. They then compiled a table of these values, using their own data and those of similar systems in the literature. Relevant data from their table are shown in Table 3.10. Although the values differ for each data set, the trend remains the same - the values increase from the methoxy analogue to the nitro analogue. Note that if σ_o is zero there is no effect, if σ_o is positive the substituent is electron withdrawing and if σ_o is negative the substituent is electron donating.

Table 3.10: Hammet σ_o values from work by Tribble and Traynham [39].

Ortho-substituent	σ_o-[a]	σ_o-[b]	σ_o-[c]
OMe	-0.37	-0.23	-0.20
Me	-0.13	-0.03	-0.17
H	0	0	0
F	0.29	-	-
Cl	0.50	-	0.40
Br	0.55	0.66	0.40
NO_2	-	1.20	-

[a]Phenols in DMSO; [b]Phenols in HMPA; [c]Anilines in DMSO.

Ignoring the nitro- and methoxy-analogues of the PTA series, the ortho effect trend fits observed NMR spectroscopy trends for the PTA-based palladacycles. The smaller the σ_o value, the broader the NMR spectroscopic signal. The deviation for the nitro- and methoxy-analogues may be due to resonance effects since the reported values were determined for simple phenol and related systems, whilst the PTA systems involve conjugation and therefore possible resonance structures.

3.3 Conclusions and future work

A variety of peak shapes for the methyl signals of the isopropyl substituents in the PTA-based palladacycle series was observed and proven to be due to a reversible symmetric site-exchange by way of variable temperature NMR spectroscopic studies and employing a computational model to describe the process. The free energy of activation ($\Delta G^{\#}$) and other thermodynamic parameters for the two-site exchange process were calculated. The rotational energy barriers lie in the range of those observed for aryl group rotations, thus it was concluded that the 2,6-dissopropylaniline moiety rotates about the N-C bond. Variable temperature NMR spectra supported this finding.

Slight deviations in the expected signal shifts were attributed to concentration-dependent molecular aggregation via association between the PTA ligands. A non-covalent aggregate was proposed and modelled. The model appears to fit the data to some degree, however further investigations are underway to attempt to confirm these initial findings.

An alternative concentration and temperature dependent dimerisation process was also proposed which could possibly explain the observed NMR changes. For this covalent dimer to form, the imine ligand needs to dissociate and a μ-chloro dimer forms. This proposal was supported to some extent by literature precedence where related dimers are reported and the presence of corresponding dimer fragments in the ESI-MS spectra of the palladacycle complexes reported in Chapter 2.

The ability of the mononuclear PTA-based palladacycles to undergo these processes was attributed to the nature of the phosphine ligand, PTA, specifically, the small cone angle and the nitrogen donor atoms of the ligand. Furthermore, we were able to show that the ortho effect could possibly account for the influence of the ortho-substituents on the rotational energy barrier for the site-exchange process.

3.4 Materials and Methods

General methods and synthetic details for the PTA-based palladacycles are reported in Chapter 2, Section 2.5. The synthesis of the non-cyclopalladated compound, **NC1**, is reported below.

NMR (^{1}H: 300 and 400 MHz; ^{13}C: 300 MHz, ^{31}P: 300 MHz) spectra were recorded on a Varian VNMRS 300 MHz or a Varian Unity Inova 400 MHz spectrometer at 273 K, unless otherwise specified, and chemical shifts are referenced to the residual protons of the deuterated solvents

and external tetramethyl silane (TMS) for ^{1}H and ^{13}C NMR, whilst ^{31}P NMR chemical shifts are referenced relative to external 85% phosphoric acid (H_3PO_4). Chemical shifts (δ) and coupling constants (*J*) are reported in ppm and Hertz (Hz), respectively. The data in brackets are as follows: multiplicity, number of atoms (as per integration), coupling constants, assignment of atoms (where ',' denotes 'and' and '/'denotes 'or').The following abbreviations were used to describe multiplicity of signals: s = singlet, d = doublet, t = triplet, q = quartet, sept = septet, m = multiplet and (br) = broad signals. Variable temperature acquisitions were performed after 30 minute thermal equilibration period at each temperature. Experimental NMR data were imported into NMRfitv12 for site-exchange modelling. Data obtained from modelling were exported to Microsoft Excel for further manipulation and plotting of graphs. Eyring plots were constructed using SciDAVis 1.D009 software [40].

Computational methods

Note that all input files can be found in Section A2.3 of Appendix 2.

All calculations employed the ORCA Density Functional program developed by Frank Neese [41]. Geometries were fully optimised and frequency scans were performed using the GGA-PBE [42] DFT functional with an additional D3-Bekce-Johnson [43;44] dispersion correction. An effective core potential (ECP) functional basis set was employed for palladium. Other Gaussian type basis sets employed in these calculations are recorded in Table 3.11. Optimisation using an implicit solvent model, namely the conductor-like screening model (COSMO) [45] with the parameters of acetonitrile was done with the aforementioned combinations of functionals and basis sets. Both the monomer and dimer were characterised as true minima on the potential energy surface (PES), as was indicated by the non-negative vibrational frequencies.

Table 3.11: Gaussian type basis sets and auxiliary basis sets.

Atom	Basis set	Auxiliary Basis set
Pd	LANTZ [46]	LAN(28) ECP [47]
C	Ahlrich Def2-TZVP [48;49]	Def2-TZVP/J [50]
H	Ahlrich Def2-TZVP	Def2-TZVP/J
Cl	Ahlrich ma-Def2-TZVP [49;51]	Def2-TZVP/J
N	Ahlrich ma-Def2-TZVP	Def2-TZVP/J
P	Ahlrich ma-Def2-TZVP	Def2-TZVP/J

The non-covalent interactions (NCI) [52] analysis were carried out using the AIMAII software package [53] on geometry optimised structures that were obtained with ORCA. Wave functional files (.wfx) used were created using Gaussian 09 [54].

Synthesis of non-cyclopalladated analogue, $[Pd(PTA)_2(C_6H_4)CH=N\{2,6\text{-}(^iPr)\text{-}C_6H_3\}Cl]$

$[Pd(PTA)_2(C_6H_4)CH=N\{2,6\text{-}(^iPr)\text{-}C_6H_3\}Cl]$ (NC1)

NC1 was synthesised by stirring a solution of **B1** (0.100 g, 0.123 mmol) in dichloromethane (5 mL) in a Schlenk tube. PTA (0.077 g, 0.49 mmol, 4 equivalents) was added. The solution was stirred for 2 hours in an oil bath at ± 25 °C. The reaction mixture was filtered through celite. Solvent was removed to obtain a yellow oily residue. The product was obtained by layering with ether to promote precipitation. The solution was kept at room temperature overnight. The white solid was isolated by vacuum filtration and rinsed with ether. The solid was dried under high vacuum. Yield: 0.090 g, 58%. FT-IR ($\nu_{C=N}$, cm^{-1}) 1614.03. m.p.: > 200 °C. ^1H NMR (599.98 MHz, $CDCl_3$): δ 8.49 (s, 1H, C*H*=N); δ 7.95 (d, 1H, $^3J_{H\text{-}H}$ 7.6 Hz, Ph); δ 7.39 (d, 1H, $^3J_{H\text{-}H}$ 6.5 Hz, Ph); δ 7.14-7.27 (m, 6H, Ph); δ 4.37 (dd, 12H, $^2J_{H\text{-}P}$ 46 Hz and $^4J_{H\text{-}P}$ 13 Hz, P-CH_2-N); δ 3.94 (s (br), 12H, N-CH_2-N); δ 3.08-3.15 (m, 2H, ^{i}Pr-C*H*);δ 1.27 (d, 12H, $^3J_{H\text{-}H}$ 6.5 Hz, CH_3). $^{31}P\{^1H\}$ NMR (242.88 MHz, $CDCl_3$): δ -63.37 (s). ESI-MS: $[M+H]^+$ 722.2; $[M\text{-}Cl]^+$ 684.2; $[M\text{-}Cl\text{-}PTA]^+$ 527.2; $[M\text{-}Cl\text{-}2PTA]^+$ 370.1; $[M\text{-}Cl\text{-}2PTA+MeCN]^+$ 411.1. Anal. Found: C, 47.7; H, 6.14; N, 12.6. Calc. for $C_{31}H_{46}N_7P_2ClPd.1CH_2Cl_2$: C, 47.7; H, 6.01; N, 12.2.

3.5. References

1. M. H. Levitt, *Spin dynamics: basics of nuclear magnetic resonance*, Chichester, England: John Wiley & Sons, 2008.
2. J. W. Akitt, *NMR and chemistry: an introduction to modern NMR spectroscopy*, Cheltenham: Thornes, 2000.
3. D. L. Pavia, *Introduction to spectroscopy*, Australia; Belmont, CA: Brooks/Cole Cengage Learning, 2009.
4. D. F. Hansen, P. Vallurupalli and L. E. Kay, *J. Phys. Chem. B*, 2008, **112**, 5898-5904.
5. D. L. Hasha, T. Eguchi and J. Jonas, *J. Am. Chem. Soc.*, 1982, **104**, 2290-2296.
6. A. D. Bain and G. J. Duns, *Can. J. Chem*., 1996, **74**, 819-824.
7. G. Binsch, *J. Am. Chem. Soc.*, 1969, **91**, 1304-1309.

8. J. Cavanagh, *Protein NMR spectroscopy: principles and practice*, San Diego: Academic Press, 1996.
9. H. M. McConnell, *J. Chem. Phys.*, 1958, **28**, 430-431.
10. R. Freeman, *Handbook of NMR*, Harlow, Essex, England: Longman Scientific & Technical,1987.
11. A. D. Bain, *Progress in Nuclear Magnetic Resonance Spectroscopy*, 2003, **43**, 63-103.
12. M. Girvin and S, Cahill, Chemical exchange in NMR spectroscopy, Lecture notes for NMR for Chemistry and Enzymology course, 28 March 2012, Albert Einstein College of Medicine.
13. D. Idiyatullin, S. Michaeli and M. Garwood, *J. Mag. Res.*, 2004, **171**, 330-337.
14. D. J. Winzor and C. M. Jackson, *J. Mol. Recognit.*, 2006, **19**, 389-407.
15. A. J. Swarts, *Mononuclear and Multinuclear Palladacycles as Catalyst Precursors*, M.Sc. Thesis Stellenbosch University, 2011.
16. D. M. E. van Niekerk, *Reactivity of metallacycles of palladium: Experimental and computational studies*, M.Sc. Thesis Stellenbosch University, 2012.
17. P. Vallurupalli, Chemical Exchange, Workshop Series on NMR and related topics, 24 February 2009, Tata Institute of Fundamental Research (TIFR) Mumbai.
18. F. Bloch, *Phys. Rev.*, 1946, **70**, 460-474.
19. F. P. Gasparro and N. H. Kolodny, *J. Chem. Ed.*, 1977, **54**, 258-261.
20. S. J. O'Kennedy, *A Kinetic Thermodynamic Study of Procyanidin Oligomer Conformation by ^{1}H NMR and DFT*, M.Sc. Thesis Stellenbosch University, 2015.
21. P. J. Hill, T. J. Herrington, N. H. Rees, A. J. P. White and A. E. Ashley, *Dalton Trans.*, 2015, **44**, 8984-8992.
22. L. Ortega-Moreno, R. Peloso, C. Maya, A. Suárez and E. Carmona, *Chem. Commun.*, 2015, **51**, 17008-17011.
23. T. Fukuda, R. Itoyama, T. Minagawa and M. Iwao, *Heterocycles*, 2014, **88**, 1121-1133.
24. J. Ruiz, N. Cutillas, F. López, G. López and D. Bautista, *Organometallics*, 2006, **25**, 5768-5773.
25. J. M. Forward, Z. Assefa, R. J. Staples and J. P. Fackler, Jr., *Inorg. Chem.*, 1996, **35**, 16-22.
26. Ł. Jaremko, A. M. Kirillov, P. Smoleński and A. J. L. Pombeiro, *Cryst. Growth Des.*, 2009, **9**, 3006-3010.
27. B. Ośmiałowski, E. Kolehmainen, S. Ikonen, A. Valkonen, A. Kwiatkowski, I. Grela and Esa Haapaniemi, *J. Org. Chem.*, 2012, **77**, 9609-9619.
28. S. R. LaPlante, R. Carson, J. Gillard, N. Aubry, R. Coulombe, S. Bordeleau, P. Bonneau, M. Little, J. O'Meara and P. L. Beaulieu, *J. Med. Chem.*, 2013, **56**, 5142-5150.

29. E. R. Johnson, S. Keinan, P. Mori-Sanchez, J. Contreras-Garcia, A. J. Cohen and W. Yang, *J. Am. Chem. Soc*., 2010, **132**, 6498-6506.
30. J. Vicente, M. T. Chicote, J. Martin, M. Artigao, X. Solans, M. Font-Altaba and M. Aguiló, *J. Chem. Soc. Dalton Trans*., 1988, **1**, 141-147.
31. K. R. Chaudhari, A. P. Wadawale and V. K. Jain, *J. Organomet. Chem*., 2012, **698**, 15-21.
32. F. Tjosaas and A. Fiksdahl, *J. Organomet. Chem.*, 2007, **692**, 5429-5439.
33. W. Zawartka, A. Gniewek, A. M. Trzeciak, J. J. Ziółkowski and J. Pernak, *J. Mol. Cat. A Chem.*, 2009, **304**, 8-15.
34. N. Mungwe, A. J. Swarts, S. F. Mapolie and G. Westman, *J. Organomet. Chem.*, 2011, **696**, 3527-3535.
35. J. Bravo, S. Bolaño, L. Gonsalvi and M. Peruzzini, *Coord. Chem. Rev.*, 2010, **254**, 555-607.
36. D. M. P. Mingos, *Essential trends in inorganic chemistry*, Oxford: Oxford University Press, 1998.
37. H. Clavier and S. P. Nolan, *Chem. Commun.*, 2010, **46**, 841-861.
38. W. W. Hussey and A. J. Diefenderfer, *J. Am. Chem. Soc.*, 1967, **89**, 5359-5362.
39. M. T. Tribble and J. G. Traynham, *J. Am. Chem. Soc.*, 1969, **91**, 379-388.
40. T. Benkert, K. Franke, D. Pozitron and R. Standish, SciDAVis 1.D009 software. Accessed at http://scidavis.sourceforge.net/.
41. F. Neese, *Wiley Interdiscip. Rev. Comput. Mol. Sci*., 2012, **2**, 73-78.
42. J. P. Perdew, K. Burke and M. Ernzerhof, Phys. Rev. Lett., 1996, 77, 3865-3868.
43. S. Grimme, J. Antony, S. Ehrlich and H. Krieg, *J. Chem. Phys*., 2010, **132**, 154104.
44. S. Grimme, C. Diedrich and M. Korth, *Angew. Chem. Int. Ed.*, 2006, **45**, 625-629.
45. A. Klamt and G. Schüürmann, *J. Chem. Soc., Perkin Trans. 2*, 1993, **1**, 799-805.
46. L. E. Roy, P. J. Hay and R. L. Martin, *J. Chem. Theory Comput.*, 2008, **4**, 1029-1031.
47. P. J. Hay and W. R. Wadt, *J. Chem. Phys.*, 1985, **82**, 299-310.
48. A. Schfer, H. Horn and R. Ahlrichs, *J. Chem. Phys.*, 1992, **97**, 2571-2577.
49. F. Weigend and R. Ahlrichs, *Phys. Chem. Chem. Phys.*, 2005, **7**, 3297-3305.
50. F. Weigend, *Phys. Chem. Chem. Phys.*, 2006, **8**, 1057-1065.
51. J. Zheng, X. Xu and D. G. Truhlar, *Theor. Chem. Acc.*, 2011, **128**, 295-305.
52. E. R. Johnson, S. Keinan, P. Mori-Sanchez, J. Contreras-Garcia, A. J. Cohen and W. Yang, *J. Am. Chem. Soc*., 2010, **132**, 6498-6506.
53. T. A. Keith, AIMAII (Version 15.05.18), TK Gristmill Software, Overland Park KS, USA, 2015.
54. M. J. Frisch, G. W. Trucks, H. B. Schlegel, G. E. Scuseria, M. A. Robb, J. R. Cheeseman, G. Scalmani, V. Barone, B. Mennucci, G. A. Petersson, H. Nakatsuji, M.

Caricato, X. Li, H. P. Hratchian, A. F. Izmaylov, J. Bloino, G. Zheng, J. L. Sonnenberg, M. Hada, M. Ehara, K. Toyota, R. Fukuda, J. Hasegawa, M. Ishida, T. Nakajima, Y. Honda, O. Kitao, H. Nakai, T. Vreven, J. A. Montgomery, Jr., J. E. Peralta, F. Ogliaro, M. Bearpark, J. J. Heyd, E. Brothers, K. N. Kudin, V. N. Staroverov, T. Keith, R. Kobayashi, J. Normand, K. Raghavachari, A. Rendell, J. C. Burant, S. S. Iyengar, J. Tomasi, M. Cossi, N. Rega, J. M. Millam, M. Klene, J. E. Knox, J. B. Cross, V. Bakken, C. Adamo, J. Jaramillo, R. Gomperts, R. E. Stratmann, O. Yazyev, A. J. Austin, R. Cammi, C. Pomelli, J. W. Ochterski, R. L. Martin, K. Morokuma, V. G. Zakrzewski, G. A. Voth, P. Salvador, J. J. Dannenberg, S. Dapprich, A. D. Daniels, O. Farkas, J. B. Foresman, J. V. Ortiz, J. Cioslowski, and D. J. Fox, Gaussian 09, Revision D.01, Gaussian, Inc., Wallingford CT, 2013.

Chapter 4
Binuclear Palladacycles: Synthesis and Characterisation

4.1 Introduction

The advantages of employing palladacycles in biological applications were previously described in Chapter 2. The main advantages being the rich coordination chemistry, facile synthesis, ease of handling and rapid library generation. The focus of Chapter 2 was the design and synthesis of mononuclear palladacycles, emphasising the use of lower molecular weight and water-soluble ligands, as a means to improve the water solubility. This chapter will discuss the design and synthesis of binuclear palladacycles, focusing of the choice of ligands and the use of water-soluble substituents to improve activity and enhance water solubility.

4.1.1 Binuclear palladacycle anti-cancer agents previously reported in the literature

Polymetallic species are by no means a new class of compounds in the field of chemotherapeutic agents or palladacycles. It has been suggested that the highly positively charged nature of polymetallic species in solution leads to stronger electrostatic interactions with DNA, thus making these complexes more active than their mononuclear counterparts [1]. The most well-known example of such complexes is the polymetallic platinum complex, [{*trans*-PtCl$(NH_3)_2$}$_2$-(μ-*trans*-{Pt$(NH_3)_2(NH_2(CH_2)_6NH_2)_2$})]$^{4+}$ (BBR3464), a trinuclear complex which has shown *in vitro* and *in vivo* cytotoxicity. This complex has been evaluated in Stage I clinical trials and its activity has been ascribed to its ability to form flexible adducts with DNA [1].

Similarly, Rodrigues *et al.* reported a series of mono-, binuclear and cationic palladacycles with bisphosphinic ligands and amine functionalities [obtained from *N*,*N*-dimethyl-1-phenethylamine (dmpa) ligands] [2]. Evaluation of the palladacycles as anti-cancer agents against syngeneic B16F10 murine melanoma, showed that the binuclear and cationic dppe analogues, [$Pd_2(S_{(-)}C^2,N$-dmpa$)_2$(μ-dppe)Cl_2] and [Pd($S_{(-)}C^2,N$-dmpa)(dppe)]Cl, were the most active compounds *in vitro*. However, *in vivo*, only the binuclear analogue was found to be active and, in agreement with the findings above, it was also more active than its monomeric analogue (Figure 4.1 and 4.2). This work suggests that binuclear palladacycles with bridging

dppe ligands may be highly active anti-cancer agents, possibly forming flexible adducts with DNA through electrostatic interactions [2].

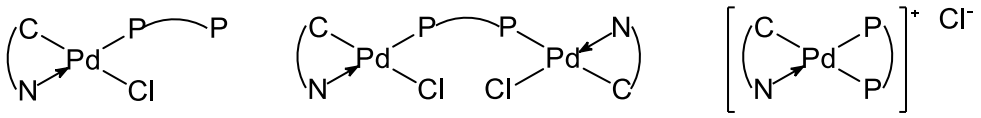

Figure 4.1: General structures for the monomeric and binuclear palladacycles, where P^P = dppe [2].

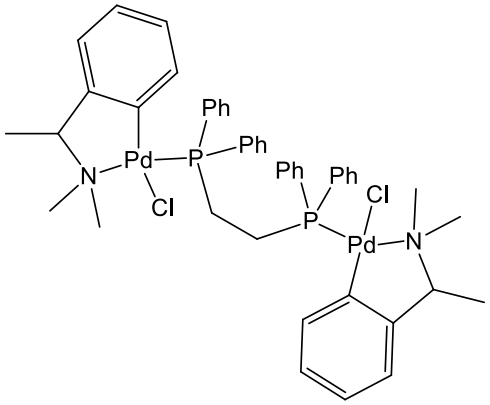

Figure 4.2: Binuclear dppe-bridged palladacycle, [Pd_2($S_{(-)}C^2$,*N*-dmpa)$_2$(μ-dppe)Cl_2], that showed the highest activity [2].

Following this work, Bincoletto *et al*., synthesised the dppf analogue, [Pd_2(C^2,$NS_{(-)}$dmpa)$_2$(μ-dppf)Cl_2], of the above complexes (Figure 4.3). Since ferrocene, on its own, is known for its anti-cancer properties, it could be incorporated into these binuclear palladacycles, in the form of dppf, to perhaps enhance the anti-cancer activity. Evaluation of this binuclear complex against Walker tumour-bearing rats showed a 90% inhibition of growth, again confirming that these bisphosphine-type ligands are promising scaffolds for palladacycles with potential application as anti-cancer agents [3].

Based on these publications and a number of other results obtained with similar μ-bisphosphine palladacycle complexes, these ligands could be used to design binuclear palladacycles with significant anti-cancer activity. Thus, μ-bisphosphine ligands were incorporated into the palladacycle system to form binuclear palladacycles, similar to **AJ5**, with the potential to bind to DNA through electrostatic interactions.

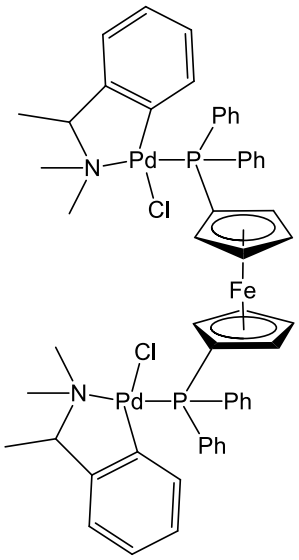

Figure 4.3: Ferrocene analogue [3] of the dppe palladacycle reported by Rodrigues *et al*. [2].

4.1.2 Influencing complex solubility by varying substituents on the ligands

Recently, Albert *et al*., reported the significant effect that small structural changes, such as a linker molecule, can have on the cytotoxicity of potential drug compounds [1]. Two series of doubly cyclopalladated diimines, previously referred to in Chapter 1, were recently reported. Briefly, the design of these palladacycles was based on the need to balance both lipophilicity and reactivity, as the lipophilicity controls the degree of cellular uptake, whilst the kinetic reactivity determines the amount of metal which can bind to the DNA. As discussed in Chapter 1, the reactivity of palladacycles can be controlled by strongly coordinating- or chelating ligands. Lipophilicity, on the other hand, is controlled by functional groups. To this end, the authors made use of two linker molecules, NCH_2CH_2N and $N(CH_2)_2O(CH_2)_2O(CH_2)_2N$, to vary flexibility, lipophilicity and hydrophilicity (Figure 4.4).

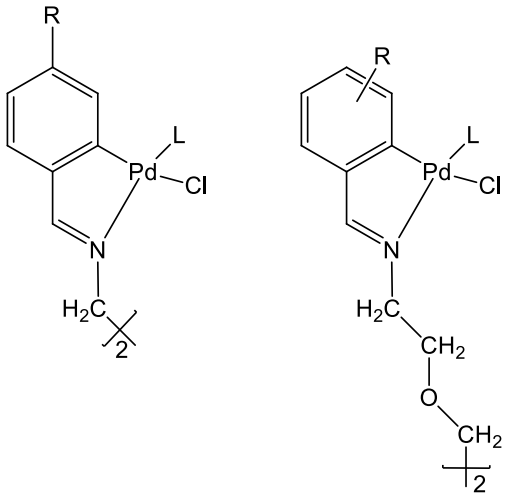

Figure 4.4: General structure of the diimine palladacycles reported by Albert *et al*. [1].

Their results showed that all complexes with the shorter NCH_2CH_2N linker were inactive, whilst the complexes with the longer linker showed activity. This corresponds to the work on the trinuclear platinum complex, BBR3464, where the flexible adducts formed with DNA correlate with higher activity. Furthermore, the oxygen atoms present in the longer linker allowed for the possibility of hydrogen-bonding with water molecules which increased the hydrophilicity of the complex [1].

Given the findings reported by Albert *et al*. [1], it was decided to functionalise the benzylidene moieties in the binuclear palladacycles previously prepared by us, with ethylene glycol-type tethers with the aim of improving water solubility and facilitating interaction of the complex with biological targets via potential hydrogen bond formation.

4.2 Synthetic routes

Based on the information above and a comprehensive study of the literature, as well as the results obtained with **AJ5**, the following series of binuclear palladacycles, shown in Figure 4.5, was designed.

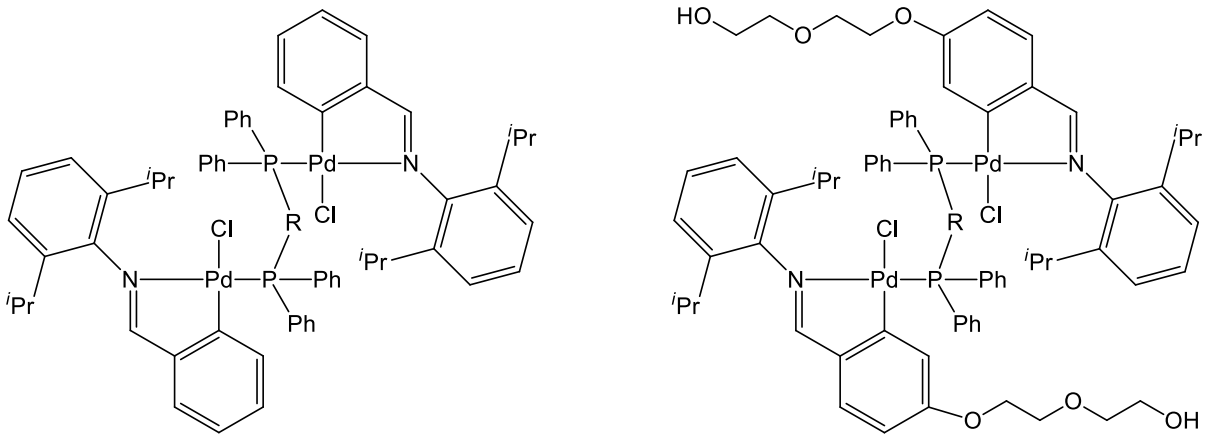

BC1-BC4 **BTC1-BTC4**

Figure 4.5: General structures of binuclear palladacycles with μ-bisphosphine ligands, R, where R = dppm, dppe, dppp or dppf. Left = unsubstituted analogues and right = ethylene glycol-tethered analogues.

The unsubstituted complexes, **BC1-BC4**, were synthesised in a three step process, similar to that used for the synthesis of the mononuclear palladacycles reported in Chapter 2. Briefly, the synthesis comprised of Schiff base condensation, cyclopalladation and finally, reaction with the bisphosphine ligands in a 1:1 ratio with the μ-chloro cyclopalladated complex. The Schiff base condensation reaction used to form the imine ligand, **L1**, and the cyclopalladation reaction to form the μ-chloro palladacycle, **B1**, is reported in Chapter 2, along with the

characterisation of these compounds. The final cleavage of the μ-chloro palladacycle with the various bisphosphines is shown in Scheme 4.1 and will be discussed in Section 4.3.

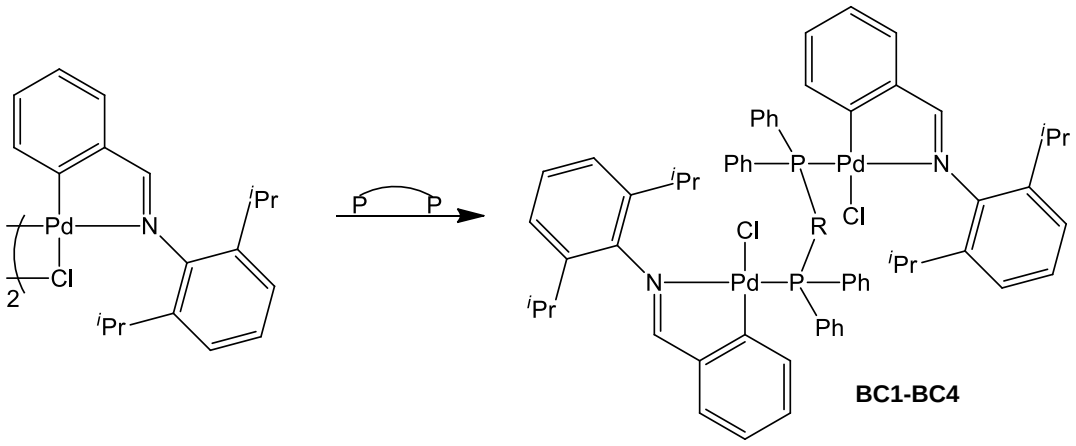

Scheme 4.1: General synthetic scheme with bisphosphines, where P^P = dppm, dppe, dppp or dppf.

The synthesis of the substituted or tethered analogues, **BTC1**-**BTC4**, was a four step process. Firstly, the aldehyde moiety was modified by adding an ethylene glycol-type tether, which could improve water solubility through hydrogen-bonding. Once the aldehyde was modified, the following three steps were the same as those for the unsubstituted series. The full four-step synthesis is shown in Scheme 4.2 and will be discussed in Section 4.3.

Finally, the bisphosphine ligands, 1,1-bis(diphenylphosphino)methane (dppm), dppe and 1,3-bis(diphenylphosphino)propane (dppp) were chosen to compare the effect of the aliphatic chain on activity and solubility. This choice was partially inspired by a paper by Caires *et al*. [4]. They reported three binuclear palladacycles with the bisphosphine bridging ligands, dppe, dppp and dppb (Figure 4.6). Interestingly, the dppe and dppb analogues were far more active than the dppp complexes and the dppb analogue was more active than the dppe analogue across three cell lines. Their data suggest that in the systems synthesised, the aliphatic chain length influenced the anti-cancer activity through the formation of more or less favourable adducts.

Furthermore, dppf was selected to allow the incorporation of ferrocene without significantly changing the structure of the designed palladacycles. The reason for incorporating ferrocene is its inherent anti-cancer activity. Thus, it could potentially enhance the anti-cancer activity of the complex, as reported by Bincoletto *et al*. (Figure 4.3) [3].

All novel compounds were characterised by FT-IR- and NMR (^{1}H, ^{13}C and ^{31}P) spectroscopy, mass spectrometry, micro analysis and melting point and single crystal analysis, where applicable. In addition, the complex solubilities were determined in water, dimethyl sulfoxide and water/dimethyl sulfoxide mixtures.

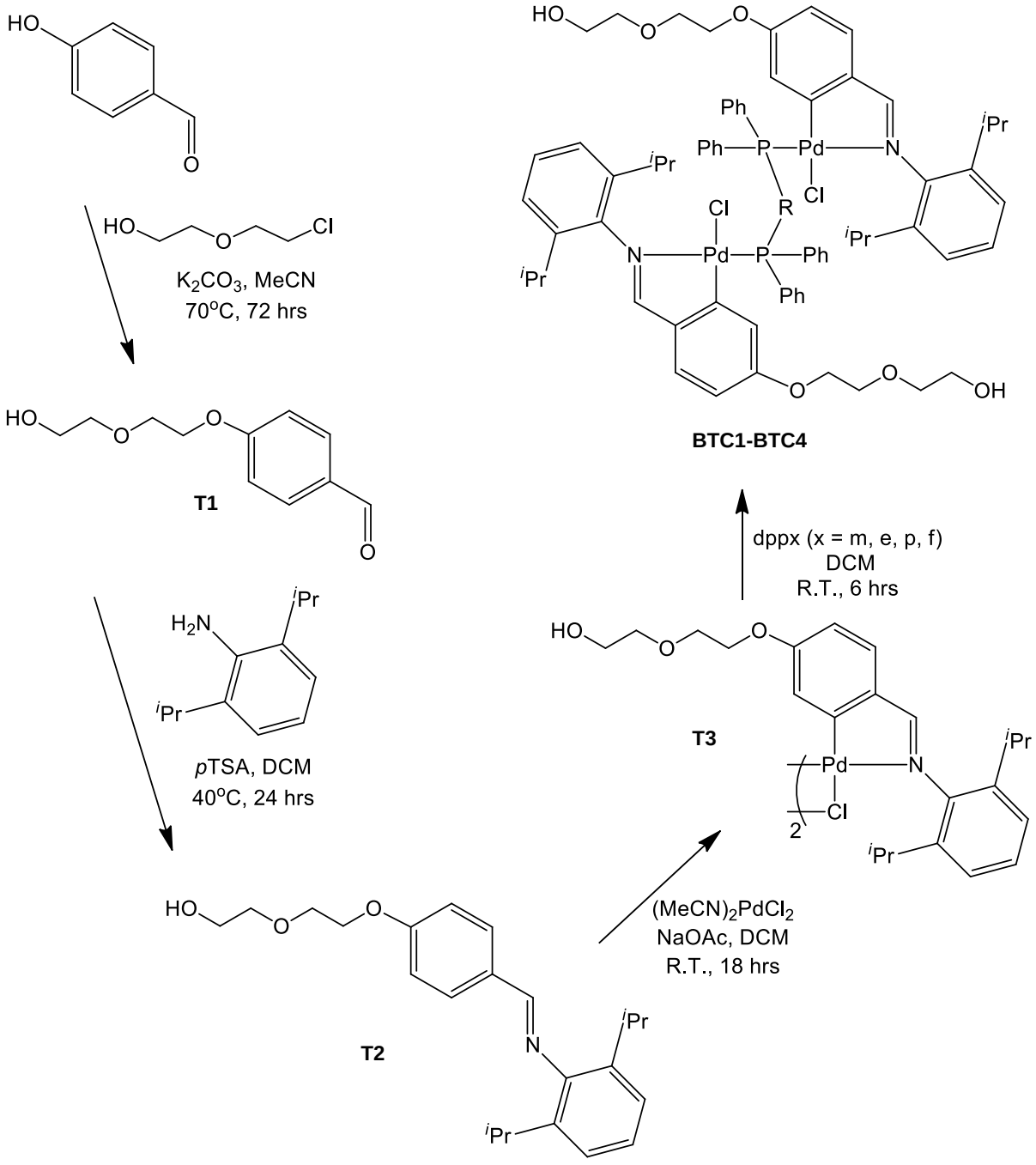

Scheme 4.2: Four-step synthesis for the tethered μ-bisphosphine palladacycles, where R = CH_2, $(CH_2)_2$, $(CH_2)_3$ or $C_5H_4FeC_5H_4$.

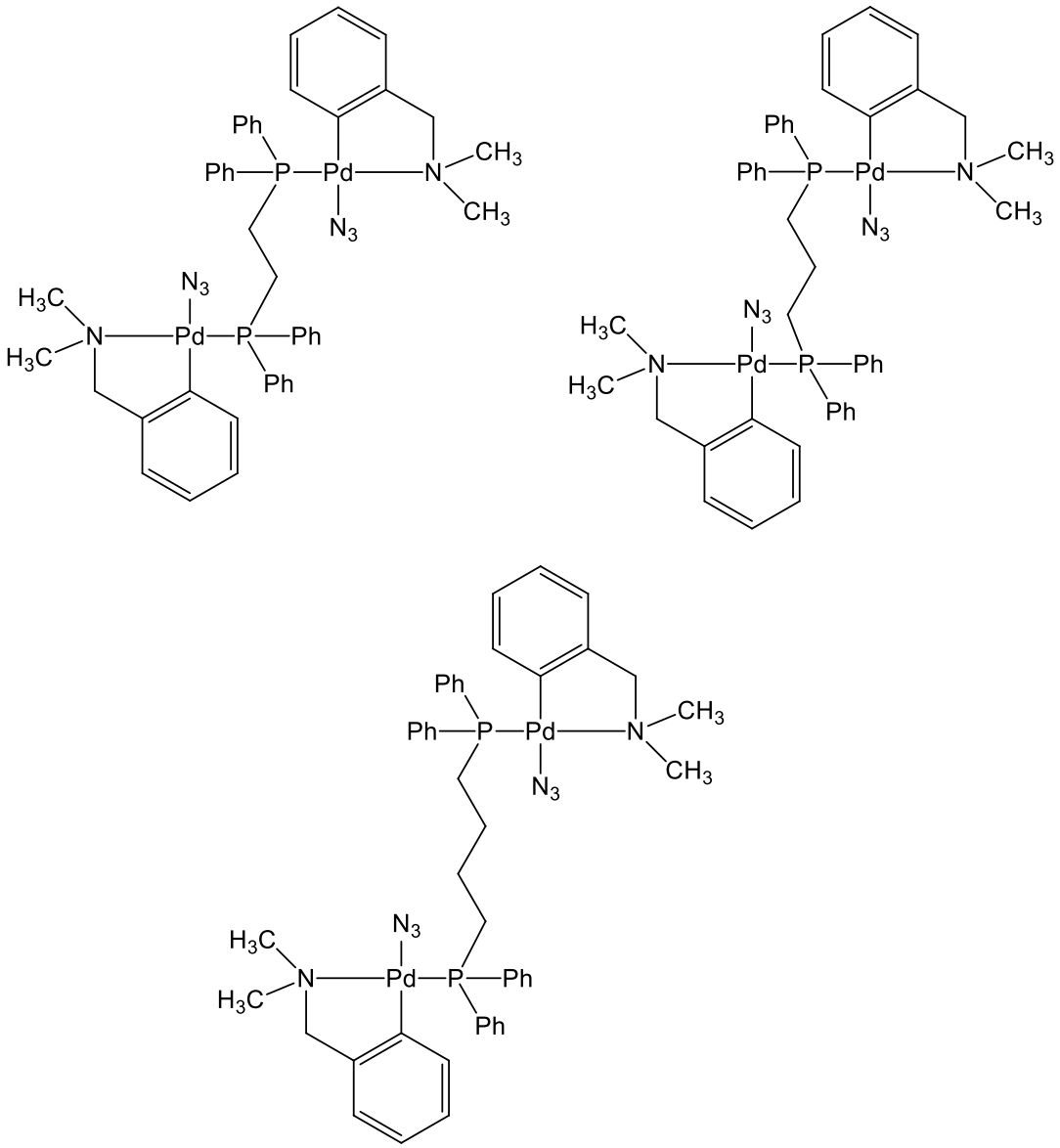

Figure 4.6: Bisphosphine bridged palladacycles reported by Caires *et al*. [4].

4.3 Results and discussion

4.3.1 Functionalisation of 4-hydroxybenzaldehyde

The functionalised aldehyde was synthesised by the method reported by Zhao *et al*. [5]. 4-Hydroxybenzaldehyde was reacted with 2-(2-chloroethoxy)ethanol to form the functionalised aldehyde, 4-[2-(2-hydroxyethoxy)ethoxy]benzaldehyde (**T1**), as shown in Scheme 4.3.

The product was isolated as a pale orange oil in a fair yield. At low temperatures, the oil solidified to a pale orange solid. The formation of the product was confirmed by FT-IR- and ^{1}H NMR spectroscopy and was found to match the literature data [5].

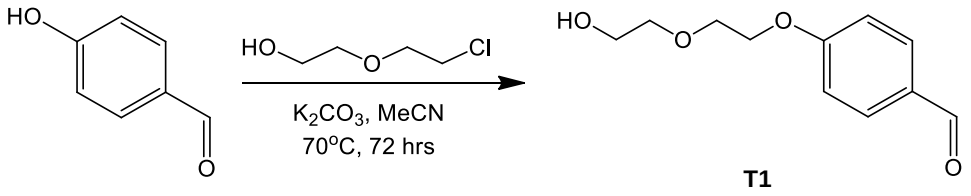

Scheme 4.3: Synthesis of 4-[2-(2-hydroxyethoxy)ethoxy]benzaldehyde (T1).

The FT-IR spectrum showed the carbonyl $\nu_{C=0}$ band shifts from 1664 cm^{-1} for 4-hydroxybenzaldehyde to 1679 cm^{-1} for the product. Furthermore, we observe the appearance of a band at 3428 cm^{-1}, corresponding to an O-H stretch and thus accounting for the hydroxyl group on the tether. The phenyl alkyl ether stretches were observed at 1254 cm^{-1} and 1046 cm^{-1} and the aliphatic ether stretch was observed at 1125 cm^{-1}.

The ^{1}H NMR spectrum of the product showed an aldehyde signal at 9.84 ppm. The proton next to the phenyl alkyl ether occurs as a triplet at 4.18-4.20 ppm, the aliphatic ether protons occur in the region of 3.60-3.90 ppm. This corresponded to the reported values [5].

4.3.2 Preparation of Schiff base ligands

The Schiff base ligand (**T2**) synthesis was adapted from the method described by Mungwe *et al*. [6]. The ligand was prepared by reacting 4-[2-(2-hydroxyethoxy)ethoxy]benzaldehyde (**T1**) with 2,6-diisopropylaniline in DCM, as shown in Scheme 4.4. A catalyst was required for this reaction to occur; thus, *para*-toluene sulfonic acid (*p*TSA) was added and the reaction was heated to 40 °C. The product was isolated as white needle crystals in a fair yield of approximately 60%.

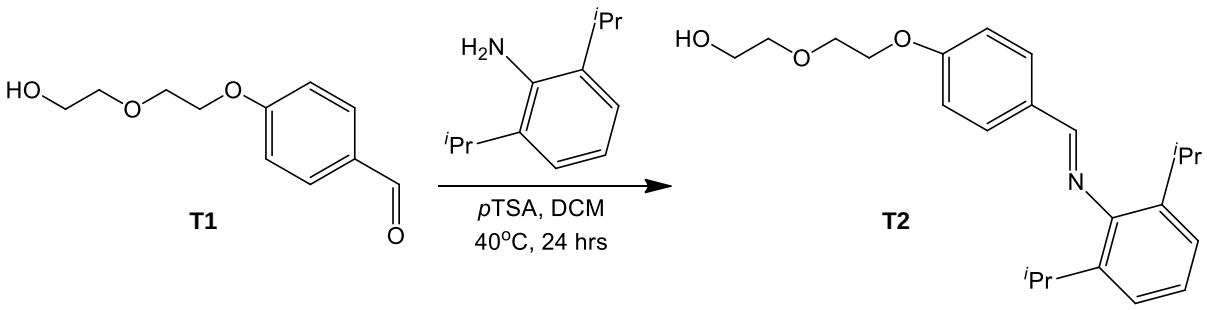

Scheme 4.4: Schiff base condensation of the tethered imine, T2.

FT-IR spectroscopy was used to determine whether the imine had been formed successfully. The disappearance of the carbonyl (C=O) band and the appearance of the imine (C=N) band was monitored. The imine C=N stretch was observed at 1630 cm^{-1}, with no evidence of the aldehyde C=O band at 1679 cm^{-1} (Figure 4.7).

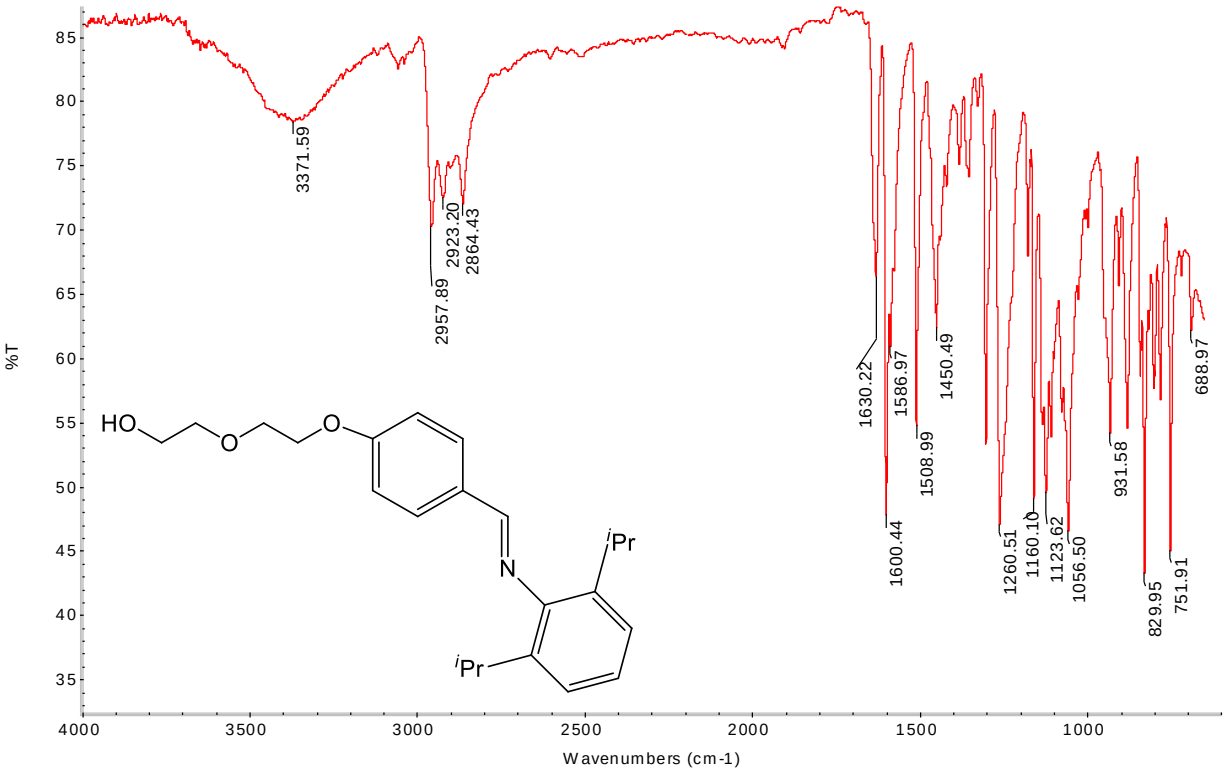

Figure 4.7: FT-IR spectrum of T2 (4000-600 cm^{-1}).

These findings were confirmed by ^{1}H NMR spectroscopy. The spectrum showed the imine signal at 8.12 ppm, which was the most deshielded signal in the spectrum. This signal was more upfield than the imine signal of **L1**, the unsubstituted analogue. The proton next to the phenyl alkyl ether was observed as a multiplet at 4.23-4.25 ppm, which was shifted 0.05 ppm downfield from the same signal in the aldehyde. The aliphatic ether protons appeared in the region of 3.7-4.0 ppm, a 0.1 ppm downfield shift from same signals in the aldehyde. The characteristic methine and methyl signals of the isopropyl substituents in the Schiff base ligands were observed at approximately 3.00 ppm and 1.18 ppm, respectively. These chemical shifts were similar to those observed for the unsubstituted ligand, **L1**.

ESI-MS and elemental analysis were also used to confirm product formation and purity, respectively. The mass spectrum showed the molecular ion, $[M+H]^{+}$, and the elemental analysis confirmed that the product was correct, with the incorporation of a small amount of water, which was also observed in the ^{1}H NMR spectrum.

A single crystal was grown from DCM layered with hexane at low temperature (-16 °C). The crystal structure was determined by single crystal X-ray diffraction.

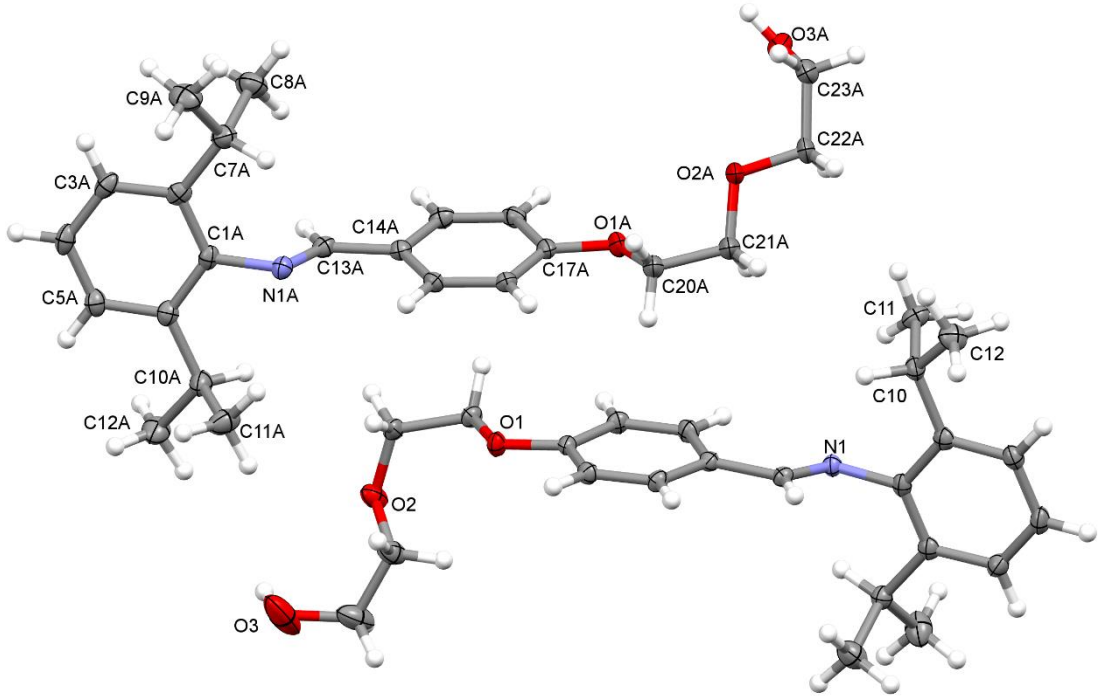

Figure 4.8: ASU of T2, with thermal ellipsoids rendered at the 50% probability level. H atoms are rendered as spheres with arbitrary fixed radii. Selected non-H atoms are labelled.

The asymmetric unit contains two independent molecules, A (top) and B (bottom), as shown in Figure 4.8. The molecules have the same composition, but slightly different conformations of the tether. Furthermore, although not shown in Figure 4.8, several atoms of the isopropyl groups closest to the tethers (labelled C10-C12 and C10A-C12A) were disordered over two positions. As observed in the crystal structure of **B6**, the disorder of the isopropyl groups is most likely via fluxional motion about a carbon (sp^2)-carbon (sp^3) bond axis. The major components have site-occupancy factors of 0.836(3) for A and 0.849(3) for B, whilst the minor components have site-occupancy factors of 0.151(3) and 0.164(3) for A and B, respectively.

The different conformations of the two molecules are clearly reflected in the torsion angle C1-N1-C13-C14 (τ) which is different for A (τ_A = -177.10(12)˚) and B (τ_B = 175.82(12)˚). These conformational differences result in different orientations and different packing. The molecules designated as A (orange) pack in a head-to-tail conformation, whilst those designated as B (purple) pack in a tail-to-tail fashion. Alternating columns of A and B are observed in the crystal packing (Figure 4.9) as an ···ABAB··· array of offset columns which repeats along the *a*-axis. The crystal structure also shows intermolecular hydrogen bonding involving the tethers of two B molecules. The terminal hydroxyl group of one molecule is hydrogen bonded to the ether oxygen atom of the other molecule (O3A-H3AA···O2A); thus forming a ring with an inversion centre and the Etter notation $R^2_2(10)$ [7]. These hydrogen bonds are bifurcate, as an additional interaction with the tether of an A molecule, as shown in Figure 4.10 is also observed. This is

an interaction between the two terminal hydroxyl groups (O3-H3···O3A). The numerical data pertaining to these hydrogen bonds can be found in Table 4.1.

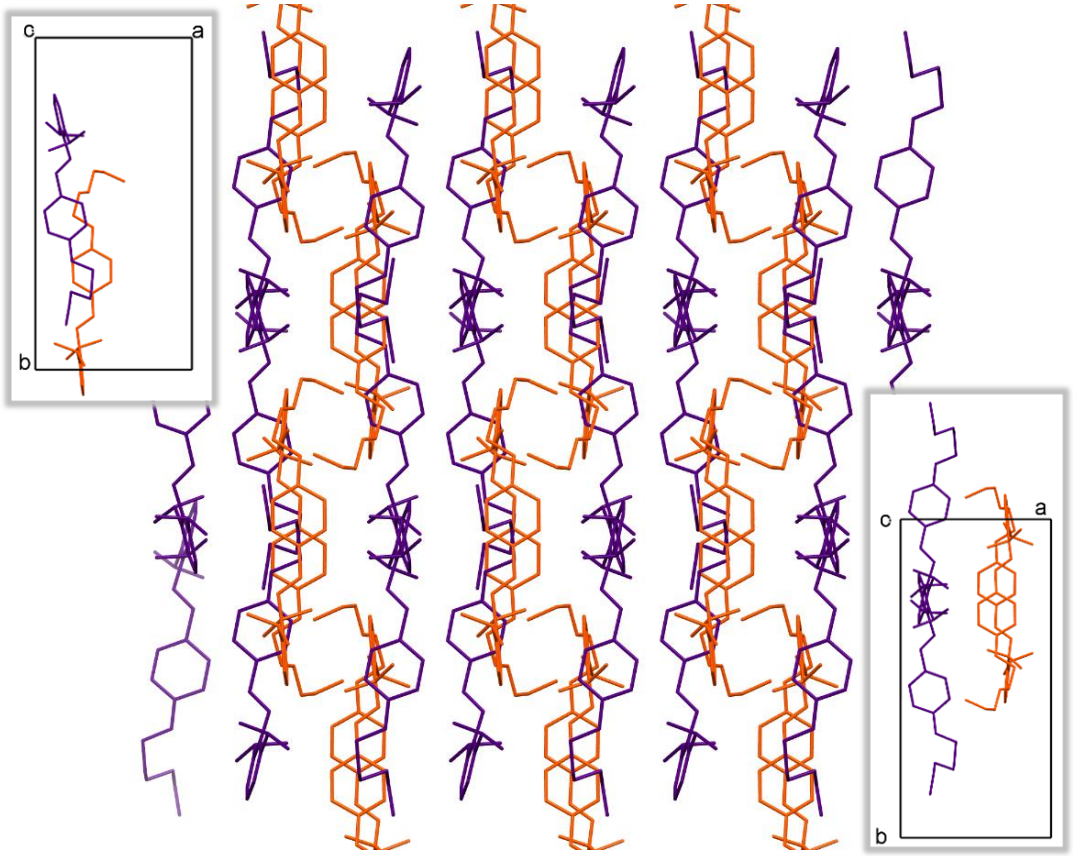

Figure 4.9: Crystal packing of T2 along the *a*-axis showing columns of A (orange), B (purple) and the rings formed by tail-to-tail packing of A. Inset (top left): Unit cell showing A and B in the ASU. Inset (bottom right): Partially packed unit cell showing columns of A and B.

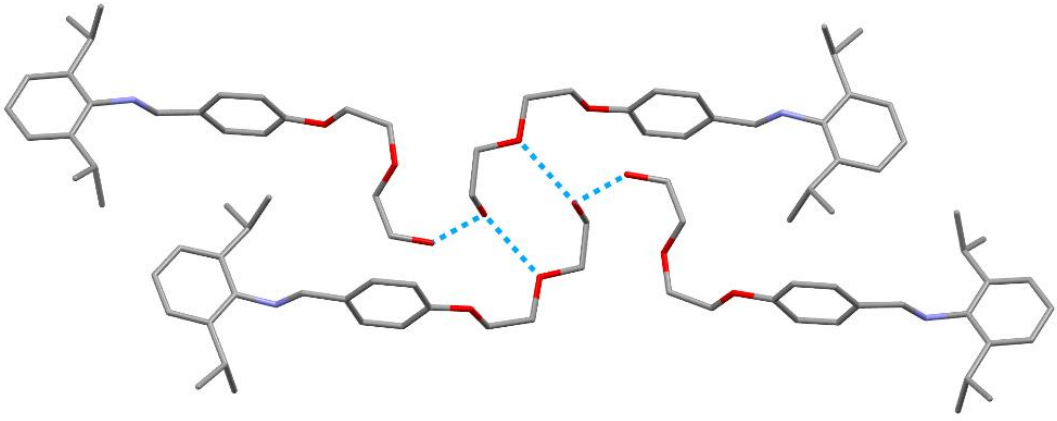

Figure 4.10: Hydrogen-bonding interactions in the crystal structure of T2. Hydrogen atoms have been omitted for clarity.

Table 4.1: Hydrogen-bond parameters

D—H···*A*	*D*—H (Å)	H···*A* (Å)	*D*···*A* (Å)	*D*—H···*A* (°)
O3—H3···O3A^{i}	0.88(3)	1.88(3)	2.748(2)	168(2)
O3A—H3AA···O2A^{ii}	0.87(3)	1.96(3)	2.790(2)	159(2)

Note: D-H = proton donor group, A = proton acceptor atom;
Symmetry codes: (i) -*x*+1, *y*+1/2, -*z*+3/2; (ii) -*x*+1, -*y*+1, -*z*+2.

Similar hydrogen bonding was observed in the reported structure of an aza podand which was obtained by opening of the macrocycle of 4',4"(5")-dinitrodibenzo-18-crown-6 ethers with $MeNH_2$ [8]. The centrosymmetric dimer, formed through bifurcate H-bonding in this case, is shown in Figure 4.11. Two O-H···O bonds were observed between the terminal hydroxyl group and the two ether oxygen atoms. The O(3)-H···O(2A) and O(3)-H···O(1A) bond distances were reported as 2.26(8) and 2.48(8) Å, whilst the angles at the hydrogen atom were reported as 124(7)° and 129(7)°, respectively. These bond distances are significantly shorter that those observed in the crystal structure of **T2**, suggesting that the intermolecular hydrogen bonding in **T2** is quite weak. This could be attributed to the degree of disorder observed in the tether of **T2**, as confirmed by the large ellipsoids observed for O2 and O3 in Figure 4.8, whereas the reported structure, the aza podand dimer mentioned above, has a total of six intermolecular hydrogen bonds "locking" the tether in place, as indicated by the more uniformly sized ellipsoids observed throughout the structure (Figure 4.11).

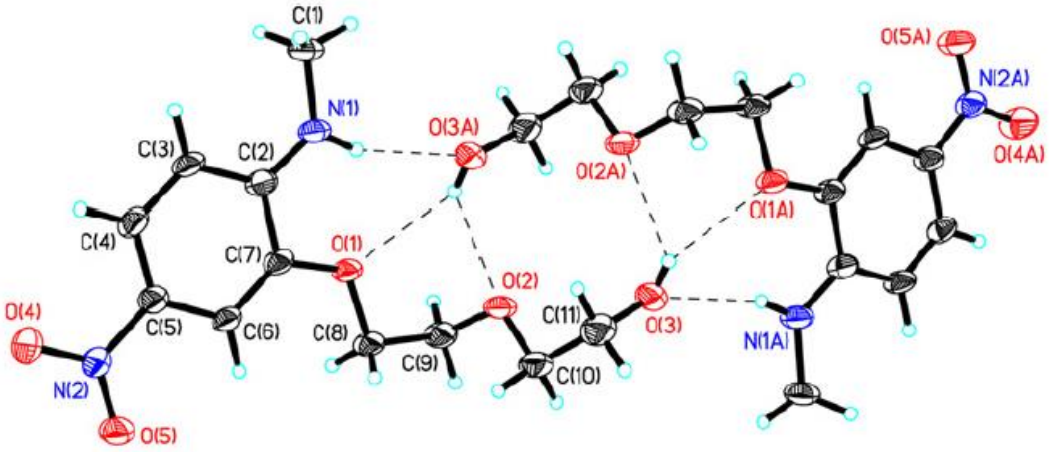

Figure 4.11: Structure of an aza podand showing dimer formation through bifurcate H-bonding. Thermal ellipsoids are drawn at 40% probability and hydrogen bonds are drawn as dashed lines [8].

Finally, it should be noted that the crystal structure included water. This water of crystallisation was also observed in the ^{1}H NMR spectrum and the elemental analysis which calculated for $C_{23}H_{31}NO_3$•$0.9H_2O$, however; the solvent was "squeezed" out, as a satisfactory model could not be found. Further experimental crystallographic data can be found in Table 4.2 and additional geometric parameters can be found in Appendix 1, Tables A1.11 and A1.12.

Table 4.2: Experimental crystallographic data for T2.

Parameter	T2
Chemical formula	$C_{23}H_{31}NO_3$
Formula weight	369.49
Temperature (K)	100(2)
Wavelength (Å)	0.71073
Crystal system	Monoclinic
Space group	$P2_1/c$
a (Å)	9.845(6)
b (Å)	20.87(1)
c (Å)	20.73(1)
α (°)	90.000
β (°)	90.54(1)
γ (°)	90.000
V (Å^3)	4258(5)
Z	8
D_{calc} [Mg/m^3]	1.153
Absorption coefficient (mm^{-1})	0.075
F(000)	1600
Final *R* indices [$I>2\sigma(I)$]	R_1 = 0.0468, wR_2 = 0.1066
Reflections collected	26919
Completeness to θmax (%)	94.3
Goodness-of-fit on F^2	1.064
Largest difference peak and hole (e Å^{-3})	0.359, -0.405

4.3.3 μ-Chloro palladacycles

Cyclopalladation of the Schiff base ligand, via electrophilic C-H bond activation, was carried out to obtain the μ-chloro bridged palladacycle. The synthesis was performed as described by Mungwe *et al.* [6], using two equivalents of Schiff base ligand, two equivalents of bis(acetonitrile)palladium dichloride and four equivalents of sodium acetate to form one equivalent of the palladacycle, **T3** (Scheme 4.5) [6].

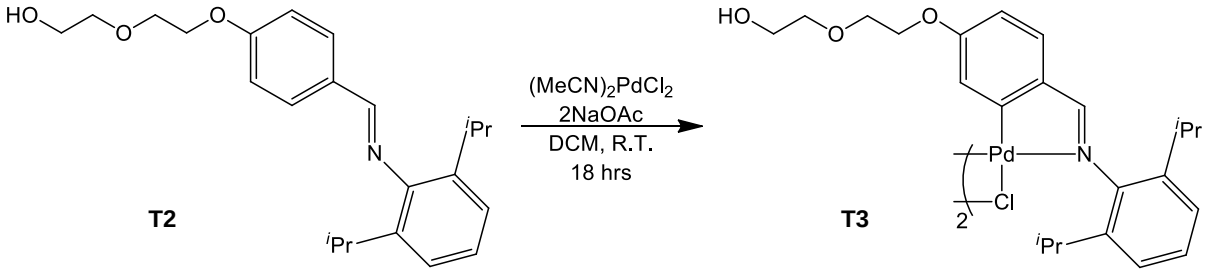

Scheme 4.5: Cyclopalladation of tethered imine, T2, to form tethered bridged complex, T3.

In this way **T3**, a yellow crystalline solid, was isolated in a high yield. The material was found to be sparingly soluble in DCM and DMSO. The product's structure was confirmed by FT-IR spectroscopy and ESI-MS. The use of other characterisation techniques was not possible due to the low solubility of the complex.

The FT-IR spectrum showed the imine $\nu_{C=N}$ stretch at 1596 cm^{-1}. This was a large shift to lower wavenumbers of approximately 30 cm^{-1} relative to the free ligand, as was expected for coordination to the metal through the imine nitrogen [9].

The mass spectrum showed a number of fragments, of which the most significant for confirming the formation of the product were the $[M\text{-}Cl+2MeCN]^+$ and $[(M/2)\text{-}Cl]^{2+}$ fragments at 1065 and 474.1 *m/z* (Figure 4.12). The simulated fragment pattern for the $[M\text{-}Cl+2MeCN]^+$ fragment matches the fragment pattern of the base peak perfectly, whilst the $[(M/2)\text{-}Cl]^{2+}$ fragment overlaps with a second fragment, thus obscuring the fragmentation pattern.

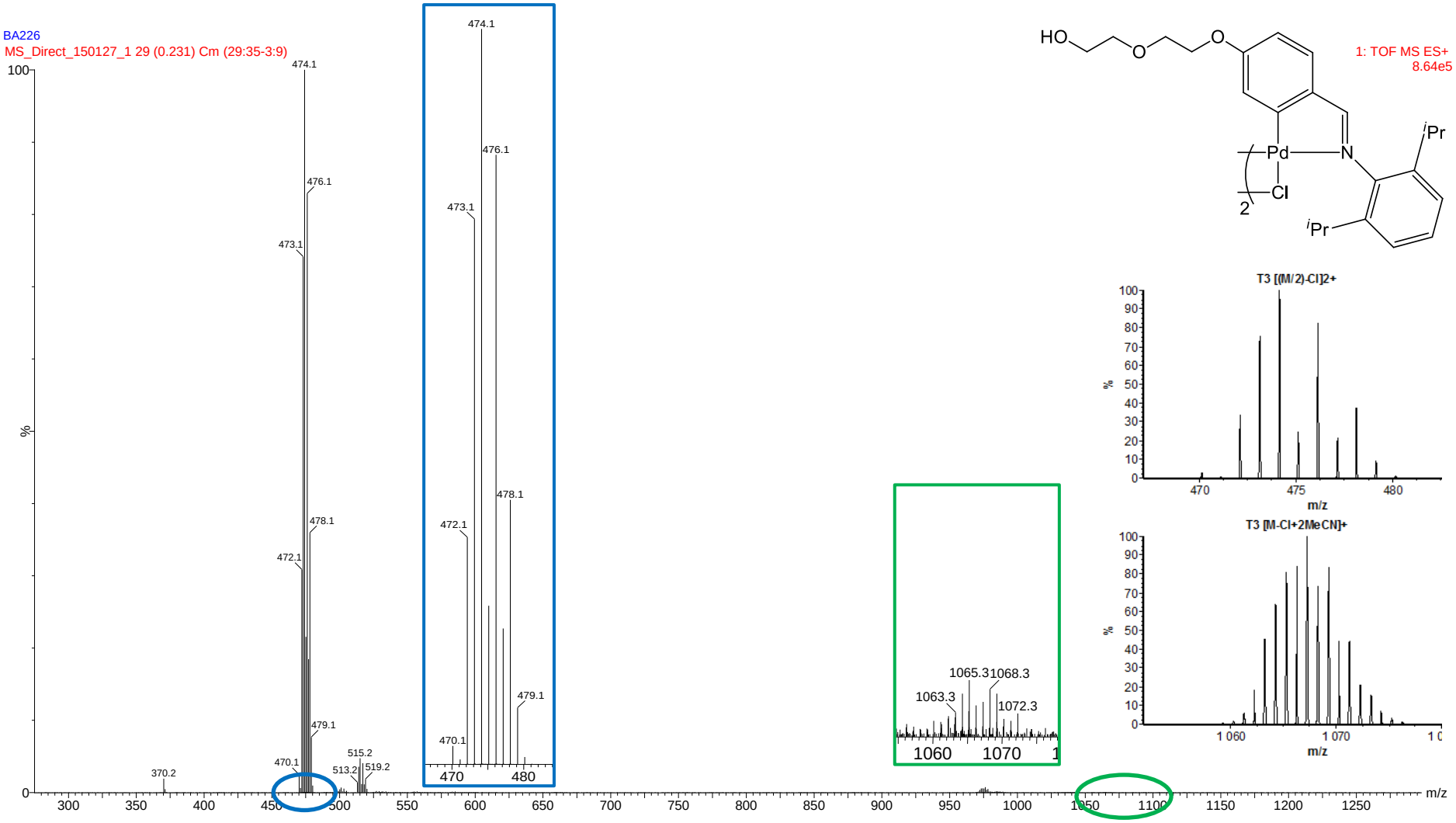

Figure 4.12: ESI-MS spectrum of T3 with inserts of zoomed in spectra showing base peak and higher molecular weight clusters, as well as the simulated fragment patterns.

4.3.4 Bisphosphine-bridged palladacycles

With the μ-chloro bridged palladacycles, **B1** and **T3** in hand, the final synthetic step was to react these binuclear palladacycles with the various bisphosphines, to obtain the desired μ-bisphosphine-bridged palladacycles. The synthetic details for this step are given in Scheme 4.6. All compounds were isolated as crystalline or amorphous solids in acceptable to good yields (42-89%). Note that the characterisation data for **AJ5**, the previously reported binuclear palladacycle, have been included in the discussion to follow, for the sake of comparison.

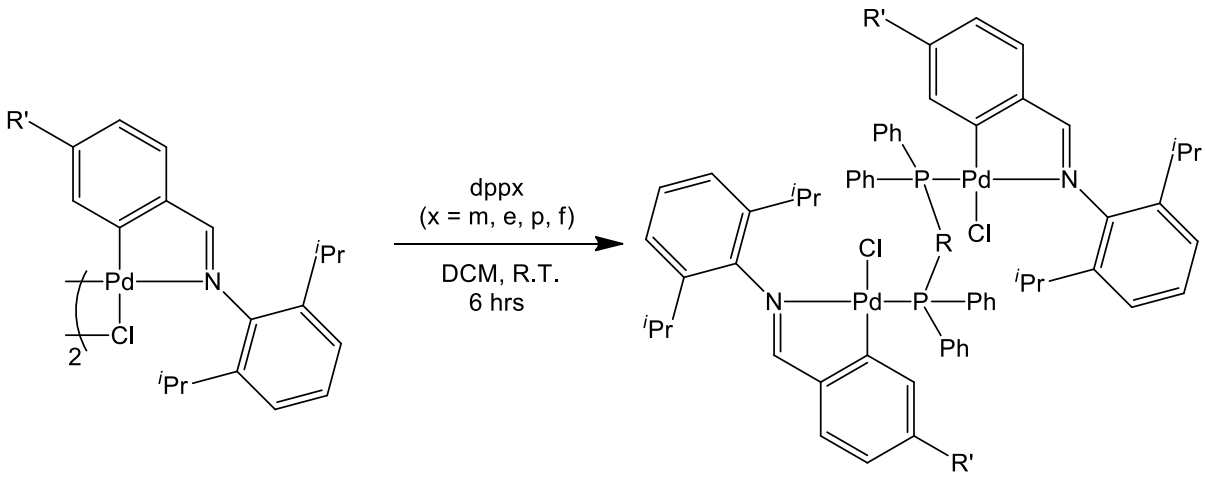

B1: R' = H
T3: R' = -$(OCH_2CH_2)_2OH$

BC1-4: R' = H (unsubstituted)
BTC1-4: R' = -$(OCH_2CH_2)_2OH$ (tether)

BC1 and **BTC1**: R = dppm
AJ5 and **BTC2**: R = dppe
BC3 and **BTC3**: R = dppp
BC4 and **BTC4**: R = dppf

Scheme 4.6: General synthetic scheme for the reaction of the μ-chloro palladacycles with various bisphosphines to obtain the unsubstituted- (BC1-BC4) and the tethered binuclear palladacycles (BTC1-BTC4).

FT-IR spectroscopy confirmed the successful displacement of the μ-chloro bridge with the μ-bisphosphine bridge for all compounds. This was confirmed by the change in the $\nu_{C=N}$ stretch from 1599 cm^{-1} (**B1**) and 1596 cm^{-1} (**T3**) to slightly higher wavenumbers in the range of 1608-1611 cm^{-1} for **BC1**-**BC4** and 1605-1606 cm^{-1} for **BTC1**-**BTC4** (Table 4.3). This shift can be explained by the fact that the phosphine ligand is a better sigma donor than the chloride ligand, thus resulting in increased electron density on the metal centre. Consequently, there is increased back donation from the metal to the ligands. Since tertiary phosphines are better pi-acceptor ligand than the imine, there is less back donation onto the imine than in the case of the μ-chloro bridged palladacycles. Thus, the imine bond is stronger and the corresponding shift to higher wavenumbers is observed [10;11].

Table 4.3: Analytical data for binuclear palladacycles, BC1-BC4 and BTC1-BTC4.

Complex	FT-IR ($\upsilon_{C=N}$, cm^{-1})[a]	ESI-MS (*m/z*) $[M-Cl]^+$	Melting point (˚C)[b]
BC1	1609	1161	246-249[d]
AJ5[c]	1612	1175	257-260[d]
BC3	1609	1189	245-248[d]
BC4	1608	1331	181-186[d]
BTC1	1606	1369	227-231[e]
BTC2	1605	1381	158-162[f]
BTC3	1605	1397	146-147[f]
BTC4	1606	-	87.5-89.4[d]

[a]IR spectra were recorded neat using an ATR accessory. [b]Melting points were recorded in glass capillaries and are reported as uncorrected. [c]Data from previously published results [12]. [d]Decomposition without melting. [e]Decomposition, followed by melting. [f]Melting followed by decomposition.

^{1}H NMR spectroscopy was used to confirm that the correct products were isolated. The imine resonances were observed as a doublet in the range of 7.80-8.10 ppm. The fine structure of the signals are due to $^4J_{H-P}$ coupling between the imine proton and the phosphorous atom of the bisphosphine ligand. These imine resonances were shifted approximately 0.2 ppm downfield compared to the μ-chloro palladacycles. This could, once again, be explained by the fact that the phosphine ligands are better sigma donors than the chloride ligands. This led to increased electron density on the metal centres and subsequent back-donation to the pi-acceptor ligands. Since the imine has more double bond character (due to the reduced degree of back-donation in the presence of the phosphine), it experiences greater anisotropic effects [10;11;13]. Both the multiplicity and the shift in the imine resonances confirmed coordination of the phosphine ligand. Tables 4.4 and 4.5 show the assignments of the signals in the ^{1}H NMR spectra for the two series of palladacycles. It was clear from the tables that the tether in the substituted palladacycles, **BTC1**-**BTC4**, leads to shielding of the imine protons, as these signals are not shifted as far downfield as is the case for the unsubstituted palladacycles. This could be due to electron donating effects of the ether functionalities in the tether, resulting in shielding of the aromatic ring protons in the ortho and para positions [13].

Further evidence for coordination of the phosphine was observed by the increased complexity of the aromatic region due to the phenyl rings of the bisphosphine ligand which appear as broad multiplets in this region. Again, as with the imine signal, the aromatic signals of the tethered analogues were more shielded (5.62-8.14 ppm) than those of the unsubstituted analogues (6.07-8.13 ppm).

The presence of only one bridging bisphosphine ligand could be confirmed by the signals resonances for these ligands in the aliphatic region. The chemical shift of the methylene protons of dppm was found at approximately 5.10 ppm, whilst dppe and dppp had resonances in the region of 1.60-3.03 ppm and the chemical shifts of the cyclopentadienyl rings of dppf are found in the region of 4.42-5.09 ppm. The remaining signals were assigned to the isopropyl groups, where the methine occurs in the region of 3.29-3.52 ppm, the methyls arise at 1.15-1.49 ppm and the methylene protons of the tether occurred as 3-4 multiplets with chemical shifts in the region of 3.10-3.68 ppm (Figure 4.13 and 4.14).

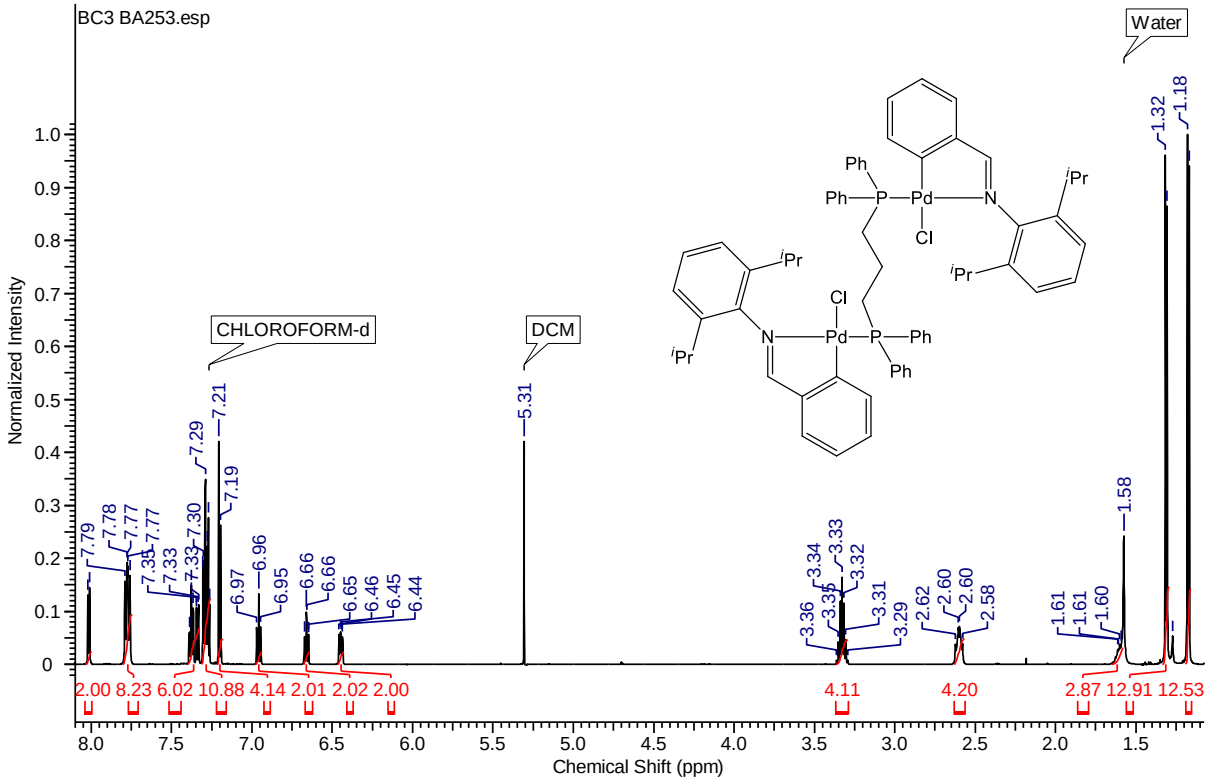

Figure 4.13: ^{1}H NMR spectrum of BC3.

^{13}C NMR spectroscopy showed the same trend in chemical shifts as ^{1}H NMR spectroscopy. The imine carbon signals were found in the region of 176-179 ppm for **BC1**-**BC4** and 175-176 ppm for **BTC1**-**BTC4**. The aromatic carbon coupled to the imine functionality (-*C*CH=N-) was found in the region of 158-161 ppm for all complexes and the ortho-mutilated carbon signal arose at approximately 145 ppm. For the tethered complexes, the aromatic carbon with the attached tether (-*C*-$(OCH_2CH_2)_2OH$) arose at a chemical shift of 161-162 ppm. There were also a number of multiplets due to $J_{C\text{-}P}$ coupling in the aromatic region. The aliphatic region was not too complex with the resonances for the isopropyl methines and methyls occurring at 27-28 ppm and 23-24 ppm, respectively. The chemical shifts of the aliphatic carbons of the bisphosphine ligand were observed in the range of 21-23 ppm and the cyclopentadienyl ring

signals of **BTC4** were found at 75-77 ppm. The chemical shifts for the tether in **BTC1**-**BTC4** occurred in the region of 61-72 ppm.

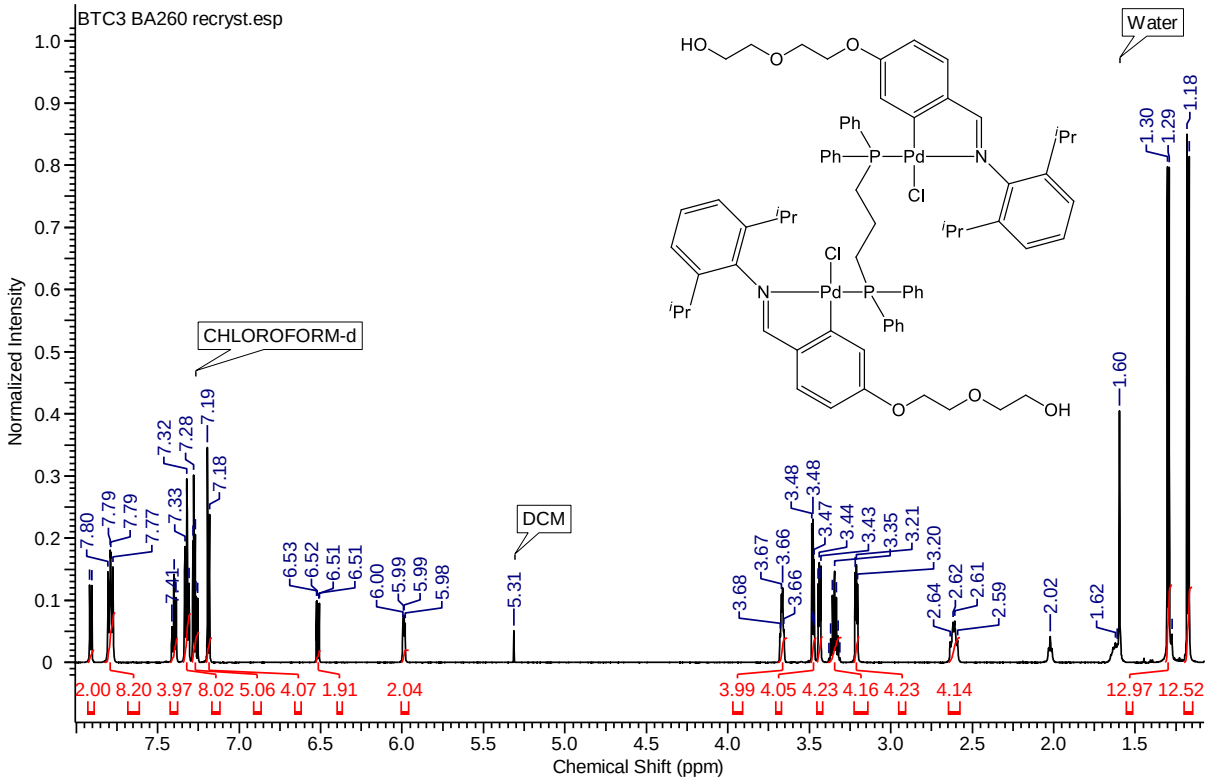

Figure 4.14: ^{1}H NMR spectrum of BTC3.

The ^{31}P NMR spectra showed single resonances for each of the complexes in the chemical shift region of 31-40 ppm (Table 4.6). Thus, confirming the equivalence of the phosphines and the formation of a pure product.

Table 4.4: ^{1}H NMR data for unsubstituted binuclear palladacycles, BC1-BC4.

Complex	C*H*=N	Aromatic Region	Aliphatic region		
			P-$(CH_2)_n$-P	$(CH_3)_2CH$	$CH(CH_3)_2$
BC1	7.99 (d, 2H, $^{4}J_{H-P}$ 7.0 Hz)	8.10-8.13 (m, 8H); 7.27-7.29 (m, 4H); 7.21-7.23 (m, 8H); 7.14-7.17 (m, 8H); 6.90-6.92 (m, 2H); 6.55-6.57 (m, 2H); 6.07-6.09 (m, 2H)	5.09-5.13 (m, 2H)	3.40-3.47 (m, 4H)	1.49 (d, 12H, $^{3}J_{H-H}$ 6.5 Hz) 1.23 (d, 12H, $^{3}J_{H-H}$ 6.5 Hz)
AJ5[a]	8.02 (d, 2H, $^{4}J_{H-P}$ 7.2 Hz)	7.88-7.94 (m, 8H); 7.20-7.34 (m, 20H); 6.93 (t, 2H, $^{3}J_{H-H}$ 7.34 Hz); 6.61 (t, 2H, $^{3}J_{H-H}$) 7.63 Hz); 6.34 (br. t, 2H, $^{4}J_{H-P}$ 7.2 Hz)	3.00 (br m, 4H)	3.37-3.46 (m, 4H)	1.33 (d, 12H, $^{3}J_{H-H}$ 6.8 Hz) 1.19 (d, 12H, $^{3}J_{H-H}$ 6.9Hz)
BC3	8.02 (d, 2H, $^{4}J_{H-P}$ 7.6 Hz)	7.76-7.79 (m, 8H); 7.33-7.39 (m, 6H); 7.26-7.30 (m, 10H), 7.20 (d, 4H, $^{3}J_{H-H}$ 7.6 Hz); 6.94-6.97 (m, 2H); 6.65-6.67 (m, 2H); 6.44-6.46 (m, 2H)	2.58-2.62 (m, 4H); 1.60 (m, 2H)	3.29-3.36 (m, 4H)	1.32 (d, 12H, $^{3}J_{H-H}$ 6.5 Hz) 1.18 (d, 12H, $^{3}J_{H-H}$ 7.0 Hz)
BC4	8.06 (d, 2H, $^{4}J_{H-P}$ 7.6 Hz)	7.60-7.64 (m, 8H); 7.36-7.40 (m, 6H); 7.23-7.27 (m, 10H); 7.18 (d, 4H, $^{3}J_{H-H}$ 7.6 Hz); 7.01-7.04 (m, 2H); 6.68-6.72 (m, 2H); 6.35-6.38 (m, 2H)	4.98 (br s, 4H, CP ring); 4.42-4.43 (m, 4H, CP ring)	3.37-3.44 (m, 4H)	1.37 (d, 12H, $^{3}J_{H-H}$ 7.0 Hz) 1.17 (d, 12H, $^{3}J_{H-H}$ 7.0 Hz)

[a]Data from references [12]. Spectra run in $CDCl_3$ at 25 ˚C. Chemical shifts reported in ppm, referenced relative to residual solvent peak.

Table 4.5: ^{1}H NMR data for substituted binuclear palladacycles, BTC1-BTC4.

Complex	C*H*=N	Aromatic Region	Aliphatic region			
			P-$(CH_2)_n$-P	-$(OCH_2CH_2)_2OH$	$(CH_3)_2CH$	$CH(CH_3)_2$
BTC1	7.89 (d, 2H, $^{4}J_{H-P}$ 7.9 Hz)	8.14-8.20 (m, 8H); 7.15-7.31 (m, 20H); 6.47 (dd, 2H, $^{3}J_{H-H}$ 8.2 Hz and $^{4}J_{H-H}$ 2.2 Hz); 5.62-5.65 (m, 2H)	5.04-5.13 (m, 2H)	3.66-3.67 (m, 4H, Ph-OC*H*$_2$-); 3.39-3.52 (m, 8H, Ph-OCH_2CH_2-and -C*H*$_2CH_2OH$); 3.16-3.19 (m, 4H, -CH_2CH_2OH)	3.39-3.52 (m, 4H)	1.48 (d, 12H, $^{3}J_{H-H}$ 6.8 Hz); 1.24 (d, 12H, $^{3}J_{H-H}$ 6.9 Hz)
BTC2	7.88-7.89 (m, 2H)	7.84-7.87 (m, 8H); 7.28-7.31 (m, 4H); 7.23-7.26 (m, 12H); 7.17 (d, 4H, $^{3}J_{H-H}$ 7.6 Hz); 6.47 (dd, 2H, $^{3}J_{H-H}$ 8.2 Hz and $^{4}J_{H-H}$ 2.3 Hz); 5.85-5.86 (m, 2H)	3.03 (br d, 4H, $^{3}J_{H-H}$ 2.3 Hz)	3.60-3.61 (m, 4H, Ph-OC*H*$_2$-); 3.34-3.42 (m, 8H, Ph-OCH_2CH_2-and -C*H*$_2CH_2OH$); 3.11 (t, 4H, $^{3}J_{H-H}$ 4.7 Hz, -CH_2CH_2OH)	3.34-3.42 (m, 4H)	1.32 (d, 12H, $^{3}J_{H-H}$ 7.0 Hz); 1.17 (d, 12H, $^{3}J_{H-H}$ 7.0 Hz)
BTC3	7.91 (d, 2H, $^{4}J_{H-P}$ 7.6 Hz)	7.77-7.80 (m, 8H); 7.39-7.41 (m, 4H); 7.31-7.33 (m, 8H), 7.25-7.28 (m, 4H); 7.19 (d, 4H, $^{3}J_{H-H}$ 7.6 Hz); 6.52 (dd, 2H, $^{3}J_{H-H}$ 8.2 Hz and $^{4}J_{H-H}$ 2.3 Hz); 5.98-6.00 (m, 2H)	2.59-2.64 (m, 4H); 1.60 (m, 2H)	3.66-3.68 (m, 4H, Ph-OC*H*$_2$-); 3.47-3.48 (m, 4H, Ph-OCH_2CH_2-); 3.43-3.45 (m, 4H, -C*H*$_2CH_2$OH); 3.20-3.22 (m, 4H, -CH_2CH_2OH)	3.31-3.38 (m., 4H)	1.30 (d, 12H, $^{3}J_{H-H}$ 6.5 Hz) 1.18 (d, 12H, $^{3}J_{H-H}$ 7.0 Hz)
BTC4	7.95 (d, 2H, $^{4}J_{H-P}$ 8.8 Hz)	7.59-7.63 (m, 8H); 7.36-7.39 (m, 4H); 7.33-7.34 (m, 2H); 7.24-7.27 (m, 8H); 7.22 (d, 2H, $^{3}J_{H-H}$ 7.6 Hz); 7.16 (d, 4H, $^{3}J_{H-H}$ 7.3 Hz); 6.60 (dd, 2H, $^{3}J_{H-H}$ 8.2 Hz and $^{4}J_{H-H}$ 2.3 Hz); 6.03 (dd, 2H, $^{3}J_{H-H}$ 5.7 Hz and $^{4}J_{H-H}$ 2.3 Hz)	5.09 (br s, 4H, CP ring); 4.42-4.43 (m, 4H, CP ring)	3.68-3.70 (m, 4H, Ph-OC*H*$_2$-); 3.52-3.54 (m, 8H, Ph-OCH_2CH_2-and -C*H*$_2CH_2OH$); 3.23 (br t, 4H, $^{3}J_{H-H}$ 4.7 Hz, -CH_2CH_2OH)	3.36-3.43 (m, 4H)	1.34 (d, 12H, $^{3}J_{H-H}$ 7.0 Hz) 1.16 (d, 12H, $^{3}J_{H-H}$ 7.0 Hz)

Spectra run in $CDCl_3$ at 25 ˚C. Chemical shifts reported in ppm, referenced relative to residual solvent peak.

Table 4.6: ^{31}P NMR shifts of binuclear palladacycles, BC1-BC4 and BTC1-BTC4.

Complex	δ (ppm)
BC1	33.99
AJ5*	39.54
BC3	35.21
BC4	31.38
BTC1	34.39
BTC2	40.63
BTC3	35.46
BTC4	31.38

*Data from previously published results [12].

ESI-MS was used as further confirmation that the correct product was formed. The molecular ion was not detected in any of the spectra; however, the $[M\text{-}Cl]^+$ fragment, a common fragment in many palladium chloride complexes and also observed in the mononuclear palladacycle series, was detected for all complexes, except **BTC4**. This fragment confirms the correct product was formed. Another common fragment across the unsubstituted and tethered series was $[M\text{-}2Cl\text{-}Pd\text{-}L1/T2]^+$. This corresponds to the loss of the labile chloride ligands, followed by the loss of a palladium atom and the coordinated ligand [12]. This fragmentation pathway is shown in Figure 4.15 and the various fragments are assigned in Table 4.7.

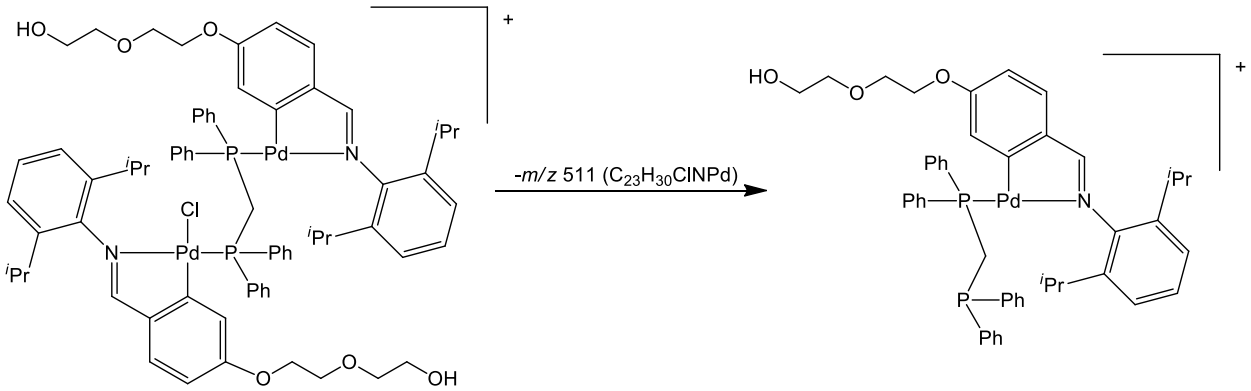

Figure 4.15: Possible fragmentation pathway for BTC1 with major fragments assigned in Table 4.7.

The solubility of the compounds was tested in water, DMSO and a DMSO/water mixture, as reported in Chapter 2. Table 4.8 shows the results of this study. The binuclear complexes were found to be far more soluble in both DMSO and the water/DMSO mixture than the mononuclear complexes. In addition, the tethered series was generally more soluble than the unsubstituted series. Despite the increased solubility, all of the complexes were insoluble in water.

Table 4.7: Ion fragments detected by ESI-MS for binuclear palladacycles, BC1-BC4 and BTC1-BTC4.

Complex	$[M\text{-}Cl]^+$	$[M\text{-}2Cl\text{-}Pd\text{-}L1/A2]^+$
BC1	1161	754
AJ5*	1175	-
BC3	1189	577
BC4	1331	924
BTC1	1369	858
BTC2	1381	872
BTC3	1397	886
BTC4	-	1028

*Data from previously published results [12].

Table 4.8: Solubilities for binuclear palladacycles, BC1-BC4 and BTC1-BTC4.

Complex	Solubility in water (mg/mL)	Solubility in DMSO (mg/mL)	%DMSO in water/DMSO solution
AJ5	0	4.38	57
BC1	0	6.32	62
BC3	0	2.02	78
BC4	0	57.2	91
BTC1	0	2.85	28
BTC2	0	32.6	76
BTC3	0	76.0	54
BTC4	0	53.7	98

4.4 Conclusions and future work

Two series of binuclear palladacycles with bridging bisphosphine ligands were synthesised and fully characterised. The series with the ethylene glycol-type tether was found to be more soluble than the analogous unsubstituted series and the mononuclear PTA-based series. However, despite the improved solubility, none of the complexes were water-soluble.

Incorporation of alternative water-soluble moieties should be investigated as a continuation of this work. Some possibilities include replacing 2,6-diisopropylaniline moiety with the more water-soluble analogues, 4-aminophenol [14] and sulfanilic acid [15]. These analogues are less sterically hindered, more soluble and sulfanilic acid is currently used in medicinal applications as it has low toxicity. In addition to varying the aniline moiety, the tether can also be modified to be either shorter or longer (fewer or more oxygen atoms), thus allowing variation in the lipophilicity and hydrophilicity of the complexes [1].

4.5 Materials and Methods

General methods are reported in Chapter 2, Section 2.5.

Synthesis of unsubstituted binuclear palladacycles with μ-bisphosphine ligands

[{PdCl(C_6H_4)CH=N(2,6-^{i}Pr$_2$-C_6H_3)}$_2$(μ-$Ph_2PCH_2PPh_2$)] (BC1)

BC1 was synthesised by preparing a solution of **B1** (0.092 g, 0.11 mmol) in dichloromethane (5 mL) in a Schlenk tube. Dppm (0.044 g, 0.11 mmol) was added. The solution was stirred for 6 hours in an oil bath at ± 25 °C. The reaction solution was filtered through celite and the solvent volume was reduced to obtain a slightly viscous yellow solution. The product was recrystallised by layering the dichloromethane solution with hexane at low temperature (-16 °C). The solution was kept at low temperature (-16 °C) overnight. The yellow crystals were isolated by vacuum filtration and rinsed with hexane. The material was dried under vacuum. Yield: 0.119 g, 88%. FT-IR ($\nu_{C=N}$, cm^{-1}) 1609. m.p.: 246-249 °C. ^{1}H NMR (599.99 MHz, $CDCl_3$): δ 8.10-8.13 (m, 8H, Ph); δ 7.99 (d, 2H, $^4J_{H-P}$ 7.0 Hz, C*H*=N); δ 7.27-7.29 (m, 4H, Ph); δ 7.21-7.23 (m, 8H, Ph); δ 7.14-7.17 (m, 8H, Ph); δ 6.90-6.92 (m, 2H, Ph); δ 6.55-6.57 (m, 2H, Ph); δ 6.07-6.09 (m, 2H, Ph); δ 5.09-5.13 (m, 2H, -PC*H*$_2$P-); δ 3.40-3.47 (m, 4H, ^{i}Pr-C*H*); δ 1.49 (d, 12H, $^3J_{H-H}$ 6.5 Hz, ^{i}Pr-C*H*$_3$); δ 1.23 (d, 12H, $^3J_{H-H}$ 6.5 Hz, ^{i}Pr-C*H*$_3$). ^{13}C{^{1}H} NMR ($CDCl_3$, 100.57 MHz): δ 176.27 (*C*H=N); δ 158.12 (-

*C*CH=N-); δ 146.38 (o-metallated C); δ 144.46 (C_{Ar}); δ 139.88 (C_{Ar}); δ 136.67 (t, J_{C-P} 4.6 Hz, C_{Ar}); δ 134.39 (t, J_{C-P} 6.3 Hz, C_{Ar}); δ 129.54 (C_{Ar}); δ 129.33 (C_{Ar}); δ 127.56 (C_{Ar}); δ 126.89-126.99 (m, C_{Ar}); δ 126.07 (C_{Ar}); δ 123.01 (C_{Ar}); δ 121.87 (C_{Ar}); δ 27.54 (^{i}Pr-*C*H); δ 23.64 (^{i}Pr-*C*H_3); δ 22.04 (-P*C*H_2P-). $^{31}P\{^{1}H\}$ NMR ($CDCl_3$, 161.89 MHz): δ 33.99 (s). ESI-MS: $[M-Cl]^+$1161.25, $[M-2Cl-Pd-L1]^+$ 754.200, $[M-2Cl-Pd-L1-(Ph)_2PCH_2P(Ph)_2+MeCN]^+$ 411.11. Anal. Found: C, 61.8; H, 4.95; N, 1.91. Calc. for $C_{63}H_{66}Cl_2N_2P_2Pd_2$•0.6$CH_2Cl_2$: C, 61.4; H, 5.44; N, 2.25. Solubility: DMSO 6.32 mg/mL; 62% DMSO in water.

[{PdCl(C_6H_4)CH=N(2,6-^{i}Pr$_2$-C_6H_3)}$_2$(μ-$Ph_2P(CH_2)_3PPh_2$)] (BC3)

BC3 was synthesised as above, using dppp as the bridging bis(phosphine) and the quantities as indicated: **B1** (0.092 g, 0.11 mmol), dichloromethane (5 mL) and dppp (0.047 g, 0.11 mmol). Yield: 0.123 g, 89%. FT-IR ($\nu_{C=N}$, cm^{-1}) 1609. m.p.: 245-248 °C. ^{1}H NMR ($CDCl_3$, 599.99 MHz): δ 8.02 (d, 2H, $^{4}J_{H-P}$ 7.6 Hz, C*H*=N); δ 7.76-7.79 (m, 8H, Ph); δ 7.33-7.39 (m, 6H, Ph); δ 7.26-7.30 (m, 10H, Ph); δ 7.20 (d, 4H, $^{3}J_{H-H}$ 7.6 Hz, Ph); δ 6.94-6.97 (m, 2H, Ph); δ 6.65-6.67 (m, 2H, Ph); δ 6.44-6.46 (m, 2H, Ph); δ 3.29-3.36 (m, 4H, ^{i}Pr-C*H*); δ 2.58-2.62 (m, 4H, -PC*H*$_2$CH_2C*H*$_2$P-); δ 1.60 (m, 2H, -PCH_2C*H*$_2$CH_2P-); δ 1.32 (d, 12H, $^{3}J_{H-H}$ 6.5 Hz, ^{i}Pr-C*H*$_3$); δ 1.18 (d, 12H, $^{3}J_{H-H}$ 7.0 Hz, ^{i}Pr-C*H*$_3$). $^{13}C\{^{1}H\}$ NMR ($CDCl_3$, 150.88 MHz): δ 176.73 (*C*H=N); δ 159.15 (-*C*CH=N-); δ 147.68 (*o*-metallated C); δ 145.06 (C_{Ar}); δ 140.82 (m, C_{Ar}); δ 137.72-137.79 (m, C_{Ar}); δ 134.19 (t, J_{C-P} 5.7 Hz, C_{Ar}); δ 130.89 (C_{Ar}); δ 130.54 (m, C_{Ar}); δ 130.22 (m, C_{Ar}); δ 129.91 (C_{Ar}); δ 128.78 (C_{Ar}); δ 128.34 (t, J_{C-P} 5.7 Hz, C_{Ar}); δ 126.91 (C_{Ar}); δ 123.97 (C_{Ar}); δ 122.76 (C_{Ar}); δ 28.45 (^{i}Pr-*C*H); δ 24.37 (^{i}Pr-*C*H_3); δ 23.16 (-PCH_2*C*H_2CH_2P-); δ 21.36 (-P*C*H_2CH_2*C*H_2P-). $^{31}P\{^{1}H\}$ NMR ($CDCl_3$, 161.89 MHz): δ 35.21 (s). ESI-MS: $[M-Cl]^+$ 1189.28, $[M-2Cl-Pd-L1]^+$ 782.232, $[M-2Cl]^{2+}$ 577.156, $[M-2Cl-Pd-L1-(Ph)_2P(CH_2)_3P(Ph)_2+MeCN]^+$ 411.104. Anal. Found: C, 59.6; H, 5.05; N, 1.60. Calc. for $C_{65}H_{70}Cl_2N_2P_2Pd_2$•0.7$H_2O$·1.3$CH_2Cl_2$: C, 59.2; H, 5.54; N, 2.08. Solubility: DMSO 2.02 mg/mL; 78% DMSO in water.

[{PdCl(C_6H_4)CH=N(2,6-^{i}Pr$_2$-C_6H_3)}$_2$(μ-$Ph_2PC_5H_4FeC_5H_4PPh_2$)] (BC4)

BC4 was synthesised as above, using dppf as the bridging bis(phosphine) and the quantities as indicated: **B1** (0.092 g, 0.11 mmol), dichloromethane (5 mL) and dppf (0.063 g, 0.11 mmol). Yield: 0.072 g, 47%. FT-IR ($\nu_{C=N}$, cm^{-1}) 1608. m.p.: 181-186 °C. ^{1}H NMR ($CDCl_3$, 599.99 MHz): δ 8.06 (d, 2H, $^4J_{H-P}$ 7.6 Hz, C*H*=N); δ 7.60-7.64 (m, 8H, Ph); δ 7.36-7.40 (m, 6H, Ph); 7.23-7.27 (m, 10H, Ph); δ 7.18 (d, 4H, $^3J_{H-H}$ 7.6 Hz, Ph); δ 7.01-7.04 (m, 2H, Ph); δ 6.68-6.72 (m, 2H, Ph); δ 6.35-6.38 (m, 2H, Ph); δ 4.98 (br s, 4H, Cp ring); δ 4.42-4.43 (m, 4H, Cp ring); δ 3.37-3.44 (m, 4H, ^{i}Pr-C*H*); δ 1.37 (d, 12H, $^3J_{H-H}$ 7.0 Hz, ^{i}Pr-C*H*$_3$); δ 1.17 (d, 12H, $^3J_{H-H}$ 7.0 Hz, ^{i}Pr-C*H*$_3$). ^{13}C{^{1}H} NMR ($CDCl_3$, 100.57 MHz): δ 177.25 (*C*H=N); δ 159.11 (-*C*CH=N-); δ 147.36 (o-metallated C); δ 145.44 (C_{Ar}); δ 140.86 (C_{Ar}); δ 135.37 (t, J_{C-P} 6.3 Hz, C_{Ar}); δ 130.53 (m, C_{Ar}); δ 130.31 (C_{Ar}); δ 128.54 (C_{Ar}); δ 127.87-127.97 (m, C_{Ar}); δ 127.05 (C_{Ar}); δ 123.99 (C_{Ar}); δ 122.86 (C_{Ar}); δ 77.20 (m, Cp ring); δ 28.52 (^{i}Pr-*C*H); δ 24.62 (^{i}Pr-*C*H$_3$); δ 23.02 (^{i}Pr-*C*H$_3$). ^{31}P{^{1}H} NMR ($CDCl_3$, 161.89 MHz): δ 31.38 (s). ESI-MS: [M-Cl]$^+$ 1331.22, [M-2Cl-Pd-L1]$^+$ 924.186, [M-2Cl]$^{2+}$ 648.133, [M-2Cl-Pd-L1-{(Ph)$_2$PC$_5$H$_4$FeC$_5$H$_4$P(Ph)$_2$}+MeCN]$^+$ 411.106. Anal. Found: C, 60.9; H, 4.79; N, 1.51. Calc. for $C_{72}H_{72}Cl_2FeN_2P_2Pd_2$•$CH_2Cl_2$: C, 60.4; H, 5.14; N, 1.93. Solubility: DMSO 57.2 mg/mL; 91% DMSO in water.

Synthesis of binuclear palladacycles with 2-(2-hydroxyethoxy)ethoxy tether and μ-bisphosphine ligands

4-[2-(2-Hydroxyethoxy)ethoxy]benzaldehyde (T1)

T1 was synthesised by stirring a solution of 4-hydroxybenzaldehyde (1.22 g, 10.0 mmol) in dry acetonitrile (75.0 mL) in a 2-neck round bottom flask. 2-(2-Chloroethoxy)ethanol (1.24 g, 10.0 mmol) was added to the solution, followed by potassium carbonate (6.50 g, 40.0 mmol). The resulting suspension was heated for 72 hours in an oil bath at ± 70 °C. The mixture was then cooled to room temperature and the solvent was removed under reduced pressure. The residue was dissolved in dichloromethane (100 mL) and the solution was washed with water (3 x 75 mL portions). The organic layer was dried over anhydrous magnesium sulphate after which the magnesium sulphate was removed by filtration. Solvent was removed from the filtrate to obtain an orange oily residue. The product was dried on high vacuum to remove any remaining solvent. Yield: 1.068 g, 65%. FT-IR ($\nu_{C=O}$, cm^{-1}) 1679; (ν_{C-O}, cm^{-1}) 1254 (phenyl alkyl ether), 1046 (phenyl alkyl ether) and 1125 (aliphatic ether). ^{1}H NMR (599.99 MHz, $CDCl_3$): δ 9.84 (s, 1H, C*H*=O); δ 7.78-7.81 (m, 2H, Ph); δ 6.98-7.00 (m, 2H, Ph); δ 4.19 (t, 2H, $^3J_{H-H}$ 4.7 Hz, Ph-OC*H*$_2$CH$_2$-); δ 3.87

(t, 2H, $^{3}J_{H\text{-}H}$ 4.7 Hz, Ph-OCH$_2$C*H*$_2$-); δ 3.74 (t, 2H, $^{3}J_{H\text{-}H}$ 4.7 Hz, -C*H*$_2$CH$_2$OH); δ 3.64-3.66 (m, 2H, -CH$_2$C*H*$_2$OH).

4-[2-(2-Hydroxyethoxy)ethoxy]-2,6-diisopropylphenylamine (T2)

T2 was synthesised by stirring **T1** (0.365 g, 1.74 mmol) in chloroform (10.0 mL). 2,6-Diisopropylaniline (0.327 mL, 1.74 mmol) was added, followed by a catalytic amount of *p*TSA (1 crystal). The solution was refluxed for 24 hours at ± 55 °C. The product was purified by column chromatography with 2:1 ethyl acetate/hexane as eluent. The product-containing fractions were combined and the solvent was removed. The residue was dissolved in DCM, the solution was concentrated and then layered with hexane at room temperature. Fine, white needle crystals formed and were isolated by vacuum filtration. The crystals were dried under vacuum. Yield: 0.404 g, 63%. FT-IR ($\nu_{C=N}$, cm^{-1}) 1630. m.p.: 89.8-94.5 °C. ^{1}H NMR (399.99 MHz, CDCl$_3$): δ 8.12 (s, 1H, C*H*=N); δ 7.85-7.87 (m, 2H, Ph); δ 7.15-7.17 (m, 2H, Ph); δ 7.08-7.12 (m, 1H, Ph); δ 7.04-7.07 (m, 2H, Ph); δ 4.23-4.25 (m, 2H, Ph-OC*H*$_2$CH$_2$-); δ 3.91-3.94 (m, 2H, Ph-OCH$_2$C*H*$_2$-); δ 3.78-3.82 (m, 2H, -C*H*$_2$CH$_2$OH); δ 3.70-3.72 (m, 2H, -CH$_2$C*H*$_2$OH); δ 2.94-3.04 (m, 2H, ^{i}Pr-C*H*); δ 1.18 (d, 12H, $^{3}J_{H\text{-}H}$ 6.6 Hz, ^{i}Pr-C*H*$_3$). ^{13}C{^{1}H} NMR (CDCl$_3$, 599.99 MHz): δ 161.33 (C$_{Ar}$); δ 161.02 (*C*H=N); δ 149.38 (C$_{Ar}$); δ 137.77 (C$_{Ar}$); δ 130.19 (C$_{Ar}$); δ 129.34 (C$_{Ar}$); δ 123.88 (C$_{Ar}$); δ 122.94 (C$_{Ar}$); δ 114.80 (C$_{Ar}$); δ 72.61 (-*C*H$_2$CH$_2$OH); δ 69.51 (Ph-OCH$_2$*C*H$_2$-); δ 67.58 (Ph-O*C*H$_2$CH$_2$-); δ 61.77 (-CH$_2$*C*H$_2$OH); δ 28.48 (^{i}Pr-*C*H); δ 24.81 (^{i}Pr-*C*H$_3$); δ 23.10 (^{i}Pr-*C*H$_3$). ESI-MS: [M+H]$^{+}$ 370.2. Anal. Found: C, 72.0; H, 8.95; N, 3.46. Calc. for C$_{23}$H$_{31}$NO$_3$•0.9H$_2$O: C, 71.6; H, 8.57; N, 3.63.

[PdCl{4-[2-(2-hydroxyethoxy)ethoxy]}CH=N{2,6-^{i}Pr-C$_6$H$_3$}]$_2$ (T3)

T3 was synthesised by stirring a solution of bis(acetonitrile)palladium dichloride (0.100 g, 0.386 mmol) in acetonitrile (5.00 mL). **T2** (0.142 g, 0.386 mmol) and sodium acetate (0.063 g, 0.77 mmol) were added to the solution. The resulting orange mixture was stirred for 18 hours in an oil bath at ± 25 °C. The solvent was removed to obtain a yellow oily residue which was dissolved in DCM (50.0 mL) and filtered through celite to remove any metallic palladium. The solvent volume was reduced and the solution was then layered with hexane at low temperature (-16 °C) to crystallise the product. The yellow crystalline solid was isolated by vacuum filtration and rinsed with hexane. The product was dried under vacuum. Yield: 0.156 g, 80%. FT-IR ($\nu_{C=N}$, cm^{-1}) 1597. m.p.: 150-154 °C. ESI-MS: [M-Cl+2MeCN]$^{+}$ 1065; [(M/2)-Cl]$^{2+}$ 474.1. Anal. Found: C, 53.6; H, 5.98; N, 2.36. Calc. for C$_{46}$H$_{60}$Cl$_2$N$_2$O$_6$Pd$_2$: C, 54.1; H, 5.92; N, 2.74.

Synthesis of μ-bis(phosphines) palladacycles with bidentate phosphines and 2-(2-hydroxyethoxy)ethoxy tether

[(PdCl{4-[2-(2-hydroxyethoxy)ethoxy]}CH=N{2,6-^{i}Pr$_2$-C$_6$H$_3$})$_2$(μ-Ph$_2$PCH$_2$PPh$_2$)] (BTC1)

BTC1 was synthesised by stirring a solution of **T3** (0.115 g, 0.113 mmol) in dichloromethane (5 mL) in a Schlenk tube. Dppm (0.043 g, 0.11 mmol) was added. The solution was stirred for 6 hours in an oil bath at ± 25 °C. The solvent volume was reduced by rotary evaporator to obtain a yellow oily residue. The product was recrystallised by layering the dichloromethane solution with hexane at low temperature. The solution was kept at low temperature (-16 °C) overnight. The off-white solid was isolated by vacuum filtration and rinsed with hexane. The recrystallisation was repeated and the crystals were dried under vacuum. Yield: 0.080 g, 50%. FT-IR ($\nu_{C=N}$, cm^{-1}) 1606. m.p.: 227-231 °C. ^{1}H NMR (299.74 MHz, $CDCl_3$): δ 8.14-8.20 (m, 8H, Ph); δ 7.89 (d, 2H, $^{4}J_{H-P}$ 7.9 Hz, C*H*=N); δ 7.15-7.31 (m, 20H, Ph); δ 6.47 (dd, 2H, $^{3}J_{H-H}$ 8.2 Hz and $^{4}J_{H-H}$ 2.2 Hz, Ph); δ 5.62-5.65 (m, 2H, Ph); δ 5.04-5.13 (m, 2H, -PC*H*$_2$P-); δ 3.66-3.67 (m, 4H, Ph-OC*H*$_2$-); δ 3.39-3.52 (m, 12H, Ph-OCH$_2$C*H*$_2$-, -C*H*$_2$CH$_2$OH and ^{i}Pr-C*H*); δ 3.16-3.19 (m, 4H, -CH$_2$C*H*$_2$OH); δ 1.48 (d, 12H, $^{3}J_{H-H}$ 6.8 Hz, ^{i}Pr-C*H*$_3$); δ 1.24 (d, 12H, $^{3}J_{H-H}$ 6.9 Hz, ^{i}Pr-C*H*$_3$). ^{13}C{^{1}H} NMR ($CDCl_3$, 75.38 MHz): δ 175.87 (*C*H=N); δ 161.96 (*C*$_{Ar}$-OCH$_2$CH$_2$-); δ 159.55 (-*C*CH=N-); δ 145.54 (o-metallated C); δ 141.21 (C$_{Ar}$); δ 140.33 (C$_{Ar}$); δ 135.44-135.61 (m, C$_{Ar}$); δ 130 (C$_{Ar}$); δ 129.93 (C$_{Ar}$); δ 128.02-128.17 (m, C$_{Ar}$); δ 126.98 (C$_{Ar}$); δ 122.86 (C$_{Ar}$); δ 122.38 (t, J_{C-P} 5.1 Hz, C$_{Ar}$); δ 112.11 (C$_{Ar}$); δ 72.33 (-*C*H$_2$CH$_2$OH); δ 69.05 (Ph-OCH$_2$*C*H$_2$-); δ 66.68 (Ph-O*C*H$_2$CH$_2$-); δ 61.68 (-*C*H$_2$CH$_2$OH); δ 28.55 (^{i}Pr-*C*H); δ 24.70 (^{i}Pr-*C*H$_3$); δ 23.11 (-P*C*H$_2$P-). ^{31}P{^{1}H} NMR ($CDCl_3$, 161.89 MHz): δ 34.39 (s). ESI-MS: [M-Cl]$^{+}$ 1369.34, [M-2Cl-Pd-T2]$^{+}$ 858.249, [M-2Cl-Pd-T2-{(Ph)$_2$PCH$_2$P(Ph)$_2$}+MeCN]$^{+}$ 474.127, [M-2Cl-Pd-T2-{(Ph)$_2$PCH$_2$P(Ph)$_2$}-C$_4$H$_9$O$_3$+MeCN]$^{+}$ 411.105. Anal. Found: C, 59.8; H, 5.87; N, 1.47. Calc. for $C_{71}H_{82}Cl_2N_2O_6P_2Pd_2$•$H_2O$: C, 59.9; H, 5.95; N, 1.97. Solubility: DMSO 2.85 mg/mL; 28% DMSO in water.

[(PdCl{4-[2-(2-hydroxyethoxy)ethoxy]}CH=N{2,6-^{i}Pr$_2$-C$_6$H$_3$})$_2$(μ-Ph$_2$P(CH$_2$)$_2$PPh$_2$)] (BTC2)

BTC2 was synthesised as above, using dppe as the bridging bis(phosphine) and the quantities as indicated: **T3** (0.115 g, 0.113 mmol), dichloromethane (5.00 mL) and dppe (0.045 g, 0.11 mmol). Yield: 0.108 g, 68%. FT-IR ($\nu_{C=N}$, cm^{-1}) 1605. m.p.: 158-162 °C. ^{1}H NMR (599.99 MHz, $CDCl_3$): δ 7.88-7.89 (m, 2H, C*H*=N); δ 7.84-7.87 (m, 8H, Ph); δ 7.28-7.31 (m, 4H, Ph); δ 7.23-7.26 (m, 12H, Ph); δ 7.17 (d, 4H, $^{3}J_{H-H}$ 7.6 Hz, Ph); δ 6.47 (dd, 2H, $^{3}J_{H-H}$ 8.2 Hz and $^{4}J_{H-H}$ 2.3 Hz, Ph); δ 5.85-5.86 (m, 2H, Ph); δ 3.60-3.61 (m, 4H, Ph-OC*H*$_2$-); δ 3.34-3.42 (m, 12H, Ph-OCH$_2$C*H*$_2$-, -C*H*$_2$CH$_2$OH and ^{i}Pr-C*H*); δ 3.11 (t, 12H, $^{3}J_{H-H}$ 4.7 Hz, -CH$_2$C*H*$_2$OH); δ 3.03 (br d, 4H, $^{3}J_{H-H}$ 2.3

Hz, -P(CH_2)$_2$P-); δ 1.32 (d, 12H, $^3J_{H-H}$ 7.0 Hz, ^{i}Pr-CH_3); δ 1.17 (d, 12H, $^3J_{H-H}$ 7.0 Hz, ^{i}Pr-CH_3). ^{13}C{^{1}H} NMR ($CDCl_3$, 75.38 MHz): δ 175.61 (*C*H=N); δ 162.43 (C_{Ar}-OCH$_2$CH$_2$-); δ 159.86 (-*C*CH=N-); δ 145.09 (o-metallated C); δ 141.28 (C_{Ar}); δ 140.43 (C_{Ar}); δ 134.27-134.43 (m, C_{Ar}); δ 130.71 (C_{Ar}); δ 130.04 (C_{Ar}); δ 128.39-128.53 (m, C_{Ar}); δ 126.78 (C_{Ar}); δ 122.78 (C_{Ar}); δ 122.37-122.51 (m, J_{C-P}, C_{Ar}); δ 112.23 (C_{Ar}); δ 72.33 (-*C*H$_2$CH$_2$OH); δ 69.05 (Ph-OCH$_2$*C*H$_2$-); δ 66.68 (Ph-O*C*H$_2$CH$_2$-); δ 61.68 (-*C*H$_2$CH$_2$OH); δ 28.55 (^{i}Pr-*C*H); δ 24.70 (^{i}Pr-*C*H$_3$); δ 23.11 (-P(*C*H$_2$)$_2$P-). ^{31}P{^{1}H} NMR ($CDCl_3$, 161.89 MHz): δ 40.63 (s). ESI-MS: [M-Cl]$^+$ 1381.38; [M-2Cl-Pd-T2]$^+$ 872.266, [M-2Cl-Pd-T2-{(Ph)$_2$P(CH$_2$)$_2$P(Ph)$_2$}+MeCN]$^+$ 474.127, [M-2Cl-Pd-T2-{(Ph)$_2$P(CH$_2$)$_2$P(Ph)$_2$}-C$_4$H$_9$O$_3$+MeCN]$^+$ 411.105. Anal. Found: C, 59.6; H, 6.04; N, 1.55. Calc. for C$_{72}$H$_{84}$Cl$_2$N$_2$O$_6$P$_2$Pd$_2$•2H$_2$O: C, 59.4; H, 6.10; N, 1.93. Solubility: DMSO 32.6 mg/mL; 76% DMSO in water.

[(PdCl{4-[2-(2-hydroxyethoxy)ethoxy]}CH=N{2,6-^{i}Pr$_2$-C$_6$H$_3$})$_2$(μ-Ph$_2$P(CH$_2$)$_3$PPh$_2$)] (BTC3)

BTC3 was synthesised as above, using dppp as the bridging bis(phosphine) and the quantities as indicated: **T3** (0.115 g, 0.113 mmol), dichloromethane (5.00 mL) and dppp (0.047 g, 0.11 mmol). Yield: 0.067 g, 42%. FT-IR ($\nu_{C=N}$, cm^{-1}) 1605. m.p.: 146-147 °C. ^{1}H NMR (599.99 MHz, $CDCl_3$): δ 7.91 (d, 2H, $^4J_{H-P}$ 7.6 Hz, C*H*=N); δ 7.77-7.80 (m, 8H, Ph); δ 7.39-7.41 (m, 4H, Ph); δ 7.31-7.33 (m, 8H, Ph); δ 7.25-7.28 (m, 4H, Ph); δ 7.19 (d, 4H, $^3J_{H-H}$ 7.6 Hz, Ph); δ 6.52 (dd, 2H, $^3J_{H-H}$ 8.2 Hz and $^4J_{H-H}$ 2.3 Hz, Ph); δ 5.98-6.00 (m, 2H, Ph); δ 3.66-3.68 (m, 4H, Ph-OC*H*$_2$CH$_2$-); δ 3.47-3.48 (m, 4H, Ph-OCH$_2$C*H*$_2$-); δ 3.43-3.45 (m, 4H, -C*H*$_2$CH$_2$OH); δ 3.31-3.38 (m, 4H, ^{i}Pr-C*H*); δ 3.20-3.22 (m, 4H, -CH$_2$C*H*$_2$OH); δ 2.59-2.64 (m, 4H, -PC*H*$_2$CH$_2$C*H*$_2$P-); δ 1.60 (m, 2H, -PCH$_2$C*H*$_2$CH$_2$P-); δ 1.30 (d, 12H, $^3J_{H-H}$ 6.5 Hz, ^{i}Pr-C*H*$_3$); δ 1.18 (d, 12H, $^3J_{H-H}$ 7.0 Hz, ^{i}Pr-C*H*$_3$). ^{13}C{^{1}H} NMR ($CDCl_3$, 100.57 MHz): δ 175.71 (*C*H=N); δ 162.23 (C_{Ar}-OCH$_2$CH$_2$-); δ 160.10 (t, J_{C-P} 3.0 Hz, -*C*CH=N-); δ 145.47 (*o*-metallated C); δ 141.45 (C_{Ar}); δ 140.93 (C_{Ar}); δ 134.48-134.60 (m, C_{Ar}); δ 130.99 (C_{Ar}); δ 130.76 (C_{Ar}); δ 130.41 (C_{Ar}); δ 130.30 (C_{Ar}); δ 128.76-128.86 (m, C_{Ar}); δ 127.08 (C_{Ar}); δ 123.03 (C_{Ar}); δ 122.78-122.89 (m, C_{Ar}); δ 112.39 (C_{Ar}); δ 72.61 (-*C*H$_2$CH$_2$OH); δ 69.32 (Ph-OCH$_2$*C*H$_2$-); δ 67.14 (Ph-O*C*H$_2$CH$_2$-); δ 61.97 (-*C*H$_2$CH$_2$OH); δ 28.74 (^{i}Pr-*C*H); δ 24.68 (^{i}Pr-*C*H$_3$); δ 23.48 (-PCH$_2$*C*H$_2$CH$_2$P-); δ 21.62 (-P*C*H$_2$CH$_2$*C*H$_2$P-). ^{31}P{^{1}H} NMR ($CDCl_3$, 161.89 MHz): δ 35.46 (s). ESI-MS: [M-Cl]$^+$ 1397.37; [M-2Cl-Pd-T2]$^+$ 886.280, [M-2Cl-Pd-T2-{(Ph)$_2$P(CH$_2$)$_3$P(Ph)$_2$}+MeCN]$^+$ 474.127. Anal. Found: C, 59.6; H, 5.94; N, 1.47. Calc. for C$_{73}$H$_{86}$Cl$_2$N$_2$O$_6$P$_2$Pd$_2$•2H$_2$O: C, 59.7; H, 6.17; N, 1.91. Solubility: DMSO 76.0 mg/mL; 54% DMSO in water.

[(PdCl{4-[2-(2-hydroxyethoxy)ethoxy]}CH=N{2,6-^{i}Pr$_2$-C$_6$H$_3$})$_2$(μ-Ph$_2$P(C$_5$H$_4$)Fe(C$_5$H$_4$)PPh$_2$) (BTC4)

BTC4 was synthesised as above, using dppf as the bridging bis(phosphine) and the amounts as indicated here: **T3** (0.115 g, 0.113 mmol), dichloromethane (5.00 mL) and dppf (0.063 g, 0.11 mmol). Yield: 0.115 g, 65%. FT-IR ($\nu_{C=N}$, cm^{-1}) 1605. m.p.: 87.5-89.4 °C. ^{1}H NMR (599.99 MHz, $CDCl_3$): δ 7.95 (d, 2H, $^{4}J_{H-P}$ 8.8 Hz, C*H*=N); δ 7.59-7.63 (m, 8H, Ph); δ 7.36-7.39 (m, 4H, Ph); δ 7.33-7.34 (m, 2H, Ph); δ 7.24-7.27 (m, 8H, Ph); δ 7.22 (d, 2H, $^{3}J_{H-H}$ 7.6 Hz, Ph); δ 7.16 (d, 4H, $^{3}J_{H-H}$ 7.3 Hz, Ph); δ 6.60 (dd, 2H, $^{3}J_{H-H}$ 8.2 Hz and $^{4}J_{H-H}$ 2.3 Hz, Ph); δ 6.03 (dd, 2H, J_{H-H} 5.9 Hz and 2.34 Hz, Ph); δ 5.09 (br s, 4H, Cp ring); δ 4.42-4.43 (m, 4H, Cp ring); δ 3.68-3.70 (m, 4H, Ph-OC*H*$_2$-); δ 3.52-3.54 (m, 8H, Ph-OCH$_2$C*H*$_2$- and -C*H*$_2$CH$_2$OH); δ 3.36-3.43 (m, 4H, $^{3}J_{H-H}$, ^{i}Pr-C*H*); δ 3.23 (br t, 4H, $^{3}J_{H-H}$ 4.7 Hz, -CH$_2$C*H*$_2$OH); δ 1.34 (d, 12H, $^{3}J_{H-H}$ 7.0 Hz, ^{i}Pr-C*H*$_3$); δ 1.16 (d, 12H, $^{3}J_{H-H}$ 7.0 Hz, ^{i}Pr-C*H*$_3$). ^{13}C{^{1}H} NMR ($CDCl_3$, 75.38 MHz): δ 176.12 (*C*H=N); δ 161.58 (d, J_{C-P} 2.2 Hz, *C*$_{Ar}$-OCH$_2$CH$_2$-); δ 159.62 (d, J_{C-P} 5.5 Hz, -*C*CH=N-); δ 145.14 (*o*-metallated C); δ 141.30 (C$_{Ar}$); δ 140.83 (C$_{Ar}$); δ 134.34-134.50 (m, C$_{Ar}$); δ 132.46 (C$_{Ar}$); δ 131.79 (C$_{Ar}$); δ 130.56 (C$_{Ar}$); δ 130.32 (C$_{Ar}$); δ 127.89 (d, J_{C-P} 10.5 Hz, C$_{Ar}$); δ 126.76 (C$_{Ar}$); δ 123.47 (d, J_{C-P} 9.4 Hz, C$_{Ar}$); δ 122.67 (C$_{Ar}$); δ 112.17 (C$_{Ar}$); δ 76.91 (m, Cp ring); δ 75.72 (d, J_{C-P} 8.06 Hz, Cp ring); δ 72.36 (-*C*H$_2$CH$_2$OH); δ 69.13 (Ph-OCH$_2$*C*H$_2$-); δ 66.68 (Ph-O*C*H$_2$CH$_2$-); δ 61.68 (-*C*H$_2$CH$_2$OH); δ 28.48 (^{i}Pr-*C*H); δ 24.81 (^{i}Pr-*C*H$_3$); δ 23.10 (^{i}Pr-*C*H$_3$). ^{31}P{^{1}H} NMR ($CDCl_3$, 161.89 MHz): δ 31.38 (s). ESI-MS: [M-2Cl-Pd-T2]$^{+}$ 1028.23, [M-2Cl]$^{2+}$ 752.179; [M-2Cl-Pd-**T2**-{(Ph)$_2$PC$_5$H$_4$FeC$_5$H$_4$P(Ph)$_2$}+MeCN]$^{+}$ 474.127. Solubility: DMSO 53.7 mg/mL; 98% DMSO in water.

4.6. References

1. J. Albert, R. Bosque, M. Cadena, L. D'Andrea, J. Granell, A. González, J. Quirante, C. Calvis, R. Messeguer, J. Badiá, L. Baldomà, T. Calvet and M. Font-Bardia, *Organometallics*, 2014, **33**, 2862-2873.
2. E. G. Rodrigues, L. S. Silva, D. M. Fausto, M. S. Hayashi, S. Dreher, E. L. Santos, J. B. Pesquero, L. R. Travassos and A. C. F. Caires, *Int. J. Cancer*, 2003, **107**, 498-504.
3. C. Bincoletto, I. L. S. Tresariol, C. R. Oliveira, S. Dreher, D. M. Fausto, M. A. Soufen, F. D. Nascimento and A. C. F. Caires, *Bioorg. Med. Chem.*, 2005, **13**, 3047-3055.
4. A. C. F. Caires, E. T. Almeida, A. E. Mauro, J. P. Hemerly and S. R. Valentini, *Quim. Nova*, 1999, **22**, 329-334.

5. Y. Zhao, Y. Li, Y. Li, C. Huang, H. Liu, S.-W. Lai, C.-M. Che and D. Zhu, *Org. Biomol. Chem.*, 2010, **8**, 3923-3927.
6. N. Mungwe, A. J. Swarts, S. F. Mapolie and G. Westman, *J. Organomet. Chem.*, 2011, **696**, 3527-3535.
7. J. Bernstein, R. E. Davies, L. Shimoni and N.-L. Chang, *Angew. Chem.*, *Int. Ed. Engl.*, 1995, **34**, 1555-1573.
8. S. N. Dmitrieva, M. V. Churakova, A. I. Vedernikov, L. G. Kuz'mina and S. P. Gromov, *Tetrahedron*, 2011, **67**, 2530-2535.
9. H. Onoue and I. Moritani, *J. Organomet. Chem*., 1972, **43**, 431-436.
10. H. Masui, *Coord. Chem. Rev*., 2001, **219**-**221**, 957-992.
11. J. Albert, M. Gomez, J. Granell, X. Solans and J. Sales, *Organometallics*, 1990, **9**, 1405-1413.
12. A. J. Swarts, *Mononuclear and Multinuclear Palladacycles as Catalyst Precursors*, M.Sc. Thesis Stellenbosch University, 2011.
13. D. L. Pavia, *Introduction to spectroscopy*, Australia; Belmont, CA: Brooks/Cole Cengage Learning, 2009.
14. National Center for Biotechnology Information. PubChem Compound Database; CID=403. Accessed at https://pubchem.ncbi.nlm.nih.gov/compound/403 on January 27, 2016.
15. National Center for Biotechnology Information. PubChem Compound Database; CID=8479. Accessed at https://pubchem.ncbi.nlm.nih.gov/compound/8479 on January 27, 2016.

Chapter 5
Biological evaluation and DNA binding studies of synthesised palladacycles

5.1 Introduction

5.1.1 *In vitro* studies

In vitro studies are not a new phenomenon in cancer research. These cell culture-based experiments allow fast and efficient testing of potential drug candidates. Various aspects of drug candidates may be tested against many different human- and animal species cell lines. These include beneficial properties, such as the ability to prevent cell proliferation, and negative effects, such as toxicity. Importantly, *in vitro* assays are less expensive and do not have the ethical issues associated with *in vivo* testing [1].

One of the major drawbacks of *in vitro* studies is that the cell culture-based systems employed to conduct these tests are “over simplified” compared to actual biological systems. Hence, there is not always a direct correlation between *in vitro* and *in vivo* results. In cell cultures, each cell type is cultured and tested in isolation, whilst in the body, human and animal, there are interactions between the various systems or cell types which could affect the toxicity and or efficacy of the drug [2]. Despite this drawback, these studies are a valuable tool for initial screening of potential drug compounds.

A great example of the value of *in vitro* testing is that of the Developmental Therapeutics Program (DTP) at the National Cancer Institute (NCI). This is a potential drug screening program which uses *in vitro* assays for the initial stages of testing, with the aim of keeping costs low and allowing a larger number of compounds to be screened per annum. The pre-screen is against three human cancer cell lines, MCF-7 breast cancer, NCI-H460 large-cell lung cancer and SF-268 glioblastoma cell lines. The next step involves the NCI60 human tumour cell line anti-cancer drug screen, where the drug compound is screened against 60 different human cancer cell lines [3]. Currently, approximately 2500 drugs per annum undergo this first stage of screening. Of these, only 2% will continue on to the second stage of testing which is *in vivo* testing, of which an even smaller fraction goes into clinical trials. Thus, the *in vitro* tests aid in the elimination of more than 98% of

potential drug candidates, allowing only the most promising drugs to move forward into clinical trials, which are both costly and time consuming [4].

Two of the most common *in vitro* assays were employed in this project; the first was a 3-(4,5-dimethylthiazol-2-yl)-2,5-diphenyltetrazolium bromide (MTT) assay which is used to determine cell viability and half maximal inhibitory concentration (IC_{50}) values. The second assay was a Western Blot to determine if there is any DNA damage or induction of apoptosis as a response to the potential drug compound.

5.1.1.1 MTT assay

The MTT assay is quite simple. Cells are cultured and then treated with the drug for a specific period of time. MTT, a yellow tetrazole, is then added to the cell culture. Viable cells will reduce the MTT to an insoluble purple formazan (Reaction Scheme 5.1). The formazan is then solubilised and quantified by absorbance spectroscopy. The more viable cells there are, the more formazan is produced and consequently, a higher absorbance value is obtained [5;6].

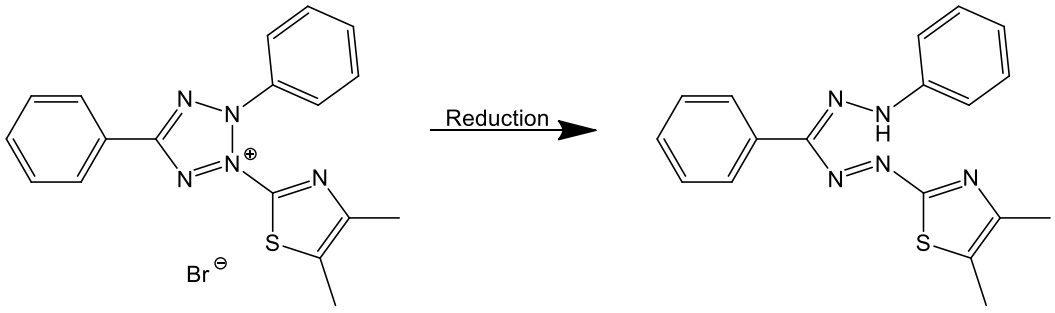

Scheme 5.1: Reduction of MTT to formazan.

From these data, the half maximal inhibitory concentration (IC_{50}) value was determined, as the concentration at which the compound inhibits growth of half of the treated cells, relative to the untreated cells [7].

5.1.1.2 Western Blot assay

Western blotting is one of the most important techniques used in cell biology. It is used to detect specific proteins, isolated from a mixture (extracted from cells). The technique consists of three main steps, i) size separation by gel electrophoresis, ii) transfer of the separated proteins to a

solid membrane and iii) labelling of the desired protein using primary and secondary antibodies to visualise the protein by various methods of detection, including colorimetric and radioactive detection, chemiluminescence and fluorescence [8]. The usefulness of this assay for evaluation of potential drugs is that it can be used to determine biochemical changes in the cells once exposed to (or treated with) the drug compound [9], as the presence of specific proteins provides information about the mode of anti-cancer activity [10;11]. The most important proteins which are employed as markers for potential anti-cancer drugs, are γ-H2AX, which, if present, is an indication of DNA damage and PARP, which if cleaved, is an indication that apoptosis has been induced. The presence of both of these proteins confirms that the drug targets DNA and induces cell death via apoptosis, the preferred mechanism of drug-induced cell death.

Palladacycles have previously been shown to exert cytotoxicity by inducing DNA double strand cleavage [12;13]. This was determined by the presence of γ-H2AX in the cells. Additionally, induction of apoptosis by the drug can be detected by the presence of the cleaved PARP proteins, where the PARP proteins are usually cleaved from 116 KD to 86KD. Similar experiments were carried out by Ulukaya *et al*. [13]. They tested for apoptosis by looking for the presence of the cleaved caspase-3 protein using a Western blot assay, whilst DNA double strand breaks were tested for by a nuclear stain which detects γ-H2AX nuclear foci. The palladacycle, [PdCl(terpy)](sac)·2H_2O, where terpy = 2,2':6'2"-terpyridine and sac = saccarinate, tested by these authors showed both double strand breaks and induction of apoptosis at higher concentrations [13].

5.1.2 DNA binding studies

DNA is a common target for many anti-cancer drugs. It controls cell growth, differentiation, replication and cell death. By binding to DNA, drug molecules can interfere with or inhibit transcription and replication processes which will lead to retarded or inhibited cell growth and division [14]. Current research seeks to understand and exploit the interactions between drug molecules and the DNA double helix, in order to use the information for rational drug design. Before understanding these interactions, they need to be identified and classified. This is where DNA binding studies come into play [15;16], as drug-DNA interactions influence the shape and conformation of both the drug and DNA molecules [14].

There are two types of drug-DNA binding: covalent- and non-covalent binding interactions [17]. Each of these will be discussed in more detail in the following sections.

5.1.2.1 Covalent binding

Covalent bonding of a compound to DNA is a strong, irreversible interaction, leading to irreparable changes in the DNA structure, thus hindering DNA replication. Cisplatin is known to bind to DNA in this manner, thus forming intrastrand DNA adducts and interstrand crosslinks. The major binding type, occurring when cisplatin interacts with DNA, is an intrastrand 1,2-d(GpG) binding where the soft Pt^{2+} ion binds to the harder N_7 atoms on sequential guanine nucleoside bases (Figure 5.1) [18]. The binding of cisplatin to DNA prevents replication, thus inducing apoptosis which consequently prevents cell division and therefore promoting the anti-tumour activity of the metallodrug.

Similarly, Katsarou *et al*. reported the formation of an intrastrand GNG($G_2C_3G_4$)(N_7-N_7) chelation of the palladium complexes, *trans*-Cl_2Pd(glyglyOH)$_2$ and *trans*-Cl_2Pd(glynvalOH)$_2$ where glyglyOH and gly-*L*-nvalOH (glynvalOH) were the dipeptides employed as ligands, with the dodecamer d[CGCGAATTCGCG]$_2$ duplex. Earlier studies of palladium compounds, $[Pd(dien)(H_2O)]^{2+}$, $[Pd(en)(H_2O)_2]^{2+}$ and K_2PdCl_4, with this dodecamer showed preferential attack at the terminal region for the monofunctional species, with selectively binding to the G_2 and G_{10} bases, whilst the bifunctional species bound selectively to the N_7 atom of the G_4 base, as observed by Katsarou *et al*. Furthermore, the hexaaqua palladium (II) species, $[Pd(H_2O)_6]^{2+}$, showed selectivity for the G_2 and G_4 bases [19;20]. These results suggested that there is, to some degree, a structure-activity relationship for the formation of palladium-DNA adducts. More importantly, these results show that palladium complexes can bind to DNA covalently and thus, palladium complexes can potentially prevent DNA replication and induce apoptosis, in a similar manner to cisplatin [21].

5.1.2.2 Non-covalent binding

In contrast to covalent bonding, non-covalent interactions with DNA are weaker and thus, reversible. These interactions are usually preferred over covalent bonding, as covalent binding drugs, such as cisplatin, cause severe toxicity, whilst reversibly binding drugs could potentially be less toxic. There are three sub-classes of non-covalent interactions: intercalation, non-covalent groove binding (major and minor) and electrostatic binding, as shown in Figure 5.2 [23-26].

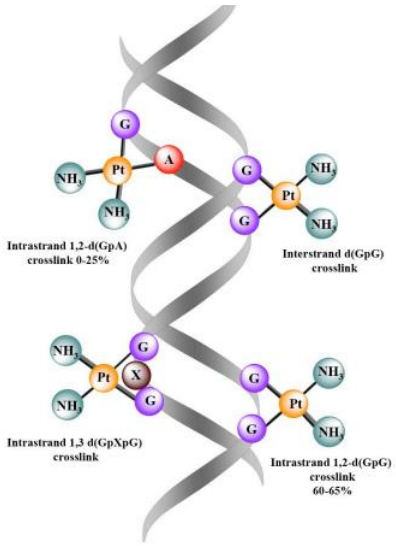

Figure 5.1: DNA adducts formed with cisplatin [22].

5.1.2.2.1 Intercalation

Intercalation is the most common type of DNA binding and hence, the most studied [15]. It occurs when a planar portion, usually an aromatic fragment, of a drug molecule binds between base pairs of the DNA double helix. Molecules that intercalate into the DNA double helix cause changes in the DNA. Such changes include elongation and unwinding of the helix [15;27]. There may also be increased stabilisation of the drug (and the DNA) in this adduct, provided by π-π stacking interactions and dipole-dipole interactions between the drug and the DNA [14-16;28]. Well known intercalators include ethidium bromide (Figure 5.3), anthracyclines and other heterocyclic dyes [16].

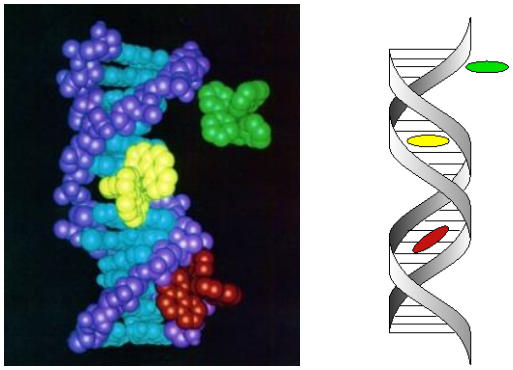

Figure 5.2: Computer generated (left) and diagrammatic (right) representations of the three types of DNA binding, where yellow represents intercalation, red represents groove binding and green represents electrostatic interactions [29].

5.1.2.2.2 Non-covalent groove binding

Groove binding is associated with hydrogen-bonding and van der Waals interactions of drug molecules with functional groups along the grooves in the DNA double helical structure [16]. The binding can be either in the major- or the minor groove in the DNA helix.

Minor groove binding

Most minor groove binders replace the “spine of hydration” (water molecules bound to DNA backbone), allowing them to fit well into the small space. Groove binders may just replace the water molecules bound to the DNA backbone, or there may be significant interactions between the DNA and the drug molecules which influence the shape and conformation of the DNA. These structures are stabilised by electrostatic, hydrophobic and hydrogen-bonding interactions. Hoechst 33258, a dye molecule, is a well-known minor groove binder (Figure 5.3) [14;28].

Major groove binder

Methyl green, another organic dye, was the first reported major groove binder (Figure 5.3). A number of other natural products have also been identified as major groove binders. These species interact through intercalation between the base pairs in the major groove, whilst non-covalent interactions are used to position the drug within the groove [25;28].

5.1.2.2.3 Electrostatic binding

This type of binding is defined as the binding of a cationic drug molecule to the negatively charged phosphate groups in the DNA backbone. These interactions are non-selective and can occur anywhere along the sugar-phosphate backbone of DNA [16]. This mode of binding is more prevalent for cationic coordination compounds. One such example is *L*-$[Ru(dpphen)_3]^{2+}$ (where dpphen = 4,7-diphenyl-1,10-phenanthroline) (Figure 5.4), which was shown to bind to DNA exclusively through electrostatic interactions [26].

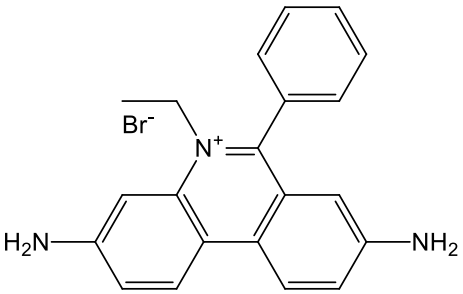

Ethidium bromide
DNA intercalator

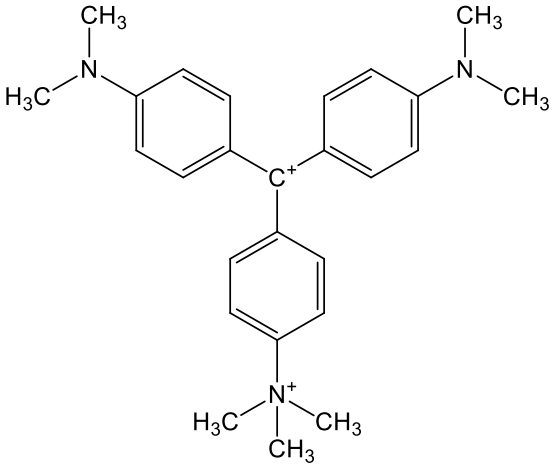

Methyl green
DNA major groove binder

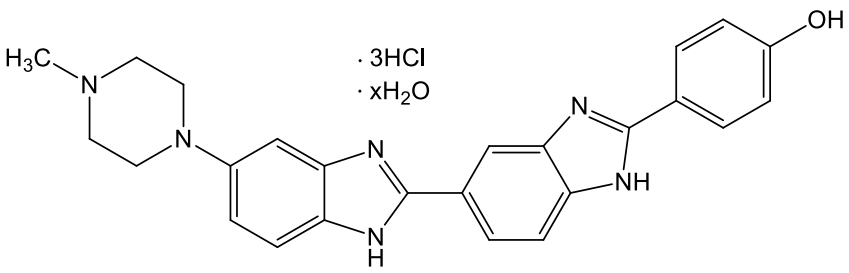

Hoechst 33258
DNA minor groove binder

Figure 5.3: Chemical structures of DNA intercalators and groove binders [14;16;28].

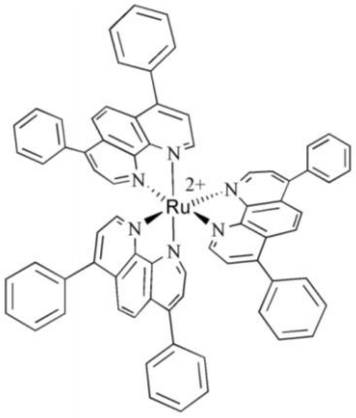

Figure 5.4: Structure of electrostatic DNA binder, *L*-[Ru(dpphen)$_3$]$^{2+}$ [26].

5.1.3 Analytical techniques for determining DNA binding interactions

Various analytical techniques can be used to monitor the changes which occur in DNA and the drug molecules, as a result of the DNA binding interactions described above. These techniques include classical spectroscopic methods, electrophoresis, isothermal titration calorimetry and many others. The more classical and most commonly used techniques, electrophoresis, UV-, CD- and NMR spectroscopy, were employed in this project [24;30].

Electrophoresis

Agarose gel electrophoresis is a simple and robust, yet very effective technique for determining whether DNA is the biological target for a potential drug compound. The ability of a compound to bind to DNA is determined by its ability to change the electrophoretic mobility of plasmid DNA [31].

Plasmid DNA has three different forms, namely: closed circular superhelical (ccc), open circular (oc) and linear. Each of these forms have a different electrophoretic mobility, based on its overall size and shape. The superhelical form is tightly coiled onto itself, making the overall physical size significantly smaller than the open circular form. Therefore, it migrates through the agarose gel significantly faster than the linear and open circular form. The linear form migrates faster than the open circular form, as its narrow shape allows it to pass through the channels in the gel easily. The open circular form has the slowest mobility due to its large floppy nature [32;33].

Recently, there have been a number of publications demonstrating the use of electrophoresis for determining DNA binding. Albert *et al*. incubated their diimine palladacycle compounds with pBluescript SK+ plasmid DNA at various concentrations (2.5-200 μM). Cisplatin and ethidium bromide were also included, as controls. The results from the agarose gel electrophoresis analysis are shown in Figure 5.5 [31].

Cisplatin showed significant changes in the electrophoretic mobility of both the open circular and superhelical forms of DNA. This was ascribed to the strong covalent bonding of cisplatin to DNA, specifically, the formation of cross-links. The non-covalent intercalation of ethidium bromide into the DNA helix was weaker and thus the changes in the electrophoretic mobility of DNA were far less significant.

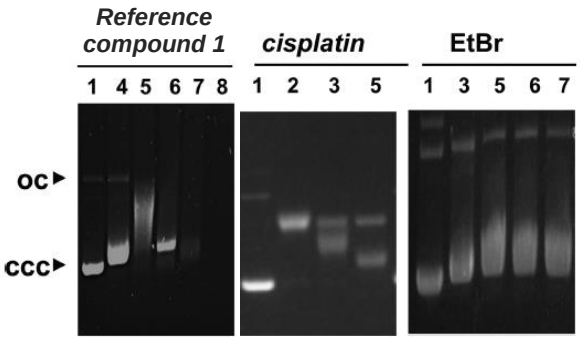

Figure 5.5: Images of agarose gel showing the interaction of compounds with plasmid DNA, where 1 = DNA, 2 = 2.5 µM compound, 3 = 5 µM compound, 4 = 10 µM compound, 5 = 25 µM compound, 6 = 50 µM compound, 7 = 100 µM compound and 8 = 200 µM compound [31].

For cisplatin, the open circular (oc) band runs through the gel slightly faster for all concentrations, whist the superhelical (ccc) band changes significantly with increasing concentration. At low concentration, 2.5 µM, the ccc band was retarded to the point at which it coalesces with the open circular DNA. Therefore, only one broad band was observed in lane 2. This coalescence corresponded to complete removal of the supercoils so that the ccc form has changed to the oc form. This uncoiled DNA is called negatively supercoiled DNA and is considered to be an underwound form of DNA, as it has fewer coils than DNA in its natural state. Lanes 3 and 5 (5-25 µM) show the separation of the bands again. The increase in the electrophoretic mobility of the ccc band is indicative of the conversion of the DNA from the negatively supercoiled form to the positively supercoiled or overwound form of DNA. Unlike the negatively supercoiled DNA, which has a right-handed supercoil, the positively supercoiled DNA has a left-handed supercoil [31;34]. Thus, the binding of cisplatin to DNA results in the uncoiling of DNA at lower concentrations, and at higher concentrations increased supercoiling with an opposite handedness is observed.

As stated, ethidium bromide showed only slight retardation of both the open circular and superhelical bands [31]. This corresponded to the slight unwinding of the DNA helix upon intercalation. Furthermore, the extent of streaking observed is typically an indication of DNA damage (such as the unwinding due to intercalation); however, at a more fundamental level, streaking is a result of incomplete separation of DNA plasmids with slightly different forms, or in this case, slightly different degrees of DNA binding and therefore, unwinding. In order to separate these forms, a higher resolution separation was required. Polyacrylamide gels are often selected over agarose gels for separations requiring higher resolutions [35]. For the purpose of determining whether or not a drug compound binds to DNA, agarose gels are sufficient, as separation of the three forms of plasmid DNA is easily achieved.

These authors studied the DNA binding of the palladacycle, Reference compound **1**, and found that it showed the same trend as cisplatin, with coalescence (lane 5) followed by positive supercoiling (lane 6) (Figure 5.6). At higher concentrations (lane 7 and 8), little to no DNA was observed. This disappearance of the DNA bands was explained as the complete breakdown of the DNA as a result of interaction with the compound [31], resulting in insufficient amounts of DNA being present to interact with the staining dye and for any appreciable detection of DNA [31].

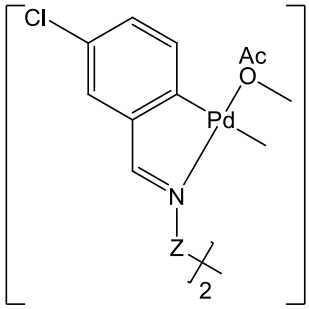

Figure 5.6: Structure of Reference compound 1, where Z = $CH_2CH_2OCH_2$ [31].

UV-Vis spectroscopy

UV-Vis spectroscopy can also be used to determine the interaction between drug molecules and DNA, by monitoring the changes in the absorbance of DNA or the drug. DNA has a characteristic absorbance maximum at approximately 260 nm. This absorbance is due to the purine and pyrimidine groups in the nucleoside bases which are chromophores. Comparison of the free drug and the drug-DNA complex should show the changes due to the interaction of the drug with the DNA, if there are any (Figure 5.7) [36]. The changes in the spectra could include bathochromic shifts in the absorption maxima of DNA and hypo- or hyperchromic effects. Weaker interacting drugs may show only hypo- or hyperchromic effects and no significant shifts in the absorbance maxima [24;36]. By recording a series of spectra, with increasing amounts of DNA, the drug-DNA association constants can be determined based on the quantitative changes. This is the most common method for determining drug-DNA interaction, as it is sensitive, simple and shows good reproducibility [24;30;36;37].

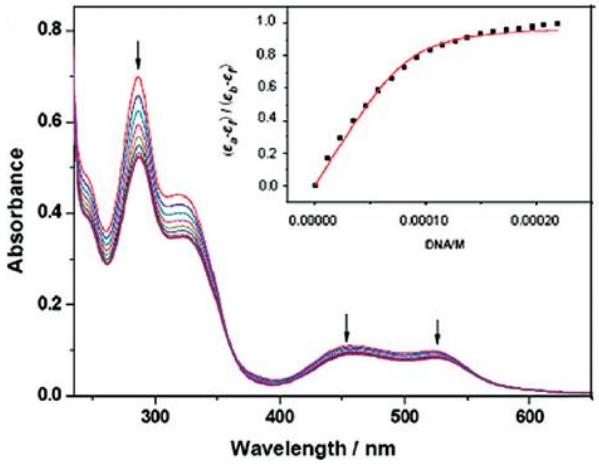

Figure 5.7: UV absorption spectra showing the changes in absorbance of the free drug upon addition of DNA (from top to bottom), due to drug-DNA interactions. Inset: plot of $(\varepsilon_a-\varepsilon_f)/(\varepsilon_b-\varepsilon_f)$ vs. DNA/M and the nonlinear least squares fit for the titration of DNA to the drug compound [36].

Circular dichroism spectroscopy

Circular dichroism (CD) is defined as the difference in absorbance of left and right circularly polarised light. It is a very powerful technique for studying drug-DNA interactions. Its most attractive quality is the small amount of sample required. The CD spectrum of DNA shows two bands, a positive band at 260-280 nm due to base stacking and a negative band at approximately 245 nm due to right-handed helicity of the double helical structure [25;31]. Achiral complexes (like most drug molecules) do not display a CD spectrum; however, when there is drug-DNA interaction, an induced CD (ICD) spectrum may be observed. Drug-DNA interaction causes changes in the conformation of the DNA helix and the drug molecule, which reflect as changes in the CD spectra or an induction of a spectrum, as the absorbance of light will differ. Changes in the CD spectra are most often observed as changes in intensities of the positive and negative bands and shifts in the wavelengths of the bands with varying drug- or DNA concentration. The observed spectra are due to the CD and ICD contributions of the DNA, the drug and the drug-DNA complex, making interpretation of these changes quite complex. However, if an ICD is observed in the absorption band of an achiral ligand, it is evidence of drug-DNA interaction [25].

Based on the information above, *in vitro* evaluation of the complexes prepared and discussed in Chapters 2 and 4 was carried out to determine their potential as anti-cancer agents. Complexes showing biological activity were further subjected to DNA binding studies in order to determine the mode of activity. By studying the interactions between the palladacycles and DNA, it was hoped to gain insight and understanding into the role of various moieties and functional groups on the metallodrug in its DNA binding ability.

5.2 Results and Discussion

5.2.1 *In vitro* results

In vitro tests were performed to determine if the complexes prepared as part of this study were active as anti-cancer agents against human breast adenocarcinoma MCF7 (estrogen receptor positive) and MDA-MB231 (estrogen receptor negative) cell lines. These included cell viability tests using a MTT assay, and in some cases Western blots to test for DNA damage using γ-H_2AX and PARP cleavage to determine whether or not apoptosis takes place. The complexes which were evaluated are shown in Figures 5.8 and 5.9.

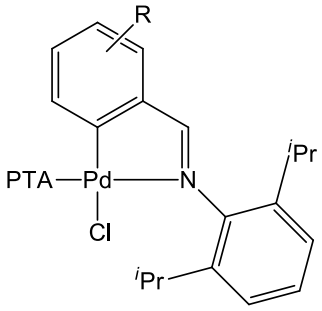

C1: R = 2-H
C2: R = 2-Cl
C3: R = 2-Br
C4: R = 2-Me
C5: R = 4-Me
C6: R = 2-F
C7: R = 2-NO_2
C8: R = 2-OMe

Figure 5.8: Mononuclear palladacycles evaluated as potential anti-cancer agents.

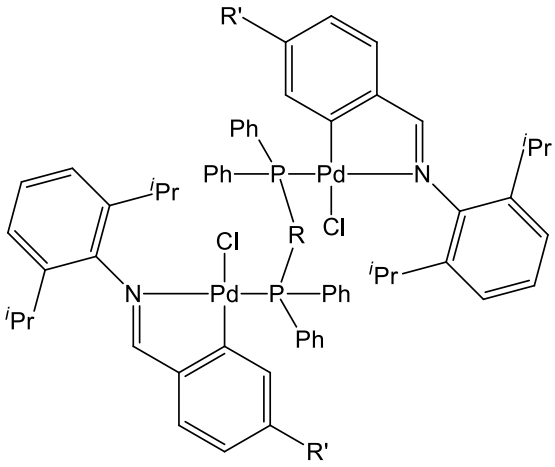

BC1: R = dppm and R' = H
BC2 / AJ5: R = dppe and R' = H
BC3: R = dppp and R' = H
BC4: R = dppf and R' = H
BTC1: R = dppm and R' = $(OCH_2CH_2)_2OH$
BTC2: R = dppe and R' = $(OCH_2CH_2)_2OH$
BTC3: R = dppp and R' = $(OCH_2CH_2)_2OH$
BTC4: R = dppf and R' = $(OCH_2CH_2)_2OH$

Figure 5.9: Binuclear palladacycles evaluated as potential anti-cancer agents. Note that BC2 is the same complex as AJ5, the binuclear palladacycle with μ-dppe, however, this complex will only be referred to as AJ5 throughout this chapter.

5.2.1.1 Cell viability assays

The MTT assay data were plotted to show the percentage cell survival at various compound concentrations. For active compounds, a visible decrease in cell survival was observed with increasing compound concentration (Figure 5.10), whilst weakly active or inactive compounds showed little to no change in the cell survival (Figure 5.11).

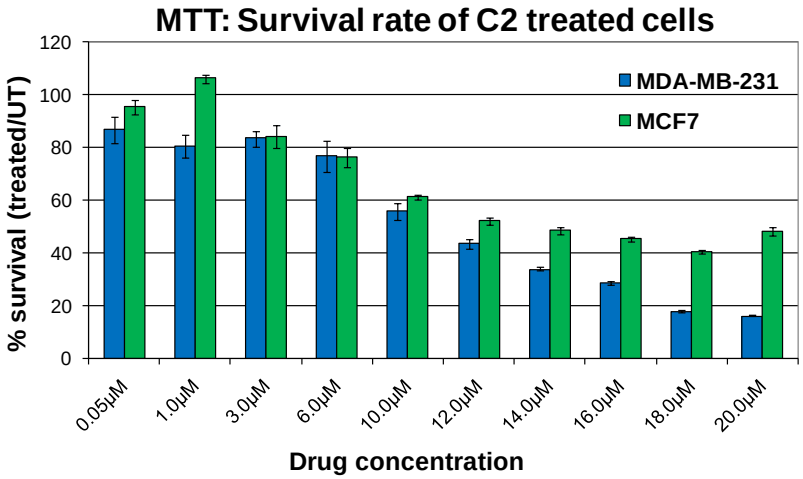

MCF7 IC_{50} = 19 μM

MDA-MB-231 IC_{50} = 17 μM

Figure 5.10: MTT assay data for active palladacycle, C2.

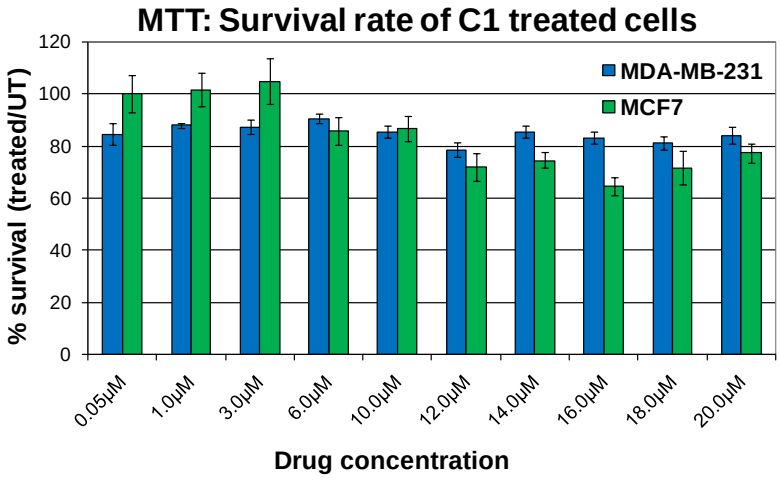

MCF7 IC_{50} = 46 μM

MDA-MB-231 IC_{50} = >54 μM

Figure 5.11: MTT assay data for weakly active palladacycle, C1.

As stated in the introduction, MTT assays are also used to determine the IC_{50} values of potential drug compounds. These values are summarised in Table 5.1. For this study, the obtained values were compared to the IC_{50} values of **AJ5**, the binuclear μ-bisphosphine palladacycle, in the

respective cell lines, as the aim of this project was to improve the solubility of the compounds, whilst maintaining the same level of activity.

The most noticeable trend in Table 5.1, is that the binuclear palladacycles were more active (i.e. have lower IC_{50} values) than the mononuclear palladacycles. Although similar studies by da Rocha *et al*. and Higgins *et al*, showed that mononuclear palladacycles showed significantly lower IC_{50} values than the binuclear forms, this improvement in activity was accompanied by, and potentially as a result of, enhanced solubility [38;39]. Based on these and other reports, the solubility of the complexes in DMSO and the ability of the complexes to tolerate water (solubility in a mixture of water/DMSO) were compared. No direct correlation between the solubility and the activity was observed. Since mononuclear and binuclear palladacycles were being compared, the concentration of palladium present may also have had an effect on the activity, thus leading to enhanced activity with increasing metal concentration, especially in the case of the binuclear palladacycles. However, when the concentration plots were compared, it was observed that even at half of the IC_{50} value concentration, the binuclear palladacycles were more active than the mononuclear palladacycles. These findings agree with results reported in the literature and discussed in Chapter 4, where examples of binuclear and polymetallic species were shown to be more effective as anti-cancer agents. This enhanced activity is possibly due to improved electrostatic interactions when two or more metal centres are present and the formation of flexible DNA adducts, as explained in Chapter 4.

Closer inspection of the mononuclear series showed that although these complexes were not as active as the binuclear complexes, **C2**, **C3** and **C5** exhibited IC_{50} values of less than 20 μM, which is still significant, as the IC_{50} values of cisplatin are approximately 19.6 μM for the MCF7 cell line and 43.5 μM for the MDA-MB231 cell line [40;41]. Thus, although these compounds are not as effective as **AJ5** and the other binuclear complexes reported here, they are as and in some cases more effective than cisplatin. Importantly, these mononuclear palladacycles are also more active against the MDA-MB231 cell line (lower IC_{50} values obtained), which, from the IC_{50} values for cisplatin, is the more resistant cell line. This suggests that these compounds could be potential alternatives in cisplatin-resistant cell lines.

Table 5.1: IC_{50} values and solubilities of palladacycles.

Complex	IC_{50} (μM) MCF7*	IC_{50} (μM) MDA-MB-231*	Solubility in DMSO (mg/mL)	%DMSO in water/DMSO mixture
AJ5	0.18 ± 0.048	0.19 ± 0.015	4.38	57
C1	>20	>20	8.32	66
C2	19 ± 1.0	17 ± 1.6	1.91	72
C3	11 ± 1.9	7.5 ± 1.0	2.34	72
C4	inactive	>20	6.72	69
C5	16 ± 5.3	7.6 ± 3.5	12.3	49
C6	>20	inactive	10.6	68
C7	inactive	inactive	0.459	57
C8	>20	inactive	6.32	58
BC1	2.7 ± 0.21	2.2 ± 0.19	6.32	62
BC3	5.8 ± 0.28	5.0 ± 0.075	2.02	78
BC4	inactive	inactive	57.2	91
BTC1	2.1 ± 0.21	2.5 ± 0.13	2.85	28
BTC2	0.49 ± 0.02	0.58 ± 0.012	32.6	76
BTC3	2.5 ± 0.26	2.3 ± 0.19	76.0	54
BTC4	inactive	inactive	53.7	98

*Note that the IC_{50} values reported here are a statistical average and were not read directly from the representative MTT assay graphs in Figures 5.10 and 5.11.

In contrast to the mononuclear complexes, the binuclear complexes do not appear to exhibit any significant selectivity between the two cell lines based on the data in Table 5.1. However, these compounds were far more active, with IC_{50} values well below those achieved with cisplatin and the mononuclear compounds, but not as low as the values reported for **AJ5**. Furthermore, the tethered compounds (**BTC1**-**BTC4**) do not appear to have significantly different activities to the unsubstituted compounds, despite the presence of the hydrophilic tether. The variation in activity can be correlated with the bisphosphine moiety instead. The results in Table 5.1 clearly show that dppe is the optimal bisphosphine ligand for these compounds, as both **AJ5** and its tethered analogue, **BTC2**, are the most active compounds by quite a significant margin. The dppm and dppp compounds which differ from dppe by only one methylene group, have significantly higher IC_{50} values while the dppf analogues were found to be inactive. The inactivity of the dppf

compounds can be explained in terms of their solubility in the test medium, as both **BC4** and **BTC4** are highly soluble in DMSO (>50 mg/mL) and polar organic solvents, but they are completely intolerant of water, instantly precipitating upon addition of aqueous medium.

Based on the IC_{50} values, further studies were carried out on the best/most representative palladacycle in each of the three series, **C2** for the mononuclear compounds, **AJ5** for the unsubstituted binuclear series and **BTC2** for the tethered binuclear series. The choice of **C2** over **C3** for the mononuclear palladacycles was based on the instability of **C3**, as the latter compound tends to be slightly unstable. Furthermore, the next most active mononuclear palladacycle is **C5**; however, this is a para-substituted species, whilst the rest of the complexes in the series of ortho-substituted. Therefore, **C2**, was selected as the most representative complex for the mononuclear series.

5.2.1.2 Western blot assays

Once the IC_{50} values were determined and the most promising compounds identified, Western blot assays were then used to determine how the active palladacycle complexes bring about the growth inhibition as determined by the MTT assay. Previous data showed that **AJ5** induces both DNA damage and apoptosis [42]. The Western blot results for **C2** and **BTC2** are shown in Figures 5.12 and 5.13.

W Blot	UT	C2	
Time (hrs)	0	24	48
γ-H2AX			
P38			

W Blot	UT	BTC2	
Time (hrs)	0	24	48
γ-H2AX			
P38			

Figure 5.12: Western Blot showing γ-H2AX for C2 and BTC2, where UT = untreated.

W Blot	UT	C2
Time (hrs)	0	24
Total PARP 116 KD		
Cleaved PARP 86 KD		
P38		

W Blot	UT	BTC2
Time (hrs)	0	24
Total PARP 116 KD		
Cleaved PARP 86 KD		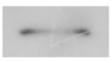
P38		

Figure 5.13: Western Blot showing cleaved PARP for C2 and BTC2, where UT = untreated.

As discussed in the introduction, the most important proteins which are employed as markers for potential anti-cancer drugs are γ-H2AX, which, if present, is an indication of DNA damage and PARP, which if cleaved, is an indication that apoptosis has been induced. In order to allow for relative quantification of the proteins being detected, a loading control, P38, was used to ensure that loading discrepancies are not interpreted as drug-induced changes.

Figure 5.12 shows that there is little to no γ-H2AX for the untreated cells. This is expected, as γ-H2AX is a DNA damage response agent which gathers at the site of DNA double-strand breaks [42]. Treatment of the cells with **C2** and **BTC2** for 24 and 48 hours, respectively, show a significant amount of γ-H2AX. The results match those obtained for **AJ5** [42].

Figure 5.13, shows the presence of PARP for both the untreated and treated cells at 0 and 24 hours and little to no cleaved PARP. Drug-induced apoptosis leads to increased amounts of cleaved PARP, the molecular marker of apoptosis [42]. The presence of cleaved PARP (86 KD) in the cells after treatment with **C2** and **BTC2** for 24 hours indicates that both palladacycles induce apoptosis. Again, these data match that obtained for **AJ5** [42]. The induction of apoptosis is preferable to necrosis, an alternative form of cell death. Necrosis is a detrimental mode of cell death, leading to inflammation in the host and often it is fatal. Apoptosis or programmed cell death is favourable, as it does not cause undesired negative effects and is usually beneficial to the host. Thus, making the mode of cell death caused by these palladacycles suited to their application as potential anti-cancer agents.

5.2.2 DNA binding studies

The *in vitro* studies above show that not only are these palladacycles active as anti-cancer agents, but they induce both DNA damage and apoptosis. Thus, DNA binding studies were performed to probe these interactions further in order to gain insight and understanding into the activity demonstrated above.

5.2.2.1 Agarose gel electrophoresis

Electrophoresis was employed to determine whether the palladacycles cause DNA damage. Changes in the electrophoretic mobility of the various forms of plasmid DNA are considered to be evidence of metal-DNA binding [43]. Using the protocols reported by Frik *et al*. and Albert *et al*. [31;43], an assay was developed and the selected palladacycles along with cisplatin were evaluated.

Initially, samples of both the mono- and binuclear palladacycles were prepared at the following three palladium concentrations: 10, 100 and 200 μM. The DNA was added and the concentration was kept constant at 0.4 μg/sample. The percentage solvent used for dissolution of the compounds (DMSO for palladacycles and saline for cisplatin) was also kept constant for all samples. Control samples of plasmid DNA with the same solvent system as for the compound-containing samples were also prepared to ensure that the changes observed are due to complex-DNA interaction and not solvent-DNA interaction. Samples were incubated overnight, after which loading dye was added and the gel was loaded and run. The gel was visualised by staining with ethidium bromide. Based on the initial results, another gel was run with a narrower concentration range (10-75 μM metal). The results of this study are shown in Figures 5.14 and 5.15 (10-200 μM) and 5.16 and 5.17 (10-75 μM).

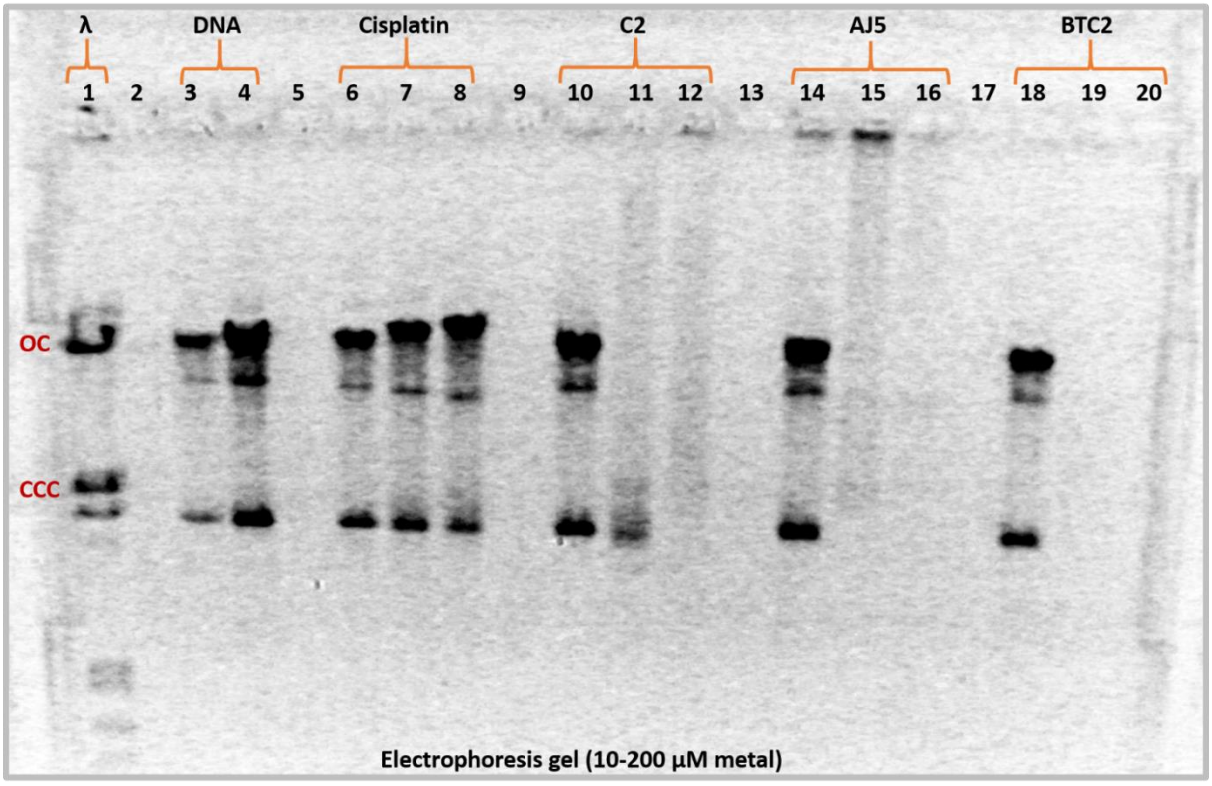

Figure 5.14: Interaction of pBluescript plasmid DNA (0.4 µg) in buffer (lane 3) and DNA in DMSO/buffer (lane 4) with increasing concentrations of compounds cisplatin, C2, AJ5 and BTC2. Gel stained with ethidium bromide stain (15 µL in 100 mL 1x TBE buffer) after running. Lane 1: λ marker.

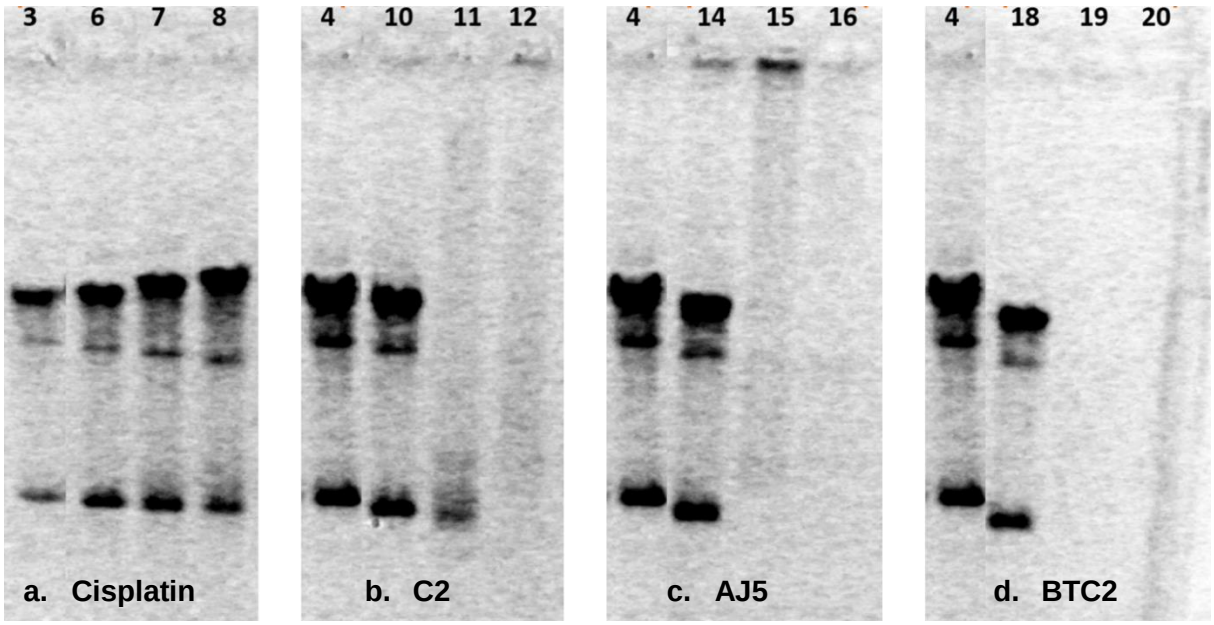

Figure 5.15: More detailed depiction of gel, where all lanes contain DNA, as well as the components listed, unless otherwise stated. a) Lane 3: Saline. Lane 5: 200 µM (no DNA). Lane 6: 10 µM. Lane 7: 100 µM. Lane 8: 200 µM. b) Lane 4: DMSO. Lane 9: 200 µM (no DNA). Lane 10: 10 µM. Lane 11: 100 µM. Lane 12: 200 µM. c) Lane 4: DMSO. Lane 13: 200 µM (no DNA). Lane 14: 10 µM. Lane 15: 100 µM. Lane 16: 200 µM. d) Lane 4: DMSO. Lane 17: 200 µM (no DNA). Lane 18: 10 µM. Lane 19: 100 µM. Lane 20: 200 µM.

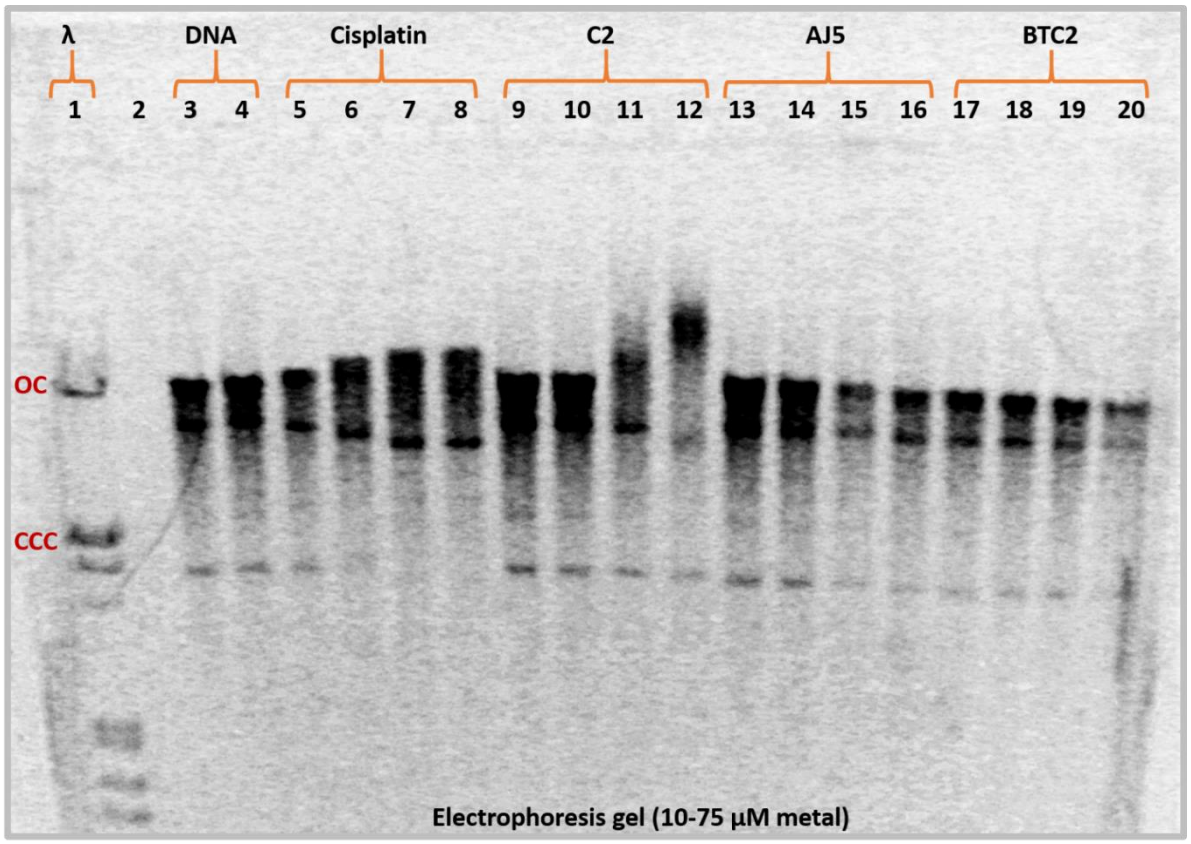

Figure 5.16: Interaction of pBluescript plasmid DNA (0.4 µg) in buffer (lane 3) and DNA in DMSO/buffer (lane 4) with increasing concentrations of compounds cisplatin, C2, AJ5 and BTC2. Gel stained with ethidium bromide stain (15 µL in 100 mL 1x TBE buffer) after running. Lane 1: λ marker.

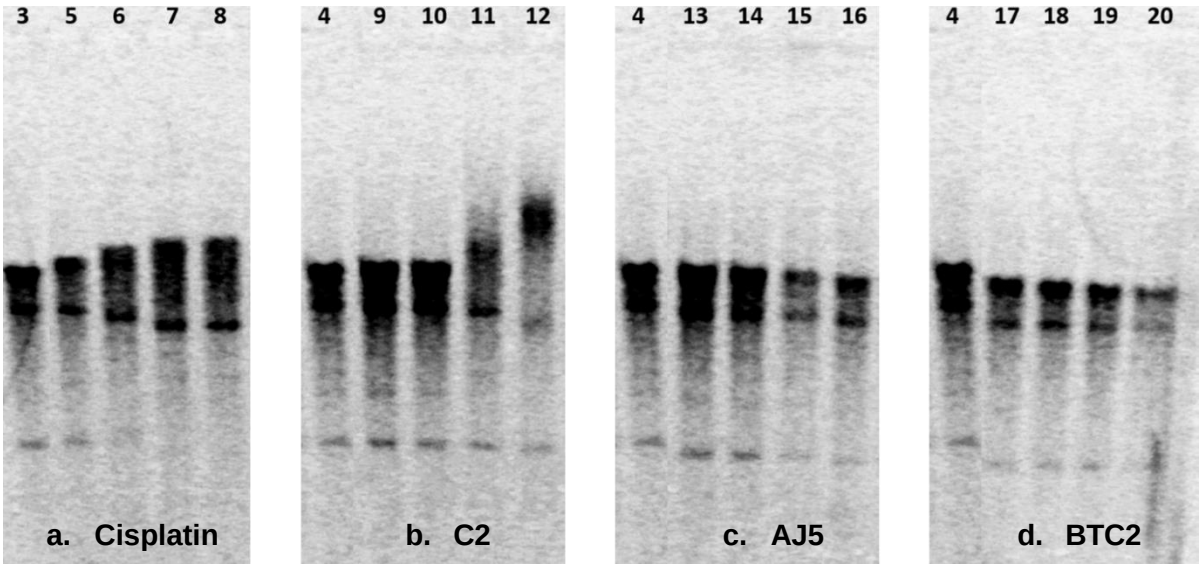

Figure 5.17: More detailed depiction of gel, where all lanes contain DNA, as well as the components listed. a) Lane 3: Saline. Lane 5: 10 µM. Lane 6: 25 µM. Lane 7: 50 µM. Lane 8: 75 µM. b) Lane 4: DMSO. Lane 9: 10 µM. Lane 10: 25 µM. Lane 11: 50 µM. Lane 12: 75 µM. c) Lane 4: DMSO. Lane 13: 10 µM. Lane 14: 25 µM. Lane 15: 50 µM. Lane 16: 75 µM. d) Lane 4: DMSO. Lane 17: 10 µM. Lane 18: 25 µM. Lane 19: 50 µM. Lane 20: 75 µM.

From Figure 5.14 and 5.15, it is clear that the palladacycles induce changes in the DNA; thus, it was concluded that all of the palladacycles tested bind to and damage the DNA [43]. Furthermore, these gels clearly show that the palladacycles induce far more significant changes in the DNA than cisplatin. Figures 5.16 and 5.17 show that the mononuclear palladacycle, **C2**, exhibits slightly different electrophoretic behaviour to the binuclear palladacycles, **AJ5** and **BTC2**, based on the trends observed in the electrophoretic mobilities of the three forms of DNA. **AJ5** and **BTC2** also show distinctly different behaviour to cisplatin. Unlike cisplatin, both **C2** and **AJ5** showed precipitated DNA in the wells at higher concentrations. This suggested the formation of insoluble aggregates by condensation of the DNA. Electrostatic forces are often the driving force behind the formation of these aggregates [44;45]. Hoechst 33258-DNA aggregation (Figure 5.18) is an example of this process, taken from the literature [44].

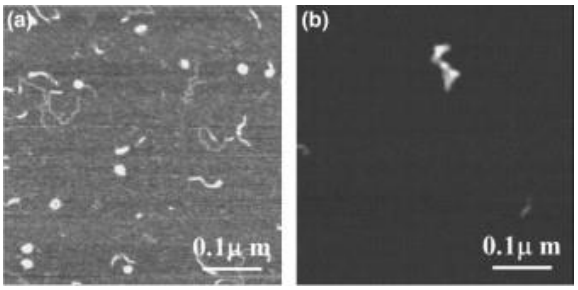

Figure 5.18: Atomic force microscopy (AFM) images of (a) 1.5 μM Hoechst 33258-DNA complex showing random free complexes and (b) 60 μM Hoechst 33258-DNA complex showing condensed aggregate [44].

Figures 5.15a and 5.17a show the changes induced by cisplatin. Initially, the oc and ccc bands are retarded, whilst the linear fragment migrates slightly faster through the gel. The disappearance of the ccc band (Figure 5.17a, lane 7 and 8) is actually retardation, observed as streaking, until the ccc band coalesces with the oc and linear bands. At higher concentrations (Figure 5.15a, lane 7 and 8), the ccc band migrates slightly faster through the gel. This is normally associated with a more condensed form of the DNA which can migrate through the gel faster than the control DNA in lane 3. This more condensed form of DNA is positively supercoiled DNA, which has a left-handed supercoil. These data agree with literature findings, such as those discussed in the introduction, where the interaction of cisplatin with plasmid DNA was found to uncoil DNA at low concentrations but increases the extent of supercoiling of the DNA (recoil DNA with opposite handedness) at higher concentrations [31;43].

Lower concentration data for the mononuclear palladacycle, **C2**, show retardation and streaking of the oc band, whilst the linear band migrates slightly faster and becomes broader (Figure 5.17b, lane 12). The ccc band becomes more feint and migrates slightly faster, however, the change in

migration is minimal. The observed retarding (Figure 5.17b, lane 10-12) followed by increased electrophoretic mobility (Figure 5.15b, lane 10 and 11) of the oc band corresponds to unwinding of the DNA followed by the induction of positive (left-handed) supercoiling. Thus, as the concentration increases, the DNA is unwound and rewound tighter with a left-handed helix, thus allowing it to migrate through the gel faster [31;34;43]. Furthermore, this left-handed supercoiled DNA could correspond to Z-form DNA. This is an unfavourable form of DNA which has opposite handedness to normal B-form DNA (right-handed helix) and is more compact [46], explaining the ability to migrate through the gel faster than B-form DNA. Notably, **C2** influences the oc band the most whilst cisplatin influenced the ccc band. This could be due to the size of the complexes, as the larger palladacycle structure may not be able to interact with the tightly coiled ccc plasmid. Higher concentration data for **C2** (Figure 5.15b) show streaking and an increase in the electrophoretic mobility of the ccc band (lane 11). Eventually, no bands were discernible aside from a feint streak (lane 12). At lower concentrations, **C2** appears to interact with DNA in a slightly different mode to the binuclear palladacycles, however, at higher concentrations, the palladacycles all exhibit the same trends. We propose that **C2** exhibits the same type of interaction with DNA as the binuclear palladacycles, just not to the same extent (possibly due to the mononuclear nature of the complex).

The binuclear palladacycles, **AJ5** and **BTC2**, show similar trends to each other at all concentrations. The lower concentration data (Figures 5.17c and 5.17d) show increased electrophoretic mobilities for all of the bands, to a lesser or greater extent, with the degree of band fading becoming more obvious with increasing concentration; however, no initial unwinding of the DNA was observed. The higher concentration data (Figure 5.15c and d) show feint streaking (Figure 5.15c, lane 15) or no visible DNA (Figure 5.15c, lane 16 and Figure 5.15d, lane 19-20). The increased electrophoretic mobilities correspond to increased supercoiling of the DNA forms, making the fragments more compact and allowing easier passage through the gel [34].

The observed streaking and absence of observable DNA bands can be related to severe damage which can possibly be accounted for by a number of processes, viz. the formation of single strand DNA (ssDNA) to which the ethidium bromide stain cannot bind, competitive binding of the complexes and ethidium bromide to double-stranded DNA which could lead to the palladacycles saturating the ethidium bromide binding sites and preventing the stain from binding, loss of the 3D superstructure of the DNA or even complete destruction of the DNA [31;47-49].

To conclude, the agarose gel electrophoresis DNA binding assay showed that the palladacycles interact with DNA by a mode different to that of cisplatin. The complexes induced DNA aggregation which, based on literature, is most likely driven by electrostatic forces. Furthermore, the induction of positive supercoiling was observed. The tightly coiled DNA with left-handed helicity could correspond to Z-form DNA. Finally, the fading/disappearing DNA bands suggested conversion of the DNA to a form that cannot be stained by ethidium bromide, such as ssDNA or DNA that has lost its 3D superstructure or possibly been completely destroyed. Alternatively, there could be competitive binding of the palladacycles with ethidium bromide, such that the palladacycles saturate the ethidium bromide binding sites and consequently prevent staining of the DNA.

To investigate the interactions of these complexes with DNA further, some spectroscopic techniques were employed.

5.2.2.2 UV-Vis spectroscopy

Generally, DNA binding studies by UV-Vis spectroscopy are carried out as absorbance titrations, where either the metal or DNA concentrations are kept constant while the other component is varied. We started out employing assays which had previously been utilised for the evaluation of DNA binding studies of metal compounds, such as the methods employed by Tarushi *et al*. and Cheng-Yong *et al*., however, these methods proved to be ineffective in the case of our compounds [16;50]. These interactions are usually monitored at a wavelength where only the DNA or the compound absorbs. Unfortunately such a wavelength did not exist for these novel palladacycles as the spectra of these compounds overlap with that of DNA. For this reason, many of our initial attempts failed, accompanied by the low solubility of the complexes, which necessitated the use of at least 10% DMSO to keep the compounds in solution. Inconclusive data was obtained or no apparent DNA binding was observed, which we knew could not be the case, based on the results of the Western blot assays and the electrophoresis study of DNA binding discussed earlier.

While searching the literature, a less commonly employed method reported by Aslanoğlu and Öge for their work on the interaction of norepinephrine with DNA was discovered [51]. This method allowed for simple comparison and interpretation of the results, as it compares the summed absorbance obtained from pure compound and pure DNA solutions measured separately, where there is no interaction, to the absorbance of the solution containing a mixture of DNA and the

compound, where, it has already been proven that there is an interaction. Thus, any changes observed in the spectra are due to interaction of the compound with the DNA [51].

Since these DNA binding protocols are new to the laboratory and the method employed is not widely reported, it was decided to test the method using a known DNA binding compound as a model compound to ensure that the method is viable and that the DNA employed in the absence of a binding agent is not being denatured as a result of experimental conditions employed. The compounds also served as models for the type of DNA binding. Ethidium bromide, an intercalator [52], methylene blue, a semi-intercalator and electrostatic binder [53] and methyl green, a major groove binder [54] were included as references. The results for these experiments are shown in the appendix (Figures A3.1-A3.3) and will not be discussed unless pertinent to the interpretation of the interaction of the palladacycles with DNA. However, from the data it was ascertained that the assay is viable and that results resembling those reported in the literature, could be obtained.

The DNA binding experiments were then carried out using **C2**, **AJ5** and **BTC2** with cisplatin, as a control for covalent binding. **AJ5** was used as a benchmark for the novel complexes, as well as being representative of the unsubstituted binuclear series, whilst **C2** and **BTC2** were the representative compounds for the mononuclear and tethered binuclear series, respectively. The results are shown in Figures 5.19-5.22. Note that the samples containing both DNA and compound are denoted in the legends as DNA_Compound x, where x is the micromolar metal concentration. The spectra which represent the summed absorbance obtained from pure compound and pure DNA solutions measured separately, are denoted in the legends as (DNA) + (Compound x), where x is again the micromolar metal concentration. Note that blue arrows have been included on the graphs to highlight the changes observed due to DNA binding interactions.

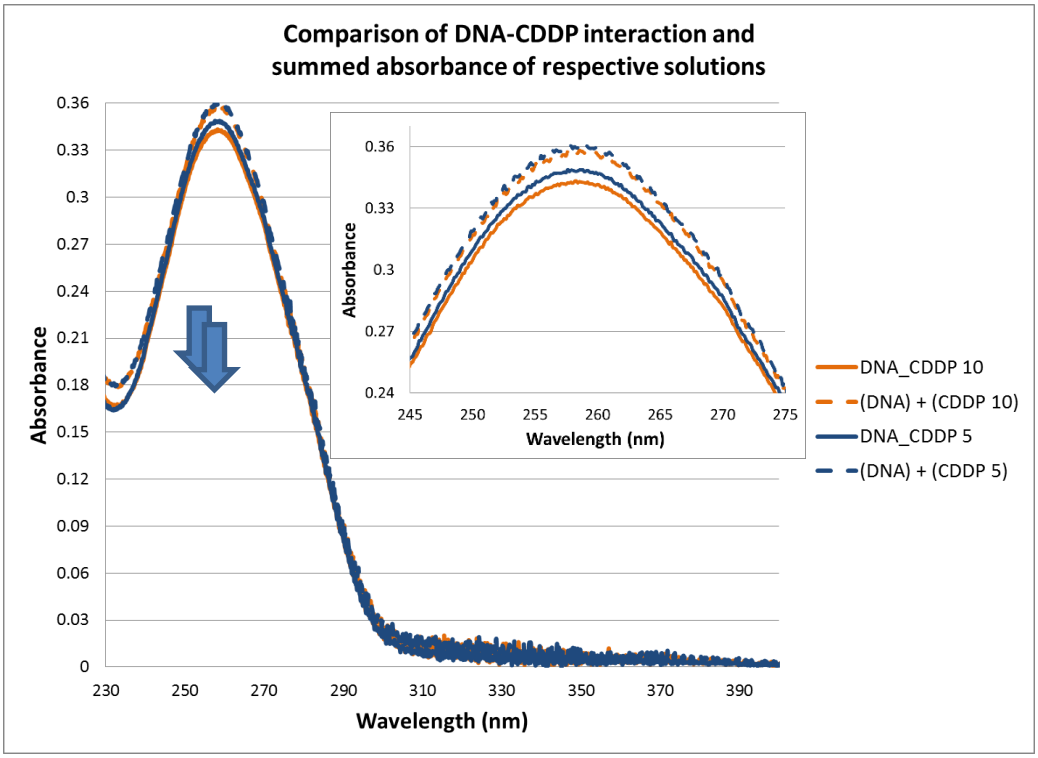

Figure 5.19: UV-Vis spectra of cisplatin interaction with DNA and the summed absorbances of pure cisplatin and pure DNA at various concentrations. Inset: Magnified area at maximum absorbance. (Consult text above for detailed explanation of the legends.)

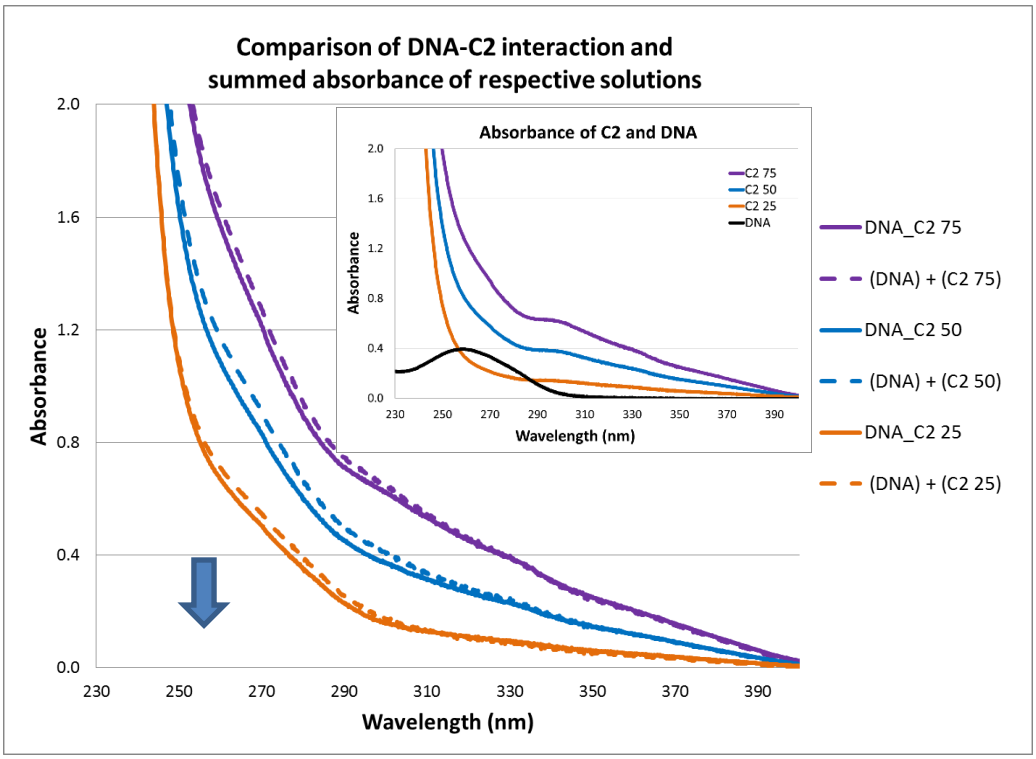

Figure 5.20: UV-Vis spectra of C2 interaction with DNA and the summed absorbances of pure C2 and pure DNA at various concentrations. Inset: Absorbance spectra of C2 (various concentrations) and DNA.

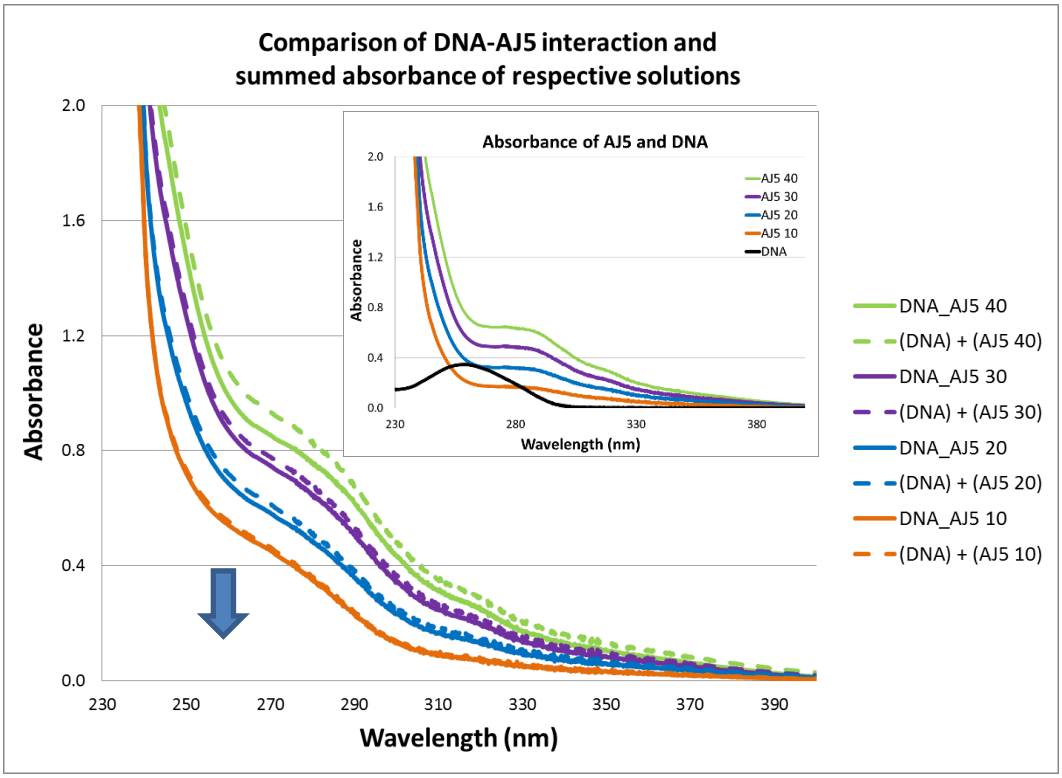

Figure 5.21: UV-Vis spectra of AJ5 interaction with DNA and the summed absorbances of pure AJ5 and pure DNA at various concentrations. Inset: Absorbance spectra of AJ5 (various concentrations) and DNA.

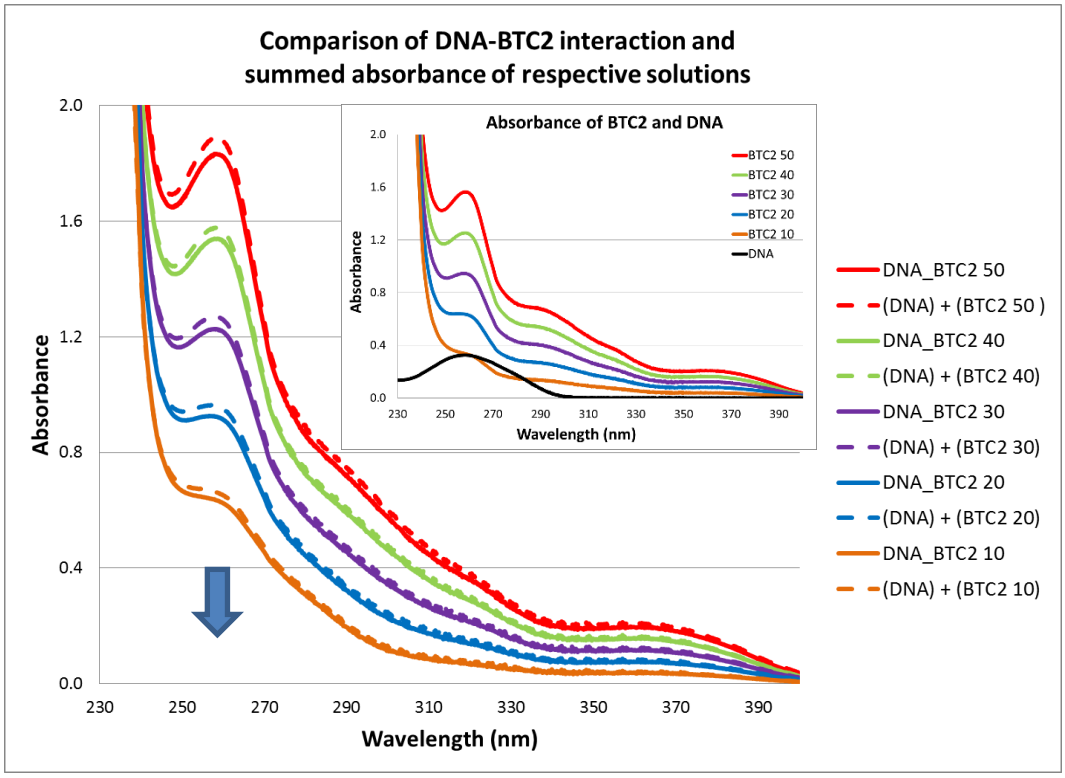

Figure 5.22: UV-Vis spectra of BTC2 interaction with DNA and the summed absorbances of pure BTC2 and pure DNA at various concentrations. Inset: Absorbance spectra of BTC2 (various concentrations) and DNA.

For cisplatin, a hypochromic effect was observed. The summed spectra showed no change with increasing metal concentration, as cisplatin does not absorb in this region, whilst the samples containing both DNA and cisplatin showed a hypochromic effect. As expected, the sample with a higher concentration of cisplatin showed a larger hypochromic effect than the lower concentration sample. The extent of interaction with DNA (hypochromism) is greater than the change in absorbance due to varying metal concentration, as can be seen by comparing the change in absorbance between the 5 and 10 μM samples and the summed spectra. The samples experience a small change in absorbance due to increasing metal concentration (0.005 AU) compared to the overall hypochromic effect relative to the summed spectra (0.013 AU). This correlated to the strength of DNA-binding rather than the type, as it is well known that cisplatin forms covalent bonds with DNA. Furthermore, comparison of the cisplatin spectra with the known binders showed that none of the known binders exhibit hypochromism to this extent.

All three palladacycles show the same effect in the UV-Vis spectra – hypochromism. In contrast to cisplatin, the degree of hypochromism is far less than the change in absorbance due to the changes in metal concentration. This suggests that these compounds do not bind as strongly to DNA. Thus, the binding observed here corresponds to the formation of weaker non-covalent bonds rather than the covalent bonds observed for cisplatin. Based on the literature, hypochromism is an indication of either groove or electrostatic binding [24;30;37;55]. This was confirmed by comparison with the spectra obtained for methylene blue and methyl green (Figures A3.2 and A3.3 in the appendix), where methylene blue, with intercalation and electrostatic interactions, showed hyperchromism and methyl green, with groove binding interactions, showed hypochromism. The reason for the observation of hyperchromism, rather than hypochromism for methylene blue, is that intercalation causes more significant changes in the structure of the DNA helix, which are then more easily detected by UV-Vis spectroscopy [53].

Both **C2** and **AJ5** showed a deviation from the hypochromic effect at higher concentrations. This was due to the formation of a precipitate at these high concentrations. Not only was this visible to the naked eye, during the experiment, but by recording the absorbance at 620 nm, non-zero absorbances were observed which were indicative of the presence of particles in solution [56]. The recorded data are shown in Table 5.2.

Table 5.2: Absorbances values recorded at 620 nm.

Sample	A_{620} (nm)*
DNA	0
C2 50	0
C2 75	0
C2 100	0.3
C2 125	0.3
DNA_C2 50	0
DNA_C2 75	0
DNA_C2 100	0
DNA_C2 125	0.4
AJ5 20	0
AJ5 30	0
AJ5 40	0
AJ5 50	0.001
DNA_AJ5 20	0
DNA_AJ5 30	0
DNA_AJ5 40	0
DNA_AJ5 50	0

*Non-zero absorbances are indicated in red text.

The presence of a precipitate corresponds to the formation of insoluble aggregates, as observed in the electrophoresis data. Thus, the next step in this study was to try to determine if the DNA binding mode was groove- or electrostatic binding. Thus, CD spectroscopy was employed, as it is more sensitive to changes in the DNA structure than UV-Vis spectroscopy.

5.2.2.3 CD spectroscopy

Based on the success of the UV-Vis spectroscopy studies, the same method was employed for the CD spectroscopy studies. There were two reasons for selecting this method. Firstly, the method was used very successfully for the UV-Vis spectra and the Chirascan instrument used allowed for simultaneous recording of CD and UV-Vis data, thus, the two sets of UV-Vis data could be compared to ensure that the experiment was successful. Secondly, the sensitivity of this

technique is advantageous; however, the more complex results are far more difficult to understand and interpret. Thus, having the summed data for comparison with the data where there are various spectral changes due to interaction of the compound with DNA aids in the interpretation of the data. Furthermore, as stated in the protocol by Garbett *et al*., the spectra should be recorded at wavelengths where no signal overlap occurs, as overlapping signals make interpretation difficult, as the signals may result from an induced CD (ICD) spectrum or structural changes in the DNA [57].

The known DNA binding compounds, ethidium bromide, methylene blue and methyl green, were again included, to ensure that the method was effective. These results are shown in the appendix (Figures A3.4 – A3.6) and will not be discussed unless pertinent to the interpretation of the interaction of the palladacycles with DNA. From the data, it was ascertained that the assay works and that the literature trends could be replicated.

The DNA binding experiments were then carried out on **C2**, **AJ5** and **BTC2** with cisplatin, as a control for covalent binding. **AJ5** was used as a benchmark for the novel complexes, as well as being representative of the unsubstituted binuclear series, whilst **C2** and **BTC2** were the representative compounds for the mononuclear and tethered binuclear series, respectively. The results are shown in Figures 5.23-5.26.

After the data were collected, it was confirmed that the compounds themselves do not have CD spectra. This was expected, as the compounds are achiral. Therefore, the summed spectra are not included in the results, as the spectra are the same as that of DNA on its own. As in the case of the UV-Vis spectroscopic studies, the samples containing both DNA and compound are denoted in the legends as DNA_Compound x, where x is the micromolar metal concentration.

For cisplatin, there is an overall decrease in the intensity of the positive band (284 nm), which corresponds to a decrease in the base stacking. The negative band (244 nm) shows an increase intensity which corresponds to an increase in the helicity of the DNA [58;59]. The observed changes in the DNA signal intensities correspond a transformation of the DNA from the B→C form with increased helicity, as reported for cisplatin in the literature [59].

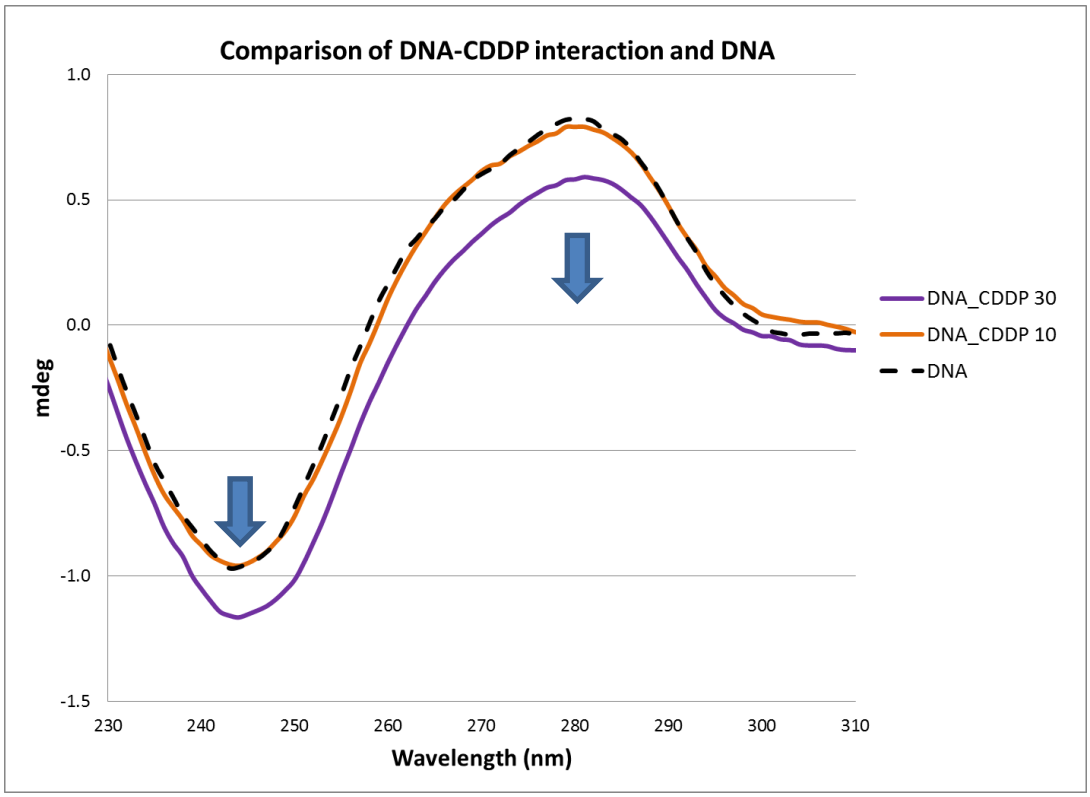

Figure 5.23: CD spectra of cisplatin interaction with DNA at various metal concentrations.

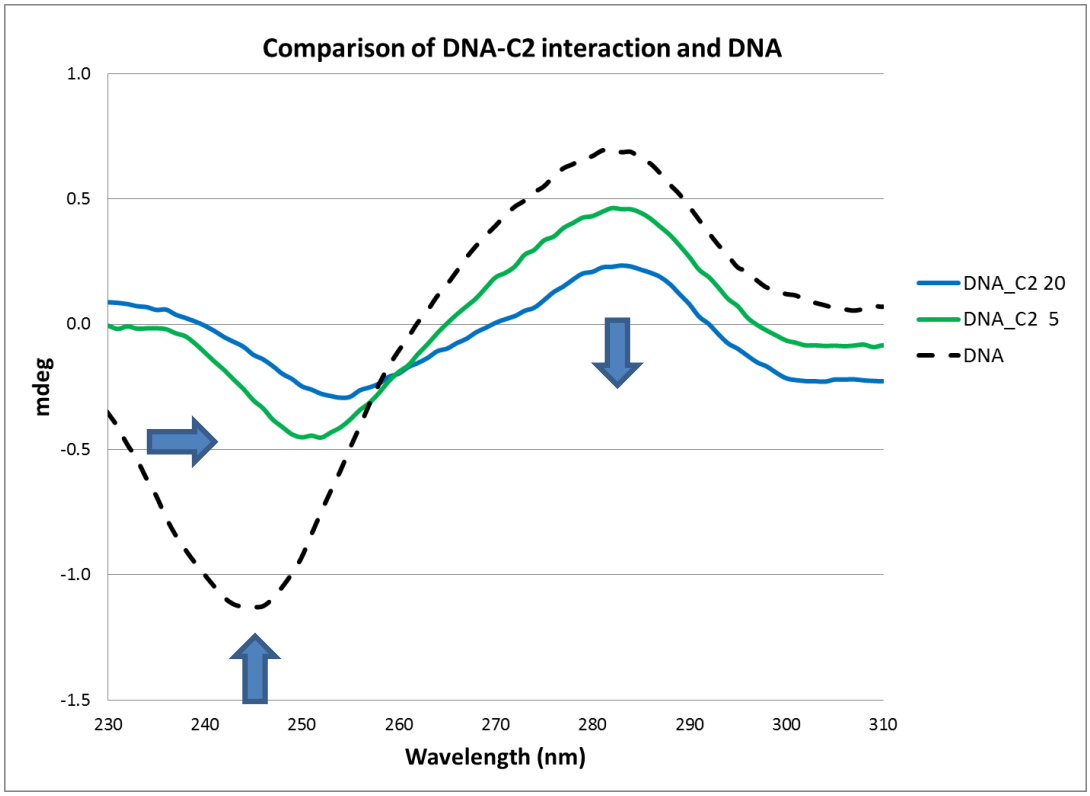

Figure 5.24: CD spectra of C2 interaction with DNA at various metal concentrations.

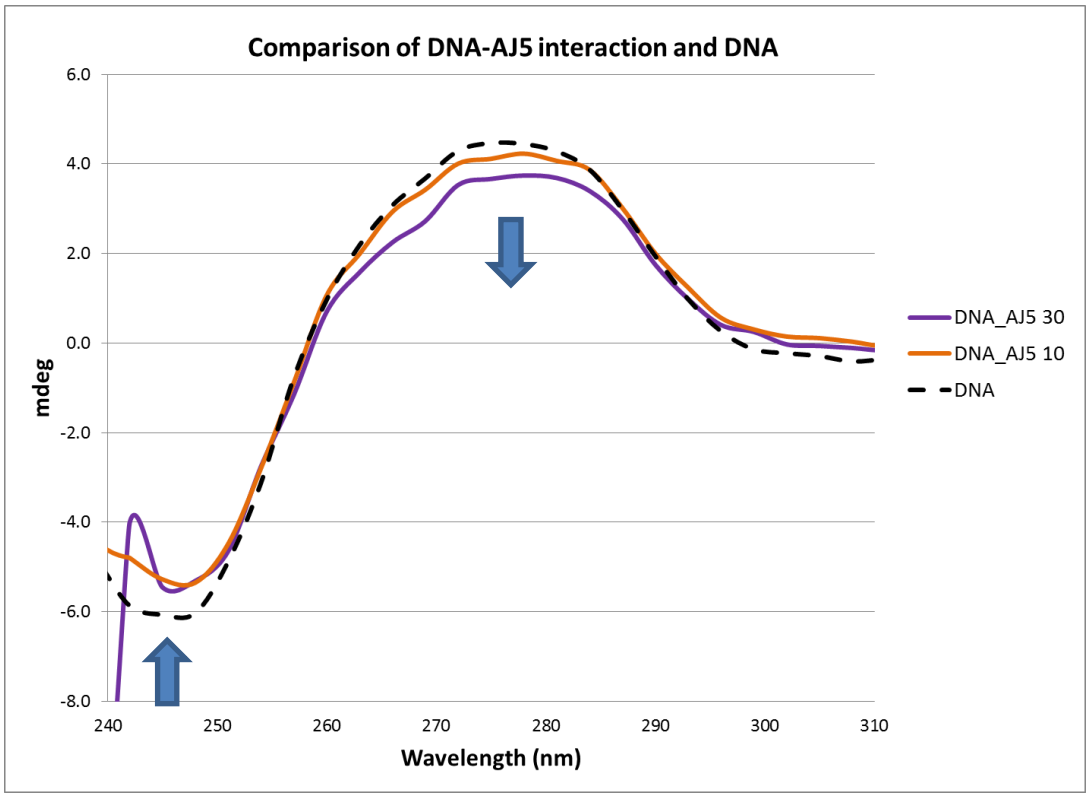

Figure 5.25: CD spectra of AJ5 interaction with DNA at various metal concentrations.

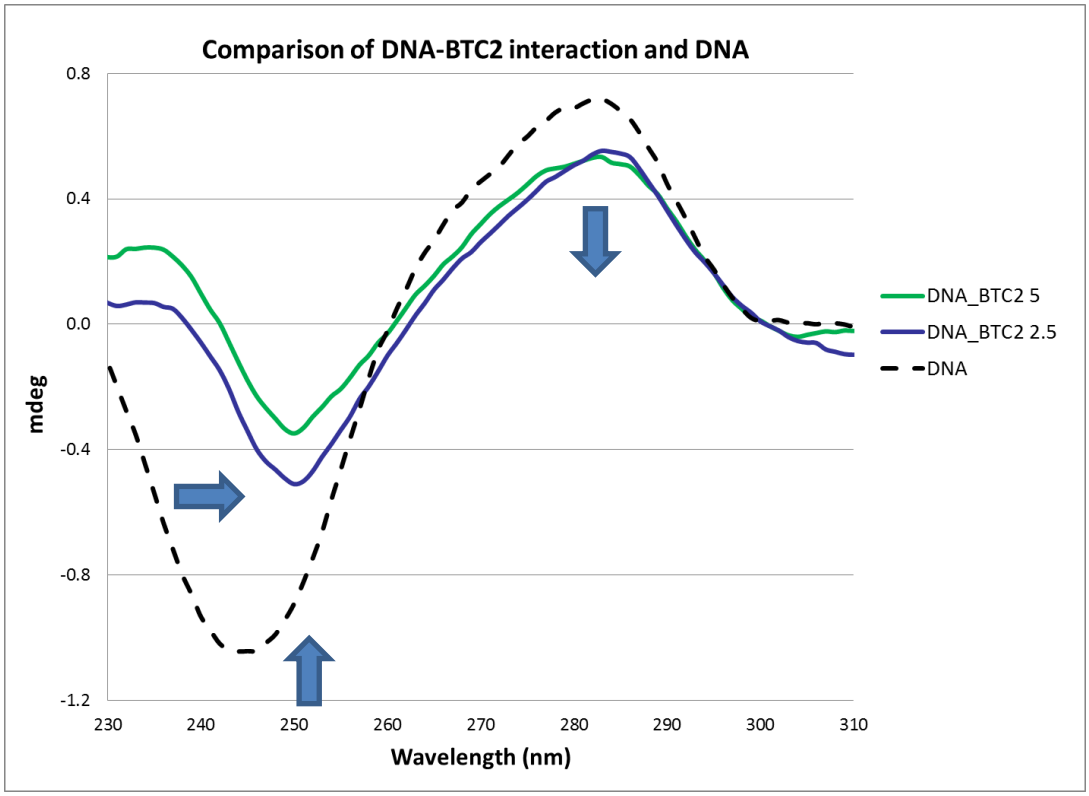

Figure 5.26: CD spectra of BTC2 interaction with DNA at various metal concentrations.

Upon interaction of the palladacycles with DNA, there was a decrease in the intensity of both the positive and negative bands. The changes are more pronounced for **C2** and **BTC2** and in fact, these two complexes show fairly similar trends. In both cases there was a clear shift in the negative bands of **C2** and **BTC2**, to higher wavelengths. The decreased intensity of both the positive and negative bands are an indication of decreased base stacking and helicity. At higher metal concentrations (50-125 μM), **C2** and **BTC2** showed CD spectra which have almost indiscernible positive and negative bands. Initially, these results were thought to be ambiguous, however, when considered with the lower concentration data, the results could most likely be correlated to a number of different possible effects, including the formation of ssDNA, a transformation in the DNA from B→Z form or the formation of achiral aggregates.

Comparison of these results with those usually obtained for the known DNA binders appears to indicate that the same trends were observed as is the case for the known major groove binder, methyl green. Despite the similarity in the observed trends, the negative bands of the CD spectra for the interaction of the palladacycles (more specifically **C2** and **BTC2**) with DNA showed a shift to higher wavenumbers, which was not the case for the groove binder, methyl green. Therefore, groove binding was unlikely as no shift in the negative band was expected. Furthermore, these compounds do not have the curved shape observed for reported groove binders (Figure 5.3). Since the electrophoresis results suggested the formation of aggregates, driven by electrostatic forces, and the UV-Vis spectra showed hypochromism which suggests either groove- or electrostatic binding, these palladacycles most likely bind to DNA through electrostatic interactions.

Next, NMR spectroscopy was attempted with the hope of gaining further insight into the interaction of the palladacycles with DNA.

5.2.2.4 Attempt to study DNA binding via NMR spectroscopy

Based on the various analytical techniques explored above, it would appear that the palladacycles bind to DNA through weak non-covalent interactions and that at high metal concentrations, the formation of insoluble metal-DNA aggregates were observed. However, experiments to determine whether these weak interactions were groove or electrostatic in nature were inconclusive. Thus, NMR spectroscopy was employed in an attempt to gain greater insight into the nature of the weak interactions between the palladacycles and DNA. **C6**, the fluoro analogue, was selected for this

experiment, as it is one of the more soluble complexes (in DMSO), as well as affording the opportunity to monitor a second nucleus, the NMR active fluorine-19 nucleus (^{19}F).

^{19}F and ^{31}P NMR spectra were recorded for **C6**, the fluoro-analogue, with varying ratios of salmon sperm DNA. **C6** was chosen, as it was one of the more soluble complexes and allowed the recording of spectra for both nuclei. All samples were prepared in 20% D_2O in DMSO-d6 to ensure that **C6** remained in solution. DNA:metal ratios of 1:10, 1:4, 1:2 and 1:1 were investigated.

All ^{19}F NMR spectroscopic signals were observed as broad singlets. The chemical shifts are recorded in Table 5.3. The ^{31}P NMR spectra are shown in Figures 5.27-5.29.

Table 5.3: ^{19}F NMR spectroscopic data.

Sample (DNA:C6)	^{19}F NMR signal shift (ppm)
DNA	No signal
C6 (2-Fluoro analogue)	-109.51
1:10	-109.53
1:4	-109.55
1:2	-109.54
1:1	-109.54

No changes were observed in the ^{19}F NMR signal of **C6**, which was observed as a broad signal at -109.5 ppm. No ^{19}F-^{1}H coupling was observed, however, this was attributed to the very low concentration of the sample.

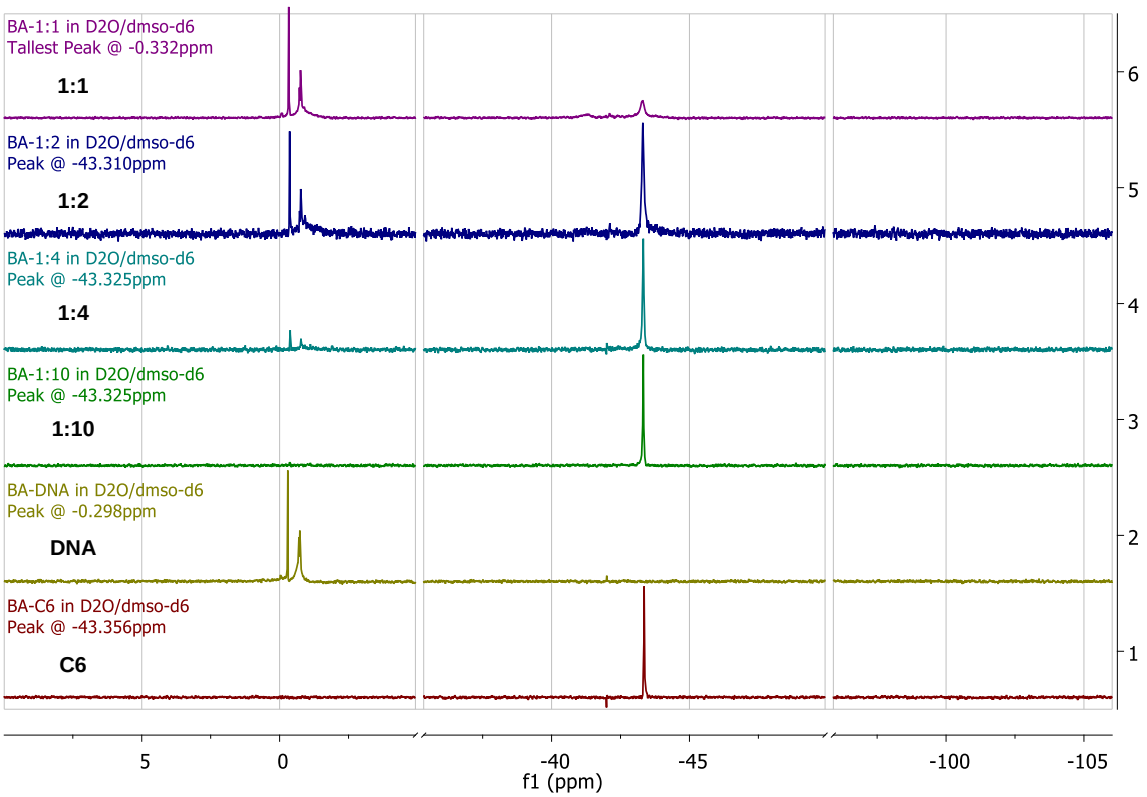

Figure 5.27: ^{31}P NMR spectra of C6 (spectrum 1), DNA (spectrum 2) and various DNA:C6 ratios (spectra 3-6).

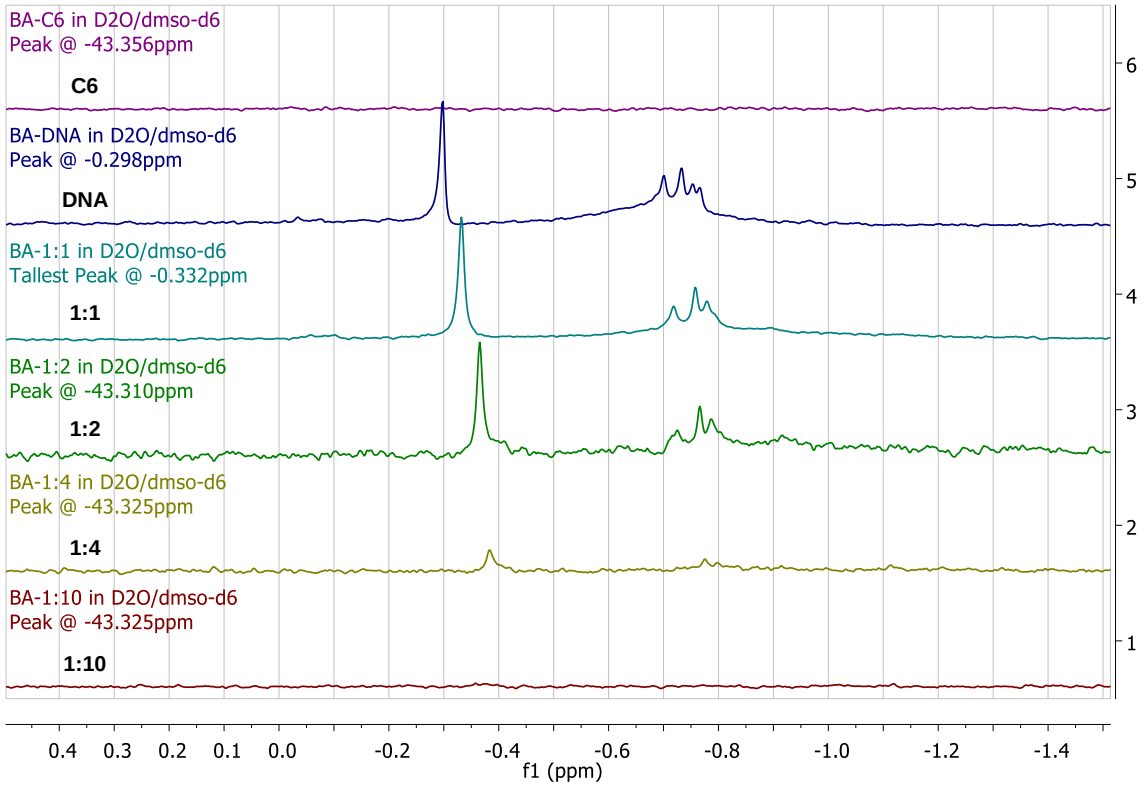

Figure 5.28: ^{31}P NMR spectra of C6 (spectrum 1), DNA (spectrum 2) and various DNA:C6 ratios (spectra 3-6) in the range of 0.5 to -1.5. Only the DNA signals are shown in the spectra.

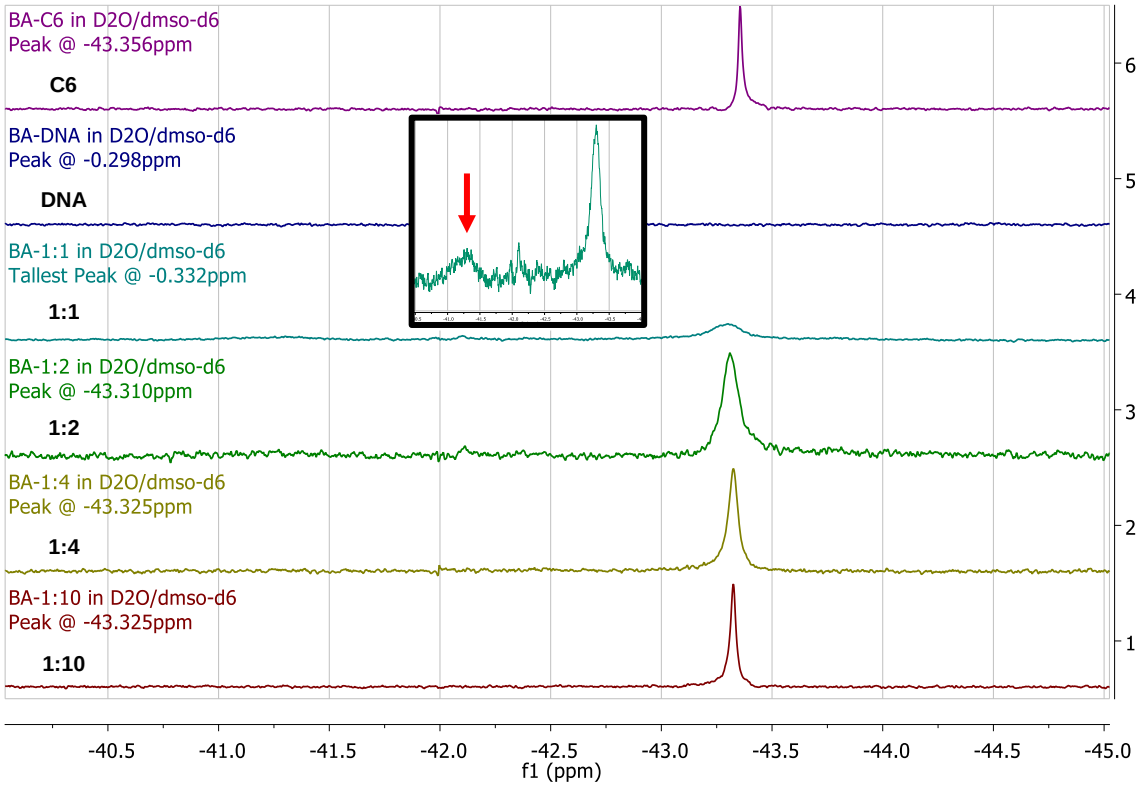

Figure 5.29: ^{31}P NMR spectra of C6 (spectrum 1), DNA (spectrum 2) and various DNA:C6 ratios (spectra 3-6). Only the C6 signal is shown. Inset of 1:1 DNA:C6 in the range of 40-45 ppm showing broad second signal.

The ^{31}P NMR spectra showed no dramatic shifts in the DNA and **C6** signals, however, a new broad signal started appearing at approximately -41 ppm, just downfield of the **C6** signal at a 1:1 ratio of DNA to **C6** (Figure 5.27). Closer inspection of the DNA signals showed an overall upfield shift of both signals (a singlet at approximately -0.3 ppm and a multiplet at -0.80 - -0.65 ppm) from the free DNA to the metal-DNA complex. Increasing the metal led to an upfield shift of these signals (Figure 5.28). The complex ^{31}P signal broadened, shifted slightly downfield with increasing DNA concentration (Figure 5.29). A new signal starts appearing at -41.25 ppm with increasing DNA concentration (Figure 5.29 inset).

Considering the ^{31}P NMR signals for both the DNA and metal complex, the slight changes observed in the NMR spectra could possibly suggest very weak interactions between the palladacycle and DNA, however, the formation of a new ^{31}P signal in the region of the complex signal confirms that the DNA does interact with and change the complex, leading to the formation of a second signal.

In order to ascertain the mode of DNA binding, all the DNA binding study data must be taken together. The evaluation of the data is discussed in the section below.

Electrophoresis showed that the palladacycles bind to the DNA by a mode different to that of cisplatin. The mononuclear compound, **C2**, exhibited a slightly different electrophoretic behaviour to that of the binuclear compounds, **AJ5** and **BTC2**, at lower metal concentrations, whilst all three palladacycles showed fairly similar trends at higher metal concentration. The palladacycles were thought to induce positive supercoiling, so that the DNA has a left-handed supercoil and migrates through the gel faster than the DNA control [34]. This left-handed supercoiled DNA could correspond to Z-form DNA which has the opposite handedness to normal B-form DNA and is more compact. The presence of precipitated DNA in the wells at higher concentrations suggested the formation of insoluble aggregates by condensation of the DNA helix through electrostatic interactions [44;45]. Finally, the observed streaking and absence of observable DNA bands at higher metal concentration was attributed to possible competitive electrostatic binding to DNA (between the complex and ethidium bromide stain), loss of 3D superstructure and/or complete DNA destruction.

The formation of smaller, more flexible ssDNA was unlikely, since **C2** and **AJ5** showed precipitation of material in the wells which suggested the formation of large insoluble aggregates. The UV-Vis spectroscopic data (reported in Section 5.2.2.2) were used to verify this, as the conversion from double strand DNA (dsDNA) to ssDNA is expected to be observed as a 40% hyperchromic shift at 260 nm in the UV-Vis spectrum. The UV-Vis spectra did not show any such hyperchromic effects, thus, ssDNA formation was ruled out.

Next, possible competitive electrostatic DNA binding was considered and thought to be improbable, as ethidium bromide is an intercalator and the UV- and CD spectroscopic data did not show the same DNA binding trends as ethidium bromide (Figures A3.1 and A3.4). However, literature reports showed that ethidium bromide has a secondary electrostatic binding site [48;49]. Therefore, it was possible that the palladacycles could block the electrostatic binding site, thus lowering the fluorescence and leading to the observed band fading.

Loss of the 3D superstructure and or complete destruction of the DNA could also explain the absence of observable DNA, as these changes to the structure of the DNA will prevent ethidium bromide from binding and visualising the DNA. Furthermore, the data obtained here resembles the data for **Reference compound 1** reported by Albert *et al.* [31] and discussed in Section 5.1.3 of the introduction (Figure 5.5). The active diimine palladacycle showed no observable DNA at

high complex concentrations. This could possibly be attributed to destruction of the DNA. However, for the palladacycles evaluated in this chapter, the NMR spectroscopy data showed only slight changes in the DNA signals upon interaction with the palladacycles at various DNA:palladacycle ratios. Therefore, loss of 3D structure and complete destruction of the DNA are unlikely.

Furthermore, UV-Vis spectroscopic data showed that all three palladacycles induce the same effect in the absorbance spectra – hypochromism. Based on the literature, hypochromism is an indication of either groove or electrostatic binding. Additionally, both **C2** and **AJ5** showed a deviation from the hypochromic effect at higher concentrations. This was due to the presence of a precipitate. The presence of a precipitate corresponds to the formation of insoluble aggregates, as observed in the electrophoresis data.

Thus, from the electrophoresis and UV-Vis spectroscopy data, the palladacycles could possibly induce the following DNA binding types: Z-form DNA, insoluble aggregates, competitive electrostatic binding forces and groove binding. The formation of ssDNA and loss of 3D structure and/or complete destruction of the DNA were ruled out.

The CD spectroscopy, like UV-Vis spectroscopy, showed similar data for all three palladacycles. Upon interaction with DNA, there was a decrease in the intensity of both the positive and negative bands of the CD spectra of DNA, which indicated decreased base stacking and helicity. The changes were more pronounced for **C2** and **BTC2** and there was also a clear shift in the negative bands, to higher wavelengths. The data suggested possible formation of ssDNA, a transformation in the DNA from B→Z form or the formation of achiral aggregates.

From the electrophoresis and UV-Vis spectroscopy data, ssDNA formation was ruled out. Thus, only a transformation in the DNA from B→Z form or the formation of achiral aggregates were considered.

Z-form DNA has an inverted CD spectrum of B-form DNA, due to opposite handedness of the B- and Z-form helices [34;55]. So the CD spectrum of Z-form DNA would exhibit a positive band at approximately 260 nm and a negative band at approximately 290 nm [60]. Although the CD spectra show a shift in the negative band to higher wavenumbers, no shift in the positive band was observed. Despite the decreasing band intensities with increasing metal concentration, a complete B→Z form transition was not observed, however, the electrophoresis data also suggested the possible formation of Z-form DNA.

Finally, the formation of achiral aggregates was quite possible, as these aggregates would not have a CD spectrum. The loss of band intensities with increasing metal concentration could correspond to the formation of achiral aggregates. More importantly, the formation of insoluble aggregates was observed in both the electrophoresis and UV-Vis spectroscopic data.

Finally, the ^{31}P NMR spectra showed subtle shifts in the DNA signals and no clear changes in the complex signal, however, a new signal starts appearing at -41.25 ppm with increasing metal concentration. Taken together, these data suggest very weak interactions between the palladacycle and DNA as very little change was observed in the NMR spectra.

Thus, from all the DNA binding study data, discussed in Sections 5.2.2.1-5.2.2.4, it was concluded that the palladacycles induce the formation of insoluble aggregates. Additionally, a B→Z form transformation in the DNA is possible. Of the possible groove and electrostatic binding forces, the most likely driving force behind the formation of insoluble aggregates and a B→Z form transition is electrostatic binding.

Since the palladacycles are neutral, the nature of the proposed electrostatic interaction is uncertain, however, from the NMR experiments, it is clear that PTA ligand dissociation does not occur, as no signal for the free phosphine at -102 ppm is detected when **C6** is examined in solution. Thus, it is proposed that the Pd-Cl bond undergoes hydrolysis to form the aquated species, which is cationic in nature (Figure 5.30), however, further studies are required to confirm this structure. Similar hydrolysis processes are reported throughout the literature for platinum anti-cancer agents [59].

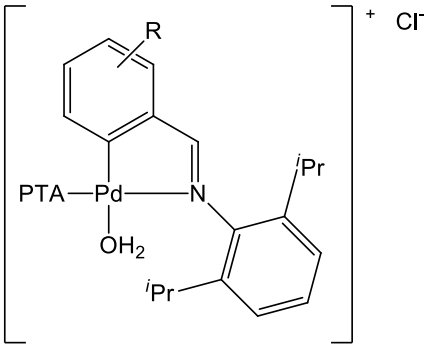

Figure 5.30: Proposed aquated species which is cationic in nature.

5.2.3 Quantitative DNA binding studies

In an attempt to establish whether the DNA binding constants could be determined, an alternative UV-Vis spectroscopic assay was investigated. The work carried out by Yang *et al.* [61] was used as a starting point to develop the assay.

Absorption titrations of the palladacycles, **C2**, **AJ5** and **BTC2** were carried out in 10% DMSO in tris-HCl buffer using a fixed palladium concentration (10 μM). Aliquots (2-10 μL) of DNA stock solution (1.0 mM) were added to both the sample and reference (10% DMSO in buffer) cuvettes in order to eliminate the absorbance of the DNA. Samples were mixed by inversion and then recorded after a 5 minute incubation period. According to literature, the titrations should be continued until the absorbance remains unchanged for four titrations, however, in the case of these palladacycles precipitation was observed before this point of binding saturation was achieved. Unfortunately, the precipitate caused interference with the absorbance trends and the experiment had to be aborted. Figure 5.31 is a representative graph of the data obtained.

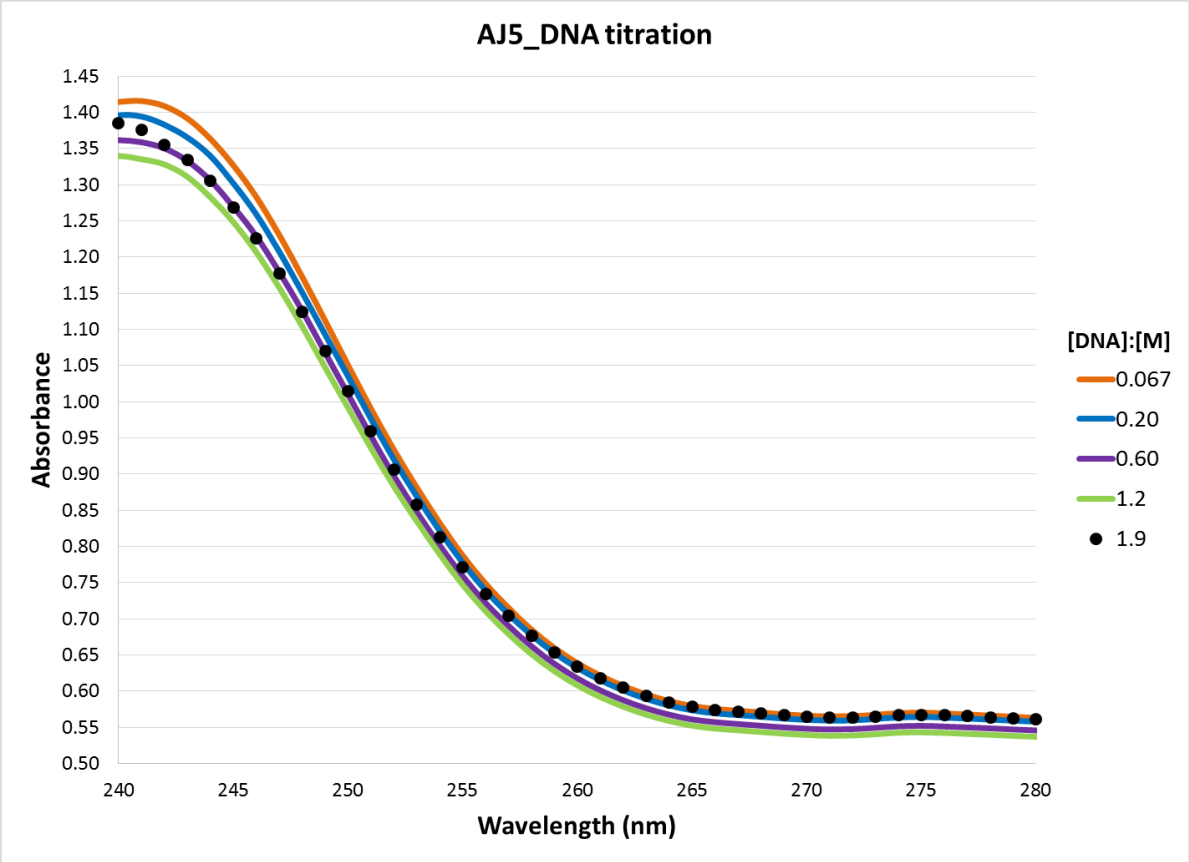

Figure 5.31: UV-Vis spectra of AJ5 titrated with DNA at various concentrations. The [DNA]:[M] ratio represented with black dots indicates the ratio at which precipitation was observed.

Based on the inability to obtain a point of DNA binding saturation due to the low solubility of the complexes and/or the formation of insoluble DNA aggregates, binding constants could not be calculated and the DNA binding studies reported will have to be viewed as only qualitative in nature.

5.3 Conclusions

In vitro studies show that the binuclear palladacycles were far more active than the mononuclear palladacycles. This was most likely due to the low solubility of the mononuclear complexes. The significantly lower IC_{50} values of the binuclear palladacycles were attributed to improved solubility and the ability to form flexible adducts with DNA. Furthermore, the presence of two metal centres could result in improved electrostatic interactions with the DNA. Interestingly, the mononuclear complexes were more cytotoxic towards human breast adenocarcinoma MDA-MB231 (triple negative) cells which are notoriously difficult to treat, whilst the binuclear complexes showed no selectivity between the different cell lines. Western blot assays showed that the palladacycles induce DNA double strand breaks and apoptosis.

DNA binding studies using electrophoresis and various spectroscopic techniques suggested that all of the palladacycles interact with DNA in a similar manner. The data obtained from these studies showed that the palladacycles bind to DNA in a mode different to that of cisplatin. The data also showed that the palladacycles induced the formation of insoluble aggregates and that the palladacycles possibly induce a B→Z form transition in the DNA. Furthermore, considering the data obtained and the reported literature trends, the results of this study suggested that the most likely form of DNA binding present is an electrostatic binding mode. Since the palladacycles are neutral, the nature of the proposed electrostatic interaction is uncertain, however, from the NMR data, it is clear that PTA ligand dissociation can be ruled out. Furthermore, hydrolysis of the Pd-Cl bond was proposed, as this process would result in a cationic species, but further studies are required to probe this experimentally.

5.4 Materials and Methods

Calf thymus DNA (CT DNA), ethidium bromide and trisodium citrate, tris(hydroxymethyl)aminomethane were obtained from Sigma Aldrich. Salmon sperm DNA solution was obtained from Thermo Scientific. Boric acid and DMSO were obtained from Merck.

Sodium chloride and bromophenol blue were obtained from Saarchem. Glycerin was obtained from BARRS Industrial Enterprises. Methylene blue was obtained from Riedel de Haan and methyl green was obtained from Dr. Theodore Schuchardt. Agarose gel was obtained from Bio-Rad, pBluescript cultures and EcoR 1+Hind III λ marker were obtained from the Microbiology department at Stellenbosch University. Distilled water was used to prepare buffers for DNA binding. All buffers were prepared according to standard protocols.

In vitro assays were carried out at the Tbox laboratory at the UCT Medical School, with the assistance of Prof. Prince and her students. Human MCF7 breast adenocarcinoma (estrogen receptor positive) cells were maintained in RPMI 1640 medium and human breast adenocarcinoma MDA-MB231 (triple negative) cells were maintained in Dulbecco's Modified Eagle's Medium (DMEM). Both were obtained from Highveld Biological, Lyndhurst, South Africa. Both media were supplemented with 10% fetal bovine serum (FBS), 100 U/mL penicillin, 100 μg/mL streptomycin and 1 mM sodium pyruvate. Cells were maintained at 37˚C in a 5% CO_2 – 95% air-humidified incubator. 3-(4,5-Dimethylthiazol-2-yl)-2,5-diphenyyltetrazolium bromide (MTT) assay was obtained from Roche, USA. Hybond ECL membranes were obtained from Amersham Biosciences. The primary antibodies PARP ½ (sc-7150) and phospo-H2AX (#2577) were obtained from Santa Cruz, California, USA, whilst the p38 antibody (M0800) was obtained from Sigma Aldrich. Antibody-reactive proteins were visualised using the chemiluminescence reaction (ECL) detection system from Thermo Scientific, Hudson, NH, USA.

Physiological saline solution, 1x TBE buffer, tris-HCl buffer (pH 7.2) [62], 1x loading dye and ethidium bromide stain (10 mg/mL) were prepared according to standard protocols. Plasmid DNA concentration was determined using a NanoDrop ND1000. Agarose gel electrophoresis was carried out in a horizontal midi gel apparatus system, from OMEG Scientific, connected to an Enduro 250V power supply. Photographs of the gel were taken in a dark room by UV light with a Fujifilm Finepix S2000HD camera. Photographs were processed using ImageJ 1.50b software [63]. A GBC UV/VIS 920 spectrometer was used to determine DNA concentration and UV-Vis spectra. Spectra were recorded in the range of 200-630 nm. A 10.00 mm path quartz cuvette was used with 300 $nm.min^{-1}$/ 0.133 nm step size and 2 nm slit width. Simultaneous CD and UV-Vis spectra were recorded on a Chirascan-plus CD spectrometer. Spectra were recorded in the range of 200-400 nm. A 10.00 mm path quartz cuvette was used with a scan speed of 0.3 nm s^{-1}, a step of 1 nm, response time: 0.3 s and spectral band width of 1.0 nm. Three accumulations were recorded for each sample.

Note that all DNA binding studies were carried out at metal concentrations and not complex concentrations, to ensure that the mononuclear and binuclear palladacycle data were comparable.

In vitro studies

Cytotoxicity (MTT) assay

The complex solutions were prepared by dissolution in DMSO to obtain 5 mM stock solutions. Solutions were stored at room temperature for no more than a week. Human MCF7 breast adenocarcinoma cells in RPMI 1640 medium and human breast adenocarcinoma MDA-MB231 cells in DMEM were seeded in 96-well plates at 3-6 x 10^{-3} cells per well. After 48 hours, the cells were treated with various concentrations of complex (0-1 μM) or the vehicle for 48 hours. The 3-(4,5-dimethylthiazol-2-yl)-2,5-diphenyyltetrazolium bromide (MTT) assay was then used, as described by the manufacturer's instructions: 10 μL of MTT solution was added to each well. Well plates were then incubated at 37 °C for 4 h. This was followed by addition of 100 μL solubilisation buffer (10% SDS in 0.01 M HCl) and incubation overnight at 37 °C. Absorbance at 585 nm was then determined for each well and the mean cell viability was calculated as a percentage of the mean vehicle control. The experiments were performed in triplicate and the data were used to determine the half maximal inhibitory concentration values (IC_{50}).

Western Blot assays

The complex solutions were prepared by dissolution in DMSO to obtain 0.1 and 0.2 μM stock solutions. Solutions were stored at room temperature for no more than a week. Human MCF7 breast adenocarcinoma cells in RPMI 1640 medium were plated in 6 cm petri dishes at 6 x 10^5 cells per plate. The cells were treated with the complex solutions for 24 or 48 hours. Cells were then lysed using whole cell lysis buffer (0.5 M tris-HCl, pH 6.8, 2% SDS, 10% glycerol, 1% β-mercaptoethanol and 0.02% bromophenol blue). Samples were boiled for 10 minutes. The proteins were resolved using SDS/PAGE (8-15% gels) as required. They were then transferred to Hybond ECL membranes which were then incubated with primary antibodies against PARP ½ (sc-7150), phospho-H2AX (#2577) and p38 (M0800).Thereafter, the membranes were incubated with HRP-conjugated secondary antibodies (1:5000). The antibody-reactive proteins were visualised with a chemiluminescence reaction (ECL) detection system.

DNA binding studies

Agarose gel electrophoresis

High concentration gels

pBluescript plasmid was isolated with a Zyppy plasmid isolation kit, following the product protocol. DNA concentration was determined and adjusted to 40 μg/mL with 1x TBE buffer. Stock solutions (34, 340 and 680 M) of palladacycles were prepared in DMSO and stock solutions of cisplatin were prepared in physiological saline solution and kept in the dark. Samples (15 μL) were prepared with constant DNA volume (10 μL) and the metal concentration was varied by adding the different stock solutions (5 μL) to obtain samples with final metal concentrations of 10, 100 and 200 μM. Compound control samples were prepared with buffer (10 μL) and the highest metal concentration (5 μL 680 M stock), to ensure that compounds to not fluoresce. DNA controls were prepared with DNA stock (10 μL) and DMSO or saline (5 μL) to ensure determine the effect of these reagents on the DNA. All samples were incubated in the dark for 22 hours at 37 °C.

Low concentration gels

pBluescript plasmid was isolated with a Zyppy plasmid isolation kit, following the product protocol. DNA concentration was determined and adjusted to 32 μg/mL with 1x TBE buffer. For the high concentration gels, stock solutions (33, 83, 166 and 249 M) of palladacycles were prepared in DMSO and stock solutions of cisplatin were prepared in physiological saline solution and kept in the dark. Samples (20 μL) were prepared with constant DNA volume (12.5 μL) and the metal concentration was varied by adding the different stock solutions (6.25 μL) to obtain samples with final metal concentrations of 10, 25, 50 and 75 μM. DNA controls were prepared with DNA stock (12.5 μL) and DMSO or saline (6.25 μL) to ensure determine the effect of these reagents on the DNA. All samples were incubated in the dark for 22 hours at 37 °C.

Agarose gel (0.800 g/100 mL) was prepared in 1x TBE buffer. Gel was allowed to set at room temperature for at least 1 hour. Loading dye (2 μL) was added to each sample. Samples were loaded and a λ marker was included. Gels were run for 3 hours at 80 V in 1x TBE buffer. The gel was then stained in 1x TBE buffer containing ethidium bromide stain (15 μL) for 15 min, followed by destaining in water for 5 min. Gels were then photographed under UV light (254 nm).

(Qualitative) UV-Vis spectroscopy

Calf thymus DNA was reconstituted in tris-HCl buffer (pH 7.2) for 48 hours at room temperature. DNA concentration was determined spectrophotometrically, as described by Sigma, and adjusted to 0.5 mM with tris-HCl buffer. Stock solutions (0.5 mM or 1.25 mM) of palladacycles were prepared in DMSO and stock solutions of cisplatin were prepared in physiological saline solution and kept in the dark. Samples (4.0 mL) were prepared with constant DNA volume (0.4 mL) and the metal concentration was varied by adding different volumes of the stock solution (0.0 - 0.4 mL) to obtain samples with final metal concentrations of 2.5-7.5 μM (cisplatin), 25-125 μM (**C2**) and 10-50 μM (**AJ5** and **BTC2**). Solubilising agents were added in various quantities (0.0 – 1.0 mL) to ensure a constant percentage in all samples. Finally, buffer was added to bring the sample volume to a total of 4 mL. Compound control samples were prepared in the same way, no DNA was added. All samples were incubated in the dark for 1 hour at 25 °C. Samples were scanned and the data recorded for further processing.

Attempted quantitative UV-Vis spectroscopy

Calf thymus DNA was reconstituted as described above and its concentration adjusted to 1.0 mM with tris-HCl buffer. Stock solutions (0.1 mM metal) of palladacycles were prepared in DMSO. Samples (3.0 mL) were prepared with constant metal concentration (10 μM; 0.3 mL of 0.1 mM stock solution) and constant buffer volume (2.7 mL) to obtain samples with final metal concentrations of 10 μM. The DNA concentration was varied by adding different volumes of the stock solution (2-10 μL). All samples were mixed by inversion of the cuvettes and were then incubated in the cell holder for 5 minutes at 25 °C. Samples were scanned and the data recorded for further processing.

CD spectroscopy

Calf thymus DNA was reconstituted and the concentration was determined as for the UV-Vis spectroscopy assay. Samples (1.0 mL) were prepared as described above, however, the quantities were adjusted to obtain a final sample volume of 1 mL. All samples were incubated in the dark for 1 hour at 25 °C. Samples were scanned at 25 °C and the data recorded for further processing.

Attempted DNA binding study via NMR spectroscopy

Salmon sperm DNA solution (10 mg/mL) was used as received. A stock solution of **C6** in DMSO-d6 (2 mg/mL) was prepared. Samples were prepared as 20% D_2O in DMSO-d6 with a total volume of 1 mL. Samples were scanned at 25 °C and the data recorded for further processing. NMR (^{19}F and ^{31}P: 400 MHz) spectra were recorded on Varian NMR spectrometer at 273 K and chemical shifts are referenced relative to external standards. Trichlorofluoromethane ($CFCl_3$) was used for the ^{19}F NMR and 85% phosphoric acid (H_3PO_4) for ^{31}P NMR. Chemical shifts (δ) and coupling constants (*J*) are reported in ppm and Hertz (Hz), respectively.

5.5 References

1. D. D. Allen, R. Caviedes, A. M. Cárdenas, T. Shimahara, J. Segura-Aguilar and P. A. Caviedes, *Drug Dev. Ind. Pharm.*, 2005, **31**, 757-768.
2. A. P. Li, *Drug Discov. Today Technol.*, 2005, **2**, 179-185.
3. R. H. Shoemaker, *Nat. Rev. Cancer*, 2006, **6**, 813-823.
4. National Cancer Institute: Developmental Therapeutics Program. Accessed at http://dtp.nci.nih.gov/index.html on June 24, 2013.
5. G. Fotakis and J. A. Timbrell, *Toxicol. Lett.*, 2006, **160**, 171-177.
6. T. Mosmann, *J. Immunol. Methods*, 1983, **65**, 55-63.
7. S. Ray, R. Mohan, J. K. Singh, M. K. Samantaray, M. M. Shaikh, D. Panda and P. Ghosh, *J. Am. Chem. Soc.*, 2007, **129**, 15042-15053.
8. T. Mahmood and P.-C. Yang, *N. Am. J. Med. Sci.*, 2012, **4**, 429-434.
9. J. Reineke, Western Blot Analysis. In *Nanotoxicity methods and protocols,* **926**, 87–97. New York: Humana Press, 2012.
10. C. Moore, *Introduction to Western Blotting*, Kidlington, Oxford: MorphoSys UK Ltd., 2009.
11. Thermo Scientific, *Western Blotting Handbook and Troubleshooting Tools*, Rockford, Illinois: Thermo Fisher Scientific Inc., 2010.
12. M. Tanaka, H. Kataoka, S. Yano, H. Ohi, K. Kawamoto, T. Shibahara, T. Mizoshita, Y. Mori, S. Tanida, T. Kamiya and T. Joh, *BMC Cancer*, 2013, **13**, 237-245.
13. E. Ulukaya, F. M. Frame, B. Cevatemre, D. Pellacani, H. Walker, V. M. Mann, M. S. Simms, M. J. Stower, V. T. Yilmaz and N. J. Maitland, *PLoS ONE*, 2013, **8**, e64278.
14. O. Kennard, *Pure Appl. Chem.*, 1993, **65**, 1213-1222.
15. A. H-J. Wang, *Curr. Opin. Struct. Biol.*, 1992, **2**, 361-368.

16. Z. Cheng-Yong, X. Xiao-Li and Y. Pin, *Biochemistry (Moscow, Russ. Fed.)*, 2007, **72**, 37-43.
17. V. González-Ruiz, A. I. Olives, M. A. Martín, P. Ribelles, M. T. Ramos and J. C. Menéndez. *An Overview of Analytical Techniques Employed to Evidence Drug-DNA Interactions. Applications to the Design of Genosensors, Biomedical Engineering, Trends, Research and Technologies*, Dr. Sylwia Olsztynska (Ed.). InTech, 2011.
18. C. J. Jones and J. Thornback, *Medicinal applications of coordination chemistry,* The Royal Society of Chemistry, 2007.
19. E. Katsarou, A. Kolstad, N. Hadjiliadis and E. Sletten, *J. Inorg. Biochem.*, 1998, **70**, 265-269.
20. S. Steinkopf, A. Garoufis, W. Nerdal and E. Sletten, *Acta Chim. Scand.*, 1995, **49**, 495-502.
21. E. Gao, C. Liu, M. Zhu, H. Lin, Q. Wu and L. Liu, *Anticancer Agents Med. Chem*. 2009, **9**, 356-368.
22. T. Boulikas, A. Pantos, E. Bellis and P. Christofis, *Cancer Ther.*, 2007, **5**, 537-583.
23. Y. Cao and X.-w. He, *Spectrochim. Acta, Part A*, 1998, **54**, 883-892.
24. M. Komorowska, S. Olsztynska-Janus and In Tech (Croatia), *Biomedical engineering, trends, research and Technologies*, Rijeka, Croatia : InTech, 2011.
25. P. L. Hamilton and D. P. Arya, *Nat. Prod. Rep.*, 2012, **29**, 134-143.
26. C. Metcalfe and J. A. Thomas, *Chem. Soc. Rev.*, 2003, **32**, 215-224.
27. D. Suh and J. B. Chaires, *Bioorg. Med. Chem.*, 1995, **3**, 723-728.
28. S. K. Kim and B. Nordén, *FEBS Lett.*, 1993, **315**, 61-64.
29. N. J. Turro, J. K. Barton and D. A. Tomalia, *Acc. Chem. Res.*, 1991, **24**, 332-340.
30. L-M. Chen, J. Liu, J-C. Chen, C-P. Tan, S. Shi, K-C. Zheng and L-N. Ji, *J. Inorg. Biochem.*, 2008, **102**, 330-341.
31. J. Albert, R. Bosque, M. Cadena, L. D'Andrea, J. Granell, A. González, J. Quirante, C. Calvis, R. Messeguer, J. Badiá, L. Baldomà, T. Calvet and M. Font-Bardia, *Organometallics*, 2014, **33**, 2862-2873.
32. Electrophoresis. Accessed at www.bioinformatics.nl/molbi/SimpleCloningLab/electrophoresis.htm on July 24, 2015.
33. How to identify supercoils, nicks and circles in plasmid preps. Accessed at http://bitesizebio.com/13524/how-to-identify-supercoils-nicks-and-circles-in-plasmid-preps/ on July 24, 2015.

34. K. Wilson and T. Walker, *Principles and Techniques of Practical Biochemistry*, Cambridge, Cambridge University Press, 2000.
35. R. R. Sinden, *DNA structure and function*. San Diego, Academic Press, 1994.
36. X. Yang, Y. Liu, S. Yao, Y. Xia, Q. Li, W. Zheng, L. Chen and J. Liu, *J. Coord. Chem.*, 2011, **64**, 1491-1502.
37. Y-M. Chang, C. K-M. Chen and M-H. Hou, *Int. J. Mol. Sci.*, 2012, **13**, 3394-3413.
38. M. C. da Rocha, A. M. Santana, S. R. Ananias, E. T. De Almeida, A. E. Mauro, M. C. P. Placeres and I. Z. Carlos, *J. Braz. Chem. Soc*., 2007, **18**, 1473-1480.
39. J. D. Higgins III, L. Neely and S. Fricker, *J. Inorg. Biochem.*, 1993, **49**, 149-156.
40. R. Vrzal, P. Štarha, Z. Dvořák and Z. Trávníček, *J. Inorg. Biochem.*, 2010, **104**, 1130-1132.
41. T. L. Fuller and R. G. Canada, *Cancer Chemother. Pharmacol.*, 1999, **44**, 249-252.
42. S. Aliwaini, J. Peres, W. L. Kröger, A. Blanckenberg, J. de la Mare, A. L. Edkins, S. Mapolie and S. Prince, *Cancer Lett.*, 2015, **357**, 206-218.
43. M. Frik, J. Jiménez, V. Vasilevski, M. Carreira, A. de Almeida, E. Gascón, F. Benoit, M. Sanaú, A. Casini and M. Contel, *Inorg. Chem. Front.*, 2014, **1**, 231-241.
44. M. Kobayashi, T. Kusakawa, M. Saito, S. Kaji, M. Oomura, S. Iwabuchi, Y. Morita, Q. Hasan and E. Tamiya, *Electrochem. Commun.*, 2004, **6**, 337-343.
45. J. Pelta, F. Livolant and J.-L. Sikorav, *J. Biol. Chem.*, 1996, **271**, 5656-5662.
46. M. A. Kastenholz, T. U. Schwartz and P. H. Hünenberger, *Biophys. J.*, 2006, **91**, 2976-2990.
47. M. Rosa, R. Dias, M. de Graça Miguel and B. Lindman, *Biomacromolecules*, 2005, **6**, 2164-2171.
48. M. J. Waring, *J. Mol. Biol.*, 1965, **13**, 269-282.
49. J.-B. LePecq and C. Paoletti, *J. Mol. Biol.*, 1967, **27**, 87-106.
50. A. Tarushi, P. Christofis and G. Psomas, *Polyhedron*, 2007, **26**, 3963-3972.
51. M. Aslanoğlu and N. Öge, *Turk. J. Chem.*, 2005, **29**, 477-485.
52. J.-B. Lepecq and C. Paoletti, *J. Mol. Biol.*, 1967, **27**, 87-106.
53. P.O. Vardevanyan, A. P. Antonyan, M. A. Parsadanyan, M. A. Shahinyan and L. A. Hambardzumyan, *J. Appl. Spectrosc.*, 2013, **80**, 595-599.
54. S. K. Kim and B. Nordén, *FEBS*, 1993, **315**, 61-64.
55. Q. Guo, M. Lu, L. A. Marky and N. R. Kallenbach, *Biochemistry*, 1992, **31**, 2451-2455.
56. Turbidimetric Solubility Assay. Accessed at http://www.cyprotex.com/physicochemicalprofiling/physicochemical-properties/turbidimetric-solubility on August 20, 2015.

57. N. C. Garbett, P. A. Ragazzon and J. B. Chaires, *Nature Protocols*, 2007, **2**, 3166-3172.
58. N. Shahabadi, F. Darabi, M. Maghsudi and S. Kashanian, *DNA Cell Biol.*, 2010, **29**, 329-336.
59. J. L. Butour, S. Wimmer, F. Wimmer and P. Castan, *Chem. Biol. Interact.*, 1977, **104**, 165-178.
60. Y.-M. Chang, C. K.-M. Chen and M.-H. Hou, *Int. J. Mol. Sci.*, 2012, **13**, 3394-3413.
61. X. Yang, Y. Liu, S. Yao, Y. Xia, Q. Li, W. Zheng, L. Chen and J. Lui, *J. Coord. Chem.*, 2011, **64**, 1491-1502.
62. Quiagen, *Quiagen bench guide*, QUIAGEN handbooks, protocols, and other resources. Accessed at www.qiagen.com/literature/litrequest.asp on September 18, 2012.
63. Rasband, W.S., ImageJ, U. S. National Institutes of Health, Bethesda, Maryland, USA, http://imagej.nih.gov/ij/, 1997-2015.

Chapter 6
Conclusions and future work

6.1 Concluding remarks

Mononuclear and binuclear (unsubstituted and substituted) palladacycles, were designed and synthesised based on the structure and properties of **AJ5** (Figure 6.1), a binuclear palladacycle with significant anti-cancer activity [1;2].

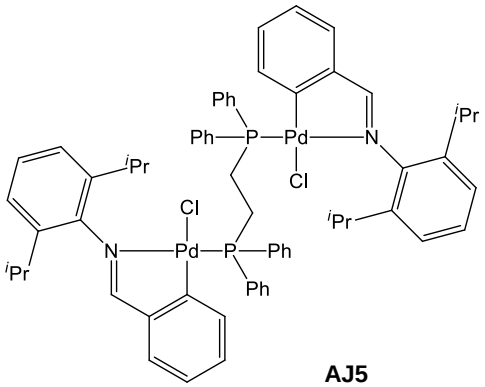

AJ5

Figure 6.1: Promising palladacycle, AJ5.

The mononuclear series of novel PTA-based palladacycles was synthesised and characterised successfully. Despite the fact that the complexes are mononuclear and have a water-soluble phosphine ligand, PTA, they were found to be insoluble in water and generally less soluble than **AJ5** in organic solvents. Variable temperature ^{1}H NMR spectroscopy showed that these palladacycles exhibit a reversible symmetric site-exchange of the methyls of the isopropyl groups via rotation of the 2,6-diisopropylaniline moiety about the N-C bond. This was confirmed by employing a computational model which showed that the experimental data lie within the 95% confidence limits. Slight deviations in the expected signal shifts were attributed to concentration-dependent chemical exchange processes, of which dimerisation by imine ligand dissociation was supported by literature precedence and ESI-MS dimer fragments, and the formation of a non-covalent dimer by PTA self-association was shown to be feasibly by a computational model of the aggregate. The ability of these species to undergo chemical exchange processes was linked to the tertiary phosphine ligand, PTA, specifically, its small cone angle and the nitrogen donor atoms.

Furthermore, the “ortho effect” was shown to account for the influence of the ortho-substituents on the free energy of activation.

Two series of binuclear palladacycles with bridging bisphosphine ligands and in the case of the substituted series, an ethylene glycol-type tether, were successfully synthesised and characterised. As expected, the substituted complexes showed significantly improved solubility in organic solvents compared to the unsubstituted complexes and **AJ5**. However, in spite of the enhanced solubility in non-aqueous media, none of the binuclear palladacycles were water-soluble.

In vitro evaluation of the mono- and binuclear palladacycles was performed against mammalian breast cancer cell lines, MCF7 and MDA-MB231. These studies showed that most of the complexes are cytotoxic, with the binuclear palladacycles showing better activity than the mononuclear palladacycles. IC_{50} values of some of the palladacycles were better than those of cisplatin (below 20 μM) and the IC_{50} values for the substituted-binuclear palladacycle, **BTC2** (Figure 6.2), were found to be comparable to those of **AJ5**. The complexes were found to induce DNA damage and apoptosis. DNA binding studies were carried out on the most active palladacycle in each series to determine the mode of action. DNA binding studies by ultraviolet-visible-, circular dichroism- and NMR spectroscopy suggest that all of the palladacycles bind to DNA in a mode different from cisplatin. The most likely mode of DNA binding was identified as an electrostatic binding mode. Thus, the formation of a cationic species was proposed to form via hydrolysis of the Pd-Cl bond (Figure 6.3), a commonly reported process for platinum anti-cancer agents. Additionally, attempts were made to determine the DNA binding constants of the palladacycles, however these quantitative studies were aborted, as the compounds were not suitably soluble.

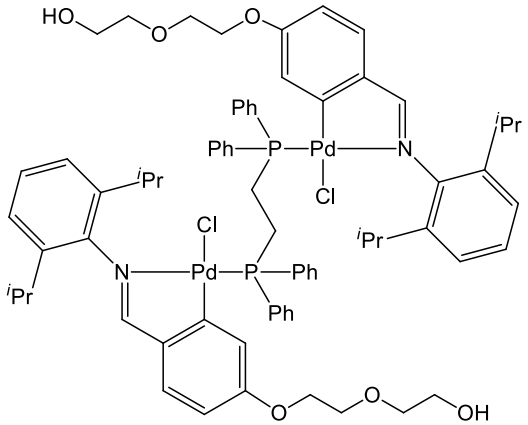

Figure 6.2: Modified palladacycle, BTC2.

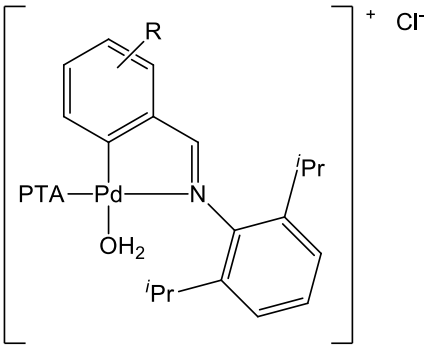

Figure 6.3: Proposed cationic species which can bind to DNA through electrostatic interactions.

In summary, a range of palladacycles with varying degrees of solubility and water-tolerance were design and synthesised successfully. A number of these palladacycles are more active, *in vitro*, than cisplatin, whilst **BTC2**, a binuclear dppe-bridged palladacycle with an ethylene glycol-type tether, exhibits comparable biological activity to **AJ5** and was found to be more soluble than **AJ5**. Furthermore, the results from the *in vitro* assays were used to identify the most promising palladacycles in each of the three series and then employed these palladacycles in DNA binding studies in an attempt determine their mode of action. The most likely mode of action was determined to be an electrostatic DNA binding mode.

6.2 Future work

From the review in Chapter 1, entitled “Palladium and its complexes as potential anti-cancer agents”, it is clear that palladium complexes could provide viable alternatives to the current metal-based anti-cancer drugs, both in terms of reduced toxicity and the ability to overcome cisplatin drug resistance. The literature provides a vast library of these palladium complexes, including some examples where the palladium complexes are significantly more active than cisplatin, yet not as toxic. Despite the overwhelming number of promising palladium complexes in the literature, there has been limited success with these complexes beyond the laboratory. This lack of advancement has been ascribed to the absence of data regarding the mode of action of these drugs. This need for more in-depth information justifies the ongoing research in this field.

The aim of this project was to synthesise novel water-soluble palladacycles for testing as anti-cancer agents. The approach employed was to impart enhanced water solubility to the palladium complexes by introducing hydrophilic functional groups on the aldehyde starting materials. Furthermore, the bridged palladacycles were cleaved with the hydrophilic tertiary phosphine, PTA

or bis(tertiary phosphine) ligands, in an attempt to increase water-solubility whilst maintaining biological activity.

6.2.1 Solubility

In terms of the latter aim, initially the use of the water-soluble phosphine, PTA, as a ligand was investigated, but this did not lead to any significant enhancement of water solubility of the complexes. In contrast to this, the incorporation of the hydrophilic ethylene glycol-type tether led to a considerable increase in solubility without significantly altering the biological activity of the compounds. However, complete water-solubility was not achieved. Comparison of the solubilities and biological activity of the palladacycles (Figure 6.4) allowed us to come to the following conclusions: The most soluble complexes (in DMSO), **BC4** and **BTC4**, were completely inactive as they did not tolerate water well, whilst the most water tolerant (lowest % DMSO in water/DMSO mixture required to keep complex in solution) complex, **BTC1**, was also not the most active complex. Furthermore, comparison of the data for the mononuclear palladacycles show that **C2** and **C3** are the most active biologically, yet both complexes have low solubility and low water tolerance. Similarly, **AJ5** which has significant biological activity has low solubility, but better water tolerance. Contrastingly, **BTC2** has high solubility but low water tolerance, yet its biological activity in on par with that of **AJ5**. These data confirmed that water-solubility is not the main factor controlling biological activity.

From the literature, it is known that the lipophilicity of compounds influences tissue permeability. As reported by Garcia *et al.*, tissue permeability of a compound affects the localisation of the compound in the targeted tissue and the capacity of the compound to bind to biomolecules, making it one of the most influential properties for biological activity. Therefore, the lipophilicity of the palladacycles should be determined and compared with the biological data to see if there is a correlation. The simplest method for determining the lipophilicity is by using a shake-flask method. The *n*-octanol/water partition coefficient (log $P_{o/w}$) is measured and the higher the value, the more lipophilic the compound [3-5]. Should there be a correlation, the data can be used to improve the design of these palladacycles.

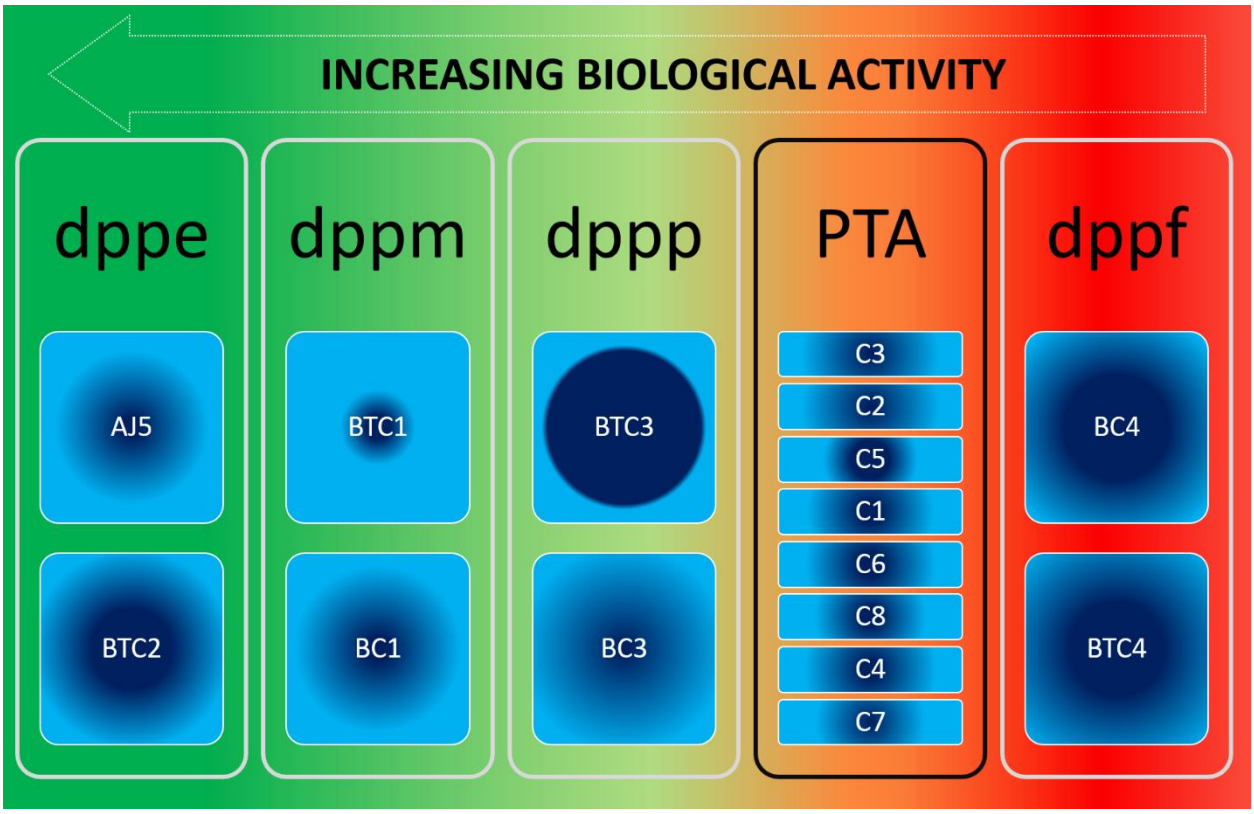

Figure 6.4: Biological activity and solubility trends of palladacycles, where palladacycles are grouped according to phosphine ligands. The mononuclear palladacycles are grouped in a black box, whilst the binuclear palladacycles are grouped in white boxes. For the solubility trends, dark blue represents solubility in DMSO and light blue represents water tolerance in water/DMSO mixtures

Furthermore, the incorporation of alternative water-soluble moieties should also be investigated for the mononuclear palladacycles. Some possibilities include replacing the 2,6-diisopropylaniline moiety with more soluble analogues, such as 4-aminophenol [6] and sulfanilic acid [7]. These analogues are also less sterically hindered, so perhaps a series of palladacycles can be prepared where the effects of varying solubility and steric bulk of the aniline ring moiety on the solubility and biological activity of the palladacycles are evaluated, as shown in Figure 6.5. Should this be effective, it could be implemented for the binuclear palladacycles as well.

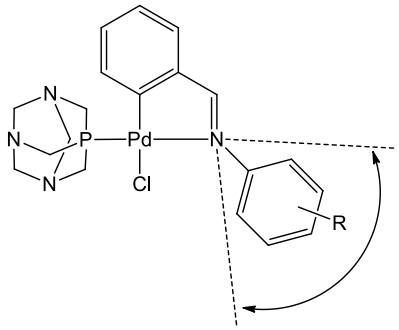

Figure 6.5: Proposed series of palladacycles with different aniline moieties, varying both solubility (R) and steric bulk.

Furthermore, the lipophilicity and hydrophilicity of **BTC2** (and the other palladacycles) can be varied, by changing the length and consequently the oxygen atom content of the ethylene glycol-type tether [8]. Since the tether did not appear to influence the biological activity of the palladacycles, this may be an effective way in which to tweak the solubility to facilitate easier *in vitro* testing of the palladacycles.

6.2.2 NMR spectroscopy study to confirm the concentration dependent processes

As mentioned in the conclusions above, three chemical exchange processes were proposed to occur in the PTA palladacycle system, a site-exchange, PTA-self aggregation and dimerisation by imine ligand dissociation. Both the site-exchange and dimerisation processes were attributed to the small cone angle of PTA, whilst the aggregation process via PTA self-association was attributed to the presence of the nitrogen donor atoms and the consequent distribution of electron density on the ligand surface. The site-exchange process was proven satisfactorily, but the concentration dependent processes were a bit more complex. Both processes were shown to be feasibly and the dimerisation was supported by literature precedence and the detection of corresponding dimer fragments in the ESI-MS data, but the shifts in the imine signal were smaller than expected. Furthermore, no experimental support was obtained for the aggregation via PTA self-association.

Thus, further modelling studies are proposed, where the changes in bond distances and electron density on the atoms are studied more in-depth. Furthermore, the site-exchange computational model should also be adjusted to include parameters that account for the observed concentration effects, possible aggregation and dimerisation via dissociation of the imine ligand. This would require rewriting of the calculations for the in-house program, NMRfitv12, used for modelling the site-exchange process, which is outside the scope of this project. However, obtaining a fit for all three processes occurring simultaneously or for the site-exchange occurring simultaneously with either an aggregation process or a dimerisation process would provide more concrete evidence to support these proposals.

6.2.3 DNA binding studies

Based on the literature review in Chapter 1, it is clear that there is still very little known about the mode of action of palladium compounds, despite the large quantity of data highlighting the potential of these compounds as anti-cancer agents. This gap in the understanding of the mode of action of palladium compounds has been offered as the reason why the progress of palladium compounds has not progressed beyond pre-clinical work. Therefore, as stated in the aims of this project, the DNA binding studies were carried out to determine the mode of action of the palladacycles and hopefully provide insight into the role of the various moieties and functional groups in the interaction of these metallodrugs with DNA. The four techniques employed each pointed to a number of different DNA binding interactions, but taken together, the results suggested an electrostatic DNA binding mode, for which a possible active species – an aquated cationic species – was proposed. Thus, it is proposed that hydrolysis studies be performed on the palladacycles.

A very simple assay was developed by Cui and Mester for the hydrolysis and detection of cisplatin and its hydrates [9], where varying concentrations of cisplatin were incubated in water at 37 °C for 1,2,3,4,5 and 24 hours. Samples were analysed by both ESI-MS and the results were further confirmed with LC/ESI-MS. Cisplatin and its hydrates were unambiguously identified with LC/ESI-MS. This would be a simple way to determine if the proposed cationic species forms.

6.3 References

1. S. Aliwaini, A. J. Swarts, A. Blanckenberg, S. F. Mapolie and S. Prince, *Biochem. Pharmacol.*, 2013, **86**, 1650-1663.
2. S. Aliwaini, J. Peres, W. L. Kröger, A. Blanckenberg, J. de la Mare, A. L. Edkins, S. Mapolie and S. Prince, *Cancer Lett.*, 2015, **357**, 206-218.
3. T. S. Morais, F. C. Santos, T. F. Jorge, L. Côrte-Real, P. J. Amorim Madeira, F. Marques, M. Paula Robalo, A. Matos, I. Santos and M. H. Garcia, J. *Inorg. Biochem.*, 2014, **130**, 1-14.
4. E. Rutkowska, K. Pajak and K. Jóźwiak, *Acta Pol. Pharm.*, 2013, **70**, 3-18.
5. J. A. Arnott and S. Lobo Planey, *Expert Opin. Drug Discov*., 2012, **7**, 863-875.
6. National Center for Biotechnology Information. PubChem Compound Database; CID=403. Accessed at https://pubchem.ncbi.nlm.nih.gov/compound/403 on January 27, 2016.

7. National Center for Biotechnology Information. PubChem Compound Database; CID=8479. Accessed at https://pubchem.ncbi.nlm.nih.gov/compound/8479 on January 27, 2016.
8. J. Albert, R. Bosque, M. Cadena, L. D'Andrea, J. Granell, A. González, J. Quirante, C. Calvis, R. Messeguer, J. Badiá, L. Baldomà, T. Calvet and M. Font-Bardia, *Organometallics*, 2014, **33**, 2862-2873.
9. M. Cui and Z. Mester, *Rapid Commun. Mass Spectrom.*, 2003, **17**, 1517-1527.

Appendix 1
Crystallography data for Chapter 2 and Chapter 4

A1.1 Crystal data for **L7**

Table A1.1: Bond distances (Å) in the crystal structure of L7.

C1A—C2A	1.395(2)	C14A—C15A	1.525(2)
C1A—C6A	1.399(2)	C14A—C16A	1.534(2)
C1A—C7A	1.480(2)	C14A—H14A	1.0000
C1B—C2B	1.398(2)	C14B—C15B	1.532(2)
C1B—C6B	1.393(2)	C14B—C16B	1.525(5)
C1B—C7B	1.485(2)	C14B—H14B	1.0000
C2A—C3A	1.383(2)	C15A—H15A	0.9800
C2B—C3B	1.385(2)	C15A—H15B	0.9800
C3A—C4A	1.383(2)	C15A—H15C	0.9800
C3A—H3A	0.9500	C15B—H15D	0.9800
C3B—C4B	1.384(2)	C15B—H15E	0.9800
C3B—H3B	0.9500	C15B—H15F	0.9800
C4A—C5A	1.390(2)	C16A—H16A	0.9800
C4A—H4A	0.9500	C16A—H16B	0.9800
C4B—C5B	1.389(2)	C16A—H16C	0.9800
C4B—H4B	0.9500	C16B—H16D	0.9800
C5A—C6A	1.385(2)	C16B—H16E	0.9800
C5A—H5A	0.9500	C16B—H16F	0.9800
C5B—C6B	1.387(2)	C17A—C18A	1.530(2)
C5B—H5B	0.9500	C17A—C19A	1.527(2)
C6A—H6A	0.9500	C17A—H17A	1.0000
C6B—H6B	0.9500	C17B—C18B	1.533(2)
C7A—H7A	0.9500	C17B—C19B	1.537(2)
C7B—H7B	0.9500	C17B—H17B	1.0000
C8A—C9A	1.405(2)	C18A—H18D	0.9800
C8A—C13A	1.403(2)	C18A—H18E	0.9800
C8B—C9B	1.407(2)	C18A—H18F	0.9800
C8B—C13B	1.407(2)	C18B—H18G	0.9800
C9A—C10A	1.390(2)	C18B—H18H	0.9800

C9A—C17A	1.518(2)	C18B—H18I	0.9800
C9B—C10B	1.396(2)	C19A—H19D	0.9800
C9B—C17B	1.520(2)	C19A—H19E	0.9800
C10A—C11A	1.387(2)	C19A—H19F	0.9800
C10A—H10A	0.9500	C19B—H19G	0.9800
C10B—C11B	1.381(2)	C19B—H19H	0.9800
C10B—H10B	0.9500	C19B—H21I	0.9800
C11A—C12A	1.384(2)	N1A—C2A	1.472(2)
C11A—H11A	0.9500	N1A—O2A	1.232(2)
C11B—C12B	1.387(2)	N1B—C2B	1.467(2)
C11B—H11B	0.9500	N1B—O2B	1.226(2)
C12A—C13A	1.398(2)	N2A—C7A	1.263(2)
C12A—H12A	0.9500	N2A—C8A	1.431(2)
C12B—C13B	1.396(2)	N2B—C7B	1.268(2)
C12B—H12B	0.9500	N2B—C8B	1.431(2)
C13A—C14A	1.522(2)	O1A—N1A	1.225(2)
C13B—C14B	1.523(2)	O1B—N1B	1.229(1)

Table A1.2: Bond angles (°) in the crystal structure of L7.

O1A—N1A—O2A	124.5(1)	O2B—N1B—O1B	123.4(1)
O1A—N1A—C2A	117.6(1)	O2B—N1B—C2B	118.0(1)
O2A—N1A—C2A	117.9(1)	O1B—N1B—C2B	118.7(1)
C2A—C1A—C6A	116.8(1)	C6B—C1B—C2B	116.8(1)
C2A—C1A—C7A	122.1(1)	C6B—C1B—C7B	118.3(1)
C6A—C1A—C7A	121.0(1)	C2B—C1B—C7B	124.8(1)
C7A—N2A—C8A	116.9(1)	C7B—N2B—C8B	118.1(1)
C3A—C2A—C1A	123.5(1)	C3B—C2B—C1B	122.9(1)
C3A—C2A—N1A	116.8(1)	C3B—C2B—N1B	117.5(1)
C1A—C2A—N1A	119.7(1)	C1B—C2B—N1B	119.5(1)
C2A—C3A—C4A	118.2(1)	C4B—C3B—C2B	118.8(1)
C2A—C3A—H3A	120.9	C4B—C3B—H3B	120.6
C4A—C3A—H3A	120.9	C2B—C3B—H3B	120.6
C3A—C4A—C5A	120.2(1)	C3B—C4B—C5B	119.9(1)
C3A—C4A—H4A	119.9	C3B—C4B—H4B	120.1
C5A—C4A—H4A	119.9	C5B—C4B—H4B	120.1
C6A—C5A—C4A	120.6(1)	C6B—C5B—C4B	120.3(1)
C6A—C5A—H5A	119.7	C6B—C5B—H5B	119.8
C4A—C5A—H5A	119.7	C4B—C5B—H5B	119.8
C5A—C6A—C1A	120.7(1)	C5B—C6B—C1B	121.3(1)
C5A—C6A—H6A	119.7	C5B—C6B—H6B	119.4
C1A—C6A—H6A	119.7	C1B—C6B—H6B	119.4

N2A—C7A—C1A	121.1(1)	N2B—C7B—C1B	119.5(1)
N2A—C7A—H7A	119.4	N2B—C7B—H7B	120.2
C1A—C7A—H7A	119.4	C1B—C7B—H7B	120.2
C13A—C8A—C9A	121.7(1)	C9B—C8B—C13B	122.3(1)
C13A—C8A—N2A	121.3(1)	C9B—C8B—N2B	116.9(1)
C9A—C8A—N2A	116.9(1)	C13B—C8B—N2B	120.4(1)
C10A—C9A—C8A	118.2(1)	C10B—C9B—C8B	117.6(1)
C10A—C9A—C17A	122.1(1)	C10B—C9B—C17B	122.4(1)
C8A—C9A—C17A	119.8(1)	C8B—C9B—C17B	119.9(1)
C11A—C10A—C9A	121.1(1)	C11B—C10B—C9B	121.1(1)
C11A—C10A—H10A	119.5	C11B—C10B—H10B	119.4
C9A—C10A—H10A	119.5	C9B—C10B—H10B	119.4
C12A—C11A—C10A	119.8(1)	C10B—C11B—C12B	120.2(1)
C12A—C11A—H11A	120.1	C10B—C11B—H11B	119.9
C10A—C11A—H11A	120.1	C12B—C11B—H11B	119.9
C11A—C12A—C13A	121.4(1)	C11B—C12B—C13B	121.3(1)
C11A—C12A—H12A	119.3	C11B—C12B—H12B	119.3
C13A—C12A—H12A	119.3	C13B—C12B—H12B	119.3
C12A—C13A—C8A	117.6(1)	C12B—C13B—C8B	117.2(1)
C12A—C13A—C14A	119.7(1)	C12B—C13B—C14B	122.0(1)
C8A—C13A—C14A	122.7(1)	C8B—C13B—C14B	120.6(1)
C13A—C14A—C15A	111.5(1)	C13B—C14B—C16B	114.2(1)
C13A—C14A—C16A	110.7(1)	C13B—C14B—C15B	109.7(1)
C15A—C14A—C16A	110.7(1)	C16B—C14B—C15B	109.6(1)
C13A—C14A—H14A	108.0	C13B—C14B—H14B	107.7
C15A—C14A—H14A	108.0	C16B—C14B—H14B	107.7
C16A—C14A—H14A	108.0	C15B—C14B—H14B	107.7
C14A—C15A—H15A	109.5	C14B—C15B—H15E	109.5
C14A—C15A—H15B	109.5	C14B—C15B—H15F	109.5
H15A—C15A—H15B	109.5	H15E—C15B—H15F	109.5
C14A—C15A—H15C	109.5	C14B—C15B—H15D	109.5
H15A—C15A—H15C	109.5	H15E—C15B—H15D	109.5
H15B—C15A—H15C	109.5	H15F—C15B—H15D	109.5
C14A—C16A—H16A	109.5	C14B—C16B—H16D	109.5
C14A—C16A—H16B	109.5	C14B—C16B—H16F	109.5
H16A—C16A—H16B	109.5	H16D—C16B—H16F	109.5
C14A—C16A—H16C	109.5	C14B—C16B—H16E	109.5
H16A—C16A—H16C	109.5	H16D—C16B—H16E	109.5
H16B—C16A—H16C	109.5	H16F—C16B—H16E	109.5
C9A—C17A—C19A	111.7(1)	C9B—C17B—C18B	113.0(1)
C9A—C17A—C18A	112.6(1)	C9B—C17B—C19B	112.0(1)
C19A—C17A—C18A	110.6(1)	C18B—C17B—C19B	109.6(1)

C9A—C17A—H17A	107.2	C9B—C17B—H17B	107.3
C19A—C17A—H17A	107.2	C18B—C17B—H17B	107.3
C18A—C17A—H17A	107.2	C19B—C17B—H17B	107.3
C17A—C18A—H18D	109.5	C17B—C18B—H18G	109.5
C17A—C18A—H18F	109.5	C17B—C18B—H18I	109.5
H18D—C18A—H18F	109.5	H18G—C18B—H18I	109.5
C17A—C18A—H18E	109.5	C17B—C18B—H18H	109.5
H18D—C18A—H18E	109.5	H18G—C18B—H18H	109.5
H18F—C18A—H18E	109.5	H18I—C18B—H18H	109.5
C17A—C19A—H19D	109.5	C17B—C19B—H19G	109.5
C17A—C19A—H19E	109.5	C17B—C19B—H19H	109.5
H19D—C19A—H19E	109.5	H19G—C19B—H19H	109.5
C17A—C19A—H19F	109.5	C17B—C19B—H21I	109.5
H19D—C19A—H19F	109.5	H19G—C19B—H21I	109.5
H19E—C19A—H19F	109.5	H19H—C19B—H21I	109.5

A1.2 Crystal data for **B6**

Table A1.3: Bond distances (Å) in the crystal structure of B6.

C1—C2	1.384(3)	C14—C15	1.529(4)
C1—C6	1.413(2)	C14—C16	1.521(4)
C1—C7	1.438(2)	C14—C21	1.526(2)
C2—C3	1.374(3)	C14—C22	1.526(2)
C3—C4	1.389(3)	C17—C18	1.522(3)
C4—C5	1.392(3)	C17—C19	1.525(3)
C5—C6	1.389(2)	Cl1—Pd1^{i}	2.3193(4)
C8—C9	1.399(2)	F1—C2	1.361(2)
C8—C13	1.399(2)	N(1)—C(7)	1.292(2)
C9—C10	1.385(3)	N1—C8	1.439(2)
C9—C17	1.519(3)	Pd(1)—C(6)	1.975(2)
C10—C11	1.385(3)	Pd(1)—Cl(A)	2.4454(5)
C11—C12	1.382(3)	Pd(1)—Cl(1)^{i}	2.3192(4)
C12—C13	1.395(3)	Pd(1)—N(1)	2.015(1)
C13—C14	1.521(3)		

Symmetry code: (i) *-x*, *-y*, *-z*.

Table A1.4: Bond angles (°) in the crystal structure of B6.

C2—C1—C6	119.5(2)	C12—C13—C8	117.1(2)
C2—C1—C7	125.1(2)	C12—C13—C14	121.2(2)
C6—C1—C7	115.3(2)	C13—C14—C15	112.0(3)
C3—C2—C1	122.7(2)	C13—C14—C21	111(1)
F1—C2—C1	118.4(2)	C13—C14—C22	113(1)
F1—C2—C3	118.9(2)	C16—C14—C13	110.9(3)
C2—C3—C4	117.3(2)	C16—C14—C15	110.8(3)
C3—C4—C5	122.0(2)	C16—C14—C21	125(1)
C6—C5—C4	120.0(2)	C22—C14—C15	97.2(8)
C1—C6—Pd1	112.2(1)	C22—C14—C21	112(1)
C5—C6—C1	118.5(2)	C9—C17—C18	111.9(2)
C5—C6—Pd1	129.2(1)	C9—C17—C19	110.7(2)
N1—C7—C1	115.6(2)	C18—C17—C19	111.4(2)
C9—C8—N1	117.6(2)	Pd1^{i}—Cl1—Pd1	92.75(2)
C13—C8—C9	123.2(2)	C7—N1—C8	121.4(2)
C13—C8—N1	119.1(2)	C7—N1—Pd1	115.5(1)
C8—C9—C17	121.7(2)	C8—N1—Pd1	123.0(1)
C10—C9—C8	117.1(2)	C(6)—Pd(1)—Cl(1)^{i}	95.33(5)
C10—C9—C17	121.2(2)	C(6)—Pd(1)—Cl(A)	177.25(5)
C11—C10—C9	121.4(2)	C(6)—Pd(1)—N(1)	81.37(7)
C12—C11—C10	120.2(2)	Cl(1)^{i}—Pd(1)—Cl(1)	87.25(2)
C11—C12—C13	121.1(2)	N(1)—Pd(1)—Cl(A)	96.06(4)
C8—C13—C14	121.8(2)	N(1)—Pd(1)—Cl(1)^{i}	176.68(4)

Symmetry code: (i) *-x*, *-y*, *-z*.

A1.3 Crystal data for **C1**

Table A1.5: Bond distances (Å) in the crystal structure of C1.

C1B—C2B	1.398(4)	C18A—H18B	0.9810
C1B—C6B	1.419(3)	C18A—H18C	0.9800
C1B—C7B	1.443(4)	C18B—H18D	0.9800
C2A—C1A	1.399(3)	C18B—H18E	0.9800
C2A—C3A	1.385(3)	C18B—H18F	0.9790
C2A—H2A	0.9500	C19A—H19A	0.9800
C2B—C3B	1.391(4)	C19A—H19B	0.9810
C2B—H2B	0.9500	C19A—H19C	0.9790
C3A—H3A	0.9510	C19B—H19D	0.9800
C3B—H3B	0.9490	C19B—H19E	0.9800
C4A—C3A	1.388(4)	C19B—H19F	0.9790

C4A—C5A	1.389(4)	C20A—H20A	0.9890
C4A—H4A	0.9490	C20A—H20B	0.9910
C4B—C3B	1.382(4)	C20B—H20C	0.9890
C4B—C5B	1.393(4)	C20B—H20D	0.9900
C4B—H4B	0.9500	C21A—H21A	0.9900
C5A—H5A	0.9500	C21A—H21B	0.9910
C5B—H5B	0.9500	C21B—H21C	0.9900
C6A—C1A	1.417(3)	C21B—H21D	0.9910
C6A—C5A	1.398(3)	C22A—H22A	0.9890
C6B—C5B	1.398(4)	C22A—H22B	0.9900
C7A—C1A	1.447(3)	C22B—H22C	0.9900
C7A—H7A	0.9490	C22B—H22D	0.9900
C7B—H7B	0.9490	C23A—H23A	0.9900
C8B—C9B	1.394(4)	C23A—H23B	0.9890
C8B—C13B	1.408(4)	C23B—H23C	0.9890
C9A—C8A	1.397(4)	C23B—H23D	0.9900
C9B—C10B	1.393(3)	C24A—H24A	0.9900
C9B—C14B	1.525(4)	C24A—H24B	0.9910
C10A—C9A	1.392(3)	C24B—H24C	0.9890
C10A—H10A	0.9500	C24B—H24D	0.9900
C10B—H10B	0.9500	C25A—H25A	0.9910
C11A—C10A	1.381(4)	C25A—H25B	0.9890
C11A—C12A	1.381(4)	C25B—H25C	0.9910
C11A—H11A	0.9500	C25B—H25D	0.9900
C11B—C10B	1.380(4)	N1A—C7A	1.275(3)
C11B—C12B	1.384(4)	N1A—C8A	1.441(3)
C11B—H11B	0.9500	N1B—C7B	1.286(3)
C12A—C13A	1.388(4)	N1B—C8B	1.448(3)
C12A—H12A	0.9500	N2A—C20A	1.471(3)
C12B—H12B	0.9500	N2A—C23A	1.473(4)
C13A—C8A	1.403(4)	N2A—C25A	1.462(4)
C13A—C17A	1.514(4)	N2B—C22B	1.479(3)
C13B—C12B	1.392(3)	N2B—C24B	1.462(4)
C13B—C17B	1.521(4)	N2B—C25B	1.469(4)
C14A—C9A	1.511(4)	N3A—C21A	1.477(3)
C14A—C15A	1.523(4)	N3A—C23A	1.473(3)
C14A—C16A	1.528(4)	N3A—C24A	1.468(4)
C14A—H14A	1.000	N3B—C20B	1.475(3)
C14B—C15B	1.528(4)	N3B—C23B	1.477(3)
C14B—C16B	1.516(4)	N3B—C25B	1.459(3)
C14B—H14B	1.001	N4A—C22A	1.476(3)
C15A—H15A	0.9800	N4A—C24A	1.468(4)

C15A—H15B	0.9800	N4A—C25A	1.467(4)
C15A—H15C	0.9800	N4B—C21B	1.464(3)
C15B—H15D	0.9800	N4B—C23B	1.459 (4)
C15B—H15E	0.9800	N4B—C24B	1.471(4)
C15B—H15F	0.9800	P1A—C20A	1.840(3)
C16A—H16A	0.9800	P1A—C21A	1.834(3)
C16A—H16B	0.9790	P1A—C22A	1.842(3)
C16A—H16C	0.9790	P1B—C20B	1.842(3)
C16B—H16D	0.9810	P1B—C21B	1.848(3)
C16B—H16E	0.9800	P1B—C22B	1.850(3)
C16B—H16F	0.9800	Pd1A—C6A	2.011(3)
C17A—C18A	1.509(4)	Pd1A—Cl1A	2.3750(8)
C17A—C19A	1.520(5)	Pd1A—N1A	2.101(2)
C17A—H17A	1.001	Pd1A—P1A	2.2176(8)
C17B—C18B	1.534(4)	Pd1B—C6B	2.015(3)
C17B—C19B	1.527(4)	Pd1B—Cl1B	2.3701(8)
C17B—H17B	1.000	Pd1B—N1B	2.112(2)
C18A—H18A	0.9790	Pd1B—P1B	2.2220(8)

Table A1.6: Bond angles (°) in the crystal structure of C1.

C2A—C1A—C6A	122.4(2)	H18D—C18B—H18E	109.5
C2A—C1A—C7A	121.8(2)	H18F—C18B—H18D	109.5
C6A—C1A—C7A	115.8(2)	H18F—C18B—H18E	109.4
C2B—C1B—C6B	122.5(2)	C17A—C19A—H19A	109.5
C2B—C1B—C7B	121.2(2)	C17A—C19A—H19B	109.5
C6B—C1B—C7B	116.3(2)	C17A—C19A—H19C	109.6
C1A—C2A—H2A	120.0	H19A—C19A—H19B	109.5
C3A—C2A—C1A	119.9(2)	H19C—C19A—H19A	109.4
C3A—C2A—H2A	120.1	H19C—C19A—H19B	109.4
C1B—C2B—H2B	120.0	C17B—C19B—H19D	109.4
C3B—C2B—C1B	120.0(2)	C17B—C19B—H19E	109.5
C3B—C2B—H2B	120.0	C17B—C19B—H19F	109.5
C2A—C3A—H3A	120.6	H19D—C19B—H19F	109.4
C4A—C3A—C2A	118.8(2)	H19E—C19B—H19D	109.4
C4A—C3A—H3A	120.6	H19E—C19B—H19F	109.6
C2B—C3B—H3B	120.7	H20A—C20A—H20B	107.9
C4B—C3B—C2B	118.5(3)	N2A—C20A—H20A	109.1
C4B—C3B—H3B	120.8	N2A—C20A—H20B	109.1
C3A—C4A—C5A	121.3(2)	N2A—C20A—P1A	112.5(2)
C3A—C4A—H4A	119.4	P1A—C20A—H20A	109.1
C5A—C4A—H4A	119.3	P1A—C20A—H20B	109.1

C3B—C4B—C5B	121.6(3)	H20C—C20B—H20D	108.0
C3B—C4B—H4B	119.2	N3B—C20B—H20C	109.3
C5B—C4B—H4B	119.2	N3B—C20B—H20D	109.3
C4A—C5A—C6A	121.8(2)	N3B—C20B—P1B	111.5(2)
C4A—C5A—H5A	119.1	P1B—C20B—H20C	109.3
C6A—C5A—H5A	119.1	P1B—C20B—H20D	109.3
C4B—C5B—C6B	121.8(3)	H21A—C21A—H21B	107.9
C4B—C5B—H5B	119.1	N3A—C21A—H21A	109.1
C6B—C5B—H5B	119.1	N3A—C21A—H21B	109.1
C1A—C6A—Pd1A	111.9(2)	N3A—C21A—P1A	112.5(2)
C5A—C6A—C1A	115.9(2)	P1A—C21A—H21A	109.1
C5A—C6A—Pd1A	132.1(2)	P1A—C21A—H21B	109.1
C1B—C6B—Pd1B	111.8(2)	H21C—C21B—H21D	108.1
C5B—C6B—C1B	115.6(2)	N4B—C21B—H21C	109.3
C5B—C6B—Pd1B	132.5(2)	N4B—C21B—H21D	109.3
C1A—C7A—H7A	120.9	N3B—C21B—P1B	111.6(2)
N1A—C7A—C1A	118.2(2)	P1B—C21B—H21C	109.3
N1A—C7A—H7A	120.9	P1B—C21B—H21D	109.3
C1B—C7B—H7B	120.9	H22A—C22A—H22B	108.1
N1B—C7B—C1B	118.1(2)	N4A—C22A—H22A	109.4
N1B—C7B—H7B	121.0	N4A—C22A—H22B	109.5
C9A—C8A—C13A	122.7(2)	N4A—C22A—P1A	111.0(2)
C9A—C8A—N1A	118.9(2)	P1A—C22A—H22A	109.5
C13A—C8A—N1A	118.3(2)	P1A—C22A—H22B	109.4
C9B—C8B—C13B	122.3(2)	H22C—C22B—H22D	108.0
C9B—C8B—N1B	120.6(2)	N2B—C22B—H22C	109.2
C13B—C8B—N1B	117.1(2)	N2B—C22B—H22D	109.2
C8A—C9A—C14A	121.9(2)	N2B—C22B—P1B	112.0(2)
C10A—C9A—C8A	117.4(2)	P1B—C22B—H22C	109.2
C10A—C9A—C14A	120.6(2)	P1B—C22B—H22D	109.2
C8B—C9B—C14B	121.4(2)	H23A—C23A—H23B	107.6
C10B—C9B—C8B	117.3(2)	N2A—C23A—H23A	108.6
C10B—C9B—C14B	121.2(2)	N2A—C23A—H23B	108.6
C9A—C10A—H10A	119.3	N2A—C23A—N3A	114.5(2)
C11A—C10A—C9A	121.3(3)	N3A—C23A—H23A	108.6
C11A—C10A—H10A	119.4	N3A—C23A—H23B	108.6
C9B—C10B—H10B	119.3	H23C—C23B—H23D	107.5
C11B—C10B—C9B	121.5(3)	N3B—C23B—H23C	108.4
C11B—C10B—H10B	119.2	N3B—C23B—H23D	108.4
C10A—C11A—C12A	119.9(3)	N4B—C23B—H23C	108.4
C10A—C11A—H11A	120.0	N4B—C23B—H23D	108.3
C12A—C11A—H11A	120.1	N4B—C23B—N3B	115.6(2)

C10B—C11B—C12B	120.2(2)	H24A—C24A—H24B	107.4
C10B—C11B—H11B	119.9	N3A—C24A—H24A	108.4
C12B—C11B—H11B	119.9	N3A—C24A—H24B	108.4
C11A—C12A—C13A	121.6(3)	N4A—C24A—H24A	108.4
C11A—C12A—H12A	119.2	N4A—C24A—H24B	108.4
C13A—C12A—H12A	119.2	N4A—C24A—N3A	115.5(2)
C11B—C12B—C13B	120.6(3)	H24C—C24B—H24D	107.6
C11B—C12B—H12B	119.7	N4B—C24B—H24C	108.6
C13B—C12B—H12B	119.7	N4B—C24B—H24D	108.6
C8A—C13A—C17A	122.0(2)	N2B—C24B—H24C	108.7
C12A—C13A—C8A	117.1(3)	N2B—C24B—H24D	108.7
C12A—C13A—C17A	120.9(3)	N2B—C24B—N4B	114.3(2)
C8B—C13B—C17B	120.7(2)	H25A—C25A—H25B	107.6
C12B—C13B—C8B	117.8(2)	N2A—C25A—H25A	108.6
C12B—C13B—C17B	121.5(2)	N2A—C25A—H25B	108.6
C9A—C14A—C15A	110.1(2)	N2A—C25A—N4A	114.5(2)
C9A—C14A—C16A	112.0(2)	N4A—C25A—H25A	108.6
C9A—C14A—H14A	107.9	N4A—C25A—H25B	108.7
C15A—C14A—C16A	111.0(3)	H25C—C25B—H25D	107.6
C15A—C14A—H14A	107.8	N2B—C25B—H25C	108.5
C16A—C14A—H14A	107.8	N2B—C25B—H25D	108.6
C9B—C14B—C15B	109.5(2)	N3B—C25B—N2B	114.8(2)
C9B—C14B—H14B	108.0	N3B—C25B—H25C	108.5
C15B—C14B—H14B	108.1	N3B—C25B—H25D	108.6
C16B—C14B—C9B	113.1(2)	C7A—N1A—C8A	120.4(2)
C16B—C14B—C15B	109.8(3)	C7A—N1A—Pd1A	113.0(2)
C16B—C14B—H14B	108.1	C8A—N1A—Pd1A	126.5(2)
C14A—C15A—H15A	109.5	C7B—N1B—C8B	119.0(2)
C14A—C15A—H15B	109.4	C7B—N1B—Pd1B	112.7(2)
C14A—C15A—H15C	109.4	C8B—N1B—Pd1B	128.1(2)
H15A—C15A—H15B	109.5	C20A—N2A—C23A	111.4(2)
H15A—C15A—H15C	109.5	C25A—N2A—C20A	110.5(2)
H15C—C15A—H15B	109.5	C25A—N2A—C23A	108.3(2)
C14B—C15B—H15D	109.5	C24B—N2B—C22B	110.2(2)
C14B—C15B—H15E	109.4	C24B—N2B—C25B	108.7(2)
C14B—C15B—H15F	109.4	C25B—N2B—C22B	111.4(2)
H15D—C15B—H15E	109.5	C23A—N3A—C21A	110.7(2)
H15D—C15B—H15F	109.5	C24A—N3A—C21A	110.4(2)
H15F—C15B—H15E	109.5	C24A—N3A—C23A	107.7(2)
C14A—C16A—H16A	109.4	C20B—N3B—C23B	111.6(2)
C14A—C16A—H16B	109.4	C25B—N3B—C20B	110.8(2)
C14A—C16A—H16C	109.5	C25B—N3B—C23B	107.4(2)

H16B—C16A—H16A	109.4	C24A—N4A—C22A	111.5(2)
H16B—C16A—H16C	109.5	C25A—N4A—C22A	110.9(2)
H16C—C16A—H16A	109.6	C25A—N4A—C24A	108.5(2)
C14B—C16B—H16D	109.4	C21B—N4B—C24B	111.1(2)
C14B—C16B—H16E	109.4	C23B—N4B—C21B	111.3(2)
C14B—C16B—H16F	109.5	C23B—N4B—C24B	108.1(2)
H16E—C16B—H16D	109.6	C20A—P1A—C22A	97.7(1)
H16E—C16B—H16F	109.5	C20A—P1A—Pd1A	116.83(9)
H16F—C16B—H16D	109.5	C21A—P1A—C20A	97.62(1)
C13A—C17A—C19A	112.7(3)	C21A—P1A—C22A	100.2(1)
C13A—C17A—H17A	107.7	C21A—P1A—Pd1A	115.20(9)
C18A—C17A—C13A	112.1(3)	C22A—P1A—Pd1A	124.6(9)
C18A—C17A—C19A	108.9(3)	C20B—P1B—Pd1B	116.96(9)
C18A—C17A—H17A	107.6	C20B—P1B—C21B	100.4(1)
C19A—C17A—H17A	107.6	C20B—P1B—C22B	97.8(1)
C13B—C17B—C18B	112.9(2)	C21B—P1B—Pd1B	121.8(1)
C13B—C17B—C19B	111.1(2)	C21B—P1B—C22B	97.2(1)
C13B—C17B—H17B	107.6	C22B—P1B—Pd1B	118.2(9)
C18B—C17B—C19B	109.9(2)	C6A—Pd1A—Cl1A	173.27(8)
C18B—C17B—H17B	107.6	C6A—Pd1A—N1A	81.01(9)
C19B—C17B—H17B	107.6	C6A—Pd1A—P1A	94.53(7)
C17A—C18A—H18A	109.5	N1A—Pd1A—Cl1A	93.87(6)
C17A—C18A—H18B	109.5	N1A—Pd1A—P1A	170.68(6)
C17A—C18A—H18C	109.4	P1A—Pd1A—Cl1A	91.16(3)
H18A—C18A—H18C	109.5	C6B—Pd1B—Cl1B	174.08(8)
H18B—C18A—H18A	97(4)	C6B—Pd1B—N1B	81.01(9)
H18B—C18A—H18C	109.5	C6B—Pd1B—P1B	95.20(8)
C17B—C18B—H18D	109.5	N1B—Pd1B—Cl1B	93.34(6)
C17B—C18B—H18E	109.5	N1B—Pd1B—P1B	173.52(6)
C17B—C18B—H18F	109.5	P1B—Pd1B—Cl1B	90.59(2)

A1.4 Crystal data for **C2**

Table A1.7: Bond distances (Å) in the crystal structure of C2.

C1A—C2A	1.398(2)	C17B—C19B	1.535(2)
C2A—C3A	1.400(2)	C17B—H17B	1.0000
C2A—H2A	0.9500	C18A—H18A	0.9800
C2B—C1B	1.398(2)	C18A—H18B	0.9800
C2B—C3B	1.399(2)	C18A—H18C	0.9800
C2B—H2B	0.9500	C18B—H18D	0.9800
C3A—H3A	0.9500	C18B—H18E	0.9800
C3B—H3B	0.9500	C18B—H18F	0.9800
C4A—C3A	1.390(2)	C19A—H19D	0.9800
C4A—H4A	0.9500	C19A—H19E	0.9800
C4B—C3B	1.387(2)	C19A—H19F	0.9800
C4B—H4B	0.9500	C19B—H19A	0.9800
C5A—C4A	1.387(2)	C19B—H19B	0.9800
C5B—C4B	1.385(2)	C19B—H19C	0.9800
C6A—C1A	1.428(2)	C20A—H20C	0.9900
C6A—C5A	1.397(2)	C20A—H20D	0.9900
C6B—C1B	1.422(2)	C20B—H20A	0.9900
C6B—C5B	1.399(2)	C20B—H20B	0.9900
C7A—C6A	1.452(2)	C20B—N27	1.470(2)
C7A—H7A	0.9500	C21A—H21A	0.9900
C7A—N1A	1.287(2)	C21A—H21B	0.9900
C7B—C6B	1.456(2)	C21B—H21C	0.9900
C7B—H7B	0.9500	C21B—H21D	0.9900
C8A—C9A	1.406(2)	C22A—H22C	0.9900
C8A—C13A	1.403(2)	C22A—H22D	0.9900
C9A—C10A	1.396(2)	C22B—H22A	0.9900
C9A—C14A	1.523(2)	C22B—H22B	0.9900
C9B—C8B	1.405(2)	C23A—H23A	0.9900
C9B—C10B	1.398(2)	C23A—H23B	0.9900
C10A—C11A	1.380(2)	C23B—H23C	0.9900
C10A—H10A	0.9500	C23B—H23D	0.9900
C10B—C11B	1.382(2)	C24A—H24C	0.9900
C10B—H10B	0.9500	C24A—H24D	0.9900
C11A—H11A	0.9500	C24B—H24A	0.9900
C11B—H11B	0.9500	C24B—H24B	0.9900
C12A—C11A	1.385(2)	C25A—H25C	0.9900
C12A—H12A	0.9500	C25A—H25D	0.9900
C12B—C11B	1.389(2)	C25B—H25A	0.9900

C12B—H12B	0.9500	C25B—H25B	0.9900
C13A—C12A	1.395(2)	Cl2A—C5A	1.746(1)
C13A—C17A	1.519(2)	Cl2B—C5B	1.744(2)
C13B—C8B	1.404(2)	N1A—C8A	1.441(2)
C13B—C12B	1.393(2)	N2A—C20A	1.473(2)
C13B—C17B	1.515(2)	N2A—C21A	1.465(2)
C14A—C15A	1.524(2)	N2A—C24A	1.473(2)
C14A—C15C	1.523(2)	N3—C7B	1.284(2)
C14A—C16A	1.524(2)	N3—C8B	1.441(2)
C14A—C16C	1.524(2)	N3A—C21A	1.472(2)
C14A—H14A	1.0000	N3A—C22A	1.475(2)
C14B—C9B	1.523(2)	N3A—C25A	1.468(2)
C14B—C15B	1.530(2)	N4A—C23A	1.473(2)
C14B—C16B	1.532(2)	N4A—C24A	1.468(2)
C14B—H14B	1.0000	N4A—C25A	1.469(2)
C15A—H15D	0.9800	N21—C21B	1.467(2)
C15A—H15E	0.9800	N21—C22B	1.477(2)
C15A—H15F	0.9800	N21—C25B	1.475(2)
C15B—H15A	0.9800	N27—C21B	1.466(2)
C15B—H15B	0.9800	N27—C24B	1.476(2)
C15B—H15C	0.9800	N34—C23B	1.472(2)
C15C—H15G	0.9800	N34—C24B	1.474(2)
C15C—H15H	0.9800	N34—C25B	1.468(2)
C15C—H15I	0.9800	P1A—C20A	1.838(1)
C16A—H16D	0.9800	P1A—C22A	1.844(1)
C16A—H16E	0.9800	P1A—C23A	1.847(1)
C16A—H16F	0.9800	P1B—C20B	1.852(1)
C16B—H16A	0.9800	P1B—C22B	1.845(1)
C16B—H16B	0.9800	P1B—C23B	1.840(1)
C16B—H16C	0.9800	Pd1A—C1A	2.005(1)
C16C—H16G	0.9800	Pd1A—Cl1A	2.3667(3)
C16C—H16H	0.9800	Pd1A—N1A	2.092(1)
C16C—H16I	0.9800	Pd1A—P1A	2.2321(3)
C17A—C18A	1.526(2)	Pd1B—C1B	2.005(1)
C17A—C19A	1.529(2)	Pd1B—Cl1B	2.3721(3)
C17A—H17A	1.0000	Pd1B—N3	2.092(1)
C17B—C18B	1.529(2)	Pd1B—P1B	2.2404(3)

Table A1.8: Bond angles (°) in the crystal structure of C2.

C2A—C1A—C6A	117.1(1)	C17A—C18A—H18C	109.5
C2A—C1A—Pd1A	131.34(9)	H18A—C18A—H18B	109.5
C6A—C1A—Pd1A	111.55(9)	H18A—C18A—H18C	109.5
C2B—C1B—C6B	117.5(1)	H18B—C18A—H18C	109.5
C2B—C1B—Pd1B	130.7(1)	C17B—C18B—H18D	109.5
C6B—C1B—Pd1B	111.63(9)	C17B—C18B—H18E	109.5
C1A—C2A—C3A	121.3(1)	C17B—C18B—H18F	109.5
C1A—C2A—H2A	119.4	H18D—C18B—H18E	109.5
C3A—C2A—H2A	119.4	H18D—C18B—H18F	109.5
C1B—C2B—C3B	121.3(1)	H18E—C18B—H18F	109.5
C1B—C2B—H2B	119.4	C17A—C19A—H19D	109.5
C3B—C2B—H2B	119.4	C17A—C19A—H19E	109.5
C2A—C3A—H3A	119.4	C17A—C19A—H19F	109.5
C4A—C3A—C2A	121.2(1)	H19D—C19A—H19E	109.5
C4A—C3A—H3A	119.4	H19D—C19A—H19F	109.5
C2B—C3B—H3B	119.4	H19E—C19A—H19F	109.5
C4B—C3B—C2B	121.2(1)	C17B—C19B—H19A	109.5
C4B—C3B—H3B	119.4	C17B—C19B—H19B	109.5
C3A—C4A—H4A	120.9	C17B—C19B—H19C	109.5
C5A—C4A—C3A	118.3(1)	H19A—C19B—H19B	109.5
C5A—C4A—H4A	120.9	H19A—C19B—H19C	109.5
C3B—C4B—H4B	121.0	H19B—C19B—H19C	109.5
C5B—C4B—C3B	118.1(1)	H20C—C20A—H20D	107.9
C5B—C4B—H4B	121.0	N2A—C20A—H20C	109.1
C4A—C5A—C6A	121.6(1)	N2A—C20A—H20D	109.1
C4A—C5A—Cl2A	118.1(1)	N2A—C20A—P1A	112.37(8)
C6A—C5A—Cl2A	120.4(1)	P1A—C20A—H20C	109.1
C4B—C5B—C6B	122.1(1)	P1A—C20A—H20D	109.1
C4B—C5B—Cl2B	117.6(1)	H20A—C20B—H20B	107.9
C6B—C5B—Cl2B	120.3(1)	N27—C20B—H20A	109.2
C1A—C6A—C7A	115.8(1)	N27—C20B—H20B	109.2
C5A—C6A—C1A	120.4(1)	N27—C20B—P1B	112.19(9)
C5A—C6A—C7A	123.8(1)	P1B—C20B—H20A	109.2
C1B—C6B—C7B	116.2(1)	P1B—C20B—H20B	109.2
C5B—C6B—C1B	119.8(1)	H21A—C21A—H21B	107.6
C5B—C6B—C7B	124.0(1)	N2A—C21A—H21A	108.6
C6A—C7A—H7A	121.3	N2A—C21A—H21B	108.6
N1A—C7A—C6A	117.5(1)	N2A—C21A—N3A	114.5(1)
N1A—C7A—H7A	121.3	N3A—C21A—H21A	108.6
C6B—C7B—H7B	121.6	N3A—C21A—H21B	108.6

N3—C7B—C6B	116.9(1)	H21C—C21B—H21D	107.6
N3—C7B—H7B	121.6	N21—C21B—H21C	108.7
C9A—C8A—N1A	119.0(1)	N21—C21B—H21D	108.7
C13A—C8A—C9A	122.3(1)	N27—C21B—H21C	108.7
C13A—C8A—N1A	118.4(1)	N27—C21B—H21D	108.7
C9B—C8B—N3	119.1(1)	N27—C21B—N21	114.4(1)
C13B—C8B—C9B	122.5(1)	H22C—C22A—H22D	108.1
C13B—C8B—N3	118.1(1)	N3A—C22A—H22C	109.5
C8A—C9A—C14A	122.6(1)	N3A—C22A—H22D	109.5
C10A—C9A—C8A	117.2(1)	N3A—C22A—P1A	110.79(9)
C10A—C9A—C14A	120.0(1)	P1A—C22A—H22C	109.5
C8B—C9B—C14B	122.6(1)	P1A—C22A—H22D	109.5
C10B—C9B—C8B	117.2(1)	H22A—C22B—H22B	108.0
C10B—C9B—C14B	120.1(1)	N21—C22B—H22A	109.3
C9A—C10A—H10A	119.2	N21—C22B—H22B	109.3
C11A—C10A—C9A	121.6(1)	N21—C22B—P1B	111.45(9)
C11A—C10A—H10A	119.2	P1B—C22B—H22A	109.3
C9B—C10B—H10B	119.2	P1B—C22B—H22B	109.3
C11B—C10B—C9B	121.6(1)	H23A—C23A—H23B	107.9
C11B—C10B—H10B	119.2	N4A—C23A—H23A	109.2
C10A—C11A—C12A	119.9(1)	N4A—C23A—H23B	109.2
C10A—C11A—H11A	120.1	N4A—C23A—P1A	111.86(9)
C12A—C11A—H11A	120.1	P1A—C23A—H23A	109.2
C10B—C11B—C12B	119.9(1)	P1A—C23A—H23B	109.2
C10B—C11B—H11B	120.0	H23C—C23B—H23D	107.9
C12B—C11B—H11B	120.0	N34—C23B—H23C	109.2
C11A—C12A—C13A	121.2(1)	N34—C23B—H23D	109.2
C11A—C12A—H12A	119.4	N34—C23B—P1B	111.98(9)
C13A—C12A—H12A	119.4	P1B—C23B—H23C	109.2
C11B—C12B—C13B	121.1(1)	P1B—C23B—H23D	109.2
C11B—C12B—H12B	119.4	H24C—C24A—H24D	107.7
C13B—C12B—H12B	119.4	N2A—C24A—H24C	108.8
C8A—C13A—C17A	121.0(1)	N2A—C24A—H24D	108.8
C12A—C13A—C8A	117.6(1)	N4A—C24A—H24C	108.8
C12A—C13A—C17A	121.3(1)	N4A—C24A—H24D	108.8
C8B—C13B—C17B	120.1(1)	N4A—C24A—N2A	113.9(1)
C12B—C13B—C8B	117.7(1)	H24A—C24B—H24B	107.6
C12B—C13B—C17B	122.1(1)	N27—C24B—H24A	108.7
C9A—C14A—C15A	112.4(2)	N27—C24B—H24B	108.7
C9A—C14A—C15C	115.3(7)	N34—C24B—H24A	108.7
C9A—C14A—C16A	111.0(3)	N34—C24B—H24B	108.7
C9A—C14A—C16C	107.4(7)	N34—C24B—N27	114.2(1)

C9A—C14A—H14A	107.7	H25C—C25A—H25D	107.6
C15A—C14A—C16A	110.1(3)	N3A—C25A—H25C	108.6
C15A—C14A—H14A	107.7	N3A—C25A—H25D	108.6
C15C—C14A—C16C	110.4(9)	N3A—C25A—N4A	114.5(1)
C16A—C14A—H14A	107.7	N4A—C25A—H25C	108.6
C9B—C14B—C15B	109.9(1)	N4A—C25A—H25D	108.6
C9B—C14B—C16B	112.9(1)	H25A—C25B—H25B	107.7
C9B—C14B—H14B	107.9	N21—C25B—H25A	108.8
C15B—C14B—C16B	110.3(1)	N21—C25B—H25B	108.8
C15B—C14B—H14B	107.9	N34—C25B—H25A	108.8
C16B—C14B—H14B	107.9	N34—C25B—H25B	108.8
C14A—C15A—H15D	109.5	N34—C25B—N21	113.7(1)
C14A—C15A—H15E	109.5	C7A—N1A—C8A	120.2(1)
C14A—C15A—H15F	109.5	C7A—N1A—Pd1A	113.17(8)
H15D—C15A—H15E	109.5	C8A—N1A—Pd1A	125.38(8)
H15D—C15A—H15F	109.5	C21A—N2A—C20A	110.6(1)
H15E—C15A—H15F	109.5	C21A—N2A—C24A	108.5(1)
C14B—C15B—H15A	109.5	C24A—N2A—C20A	111.3(1)
C14B—C15B—H15B	109.5	C7B—N3—C8B	121.2(1)
C14B—C15B—H15C	109.5	C7B—N3—Pd1B	113.75(8)
H15A—C15B—H15B	109.5	C8B—N3—Pd1B	124.07(8)
H15A—C15B—H15C	109.5	C21A—N3A—C22A	111.7(1)
H15B—C15B—H15C	109.5	C25A—N3A—C21A	108.5(1)
C14A—C15C—H15G	109.5	C25A—N3A—C22A	111.2(1)
C14A—C15C—H15H	109.5	C24A—N4A—C23A	111.0(1)
C14A—C15C—H15I	109.5	C24A—N4A—C25A	108.1(1)
H15G—C15C—H15H	109.5	C25A—N4A—C23A	111.6(1)
H15G—C15C—H15I	109.5	C21B—N21—C22B	111.6(1)
H15H—C15C—H15I	109.5	C21B—N21—C25B	108.7(1)
C14A—C16A—H16D	109.5	C25B—N21—C22B	111.3(1)
C14A—C16A—H16E	109.5	C20B—N27—C24B	111.1(1)
C14A—C16A—H16F	109.5	C21B—N27—C20B	111.2(1)
H16D—C16A—H16E	109.5	C21B—N27—C24B	108.1(1)
H16D—C16A—H16F	109.5	C23B—N34—C24B	111.6(1)
H16E—C16A—H16F	109.5	C25B—N34—C23B	111.0(1)
C14B—C16B—H16A	109.5	C25B—N34—C24B	108.7(1)
C14B—C16B—H16B	109.5	C20A—P1A—C22A	99.33(6)
C14B—C16B—H16C	109.5	C20A—P1A—C23A	97.01(6)
H16A—C16B—H16B	109.5	C20A—P1A—Pd1A	115.28(4)
H16A—C16B—H16C	109.5	C22A—P1A—C23A	99.19(7)
H16B—C16B—H16C	109.5	C22A—P1A—Pd1A	122.85(4)
C14A—C16C—H16G	109.5	C23A—P1A—Pd1A	118.52(4)

C14A—C16C—H16H	109.5	C20B—P1B—Pd1B	109.70(4)
C14A—C16C—H16I	109.5	C22B—P1B—C20B	97.92(6)
H16G—C16C—H16H	109.5	C22B—P1B—Pd1B	127.99(4)
H16G—C16C—H16I	109.5	C23B—P1B—C20B	98.49(6)
H16H—C16C—H16I	109.5	C23B—P1B—C22B	98.43(6)
C13A—C17A—C18A	111.6(1)	C23B—P1B—Pd1B	118.93(4)
C13A—C17A—C19A	112.5(1)	C1A—Pd1A—Cl1A	173.38(4)
C13A—C17A—H17A	107.2	C1A—Pd1A—N1A	81.36(5)
C18A—C17A—C19A	110.8(1)	C1A—Pd1A—P1A	95.61(4)
C18A—C17A—H17A	107.2	N1A—Pd1A—Cl1A	92.05(3)
C19A—C17A—H17A	107.2	N1A—Pd1A—P1A	169.84(3)
C13B—C17B—C18B	113.3(1)	P1A—Pd1A—Cl1A	90.98(1)
C13B—C17B—C19B	111.0(1)	C1B—Pd1B—Cl1B	170.57(4)
C13B—C17B—H17B	107.3	C1B—Pd1B—N3	81.32(5)
C18B—C17B—C19B	110.5(1)	C1B—Pd1B—P1B	100.54(4)
C18B—C17B—H17B	107.3	N3—Pd1B—Cl1B	93.67(3)
C19B—C17B—H17B	107.3	N3—Pd1B—P1B	166.21(3)
C17A—C18A—H18A	109.5	P1B—Pd1B—Cl1B	86.23(1)
C17A—C18A—H18B	109.5		

A1.5 Crystal data for **C4**

Table A1.9: Bond distances (Å) in the crystal structure of C4.

C1A—C2A	1.408(3)	C17B—C19B	1.531(3)
C1A—C6A	1.426(3)	C20B—N2B	1.478(3)
C1A—C7A	1.442(3)	C26A—C2A	1.510(3)
C1B—C2B	1.410(3)	C26B—C2B	1.508(3)
C1B—C6B	1.420(3)	N1A—C7A	1.279(3)
C1B—C7B	1.444(3)	N1A—C8A	1.440(3)
C3A—C2A	1.383(3)	N1B—C7B	1.283(3)
C3A—C4A	1.388(3)	N1B—C8B	1.447(3)
C3B—C2B	1.387(3)	N2A—C20A	1.478(3)
C3B—C4B	1.384(3)	N2A—C23A	1.468(3)
C5A—C4A	1.392(3)	N2A—C25A	1.461(3)
C5B—C4B	1.390(3)	N2B—C23B	1.470(3)
C6A—C5A	1.392(3)	N2B—C25B	1.476(3)
C6B—C5B	1.396(3)	N3A—C21A	1.473(3)
C8A—C9A	1.399(3)	N3A—C23A	1.467(3)
C8A—C13A	1.392(3)	N3A—C24A	1.463(3)

C8B—C9B	1.394(3)	N3B—C21B	1.474(3)
C8B—C13B	1.395(3)	N3B—C23B	1.471(3)
C9A—C10A	1.396(4)	N3B—C24B	1.466(3)
C9A—C14A	1.520(4)	N4A—C22A	1.467(3)
C9B—C10B	1.395(3)	N4A—C24A	1.475(3)
C9B—C14B	1.511(3)	N4A—C25A	1.468(3)
C10A—C11A	1.377(4)	N4B—C22B	1.468(3)
C10B—C11B	1.387(3)	N4B—C24B	1.463(3)
C12A—C11A	1.382(4)	N4B—C25B	1.465(3)
C12B—C11B	1.383(3)	P1A—C20A	1.842(2)
C13A—C12A	1.388(3)	P1A—C21A	1.848(3)
C13B—C12B	1.399(3)	P1A—C22A	1.844(2)
C13B—C17B	1.512(3)	P1B—C20B	1.845(2)
C14A—C15A	1.463(4)	P1B—C21B	1.845(2)
C14A—C16A	1.441(5)	P1B—C22B	1.849(2)
C14B—C15B	1.510(4)	Pd1A—C6A	2.022(2)
C14B—C15C	1.74(2)	Pd1A—Cl1A	2.3832(6)
C14B—C16B	1.513(4)	Pd1A—N1A	2.089(2)
C14B—C16C	1.48(2)	Pd1A—P1A	2.2229(6)
C17A—C13A	1.515(3)	Pd1B—C6B	2.018(2)
C17A—C18A	1.527(3)	Pd1B—Cl1B	2.3773(6)
C17A—C19A	1.531(3)	Pd1B—N1B	2.087(2)
C17B—C18B	1.521(4)	Pd1B—P1B	2.2347(6)

Table A1.10: Bond angles (°) in the crystal structure of C4.

C2A—C1A—C6A	123.0(2)	C13B—C17B—C19B	111.4(2)
C2A—C1A—C7A	121.9(2)	C18B—C17B—C19B	111.6(2)
C6A—C1A—C7A	115.0(2)	N2A—C20A—P1A	111.7(2)
C2B—C1B—C6B	123.3(2)	N2B—C20B—P1B	112.0(2)
C2B—C1B—C7B	121.5(2)	N3A—C21A—P1A	111.4(2)
C6B—C1B—C7B	115.0(2)	N3B—C21B—P1B	111.7(2)
C1A—C2A—C26A	121.5(2)	N4A—C22A—P1A	112.0(2)
C3A—C2A—C1A	118.2(2)	N4B—C22B—P1B	111.7(2)
C3A—C2A—C26A	120.2(2)	N3A—C23A—N2A	114.4(2)
C1B—C2B—C26B	121.9(2)	N2B—C23B—N3B	114.3(2)
C3B—C2B—C1B	117.5(2)	N3A—C24A—N4A	115.0(2)
C3B—C2B—C26B	120.5(2)	N4B—C24B—N3B	114.9(2)
C2A—C3A—C4A	120.3(2)	N2A—C25A—N4A	114.6(2)
C4B—C3B—C2B	120.7(2)	N4B—C25B—N2B	113.8(2)
C3A—C4A—C5A	120.7(2)	C7A—N1A—C8A	117.9(2)
C3B—C4B—C5B	120.9(2)	C7A—N1A—Pd1A	113.3(2)

C4A—C5A—C6A	122.0(2)	C8A—N1A—Pd1A	128.8(2)
C4B—C5B—C6B	121.5(2)	C7B—N1B—C8B	117.7(2)
C1A—C6A—Pd1A	112.0(2)	C7B—N1B—Pd1B	112.9(2)
C5A—C6A—C1A	115.8(2)	C8B—N1B—Pd1B	129.2(1)
C5A—C6A—Pd1A	132.2(2)	C23A—N2A—C20A	111.3(2)
C1B—C6B—Pd1B	112.1(2)	C25A—N2A—C20A	111.1(2)
C5B—C6B—C1B	116.0(2)	C25A—N2A—C23A	108.3(2)
C5B—C6B—Pd1B	131.6(2)	C23B—N2B—C20B	111.0(2)
N1A—C7A—C1A	118.8(2)	C23B—N2B—C25B	108.3(2)
N1B—C7B—C1B	118.9(2)	C25B—N2B—C20B	111.4(2)
C9A—C8A—N1A	118.7(2)	C23A—N3A—C21A	110.8(2)
C13A—C8A—C9A	122.6(2)	C24A—N3A—C21A	111.6(2)
C13A—C8A—N1A	118.7(2)	C24A—N3A—C23A	108.3(2)
C9B—C8B—C13B	122.7(2)	C23B—N3B—C21B	110.7(2)
C9B—C8B—N1B	118.2(2)	C24B—N3B—C21B	111.6(2)
C13B—C8B—N1B	119.0(2)	C24B—N3B—C23B	108.2(2)
C8A—C9A—C14A	121.9(2)	C22A—N4A—C24A	110.9(2)
C10A—C9A—C8A	117.1(2)	C22A—N4A—C25A	110.6(2)
C10A—C9A—C14A	120.9(3)	C25A—N4A—C24A	108.5(2)
C8B—C9B—C10B	117.5(2)	C24B—N4B—C22B	111.8(2)
C8B—C9B—C14B	120.5(2)	C24B—N4B—C25B	108.6(2)
C10B—C9B—C14B	122.0(2)	C25B—N4B—C22B	110.9(2)
C11A—C10A—C9A	121.4(3)	C20A—P1A—C21A	97.7(2)
C11B—C10B—C9B	121.0(2)	C20A—P1A—C22A	97.8(1)
C10A—C11A—C12A	119.5(2)	C20A—P1A—Pd1A	118.84(8)
C12B—C11B—C10B	120.1(2)	C21A—P1A—Pd1A	121.63(8)
C11A—C12A—C13A	121.7(2)	C22A—P1A—C21A	99.8(1)
C11B—C12B—C13B	120.9(2)	C22A—P1A—Pd1A	116.56(8)
C8A—C13A—C17A	120.4(2)	C20B—P1B—C21B	97.7(1)
C12A—C13A—C8A	117.2(2)	C20B—P1B—C22B	97.6(1)
C12A—C13A—C17A	122.3(2)	C20B—P1B—Pd1B	116.87(8)
C8B—C13B—C12B	117.5(2)	C21B—P1B—C22B	99.7(1)
C8B—C13B—C17B	121.5(2)	C21B—P1B—Pd1B	118.11(8)
C12B—C13B—C17B	121.0(2)	C22B—P1B—Pd1B	122.28(8)
C15A—C14A—C9A	112.4(3)	C6A—Pd1A—Cl1A	173.80(7)
C16A—C14A—C9A	116.4(3)	C6A—Pd1A—N1A	80.88(8)
C16A—C14A—C15A	121.3(3)	C6A—Pd1A—P1A	95.02(7)
C9B—C14B—C15C	105.0(5)	N1A—Pd1A—Cl1A	93.11(5)
C9B—C14B—C16B	112.1(2)	N1A—Pd1A—P1A	175.89(5)
C15B—C14B—C9B	112.4(2)	P1A—Pd1A—Cl1A	90.98(2)
C15B—C14B—C16B	113.7(3)	C6B—Pd1B—Cl1B	171.62(6)
C16C—C14B—C9B	106.7(9)	C6B—Pd1B—N1B	81.02(8)

C16C—C14B—C15C	101(1)	C6B—Pd1B—P1B	96.04(6)
C13A—C17A—C18A	112.6(2)	N1B—Pd1B—Cl1B	91.87(5)
C13A—C17A—C19A	112.0(2)	N1B—Pd1B—P1B	176.45(5)
C18A—C17A—C19A	111.2(2)	P1B—Pd1B—Cl1B	91.21(2)
C13B—C17B—C18B	110.9(2)		

A1.6 Crystal data for **T2**

Table A1.11: Bond distances (Å) in the crystal structure of T2.

C1—C2	1.403(2)	C12A—H12H	0.9800
C1—C6	1.409(2)	C12A—H12I	0.9800
C1A—C2A	1.405(2)	C12B—H12D	0.9800
C1A—C6A	1.409(2)	C12B—H12E	0.9800
C2—C3	1.389(2)	C12B—H12F	0.9800
C2—C7	1.523(2)	C12C—H12J	0.9800
C2A—C3A	1.396(2)	C12C—H12K	0.9800
C2A—C7A	1.518(2)	C12C—H12L	0.9800
C3—C4	1.382(2)	C13—C14	1.469(2)
C3—H3A	0.9500	C13—H13	0.9500
C3A—C4A	1.380(2)	C13A—C14A	1.465(2)
C3A—H3AB	0.9500	C13A—H13A	0.9500
C4—C5	1.385(2)	C14—C15	1.400(2)
C4—H4	0.9500	C14—C19	1.396(2)
C4A—C5A	1.384(2)	C14A—C15A	1.393(2)
C4A—H4A	0.9500	C14A—C19A	1.400(2)
C5—C6	1.391(2)	C15—C16	1.379(2)
C5—H5	0.9500	C15—H15	0.9500
C5A—C6A	1.394(2)	C15A—C16A	1.385(2)
C5A—H5A	0.9500	C15A—H15A	0.9500
C6—C10	1.522(2)	C16—C17	1.394(2)
C6A—C10A	1.520(2)	C16—H16	0.9500
C7—C8	1.523(2)	C16A—C17A	1.397(2)
C7—C9	1.528(2)	C16A—H16A	0.9500
C7—H7	1.0000	C17—C18	1.395(2)
C7A—C8A	1.528(2)	C17A—C18A	1.391(2)
C7A—C9A	1.531(2)	C18—C19	1.383(2)
C7A—H7A	1.0000	C18—H18	0.9500
C8—H8A	0.9800	C18A—C19A	1.380(2)
C8—H8B	0.9800	C18A—H18A	0.9500

C8—H8C	0.9800	C19—H19	0.9500
C8A—H8AA	0.9800	C19A—H19A	0.9500
C8A—H8AB	0.9800	C20—C21	1.512(2)
C8A—H8AC	0.9800	C20—H20A	0.9900
C9—H9A	0.9800	C20—H20B	0.9900
C9—H9B	0.9800	C20A—C21A	1.503(2)
C9—H9C	0.9800	C20A—H20C	0.9900
C9A—H9AA	0.9800	C20A—H20D	0.9900
C9A—H9AB	0.9800	C21—H21A	0.9900
C9A—H9AC	0.9800	C21—H21B	0.9900
C10—C11	1.510(2)	C21A—H21C	0.9900
C10—C11B	1.523(3)	C21A—H21D	0.9900
C10—C12	1.535(2)	C22—C23	1.497(2)
C10—C12B	1.507(3)	C22—H22A	0.9900
C10—H10	1.0000	C22—H22B	0.9900
C10—H10A	1.0000	C22A—C23A	1.504(2)
C10A—C11A	1.507(2)	C22A—H22C	0.9900
C10A—C11C	1.525(4)	C22A—H22D	0.9900
C10A—C12A	1.527(2)	C23—H23A	0.9900
C10A—C12C	1.507(4)	C23—H23B	0.9900
C10A—H10B	1.0000	C23A—H23C	0.9900
C10A—H10C	1.0000	C23A—H23D	0.9900
C11—H11A	0.9800	N1—C1	1.425(2)
C11—H11B	0.9800	N1—C13	1.273(2)
C11—H11C	0.9800	N1A—C1A	1.425(2)
C11A—H11G	0.9800	N1A—C13A	1.272(2)
C11A—H11H	0.9800	O1—C17	1.361(2)
C11A—H11I	0.9800	O1—C20	1.434(2)
C11B—H11D	0.9800	O1A—C17A	1.364(2)
C11B—H11E	0.9800	O1A—C20A	1.430(2)
C11B—H11F	0.9800	O2—C21	1.420(2)
C11C—H11J	0.9800	O2—C22	1.427(2)
C11C—H11K	0.9800	O2A—C21A	1.426(2)
C11C—H11L	0.9800	O2A—C22A	1.431(2)
C12—H12A	0.9800	O3—C23	1.411(3)
C12—H12B	0.9800	O3—H3	0.88(3)
C12—H12C	0.9800	O3A—C23A	1.422(2)
C12A—H12G	0.9800	O3A—H3AA	0.87(3)

Table A1.12: Bond angles (°) in the crystal structure of T2.

C2—C1—C6	121.5(1)	C10—C12—H12B	109.5
C2—C1—N1	118.4(1)	C10—C12—H12C	109.5
C6—C1—N1	119.9(1)	H12A—C12—H12B	109.5
C2A—C1A—C6A	121.8(1)	H12A—C12—H12C	109.5
C2A—C1A—N1A	118.5(1)	H12B—C12—H12C	109.5
C6A—C1A—N1A	119.5(1)	C10A—C12A—H12G	109.5
C1—C2—C7	120.2(1)	C10A—C12A—H12H	109.5
C3—C2—C1	118.3(1)	C10A—C12A—H12I	109.5
C3—C2—C7	121.5(1)	H12G—C12A—H12H	109.5
C1A—C2A—C7A	120.6(1)	H12G—C12A—H12I	109.5
C3A—C2A—C1A	117.9(1)	H12H—C12A—H12I	109.5
C3A—C2A—C7A	121.5(1)	C10—C12B—H12D	109.5
C2—C3—H3A	119.4	C10—C12B—H12E	109.5
C4—C3—C2	121.2(1)	C10—C12B—H12F	109.5
C4—C3—H3A	119.4	H12D—C12B—H12E	109.5
C2A—C3A—H3AB	119.5	H12D—C12B—H12F	109.5
C4A—C3A—C2A	121.1(1)	H12E—C12B—H12F	109.5
C4A—C3A—H3AB	119.5	C10A—C12C—H12J	109.5
C3—C4—C5	120.0(1)	C10A—C12C—H12K	109.5
C3—C4—H4	120.0	C10A—C12C—H12L	109.5
C5—C4—H4	120.0	H12J—C12C—H12K	109.5
C3A—C4A—C5A	120.3(1)	H12J—C12C—H12L	109.5
C3A—C4A—H4A	119.8	H12K—C12C—H12L	109.5
C5A—C4A—H4A	119.8	C14—C13—H13	118.6
C4—C5—C6	121.2(1)	N1—C13—C14	122.8(1)
C4—C5—H5	119.4	N1—C13—H13	118.6
C6—C5—H5	119.4	C14A—C13A—H13A	118.3
C4A—C5A—C6A	121.1(1)	N1A—C13A—C14A	123.4(1)
C4A—C5A—H5A	119.4	N1A—C13A—H13A	118.3
C6A—C5A—H5A	119.4	C15—C14—C13	119.0(1)
C1—C6—C10	120.3(1)	C19—C14—C13	122.3(1)
C5—C6—C1	117.9(1)	C19—C14—C15	118.6(1)
C5—C6—C10	121.7(1)	C15A—C14A—C13A	122.5(1)
C1A—C6A—C10A	120.6(1)	C15A—C14A—C19A	118.4(1)
C5A—C6A—C1A	117.8(1)	C19A—C14A—C13A	119.0(1)
C5A—C6A—C10A	121.7(1)	C14—C15—H15	119.6
C2—C7—C8	113.0(1)	C16—C15—C14	120.8(1)
C2—C7—C9	110.5(1)	C16—C15—H15	119.6
C2—C7—H7	107.4	C14A—C15A—H15A	119.5
C8—C7—C9	110.9(1)	C16A—C15A—C14A	121.1(1)

C8—C7—H7	107.4	C16A—C15A—H15A	119.5
C9—C7—H7	107.4	C15—C16—C17	120.0(1)
C2A—C7A—C8A	112.4(1)	C15—C16—H16	120.0
C2A—C7A—C9A	112.1(1)	C17—C16—H16	120.0
C2A—C7A—H7A	107.2	C15A—C16A—C17A	119.5(1)
C8A—C7A—C9A	110.4(1)	C15A—C16A—H16A	120.3
C8A—C7A—H7A	107.2	C17A—C16A—H16A	120.3
C9A—C7A—H7A	107.2	C16—C17—C18	119.9(1)
C7—C8—H8A	109.5	O1—C17—C16	115.3(1)
C7—C8—H8B	109.5	O1—C17—C18	124.8(1)
C7—C8—H8C	109.5	C18A—C17A—C16A	120.3(1)
H8A—C8—H8B	109.5	O1A—C17A—C16A	124.1(1)
H8A—C8—H8C	109.5	O1A—C17A—C18A	115.6(1)
H8B—C8—H8C	109.5	C17—C18—H18	120.2
C7A—C8A—H8AA	109.5	C19—C18—C17	119.6(1)
C7A—C8A—H8AB	109.5	C19—C18—H18	120.2
C7A—C8A—H8AC	109.5	C17A—C18A—H18A	120.2
H8AA—C8A—H8AB	109.5	C19A—C18A—C17A	119.5(1)
H8AA—C8A—H8AC	109.5	C19A—C18A—H18A	120.2
H8AB—C8A—H8AC	109.5	C14—C19—H19	119.5
C7—C9—H9A	109.5	C18—C19—C14	121.0(1)
C7—C9—H9B	109.5	C18—C19—H19	119.5
C7—C9—H9C	109.5	C14A—C19A—H19A	119.4
H9A—C9—H9B	109.5	C18A—C19A—C14A	121.2(1)
H9A—C9—H9C	109.5	C18A—C19A—H19A	119.4
H9B—C9—H9C	109.5	C21—C20—H20A	110.1
C7A—C9A—H9AA	109.5	C21—C20—H20B	110.1
C7A—C9A—H9AB	109.5	H20A—C20—H20B	108.5
C7A—C9A—H9AC	109.5	O1—C20—C21	107.8(1)
H9AA—C9A—H9AB	109.5	O1—C20—H20A	110.1
H9AA—C9A—H9AC	109.5	O1—C20—H20B	110.1
H9AB—C9A—H9AC	109.5	C21A—C20A—H20C	110.4
C6—C10—C11B	111.8(4)	C21A—C20A—H20D	110.4
C6—C10—C12	113.9(1)	H20C—C20A—H20D	108.6
C6—C10—H10	107.5	O1A—C20A—C21A	106.8(1)
C6—C10—H10A	104.3	O1A—C20A—H20C	110.4
C11—C10—C6	110.1(1)	O1A—C20A—H20D	110.4
C11—C10—C12	110.2(1)	C20—C21—H21A	108.7
C11—C10—H10	107.5	C20—C21—H21B	108.7
C11B—C10—H10A	104.3	H21A—C21—H21B	107.6
C12—C10—H10	107.5	O2—C21—C20	114.3(1)
C12B—C10—C6	116.3(4)	O2—C21—H21A	108.7

C12B—C10—C11B	114.2(6)	O2—C21—H21B	108.7
C12B—C10—H10A	104.3	C20A—C21A—H21C	110.0
C6A—C10A—C11C	107.8(5)	C20A—C21A—H21D	110.0
C6A—C10A—C12A	114.4(1)	H21C—C21A—H21D	108.4
C6A—C10A—H10B	106.4	O2A—C21A—C20A	108.3(1)
C6A—C10A—H10C	106.0	O2A—C21A—H21C	110.0
C11A—C10A—C6A	111.6(1)	O2A—C21A—H21D	110.0
C11A—C10A—C12A	111.0(2)	C23—C22—H22A	110.0
C11A—C10A—H10B	106.4	C23—C22—H22B	110.0
C11C—C10A—H10C	106.0	H22A—C22—H22B	108.4
C12A—C10A—H10B	106.4	O2—C22—C23	108.6(1)
C12C—C10A—C6A	113.1(5)	O2—C22—H22A	110.0
C12C—C10A—C11C	117.0(8)	O2—C22—H22B	110.0
C12C—C10A—H10C	106.0	C23A—C22A—H22C	109.9
C10—C11—H11A	109.5	C23A—C22A—H22D	109.9
C10—C11—H11B	109.5	H22C—C22A—H22D	108.3
C10—C11—H11C	109.5	O2A—C22A—C23A	109.0(1)
H11A—C11—H11B	109.5	O2A—C22A—H22C	109.9
H11A—C11—H11C	109.5	O2A—C22A—H22D	109.9
H11B—C11—H11C	109.5	C22—C23—H23A	109.0
C10A—C11A—H11G	109.5	C22—C23—H23B	109.0
C10A—C11A—H11H	109.5	H23A—C23—H23B	107.8
C10A—C11A—H11I	109.5	O3—C23—C22	112.9(2)
H11G—C11A—H11H	109.5	O3—C23—H23A	109.0
H11G—C11A—H11I	109.5	O3—C23—H23B	109.0
H11H—C11A—H11I	109.5	C22A—C23A—H23C	109.6
C10—C11B—H11D	109.5	C22A—C23A—H23D	109.6
C10—C11B—H11E	109.5	H23C—C23A—H23D	108.1
C10—C11B—H11F	109.5	O3A—C23A—C22A	110.2(1)
H11D—C11B—H11E	109.5	O3A—C23A—H23C	109.6
H11D—C11B—H11F	109.5	O3A—C23A—H23D	109.6
H11E—C11B—H11F	109.5	C13—N1—C1	118.5(1)
C10A—C11C—H11J	109.5	C13A—N1A—C1A	118.3(1)
C10A—C11C—H11K	109.5	C17—O1—C20	118.7(1)
C10A—C11C—H11L	109.5	C17A—O1A—C20A	118.2(1)
H11J—C11C—H11K	109.5	C21—O2—C22	114.0(1)
H11J—C11C—H11L	109.5	C21A—O2A—C22A	112.5(1)
H11K—C11C—H11L	109.5	C23—O3—H3	107(2)
C10—C12—H12A	109.5	C23A—O3A—H3AA	114(2)

A1.7 CIFCHECK reports

A1.7.1 CIFCHECK report for L7

checkCIF/PLATON report

Structure factors have been supplied for datablock(s) C_

THIS REPORT IS FOR GUIDANCE ONLY. IF USED AS PART OF A REVIEW PROCEDURE FOR PUBLICATION, IT SHOULD NOT REPLACE THE EXPERTISE OF AN EXPERIENCED CRYSTALLOGRAPHIC REFEREE.

No syntax errors found. CIF dictionary Interpreting this report

Datablock: C_

```
Bond precision:  C-C = 0.0020 A          Wavelength=0.71073

Cell:          a=9.0009(13)       b=10.1457(14)    c=19.758(3)
               alpha=100.105(2)   beta=95.811(2)   gamma=105.637(2)
Temperature:   100 K
```

	Calculated	Reported
Volume	1689.5(4)	1689.4(4)
Space group	P -1	P -1
Hall group	-P 1	-P 1
Moiety formula	C19 H22 N2 O2	C19 H22 N2 O2
Sum formula	C19 H22 N2 O2	C19 H22 N2 O2
Mr	310.39	310.39
Dx,g cm-3	1.220	1.220
Z	4	4
Mu (mm-1)	0.080	0.080
F000	664.0	664.0
F000'	664.27	
h,k,lmax	12,13,26	12,13,26
Nref	8826	8081
Tmin,Tmax	0.988,0.993	0.986,0.993
Tmin'	0.986	

```
Correction method= # Reported T Limits: Tmin=0.986 Tmax=0.993
AbsCorr = MULTI-SCAN

Data completeness= 0.916          Theta(max)= 28.810

R(reflections)= 0.0451( 6393)     wR2(reflections)= 0.1084( 8081)

S = 1.040                  Npar= 423
```

The following ALERTS were generated. Each ALERT has the format
test-name_ALERT_alert-type_alert-level.
Click on the hyperlinks for more details of the test.

Alert level C

```
PLAT906_ALERT_3_C Large K value in the Analysis of Variance ......      2.611 Check
PLAT911_ALERT_3_C Missing # FCF Refl Between THmin & STh/L=  0.600         11 Report
```

Alert level G

```
PLAT005_ALERT_5_G No Embedded Refinement Details found  in the CIF     Please Do !
PLAT066_ALERT_1_G Predicted and Reported Tmin&Tmax Range Identical          ? Check
PLAT154_ALERT_1_G The s.u.'s on the Cell Angles are Equal ..(Note)       0.002 Degree
PLAT899_ALERT_4_G SHELXL97   is Deprecated and Succeeded by SHELXL       2014 Note
PLAT910_ALERT_3_G Missing # of FCF Reflection(s) Below Theta(Min)           1 Note
PLAT912_ALERT_4_G Missing # of FCF Reflections Above STh/L=  0.600        732 Note
PLAT978_ALERT_2_G Number C-C Bonds with Positive Residual Density          15 Note
```

```
   0 ALERT level A = Most likely a serious problem - resolve or explain
   0 ALERT level B = A potentially serious problem, consider carefully
   2 ALERT level C = Check. Ensure it is not caused by an omission or oversight
   7 ALERT level G = General information/check it is not something unexpected

   2 ALERT type 1 CIF construction/syntax error, inconsistent or missing data
   1 ALERT type 2 Indicator that the structure model may be wrong or deficient
   3 ALERT type 3 Indicator that the structure quality may be low
   2 ALERT type 4 Improvement, methodology, query or suggestion
   1 ALERT type 5 Informative message, check
```

It is advisable to attempt to resolve as many as possible of the alerts in all categories. Often the minor alerts point to easily fixed oversights, errors and omissions in your CIF or refinement strategy, so attention to these fine details can be worthwhile. In order to resolve some of the more serious problems it may be necessary to carry out additional measurements or structure refinements. However, the purpose of your study may justify the reported deviations and the more serious of these should normally be commented upon in the discussion or experimental section of a paper or in the "special_details" fields of the CIF. checkCIF was carefully designed to identify outliers and unusual parameters, but every test has its limitations and alerts that are not important in a particular case may appear. Conversely, the absence of alerts does not guarantee there are no aspects of the results needing attention. It is up to the individual to critically assess their own results and, if necessary, seek expert advice.

Publication of your CIF in IUCr journals

A basic structural check has been run on your CIF. These basic checks will be run on all CIFs submitted for publication in IUCr journals (*Acta Crystallographica*, *Journal of Applied Crystallography*, *Journal of Synchrotron Radiation*); however, if you intend to submit to *Acta Crystallographica Section C* or *E* or *IUCrData*, you should make sure that full publication checks are run on the final version of your CIF prior to submission.

Publication of your CIF in other journals

Please refer to the *Notes for Authors* of the relevant journal for any special instructions relating to CIF submission.

PLATON version of 30/03/2016; check.def file version of 30/03/2016

Datablock C_ - ellipsoid plot

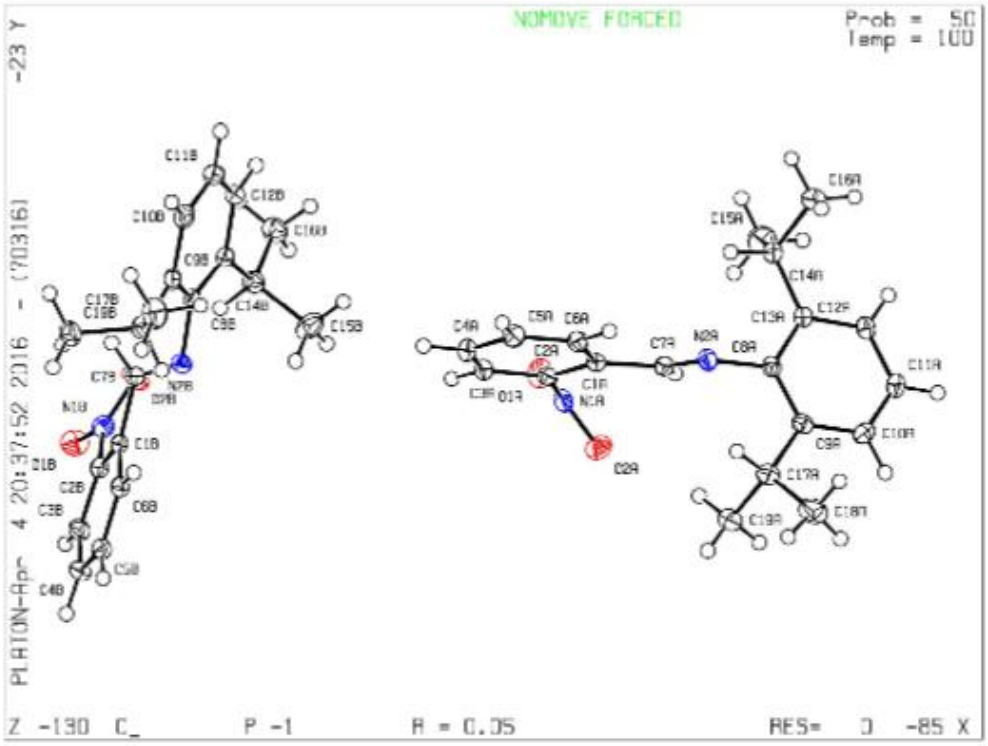

A1.7.2 CIFCHECK report for B6

checkCIF/PLATON report

Structure factors have been supplied for datablock(s) C_

THIS REPORT IS FOR GUIDANCE ONLY. IF USED AS PART OF A REVIEW PROCEDURE FOR PUBLICATION, IT SHOULD NOT REPLACE THE EXPERTISE OF AN EXPERIENCED CRYSTALLOGRAPHIC REFEREE.

No syntax errors found. CIF dictionary Interpreting this report

Datablock: C_

```
Bond precision:  C-C = 0.0031 A          Wavelength=0.71073

Cell:          a=9.6171(4)       b=9.8094(5)       c=10.6917(5)
               alpha=96.677(1)   beta=111.131(1)   gamma=94.141(1)
Temperature:   100 K
```

	Calculated	Reported
Volume	927.31(8)	927.31(7)
Space group	P -1	P -1
Hall group	-P 1	-P 1
Moiety formula	C38 H42 Cl2 F2 N2 Pd2	C38 H42 Cl2 F2 N2 Pd2
Sum formula	C38 H42 Cl2 F2 N2 Pd2	C38 H42 Cl2 F2 N2 Pd2
Mr	848.44	848.44
Dx,g cm-3	1.519	1.519
Z	1	1
Mu (mm-1)	1.152	1.152
F000	428.0	428.0
F000'	426.44	
h,k,lmax	13,13,14	13,13,13
Nref	4876	4445
Tmin,Tmax	0.861,0.861	0.865,0.869
Tmin'	0.861	

```
Correction method= # Reported T Limits: Tmin=0.865 Tmax=0.869
AbsCorr = MULTI-SCAN

Data completeness= 0.912          Theta(max)= 28.890

R(reflections)= 0.0215( 4149)     wR2(reflections)= 0.0506( 4445)

S = 1.020                  Npar= 219
```

The following ALERTS were generated. Each ALERT has the format
test-name_ALERT_alert-type_alert-level.
Click on the hyperlinks for more details of the test.

Alert level C

```
PLAT220_ALERT_2_C Non-Solvent Resd 1    C    Ueq(max)/Ueq(min) Range         3.3 Ratio
PLAT230_ALERT_2_C Hirshfeld Test Diff for     N1      --  C7       ..         5.1 s.u.
PLAT911_ALERT_3_C Missing # FCF Refl Between THmin & STh/L=  0.600            5 Report
```

Alert level G

```
PLAT002_ALERT_2_G Number of Distance or Angle Restraints on AtSite           3 Note
PLAT154_ALERT_1_G The s.u.'s on the Cell Angles are Equal ..(Note)        0.001 Degree
PLAT171_ALERT_4_G The CIF-Embedded .res File Contains EADP Records           2 Report
PLAT172_ALERT_4_G The CIF-Embedded .res File Contains DFIX Records           2 Report
PLAT232_ALERT_2_G Hirshfeld Test Diff (M-X)  Pd1     --  Cl1      ..       12.0 s.u.
PLAT232_ALERT_2_G Hirshfeld Test Diff (M-X)  Pd1     --  Cl1_a    ..        6.5 s.u.
PLAT301_ALERT_3_G Main Residue  Disorder ..... Percentage =          9 Note
PLAT367_ALERT_2_G Long?   C(sp?)-C(sp?) Bond  C13     -   C14     ..     1.52 Ang.
PLAT860_ALERT_3_G Number of Least-Squares Restraints .....           2 Note
PLAT899_ALERT_4_G SHELXL97   is Deprecated and Succeeded by SHELXL        2014 Note
PLAT912_ALERT_4_G Missing # of FCF Reflections Above STh/L=  0.600        389 Note
PLAT978_ALERT_2_G Number C-C Bonds with Positive Residual Density          16 Note
```

```
  0 ALERT level A = Most likely a serious problem - resolve or explain
  0 ALERT level B = A potentially serious problem, consider carefully
  3 ALERT level C = Check. Ensure it is not caused by an omission or oversight
 12 ALERT level G = General information/check it is not something unexpected

  1 ALERT type 1 CIF construction/syntax error, inconsistent or missing data
  7 ALERT type 2 Indicator that the structure model may be wrong or deficient
  3 ALERT type 3 Indicator that the structure quality may be low
  4 ALERT type 4 Improvement, methodology, query or suggestion
  0 ALERT type 5 Informative message, check
```

It is advisable to attempt to resolve as many as possible of the alerts in all categories. Often the minor alerts point to easily fixed oversights, errors and omissions in your CIF or refinement strategy, so attention to these fine details can be worthwhile. In order to resolve some of the more serious problems it may be necessary to carry out additional measurements or structure refinements. However, the purpose of your study may justify the reported deviations and the more serious of these should normally be commented upon in the discussion or experimental section of a paper or in the "special_details" fields of the CIF. checkCIF was carefully designed to identify outliers and unusual parameters, but every test has its limitations and alerts that are not important in a particular case may appear. Conversely, the absence of alerts does not guarantee there are no aspects of the results needing attention. It is up to the individual to critically assess their own results and, if necessary, seek expert advice.

Publication of your CIF in IUCr journals

A basic structural check has been run on your CIF. These basic checks will be run on all CIFs submitted for publication in IUCr journals (*Acta Crystallographica*, *Journal of Applied Crystallography*, *Journal of Synchrotron Radiation*); however, if you intend to submit to *Acta Crystallographica Section C* or *E* or *IUCrData*, you should make sure that full publication checks are run on the final version of your CIF prior to submission.

Publication of your CIF in other journals

Please refer to the *Notes for Authors* of the relevant journal for any special instructions relating to CIF submission.

PLATON version of 30/03/2016; check.def file version of 30/03/2016

Datablock C_ - ellipsoid plot

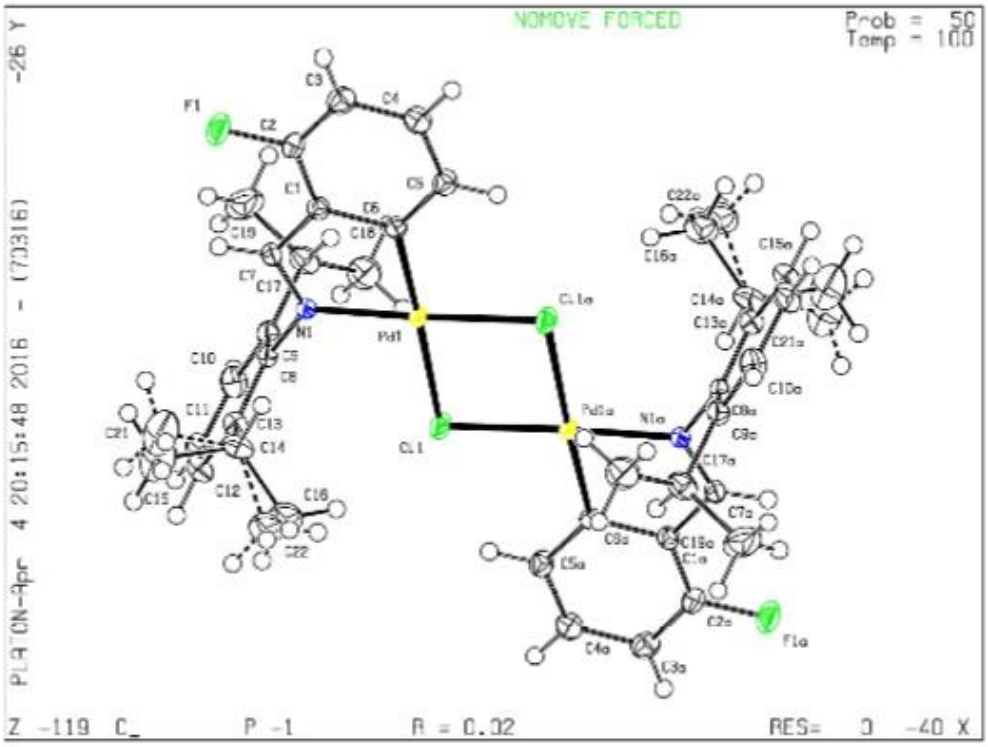

A1.7.3 CIFCHECK report for C1

checkCIF/PLATON report

Structure factors have been supplied for datablock(s) C__Users_dhaynes_Desktop_C1_AV_C1

THIS REPORT IS FOR GUIDANCE ONLY. IF USED AS PART OF A REVIEW PROCEDURE FOR PUBLICATION, IT SHOULD NOT REPLACE THE EXPERTISE OF AN EXPERIENCED CRYSTALLOGRAPHIC REFEREE.

No syntax errors found. CIF dictionary Interpreting this report

Datablock: C__Users_dhaynes_Desktop_C1_AV_C1

Bond precision: C-C = 0.0041 A Wavelength=0.71073

Cell: a=19.101(3) b=13.413(2) c=19.575(3)
alpha=90 beta=94.160(2) gamma=90
Temperature: 100 K

	Calculated	Reported
Volume	5001.9(13)	5001.8(15)
Space group	P 21/n	P 21/n
Hall group	-P 2yn	-P 2yn
Moiety formula	C25 H34 Cl N4 P Pd	C25 H34 Cl N4 P Pd
Sum formula	C25 H34 Cl N4 P Pd	C25 H34 Cl N4 P Pd
Mr	563.38	563.38
Dx,g cm-3	1.496	1.496
Z	8	8
Mu (mm-1)	0.933	0.933
F000	2320.0	2320.0
F000'	2314.55	
h,k,lmax	25,18,26	25,17,26
Nref	13199	12073
Tmin,Tmax	0.869,0.890	0.800,0.888
Tmin'	0.792	

Correction method= # Reported T Limits: Tmin=0.800 Tmax=0.888
AbsCorr = MULTI-SCAN

Data completeness= 0.915 Theta(max)= 28.923

R(reflections)= 0.0374(9527) wR2(reflections)= 0.0808(12073)

S = 1.028 Npar= 585

The following ALERTS were generated. Each ALERT has the format
test-name_ALERT_alert-type_alert-level.
Click on the hyperlinks for more details of the test.

Alert level B

```
PLAT220_ALERT_2_B Non-Solvent Resd 1    C   Ueq(max)/Ueq(min) Range         6.4 Ratio
```

Alert level C

```
PLAT220_ALERT_2_C Non-Solvent Resd 2    C   Ueq(max)/Ueq(min) Range         3.8 Ratio
PLAT222_ALERT_3_C Non-Solvent Resd 1    H Uiso(max)/Uiso(min) Range         7.2 Ratio
PLAT222_ALERT_3_C Non-Solvent Resd 2    H Uiso(max)/Uiso(min) Range         4.2 Ratio
PLAT242_ALERT_2_C Low    'MainMol' Ueq as Compared to Neighbors of        C17A Check
PLAT911_ALERT_3_C Missing # FCF Refl Between THmin & STh/L=  0.600          15 Report
PLAT977_ALERT_2_C Check the Negative Difference Density on    H19C       -0.38 eA-3
```

Alert level G

```
PLAT066_ALERT_1_G Predicted and Reported Tmin&Tmax Range Identical           ? Check
PLAT152_ALERT_1_G The Supplied and Calc. Volume s.u. Differ by ...           -2 Units
PLAT912_ALERT_4_G Missing # of FCF Reflections Above STh/L=  0.600        1078 Note
PLAT978_ALERT_2_G Number C-C Bonds with Positive Residual Density            7 Note
```

```
   0 ALERT level A = Most likely a serious problem - resolve or explain
   1 ALERT level B = A potentially serious problem, consider carefully
   6 ALERT level C = Check. Ensure it is not caused by an omission or oversight
   4 ALERT level G = General information/check it is not something unexpected

   2 ALERT type 1 CIF construction/syntax error, inconsistent or missing data
   5 ALERT type 2 Indicator that the structure model may be wrong or deficient
   3 ALERT type 3 Indicator that the structure quality may be low
   1 ALERT type 4 Improvement, methodology, query or suggestion
   0 ALERT type 5 Informative message, check
```

It is advisable to attempt to resolve as many as possible of the alerts in all categories. Often the minor alerts point to easily fixed oversights, errors and omissions in your CIF or refinement strategy, so attention to these fine details can be worthwhile. In order to resolve some of the more serious problems it may be necessary to carry out additional measurements or structure refinements. However, the purpose of your study may justify the reported deviations and the more serious of these should normally be commented upon in the discussion or experimental section of a paper or in the "special_details" fields of the CIF. checkCIF was carefully designed to identify outliers and unusual parameters, but every test has its limitations and alerts that are not important in a particular case may appear. Conversely, the absence of alerts does not guarantee there are no aspects of the results needing attention. It is up to the individual to critically assess their own results and, if necessary, seek expert advice.

Publication of your CIF in IUCr journals

A basic structural check has been run on your CIF. These basic checks will be run on all CIFs submitted for publication in IUCr journals (*Acta Crystallographica*, *Journal of Applied Crystallography*, *Journal of Synchrotron Radiation*); however, if you intend to submit to *Acta Crystallographica Section C* or *E* or *IUCrData*, you should make sure that full publication checks are run on the final version of your CIF prior to submission.

Publication of your CIF in other journals

Please refer to the *Notes for Authors* of the relevant journal for any special instructions relating to CIF submission.

PLATON version of 30/03/2016; check.def file version of 30/03/2016

Datablock C__Users_dhaynes_Desktop_C1_AV_C1 - ellipsoid plot

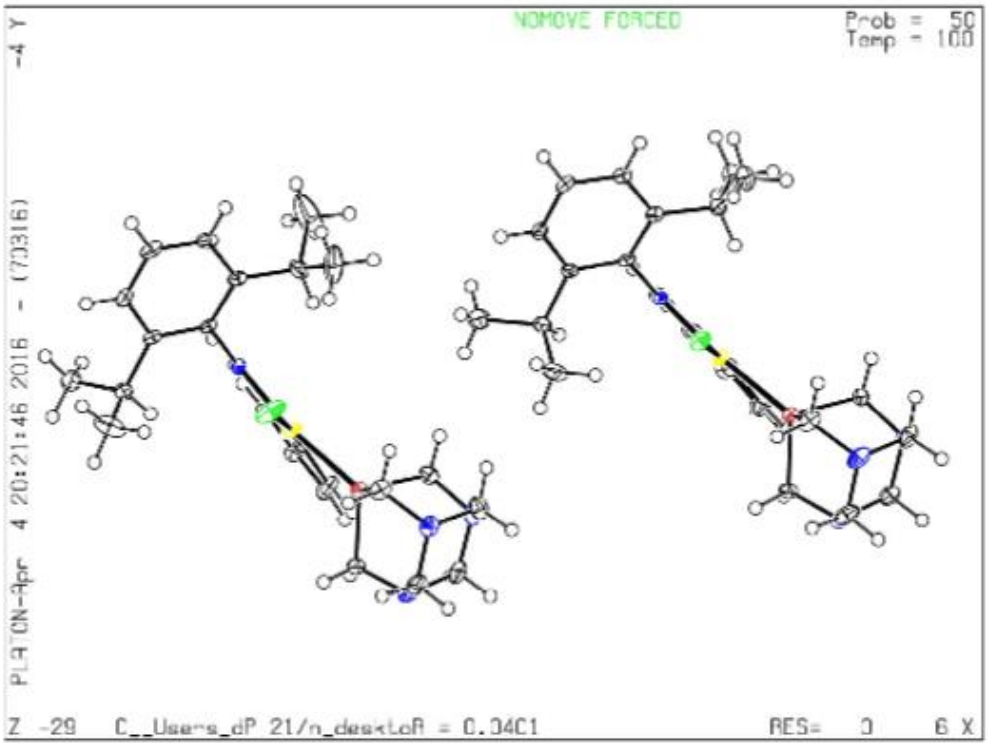

A1.7.4 CIFCHECK report for C2

checkCIF/PLATON report

Structure factors have been supplied for datablock(s) C2

THIS REPORT IS FOR GUIDANCE ONLY. IF USED AS PART OF A REVIEW PROCEDURE FOR PUBLICATION, IT SHOULD NOT REPLACE THE EXPERTISE OF AN EXPERIENCED CRYSTALLOGRAPHIC REFEREE.

No syntax errors found. CIF dictionary Interpreting this report

Datablock: C2

Bond precision: C-C = 0.0019 A Wavelength=0.71073

Cell: a=12.1991(4) b=23.1995(8) c=18.2034(6)
alpha=90 beta=93.563(2) gamma=90
Temperature: 100 K

	Calculated	Reported
Volume	5141.8(3)	5141.8(3)
Space group	P 21/c	P 21/c
Hall group	-P 2ybc	-P 2ybc
Moiety formula	C25 H33 Cl2 N4 P Pd, 0.047(O)	C25 H33 Cl2 N4 O0.05 P Pd
Sum formula	C25 H33 Cl2 N4 O0.05 P Pd	C25 H33 Cl2 N4 O0.05 P Pd
Mr	598.57	598.56
Dx,g cm-3	1.546	1.546
Z	8	8
Mu (mm-1)	1.013	1.013
F000	2451.0	2451.0
F000'	2446.73	
h,k,lmax	17,33,26	17,32,25
Nref	15996	15112
Tmin,Tmax	0.719,0.868	0.914,1.000
Tmin'	0.695	

Correction method= # Reported T Limits: Tmin=0.914 Tmax=1.000
AbsCorr = MULTI-SCAN

Data completeness= 0.945 Theta(max)= 30.718

R(reflections)= 0.0199(14027) wR2(reflections)= 0.0524(15112)

S = 1.060 Npar= 624

The following ALERTS were generated. Each ALERT has the format
test-name_ALERT_alert-type_alert-level.
Click on the hyperlinks for more details of the test.

Alert level B

PLAT220_ALERT_2_B Non-Solvent Resd 1 C Ueq(max)/Ueq(min) Range 6.2 Ratio

---

Alert level C

PLAT077_ALERT_4_C Unitcell contains non-integer number of atoms .. Please Check
PLAT213_ALERT_2_C Atom C16C has ADP max/min Ratio ..... 4.0 prolat
PLAT222_ALERT_3_C Non-Solvent Resd 1 H Uiso(max)/Uiso(min) Range 7.8 Ratio
PLAT242_ALERT_2_C Low 'MainMol' Ueq as Compared to Neighbors of C14A Check
PLAT411_ALERT_2_C Short Inter H...H Contact H23B .. H23C .. 2.02 Ang.
PLAT430_ALERT_2_C Short Inter D...A Contact N2A .. O1 .. 2.89 Ang.
PLAT480_ALERT_4_C Long H...A H-Bond Reported H20B .. Cl1B .. 2.87 Ang.
PLAT480_ALERT_4_C Long H...A H-Bond Reported H24B .. N4A .. 2.64 Ang.
PLAT480_ALERT_4_C Long H...A H-Bond Reported H23C .. Cl1B .. 2.90 Ang.
PLAT480_ALERT_4_C Long H...A H-Bond Reported H21D .. Cl2B .. 2.96 Ang.
PLAT480_ALERT_4_C Long H...A H-Bond Reported H20B .. Cl1B .. 2.87 Ang.
PLAT480_ALERT_4_C Long H...A H-Bond Reported H24B .. N4A .. 2.64 Ang.
PLAT480_ALERT_4_C Long H...A H-Bond Reported H23C .. Cl1B .. 2.90 Ang.
PLAT480_ALERT_4_C Long H...A H-Bond Reported H21D .. Cl2B .. 2.96 Ang.
PLAT480_ALERT_4_C Long H...A H-Bond Reported H20B .. Cl1B .. 2.87 Ang.
PLAT480_ALERT_4_C Long H...A H-Bond Reported H24B .. N4A .. 2.64 Ang.
PLAT480_ALERT_4_C Long H...A H-Bond Reported H23C .. Cl1B .. 2.90 Ang.
PLAT480_ALERT_4_C Long H...A H-Bond Reported H21D .. Cl2B .. 2.96 Ang.

Alert level G

PLAT002_ALERT_2_G Number of Distance or Angle Restraints on AtSite 5 Note
PLAT042_ALERT_1_G Calc. and Reported MoietyFormula Strings Differ Please Check
PLAT172_ALERT_4_G The CIF-Embedded .res File Contains DFIX Records 4 Report
PLAT232_ALERT_2_G Hirshfeld Test Diff (M-X) Pd1A -- Cl1A .. 7.4 s.u.
PLAT232_ALERT_2_G Hirshfeld Test Diff (M-X) Pd1A -- C1A .. 5.4 s.u.
PLAT232_ALERT_2_G Hirshfeld Test Diff (M-X) Pd1B -- Cl1B .. 9.3 s.u.
PLAT301_ALERT_3_G Main Residue Disorder ..... Percentage = 3 Note
PLAT302_ALERT_4_G Anion/Solvent Disorder ..... Percentage = 100 Note
PLAT304_ALERT_4_G Non-Integer Number of Atoms (0.09) in Resd. # 3 Check
PLAT311_ALERT_2_G Isolated Disordered Oxygen Atom (No H's ?) ..... O1 Check
PLAT367_ALERT_2_G Long? C(sp?)-C(sp?) Bond C9A - C14A .. 1.52 Ang.
PLAT432_ALERT_2_G Short Inter X...Y Contact O1 .. C16A .. 2.53 Ang.
PLAT860_ALERT_3_G Number of Least-Squares Restraints ..... 4 Note
PLAT912_ALERT_4_G Missing # of FCF Reflections Above STh/L= 0.600 856 Note
PLAT978_ALERT_2_G Number C-C Bonds with Positive Residual Density 15 Note

---

0 **ALERT level A** = Most likely a serious problem - resolve or explain
1 **ALERT level B** = A potentially serious problem, consider carefully
18 **ALERT level C** = Check. Ensure it is not caused by an omission or oversight
15 **ALERT level G** = General information/check it is not something unexpected

1 ALERT type 1 CIF construction/syntax error, inconsistent or missing data
13 ALERT type 2 Indicator that the structure model may be wrong or deficient
3 ALERT type 3 Indicator that the structure quality may be low
17 ALERT type 4 Improvement, methodology, query or suggestion
0 ALERT type 5 Informative message, check

It is advisable to attempt to resolve as many as possible of the alerts in all categories. Often the minor alerts point to easily fixed oversights, errors and omissions in your CIF or refinement strategy, so attention to these fine details can be worthwhile. In order to resolve some of the more serious problems it may be necessary to carry out additional measurements or structure refinements. However, the purpose of your study may justify the reported deviations and the more serious of these should normally be commented upon in the discussion or experimental section of a paper or in the "special_details" fields of the CIF. checkCIF was carefully designed to identify outliers and unusual parameters, but every test has its limitations and alerts that are not important in a particular case may appear. Conversely, the absence of alerts does not guarantee there are no aspects of the results needing attention. It is up to the individual to critically assess their own results and, if necessary, seek expert advice.

Publication of your CIF in IUCr journals

A basic structural check has been run on your CIF. These basic checks will be run on all CIFs submitted for publication in IUCr journals (*Acta Crystallographica*, *Journal of Applied Crystallography*, *Journal of Synchrotron Radiation*); however, if you intend to submit to *Acta Crystallographica Section C* or *E* or *IUCrData*, you should make sure that full publication checks are run on the final version of your CIF prior to submission.

Publication of your CIF in other journals

Please refer to the *Notes for Authors* of the relevant journal for any special instructions relating to CIF submission.

PLATON version of 30/03/2016; check.def file version of 30/03/2016

Datablock C2 - ellipsoid plot

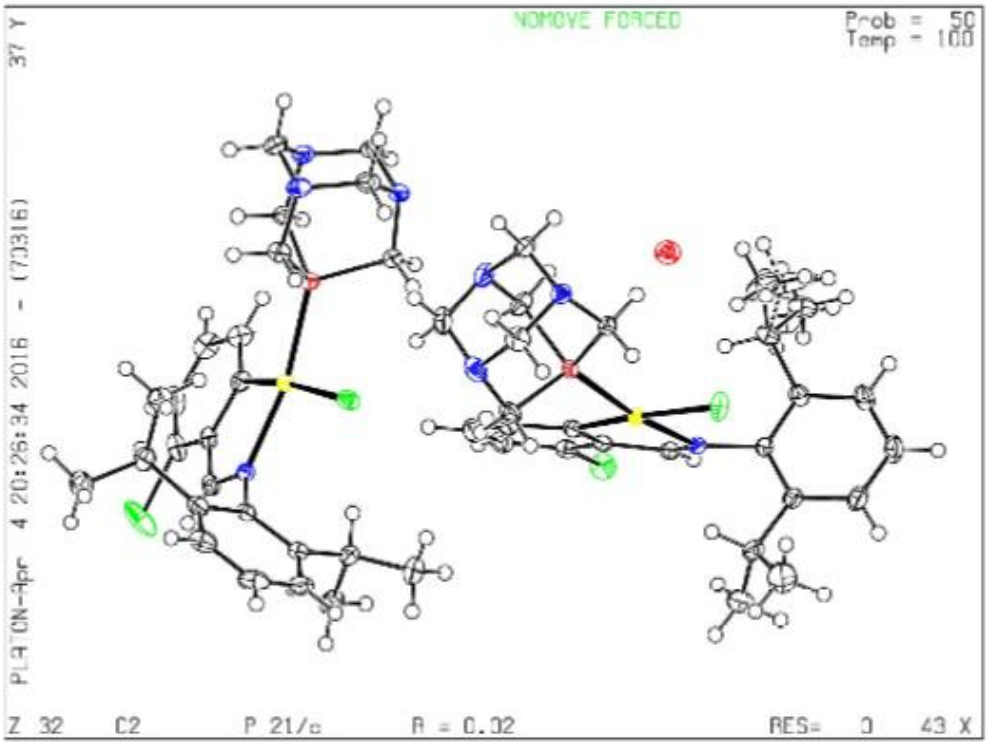

A1.7.5 CIFCHECK report for C4

checkCIF/PLATON report

Structure factors have been supplied for datablock(s) C4

THIS REPORT IS FOR GUIDANCE ONLY. IF USED AS PART OF A REVIEW PROCEDURE FOR PUBLICATION, IT SHOULD NOT REPLACE THE EXPERTISE OF AN EXPERIENCED CRYSTALLOGRAPHIC REFEREE.

No syntax errors found. CIF dictionary Interpreting this report

Datablock: C4

Bond precision: C-C = 0.0039 A Wavelength=0.71073

Cell: a=13.3048(9) b=13.7674(10) c=17.0288(12)
alpha=104.843(1) beta=105.172(1) gamma=109.699(1)
Temperature: 173 K

	Calculated	Reported
Volume	2622.8(3)	2622.8(3)
Space group	P -1	P -1
Hall group	-P 1	-P 1
Moiety formula	2(C26 H36 Cl N4 P Pd), H2 O	C26 H37 Cl N4 O0.50 P Pd
Sum formula	C52 H74 Cl2 N8 O P2 Pd2	C26 H37 Cl N4 O0.50 P Pd
Mr	1172.83	586.41
Dx,g cm-3	1.485	1.485
Z	2	4
Mu (mm-1)	0.894	0.894
F000	1212.0	1212.0
F000'	1209.31	
h,k,lmax	18,18,23	18,18,22
Nref	13867	12645
Tmin,Tmax	0.842,0.914	0.679,0.746
Tmin'	0.800	

Correction method= # Reported T Limits: Tmin=0.679 Tmax=0.746
AbsCorr = MULTI-SCAN

Data completeness= 0.912 Theta(max)= 28.945

R(reflections)= 0.0304(10738) wR2(reflections)= 0.0738(12645)

S = 1.031 Npar= 626

The following ALERTS were generated. Each ALERT has the format
test-name_ALERT_alert-type_alert-level.
Click on the hyperlinks for more details of the test.

Alert level B

PLAT412_ALERT_2_B Short Intra XH3 .. XHn H14B .. H16H .. 1.75 Ang.

Alert level C

PLAT213_ALERT_2_C Atom C15A has ADP max/min Ratio ..... 3.2 prolat
PLAT220_ALERT_2_C Non-Solvent Resd 2 C Ueq(max)/Ueq(min) Range 5.4 Ratio
PLAT222_ALERT_3_C Non-Solvent Resd 2 H Uiso(max)/Uiso(min) Range 6.0 Ratio
PLAT242_ALERT_2_C Low 'MainMol' Ueq as Compared to Neighbors of C14A Check
PLAT412_ALERT_2_C Short Intra XH3 .. XHn H10B .. H15I .. 1.80 Ang.
PLAT911_ALERT_3_C Missing # FCF Refl Between THmin & STh/L= 0.600 21 Report
PLAT977_ALERT_2_C Check the Negative Difference Density on H14A -0.34 eA-3
PLAT977_ALERT_2_C Check the Negative Difference Density on H26D -0.32 eA-3
PLAT977_ALERT_2_C Check the Negative Difference Density on H26F -0.40 eA-3

Alert level G

PLAT042_ALERT_1_G Calc. and Reported MoietyFormula Strings Differ Please Check
PLAT045_ALERT_1_G Calculated and Reported Z Differ by a Factor ... 0.50 Check
PLAT154_ALERT_1_G The s.u.'s on the Cell Angles are Equal ..(Note) 0.001 Degree
PLAT300_ALERT_4_G Atom Site Occupancy of *H26G is Constrained at 0.5 Check
PLAT300_ALERT_4_G Atom Site Occupancy of *H26H is Constrained at 0.5 Check
PLAT300_ALERT_4_G Atom Site Occupancy of *H26I is Constrained at 0.5 Check
PLAT300_ALERT_4_G Atom Site Occupancy of *H26J is Constrained at 0.5 Check
PLAT300_ALERT_4_G Atom Site Occupancy of *H26K is Constrained at 0.5 Check
PLAT300_ALERT_4_G Atom Site Occupancy of *H26L is Constrained at 0.5 Check
PLAT300_ALERT_4_G Atom Site Occupancy of *H26A is Constrained at 0.5 Check
PLAT300_ALERT_4_G Atom Site Occupancy of *H26B is Constrained at 0.5 Check
PLAT300_ALERT_4_G Atom Site Occupancy of *H26C is Constrained at 0.5 Check
PLAT300_ALERT_4_G Atom Site Occupancy of *H26D is Constrained at 0.5 Check
PLAT300_ALERT_4_G Atom Site Occupancy of *H26E is Constrained at 0.5 Check
PLAT300_ALERT_4_G Atom Site Occupancy of *H26F is Constrained at 0.5 Check
PLAT301_ALERT_3_G Main Residue Disorder ..... Percentage = 3 Note
PLAT367_ALERT_2_G Long? C(sp?)-C(sp?) Bond C2B - C26B .. 1.51 Ang.
PLAT367_ALERT_2_G Long? C(sp?)-C(sp?) Bond C2A - C26A .. 1.51 Ang.
PLAT773_ALERT_2_G Check long C-C Bond in CIF: C14B -- C15C . 1.74 Ang.
PLAT910_ALERT_3_G Missing # of FCF Reflection(s) Below Theta(Min) 1 Note
PLAT912_ALERT_4_G Missing # of FCF Reflections Above STh/L= 0.600 1188 Note
PLAT978_ALERT_2_G Number C-C Bonds with Positive Residual Density 9 Note

---

0 **ALERT level A** = Most likely a serious problem - resolve or explain
1 **ALERT level B** = A potentially serious problem, consider carefully
9 **ALERT level C** = Check. Ensure it is not caused by an omission or oversight
22 **ALERT level G** = General information/check it is not something unexpected

3 ALERT type 1 CIF construction/syntax error, inconsistent or missing data
12 ALERT type 2 Indicator that the structure model may be wrong or deficient
4 ALERT type 3 Indicator that the structure quality may be low
13 ALERT type 4 Improvement, methodology, query or suggestion
0 ALERT type 5 Informative message, check

It is advisable to attempt to resolve as many as possible of the alerts in all categories. Often the minor alerts point to easily fixed oversights, errors and omissions in your CIF or refinement strategy, so attention to these fine details can be worthwhile. In order to resolve some of the more serious problems it may be necessary to carry out additional measurements or structure refinements. However, the purpose of your study may justify the reported deviations and the more serious of these should normally be commented upon in the discussion or experimental section of a paper or in the "special_details" fields of the CIF. checkCIF was carefully designed to identify outliers and unusual parameters, but every test has its limitations and alerts that are not important in a particular case may appear. Conversely, the absence of alerts does not guarantee there are no aspects of the results needing attention. It is up to the individual to critically assess their own results and, if necessary, seek expert advice.

Publication of your CIF in IUCr journals

A basic structural check has been run on your CIF. These basic checks will be run on all CIFs submitted for publication in IUCr journals (*Acta Crystallographica*, *Journal of Applied Crystallography*, *Journal of Synchrotron Radiation*); however, if you intend to submit to *Acta Crystallographica Section C* or *E* or *IUCrData*, you should make sure that full publication checks are run on the final version of your CIF prior to submission.

Publication of your CIF in other journals

Please refer to the *Notes for Authors* of the relevant journal for any special instructions relating to CIF submission.

PLATON version of 30/03/2016; check.def file version of 30/03/2016

Datablock C4 - ellipsoid plot

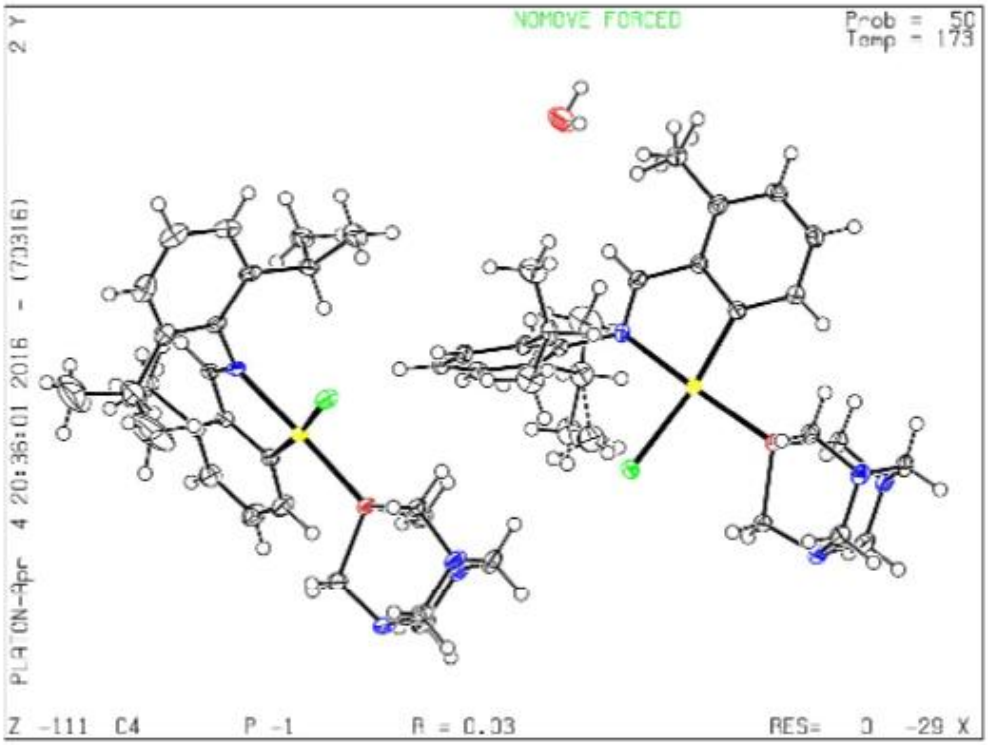

A1.7.6 CIFCHECK report for T2

checkCIF/PLATON report

Structure factors have been supplied for datablock(s) blanckenberg01_sq

THIS REPORT IS FOR GUIDANCE ONLY. IF USED AS PART OF A REVIEW PROCEDURE FOR PUBLICATION, IT SHOULD NOT REPLACE THE EXPERTISE OF AN EXPERIENCED CRYSTALLOGRAPHIC REFEREE.

No syntax errors found. CIF dictionary Interpreting this report

Datablock: blanckenberg01_sq

```
Bond precision:   C-C = 0.0021 A          Wavelength=0.71073

Cell:             a=9.845(6)     b=20.867(14)         c=20.726(13)
                  alpha=90       beta=90.540(12)      gamma=90
Temperature:      100 K

                  Calculated                  Reported
Volume            4258(5)                     4258(5)
Space group       P 21/c                      P 1 21/c 1
Hall group        -P 2ybc                     -P 2ybc
Moiety formula    C23 H31 N O3                C23 H31 N O3
Sum formula       C23 H31 N O3                C23 H31 N O3
Mr                369.49                      369.49
Dx,g cm-3         1.153                       1.153
Z                 8                           8
Mu (mm-1)         0.075                       0.075
F000              1600.0                      1600.0
F000'             1600.69
h,k,lmax          13,27,27                    12,27,27
Nref              10508                       9914
Tmin,Tmax         0.973,0.984                 0.714,0.746
Tmin'             0.970

Correction method= # Reported T Limits: Tmin=0.714 Tmax=0.746
AbsCorr = MULTI-SCAN

Data completeness= 0.943          Theta(max)= 28.230

R(reflections)= 0.0468( 7249)     wR2(reflections)= 0.1176( 9914)

S = 1.064                  Npar= 545
```

The following ALERTS were generated. Each ALERT has the format
test-name_ALERT_alert-type_alert-level.
Click on the hyperlinks for more details of the test.

Alert level C

```
PLAT220_ALERT_2_C Non-Solvent Resd 1    O    Ueq(max)/Ueq(min) Range         3.4 Ratio
PLAT220_ALERT_2_C Non-Solvent Resd 2    C    Ueq(max)/Ueq(min) Range         3.7 Ratio
PLAT222_ALERT_3_C Non-Solvent Resd 1    H Uiso(max)/Uiso(min) Range         4.3 Ratio
PLAT222_ALERT_3_C Non-Solvent Resd 2    H Uiso(max)/Uiso(min) Range         4.6 Ratio
PLAT234_ALERT_4_C Large Hirshfeld Difference C10A    --  C11C    ..        0.19 Ang.
PLAT242_ALERT_2_C Low    'MainMol' Ueq as Compared to Neighbors of       C10A Check
PLAT413_ALERT_2_C Short Inter XH3 .. XHn     H21D    ..  H12L    ..       2.03 Ang.
PLAT413_ALERT_2_C Short Inter XH3 .. XHn     H22C    ..  H12K    ..       2.00 Ang.
PLAT906_ALERT_3_C Large K value in the Analysis of Variance ......      3.270 Check
PLAT911_ALERT_3_C Missing # FCF Refl Between THmin & STh/L=  0.600          5 Report
```

Alert level G

```
PLAT002_ALERT_2_G Number of Distance or Angle Restraints on AtSite         10 Note
PLAT172_ALERT_4_G The CIF-Embedded .res File Contains DFIX Records          1 Report
PLAT230_ALERT_2_G Hirshfeld Test Diff for    C10A    --  C12C    ..       5.3 s.u.
PLAT301_ALERT_3_G Main Residue  Disorder ..... Percentage =                7 Note
PLAT605_ALERT_4_G Largest Solvent Accessible VOID in Structure ...         76 A**3
PLAT720_ALERT_4_G Number of Unusual/Non-Standard Labels ........           8 Note
PLAT860_ALERT_3_G Number of Least-Squares Restraints .............         8 Note
PLAT869_ALERT_4_G ALERTS Related to the use of SQUEEZE Suppressed          ! Info
PLAT910_ALERT_3_G Missing # of FCF Reflection(s) Below Theta(Min)          1 Note
PLAT912_ALERT_4_G Missing # of FCF Reflections Above STh/L=  0.600       569 Note
```

```
  0 ALERT level A = Most likely a serious problem - resolve or explain
  0 ALERT level B = A potentially serious problem, consider carefully
 10 ALERT level C = Check. Ensure it is not caused by an omission or oversight
 10 ALERT level G = General information/check it is not something unexpected

  0 ALERT type 1 CIF construction/syntax error, inconsistent or missing data
  7 ALERT type 2 Indicator that the structure model may be wrong or deficient
  7 ALERT type 3 Indicator that the structure quality may be low
  6 ALERT type 4 Improvement, methodology, query or suggestion
  0 ALERT type 5 Informative message, check
```

It is advisable to attempt to resolve as many as possible of the alerts in all categories. Often the minor alerts point to easily fixed oversights, errors and omissions in your CIF or refinement strategy, so attention to these fine details can be worthwhile. In order to resolve some of the more serious problems it may be necessary to carry out additional measurements or structure refinements. However, the purpose of your study may justify the reported deviations and the more serious of these should normally be commented upon in the discussion or experimental section of a paper or in the "special_details" fields of the CIF. checkCIF was carefully designed to identify outliers and unusual parameters, but every test has its limitations and alerts that are not important in a particular case may appear. Conversely, the absence of alerts does not guarantee there are no aspects of the results needing attention. It is up to the individual to critically assess their own results and, if necessary, seek expert advice.

Publication of your CIF in IUCr journals

A basic structural check has been run on your CIF. These basic checks will be run on all CIFs submitted for publication in IUCr journals (*Acta Crystallographica*, *Journal of Applied Crystallography*, *Journal of Synchrotron Radiation*); however, if you intend to submit to *Acta Crystallographica Section C* or *E* or *IUCrData*, you should make sure that full publication checks are run on the final version of your CIF prior to submission.

Publication of your CIF in other journals

Please refer to the *Notes for Authors* of the relevant journal for any special instructions relating to CIF submission.

PLATON version of 30/03/2016; check.def file version of 30/03/2016

Datablock blanckenberg01_sq - ellipsoid plot

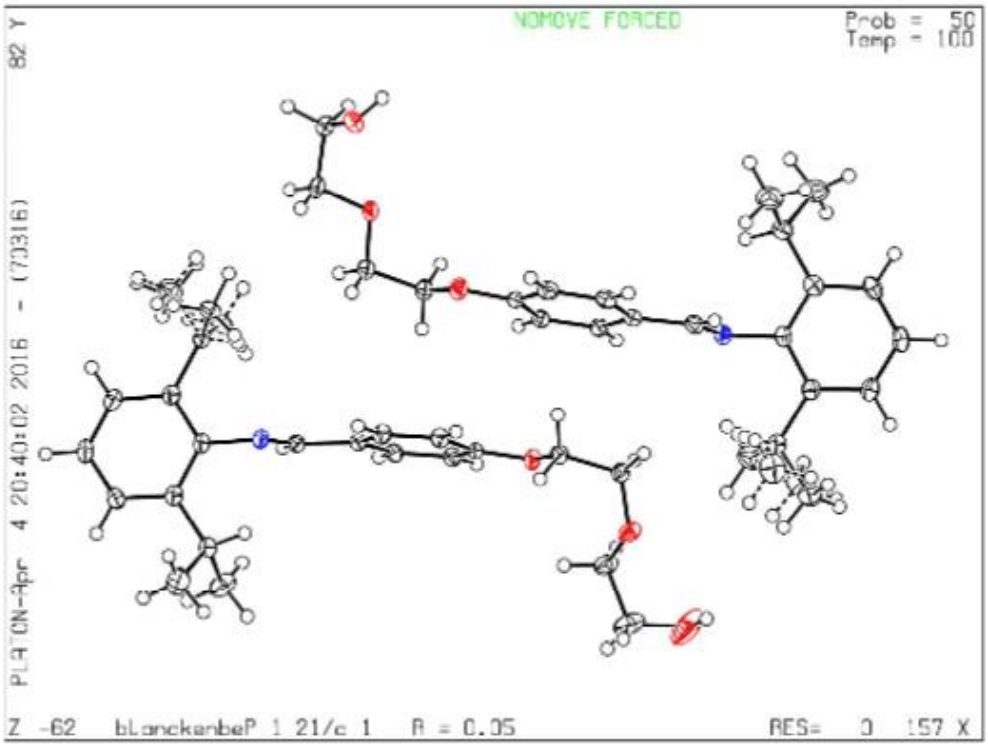

Appendix 2
Additional NMR spectroscopy study data

A2.1 Variable temperature ^{1}H NMR spectra

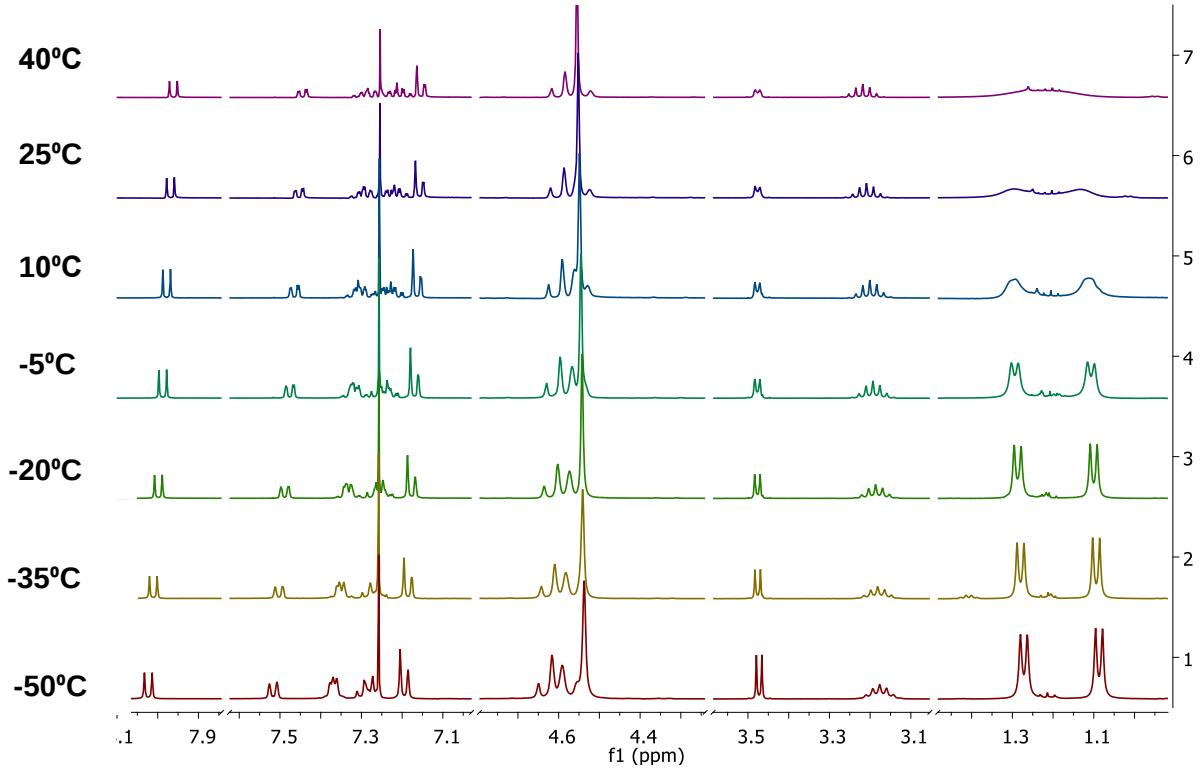

Figure A2.1: ^{1}H NMR spectroscopic array of C1 in $CDCl_3$ (-50 – 40 °C).

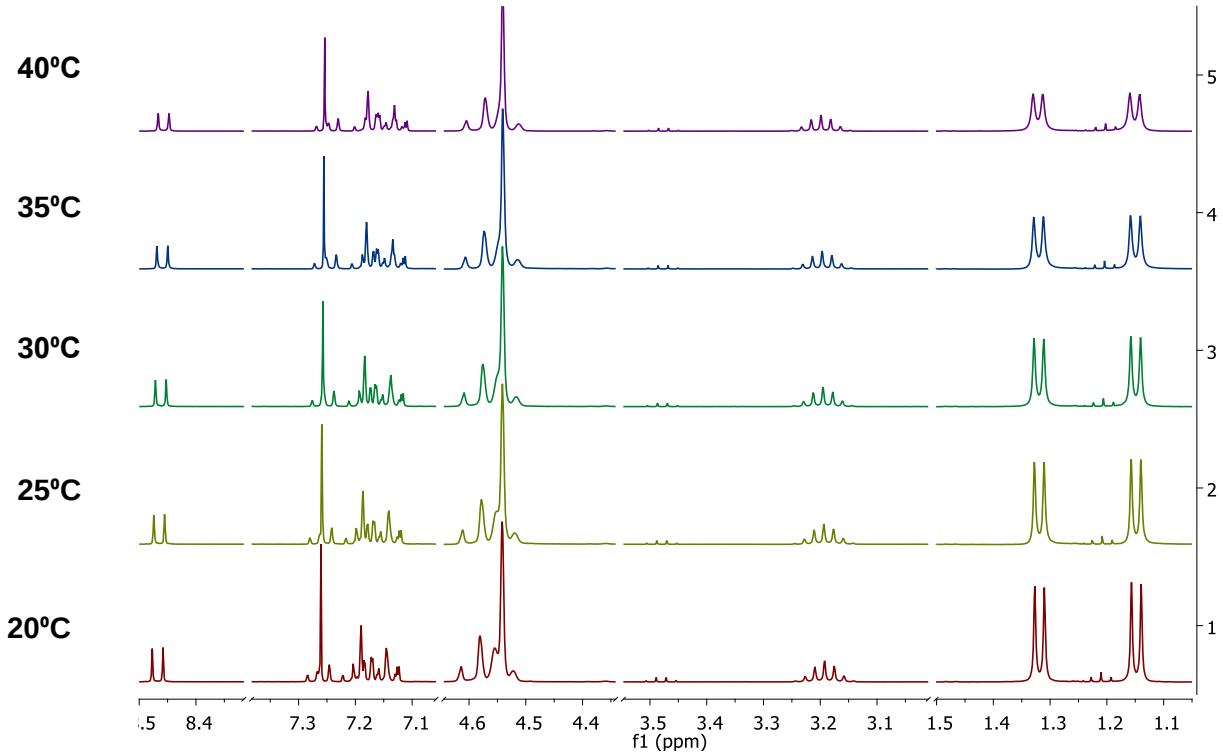

Figure A2.2: ^{1}H NMR spectroscopic array of C2 in $CDCl_3$ (20 – 40 °C).

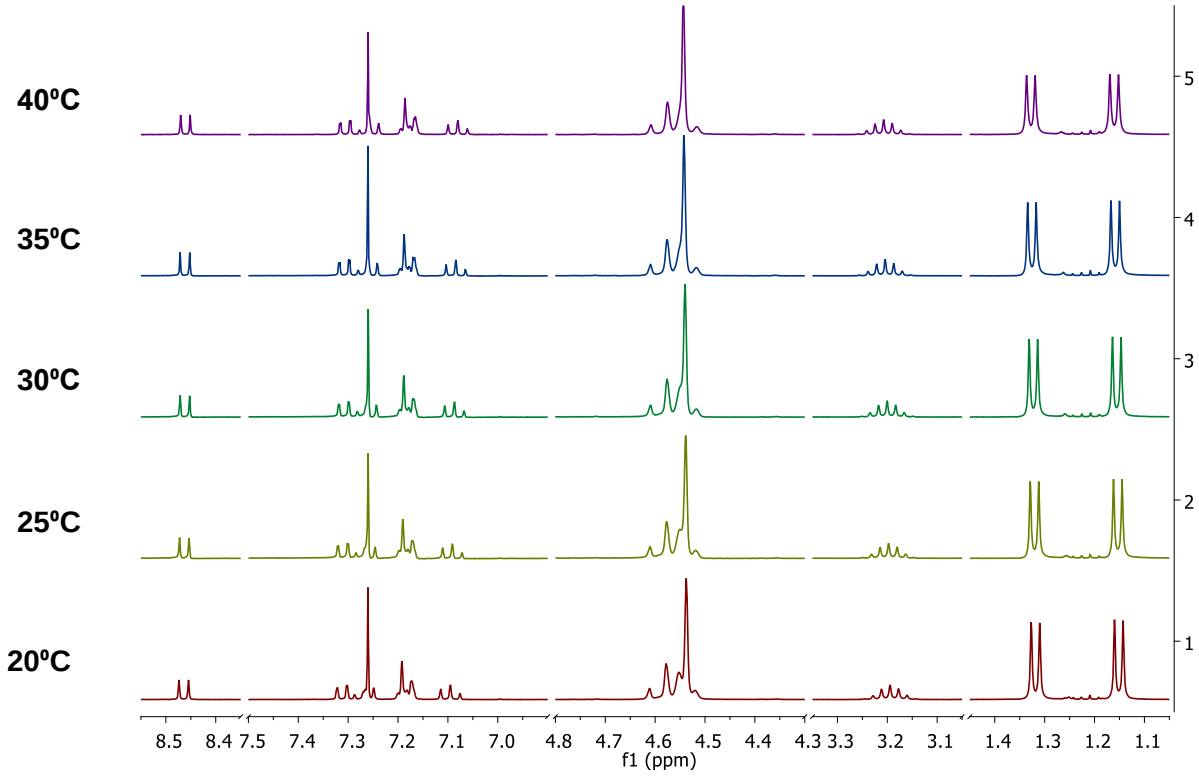

Figure A2.3: ^{1}H NMR spectroscopic array of C3 in $CDCl_3$ (20 – 40 °C).

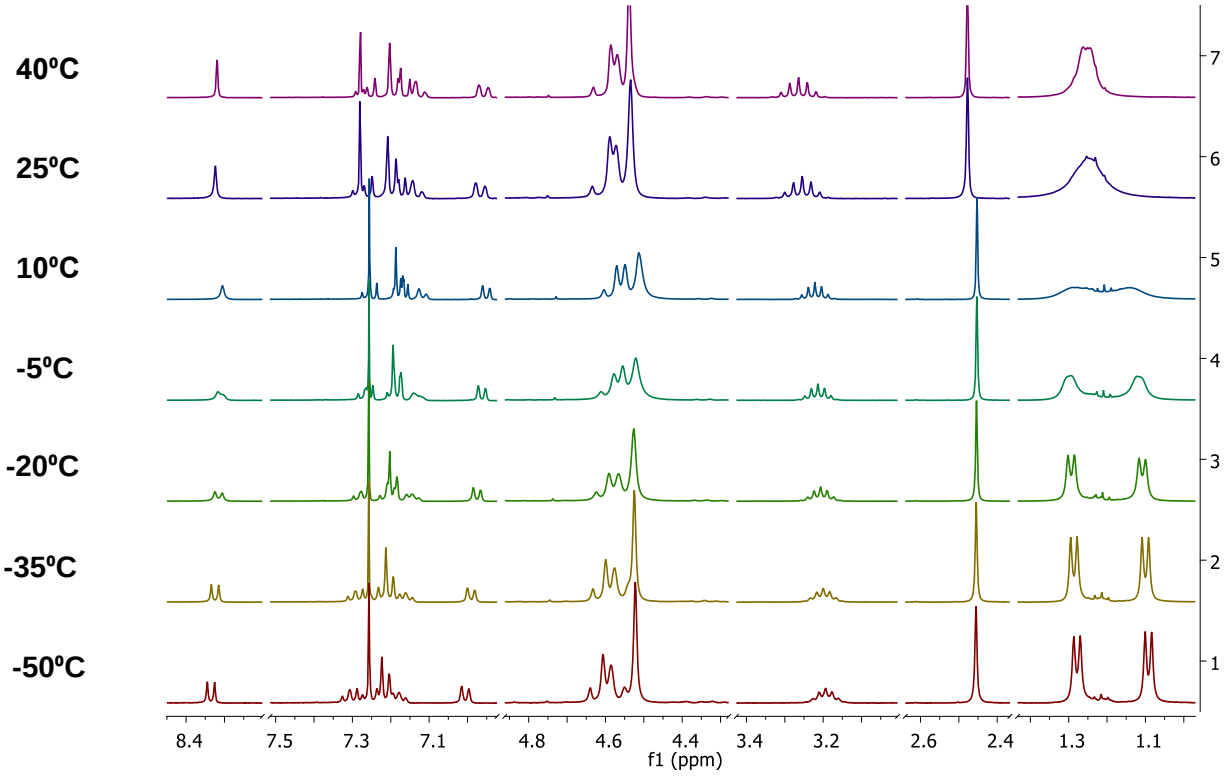

Figure A2.4: ^{1}H NMR spectroscopic array of C4 in $CDCl_3$ (-50 – 40 °C).

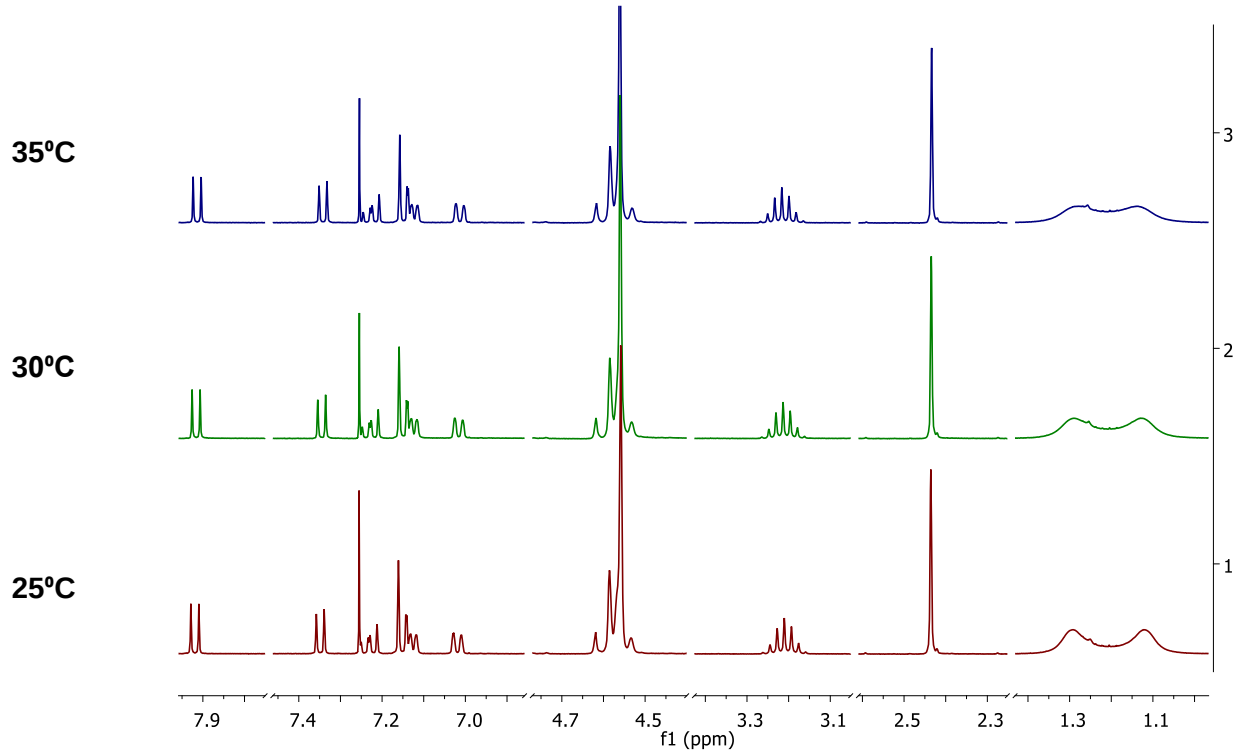

Figure A2.5: ^{1}H NMR spectroscopic array of C5 in $CDCl_3$ (25 – 35 °C).

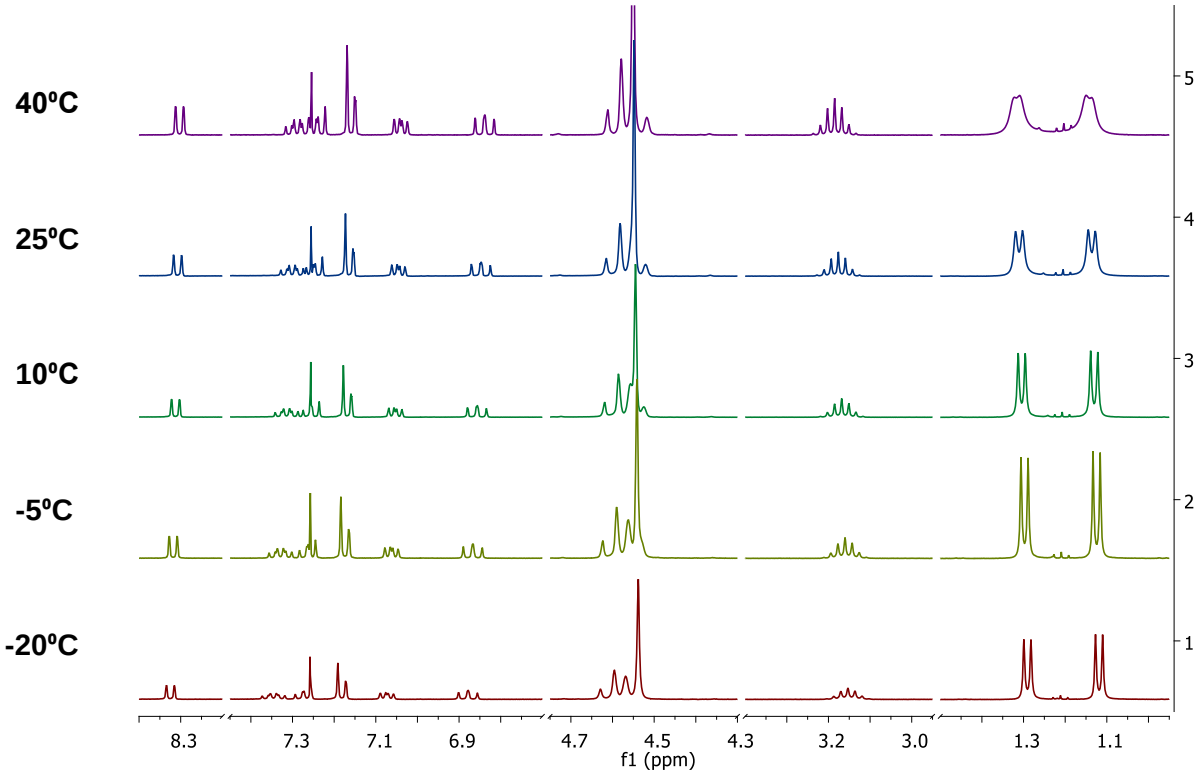

Figure A2.6: ^{1}H NMR spectroscopic array of C6 in $CDCl_3$ (-20 – 40 °C).

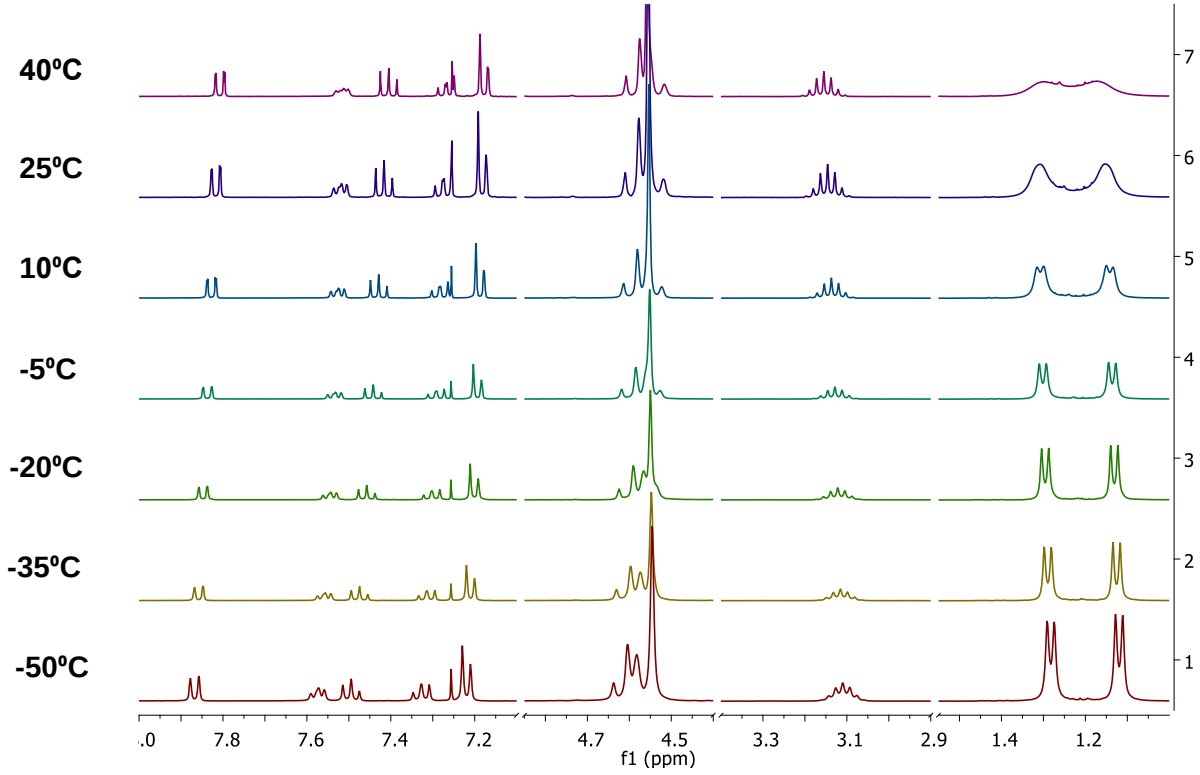

Figure A2.7: ^{1}H NMR spectroscopic array of C7 in $CDCl_3$ (-50 – 40 °C).

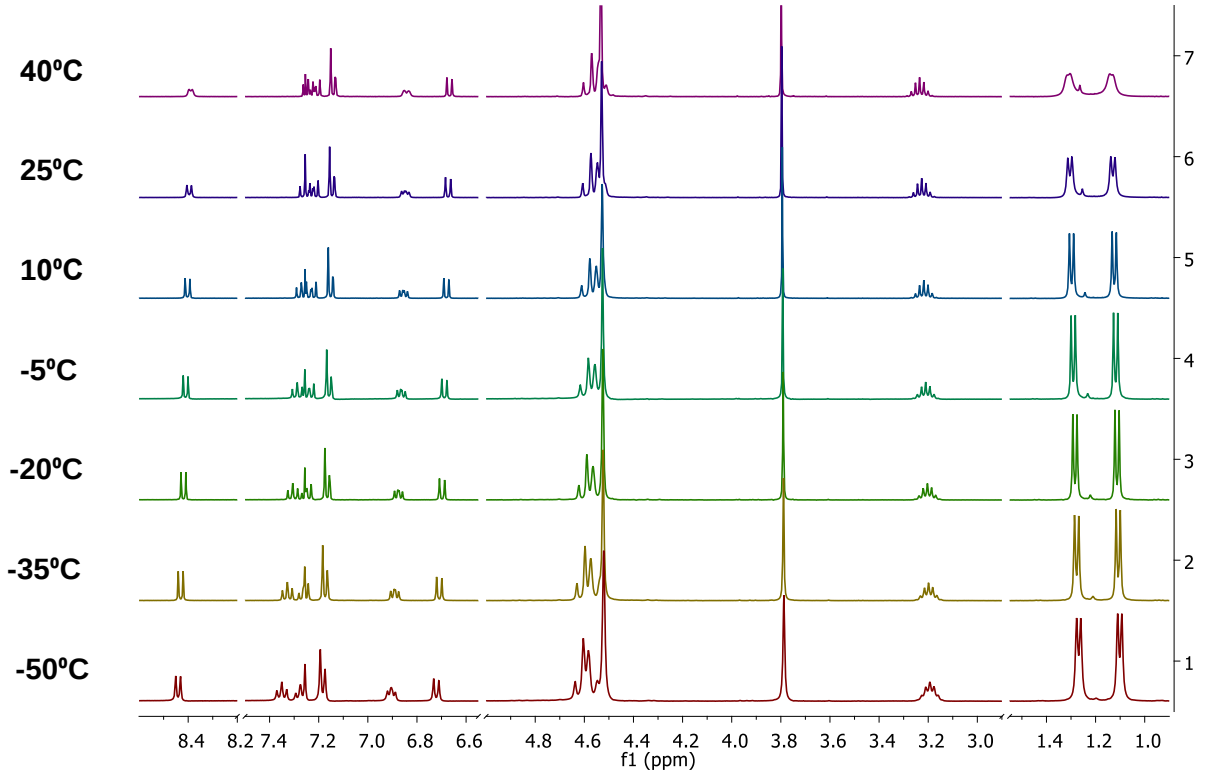

Figure A2.8: ^{1}H NMR spectroscopic array of C8 in $CDCl_3$ (-50 – 40 °C).

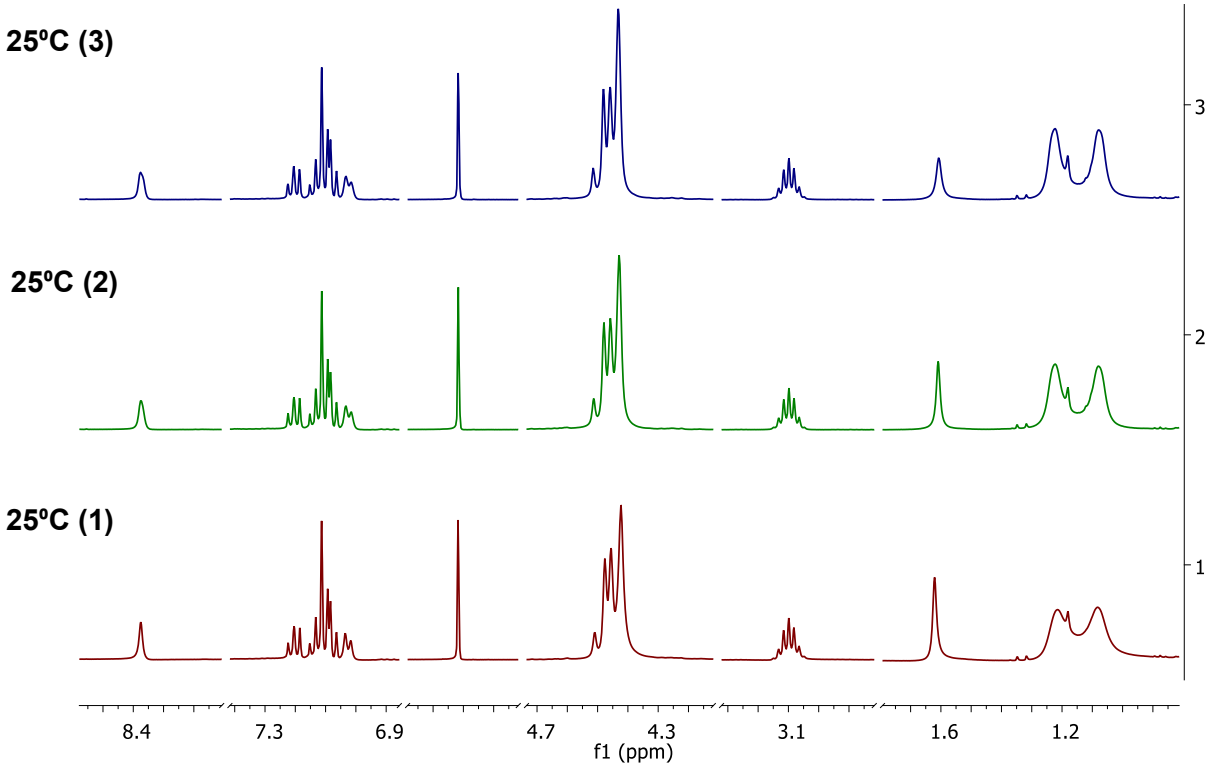

Figure A2.9: ^{1}H NMR (25 °C) of C2 in TCE-d2 showing no change after cooling, heating and cooling again. Note that the slight differences observed in the spectra may be due to slight differences in the temperature of the sample.

A2.2 Eyring plots

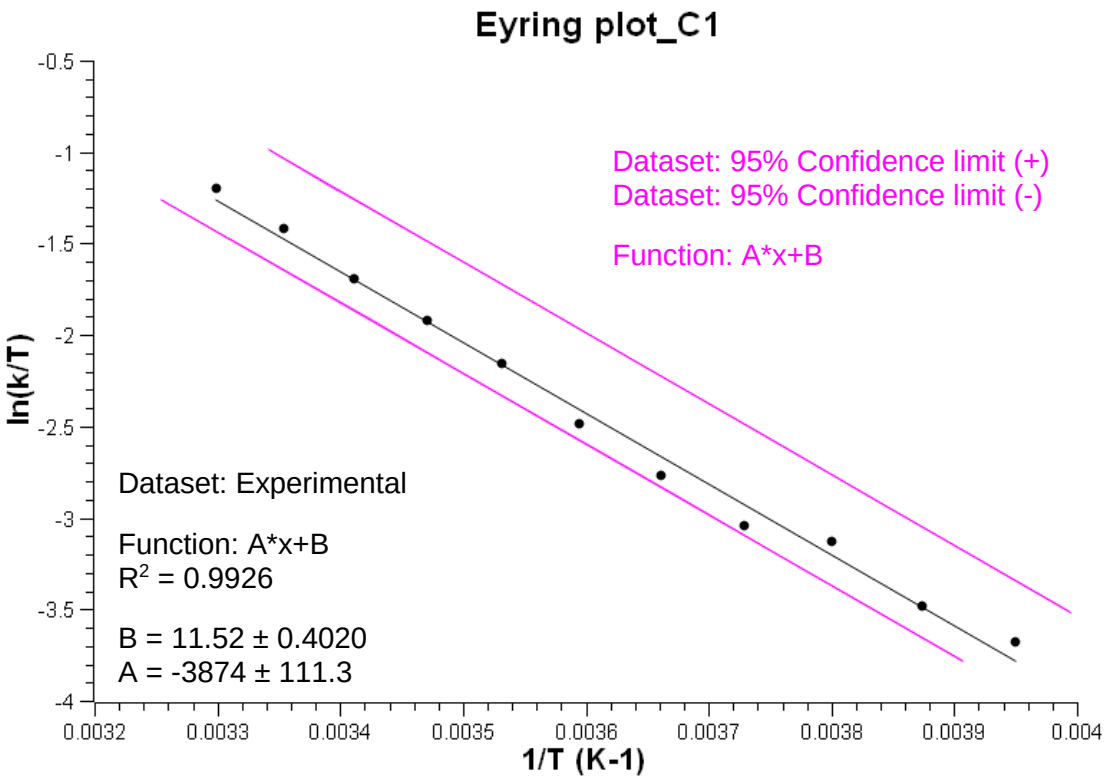

Figure A2.10: Eyring plot of C1 in $CDCl_3$.

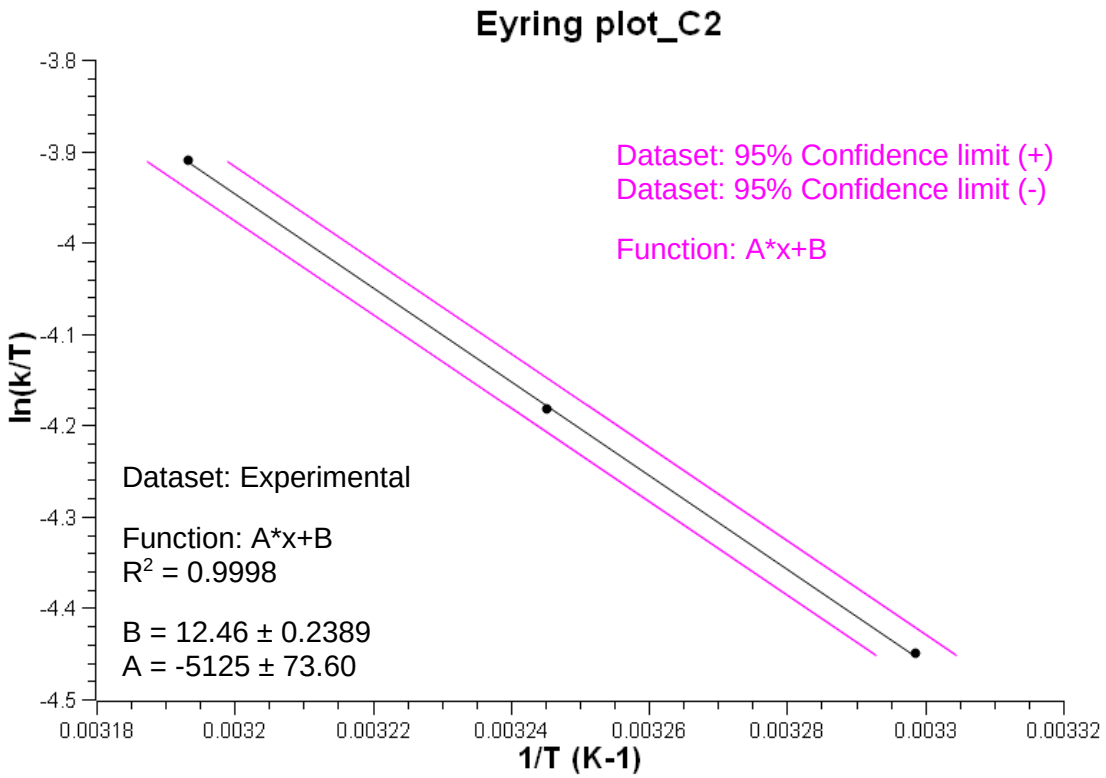

Figure A2.11: Eyring plot of C2 in $CDCl_3$.

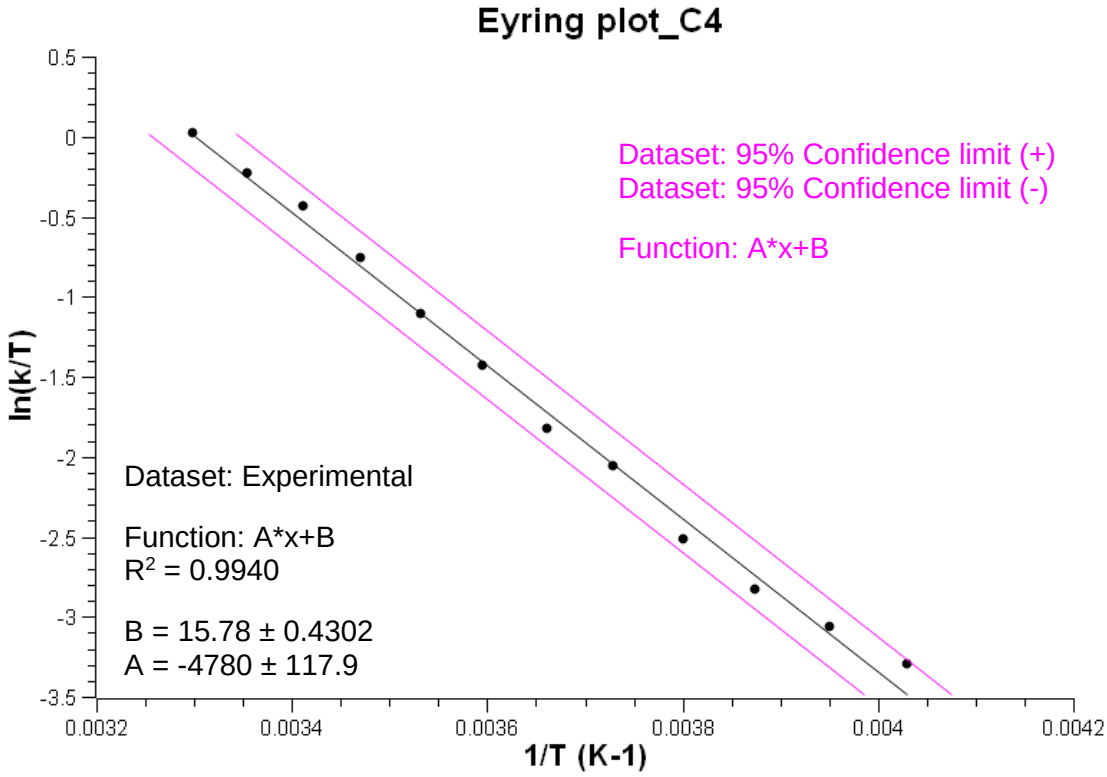

Figure A2.12: Eyring plot of C4 in $CDCl_3$.

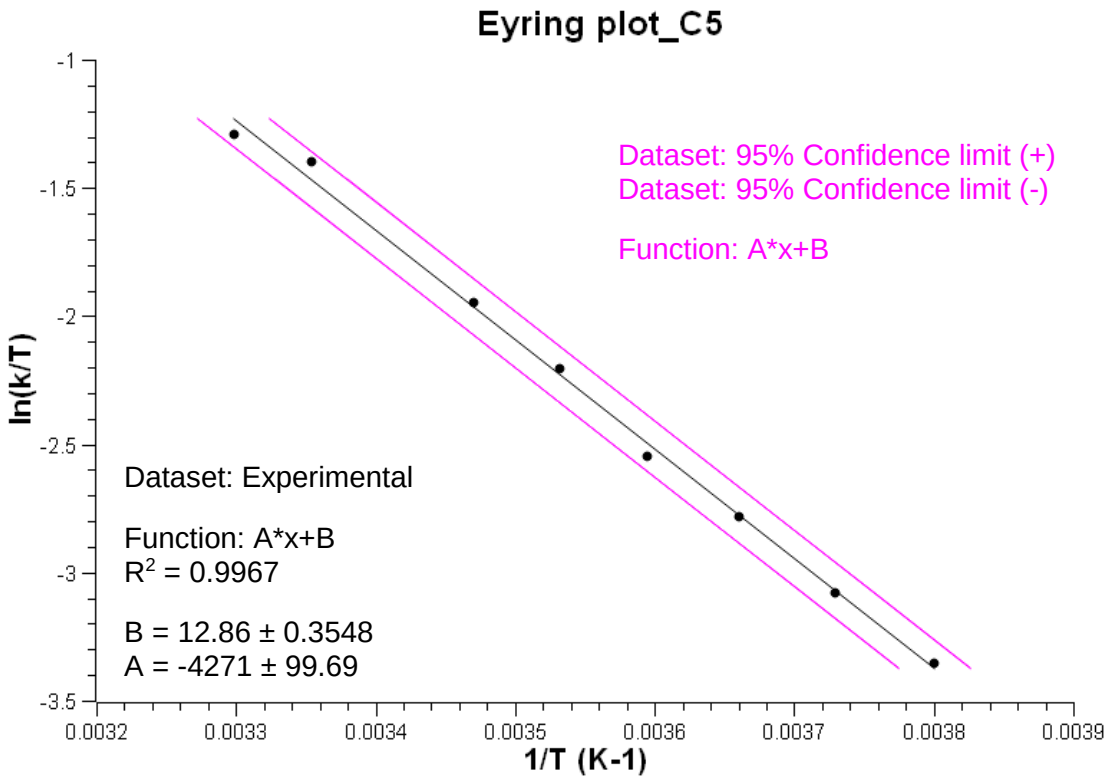

Figure A2.13: Eyring plot of C5 in $CDCl_3$.

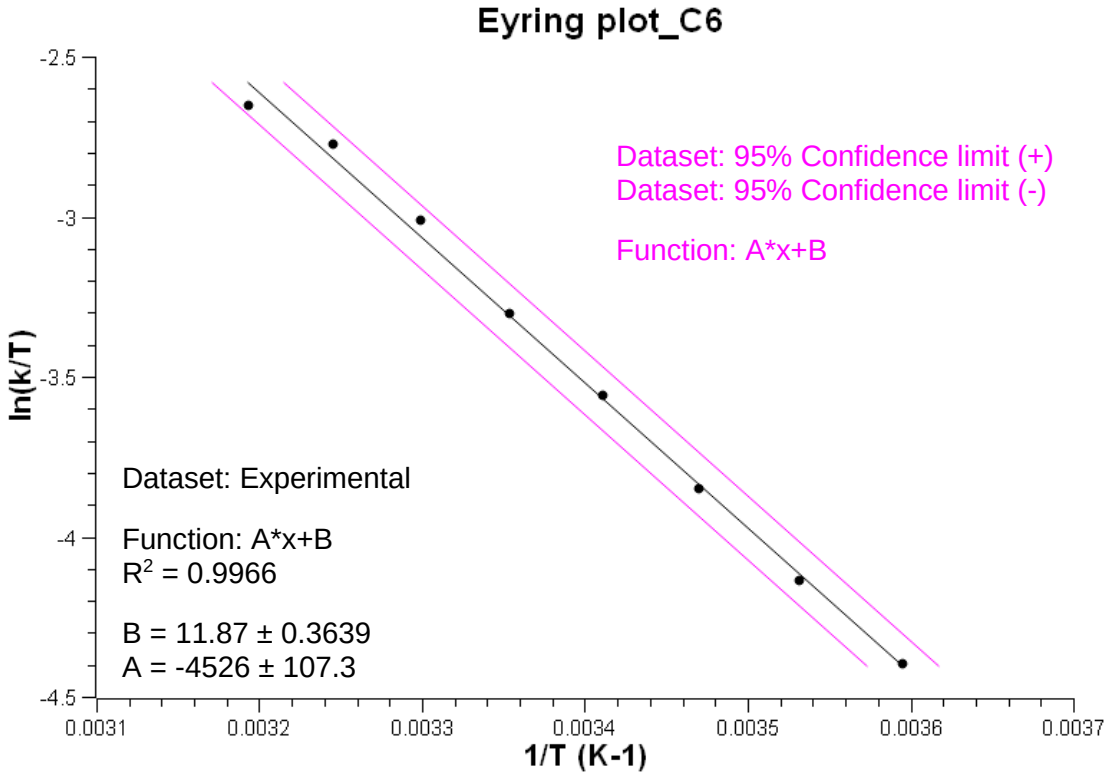

Figure A2.14: Eyring plot of C6 in $CDCl_3$.

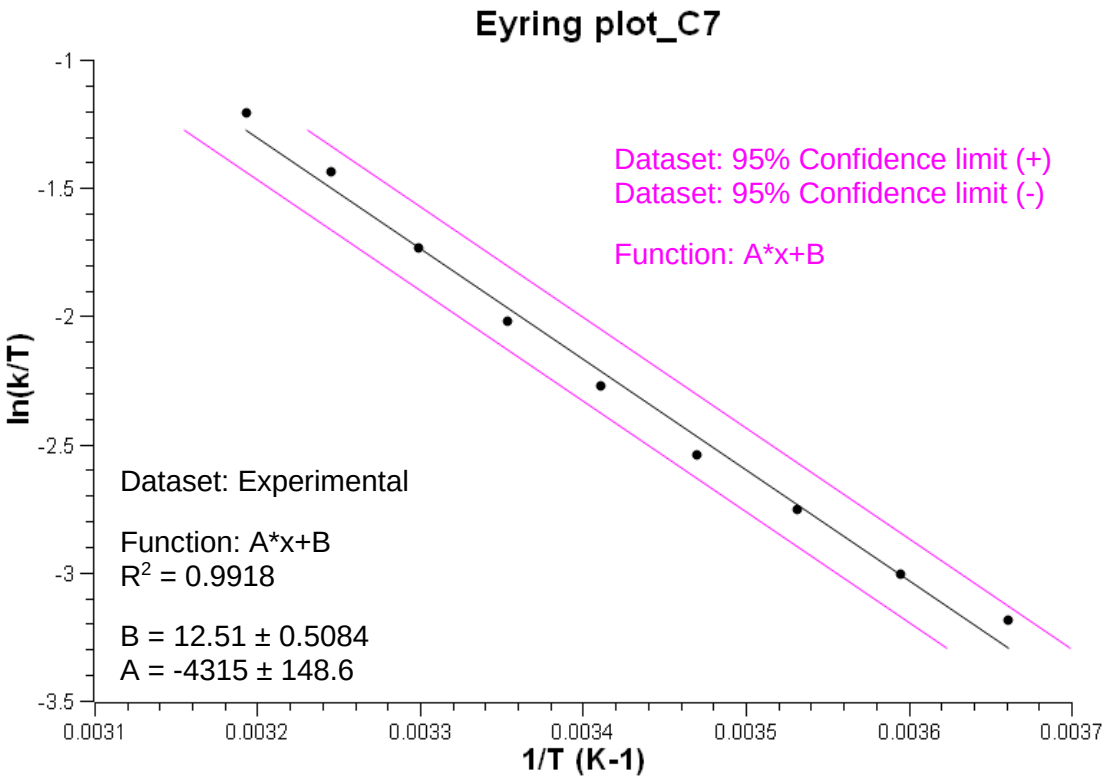

Figure A2.15: Eyring plot of C7 in $CDCl_3$.

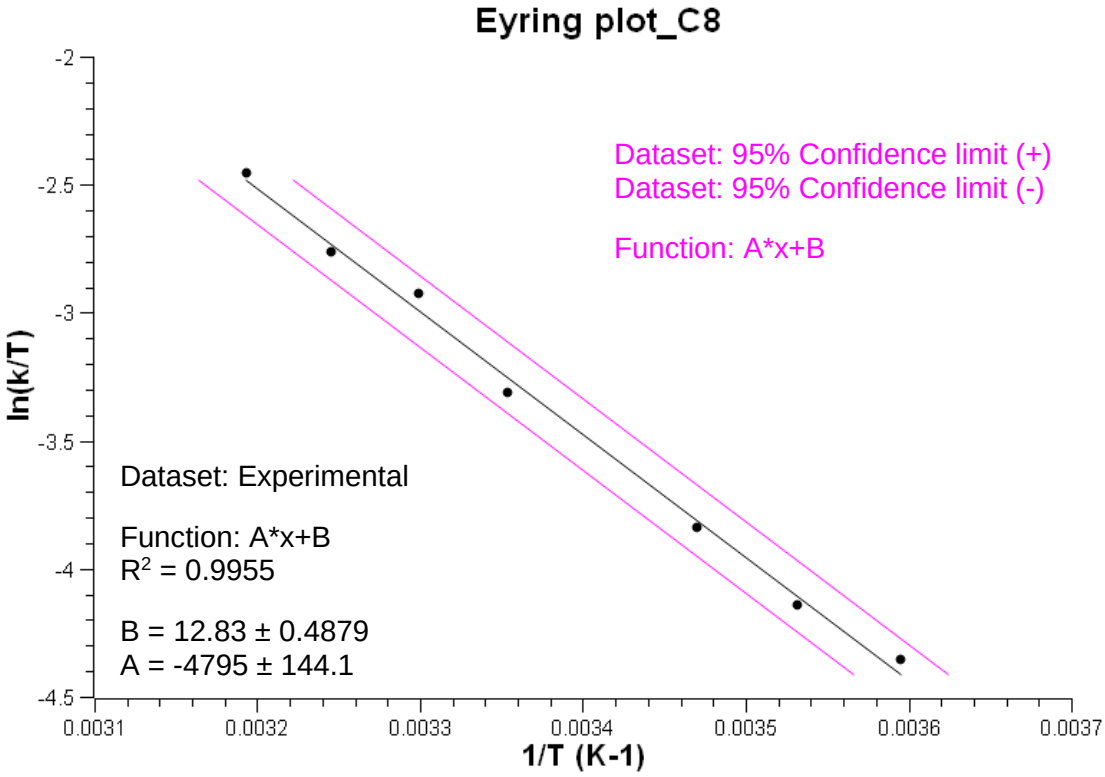

Figure A2.16: Eyring plot of C8 in $CDCl_3$.

A2.3 ORCA Input files

A2.3.1 Monomer

File: /home/15642097/Documents/ORCA...a_ACN_D3_TZVP_monomer_geop.inp Page 1 of 2

```
# ============================================================
# Orca input file made in Gabedit
# ============================================================
! Opt PBE D3 RI COSMO(Acetonitrile)
! VeryTightSCF  VerySlowConv XYZFILE
! Def2-TZVP Def2-TZVP/J AutoAux

%basis
newgto Cl "ma-def2-TZVP" end #
newgto N "ma-def2-TZVP" end #
newgto P "ma-def2-TZVP" end #
end

! ECP{LANL=[Pd]}
! NumFreq

%pal
nprocs 16
end

%output
     print[p_mos] 1
 end #output
* xyz 0   1
 Pd  8.094678 0.904377 0.061087
 H  2.777906 3.178073 -2.238690
 Cl  8.365334 2.829873 -1.375667
 N  10.171193 0.713902 0.437240
 C  8.066753 -0.722590 1.255849
 C  6.999152 -1.497122 1.715703
 C  7.203658 -2.612804 2.539333
 C  8.485157 -2.997934 2.934644
 C  9.565717 -2.240822 2.492385
 C  9.382421 -1.115943 1.665915
 C  10.466368 -0.297126 1.193274
 C  11.195920 1.550296 -0.087105
 C  11.993493 1.087033 -1.158352
 C  12.971359 1.959129 -1.652626
 C  13.147426 3.233472 -1.111766
 C  12.334615 3.669471 -0.066626
 C  11.338030 2.841182 0.460262
 C  10.459398 3.281056 1.616308
 C  10.103713 4.768632 1.572291
 C  11.103405 2.905683 2.961710
 C  11.743995 -0.270670 -1.796758
 C  12.961231 -0.843971 -2.526762
 C  10.530672 -0.196627 -2.739201
 H  9.513529 2.718628 1.531509
 H  10.985520 5.407329 1.732336
 H  9.380370 5.002648 2.367372
 H  9.650667 5.032580 0.606315
 H  11.308348 1.827192 3.027472
 H  10.437829 3.177902 3.794833
 H  12.057062 3.438227 3.096164
 H  12.739114 -1.866451 -2.863292
 H  13.846134 -0.880908 -1.874989
 H  13.218041 -0.253997 -3.419170
 H  9.633827 0.166028 -2.215842
 H  10.312839 -1.189013 -3.160979
 H  10.733678 0.497597 -3.568905
 H  11.489792 -0.982225 -0.995473
 H  12.476333 4.670011 0.343837
 H  13.921272 3.891124 -1.512674
 H  13.608689 1.638929 -2.478229
 Cl  11.173654 -2.725377 2.988029
 H  8.644143 -3.867276 3.571781
 H  6.344903 -3.194925 2.879027
```

```
 H  5.976387 -1.253614 1.445865
 C  4.448520 0.143618 0.241787
 H  4.422383 0.172512 1.341573
 H  4.574963 -0.901607 -0.077690
 H  11.507351 -0.503356 1.464646
 C  3.789973 2.892439 -1.912270
 C  5.210296 2.848079 0.061388
 N  3.845086 3.019937 -0.446895
 N  4.057634 1.532681 -2.409227
 C  5.454744 1.144657 -2.188150
 P  5.893460 1.165385 -0.374794
 C  2.928310 2.037962 0.146906
 C  3.135823 0.597589 -1.751981
 N  3.174949 0.654438 -0.284141
 H  1.904229 2.308842 -0.150609
 H  2.999299 2.091979 1.242828
 H  3.366296 -0.426487 -2.078812
 H  2.112812 0.843511 -2.075029
 H  5.219260 2.963642 1.155322
 H  5.882636 3.600549 -0.373494
 H  6.133657 1.840499 -2.700007
 H  5.629073 0.133010 -2.583811
 H  4.512572 3.587802 -2.361601
*
```

A2.3.2 Dimer

File: /home/15642097/Documents/ORCA...er2/Pd_TPa_ACN_Dimer2_freq.inp Page 1 of 3

```
# ============================================================
# Orca input file made in Gabedit
# ============================================================
! Opt PBE D3 RI COSMO(Acetonitrile)
! VeryTightSCF  VerySlowConv XYZFILE
! Def2-TZVP Def2-TZVP/J
! ECP{LANL=[Pd]}
! NumFreq

%pal
nprocs 16
end

%output
     print[p_mos] 1
 end #output
* xyz 0   1
  Pd  8.09467819923630      0.90437670823584      0.06108659838984
  H   2.77790631867497      3.17807308042603     -2.23869009761431
  Cl  8.36533384461883      2.82987271090113     -1.37566681327849
  N   10.17119298204479      0.71390181560196      0.43723957431919
  C   8.06675320032548     -0.72258979941945      1.25584918964907
  C   6.99915246091288     -1.49712161810412      1.71570347065345
  C   7.20365778702599     -2.61280382093249      2.53933265697743
  C   8.48515689502118     -2.99793382099345      2.93464373072049
  C   9.56571739354381     -2.24082231593015      2.49238510135553
  C   9.38242139691855     -1.11594340315533      1.66591459493552
  C   10.46636841353929      -0.29712644251882      1.19327412012028
  C   11.19591981615061      1.55029627745348     -0.08710519443304
  C   11.99349316851857      1.08703286563351     -1.15835248339384
  C   12.97135896242435      1.95912945003123     -1.65262610617392
  C   13.14742575585089      3.23347166884859     -1.11176573528328
  C   12.33461474282562      3.66947095208259     -0.06662556756679
  C   11.33802963385403      2.84118188380424      0.46026198962821
  C   10.45939761397685      3.28105640963698      1.61630812858104
  C   10.10371293904159      4.76863226045316      1.57229127015769
  C   11.10340454340468      2.90568343403646      2.96170957093402
  C   11.74399515983015     -0.27066986189380     -1.79675760088833
  C   12.96123112267098     -0.84397098911027     -2.52676249674212
  C   10.53067208569195     -0.19662716016201     -2.73920136561521
  H   9.51352908391979      2.71862771607790      1.53150939395348
  H   10.98552002761940      5.40732866865034      1.73233637906061
  H   9.38036998715166      5.00264845226454      2.36737226090331
  H   9.65066683094685      5.03257981499610      0.60631500061114
  H   11.30834769372857      1.82719244383829      3.02747220984781
  H   10.43782944332230      3.17790184600823      3.79483259391459
  H   12.05706204793929      3.43822714360935      3.09616429133622
  H   12.73911442019121     -1.86645149977623     -2.86329217808608
  H   13.84613441102607     -0.88090797141081     -1.87498926047587
  H   13.21804053927306     -0.25399697816375     -3.41917008755484
  H   9.63382692920540      0.16602760734464     -2.21584160068714
  H   10.31283918032262     -1.18901319115708     -3.16097902327140
  H   10.73367750611608      0.49759663176920     -3.56890546202477
  H   11.48979232997008     -0.98222461810973     -0.99547274211106
  H   12.47633304536522      4.67001095452476      0.34383732977405
  H   13.92127176135140      3.89112431625479     -1.51267413063089
  H   13.60868883711384      1.63892918022796     -2.47822866387626
  Cl  11.17365406711289     -2.72537687051249      2.98802850746895
  H   8.64414273398963     -3.86727612201980      3.57178133434008
  H   6.34490292572494     -3.19492484227963      2.87902667978922
  H   5.97638675910629     -1.25361403145443      1.44586457959411
  C   4.44851994214725      0.14361828154050      0.24178707361162
  H   4.42238297480910      0.17251176975730      1.34157271464414
  H   4.57496278870337     -0.90160682304548     -0.07769044204410
  H   11.50735123438516      -0.50335554053759      1.46464605266207
  C   3.78997346612104      2.89243909694354     -1.91227005485458
  C   5.21029589795270      2.84807889420852      0.06138753300652
```

```
N    3.84508593579501      3.01993676341292     -0.44689467778708
N    4.05763437779372      1.53268064137851     -2.40922706400652
C    5.45474371911999      1.14465669620804     -2.18815009890310
P    5.89346034900844      1.16538501838341     -0.37479370862325
C    2.92831024745514      2.03796185163052      0.14690566664812
C    3.13582279002822      0.59758860602783     -1.75198055782018
N    3.17494947455293      0.65443788146497     -0.28414121844119
H    1.90422867802184      2.30884230423905     -0.15060914337361
H    2.99929925398694      2.09197880197595      1.24282803364141
H    3.36629574868353     -0.42648736337980     -2.07881201009640
H    2.11281198766198      0.84351063476789     -2.07502877933073
H    5.21925990058046      2.96364190747215      1.15532221158847
H    5.88263608275070      3.60054870096674     -0.37349373654643
H    6.13365695024882      1.84049908065343     -2.70000656803836
H    5.62907318894064      0.13300962916514     -2.58381137954277
H    4.51257221181390      3.58780175850391     -2.36160078734835
Pd  -5.78806774667539      2.82357552028899     -2.81962331898503
H    0.34386960501086      1.83107084037014     -3.19749624384000
Cl  -5.01070280309157      2.18127431839775     -5.01697683465193
N   -7.82366024915661      2.89032323714933     -3.40067945348697
C   -6.61294689494713      3.40390096209594     -1.07053155269426
C   -6.02578837926667      3.68021630547587      0.16657221783869
C   -6.79168362632601      4.09111660068595      1.26634637393707
C   -8.17532136271545      4.24325800011142      1.17177059473232
C   -8.78449612320722      3.97352620529515     -0.04987313197350
C   -8.03458862417831      3.55767833539015     -1.16650112897243
C   -8.62015445986525      3.25619396154101     -2.44518511638302
C   -8.33317938278519      2.60217051385142     -4.69774432859549
C   -8.73888143373555      3.66396723055955     -5.53824611161967
C   -9.20764903332570      3.32936092634298     -6.81493350417476
C   -9.26786099905813      2.00189132061867     -7.24016979042377
C   -8.84728710942887      0.97592818550140     -6.39489197106360
C   -8.36369640826584      1.25488975962321     -5.11216916428288
C   -7.92931122418974      0.15360306811392     -4.16294410927493
C   -7.25134054987439     -1.02227003265012     -4.87009614505226
C   -9.11403314187470     -0.31994087697291     -3.30531912985927
C   -8.60036615191404      5.11488771174703     -5.10366293235883
C   -9.57444754554395      6.06426327769269     -5.80636540572879
C   -7.14741522255285      5.58533744204311     -5.29047967585540
H   -7.18036336678546      0.59706772249161     -3.48323159648940
H   -7.95116629588196     -1.57452567329219     -5.51535965952983
H   -6.86398507055101     -1.73028517024184     -4.12292380271729
H   -6.40972170240782     -0.67273212176284     -5.48456458160652
H   -9.56606690856927      0.51208164095308     -2.74689914173715
H   -8.78738406335304     -1.08135635257677     -2.58089404735557
H   -9.89674210497881     -0.76362916412010     -3.93995391636045
H   -9.50307805473114      7.06524828586876     -5.35719883526393
H  -10.61490067800161      5.71929819428205     -5.71329749580527
H   -9.34320877241494      6.16919744385963     -6.87689653472242
H   -6.44163017102679      4.94065428878155     -4.74620287006342
H   -7.02898289852156      6.61819453921814     -4.92945871413639
H   -6.87329038390360      5.55875743852278     -6.35610649454172
H   -8.82125101716541      5.17178439236061     -4.02625951908238
H   -8.89334011888586     -0.05816711750815     -6.73895320463842
H   -9.64257148601836      1.76704523742423     -8.23800091475474
H   -9.53135502159570      4.12099306258196     -7.49112465940272
Cl -10.52005068064030      4.16908538149561     -0.17018824692024
H   -8.76948635728518      4.56537282718275      2.02597511555835
H   -6.29781327881568      4.29752929835699      2.21813886633117
H   -4.95403510658207      3.58252876526541      0.30961268332597
C   -2.81269688720560      2.98993877358482     -0.57973294524797
H   -3.25946480642796      2.32100814616638      0.17038032219256
H   -2.99899176718678      4.03032002721589     -0.27486824783112
H   -9.70071752632884      3.31720978260880     -2.61565129174018
C   -0.74409073700682      1.97232801452492     -3.28445782841534
C   -2.85427258247493      1.00094792508592     -2.57251556556381
N   -1.40041797010720      1.01637638644708     -2.37705748045884
```

Appendix 3
Additional DNA binding study data

A3.1 UV-Vis spectroscopic data

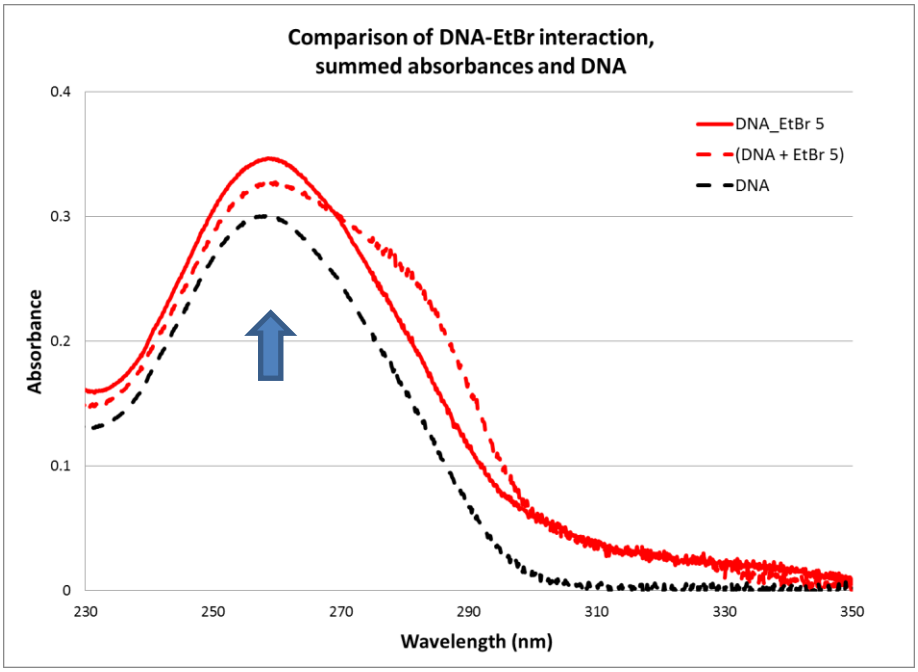

Figure A3.1: UV-Vis spectra of ethidium bromide interaction with DNA, the summed absorbances of ethidium bromide and DNA, and DNA.

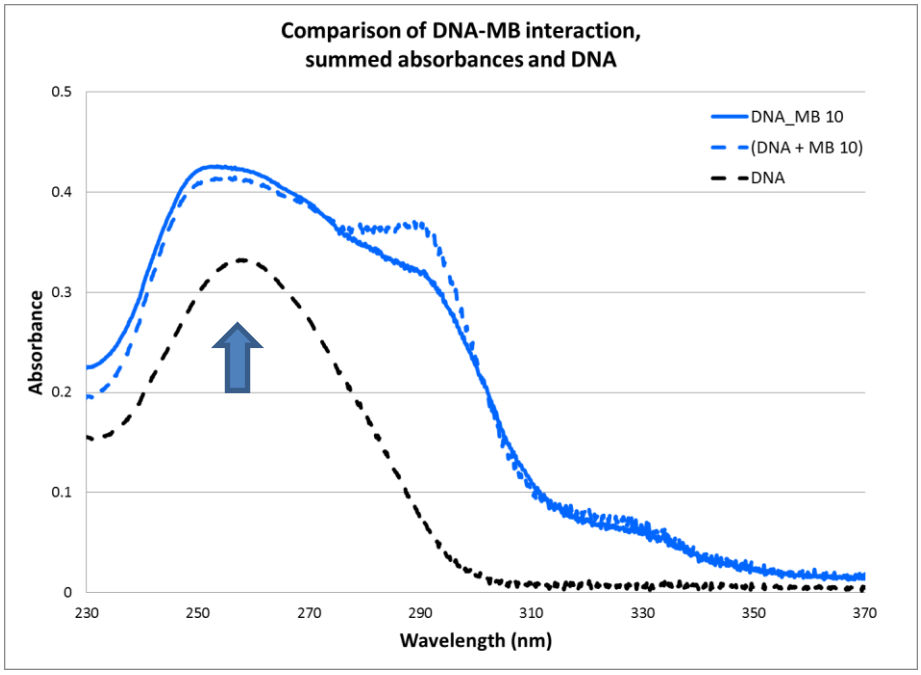

Figure A3.2: UV-Vis spectra of methylene blue interaction with DNA, the summed absorbances of methylene blue and DNA, and DNA.

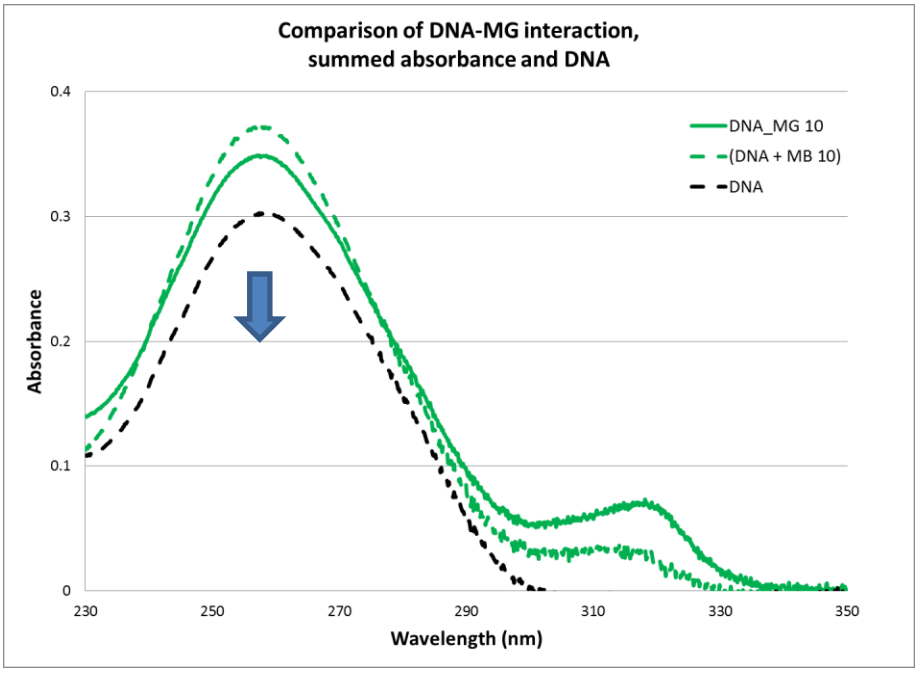

Figure A3.3: UV-Vis spectra of methyl green interaction with DNA, the summed absorbances of methyl green and DNA, and DNA.

A3.2 CD spectroscopic data

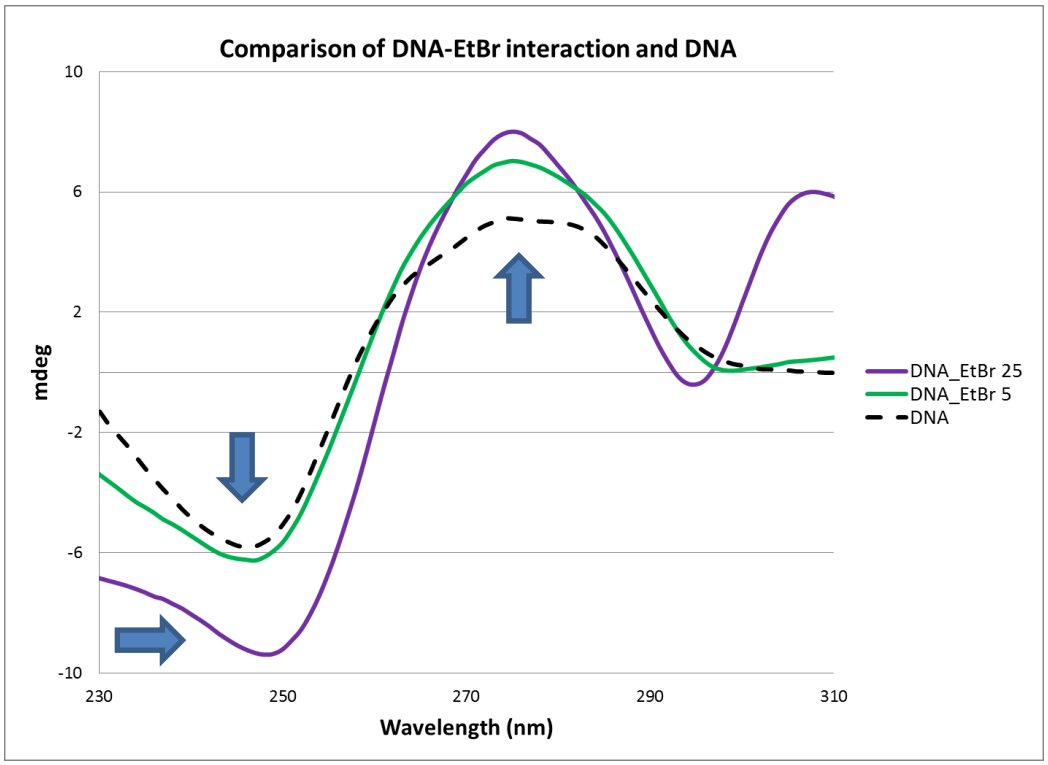

Figure A3.4: CD spectra of ethidium bromide interaction with DNA at various concentrations.

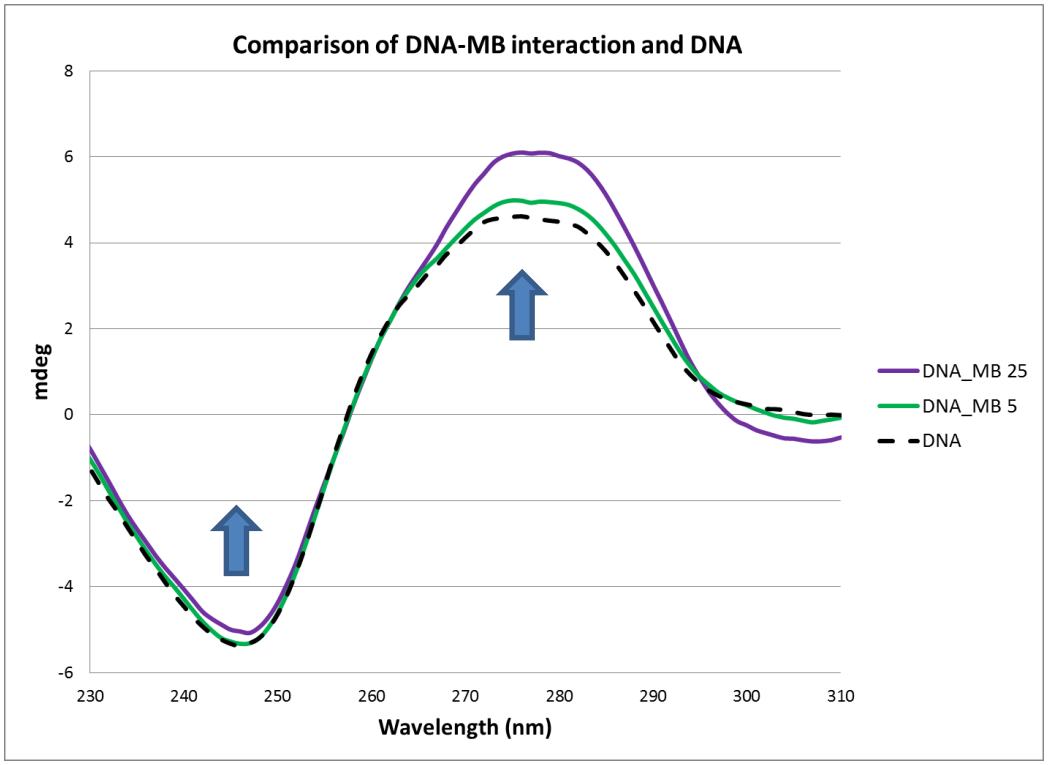

Figure A3.5: CD spectra of methylene blue interaction with DNA at various concentrations.

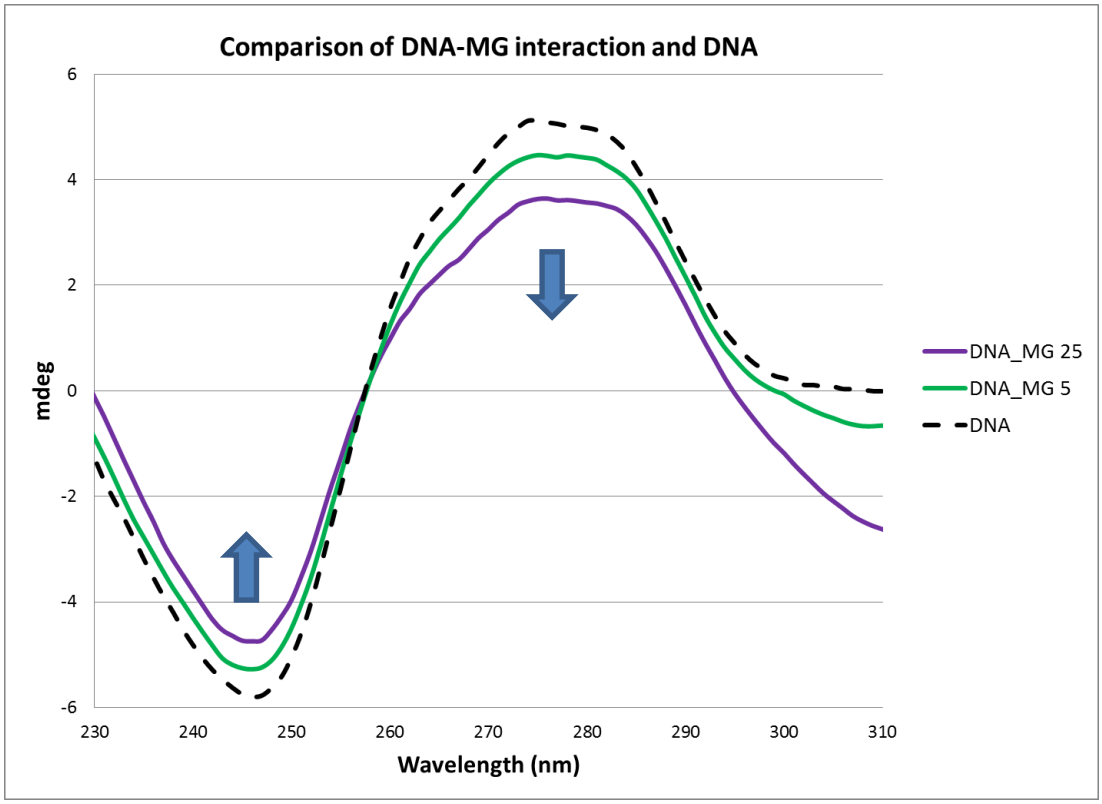

Figure A3.6: CD spectra of methyl green interaction with DNA at various concentrations.